Nanoengineering of organic light-emitting diodes

John Mark Lupton

November 2000

A thesis submitted to the faculty of science at the University of Durham for the degree of Doctor of Philosophy.

Abstract

This thesis reports nanoengineerging of the emission and transport properties of organic light-emitting diodes (LEDs). This is achieved by a control of the electronic material properties and the photonic device properties. A novel class of conjugated materials for electroluminescence (EL) applications is presented, based on successively branching, or dendritic, materials comprising an emissive core and a shielding dendritic architecture. Exciton localisation at the centre of these dendrimers is observed in both luminescence and absorption. A detailed quantum chemical investigation using an exciton model supports these findings and accurately describes the energies and oscillator strengths of transitions in the core and branches.

The dendrimer generation describes the degree of branching and gives a direct measure of the separation and interaction between chromophores. Increasing generation is found to lead to a reduction in red tail emission. This correlates with an increase in operating field and LED efficiency. Dendrimer blends with triplet harvesting dendritic phosphors are also investigated and found to exhibit unique emission properties. A numerical device model is presented, which is used to describe the temperature dependence of single layer polymer LEDs by fitting the field-dependent mobility and the barrier to hole injection. The device model is also used to obtain mobility values for the dendrimer materials, which are in excellent agreement with results obtained from time-of-flight measurements. The dendrimer generation is shown to provide a direct control of hopping mobility, which decreases by two orders of magnitude as the dendrimer generation increases from 0 to 3.

The photonic properties and spontaneous emission of an LED are modified by incorporating a periodic wavelength scale microstructure into the emitting film. This is found to double the amount of light emitted with no effect on the device current. An investigation of the angular dependence and the polarisation of the emission shows that the increase in efficiency is due to the scattering out of lossy waveguide modes in the organic film.

Declaration

The material in this thesis has not been submitted for examination for any other degree or part thereof at the University of Durham or any other institution. The material contained in this thesis is the work of the author except where formally acknowledged by reference.

Acknowledgements

I would like to thank my supervisor Prof. I. Samuel for providing an interesting research topic as well as a stimulating research environment. I am grateful to all my colleagues in Durham for many helpful and stimulating discussions as well as fruitful collaborations, in particular to Dr. Dongge Ma, Mr. B. Matterson, Dr. A. Monkman, Dr. L.O. Pålsson, Dr. A. Safonov, Miss A. Sheridan, Dr. G. Turnbull, and Mr. P. Wood. I would also like to thank all the technical and secretarial staff in Durham, in particular Mr. N. Thompson, Mr. D. Patterson, Mr. J. Scott and Ms. S. Fairless.

I am indebted to Dr. P. Burn and his group at the Dyson Perrins laboratory, Oxford, for providing many interesting materials to study as well as a healthy level of enthusiasm. I would especially like to thank Dr. R. Beavington, Mr. M. Frampton and Dr. L. Hemingway.

I also greatly appreciated the collaboration with Dr. W. Barnes of Exeter University and his encouragement and enthusiasm for my work. I am grateful to his colleagues Dr. M. Jory and Dr. M. Salt for providing gratings for me to study.

I am delighted to have had the opportunity to spend time with Prof. H. Bässler at Marburg University and would like to express my gratitude for his invitation as well as for many interesting discussions. I am grateful to the group in Marburg for enabling rapid integration and would particularly like to thank Mr. K. Book and Mr. C. Im for continued support during my stay as well as Dr. V. Nikitenko for ongoing collaboration.

The invitation by Prof. S. Mukamel to visit Rochester University was greatly appreciated as well as the keen interest he displayed in my work. I am most grateful for the many helpful discussions, which enabled me to rapidly generate some interesting results. I would also like to thank the other members of the group in Rochester, in particular Dr. M. Ottonelli, for setting me up on the CEO package.

Finally, I would also like to thank Opsys Ltd. for their interest in my work and for enabling a number of experiments to be carried out in Oxford. I am particularly grateful to Dr. O. Salata and Dr. E. Potterton.

I acknowledge financial support from the EPSRC, from Raychem Ltd. through a CASE studentship and from the German Academic Exchange Service through a Research Scholarship.

South of Hadrian's Wall:

Caelum crebris imbribus ac nebulis foedum; asperitas frigorum abest. [...] nox clara et extrema Britanniae parte brevis, ut finem atque initium lucis exiguo discrimine internoscas.[...] (solis) nec occidere et exsurgere, sed transire adfirmant. Scilicet extrema et plana terrarum humili umbra non erigunt tenebras, infraque caelum et sidera nox cadit.

C. Tacitus, Agricola, Opera Minora, ed. by: M. Winterbottom and R. M. Ogilvie, Clarendon Press (1975)

Tacitus writing on life in the North: "The climate is objectionable, with its frequent rains and mists, but there is no extreme cold. [...] The night is bright and, in the extreme North, short, with only a brief interval between evening and morning twilight. [...] (The sun) does not set and rise, but simply passes along the horizon. The reason for this must be that the ends of the earth, being flat, cast low shadows and cannot raise the darkness to any height."

Adapted from H. Mattingly, Tacitus on Britain and Germany, Penguin Classics (1951)

Table of Contents

1.

Introduction

Conducting polymers and electroactive organic materials have been at the centre of both theoretical and applied research for a number of decades. Much research effort has been focused on the development and the understanding of conducting plastics such as polyacetylenes and polyaniline [1-2]. However, the discovery of efficient electroluminescence (EL) in organic materials [3-7] sparked an explosion of interest [8-9] in this area of condensed matter physics previously only associated with high temperature superconductors. With the discovery of electrically driven lasing [10] and the observation of superconductivity [11] and the fractional quantum Hall effect [12] in organic materials, organic electronics must be taken as a serious extension if not an entirely new branch of semiconductor physics. Indeed, it has even been shown that organic semiconductors are ubiquitous in nature [13] in the form of the reaction centre of a photosynthetic light-harvesting complex, which suggests that there still remains much to be explored in this exciting field.

One reason why organic semiconductors have attracted so much attention over the past years, in particular with regards to display applications, is their relative ease in processing with respect to conventional inorganic semiconductors. In particular in view of large area display, lighting or signalling applications, the potential to cover large, even flexible, surfaces with soluble polymers or organic molecules has attracted wide ranged interest. The success of readily processable conducting polymers in applications such as electrostatic shielding or as antifouling agents, culminating in the award of the Nobel Prize in chemistry, has been seen as an indication of the potential behind semiconducting organics.

Low-dimensional electronic and photonic structures are of considerable interest as they enable new areas of physics inaccessible with bulk materials to be explored and allow a wide range of novel applications previously inconceivable [14]. Polymers and organic molecules naturally fall into the category of low dimensional materials due to their inherent anisotropy and the preferential delocalisation of π-electrons along the polymer backbone. In addition, it has also been demonstrated that organic semiconductors can readily be formed to take physical structures of dimensions of the wavelength of light, which is a significant result [15]. Since the proposition of photonic band gaps [16] there has been considerable interest in creating periodic wavelength scale structures to control the interaction of photons with matter [17-18]. The organic materials used in LEDs may

hence be seen as suitable candidates for performing nanoscale engineering both of the electronic properties as well as the photonic and optical properties.

In addition to the prospect of creating physically unique devices out of wavelength scale processable molecular semiconductors, a whole new range of device and material physics has become accessible. There are a number of differences in principle between inorganic and organic semiconducting materials, which are primarily related to the nature of bonding in the solids. Most inorganic semiconductor crystals are held together by strong covalent bonds. The intrinsic population of free carriers is hence low and carriers have to be added by doping impurities. Organic semiconductors on the other hand are held together by weak van-der-Waals bonds in the bulk, whereas covalent bonds give rise to the intramolecular bonding. The electronic density of states in organic semiconductors is hence highly anisotropic and may, to a first approximation, be treated as being one-dimensional. Charge carriers hence experience very different interactions with the lattice and are generally much more strongly coupled to lattice deformations. In addition, the nature of the π-bonds, giving rise to the free charge carriers, results in strong electronic couplings. A consequence of this and of the large anisotropy is an abnormally strong exciton binding energy, which can be orders of magnitude greater than in inorganic materials. Due to the large splitting between singlet and triplet levels, singlet and triplet excitons are not freely interchangeable in these materials through interactions with the lattice. An important demonstration of this is the harvesting of triplet excitations out of a light-emitting diode (LED) by using a phosphorescent dopant [19]. This was shown to substantially increase the device efficiency.

Significant improvements to the operation efficiency, brightness and lifetime of organic LEDs have been made thus far by the development of new materials and cleaner synthetic routes. The comparatitive investigation of different materials has led to an improved understanding of the photophysical and electronic material properties responsible for EL. An important new class of macromolecular materials, bridging the gap between polymeric and molecular compounds, are dendrimers, which possess a fractal rather than a linear geometry. Although dendrimers have been studied extensively as novel nanoscopic molecules [20] with molecular weights achievable which are greater than those of any naturally occurring macromolecular arrangement, it was not until recently that EL was demonstrated in these compounds [21-22].

Three current key issues may be identified in the field of organic EL. Firstly, and most importantly, there is still no sound understanding of the correlation between chemical structure and material properties. It has been shown that the degree of interaction between conjugated units leads to a strong modification of the emission spectrum in the solid state and also to luminescence quenching [23]. This effect is known to be strongly dependent on the material. Also, the charge transport properties are known to vary widely between seemingly related materials [24]. An understanding of the origin of these material dependent properties is imperative for the design of new and improved materials.

Secondly, the nature of excitations generated in organic materials is still not fully understood. Exciton theory is used to account for most effects observed, but there are few accurate theories predicting material properties based on exciton models. Also, triplet excitons form a significant contribution to the excitations present in LEDs [25]. Although methods have been proposed as to how to generate useful luminescence from these excitations [19], there is no full understanding of the exact processes of energy transfer due to a poor knowledge of the triplet levels in organics. It is hence of interest to investigate both the electronic nature of excitations in organic materials as well as the dynamics of triplet excitations.

Thirdly, organic LEDs are intrinsically extremely small structures with layer thicknesses significantly smaller than the wavelength of light. Due to the large difference in refractive indices of the materials comprising the LED, strong waveguiding effects occur which can give rise to a substantial loss in overall efficiency [26]. Although recent devices have yielded efficiencies far above those previously thought possible under the limits imposed by waveguide losses and triplet formation [27], there is still a significant energy loss within the LED.

This thesis aims to give new insight into the three main issues addressed above. Firstly, the nature of charge transport in organic LEDs and the relationship between chemical structure and macroscopic device properties. This is illuminated by the use of a novel class of electroluminescent materials, conjugated dendrimers. Secondly, the nature of electronic excitations in dendrimers is investigated using spectroscopic as well as quantum chemical techniques. The energy transfer in organic LEDs is explored further

and a dendrimer-based system designed to harvest triplet excitations in LEDs is presented. Finally, a wavelength scale modulation of the optically and electrically active layer of the LED is presented, which is a novel and effective approach to directly control the spontaneous emission from an LED.

The basic physics of devices is reviewed in chapter 2, after which the experimental techniques used are described in chapter 3. In chapter 4 a novel class of conjugated dendrimers are presented, which allow a direct control of the intermolecular interactions and the charge carrier mobility through the degree of dendrimer branching and chromophore separation. Exciton localisation is observed, which can account for the generation dependent features found in the charge transport and the emission. A coupled electronic oscillator model is applied to further investigate the system, and is found to yield a direct confirmation of exciton localisation in conjugated dendrimers.

In chapter 5 a detailed temperature dependent device model is presented, which can account for the observed features of a single layer MEH-PPV LED. Arrhenius type activation is observed for the mobility parameters derived from the device model, and the barrier to charge carrier injection is found to decrease with temperature in a similar manner to the band gap of the polymer.

In chapter 6, this model is used to further investigate the charge transport properties of the dendrimers presented in chapter 4. The majority carrier mobility in films of the dendrimer is measured using the time-of-flight technique and compared to values obtained using the device model. The increase in chromophore spacing regulated by the dendrimer generation is found to lead to a decrease in charge carrier mobility by 2 orders of magnitude. The scaling with the dendrimer hydrodynamic radius is in agreement with small polaron hopping theory.

A novel electrophosphorescent device is presented in chapter 7, which relies on a dendrimer architecture for both the fluorescent host molecule as well as the phosphorescent guest molecule. The emission properties of the device are investigated as a function of the driving pulse period. Whereas the steady state emission properties can be attributed to preferential charge trapping on the phosphorescent dopant, the

dependence on pulse period arises from interactions between long-lived triplet excitations.

Finally, chapter 8 addresses a novel device structure consisting of an LED fabricated on a Bragg grating. The optical as well as the electrical properties of this device are discussed. The Bragg grating structure is found to lead to a doubling of efficiency with respect to planar devices.

References

[1] E. M. Conwell, in : H. S. Nalwa (Ed.), Handbook of Organic Conductive Molecules and Polymers: Vol 4. Conductive Polymers: Transport, Photophysics and Applications, Wiley (1997)

[2] An introduction to molecular electronics, ed. by: M. C. Petty, M. R. Bryce and D. Bloor, Edward Arnold (1995)

[3] W. Helfrich, W. G. Schneider, Phys. Rev. Lett. 14, 229 (1965)

[4] M. Pope, H. P. Kallmann, and P. Magnante, J. Chem. Phys. **38**, 2042 (1962)

[5] R. H. Partridge, Polymer **24**, 755 (1983)

[6] C. W. Tang and S. A. Vanslyke, Appl. Phys. Lett. **51,** 913 (1987)

[7] J. H. Burroughes, D. D. C. Bradley, A. R. Brown, R. N. Marks, K. Mackay, R. H. Friend, P. L. Burn, and A. B. Holmes, Nature **347,** 539 (1990)

[8] R. H. Friend, R. W. Gymer, A. B. Holmes, J. H. Burroughes, R. N. Marks, C. Taliani, D. D. C. Bradley, D. A. DosSantos, J. L. Bredas, M. Logdlund, and W. R. Salaneck, Nature **397,** 121 (1999)

[9] D. Kalinowski, J. Phys. D **32,** 179 (1999)

[10] J. H. Schon, C. Kloc, A. Dodabalapur, and B. Batlogg, Science **289**, 5999 (2000)

[11] J. H. Schon, C. Kloc, B. Batlogg, Nature **403**, 324 (2000)

[12] J. H. Schon, C. Kloc, B. Batlogg, Science **288**, 2338 (2000)

[13] P. B. Lukins, Chem. Phys. Lett. **321,** 13 (2000)

[14] C. Weisbuch, H. Benisty, and R. Houdré, J. Lum. **85**, 271 (2000)

[15] M. Berggren, A. Dodabalapur, R. E. Slucher, A. Timko, and O. Nalamasu, Appl. Phys. Lett. **72**, 26 (1998)

[16] E. Yablonovitch, Phys. Rev. Lett. **58,** 2059 (1987)

[17] E. Yablonovitch and T. J. Gmitter, Phys. Rev. Lett. **63,** 1950 (1989)

[18] M. Boroditsky, T. F. Krauss, R. Coccioli, R. Vrijen, R. Bhat, and E. Yablonovitch, Appl. Phys. Lett. **75,** 1036 (1999)

[19] M. A. Baldo, D. F. Obrien, Y. You, A. Shoustikov, S. Sibley, M. E. Thompson, and S. R. Forrest, Nature **395,** 151 (1998)

[20] D. A. Tomalia, Adv. Mater. **6**, 529 (1994)

[21] P. W. Wang, Y. J. Liu, C. Devadoss, P. Bharathi, and J. S. Moore, Adv. Mater. **8**, 237 (1996)

[22] M. Halim, J. N. G. Pillow, I. D. W. Samuel, and P. L. Burn. Adv. Mater. 11. 371 (1999)

[23] I. D. W. Samuel, G. Rumbles. and R. H. Friend, in : N. S. Sariciftci (Ed.). Primary Photoexcitations in Conjugated Polymers: Molecular Exciton versus Semiconductor Band Model, World Scientific (1997)

[24] Z. G. Yu, D. L. Smith, A. Saxena, R. L. Martin. and A. R. Bishop, Phys. Rev. Lett. **84**, 721 (2000)

[25] Z. Shuai, D. Beljonne, R. J. Silbey. and J. L. Bredas, Phys. Rev. Lett. **84,** 131 (2000)

[26] N. C. Greenham, R. H. Friend, and D. D. C. Bradley. Adv. Mater. **6,** 491 (1994)

[27] J. S. Kim, P. K. H. Ho. N. C. Greenham, and R. H. Friend, J. Appl. Phys. **88**, 1073 (2000)

2.

Physical principles of light-emitting diodes

2.1 Introduction

In this chapter the most important physical aspects relevant to organic electroluminescence are reviewed, which are later drawn on in the analysis of the results. It begins by summarising the photophysics of conjugated materials and the electronic processes giving rise to absorption and emission. The specific case of intermolecular interactions and excimer formation, which leads to a modification of the electronic material properties, is addressed. The dendrimer concept is presented, which allows a unique control of the level of interaction between adjacent chromophores through the control of the molecular size. Turning to organic LEDs, the device operation is discussed in detail and a temperature dependent model for device operation is presented. Finally, optical waveguiding effects in LEDs are discussed and a method of reducing the loss due to reabsorption by incorporating a Bragg-grating-like structure into the device is presented.

2.2 Photophysics of conjugated materials

Conjugated materials are a particularly interesting class of organic compounds, which exhibit a wide variety of material properties. The term conjugation describes the bonding and a simple example is the case of ethene, shown in Fig. 2.1.

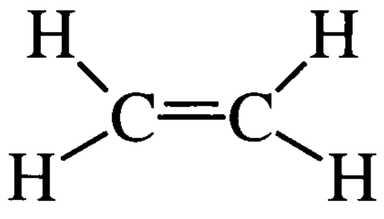

Fig. 2.1. *Chemical structure of ethene.*

The orbitals of the two carbon atoms forming the ethene compound with the double bond are shown in Fig. 2.2. There are four electrons on the outer shell of the carbon atom, which is in the $1s^2 2s^2 2p^2$ ground state configuration. In this case the outer most two p electron orbitals are unpaired and can mix with the 2s orbitals to give three equivalently hybridised orbitals in the configuration sp^2. These three orbitals lie in a plane at angles of 120° to each other. The two carbon atoms in the ethene molecule are

bonded together through the σ-orbitals by bonds known as σ-bonds. The remaining p orbital, which is described as a p_z orbital, remains unhybridised and is normal to the plane of the σ-bonds. However, due to the close proximity of the two carbon atoms the two p_z orbitals can also interact forming a further bond, known as a π-bond. It is these π-bonds which provide loosely bound electrons which are free to move along the backbone of the polymer and give rise to a host of optical and electrical material properties.

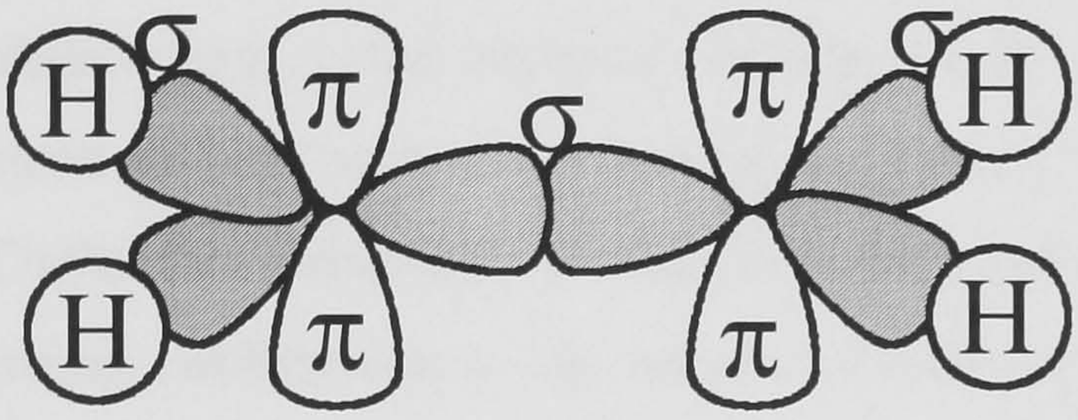

Fig. 2.2. *Electronic orbitals of ethylene.*

Small conjugated molecules provide a close analogy for the electronic structure of oligomers and polymers, as seen in Fig. 2.3. The overlap of π-orbitals also occurs in polymers, leading to electron delocalisation along the polymer backbone. However, it turns out energetically preferable to have alternating single and double bonds rather than providing a π-bond across the whole of the molecule. This phenomenon, which is known as the Peierls' distortion, gives rise to slightly varying single and double bond lengths and the opening up of a band gap in the material. The length over which electronic delocalisation occurs in a polymer chain is referred to as the conjugation length. It is limited by twists and other defects on the polymer backbone as well as by impurities such as carbonyl groups [1, 2]. It is much smaller than the molecular chain length, which can have lengths of tens of thousands of repeat units.

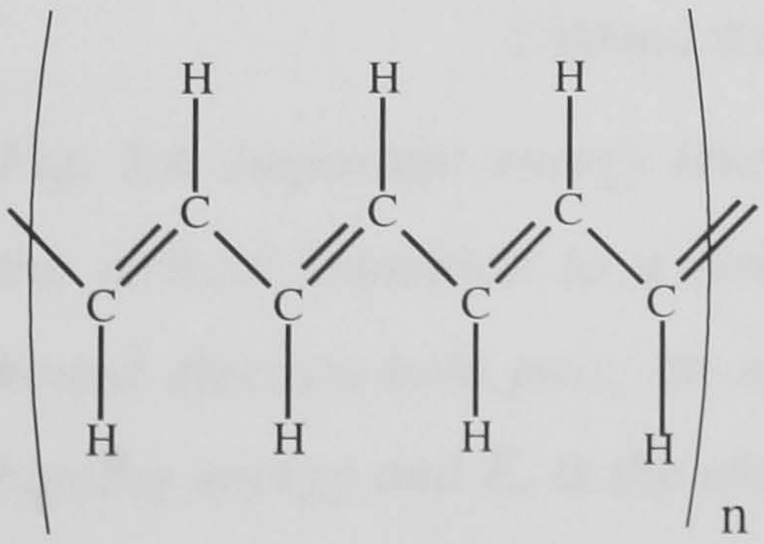

Fig. 2.3. *Structure of polyacetylene.*

The electronic structure of conjugated polymers has often been likened to that of inorganic semiconductors with delocalised states forming conduction and valence bands [3]. However, it has been realised that band theory can only provide a limited description of the optical and electronic properties of a small range of conjugated polymers. The Su-Schrieffer-Heeger model [3] has been used to successfully describe the band-gap of degenerate ground state polymers such as polyacetylene and predict the formation of exotic excitations such as solitons. However, these band based theories neglect electron-electron interactions, which are generally very strong in conjugated systems. A contrasting picture, which has provided explanations of many experimental observations, is the molecular exciton model. Rather than forming free or weakly bound electron-hole pairs upon optical excitation, electrons and holes experience a mutual Coulombic attraction resulting in a characteristic exciton binding energy. Furthermore, strong confinement to the polymer structure as well as mixing of the excited state with the continuum may lead to strong exciton binding [4]. This reduces the energy of single photon excitations with respect to the electron-hole band gap. The significant energy levels in an excitonic material are shown in Fig. 2.4.

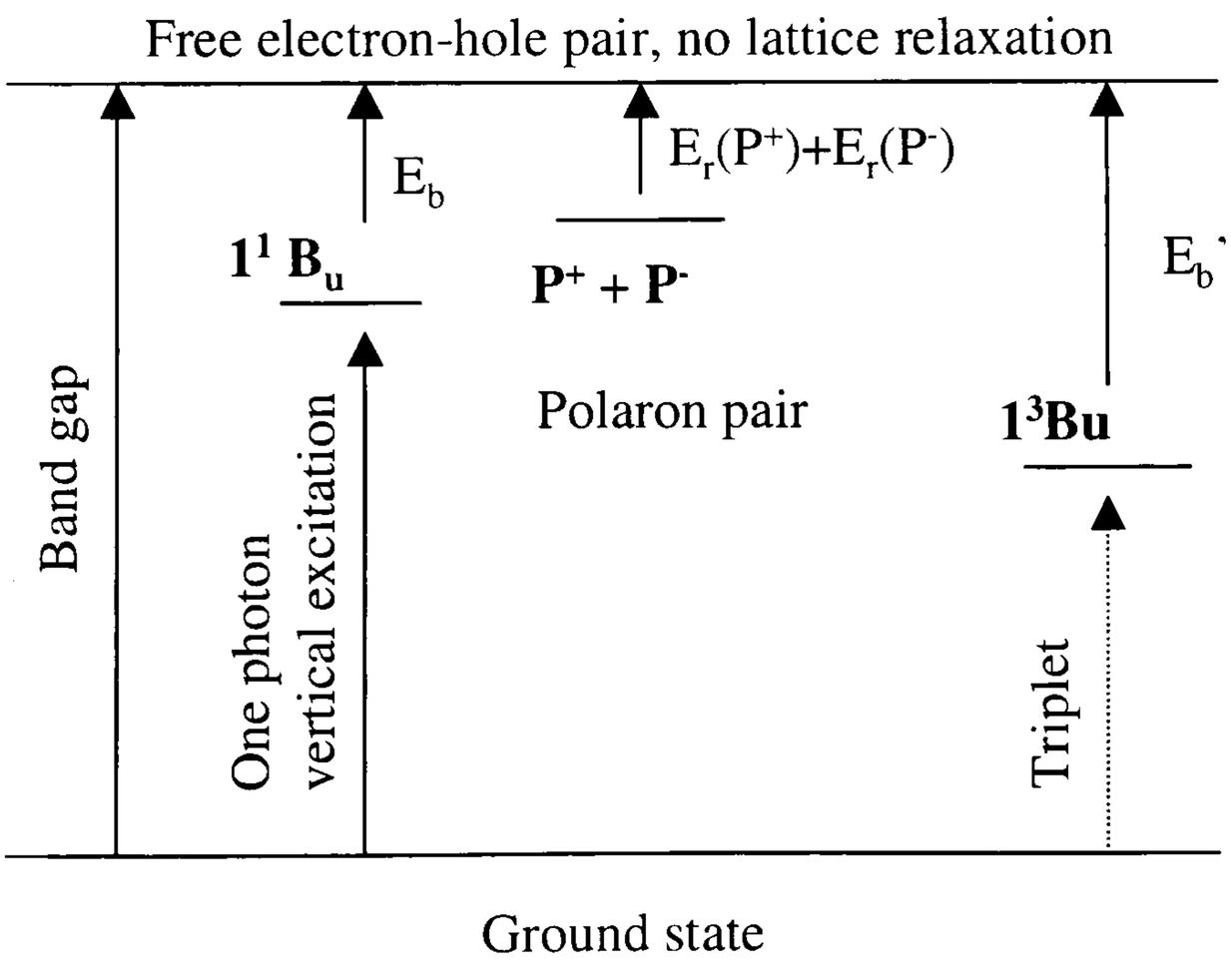

Fig. 2.4. *Important energy levels in conjugated polymers. The band gap is defined as the vertical transition to a free electron-hole pair. A one photon excitation forms a bound electron-hole pair, an exciton of binding energy E_b. E_b' is the triplet exciton binding energy and E_r is the energy required to form a radical (also known as polaron binding energy) [5].*

As a change in the charge distribution generated on the backbone of a polymer results in a molecular distortion, charge carriers exist in the form of polarons or radical cations or anions. Under electrical excitation, bound carrier pairs are hence pairs of positive and negative polarons. In PPV derivatives the EL spectra generally closely follow the fluorescence spectra, which leads to the conclusion that the joint electron-hole polaron binding energy is smaller than the exciton binding energy and electrically generated excitations hence relax to the 1^1Bu state before emitting [5]. Excitonic effects become apparent in a number of spectroscopic measurements, such as photocurrent, electroabsorption and site selective fluorescence [4, 5]. However, depending on the degree of the extent of the exciton, excitonically bound electron-hole pairs may be expected to yield hydrogenic excitation spectra, which are observed in weakly bound excitons in silicon, germanium and some metal oxides, but not in conjugated materials [5].

In polymers, the emission spectra are generally broadened for two reasons, which makes an identification of excitons on the basis of their energetic spectrum complicated. Firstly, electronic correlations are generally very strong in conjugated materials. Even a small change in charge distribution can lead to molecular distortion which gives rise to an exceptionally strong electron-phonon coupling, typically in the order of 0.2 eV. The dominant modes of this coupling are carbon-carbon stretch modes, which are visible in many spectra. Electronic correlations also exist between carriers on polymer chains, which arise in part from the strong anisotropy inherent to the quasi one-dimensional density of states of these materials. Secondly, polymeric materials are inherently disordered, which gives rise to a distribution of energy levels, typically approximated by a Gaussian. Disorder may be manifest both spatially as well as energetically. Whereas a spatial distribution in the transport sites has a strong effect on charge transport, a distribution in effective conjugation lengths will result in a distribution around the band edges which will be manifest in spectroscopic observables.

The simplest means of investigating the electronic characteristics of a conjugated material is by determining the absorption and emission properties. A common way of representing electronic transitions is in configuration co-ordinate diagrams through plots of the molecular potential energy versus molecular co-ordinate. This is shown in Fig. 2.5. The ground state wavefunction is shown in the sketch as well as the wavefunctions

of the lowest vibronic (zero phonon) level of the first excited state and the fourth level of the first excited state (ν=3), which has 3 nodes. Excitations occur from the lowest (ν=0) vibrational level of the ground state, with the transition amplitude depending on the conformation of the molecule. The conformation with the strongest transition amplitude is at the equilibrium nuclear co-ordinate position R_e. The shift of the equilibrium position between the excited and the ground state represents a configurational co-ordinate displacement of the upper state relative to the ground state, which is related to the electron-phonon coupling. Transitions occur according to the Franck-Condon principle, which states that electronic transitions take place on a much shorter time scale than nuclear rearrangements. Transitions are hence drawn as vertical lines.

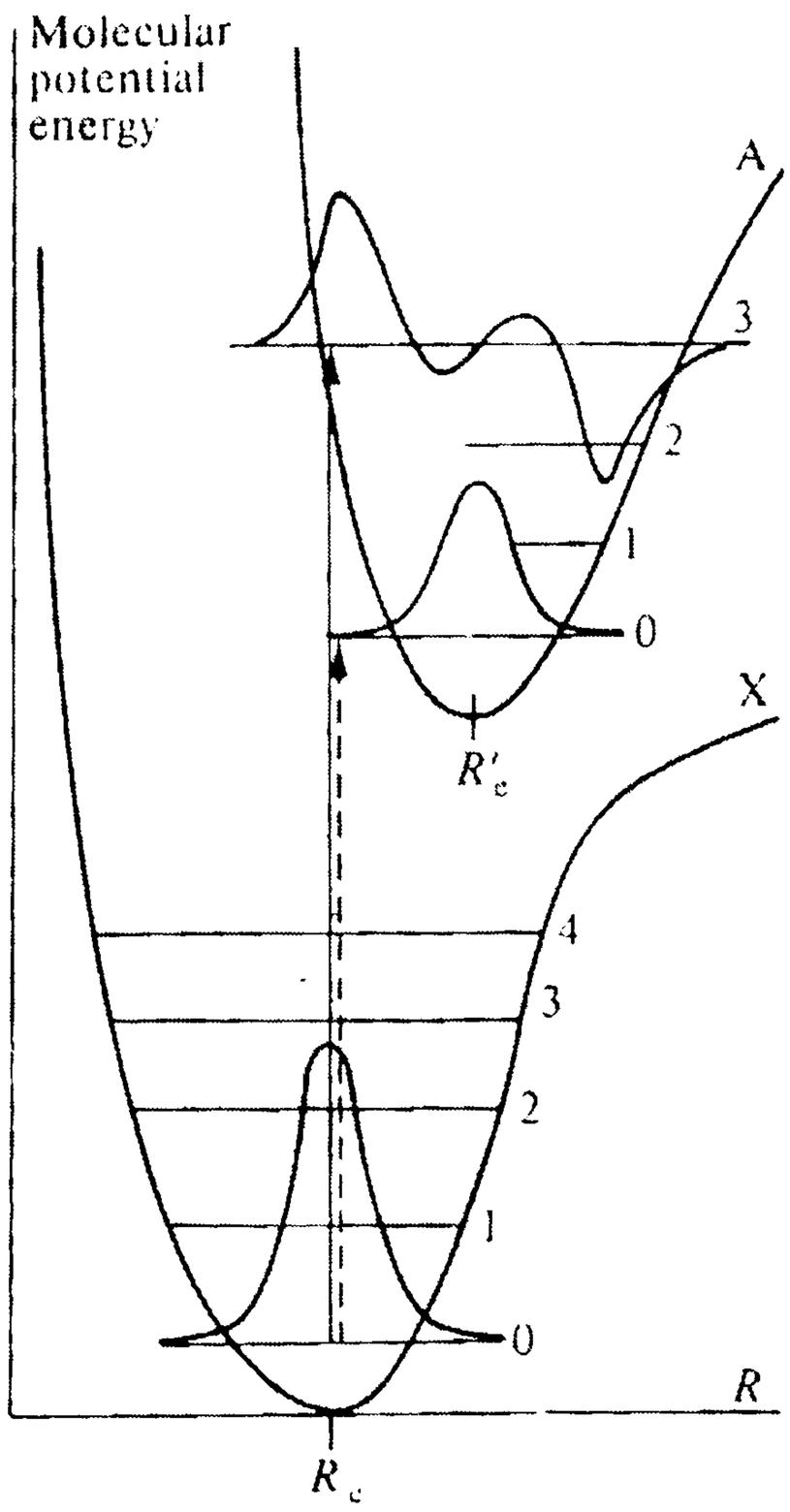

Fig. 2.5. *Configuration co-ordinate representation of optical absorption in organic molecules [6].*

Luminescence occurs following a similar principle and is described schematically in Fig. 2.6. In the simplest case, the luminescence spectrum is a mirror image of the

absorption spectrum with a certain red shift, corresponding to the Stokes' shift. Absorption occurs from the populated $\nu''=0$ level of the S_0 electronic ground state to the various vibrational levels of excited state S_1. The excited state can then undergo radiationless vibrational relaxation, leading to population of the $\nu'=0$ level of the excited state. Radiative transitions can then occur from this level to the manifold of vibrational levels of the ground state. Relaxation may also occur through non-radiative decay routes, such as through lattice interactions, which give rise to luminescence quantum yields significantly below unity in the solid state. In theory, the relative strengths of the specific transitions in absorption and luminescence are similar and the emission and absorption spectra should hence have similar shapes. However, due to the vibrational relaxation shown in the diagram, the emission spectrum appears as a mirror image of the absorption spectrum. The zero phonon transitions do not completely overlap due to the effect of the Stokes' shift between luminescence and absorption.

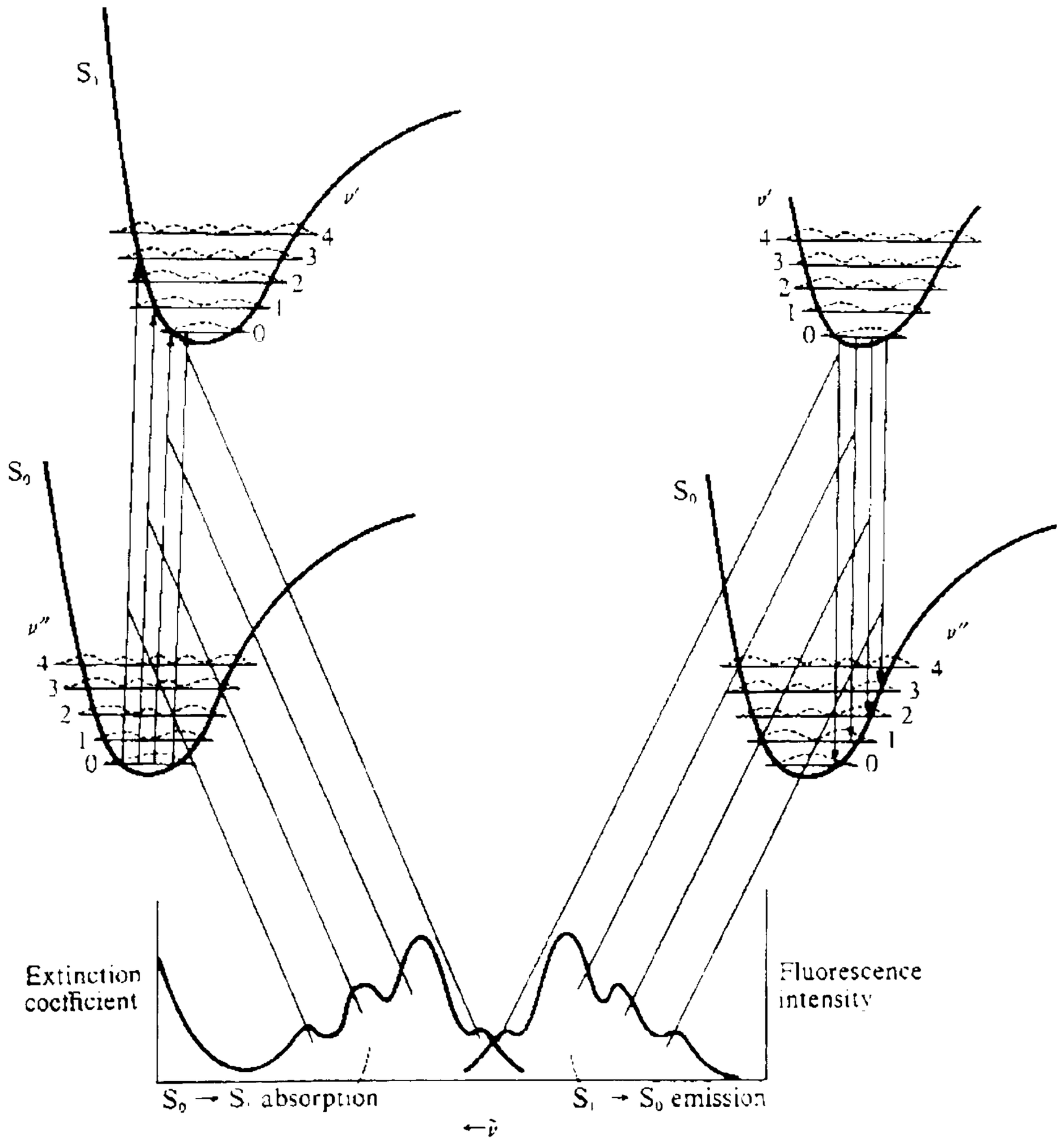

Fig. 2.6. *Configuration co-ordinate representation of absorption and emission [4].*

In many conjugated materials, deviations from the simple mirror image relationship are observed. According to the Franck-Condon principle, any nuclear rearrangement occurs after electronic transitions. However, the excited state lifetimes in many conjugated molecules are in the order of 1 ns, which provides ample time for a nuclear rearrangement of the molecule and a dramatic alteration of the excited state potential energy surface. An example of this is free-base porphyrin, where a narrow absorption band is found at 420 nm, yet emission occurs in the red in the region of 650 nm. Such a large shift between absorption and luminescence is much greater than any possible effect through phonon scattering (the Stokes' shift) but can be attributed to a conformational change of the molecule upon excitation. In addition, in polymers exciton migration may give a contribution to both the red-shift of emission with respect to the absorption as well as an asymmetry between luminescence and absorption. Due to the weakly interacting nature of excitons, they generally act as rather mobile quasi-particles and can move relatively freely along the polymer backbone. Given the comparatively long lifetime of excitations, excitons may migrate to lower energy sites in the material and accumulate there. The emission spectra, such as in PPV, hence appear narrower than the absorption, which probes the entire molecular conformation, and are also shifted to the red. As mentioned above, electronic couplings and disorder effects may lead to strong broadening which also reduces the resolution of the vibrational peaks in the emission and absorption spectra.

Depending on the spins of the excited electron and the vacant hole, excitations may exist as triplets or as singlets as described in (2.1). The singlet state is defined as having an antisymmetric spin wavefunction, whereas the triplet spin wavefunction is symmetric. There are hence three combinations of spins forming a triplet and only one possible superposition giving rise to the singlet.

$$\begin{aligned} \text{singlet} &= \frac{1}{\sqrt{2}}\left[(\uparrow\downarrow)-(\downarrow\uparrow)\right] \\ \text{triplet} &= (\uparrow\uparrow) \\ &= \frac{1}{\sqrt{2}}\left[(\uparrow\downarrow)+(\downarrow\uparrow)\right] \\ &= (\downarrow\downarrow) \end{aligned} \tag{2.1}$$

Only singlet excitations are dipole coupled to the ground state and can decay radiatively. However, both singlet and triplet levels exist in organic materials. The difference between singlet and triplet levels is highlighted in Fig. 2.7. Upon photoexcitation, charge carriers are raised into the singlet excited state level, from which they can decay radiatively. In some materials, in particular in the presence of heavy metal atoms, which allow strong spin-orbit coupling, intersystem crossing can occur between the singlet and the triplet state, as shown in the right hand side of the figure. The emission from the triplet state occurs through phosphorescence, which is much slower than straight fluorescence due to the selection rules prohibiting this transition. In general, phosphorescence in polymers is extremely inefficient and has only recently been observed [7]. The long lifetime, which can be in the range of milliseconds to seconds, facilitates quenching of the excitation through impurities, defects and bimolecular processes between the mobile excitations.

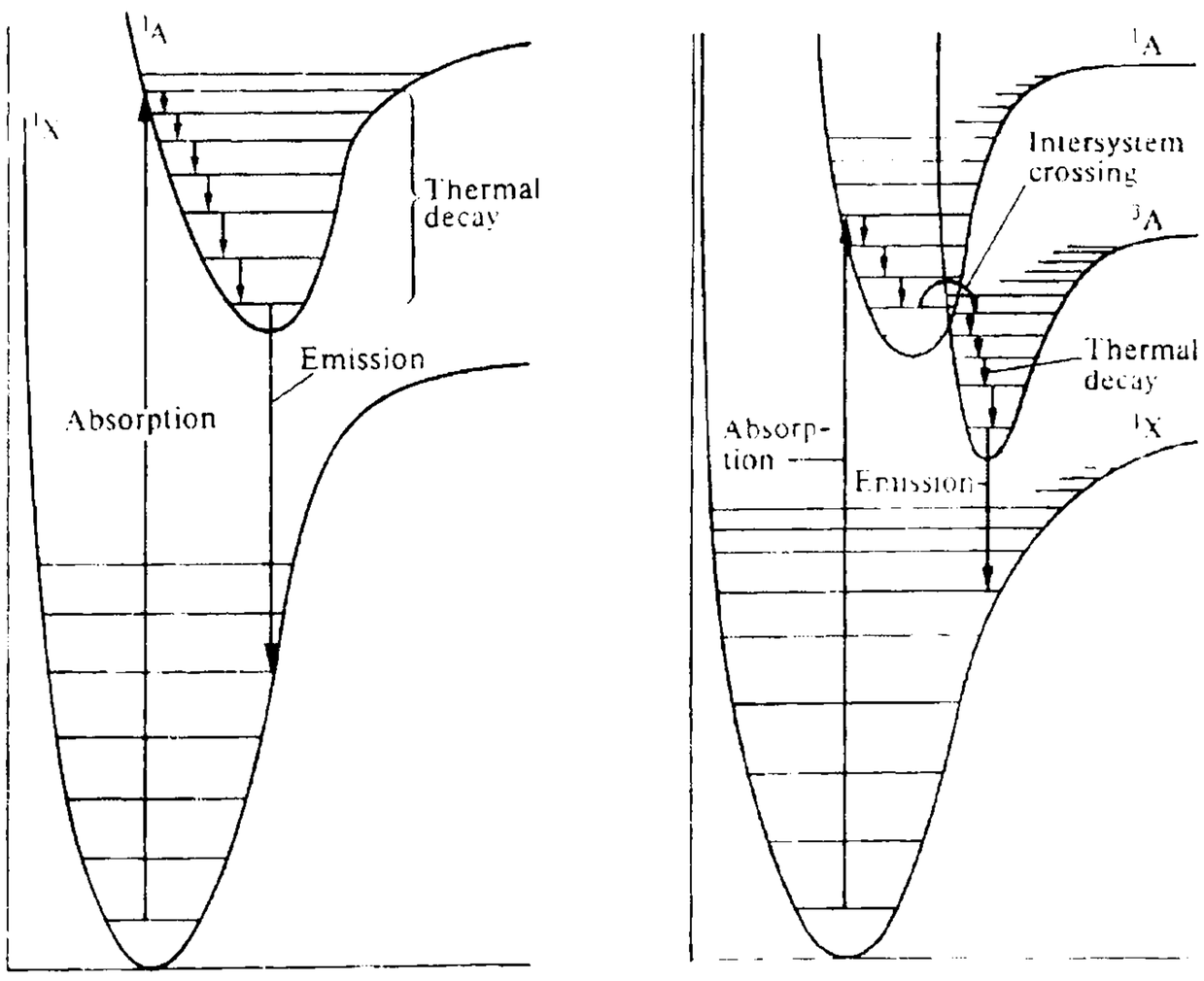

Fig. 2.7. *Fluorescence (left) and intersystem crossing leading to phosphorescence (right) [4].*

The basic photophysical processes discussed above are highly relevant to the operation of LEDs. Singlet excitons may be generated either through optical absorption of a photon or through injection of positive polarons and negative polarons at the anode and cathode of the device, respectively. This is shown schematically in Fig. 2.8. Positive and negative polarons meet up and combine to form an exciton, which can then decay

radiatively. However, injected polarons may be equally likely of either spin, so that under electrical injection of charge carriers, due to the spin statistics in (2.1), only 25 % of the excitations generated are singlets. Although this number is currently subject to heated debate [8-10] and more recent measurements suggest almost equal formation of singlets and triplets, triplet excitations nevertheless play a significant role in the operation of LEDs. Due to the presence of charge carriers in conjugated polymer LEDs, however, all triplet excitations decay non-radiatively and the phosphorescence is quenched. Through a suitable choice of phosphorescent dopant with significantly shorter lifetimes, the triplet excitations may be harvested from the device and turned into useful radiation, as was demonstrated by the Princeton group [11].

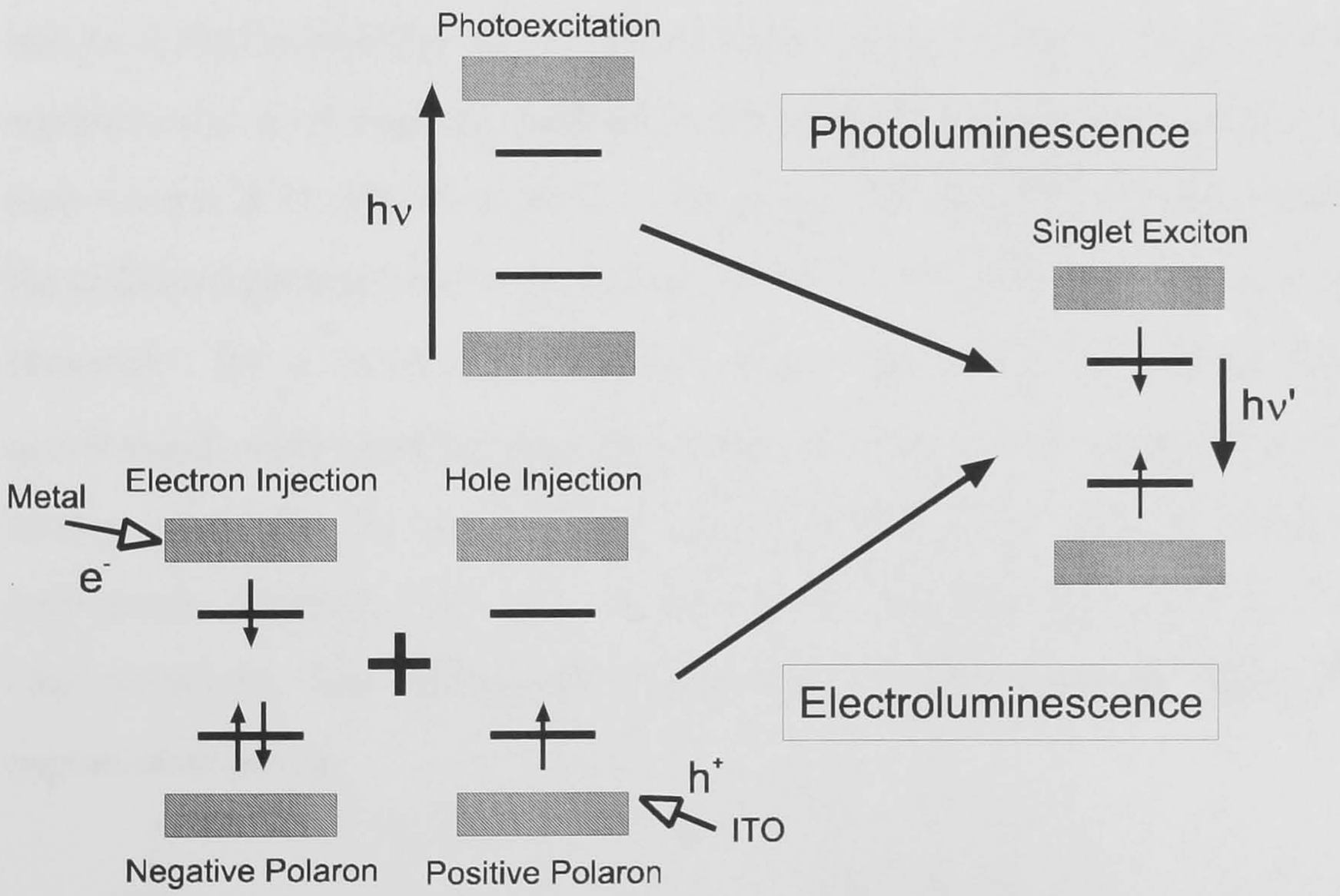

Fig. 2.8. *Basic processes leading to luminescence in conjugated materials [12].*

A problem commonly associated with excitons is the bimolecular interaction between like excited state species which can lead to quenching of the excited state and hence of the luminescence [4]. These bimolecular reaction processes are well known from the study of chemical reactions [13]. Neutral excitations are known to interact with one another. This has been studied intensively in the context of photosynthetic systems [14-16]. Bimolecular interactions can lead to quenching of excitations which reduces the luminescence yield. This has been demonstrated, for example, in the context of polymer lasers, where the linear relationship between the pump and the emission intensity breaks down above a certain pump intensity [17]. The critical parameters in bimolecular

annihilation processes are the concentration, interaction rate and excited state lifetime. For triplet excitations, the lifetime is much increased, so effects due to bimolecular annihilation are expected to be enhanced.

Bimolecular decay can be described through the bimolecular rate equation [15] given in (2.2).

$$\frac{dn}{dt} = -\gamma_1 n - \frac{1}{2}\gamma_2 n^2 \qquad (2.2)$$

Here, n is the concentration of excitons, γ_1 is the excited state decay rate of the system and γ_2 is the interaction rate or bimolecular decay constant. The non-linear differential equation can be solved through standard numerical techniques such as Euler's method (see section 2.5). The solutions for the decay of the excited state population with time for different parameters are shown in Fig. 2.9. For γ_2=0, the decay is single exponential. However, for a strong bimolecular decay rate γ_2=1, the initial decay is strongly accelerated, corresponding to a quenching of excitations through mutual interactions. At longer times the decay becomes single exponential. This is because the level of interaction depends on the concentration of excitons and is reduced at low concentrations. The intermediate case shows a more gradual approach to the single exponential decay.

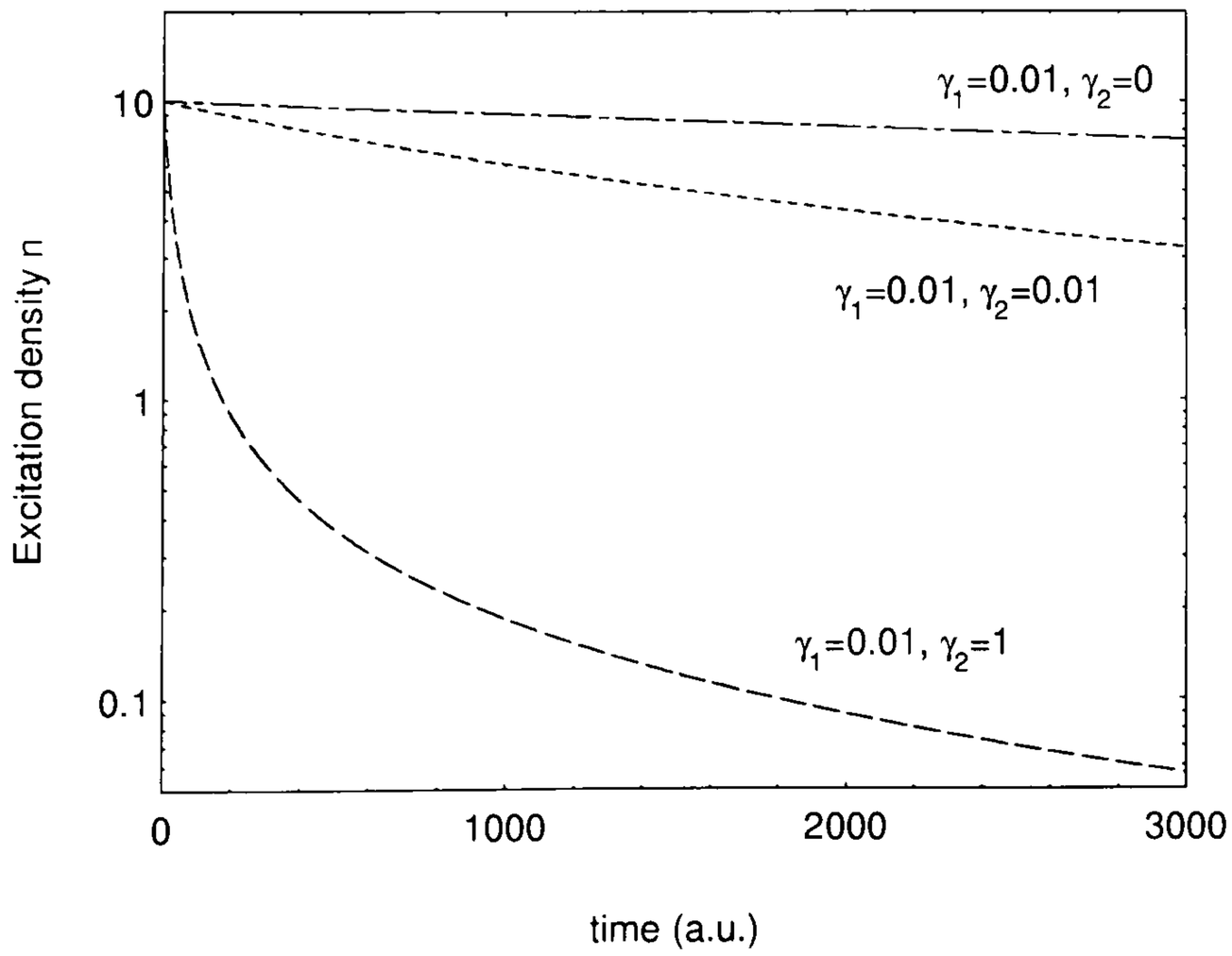

Fig. 2.9. *Exciton depopulation with varying degrees of bimolecular interaction (initial concentration n_0=10).*

The measurement of the decay dynamics of excitons requires time resolved detection techniques. However, a signature of quenching may also be seen in an integrated detection, such as the fluorescence yield measurement, as a function of concentration of excitations. In numerical terms, equation (2.2) can be solved for varying initial concentrations n_0 and the integrated excitation density $\int_0^\infty n(t)dt$ is computed, which corresponds to the fluorescence yield. The results are shown in Fig. 2.10 for a number of different parameters. There are three universal features visible. At low concentrations, the integrated decay scales linearly with the exciton concentration. Above a certain concentration a deviation is observed, giving rise to an average dependence of the integrated decay on the square root of the exciton concentration. This is in full agreement with the observations by Denton et al. [17]. For very high concentrations, the integral approaches saturation and the exponent is reduced below 0.1. It is also seen that for a reduced ratio of radiative to bimolecular decay rate, quenching occurs at lower concentrations.

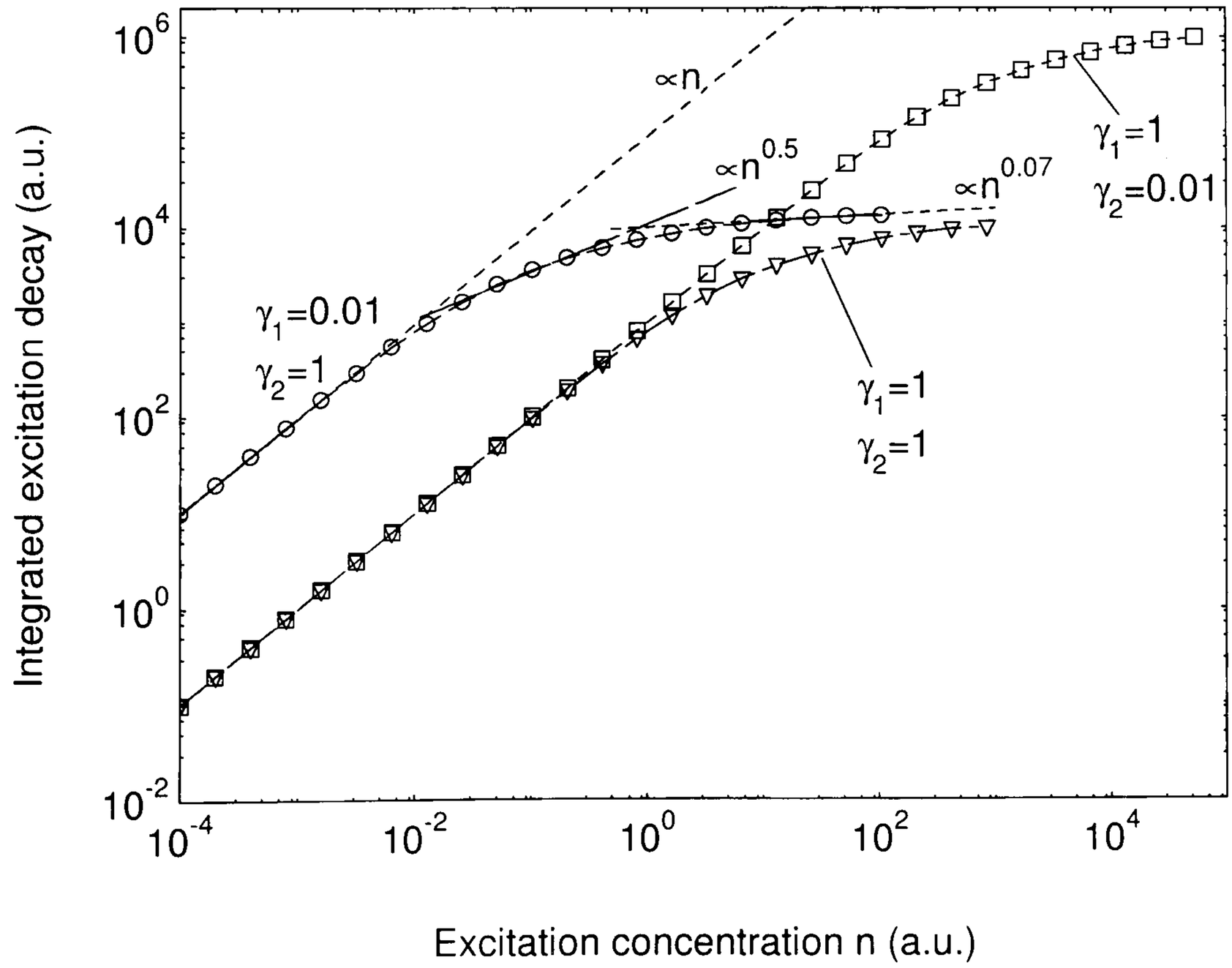

Fig. 2.10. *Exciton quenching resulting from bimolecular interaction.*

The problem of bimolecular decay has attracted considerable attention in the literature. An analytical solution was shown to exist by Campillo et al. [16] following the form (2.3)

$$\varphi_f(n) = \varphi_f^{\max} \frac{r}{n} \ln(1 + \frac{n}{r}) \qquad (2.3)$$

where φ_f is the fluorescence yield, and $r=2\gamma_1/\gamma_2$. In Fig. 2.11 it is demonstrated that the numerical simulations of the bimolecular interactions agree with this solution. The luminescence yield is normalised to be 1 and defined as the ratio of the calculated integrated decay to the linear region in Fig. 2.10.

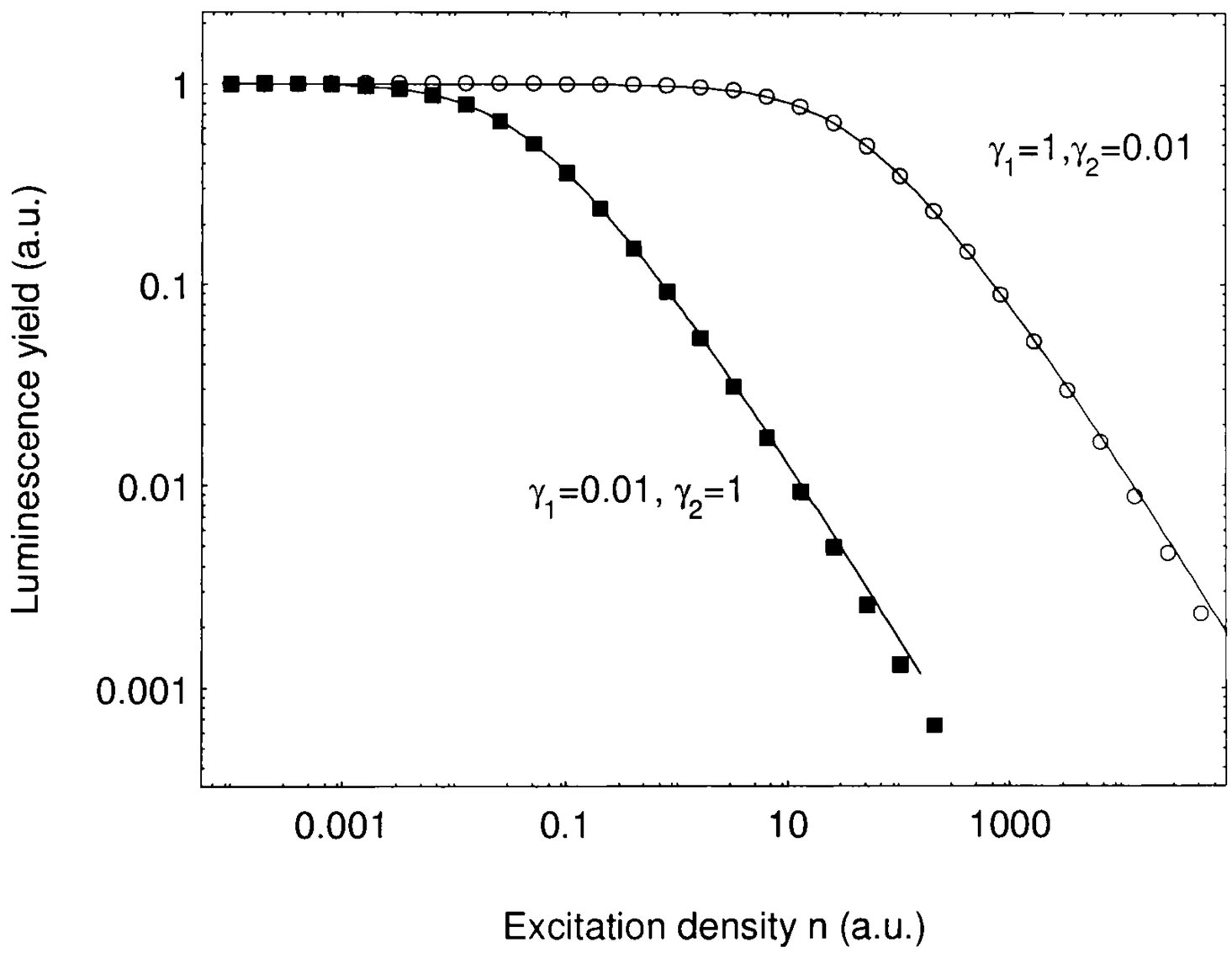

Fig. 2.11. *Analytical solution of bimolecular decay (2.3) (lines) compared to the numerical calculation above (symbols).*

It has hence been shown that quenching effects amongst excitons can have a significant effect on the detected light emission. As the critical density decreases with increasing radiative lifetime, excitation densities approachable in LEDs may suffice to give rise to quenching between triplet excitations. Indeed, this has previously been suggested on the basis of a strong decrease in electrophosphorescent device efficiency with current density [11].

2.3 Intermolecular interactions

For any physical system the observable properties of an isolated complex are modified when bulk materials are formed. This is a simple consequence of the quantum mechanical splitting arising from electronic correlations and exchange interactions. In conjugated organic materials as in many organic dye systems, the photophysical properties are vastly modified in the bulk with respect to the relatively isolated case in solution. There are two important classes of intermolecular states arising from interactions, which shall be discussed in the following. The first are aggregates, which may be considered as physical dimers, and the second are excimers, which are excited state dimers.

Aggregates result from the overlap between the wavefunctions of two identical closely spaced molecules. The ground and excited state wavefunctions of the aggregate system are formed through a mixture of the individual molecular wavefunctions. This modification of both ground and excited state results in a change of the absorption and emission spectrum. In general, aggregation effects are concentration dependent and may be observed in highly concentrated solutions as well as in films. An example of a polymer in which aggregates form is polyfluorene, where a low energy feature is observed in both absorption and luminescence [18]. The luminescence from aggregate states tends to be broad and featureless. The energy levels of the monomers and the split dimers which give rise to aggregate states are shown in Fig. 2.12. The coulombic binding energy W of the dimer pair is calculated through the expectation value of the product of the two monomeric wavefunctions operated on by the intermolecular interaction operator. The resulting excitation can be thought of as oscillating coherently between the two molecules, rather than being localised on one.

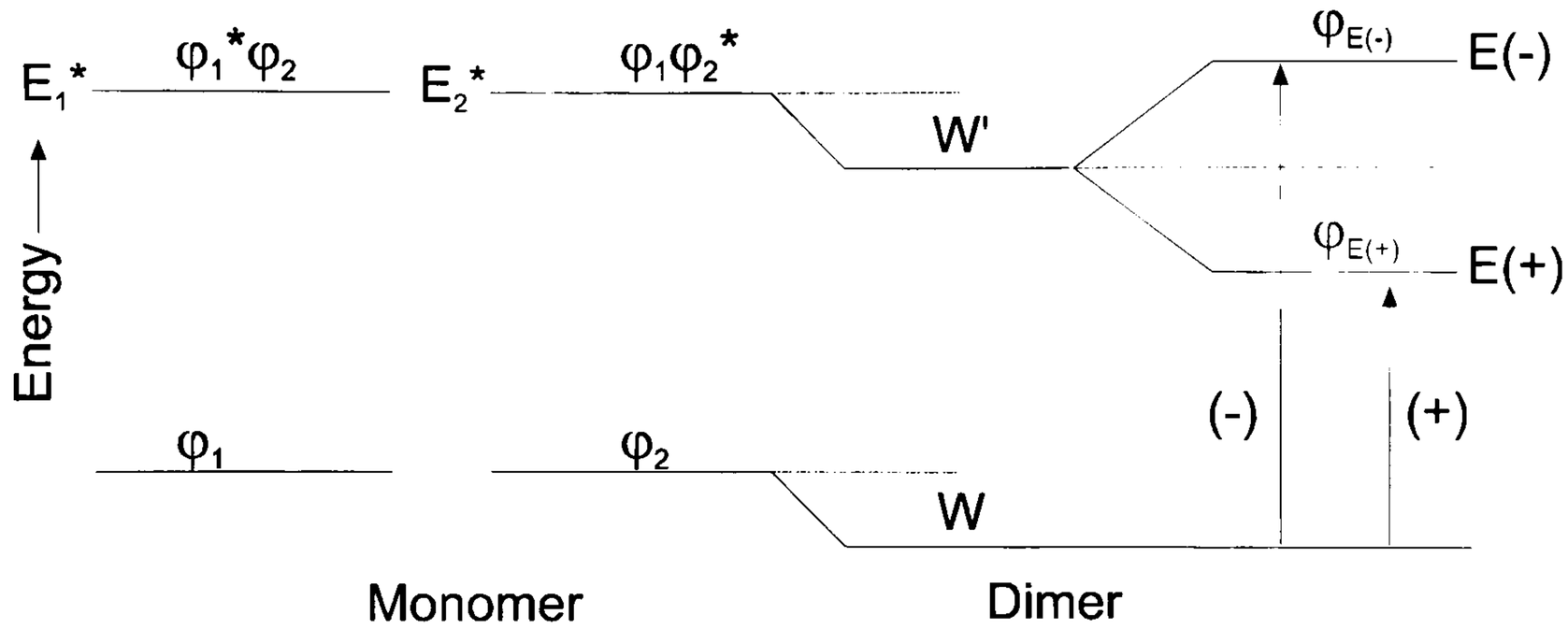

Fig. 2.12. *Energy levels of monomers and physical dimers. φ_1 and φ_2* denote equivalent excited electronic states of two identical molecules interacting with each other. In the absence of an interaction energy, φ_1*φ_2 and $\varphi_1\varphi_2$* have the same electronic energy, and the excitation will remain on the molecule initially excited. A non-zero interaction term results in a splitting of the joint levels and the formation of a red-shifted or blue-shifted feature. W' is the coulombic energy of interaction of the charge distribution of the excited state of molecule 1 with the ground state of molecule 2 [4].*

The aggregated state exhibits a splitting with respect to the monomer state. However, due to the effects of exciton migration emission will often occur from the lowest energy site. The relative contributions of the two lines of the doublet depend on the orientation of the dipoles, as shown in Fig. 2.13. For dipoles aligned in parallel, the lower energy level becomes dipole forbidden, whereas for dipoles aligned head-to-tail the higher energy level is forbidden. Randomly oriented dipoles result in a split band with contributions from both lines of the doublet. Forbidden transitions result from the vectorial nature of the monomeric dipoles, which add up to zero as seen in the figure.

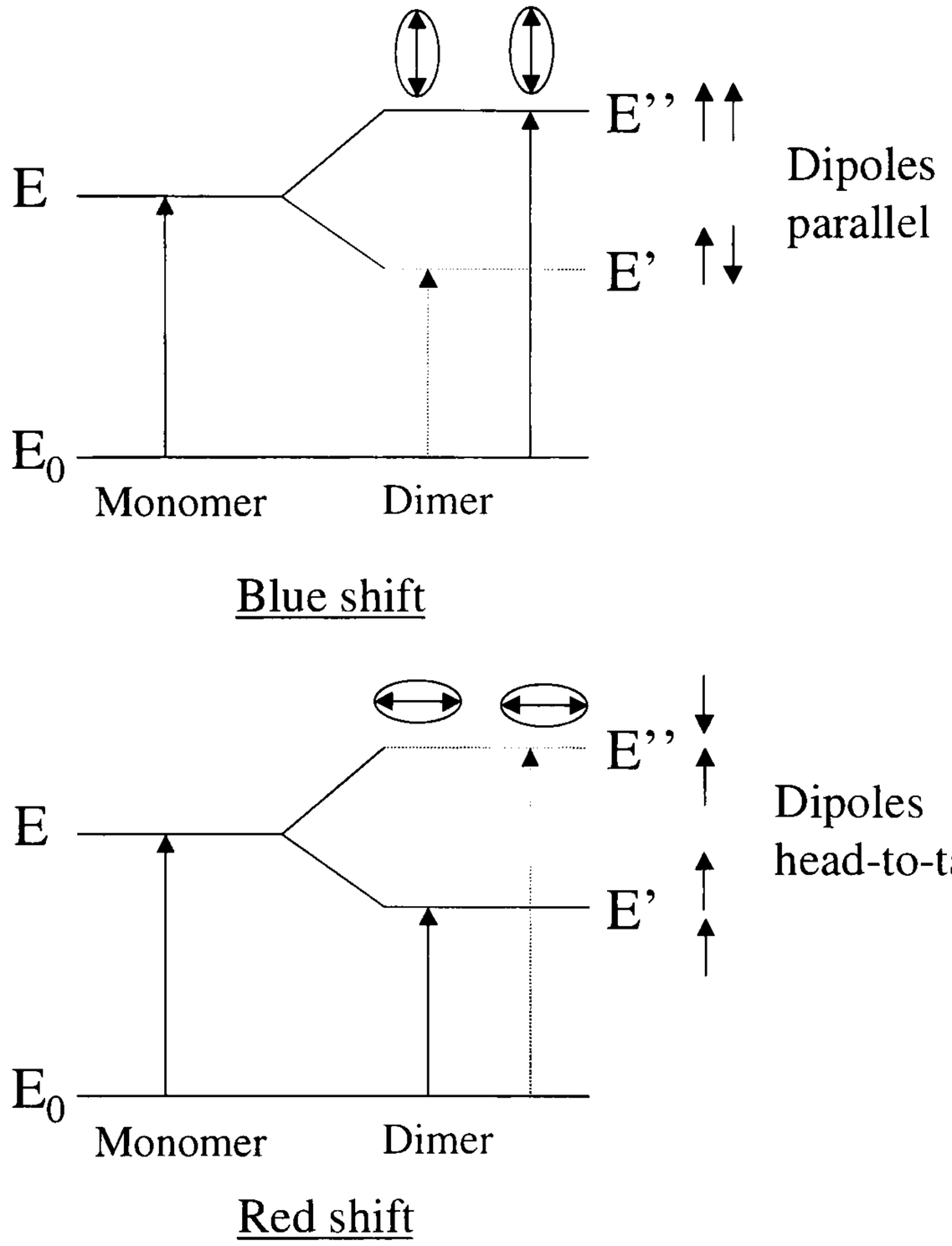

Fig. 2.13. *Exciton splitting in dimers having the two extreme geometries. The short arrows depict the orientations of the monomer transition dipoles. The dotted lines denote dipole forbidden transitions [4].*

There is a second class of intermolecular species that exhibit the optical absorption characteristics of a monomer but reveal a broad, structureless fluorescence spectrum, which is a feature of the physical dimer association. These are known as excimers, which form between an excited molecule and a molecule in the ground state, despite the repulsive ground state potential between them. The reactions that give rise to excimer formation are shown in equations (2.4)-(2.6).

Cleary, as is shown in the upper panel of Fig. 2.14, the lowest excited molecular singlet state can decay emitting normal fluorescence:

$$S_1^* \rightarrow S_0 + h\nu_M \qquad (2.4)$$

Alternatively, collisional quenching of the S_1* state by a ground state S_0 produces the excimer state E_1*:

$$S_1^* + S_0 \rightarrow E_1^* \tag{2.5}$$

Finally, the excimer may decay radiatively:

$$E_1^* \rightarrow S_0 + S_0 + h\nu_{Excimer} \tag{2.6}$$

The emission from an excimer state to a repulsive ground state which causes a spectral broadening is shown in Fig. 2.14 in comparison to the case for the ground state dimer complex.

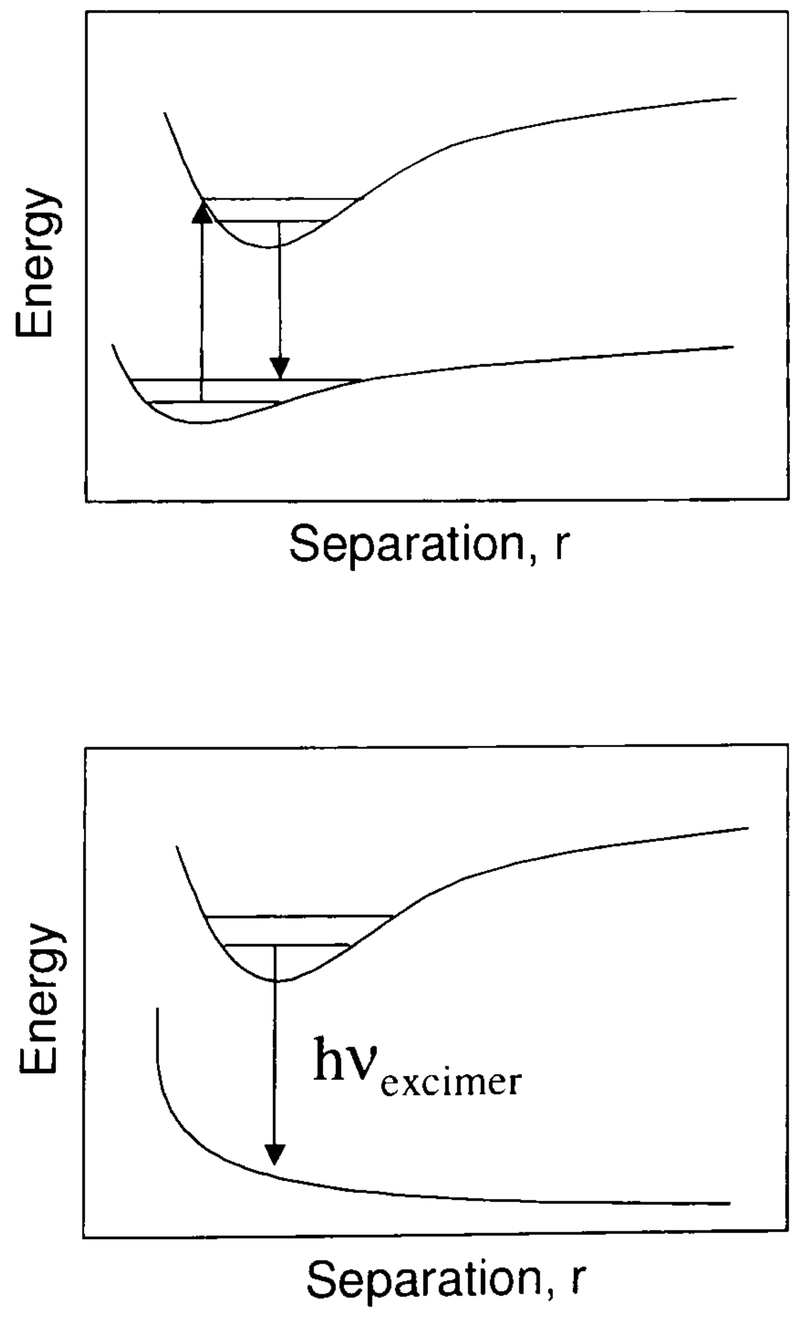

Fig. 2.14. *Electronic transitions in dimers. Upper panel: absorption and emission from an aggregated system with stable ground and excited states. Lower panel: emission into the repulsive ground state of an excimer [19].*

There has been considerable interest in the identification of the contribution of intermolecular interactions to the luminescence of conjugated polymers [20-26]. There is also a considerable body of theoretical work which has been devoted to the excimer problem and the nature of such an excited state [27-30]. Excimer emission is generally inefficient and excimer states hence act as quenching sites for luminescence. Recent calculations by Tretiak et al. [30] confirm this and demonstrate that low-lying modes with weak oscillator strengths are formed between PPV chains at proximities of less than 4 Å.

2.4 The dendrimer concept

Organic semiconductors can generally be divided into two classes of materials, small organic molecules and polymeric materials. However, there is an interesting class of macromolecular materials in between, with a branching exponential rather than a linear geometry. These materials are known as dendrimers. Over the past decade there has been rapidly increasing interest in dendritic molecules from a large variety of research areas [31-41]. A large number of publications and patents were produced by Tomalia and co-workers [31], who identified dendrimers as materials suitable to imitate naturally occurring light-harvesting complexes important to photosynthesis. Further interest in dendrimers has been as molecular drug delivery systems, employing molecular recognition features incorporated in the branches, or dendrons [31-32]. A remarkable feature of dendrimers is the ability to localise energy on the centre of the molecule through correct choice of the energy gradient between core and dendrons [33]

Dendrimers can be constructed to consist of a luminescent conjugated core region - either monomeric, polymeric or molecular – surrounded by hyperbranched, conjugated side groups or dendrons. This is shown schematically in Fig. 2.15. The conjugation is broken between the different conjugated units, which can be achieved by *meta*-conjugations or carbonyl linkers, for example. Excitations are hence not delocalised across the entire molecule.

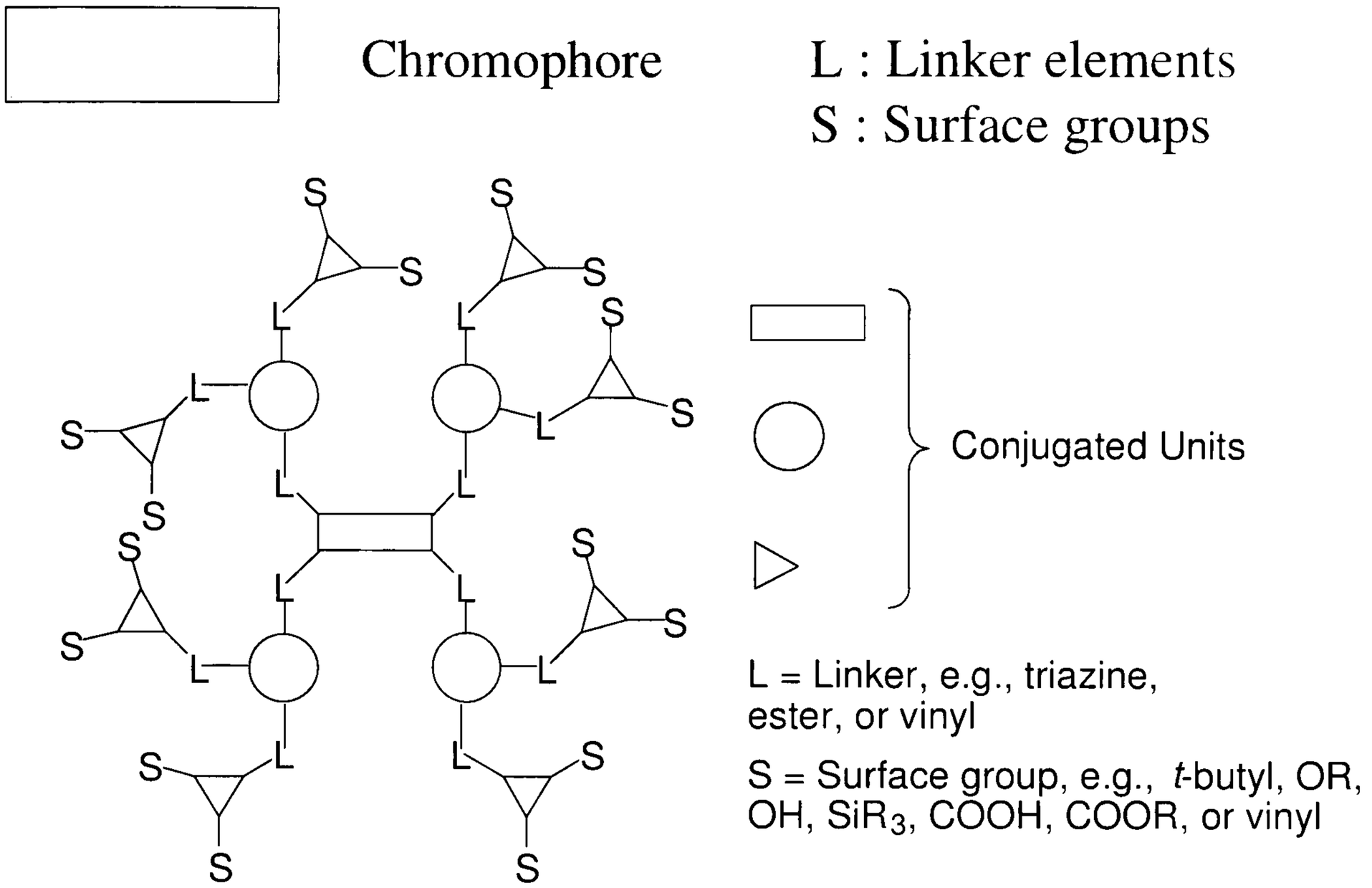

Fig. 2.15. *Schematic structure of conjugated dendrimers. A conjugated core is surrounded by doubly branched conjugated dendrons, forming a second generation dendrimer. The different conjugated groups are linked through linker units (L). The dendrimer is surrounded by surface groups (S), which control the interaction with the environment.*

Energy localisation at and funnelling to the centre of dendrimers has been demonstrated in a number of systems [33, 40-43], although to date no practical applications have been found. The fact that the dendrons posses three contact points within the dendrimer, two of which point away from the core, suggests from a mere statistical argument that excitation energy should diffuse from the core to the periphery [44]. Indeed, such systems, where the emissive centres are localised on the dendron periphery, have been demonstrated [32]. However, dendrimers can also possess a unique shielding effect, which protects excitations from interactions with the environment. This has been demonstrated conclusively by the encapsulation of emissive centres in a dendrimer architecture. In work carried out by Meijer and co-workers, a reduction in aggregate emission was observed for Bengal Rose shielded in this way [45]. A most remarkable effect of energy localisation has been demonstrated by Aida and co-workers, who found that their dendritic macromolecules could be photoisomerised by the absorption of a

number of infrared photons rather than a single ultraviolet photon [41-42]. This result, which is yet to be reproduced in the literature, suggests that the dendrimer architecture inhibits all radiative and non-radiative decay modes for excitations at the core, so that quanta of infrared radiation can simply add up, finally leading to photoisomerisation.

Although dendrimers are optically fascinating systems and may well find applications in artificial light-harvesting devices, no applications have been demonstrated as yet. A further area of interest has hence been in electroactive dendrimers [46-47] and the effect of the dendritic architecture on oxidation and reduction. Dendritic or starburst materials have also been used as charge transporting materials [48-53], in particular for organic LEDs. However, the possibility to independently control the emissive core and the dendrimer architecture, the potential shielding and localisation of excitations as well as the possibility for energy funnelling make conjugated dendrimers extremely interesting as materials for organic LEDs [54-57]. In effect, conjugated dendrimers allow a nanoscale control of the electronic properties of organic semiconductors. The wide range of emission colours available to organic LEDs has frequently been cited as a key benefit of these devices over conventional devices. Using conjugated dendrimers, Halim et al. demonstrated that the emission spectrum of dendrimers in a common architecture can be tuned throughout the visible spectrum [56]. The dendrons provide a means of controlling the ordering and microscopic packing of the emissive chromophores, which is extremely important in the operation of LEDs, as it affects both charge transport and interchromophore coupling of the emissive dipoles. Finally, the interaction of the molecule with the environment is of great importance. The surface groups of the dendrimers provide a method of controlling the solubility, which can be extremely useful in the fabrication of solution processed multilayer devices.

2.5 Primary photoexcitations in dendrimers – a quantum chemical approach

The development of quantum theory and the phenomenal success of describing the properties of atoms fuelled the desire to be able to calculate and predict the characteristics of molecules and even solids. Yet even the simplest approximations made in theories of bulk systems have only recently become practical due to the

enormous increase in computational power. A complete quantum mechanical description of a molecule requires the calculation of all orbitals as well as the interaction between all of these orbitals and the states resulting from electronic splitting. Depending on the parameters which are to be predicted, calculations may hence contain a vast amount of redundant information. A number of frameworks have been developed within the field of quantum chemistry, suitable for different applications [58]. In the field of conjugated organic semiconductors, one of the parameters of greatest interest is the band gap of the material, which ultimately controls the emission colour. In the previous section the benefits of the dendrimer concept were discussed, which provides a molecular framework for a controlled variation of the emission properties of molecules for EL applications. It would be highly desirable to be able to predict these emission properties merely on the basis of the chemical structure of the molecule.

There is an extensive body of work on the application of quantum chemical techniques to polymers and other organic materials. Both semi-empirical (e.g. intermediate neglect of differential overlap sum over states (INDO-SOS) [59, 60]) and ab-initio calculations [61] have provided rather good predictions of the electron-hole separation in PPV. However, experimental data on polymers are statistical in nature due to the intrinsic distribution of conjugated lengths, which can be a factor of 1000 shorter than the actual chain length of the polymer. In contrast, conjugated dendrimers provide ideal systems to apply the methods of quantum chemistry to, due to their well defined chemical structure and distinct chromophore. Yet to date there have been few attempts to calculate the electronic properties of dendrimers as they are simply too big for most current approaches to deal with. Whereas the polymers are linear systems and can be broken down into oligomeric components, the dendrimers are exponential and can hence be separated into different units only under special conditions.

Recently, a novel approach to calculating the spectroscopic properties of organic molecules and polymers was developed by Mukamel and co-workers in Rochester [62-66]. The coupled electronic oscillator (CEO) method is designed to calculate the excited state rather than the ground state or the perturbed ground state, by implicating the creation of a coupled hole and electron forming an exciton. This idea is particularly relevant to organic materials with large exciton binding energies and molecules with strong electron correlations, such as conjugated molecules.

The optical response of a quantum system is determined by the associated set of many-electron eigenstates $|\nu\rangle$, $|\eta\rangle$, ... and the corresponding energy eigenvalues ϵ_ν, ϵ_η, ... The many-electron wavefunctions hence describe all n-body properties of the material. However, even for the smallest of molecules computational limits are soon reached. Fortunately, most of the information contained in the quantum states of the system is redundant, as the observable optical properties of a material depend only on the expectation values of one- and two-electron quantities. An accurate picture of the relevant physical processes may hence be gained with a much reduced description of the quantum mechanical parameters governing the system. This idea of a reduced variable set is the basis of density-functional theory, which employs only the ground state charge density profile to give the ground state energy [67]. The CEO technique uses a similar concept of a reduced variable set, i.e. a functional rather than a wavefunction basis set, yet with the important difference that the excited state energy is calculated rather than the ground state energy. The CEO single-electron density matrix is hence defined as

$$\rho_{nm}^{\nu\eta} \equiv \langle \nu | c_n^+ c_m | \eta \rangle \tag{2.7}$$

where $|\nu\rangle$ and $|\eta\rangle$ are global electronic many-electron eigenstates of the molecular system and $c_n^+(c_n)$ are the electron annihilation (creation) operators for the basis set describing the electron on the n-th orbital. n and m are indices denoting the atomic basis functions, i.e. the wavefunctions describing the electrons in the individual atoms comprising the molecule. For $\nu=\eta$, ρ is the reduced single-electron density matrix of the state ν, whereas for $\nu\neq\eta$, ρ describes the density matrix resulting from a transition between the states ν and η.

Under optical excitation, the time-dependent global wavefunction of the molecule becomes a coherent superposition of states following the Fourier series

$$\Psi(t) = \sum_\nu a_\nu(t) |\nu\rangle \tag{2.8}$$

The corresponding time-dependent density matrix describing an electronic transition of the molecule from ν to η is then given by

$$\rho_{nm}(t) \equiv \left\langle \Psi(t) \middle| c_n^+ c_m \middle| \Psi(t) \right\rangle = \sum_{\nu,\eta} a_\nu^*(t) a_\eta(t) \rho_{nm}^{\nu\eta} \,. \qquad (2.9)$$

It is hence possible to relate the time-dependent single electron density matrix resulting from an external driving field to the molecular density matrix.

The optical response involves only reduced information about the global eigenstates, which is contained in the matrix subset $\rho^{\eta\nu}$ defined in (2.7). The above definition of the single-electron density $\rho^{\eta\nu}$ implies that it is necessary to first calculate the molecular eigenstates $|\eta\rangle$ and $|\nu\rangle$. Fortunately, the matrices $\rho^{\eta\nu}$ and frequencies Ω_ν can be calculated directly using the time-dependent Hartree-Fock theory. The calculation of the many-body eigenstates, which is complicated and virtually impossible for larger molecules, can hence be avoided. The time-dependent Hartree-Fock approximation states that the many-body wavefunction is determined by a single Slater determinant for all times and can hence be described by a closed equation of motion involving only the single-electron density matrix. In summary, this approximation results in an oscillator, or quasiparticle, picture of the optical excitation of the molecule.

The closed equation of motion for a molecule under excitation by an optical field E can be described in terms of the commutators of the Hartree-Fock Hamiltonian F, the dipole moment μ and the single-electron density ρ. By expanding $\rho(t)=\rho_0 + \delta\rho(t)$, one obtains

$$i\frac{\partial \rho(t)}{\partial t} = i\frac{\partial \delta\rho(t)}{\partial t} = [F(\rho), \rho] - E(t) * [\mu, \rho] \qquad (2.10)$$

which yields a set of K×K equations, where K is the number of atomic orbitals. The ground state single-electron density, which is the effective input to the CEO calculation, is obtained from INDO/S (spectroscopy) calculations involving all open shell orbitals (e.g. 1 orbital for hydrogen, 4 orbitals for carbon). The INDO/S orbitals are parameterised to reproduce the band-gap of polyacetylene at room temperature. The solution of the equation of motion can be greatly simplified by restricting the equations

to those containing only occupied (electron) – unoccupied (hole) pairs of orbitals. To do this, $\delta\rho(t)$ is decomposed into two components

$$\delta\rho(t) = \xi(t) + T(\xi(t)) \tag{2.11}$$

where ξ represents the electron-hole part of the transition matrix, the interband transition, and $T(\xi)$ represents electron-electron or hole-hole transitions, i.e. transitions within a band. The matrix elements of the interband transitions are hence given by

$$(\xi_\nu)_{nm} = \langle \nu | c_m^+ c_n | g \rangle \tag{2.12}$$

The two components of the density matrix are shown schematically in Fig. 2.16.

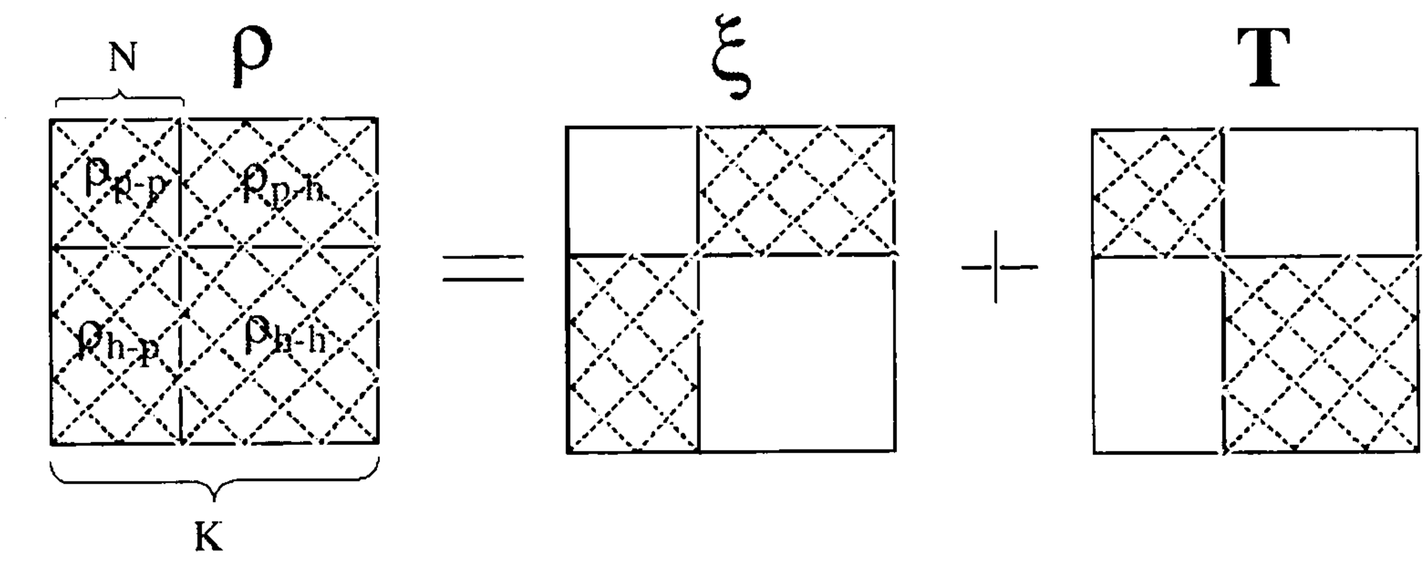

Fig. 2.16. *The single-electron density matrix in terms of the possible electronic transitions: particle-particle (p-p), particle-hole (p-h), hole-particle (h-p) and hole-hole (h-h). The dimensions of the matrix ρ are defined by the size of the basis set K (which is generally 1×No of H atoms + 4×No of C atoms). In this representation there are N occupied orbitals and K-N unoccupied orbitals [66].*

The complete expansion of the electronic density matrix in terms of the electronic normal modes ξ_ν takes the form

$$\delta\rho(t) = \sum_\nu a_\nu(t)\xi_\nu + a_\nu^*(t)\xi_\nu^* \tag{2.13}$$

where each ξ_ν has a corresponding eigenenergy Ω_ν. The electronic modes describe collective motions of electrons and holes but carry much less information than the

many-body molecular eigenstates. The diagonal elements $(\xi_v)_{nn}$ represent the net charge induced on the n-th atomic orbital in the presence of the driving electric field, whereas the off-diagonal elements $(\xi_v)_{mn}$ m≠n define the joint amplitude of an electron being on orbital m and a hole on orbital n. Electronic modes are hence directly related to the motions of optically induced charges and electronic coherences. The correspondence between the optical excitation and the real-space CEO picture is shown in Fig. 2.17.

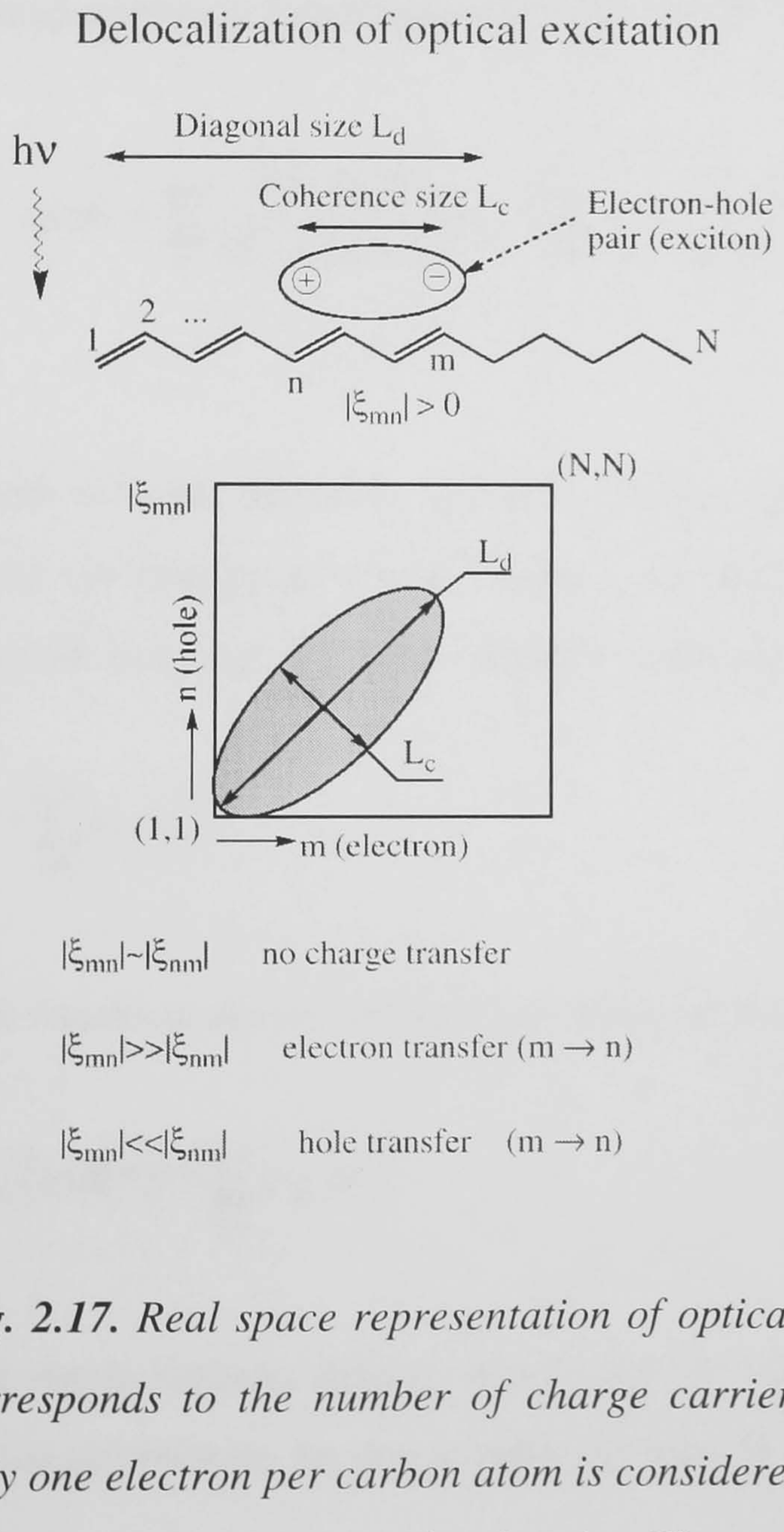

Fig. 2.17. *Real space representation of optical excitations in an N×N matrix, where N corresponds to the number of charge carriers. In the single-electron approximation only one electron per carbon atom is considered, so N hence corresponds to the number of carbon atoms or the molecular size. The exciton generated by an incident photon can be characterised in terms of the coherence length and the diagonal length. The coherence length L_c is given by the anti-diagonal width of the density matrix and defines the distance the electron and hole can move apart. The diagonal size L_d defines the distance over which the excitation can reside within the molecule, as illustrated above for the case of polyacetylene. An asymmetry within the transition matrix is indicative of a charge transfer state [66].*

Two important quantities are defined in Fig. 2.17: the coherence size L_c and the diagonal size L_d. Whereas the coherence size measures the coherence between electrons and holes on different atomic sites within the molecule, the diagonal size describes the degree of localisation of optical excitations. This form of representation is hence ideally suited to investigate the concept of energy localisation in conjugated dendrimers.

The eigenfrequencies Ω_ν and the time dependent Hartree-Fock equations provide the optical transition frequencies [65]. The linear polarisability $\alpha(\omega)$ is then given by

$$\alpha(\omega) = \sum_\nu \frac{2\Omega_\nu \mu_{g\nu}\mu_{g\nu}^*}{\Omega_\nu^2 - (\omega + i\Gamma)^2} = \sum_\nu \frac{f_\nu}{\Omega_\nu^2 - (\omega + i\Gamma)^2} \qquad (2.14)$$

where f_ν is the oscillator strength of the g (ground state) to ν transition, Γ is the line width (or relaxation rate/dephasing), and μ is the dipole moment operator. The dipole moment is a single-electron operator which may be written in the form

$$\mu = \sum_{nm} \mu_{nm} c_n^+ c_n \qquad (2.15)$$

The transition dipole operator can hence be written as

$$\mu_{g\nu} \langle g | \mu | \nu \rangle = \sum_{nm} \mu_{nm} \rho_{nm}^{g\nu} \qquad (2.16)$$

The single-electron density matrix and the corresponding eigenvalue Ω_ν hence contain all the information needed to calculate the linear optical response.

2.6 Device models

2.6.1 Introduction

In spite of the remarkable progress in the field of organic electroluminescence and the large range of improvements made to device structures and materials chemistry and

purity, organic devices remain inherently complicated in operation in contrast to their simplicity in fabrication. For example, the nature of charge transport in conjugated EL polymers is a current key interest. Time-of-flight measurements have shown that the mobility can change by orders of magnitude in seemingly related compounds, and so can the exhibited dependence on the applied field [68]. In most cases the electron mobility is smaller than the hole mobility, yet recent space charge limited current measurements on MEH-PPV suggest that electron and hole mobilities are virtually identical [69] – a result which is not matched by time-of-flight data [70]. Some devices exhibit a strong dependence on temperature, and whereas some structures have shown an increase in efficiency with increasing temperature [71], others show a decrease. (An example of this is discussed in Chapter 4, where the single layer device efficiency is found to decrease 50-fold as the device is heated from 10 K to 300 K). Overall, there has been remarkably little work on the temperature dependence of LEDs, although the temperature dependence is a standard tool of investigating charge transport in semiconductor physics. Most EL polymers are intrinsic semiconductors, but can exhibit a varying degree of doping, which is particularly strong for precursor materials [72, 73]. Yet there appears to be no intrinsic limit to the current density a device can support, provided the electrical excitation is sufficiently short to allow ohmic heat to dissipate. However, whereas the Cambridge group have suggested that the mobility decreases at high currents [74], results from Los Alamos suggest the opposite [75].

A significant complication in understanding the operation of LEDs comes from the nature of the polymer/metal interfaces in the device [76-79]. Generally, a polymer LED is fabricated by spin-coating a polymer film onto an ITO substrate and then evaporating a metal cathode on top, forming two very different interfaces. Whereas the ITO/polymer interface is extremely sensitive to ambient impurities trapped between the polymer and the electrode as well as impurities introduced by the ITO itself, the polymer/cathode interface is sensitive to the evaporating conditions such as rate and base pressure. Organic materials are chemically very sensitive and can hence decompose or react with the metal upon evaporation. Thinking in terms of a rigid band offset as for inorganic metal/semiconductor interfaces is hence an oversimplification. Furthermore, the polymers are amorphous molecular materials and hence possess no equivalent to a band continuum. Charge transport is very different to the case of inorganic materials, where scattering effects dominate in single crystals. In the case of polymers, the bands are

generally very narrow, which reduces the scattering effects, but due to the disorder inherent in these materials there is a broad distribution of energy levels, which considerably complicates the view of charge carrier injection and transport.

An extensive body of experimental and theoretical work has focused on the effect of energetic and spatial disorder on the charge transport in conjugated polymers. The most noteworthy model resulting from this research is the Gaussian Disorder Model which was developed by Bässler and co-workers on the basis of Monte Carlo simulations [80]. The key feature of this model of Miller-Abrams type hopping transport in a disordered medium is an exponential square root dependence of the mobility on electric field. This dependence, which is also known as the pseudo Poole-Frenkel effect due to the conceptional and functional similarity to the increase in conductivity in ionic media by the presence of an electric field as described by Poole and Frenkel [81], has been observed in numerous mobility measurements on polymers and other organic materials. Although the idea of a field-dependent mobility is counter intuitive and contradictory to the conventional semiconductor theories of Sommerfeld and Bloch, it has been shown to be a direct consequence of disorder. Recent analytical work has also confirmed the universality of the field dependence of the mobility in hopping transport in disordered media [68, 82].

It has recently been shown that the current-voltage characteristics of ITO/MEH-PPV/Al LEDs can be described by a model, which considers single carrier transport (hole polarons only) [83]. The model combines the injection processes of the tunnelling, thermionic emission and the interface recombination currents [84] with the bulk transport through the diode. Although the authors demonstrate that the injection terms in their model adapt well to varying work functions [85] of different injecting electrodes, the temperature dependence has not been considered [86] and comparison with data is only at room temperature.

In this section the operation of single carrier diode structures is reviewed briefly and a device model is presented, which is later used to describe the device operation of LEDs made of different materials.

2.6.2 Analytical models

The Fowler-Nordheim or field emission tunnelling theory has been widely used to analyse current-voltage characteristics in terms of the barrier to injection for majority charge carriers although its shortcomings have been discussed at length in the literature [87]. Following Parker [88], for carriers tunnelling through a triangular barrier, the logarithm of J/E^2 is proportional to the inverse of the field, which allows the determination of the barrier height:

$$J = C \times E^2 \times e^{-\frac{\kappa}{E}} \tag{2.17}$$

$$C = \frac{3e^2}{8\pi h\varphi} \tag{2.18}$$

$$\kappa = \frac{8\pi\sqrt{2em}}{3h}\varphi^{\frac{3}{2}} \tag{2.19}$$

where e is the modulus of the electron charge, h Planck's constant, m the effective mass of the hole polaron which is taken to be the electron mass and φ the barrier height to injection in eV.

Initial studies by Parker [88] on MEH-PPV clearly correlated the device performance, current-voltage characteristics and efficiency, with the work function of the injecting contact, highlighting the importance of charge carrier injection in the description of organic LEDs. Fowler-Nordheim tunnelling theory has found much attention as an explanation of the observed current-voltage characteristics in polymer diodes [88-91]. There are a number of problems with models based on tunnelling: the fits are poor in the sense that they typically only follow the measured data over one order of magnitude of current density; the tunnelling theory overestimates the current density by many orders of magnitude [90, 92] which implies the presence of other processes such as image charge effects and carrier recombination; and the barrier heights determined by a Fowler-Nordheim analysis are typically smaller than values calculated from direct measurements of the built-in electric field and the offset between the metal work function and the highest occupied molecular orbital (HOMO) of the polymer [93-95].

In contrast, thermionic emission has been invoked to explain the characteristics observed in a number of LEDs, most notably precursor PPV devices studied by the Bayreuth group [72]. Impedance spectroscopy was combined with I-V measurements to determine the width of the depletion zone of LEDs, which implied a certain level of doping [73]. Interesting results have also been obtained by combining these experiments with measurements of thermally stimulated currents [96]. The trap distributions obtained from both these techniques were found to be in remarkable agreement. Internal photoemission and electroabsorption measurements have confirmed the presence of a Schottky contact formed at the metal/polymer interface [93], although for many systems it appears that the depletion region is larger than the actual device [97]. In contrast to tunnelling, a current governed by thermionic emission is thermally activated and has an exponential bias dependence of the form

$$J = J_s(\exp\left(\frac{eV}{nkT}\right)-1) \tag{2.20}$$

where J_s is effectively a constant depending only on temperature and effective electron mass and n is the ideality factor which is ~1 at high temperature. Additionally, the Schottky effect describes the image force barrier lowering induced by the electric field present at the barrier. Although a rigorous analysis of this is complicated, a recent derivation combining Langevin type recombination and the Schottky effect specifically for the case of a metal/polymer interface led to a functional dependence of the current on the applied field which is approximated by a square root relationship [98].

An alternative approach to modelling devices by considering the injection current is to assume an ohmic contact and view the low mobility of the material as the current limiting factor. Analytical models have been used successfully to describe space charge limited conduction in ITO/PPV/Al(Ca) LEDs [97, 99-101]. Using either an exponential distribution of traps in the material or the universal concept of a field and temperature-dependent hopping mobility in the trap free limit or a combination of both, good agreement with experiment has been found. Although capacitance-voltage measurements on MEH-PPV [102] and PPV [73] clearly demonstrate the presence of traps in polymer LEDs and the creation of a Schottky barrier with a charge carrier depletion region, the contributions of these trapping sites to the actual conduction

process remains as yet unclear and appear to be linked to the variation of mobility with applied field. Conwell et al. [87] obtained equally good fits to ITO/MEH-PPV/Ca devices considering both the trap-free and the trap-filled limits.

Conjugated polymers have low mobilities in the order of 10^{-6} cm^2/Vs which tend to limit the current flow when sufficient current is injected through or over the barrier. This phenomenon is known as space charge limited current flow. Detailed models well known from inorganic semiconductor structures as presented by Lampert and Mark [103] have been applied successfully to PPV LEDs to explain I-V characteristics, transient and static capacitance voltage measurements and temperature dependence. The best fitting models assume an exponential distribution of traps around the conduction band, which is in accord with the predictions made by the disorder model [80, 97].

Space charge limited current is manifest through a voltage rather than a field dependence of the current, which is usually expressed in the form of a power law. A frequently cited form of this dependence is given by Child's law in the trap free insulator [103]

$$J \cong \varepsilon_0 \sqrt{\frac{e}{m_0}} \frac{V^{\frac{3}{2}}}{L^2} \tag{2.21}$$

A further important case of space charge limited currents is the trap filled limit, where traps with a single energy level are present in the material. This results in the often cited bias squared dependence of the space charge limited current.

$$J = \frac{9\varepsilon\varepsilon_0 \mu V^2}{8d^3} \tag{2.22}$$

In many systems the trapping levels are described by an exponential distribution, which results in more complicated power-law dependencies of the current on the bias. As will be discussed below, it is not possible to obtain a full physical picture of traps in a semiconductor merely from the I-V characteristics, as the concept of a field-dependent mobility is not compatible with large distributions of traps.

2.5.3 A combined device model

The calculations presented in chapters 5 and 6 of this thesis are based on the device model for single carrier organic diodes by Davids et al. [83]. The model gives a good description of MEH-PPV devices with various metal contacts [85] over a wide range of current densities. The creation of a Schottky barrier [102] and the resulting band bending and image charge effects are taken into account in the injection current. Due to the low mobility of the material there is a recombination current at the interface which depends on the degeneracy of the polymeric semiconductor. An extension of the model is presented here to account for the temperature dependence of device operation. Also, a number of simplifications are made to the model without impairing its physical accuracy by neglecting both the time dependence and the diffusion term of the current density, as has also been proposed by Kawabe et al. [92]. In the model by Kawabe et al., however, no experimental data are presented and the injection is described only qualitatively in the high field regime by applying the tunnelling formalism and neglecting the field dependence of the mobility.

The temperature dependence is accounted for both in the injection terms (the thermionic emission and the interface recombination current) and in the transport (through the mobility). It is assumed that other physical parameters of the material remain constant with temperature, in particular the dielectric constant, the effective charge carrier mass and the hole polaron degeneracy, which determines the charge carrier density injected into the polymer.

The model does not explicitly take into account the presence of traps in organic diodes or the effect of structural and energetic disorder. The mobility is described through the field-dependent variable range hopping process from one localised state to the next. As remarked by Pai [104], the field-dependent mobility includes the effects of charge trapping sites phenomenologically, which has previously led to difficulties combining both an exponential trap distribution and field-dependent mobility in analytical models [97]. Also, it has been demonstrated that a field-dependent mobility arises naturally from the disorder of an organic semiconductor [68, 82].

The model and calculation is based on work published by Gummel and Scharfetter [105] on inorganic diodes. It has a complete time dependence and is numerically rather intensive. For hole only devices the model may be simplified to the three equations

$$\frac{\partial p}{\partial t}+\frac{1}{e}\frac{\partial J}{\partial x}=G-R \tag{2.23}$$

$$J=e\mu(pE-\frac{kT}{e}\frac{\partial p}{\partial x}) \tag{2.24}$$

$$\frac{\partial E}{\partial x}=\frac{e}{\varepsilon}(p-n) \tag{2.25}$$

Where J is the current density, x the distance from the hole injecting anode, E the electric field, e the magnitude of the electron charge, ε the dielectric constant, μ the hole mobility, p the hole density, n the electron density (=0), G the carrier generation and R the carrier recombination rate. The continuity equation (2.23) is based on the assumption that generation and recombination is bimolecular in the absence of traps. This is an important statement, as it implies that the model physically neglects the influence of traps in the current flow. However, practically some contributions of the effect of traps on transport are included in the field-dependent mobility.

Neglecting the time dependence and the minority current, the equations take the form

$$\frac{dJ}{dx}=0 \tag{2.26}$$

$$\frac{dE}{dx}=\frac{e}{\varepsilon}p \tag{2.27}$$

$$J=e\mu pE \tag{2.28}$$

The presence of electrons in the device is ignored, as the barrier height to electron injection from aluminium (approx. 1.4 eV [83]) is more than twice the barrier height for hole injection from ITO [93]. On the basis of the internal quantum efficiency of the device which is in the order of 0.05% [88], it is estimated that the electron current is of

order 1% of the hole current for these contacts. For more efficient device configurations with calcium cathodes the electron current will contribute to the overall device current, and the effect of negative space charge on the injection of holes at the anode is likely to be of greater importance when simulating device operation. In the case of these devices with ITO and aluminium contacts the built-in potential in the LEDs is small compared with the large operating biases and has been neglected. These simplifications for effectively single carrier devices with high turn-on fields, low charge carrier concentrations and relatively high barriers to injection have no effect on the calculation of the charge carrier mobility as a function of temperature.

In the simple treatment of the diode as a parallel plate capacitor, the boundary condition at the anode, the electric field at x=0, is given by the charge density per unit area Q present on the injecting anode. This charge may be chosen arbitrarily to calculate the current for a certain boundary field and hence for a given voltage, the integral of the electric field across the device.

$$E_{(x=0)}=Q/\varepsilon \qquad (2.29)$$

The charge carrier density at the interface is given by the current injected at the interface, which is a superposition of the tunnelling current, thermionic emission and interface recombination, the time reversed thermionic emission:

$$J_{(x=0)}=J_{FN}+J_{TIE}-J_{IR} \qquad (2.30)$$

where J_{FN} is the tunnelling current taking into account the image force barrier lowering, J_{TIE} is the thermionic emission over the Schottky barrier and J_{IR} is the interface recombination current.

The low mobility and resulting interfacial build-up of space charge also results in a lowering of the injection barrier height through image force effects [106, 107]. This is expressed in a field-dependent form of the barrier height:

$$E_b = \Phi - \sqrt{\frac{e\left|E_{(x=0)}\right|}{\varepsilon}} \tag{2.31}$$

where Φ is the offset between the HOMO level of the polymer and the metal work function.

The thermionic emission current hence takes the form

$$J_{TIE} = AT^2 e^{-\frac{E_b}{kT}} \tag{2.32}$$

with A being Richardson's constant.

The recombination current is proportional to the carrier density at the interface but is otherwise of the same form as the thermionic emission current:

$$J_{IR} = \frac{AT^2}{n_0} p_{(x=0)} \tag{2.33}$$

n_0 is the density of conjugated chain segments times the number of ways that a chain segment can be occupied by an electron or hole, i.e. its degeneracy. It can be estimated by density of states calculations and a value of 10^{21} cm^{-3} has been suggested [83]. It is by no means clear how this quantity depends on temperature. Whereas conventional semiconductors ideally display an exponential dependence of the number of charge carriers on temperature, resulting from thermal excitation of electrons from valence to conduction band, adding or removing an electron from a polymer will not generate free electrons or holes at the conduction or valence band edges [108]. The physical reason for this is that the electronic degrees of freedom couple strongly to structural deformations due to the one-dimensional electronic structure, so that charge transfer leads to molecular distortion, which is known as a polaron. This effect has been widely studied in electronic energy calculations of polymers. Campbell et al. have suggested a value of 10^{20} cm^{-3} for the effective density of states but claim that the product of μn_0 is apparently temperature independent [97], indicating a temperature-dependent variation

of n_0. The dielectric constant is taken to be in the order of $3\varepsilon_0$ and is not thought to exhibit a significant temperature dependence.

The tunnelling current can be expressed in a simple form as suggested in equation (2.17), however neglecting the effects of image force. A more complete model uses the Wentzel-Kramers-Brillouin (WKB) approximation to calculate the tunnelling current under the effect of barrier lowering [106, 109]. The resulting current takes the form:

$$J_{FN} = J_t \left(\frac{E_{(x=0)}}{E_t t(y)} \right)^2 \exp\left(- \frac{E_t v(y)}{E_{(x=0)}} \right) \tag{2.34}$$

Where

$$E_t = \frac{4\sqrt{e}\Phi^{\frac{3}{2}}}{3a_0\sqrt{R}} \tag{2.35}$$

$$J_t = \frac{2\pi e^3 \Phi^2}{9(\pi a_0)^2 hR} \tag{2.36}$$

Where R is the Rydberg, a_0 the Bohr radius. Here

$$y = \frac{\sqrt{\frac{eE_{(x=0)}}{\varepsilon}}}{\Phi} \tag{2.37}$$

and

$$v(y) = (1+y)^{1/2}\left[E\left(\sqrt{\frac{1-y}{1+y}}\right) - yK\left(\sqrt{\frac{1-y}{1+y}}\right)\right] \tag{2.38}$$

$$t(y) = (1+y)^{-1/2}\left[(1+y)E\left(\sqrt{\frac{1-y}{1+y}}\right) - yK\left(\sqrt{\frac{1-y}{1+y}}\right)\right] \tag{2.39}$$

where K(r) and E(r) are complete elliptic integrals of the first and second kind, respectively.

It is clear that the model for injection is not complete. A rough calculation will show that at low biases thermionic emission is by far the dominant injection mechanism. However, as the temperature is lowered, J_{TIE} is greatly reduced and so is $p_{(x=0)}$. As the form of the tunnelling current used here is temperature independent, the model does not account for sufficient carrier injection below approx. 250 K. The inclusion of an ideality factor at low temperatures remedies this deficiency and physically implies a temperature dependence of the image charge. Indeed, the literature suggests an influence of temperature on the image force for both the tunnelling expression [103] and the thermionic emission expression [106]. It should also be noted that a temperature dependence arises for the tunnelling current by inclusion of higher orders of the electron distribution function, which is commonly approximated as a step function by setting T=0. Koehler et al. [91] demonstrated that this expansion of the model can include a moderate variation of current with temperature at high fields, but it is unlikely to be able to account for the currents at low biases and low temperatures.

Also, modifications to the above expressions have been suggested by Scott et al. in order to account for the hopping type injection process characteristic of metal/polymer contacts [98]. Furthermore, there is no continuum into which injection occurs. Instead the states are localised. In contrast to inorganic materials with rigid band offsets there is a distribution of energy sites into which injection can occur, which is due to the inherent disorder of conjugated polymers. This practically invalidates the concept of an effective electron mass, which is a further complication in the applicability of thermionic emission and tunnelling theory.

For constant temperature the field-dependent mobility takes the form [80, 82, 99-100,104, 110]

$$\mu_{(E)} = \mu_{(E=0)} \exp\left(\sqrt{\frac{E}{E_0}}\right) \tag{2.40}$$

The single carrier device model hence relies on three fitting parameters at constant temperature: the barrier to charge carrier injection; the mobility as the field tends to zero; and the field dependence of the mobility. No functional dependence of the fitting parameters on temperature is assumed so that the fitting procedure is designed to explore the whole parameter space. The temperature set in the device model merely controls the thermionic emission current at the anode. Previous measurements of the temperature dependence of the mobility in polymers through the time-of-flight technique [104, 111] and space charge limited currents [99, 100] yielded a functional dependence following

$$\mu_{(E=0)} = \mu_0 \exp(-\frac{\Delta}{k_B T}) \tag{2.41}$$

and

$$\frac{1}{\sqrt{E_0}} = B(\frac{1}{k_B T} - \frac{1}{k_B T_0}) \tag{2.42}$$

where μ_0, Δ, T_0 and B are material constants related to the morphology of the material and have been studied extensively in the context of the Gaussian Disorder Model [68, 80, 82, 110].

Neglecting the diffusion terms the equations are straightforward to solve numerically. For an initial value of the electric field at the anode the resulting steady state current density is found. The voltage is determined by integrating the electric field across the device.

The coupled non-linear differential equations were solved in chapter 5 of this thesis by standard first order numerical integration techniques, the simplest of which is Euler's method. The electric field, charge density, current and mobility are discretised. The requirements for number of lattice points increases with decreasing temperature and decreasing barrier height, as the field becomes less uniform when approaching the space charge limit. It was found that results were insensitive to the number of lattice points above 500 lattice points at room temperature and 5000 points at 100 K. In the steady state, the injected current is equal to the drift current, $J=ep\mu E$ at $x=0$, so from the

expressions for the injected current and an initial electric field value a charge carrier density at the interface is calculated. This value is then used to solve Poisson's equation for the next value of the electric field on the lattice, from which the charge carrier density one step on is calculated, taking into account the gradient of both the electric field and the mobility.

Rearranging the injection terms (2.30), the hole density at the interface is obtained as

$$p_{(x=0)} = \frac{J_{tu} + J_{TIE}}{eE\mu + \frac{AT^2}{n_0}} \tag{2.43}$$

Next, Poisson's equation is integrated up for the next lattice point using the Euler formalism

$$E(i+1) = E(i) + \Delta x \frac{e}{\varepsilon} p(i) \tag{2.44}$$

where i is the lattice index and Δx is the step size.

The continuity equation has to be written out to include the full spatial differentials of the mobility, field and hole density:

$$\frac{\partial J}{\partial x} = 0 = \frac{\partial (eEp\mu)}{\partial x} = e\left(p\mu \frac{\partial E}{\partial x} + E\mu \frac{\partial p}{\partial x} + pE \frac{\partial \mu}{\partial x} \right) \tag{2.45}$$

which can be rearranged, substituting Poisson's equation (2.27), in terms of the hole density gradient

$$\frac{\partial p}{\partial x} = -p^2 \frac{e}{\varepsilon} \left(\frac{1}{E} + \frac{1}{2\sqrt{EE_0}} \right) \tag{2.46}$$

The hole density can hence be integrated numerically following

$$p(i+1) = p(i) - \Delta x \frac{e}{\varepsilon} p^2(i) \left(\frac{1}{E(i)} + \frac{1}{2\sqrt{E_0 E(i)}} \right) \qquad (2.47)$$

The main steps of the routine are summarised in Fig. 2.18 in a block diagram.

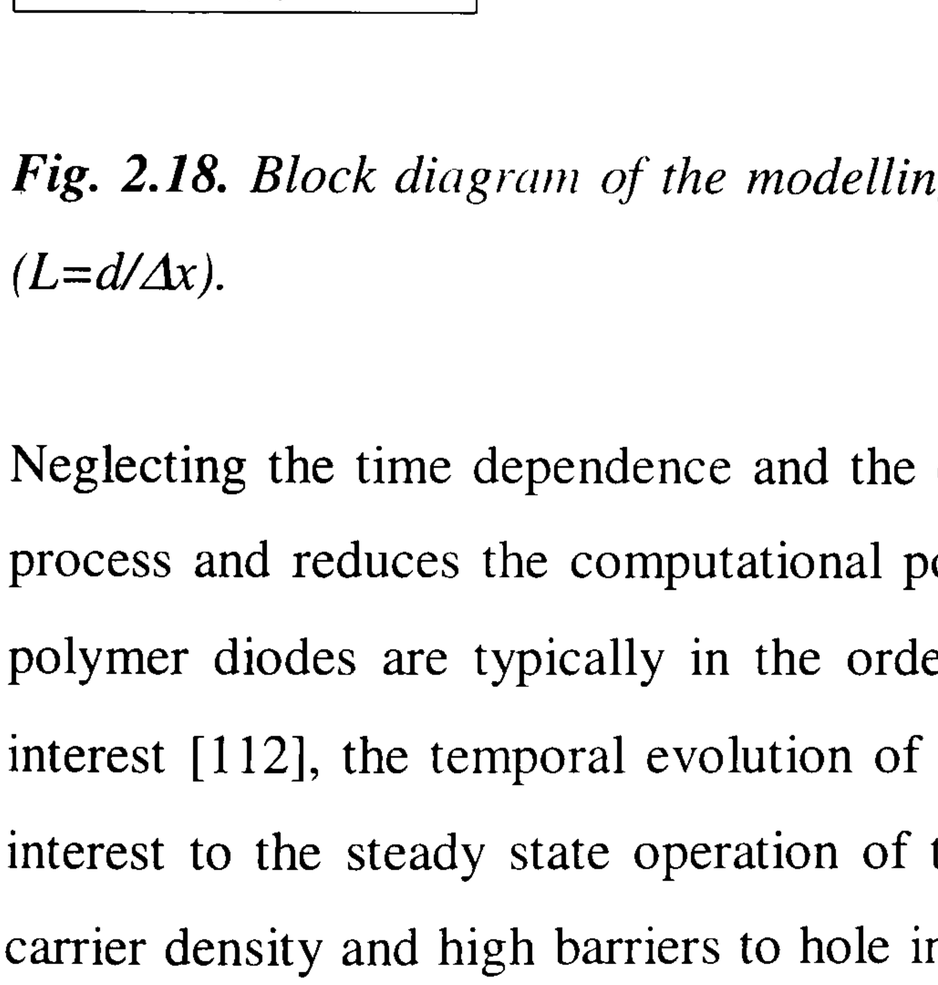

Fig. 2.18. *Block diagram of the modelling algorithm. L is the number of lattice points (L=d/Δx).*

Neglecting the time dependence and the diffusion current greatly simplifies the fitting process and reduces the computational power required. As the RC time constants for polymer diodes are typically in the order of 0.1 to 1 μs in the operation regime of interest [112], the temporal evolution of charge carrier and current density is of little interest to the steady state operation of the device. Due to the relatively low charge carrier density and high barriers to hole injection in the LED systems studied here, the diffusion current is not thought to play a major role in the transport through the polymer layer, but may become more important for low barriers to injection and at low temperatures.

2.7 Waveguiding effects in LEDs

Organic LEDs have opened up novel areas of physics not only in terms of injection and charge transport in a quasi one-dimensional density of states, but also in terms of optics

and thin film photonics. In contrast to conventional LEDs, which are point emitters with emission occurring from the p-n junction, organic LEDs are surface emitters and can potentially emit over large areas. However, the optically active materials are generally sandwiched between dielectrics and hence form an optical cavity of dimensions significantly below that of the wavelength of light. The relatively high refractive index of semiconductors, which is typically around 2 for polymers and can be in the excess of 3 for inorganic materials, gives rise to photon confinement in the form of waveguide modes in the device [113, 114]. Although for certain applications, such as optical communications, thin film waveguiding effects are highly desirable, in the context of organic LEDs they are detrimental to the device operation. As for most materials there is a significant overlap of absorption and emission, waveguided light can only travel a limited distance through the film before it is reabsorbed by the material, resulting in a reduction in the luminous efficiency.

The three main modes a photon can emit into in a polymer/metal structure are shown in Fig. 2.19.

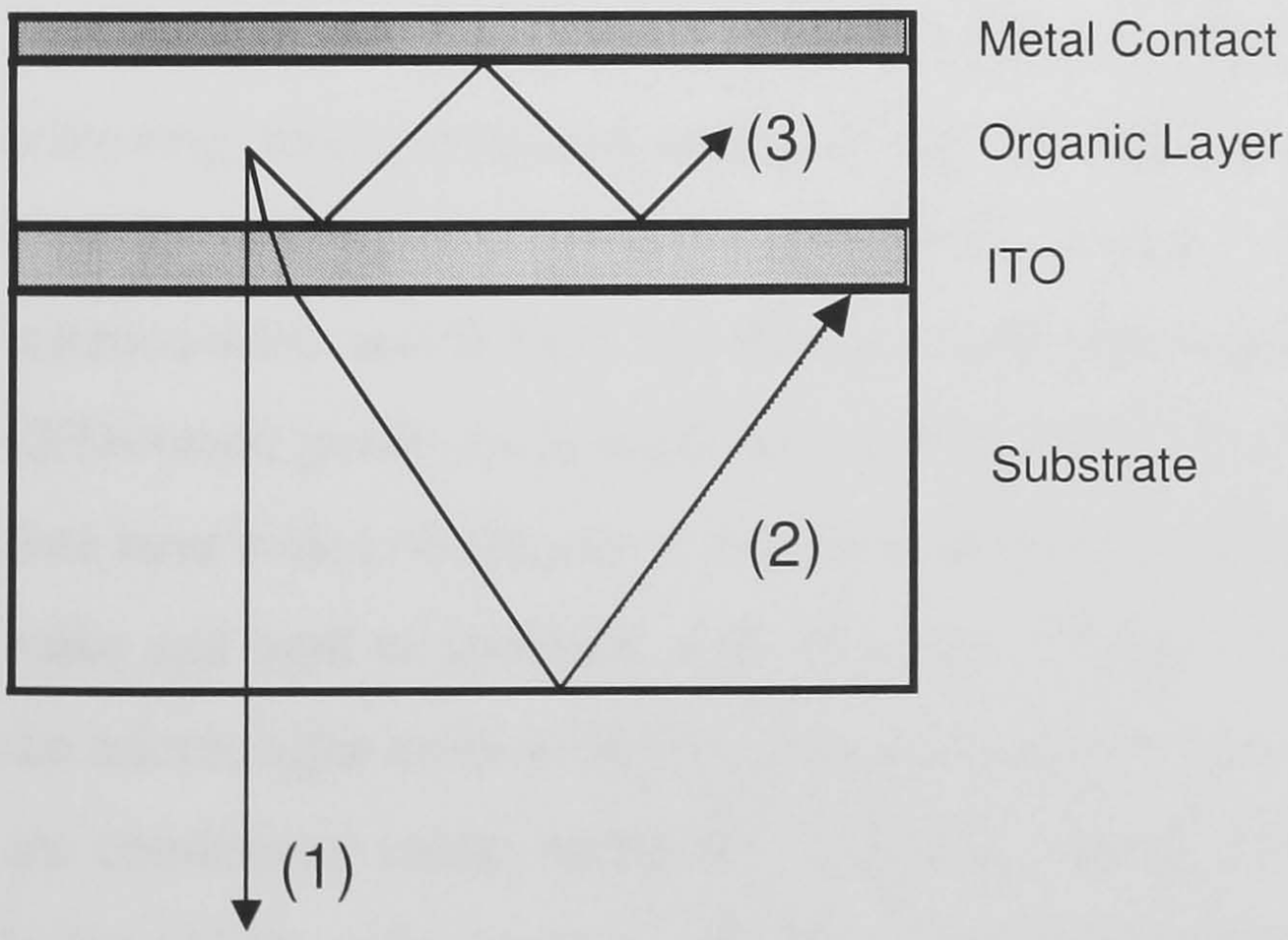

Fig. 2.19. *The three main modes an emitted photon can enter in an LED. (1) Direct emission in the forward direction; (2) Off-angle emission, giving rise to waveguiding in the substrate; (3) emission above the critical angle of the organic/ITO interface leading to waveguiding in the organic layer.*

Due to the overlap of the absorption and emission band of most organic materials, the mode (3) trapped in the organic layer is the most lossy and will result in a considerable reduction of the emission efficiency of this kind of photonic structure. There have been a number of attempts to establish the ratio between the number of photons generated within the film and the number of photons actually emitted. Initial estimates suggested that as little as $1/(2n^2)$ of the light generated is emitted from an LED [114]. In a more recent analysis, Kim et al. suggested that the actual out-coupling efficiency is a very sensitive function of dipole orientation as well as location within the LED structure and distance to the reflecting cathode [9]. They found that in ideal structures, which their LEDs are believed to be, the outcoupling efficiency can be as high as $1.2/n^2$ or 40 % for a refractive index of 1.8. However, even these numbers show that there is still considerable scope for improving the efficiency of LEDs, although the current peak device performances appear to have surpassed the theoretical limits imposed by the 1:3 spin selection rules (equation 2.1) [9-10, 71].

There are a number of methods of directly controlling the photonic properties, and hence the photon density of states, of an LED. The use of microcavities has attracted considerable attention over the past years, as they provide a very simple way of achieving much enhanced colour purity as well as colour tuneability in broad band organic emitters [115-120]. Standard device structures are basically planar microcavities, and it has been demonstrated that angular dispersion effects observed in LEDs result purely from weak microcavity effects [121]. Most microcavity structures to date have relied on the use of dielectric mirrors or Bragg stacks, which are expensive to make and hard to combine with injecting contacts. Although the most striking uses of the microscopic control of the photon density of states through the use of microcavities are continuous colour tunability [118] and the possibility of achieving low threshold lasing [117], comparatively efficient organic microcavity LEDs were not demonstrated until very recently [120]. These novel device structures employ alternating layers of differently doped conducting polymers, which provide sufficient refractive index contrast to act as a Bragg reflector. However, as the physical structure of these devices is rather different to that of conventional devices, it is hard to determine whether planar microcavities can actually lead to a reduction in lossy waveguide modes in the device and hence an overall increase in the external efficiency.

A new approach in the context of organic LEDs to modifying the photonic properties of a thin polymer/metal waveguide is the use of lateral microstructure by imposing a periodic corrugation on the optically active area. This technique has been used with great success in both organic [122-124] and inorganic [125] distributed feedback lasers where the gain is achieved in the plane of the film and stimulated emission is scattered out into the forward direction. In the context of organic LEDs this microstructure allows a novel control of spontaneous rather than stimulated emission.

The use of periodic microstructure in LEDs as a way of reducing the loss through waveguide modes in the organic layer is conceivable in two ways. Firstly, as drawn schematically in Fig. 2.20, waveguide modes can be blocked by imposing a corrugation with a period of half of the wavelength of the guided mode. Such a technique has been employed previously in inorganic materials and has been shown to lead to an increase in light extraction efficiency [126]. However, to date this concept has not been applied to electrically driven LED structures. An alternative approach is to use a periodic corrugation with a period equal to the wavelength of the trapped light to Bragg-scatter the mode out of the plane of the film into the forward direction as seen in Fig. 2.21. This technique will be employed in chapter 8 to control the emission properties of LEDs and increase the external emission efficiency.

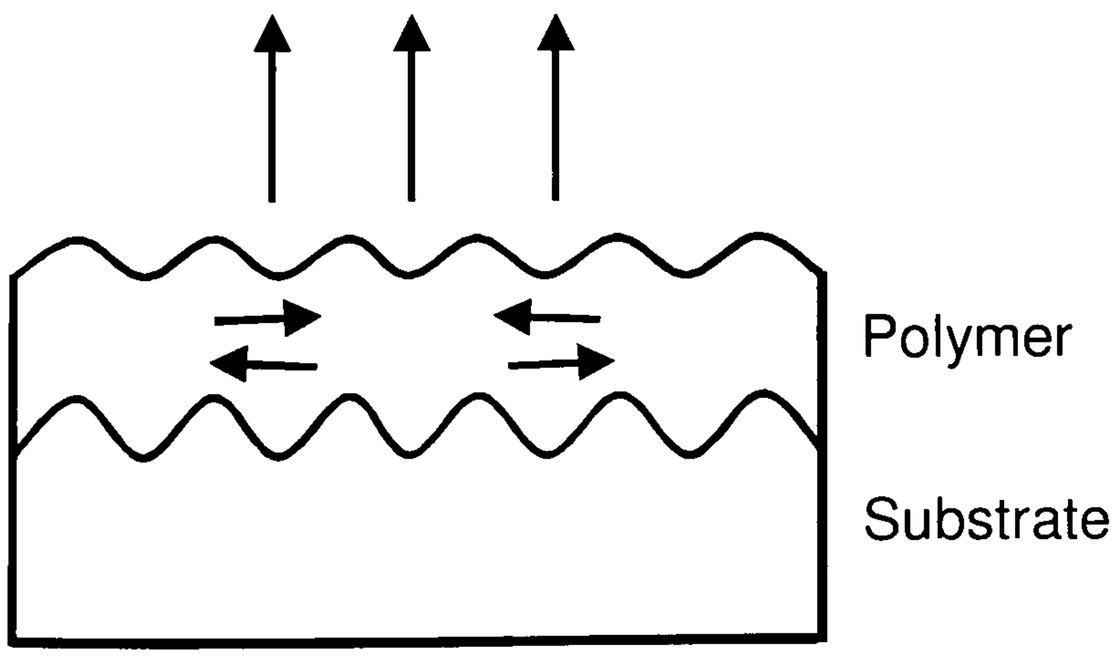

Fig. 2.20. *Blocking of waveguide modes in the organic film by a corrugation of period half the wavelength of the waveguide mode.*

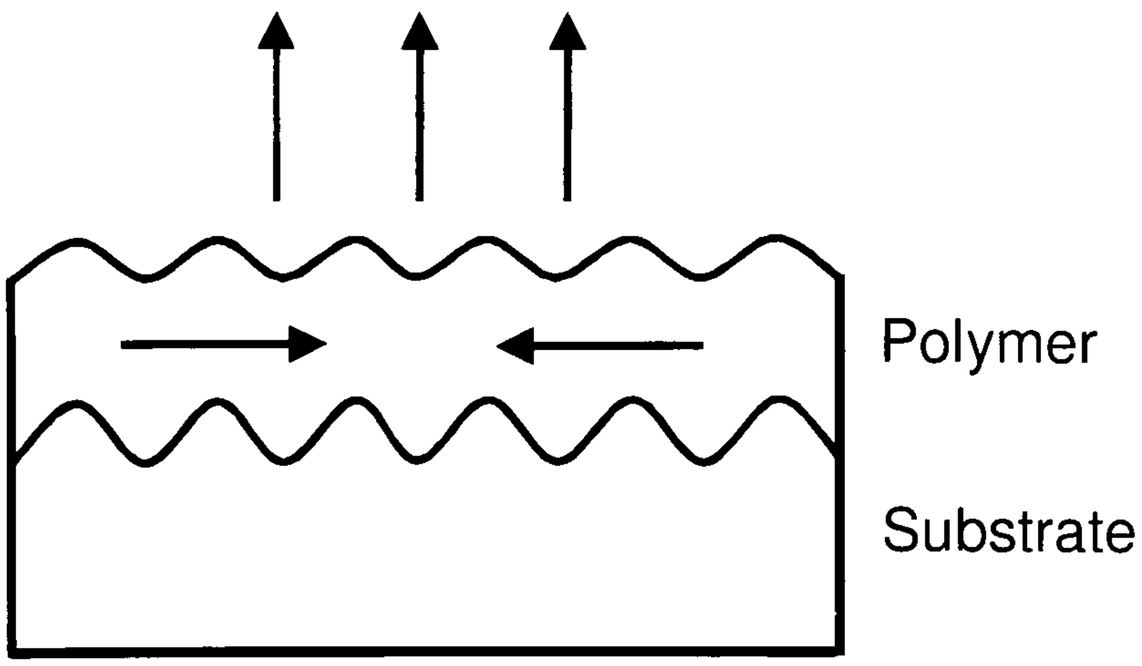

Fig. 2.21. *Scattering out of lateral waveguide modes in the organic film into the forward direction. The period of the grating is ideally equal to the wavelength of the waveguide mode.*

The basic processes of light scattering are shown in Fig. 2.22. Scattering off a single scattering centre can be thought of as absorption and re-emission of a photon. However, incident unpolarised light propagating in the z-direction will scatter into light propagating in the x-direction with polarisation in the y-direction and light propagating in the y-direction with polarisation in the x-direction. An ordered array of scattering centres separated by a distance d gives rise to constructive interference of the scattered wavefronts provided the angles of incidence and emission are identical. This condition can be written in terms of the Bragg condition as

$$2d\sin(\theta)=N\lambda \tag{2.48}$$

where θ is the angle of incidence and N is the order of the scattered peak.

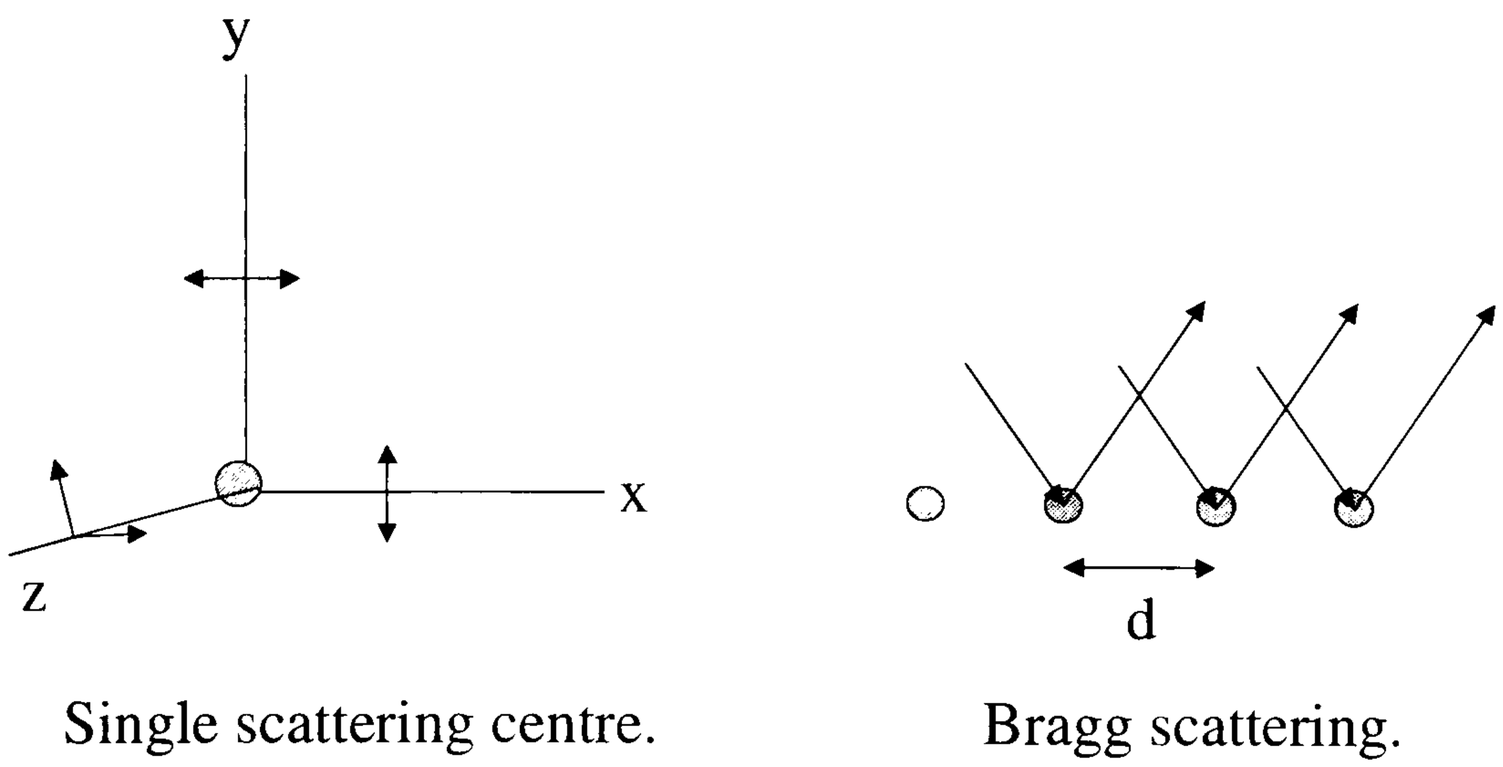

Single scattering centre. Bragg scattering.

Fig. 2.22. *Scattering of unpolarised light on a scattering centre re-emitting light polarised in the x and y direction. A regular array of scattering centres gives rise to constructive interference of the scattered wavefronts for equal angles of incidence and emission, the Bragg-scattering condition.*

Emissive species embedded in the emissive layer of an LED structure emit their energy into the available modes of the structure. These modes are primarily radiative modes, which produce useful radiation and trapped guided modes. Guided modes may be in the form of waveguide modes or surface plasmon polariton modes associated with the metal contacts. Emissive species may also lose their energy through non-radiative decay routes, such as through the generation of phonons. The different radiative modes are characterised by their frequency and in-plane wavevector. Modes having in-plane wavevectors less than the free space photons of the same frequency may escape the LED structure and are responsible for the useful radiation from planar LEDs. Modes with higher wavevectors are not able to radiate into free space, and are thus trapped, or waveguided, in one (or a number) of the layers making up the LED. Although the exact contribution of these modes is currently still a matter of dispute, there is strong experimental and theoretical evidence that the contribution of these modes to the radiative emission in LEDs lies above 50 % [9, 127].

Through Bragg-scattering a microstructured corrugation imposed on the emitting layer may change the in-plane wavevector of guided modes, as shown in Fig. 2.23. A mode with the free space wavevector $\mathbf{k_0}$ and an in-plane wavevector $\mathbf{k_g}$ propagates through the polymer film with an angle of propagation θ. The thickness of the organic layer is

labelled *t*. The presence of a periodic corrugation with a Bragg vector **G** results in the mode being scattered into the forward direction. The external angle of detection is labelled β. The vectoral nature of the Bragg-scattering process also results in a direct control of the polarisation state of the emitted radiation.

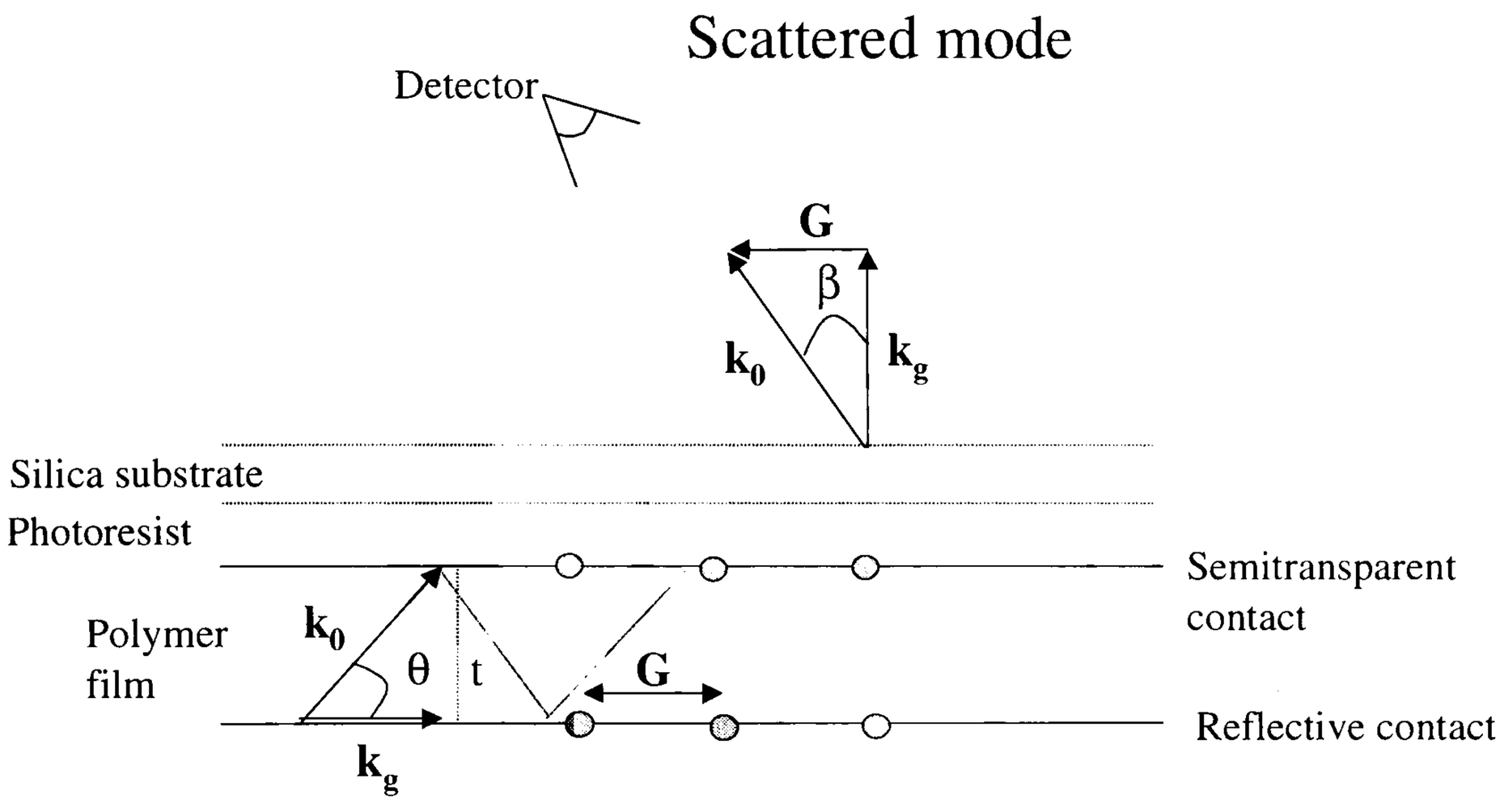

Fig. 2.23. *Propagation of waveguide modes in the organic film of the LED. The photoresist Bragg grating, which modulates the polymer film, allows scattering into the forward direction. The angle of emission β is determined experimentally. The internal angle θ is related to the refractive index of the organic.*

In reciprocal space, the wavevector of the emitted light, $\mathbf{k_0}$, is related to the in-plane wavevector of the guided mode $\mathbf{k_g}$, and the angle of emission β by

$$k_0 \sin(\beta) = \pm k_g \pm NG \tag{2.49}$$

This scattering condition gives rise to an angular dependence of the wavelength of the scattered peak characteristic of Bragg-scattering. As there are four possible combinations of adding the in-plane wavevector to the Bragg vector, the angular dispersion of the scattered peak results in four branches which are generally plotted in a characteristic X-shape as seen in Fig. 2.24.

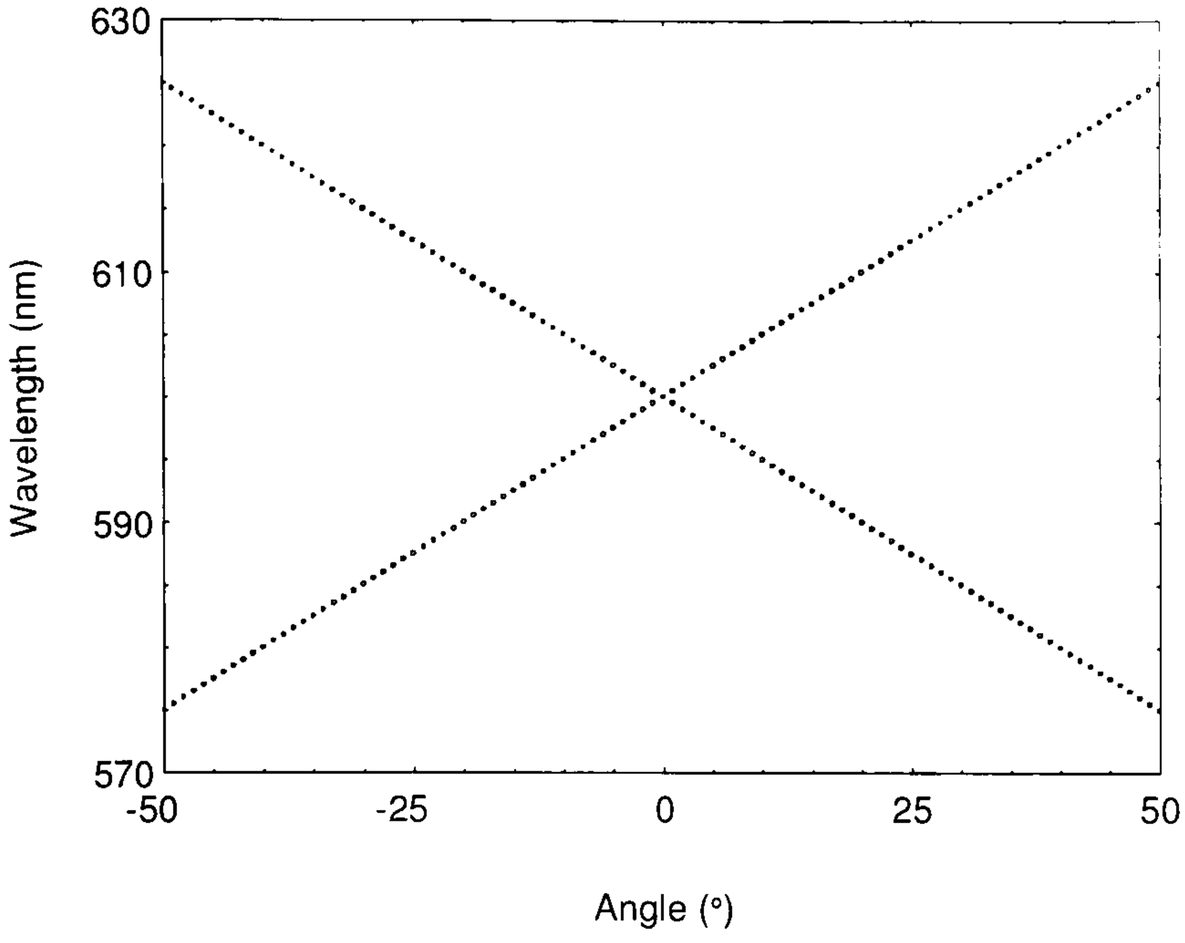

Fig. 2.24. *Plot of peak wavelength against angle of detection. A scattered peak splits into two peaks as the angle of detection is moved off-normal.*

The above splitting of the peak in real space can be converted to a dispersion diagram using equation (2.49), which is plotted in Fig. 2.25.

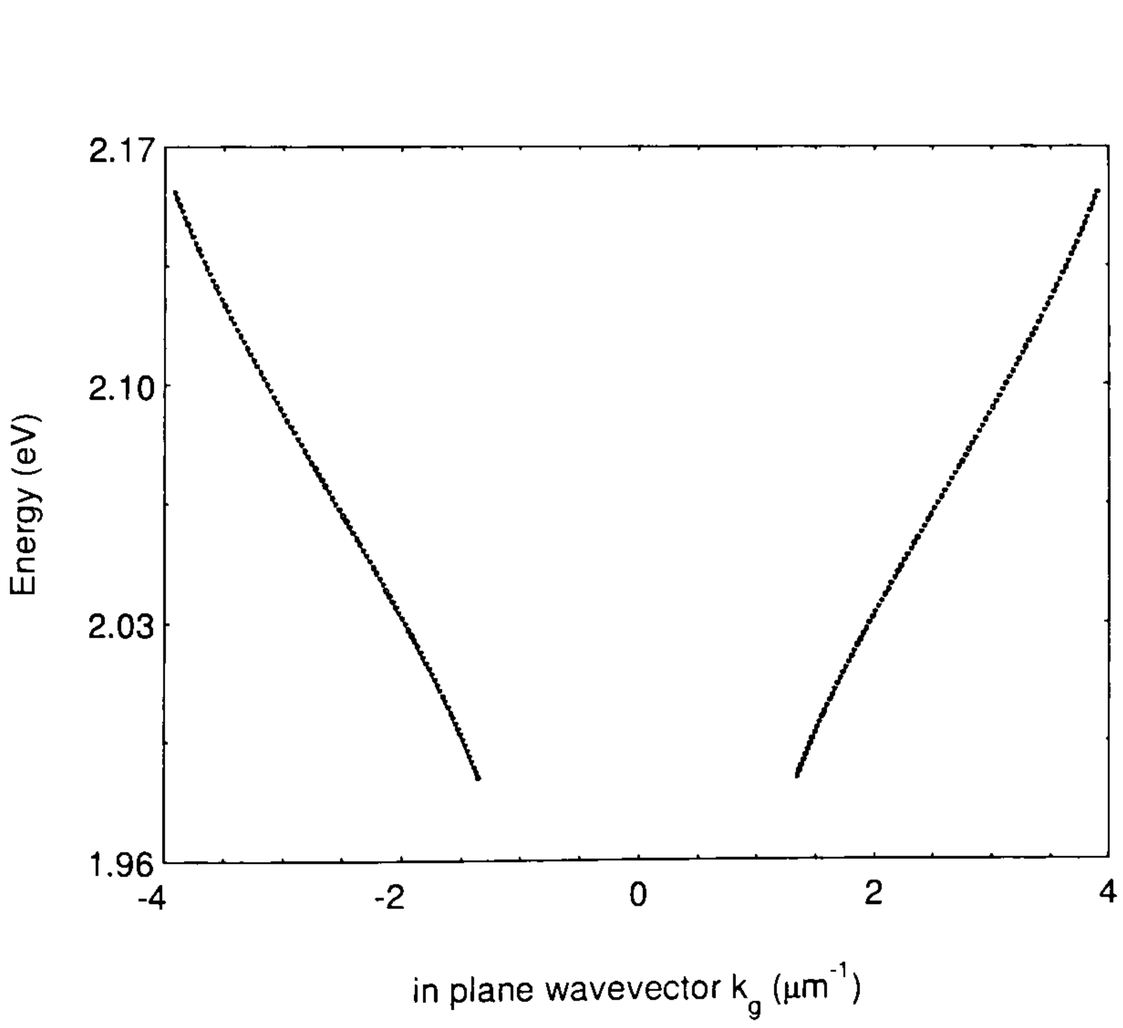

Fig. 2.25. *The same data as in Fig. 2.24 shown in a dispersion diagram. The peak splitting results from scattering either parallel or antiparallel to the grating vector.*

As the internal angle of propagation θ is related to the refractive index of the film through the free space and in-plane wavevectors by

$$k_g = k_0 \, n \, \sin(\theta) \qquad (2.50)$$

a dispersion diagram as in Fig. 2.25 can be used to determine the refractive index, given that the modestructure is known. This has been done successfully for films of MEH-PPV on metal covered substrates [128]. Within the plane wave approach the waveguide modes obey the following condition [129]

$$2\, n\, t\, k_0\, cos(\theta) = 2\, N\, \pi + \phi_1 + \phi_2 \qquad (2.51)$$

where ϕ_1 and ϕ_2 are the changes of the phase on reflection from the polymer/air and polymer/metal interfaces, respectively. In a metal/polymer structure, the lowest energy mode has been calculated to be a zero order transverse electric mode [130] for which $\phi_2=\pi$. The phase shift ϕ_1 is hence determined by

$$\phi_1 = 2\tan^{-1}\left[\frac{\sqrt{\sin^2(\theta) - n^{-2}}}{\cos(\theta)}\right] \qquad (2.52)$$

As the refractive index of MEH-PPV decreases from approx. 2.05 at 500 nm to 1.8 at 800 nm [131], the above relationships demonstrate that the dispersion will strongly influence the Bragg-scattering process.

Finally, it should be noted that equation (2.51) predicts that the free space wavevector of the scattered peak will decrease with increasing film thickness. This means that longer wavelength modes will be scattered out of thicker films. The above equations also impose boundaries on the validity of the scattering condition and result in a cut-off thickness of the organic layer, below which waveguiding will be suppressed.

Although it is more complicated to derive analytically, the scattering condition is also subject to sufficient index contrast of the corrugation with respect to the emitting layer. Previous studies on microstructured PEDOT layers [132] showed that a corrugated polymer layer beneath the optically active organic layer does not provide the level of contrast achieved with thin metal films, which appear to be necessary for fulfilling the Bragg-scattering condition.

References

[1] L. J. Rothberg, M. Yan, F. Papadimitrakopoulos, M. E. Galvin, E. W. Kwock, and T. M. Miller, Synth. Met. **80,** 41 (1996)

[2] N. T. Harrison, G. R. Hayes, R. T. Phillips, and R. H. Friend, Phys. Rev. Lett. **77**, 1881 (1996)

[3] A. J. Heeger, S. Kivelson, J. R. Schrieffer, and W. P. Su, Rev. Mod. Phys. **60**, 781 (1988)

[4] M. Pope and C. E. Swenberg, Electronic Processes in Organic Crystals, Oxford University Press (1982)

[5] Z. G. Soos, M. H. Hennessy, and D. Mukhopadhyay in : N. S. Sariciftci (Ed.), Primary Photoexcitations in Conjugated Polymers: Molecular Exciton versus Semiconductor Band Model, World Scientific (1997)

[6] P.W. Atkins, Molecular Quantum Mechanics, 2nd Edition (Oxford University Press, Oxford, 1983)

[7]Y. V. Romanovskii, A. Gerhard, B. Schweitzer, U. Scherf, R. I. Personov, and H. Bassler, Phys. Rev. Lett. **84,** 1027 (2000)

[8] Z. Shuai, D. Beljonne, R. J. Silbey, and J. L. Bredas, Phys. Rev. Lett. **84,** 131 (2000)

[9] J. S. Kim, P. K. H. Ho, N. C. Greenham, and R. H. Friend, J. Appl. Phys. **88**, 1073 (2000)

[10] P. K. H. Ho, J. S. Kim, J. H. Burroughes, H. Becker, S. F. Y. Li, T. M. Brown, F. Cacialli, and R. H. Friend, Nature **404,** 481 (2000)

[11] M. A. Baldo, D. F. Obrien, Y. You, A. Shoustikov, S. Sibley, M. E. Thompson, and S. R. Forrest, Nature **395,** 151 (1998)

[12] S. Dailey, PhD Thesis, University of Durham (1998)

[13] P. W. Atkins, Physical Chemistry, 3rd Edition (Oxford University Press), 1976

[14] V. Sundstrom, T. Gillbro, R. A. Gadonas, and A. Piskarskas, J. Chem. Phys. **89**, 2754 (1988)

[15] C. E. Swenberg, N. E. Geacintov, and M. Pope, Biophys. J. **16**, 1447 (1976)

[16] A. J. Campillo, R. C. Hyer, T. G. Monger, W. W. Parson, and S. L. Shapiro, Proc. Natl. Acad. Sci. U. S. A. **74**, 1997 (1977)

[17] G. J. Denton, N. Tessler, N. T. Harrison, and R. H. Friend, Phys. Rev. Lett .**78,** 733 (1997)

[18] D. D. C. Bradley, M. Grell, X. Long, H. Mellor, and A. Grice, SPIE **3145**. 254 (1998)

[19] I. D. W. Samuel, G. Rumbles, and R. H. Friend, in : N. S. Sariciftci (Ed.). Primary Photoexcitations in Conjugated Polymers: Molecular Exciton versus Semiconductor Band Model, World Scientific (1997)

[20] S. A. Jenekhe and J. A. Osaheni, Science **265,** 765 (1994)

[21] I. D. W. Samuel, G. Rumbles, and C. J. Collison, Phys. Rev. B **52,** 11573 (1995)

[22] I. D. W. Samuel, G. Rumbles, C. J. Collison, S. C. Moratti, and A. B. Holmes, Chem. Phys. **227,** 75 (1998)

[23] M. Yan, L. J. Rothberg, E. W. Kwock, and T. M. Miller, Phys. Rev. Lett. **75,** 1992 (1995)

[24] M. Yan, L. J. Rothberg, F. Papadimitrakopoulos, M. E. Galvin, and T. M. Miller, Phys. Rev. Lett. **72,** 1104 (1994)

[25] H. Bassler and B. Schweitzer, Acc. Chem. Res. **32,** 173 (1999)

[26] D. Hertel, B. Schweitzer, H. Bassler, H. Tillmann, and H. H. Horhold, Chem. Phys. **227,** 179 (1998)

[27] E. M. Conwell and H. A. Mizes, Phys. Rev. B **51,** 6953 (1995)

[28] E. M. Conwell, Synth. Metals **85,** 995 (1997)

[29] E. M. Conwell, Phys. Rev. B **57,** 14200 (1998)

[30] S. Tretiak, A. Saxena, R. L. Martin, and A. R. Bishop, J. Phys. Chem. B **104**, 7029 (2000)

[31] D. A. Tomalia, Adv. Mater. **6**, 529 (1994)

[32] A. W. Bosman, H. M. Janssen, and E. W. Meijer, Chem. Rev. **99**, 1665 (1999)

[33] R. Kopelman, M. Shortreed, Z. Y. Shi, W. H. Tan, Z. F. Xu, J. S. Moore, A. BarHaim, and J. Klafter, Phys. Rev. Lett. **78,** 1239 (1997)

[34] J. M. J. Frechet, Science **263,** 1710 (1994)

[35] S. K. Deb, T. M. Maddux, and L. P. Yu, J. Am. Chem. Soc. **119,** 9079 (1997)

[36] J. N. G. Pillow, M. Halim, J. M. Lupton, P. L. Burn, and I. D. W. Samuel, Macromolecules 32, 5985 (1999)

[37] L. L. Miller, R. G. Duan, D. C. Tully, and D. A. Tomalia, J. Am. Chem. Soc. **119,** 1005 (1997)

[38] V. V. Narayanan and G. R. Newkome, Top. Curr. Chem. **197,** 19 (1998)

[39] A. D. Schluter, Top. Cur. Chem. **197,** 165 (1998)

[40] D. Gust, Nature **386**, 21 (1997)

[41] D. L. Jiang, and T. Aida, Nature **388**, 454 (1997)

[42] S. Mukamel, Nature **388**, 425 (1997)

[43] J. S. Moore, Acc. Chem. Res. **30,** 402 (1997)

[44] J. Klafter, Gordon Conference on Electronic Excitations in Organic Materials, Rhode Island (2000)

[45] J. F. G. A. Jansen, E. M. M. DeBrabandderVandenberg, E. W. Meijer, Science **266**, 1226 (1994)

[46] P. J. Dandliker, F. Diederich, M. Gross, C. B. Knobler, A. Louati, and E. M. Sanford, Angew. Chem.-Int. Ed. **33,** 1739 (1994)

[47] J. Issberner, R. Moors, and F. Vogtle, Angew. Chem.-Int. Ed. **33,** 2413 (1995)

[48] X. T. Tao, Y. D. Zhang, T. Wada, H. Sasabe, H. Suzuki, T. Watanabe, S. Miyata, and I. P. Riken, Adv. Mater. **10,** 226 (1998)

[49] Y. Kuwabara, H. Ogawa, H. Inada, N. Noma, and Y. Shirota, Adv. Mater. **6,** 677 (1994)

[50] Y. Shirota, Y. Kuwabara, H. Inada, T. Wakimoto, H. Nakada, Y. Yonemoto, S. Kawami, and K. Imai, Appl. Phys. Lett. **65,** 807 (1994)

[51] Y. Shirota, Y. Kuwabara, D. Okuda, R. Okuda, H. Ogawa, H. Inada, T. Wakimoto, H. Nakada, Y. Yonemoto, S. Kawami, and K. Imai, J. Lum. **72,** 985 (1997)

[52] M. Thelakkat, R. Fink, F. Haubner, and H. W. Schmidt, Macromol. Symp. **125,** 157 (1998)

[53] J. Bettenhausen and P. Strohriegl, Adv. Mater. **8**, 507 (1996)

[54] M. Halim, J. N. G. Pillow, I. D. W. Samuel, and P. L. Burn, Adv. Mater. 11, 371 (1999)

[55] J. M. Lupton, L. R. Hemingway, I. D. W. Samuel, and P. L. Burn, J. Mat. Chem. 10, 867 (2000)

[56] M. Halim, I. D. W. Samuel, J. N. G. Pillow, and P. L Burn, Synth. Met. **102**, 1113 (1999)

[57] P. W. Wang, Y. J. Liu, C. Devadoss, P. Bharathi, and J. S. Moore, Adv. Mater. **8,** 237 (1996)

[58] P. W. Atkins, Molecular Quantum Mechanics, 3rd Edition, Chapter 9, Oxford University Press (1997)

[59] J. L. Bredas, J. Cornil, D. Beljonne, D. dosSantos, and Z. G. Shuai, Acc. Chem. Res. **32,** 267 (1999)

[60] A. Kohler, D. A. dosSantos, D. Beljonne, Z. Shuai, J. L. Bredas, A. B. Holmes, A. Kraus, K. Mullen, and R. H. Friend, Nature **392,** 903 (1998)

[61] M. Rohlfing and S. G. Louie, Phys. Rev. Lett. **82,** 1959 (1999)

[62] S. Mukamel, S. Tretiak, T. Wagersreiter, and V. Chernyak, Science **277,** 781 (1997)

[63] E. Y. Poliakov, V. Chernyak, S. Tretiak, and S. Mukamel, J. Chem. Phys. **110,** 8161 (1999)

[64] S. Tretiak, V. Chernyak, and S. Mukamel, J. Phys. Chem. B **102,** 3310 (1998)

[65] G. C. Bazan, W. J. Oldham, R. J. Lachicotte, S. Tretiak, V. Chernyak, and S. Mukamel, J. Am. Chem. Soc. **120,** 9188 (1998)

[66] S. Tretiak, PhD Thesis, University of Rochester (1998) (see also http://markov.chem.rochester.edu/serg/Publications)

[67] W. Kohn, Rev. Mod. Phys. **71**, 1253 (1999)

[68] Z. G. Yu, D. L. Smith, A. Saxena, R. L. Martin, and A. R. Bishop, Phys. Rev. Lett. **84**, 721 (2000)

[69] L. Bozano, S. A. Carter, J. C. Scott, G. G. Malliaras, and P. J. Brock, Appl. Phys. Lett. **74**, 1132 (1999)

[70] I. H. Campbell, D. L. Smith, C. J. Neef, and J. P. Ferraris, Appl. Phys. Lett. **74**, 2809 (1999)

[71] Y. Cao, I. D. Parker, G. Yu, C. Zhang, and A. J. Heeger, Nature **397,** 414 (1999)

[72] S. Karg, M. Meier, and W. Riess, J. Appl. Phys. **82,** 1951 (1997)

[73] J. Scherbel, P. H. Nguyen, G. Paasch, W. Brutting, and M. Schwoerer, J. Appl. Phys. **83,** 5045 (1998)

[74] N. Tessler, N. T. Harrison, and R. H. Friend, Adv. Mat. **10,** 64 (1998)

[75] I. H. Campbell, D. L. Smith, C. J. Neef, and J. P. Ferraris, Appl. Phys. Lett. **75,** 841 (1999)

[76] K. S. Hisao Ishii, SPIE **3148,** 213 (1997)

[77] N. Johansson, F. Cacialli, K. Z. Xing, G. Beamson, D. T. Clark, R. H. Friend, and W. R. Salaneck, Synth. Met. **92,** 207 (1998)

[78] W. R. Salaneck and M. Logdlund, Polym. Adv. Tech. **9,** 419 (1998)

[79] J. M. Lupton, V. R. Nikitenko, I. D. W. Samuel, and H. Bässler, J. Appl. Phys. (in press)

[80] H. Bässler, Phys. Status Solidi B **175,** 15 (1993)

[81] J. Frenkel, Phys. Rev **54**, 647 (1938)

[82] D. H. Dunlap, P. E. Parris, and V. M. Kenkre, Phys. Rev. Lett. **77,** 542 (1996)

[83] P. S. Davids, I. H. Campbell, and D. L. Smith, J. Appl. Phys. **82,** 6319 (1997)

[84] P. S. Davids, S. M. Kogan, I. D. Parker, and D. L. Smith, Appl. Phys. Lett. **69,** 2270 (1996)

[85] I. H. Campbell, P. S. Davids, D. L. Smith, N. N. Barashkov, and J. P. Ferraris, Appl. Phys. Lett. **72,** 1863 (1998)

[86] B. K. Crone, P. S. Davids, I. H. Campbell, and D. L. Smith, J. Appl. Phys. **84**, 833 (1998)

[87] E. M. Conwell and M. W. Wu, Appl. Phys. Lett. **70,** 1867 (1997)

[88] I. D. Parker, J. Appl. Phys. **75,** 1656 (1994)

[89] A. J. Heeger, I. D. Parker, and Y. Yang, Synth. Met. **67,** 23 (1994)

[90] H. Vestweber, J. Pommerehne, R. Sander, R. F. Mahrt, A. Greiner, W. Heitz, and H. Bässler, Synth. Met. **68,** 263 (1995)

[91] M. Koehler and I. A. Hummelgen, Appl. Phys. Lett. **70,** 3254 (1997)

[92] Y. Kawabe, G. E. Jabbour, S. E. Shaheen, B. Kippelen, and N. Peyghambarian, Appl. Phys. Lett. **71,** 1290 (1997)

[93] I. H. Campbell, T. W. Hagler, D. L. Smith, and J. P. Ferraris, Phys. Rev. Lett. **76,** 1900 (1996)

[94] M. Gross, K. Meerholz, and C. Brauchle, Synth. Met. **102**, 1147 (1999)

[95] M. Fahlman, O. Lhost, F. Meyers, J. L. Bredas, S. C. Graham, R. H. Friend, P. L. Burn, A. B. Holmes, K. Kaeriyama, Y. Sonoda, M. Logdlund, S. Stafstrom, and W. R. Salaneck, Synth. Met. **55,** 263 (1993)

[96] W. Brutting, E. Buchwald, G. Egerer, M. Meier, K. Zuleg, M. Schwoerer, Synth. Met. **84**, 677 (1997)

[97] A. J. Campbell, D. D. C. Bradley, and D. G. Lidzey, J. Appl. Phys. **82,** 6326 (1997)

[98] J. C. Scott, and G. G. Malliaras, Chem. Phys. Lett. **299**, 115 (1999)

[99] P. W. M. Blom, M. J. M. Dejong, and J. J. M. Vleggaar, Appl. Phys. Lett. **68,** 3308 (1996)

[100] P. W. M. Blom, M. J. M. deJong, and M. G. van Munster, Phys. Rev. B **55,** R656 (1997)

[101] J. C. Scott, S. Karg, and S. A. Carter, J. Appl. Phys. **82,** 1454 (1997)

[102] I. H. Campbell, D. L. Smith, and J. P. Ferraris, Appl. Phys. Lett. **66,** 3030 (1995)

[103] M.A. Lampert, P. Mark, Current injection in solids, Academic Press 1970

[104] D. M. Pai, J. Chem. Phys. **52,** 2285 (1970)

[105] D. Scharfetter, Gummel, HK, IEEE Transactions on electron devices **16**, 64 (1969)

[106] E. H. Rhoderick, R. H. Williams, Metal-Semiconductor Contacts, Oxford University Press 1988

[107] E. Tutis, M. N. Bussac, and L. Zuppiroli, Appl. Phys. Lett. **75,** 3880 (1999)

[108] W. Rehwald and H. G. Kiess in: Conjugated Conducting Polymers, H. G. Kiess (ed.), Springer (1992)

[109] H. Kleinert, Path Integrals in Quantum Mechanics, Statistics and Polymer Physics, World Scientific 1990

[110] Yu. N. Gartstein and E. M. Conwell, Chem. Phys. Lett. **245**, 351 (1995)

[111] E. Lebedev, Th. Dittrich, V. Petrova-Koch, S. Karg, and W. Brutting, Appl. Phys. Lett. **71**, 2686 (1997)

[112] N. C. Greenham, Electroluminescence in Conjugated Polymers, PhD Thesis, Cambridge University 1995, p. 162

[113] D. Wood, Optoelectronic semiconductor devices (Prentice Hall, London, 1997)

[114] N. C. Greenham, R. H. Friend, and D. D. C. Bradley, Adv. Mater. **6,** 491 (1994)

[115] A. Dodabalapur, L. J. Rothberg, R. H. Jordan, T. M. Miller, R. E. Slusher, and J. M. Phillips, J. Appl. Phys. **80**, 6954 (1996)

[116] T. Tsutsui, N. Takada, S. Saito and E. Ogino, Appl. Phys. Lett. **65**, 1868 (1994)

[117] N. Tessler, G. J. Denton, and R. H. Friend, Nature **382**, 695 (1996)

[118] H. Becker, R. H. Friend, and T. D. Wilkinson, Appl. Phys. Lett. **72**, 1266 (1998)

[119] D. G. Lidzey, D. D. C. Bradley, Chem. Phys. Lett. (1996)

[120] P. K. H. Ho, D. S. Thomas, R. H. Friend, and N. Tessler, Science **285,** 233-236 (1999)

[121] V. Bulovic, V. B. Khalfin, G. Gu, P. E. Burrows, D. Z. Garbuzov, and S. R. Forrest, Phys. Rev. B **58,** 3730 (1998)

[122] M. Berggren, A. Dodabalapur, R. E. Slucher, A. Timko, and O. Nalamasu, Appl. Phys. Lett. **72**, 26 (1998)

[123] M. D. McGehee, M. A. DiazGarcia, F. Hide, R. Gupta, E. K. Miller, D. Moses, and A. J. Heeger, Appl. Phys. Lett. **72,** 1536 (1998)

[124] C. Kallinger, M. Hilmer, A. Haugeneder, M. Perner, W. Spirkl, U. Lemmer, J. Feldmann, U. Scherf, K. Müllen, A. Gombert, and V. Wittwer, Adv. Mater. **10,** 920 (1998)

[125] H. Kogelnik, and C. V. Shank, Appl. Phys. Lett. **18**, 152 (1971)

[126] M. Boroditsky, T. F. Krauss, R. Coccioli, R. Vrijen, R. Bhat, and E. Yablonovitch, Appl. Phys. Lett. **75,** 1036 (1999)

[127] J. A. E. Wasey and W. L. Barnes, J. Mod. Opt. **47**, 725 (2000)

[128] A. N. Safonov, M. Jory, B. J. Matterson, J. M. Lupton, M. G. Salt, J. A. E. Wasey, W. L. Barnes, and I. D. W. Samuel, Synth. Met. **116**, 145 (2001)

[129] P. K. Tien, Appl. Opt. 10, 2395 (1971)

[130] S. C. Kitson, W. L. Barnes, and J. R. Sambles, IEEE Photon. Tech. Lett. **8**, 1662 (1996)

[131] A. Boudrioua, P. A. Hobson, B. J. Matterson, I. D. W. Samuel and W. L. Barnes, Synth. Met. **111**, 545 (2000)

[132] T. Granlund, T. Nyberg, L. S. Roman, M. Svensson, adn O. Inganas, Adv. Mater. **12**, 269 (2000)

3.

Experimental details

3.1 Introduction

In this chapter the basic experimental procedures used for characterising new materials and device structures will be described. One of the key advantages of organic electroluminescent materials is their ease in processing compared to the epitaxial techniques required for inorganic materials. In the simplest case, all that is required to achieve organic EL is to spin-coat a polymer onto a transparent anode such as indium tin oxide (ITO), which is widely used in LCD technology. The top electrode is generally deposited by thermal evaporation of a metal under vacuum. However, it has been demonstrated and was also observed by the author that solution processable metallic materials such as silver paint or silver electrolytes [1] are sufficient to form the electron injecting contact on precursor materials such as PPV. It was found by the author, that stable EL is observed from MEH-PPV immersed in liquid nitrogen by simply contacting the polymer, spun on an ITO substrate, with a strip of aluminium foil.

The preparation of samples and the standard optical characterisation will be outlined briefly, followed by the preparation and testing of devices. Finally, the time-of-flight technique, which is used to determine transit times and mobilities, will be described.

The materials used throughout this thesis are either poly[2-methoxy, 5-(2'-ethyl-hexyloxy)-1,4-phenylene vinylene] (MEH-PPV), which was obtained from Covion GmbH, or conjugated dendrimers, which were synthesised in the Dyson Perrins Laboratory at Oxford University. A hole injecting layer of poly(3,4-ethylenedioxythiophene)/poly(styrene) (PEDT/PSS, also referred to as PEDOT), which was obtained from Bayer, was used in a number of devices. The structures of MEH-PPV and PEDOT are shown in Fig. 3.1.

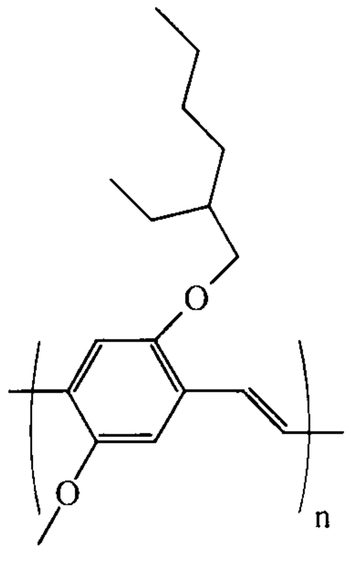

MEH-PPV

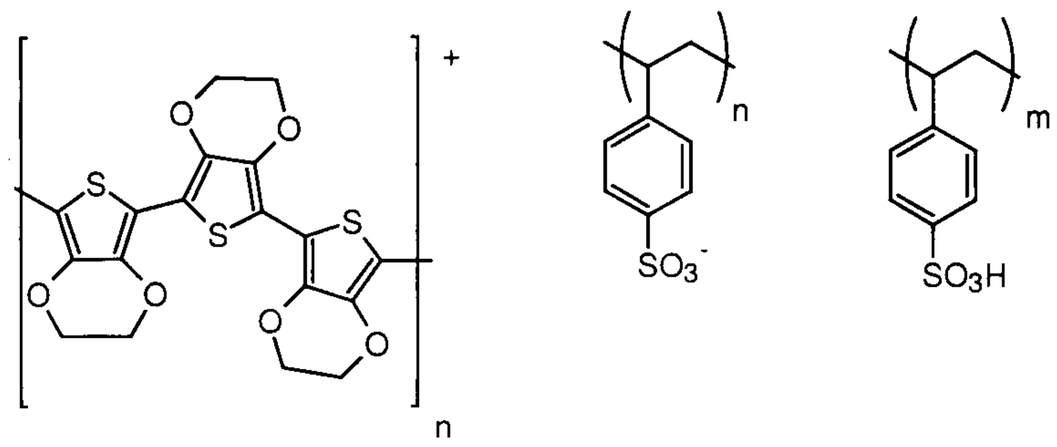

PEDOT/PSS [2]

Fig. 3.1. *Chemical structures of MEH-PPV and PEDOT.*

3.2 Sample preparation and characterisation

Dendrimer and polymer films were spin-coated from concentrated solutions. Typical concentrations are 10 mg/ml for dendrimers and 4 mg/ml for MEH-PPV. The spinning solvents used were tetrahydrofuran or chloroform for the dendrimers and chlorobenzene for MEH-PPV. Spinning speeds were typically 1000 rpm.

Film thicknesses were measured on a Tencor Alpha Step to a precision of approx. 5 nm by cutting a groove into the organic film and measuring the difference in height between the two sides of the groove and the centre.

Absorption spectra were measured on films spun onto quartz disks as well as on dilute solutions in quartz cuvettes using a Perkin-Elmer Lambda 19 absorption spectrometer. Optionally, the quartz disk could be mounted on the cold finger of a Leybold closed loop helium cryostat to investigate the change in absorption spectrum over a temperature range from 300 K to 10 K. Luminescence spectra were measured either using an Instruments S. A. (Jobin Yvon/SPEX) CCD spectrometer or an Instruments S. A. Fluoromax fluorimeter. In the case of the CCD spectrometer, the samples were

excited optically either by a laser such as an argon ion or a helium cadmium laser, or by a monochromated mercury arc lamp.

3.3 Device preparation

The standard light-emitting diodes were fabricated on ITO substrates. These were patterned by masking and etching to remove the risk of electrical shortening, yielding devices of the structure seen in Fig. 3.1. The standard structure has eight pixel, which half overlap the ITO strip and half overlap the glass substrate from which the ITO was removed. Typical device areas were 2 mm^2.

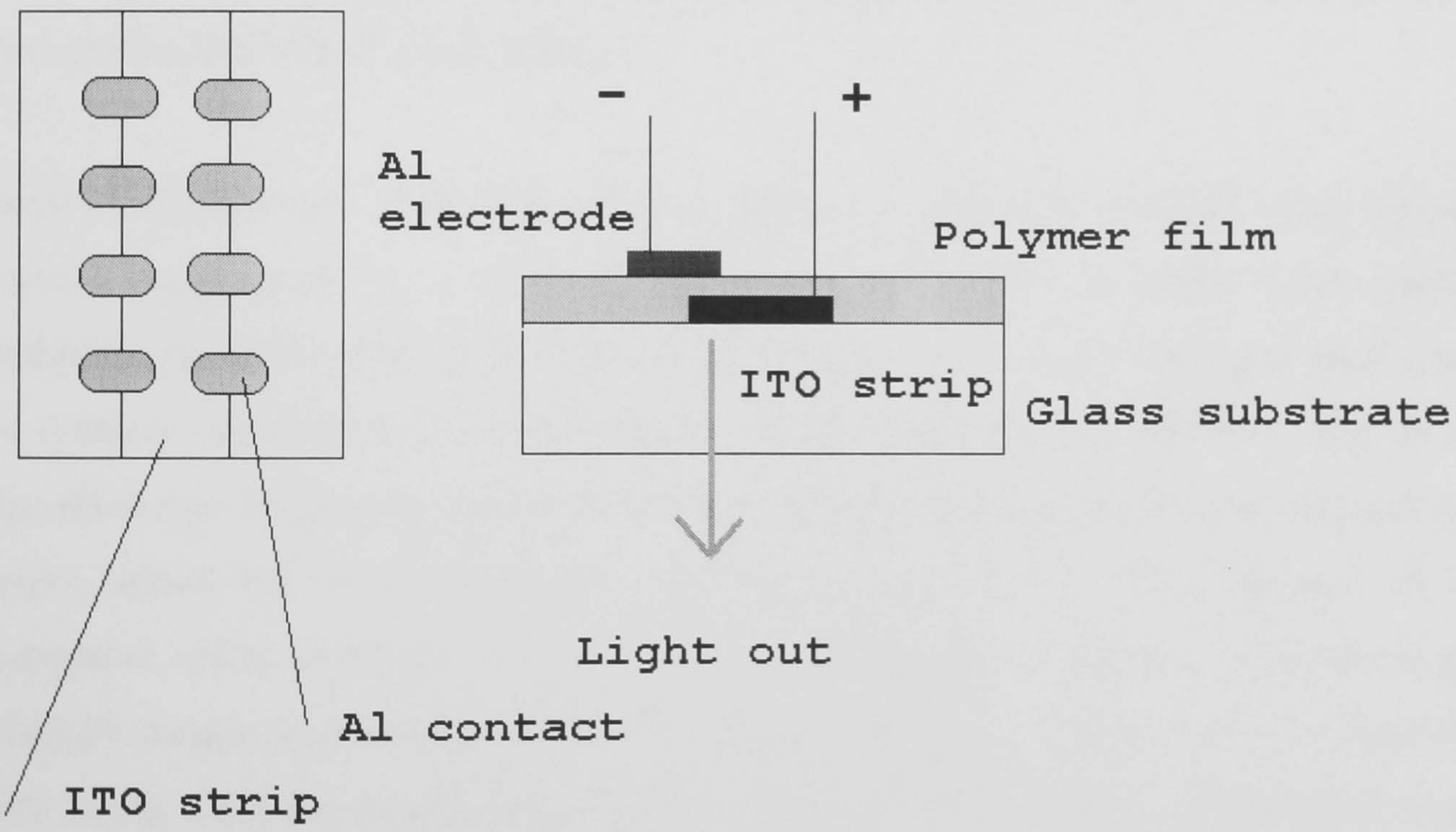

Fig. 3.1. *Top view and side view of the standard LED structure used. The device has eight pixel.*

The ITO was masked either with a standard masking pen, varnish or sellotape. A number of routes were explored for etching the ITO. For the substrates masked with varnish it was found necessary to immerse them in one molar hydrochloric acid for approx. 20 minutes at a temperature of 50° C. Alternatively, the approach used by the Marburg group involves the samples being masked with sellotape and coated in zinc powder. A 1:1 H_20:HCl mixture by weight could then be dripped onto the substrates

with a pipette, leading to a reaction with the zinc powder. After a few seconds the powder and the acid are neutralised and washed away with water.

The substrates were then cleaned in an ultrasonic bath in acetone (which also dissolves the varnish) and subsequently in isopropanol. It was found that the substrates could be kept for prolonged periods in isopropanol. Shortly before device fabrication, the substrates were dried under clean nitrogen.

Optionally, devices were coated by a hole injecting layer of PEDOT. This was spin-coated from water and required drying before further processing. The films were dried either by placing the substrates in an oven under vacuum for 1 hr at 80° C or by drying on a hot plate at approx. 80 °C for five minutes. No difference in device operation was observed between these two techniques.

Metal electrodes were deposited under a vacuum of typically $5\text{-}9\times10^{-6}$ mbar through thermal evaporation at a rate of approx. 1 Å/s. The materials used include predominantly aluminium, gold, calcium and magnesium. It was found that particularly the calcium evaporation was very sensitive to the evaporation conditions such as the deposition rate. In general, a slow deposition of calcium was indicative of outgassing of oxides, which led to an insulating, dull layer in the device. The thickness of the evaporated metal could be monitored using a piezo-electric crystal. Aluminium was generally evaporated from a tungsten filament, although it could also be evaporated from boats. Calcium, magnesium and gold were evaporated from molybdenum boats. The typical amount required for an evaporation was less than a gram. The metal layers can be 50 to 200 nm thick. Calcium electrodes need only be a few nm thin [3] and are then capped with aluminium. Magnesium is co-evaporated with aluminium from a single source, but is deposited first on the organic layer due to its lower boiling point.

Devices were also fabricated on gold anodes. In this case a transparent gold electrode the size of the standard ITO strip seen in Fig. 3.1 was evaporated to a thickness of 10 nm to 15 nm on a glass or silica substrate. It was found imperative that the further processing of the device fabrication is carried out under inert conditions in a glove box. To this end, the substrates with the gold electrode were immersed in the spinning

solvent, typically chlorobenzene, and transferred into the glove box whilst still immersed. Once inside the glove box, the substrates were dried. The polymer was then spin-coated under inert conditions. Removing the devices from the inert atmosphere in order to load them into the evaporator was not found to reverse the beneficial effect of spinning under nitrogen and washing atmospheric adhesions from the gold layer by immersing the substrate in the spinning solvent.

Devices could also be prepared in the glove box and then loaded under nitrogen into a chamber with an evaporation mask built. This could be transferred to the evaporator without having to break the inert conditions. No further increase in device efficiency was observed for this procedure with respect to atmospheric loading of the evaporator, however the device stability was found to be significantly improved.

Samples could be stored in the glove box for a number of weeks, however, testing was preferably carried out straight after fabrication.

3.4 Device testing

Unless stated otherwise, devices were tested under dynamic vacuum of 10^{-5} mbar provided by a turbomolecular pump. The devices were contacted either in a fixed arrangement using sprung gold pins or using thin copper wires and silver paint. Successful experiments with encapsulation were made by covering the device with a microscope slide under inert conditions.

3.4.1 Steady-state measurements

The standard device testing set-up is shown in Fig. 3.3. The device is driven by a Keithley 2400 source measure unit. The emitted light is detected by a large area (1 cm^2) silicon photodiode at a fixed distance of 3.5 cm to the device. The signal from the photodiode is amplified and measured by a Keithley 2000 digital voltmeter. The experiment is fully automated via a computer.

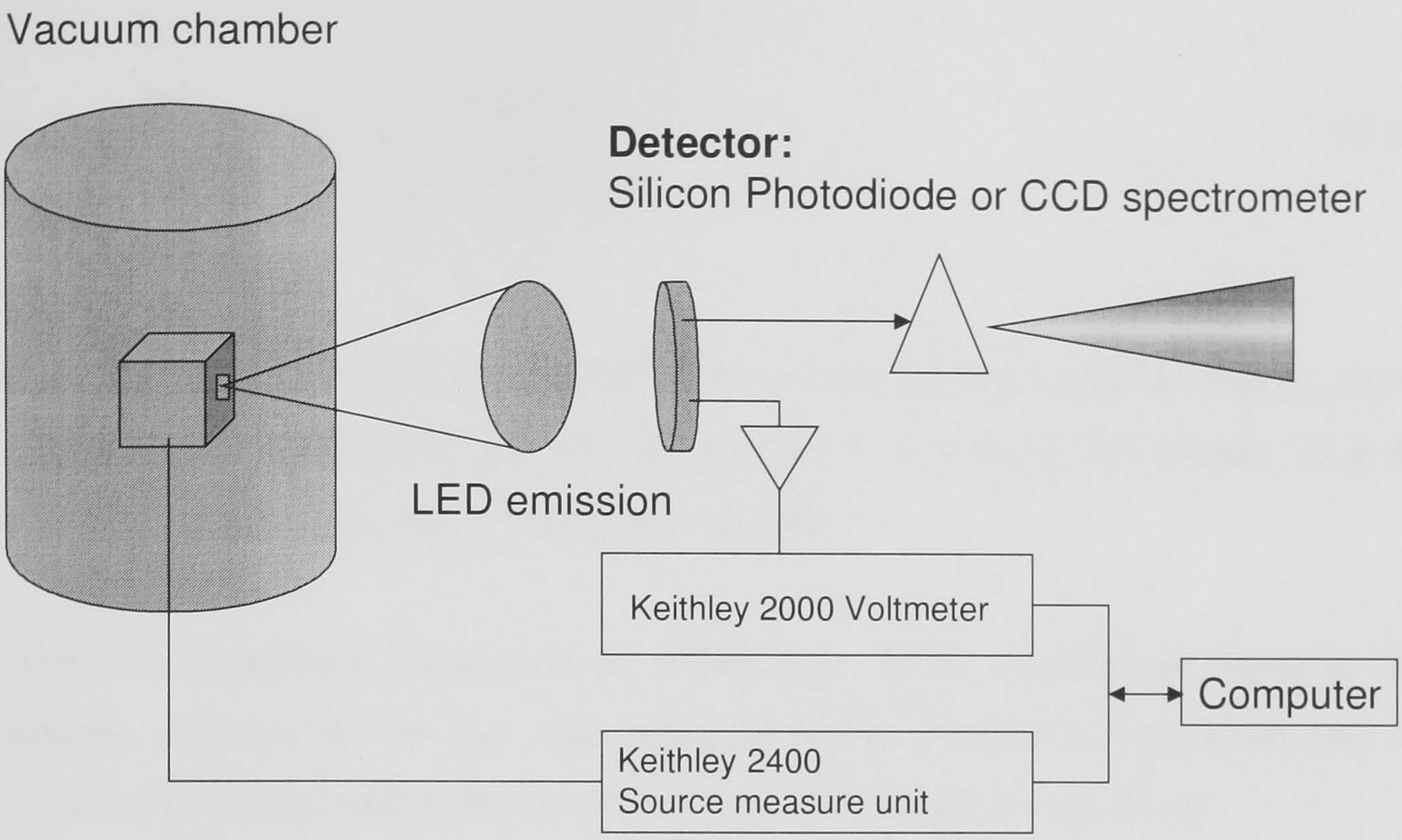

Fig. 3.3. *Experimental setup for device characterisation.*

Alternatively, a fibre coupled CCD spectrometer may be used in place of the photodiode to record the emission spectrum of the LED. The spectrometer is calibrated to give a value corresponding to the number of photons in a given wavelength interval. The spectrum can hence only be used in conjunction with a measurement of the total amount of light emitted to calculate the device brightness and efficiency.

The external quantum efficiency is defined as the number of photons emitted by the device to the number of charge carriers injected. The number of carriers injected per unit time is given by the device current, and the number of photons emitted per unit time is measured by the photodiode, which is calibrated to current per unit power (A/W). The efficiency calculations used were developed by Dailey [4] and are based on a method proposed by Greenham [5-6]. This involves the assumption that the emission is isotropic and the emitters are Lambertian resulting in an angular dependence of the emitted flux according to $F_0 cos\theta$, where θ is the angle of detection and F_0 is the photon flux in the forward direction. The light is detected by the photodiode over a given solid angle, and using the assumption of Lambertian emission, the total emission intensity in the forward direction is calculated. Using the responsivity of the photodiode $R(\lambda)$ and the measured spectrum $S(\lambda)$, the external quantum efficiency is calculated according to (3.1) [4].

$$\eta_{ext} = \frac{\pi e V_{Photodiode}}{R_{Amplifier} I_{LED} \Omega h c} \int_0^\infty \frac{S(\lambda) d\lambda}{\int_0^\infty \frac{S(\lambda) R(\lambda)}{\lambda} d\lambda} \tag{3.1}$$

where $V_{Photodiode}$ is the voltage measured from the amplified photodiode, $R_{Amplifier}$ is the tunable resistor defining the gain of the amplifier, I_{LED} is the device current, Ω is the solid angle of detection, and e, h and c are constants.

Using the Comission Internationale d'Eclairage (CIE) conventions defining the photopic response of the eye, the measured power emitted by the LED may be converted into perceived brightness, which is given in Candelas per m^2 [4].

3.4.2 Pulsed excitation

Instead of using the continuously driving source measure unit, the LED may also be driven by a pulse generator. This has the advantage that a wider range of device currents and biases may be explored than under continuous operation, as ohmic heating is reduced. The effects of ohmic heating on devices are highlighted in Fig. 3.4 for an ITO/PEDOT/MEH-PPV/Ca device driven with 9 ns pulses at a period of 310 ns and 530 ns. The applied bias was 35 V. Although the 9 ns pulsewidth is still significantly below the RC time of the system, which is in the order of 100 ns, the increase in heating and the resulting blue-shift of the spectrum are clearly seen with decreasing pulse period. Shown also are the cw spectra at two different biases, which are significantly blue-shifted with respect to the spectrum obtained under long period excitation. A more detailed investigation of thermal effects in LEDs can be found in [7].

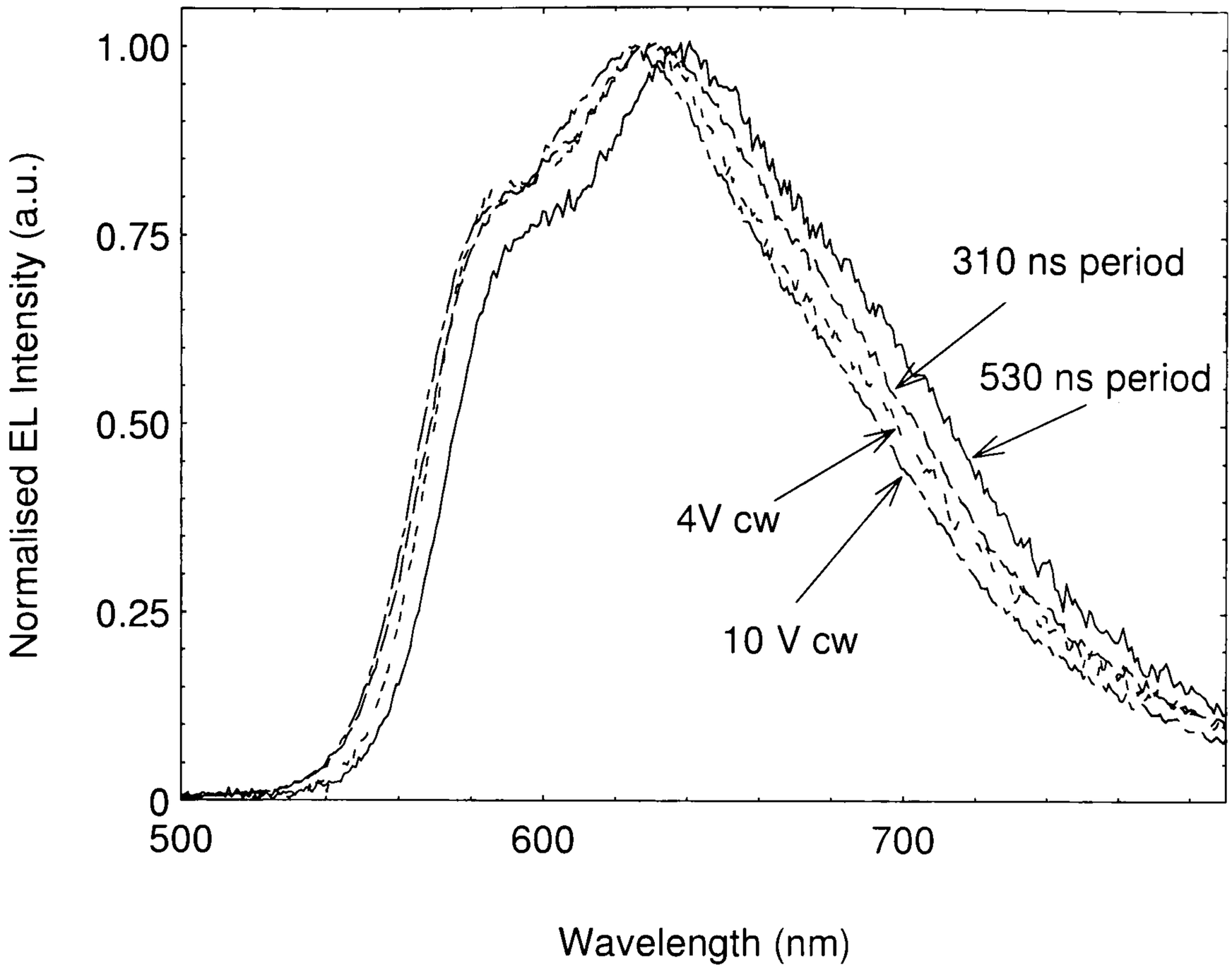

Fig. 3.4. *Steady state and pulsed EL spectra of MEH-PPV showing a blue-shift in emission due to ohmic heating.*

Pulsed excitation can also be used to probe the dynamics of charge carriers in the device by monitoring the evolution of the EL upon application and upon switching off of the voltage pulse. The transient EL [8] can be recorded using a photomultiplier in combination with a multichannel analyser, which is triggered by the pulse generator. A variable delay on the multichannel analyser allows the investigation of either the rise or the decay dynamics of EL.

3.4.3 Temperature dependent measurements

An important parameter to consider in investigating the properties of semiconductors is the dependence of material characteristics on temperature. The device EL spectra, as well as the current-voltage and EL-voltage characteristics could be measured by mounting the device in a closed loop helium cryostat. The device was attached to the copper cold finger of the cryostat using silver paint and thin copper wires were used to make contact to the electrodes. The temperature of the cold finger was measured by a

single thermocouple mounted on the cold finger. An Oxford Instruments ITC4 was used to control the temperature. The device automated characterisation routines could be run as for room temperature measurements, and the temperature controller could also be programmed by a computer. The cryostat cooled down from room temperature to 10 K within an hour, but the sample was generally left over night to reach 10 K. At least 30 minutes were left between each measurement for the system to reach thermal equilibrium.

3.5 Time-of-flight measurements

The most reliable way of measuring the transit time of charge carriers in a material is the time-of-flight (TOF) technique. In a TOF experiment, charge carriers are generated optically at one side of the sample. Under application of an external field, they are swept across the device, resulting in a current. This principle is shown in Fig. 3.5, which describes the TOF set-up used by the group in Marburg [9]. A Nd:YAG laser drives an optical parametric oscillator, which gives a tuneable emission wavelength. This is chosen appropriately to the experiment. In the experiments carried out on dendrimers, a rhodamine 6G (R6G) charge generation layer was used, as only relatively thin dendrimer films could be deposited. The R6G layer was evaporated to a thickness of 15 nm prior to the deposition of the aluminium cathode. The chamber vacuum had to be broken in between these two steps in order to change the evaporation mask. The laser light is hence tuned to pass through the ITO and the dendrimer film and is partially absorbed by the rhodamine layer. As R6G is a hole transporting material and due to the choice of polarity, electrons will migrate to the aluminium anode and holes will migrate across the dendrimer film to the ITO cathode. This current is measured over a variable series resistance using a storage oscilloscope. A voltage source with a fast response time is used to apply the field across the device. The choice of the voltage source is crucial in the experiment, as it has to maintain a steady bias with a changing current.

Laser pulses were generated at a repetition rate of 10 Hz and a manual shutter was used to expose the sample to one laser pulse. The laser beam was partially reflected from a microscope slide and shone onto a photodiode, which was used to trigger the

oscilloscope. The power of the laser beam could be varied with neutral density filters, but for most measurements the peak power was used.

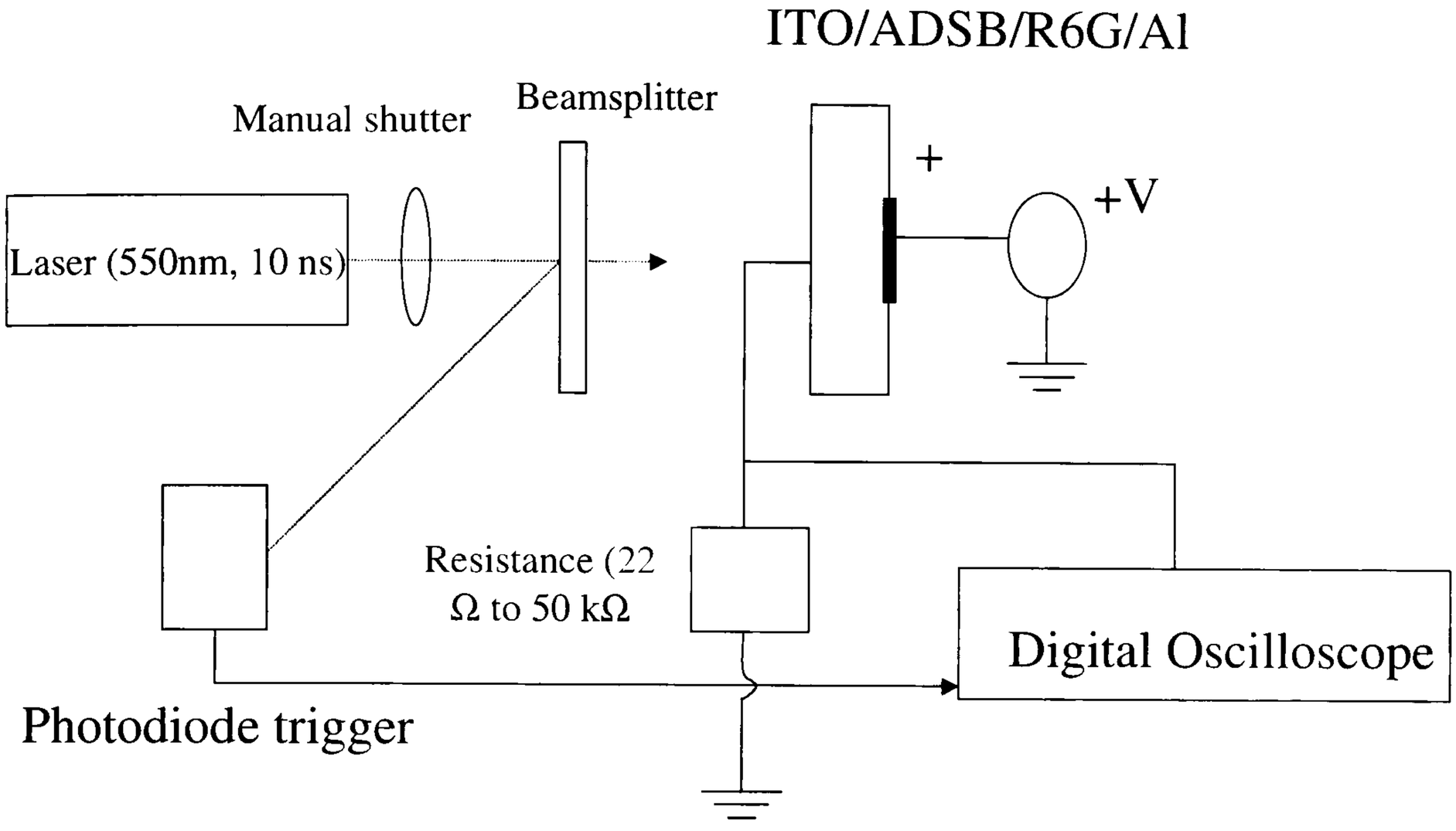

Fig. 3.5. *Experimental set-up of the time-of-flight experiment. A Nd:YAG laser drives an optical parametric oscillator, tuned to give an output of 550 nm.*

The samples were held under vacuum and the capacitances were regularly checked to ensure that the aluminium electrode was still uniform. It was found that the applied field resulted in a gradual breakdown of the electrode under repeated exposure, depending on the voltage across the structure. The RC time of the system was ideally approx. 100 ns and small electrodes of surface area 1 mm^2 were used. In TOF measurements it is important that the generated charge remains smaller than about 5% of the capacitative charge. However, in the present experiment only a small fraction of the light is actually absorbed in the rhodamine layer, so the number of charge carriers generated remains relatively small. No distortion effects with the applied bias were observed, which would be a signature of space charge effects.

References

[1] R. K. Kasim, M. Pomerantz, and R. L. Elsenbaumer, Chem. Mater. **10,** 235 (1998)

[2] A. Elschner, F. Bruder, H.-W. Heuer, F. Jonas, A. Karbach, S. Kirchmeyer, S. thurm, and R. Wehrmann, Synth. Met. **111-112**, 139 (2000)

[3] J. M. Bharathan and Y. Yang, J. Appl. Phys. **84,** 3207 (1998)

[4] S. Dailey, PhD Thesis, University of Durham (1998)

[5] N. C. Greenham, PhD Thesis, University of Cambridge (1995)

[6] N. C. Greenham, R. H. Friend, and D. D. C. Bradley, Adv. Mater. **6,** 491 (1994)

[7] N. Tessler, N. T. Harrison, D. S. Thomas, and R. H. Friend, Appl. Phys. Lett. **73,** 732 (1998)

[8] V. Savvateev, A. Yakimov, and D. Davidov, Adv. Mater. **11,** 519 (1999)

[9] C. Im, Diploma Thesis, University of Marburg (1999)

4.

Nanoscale control of intermolecular interactions in conjugated dendrimers

Acknowledgements

I am indebted to R. Beavington of Oxford University, who synthesised the dendrimers presented in this chapter and would like to thank him and P. Burn for many helpful discussions. I would like to thank L.-O. Pålsson for assistance with the photoluminescence quantum yield measurements and many helpful discussions, and Opsys Ltd. for the opportunity to use their facilities to fabricate bilayer devices, particularly O. Salata and D.-G. Moon for technical assistance. I am very grateful to S. Mukamel at Rochester University, NY, for the invitation to carry out some coupled electronic oscillator calculations on the dendrimers as well as for many helpful discussions. The help and guidance by M. Ottonelli in using the code in Rochester was very much appreciated.

4.1 Introduction

Dendritic systems and in particular conjugated dendrimers have recently attracted considerable attention from the synthetic organic chemistry community [1-17], photophysicists, in particular from the area of biophysics [16-20] and even more basic areas of research such as topology, rheology and statistical physics [21]. Geometrically, dendrimers are unique systems, as the number of atoms grows exponentially with the branching, or generation, of the dendrimer, rather than to the power of 1, 2 or 3. This exponential growth is a characteristic of an infinite dimensional system [20]. In contrast, there is only one unique connecting path across the structure between two lattice sites, i.e. units of the molecule, making the connectivity or the path of an excitation one-dimensional. This results in unusual optical properties of these macromolecules. Dendritic molecules have been synthesised and studied as a comparison to biological light-harvesting complexes [18, 22-23], and a body of both theoretical and experimental work exists on these artificial light-harvesting antennae. In these complexes, excitations are generated optically in the dendron periphery of the molecule and transferred through exciton hopping into the central region of the molecule, leading to a level of exciton confinement. This confinement is not dissimilar to that employed in quantum wells or even quantum dots [24], although the approach to achieving this confinement is, of course, very different. Excitonic effects due to this strong degree of localisation have attracted considerable attention and charge transfer complexes have been observed as well as strong coherences and Davidov-like splitting [19-20, 22, 25-27] .

In contrast to the likening to light-harvesting complexes, conjugated dendrimers may also be used as light-emitting materials [2, 4-7, 13-14]. The exciton confinement at the centre of the dendrimer allows the emitting region to be modified independently of the dendron architecture, which can be tuned to give the desired interactions with the environment such as neighbouring molecules or solvent [5, 7, 22]. Emissive excitations can hence be shielded from the environment through the periphery of the dendrimer [16-17]. This can reduce parasitic effects such as solvation effects in solution or luminescence quenching through interaction with the environment or surrounding chromophores [5, 17, 28]. Recently, conjugated dendrimers have been proposed as

emitting or transport layers in organic LEDs [4-7, 13-15, 29-35] . Dendrimers combine a number of advantageous electronic and processing properties: they possess a well defined molecular weight and can hence be synthesised reproducibly to a high purity; they are solution processable in most cases and, in contrast to conjugated polymers with very high molecular weight and viscosity, may be ideally suited for inkjet printing of LED structures, as has previously been demonstrated with polymer based materials [36]. In addition, it has been shown that the emission colour of the core region may be tuned independently of the dendron architecture across the entire visible spectrum [7]. This provides a novel tool for controlling the emission colour of organic LEDs.

A further interest in dendrimers for EL applications is the possibility of assigning different functional properties to the different components of the macromolecular structure. For instance, it is conceivable to attach moieties with hole transporting properties to the core region and electron transporting properties to the dendrons. This concept has been explored by the author and coworkers in the context of triazine dendron containing dendrimers [6], where triazine is known to have electron-donating properties. However, no conclusive evidence was found that the charge transport properties are modified by the choice of dendrons. In the structures investigated here, stilbene was used as the dendrons and was found to act as an insulator between the chromophores.

In this chapter two novel families of conjugated dendrimers for EL applications are discussed. Exciton localisation at the core region is observed for all four generations of the dendrimers. The dendron periphery and the dendrimer generation hence provide a unique method of investigating the effect of chromophore spacing on the emission and transport properties of LEDs. There is considerable interest in understanding the nature of the emissive species responsible for EL in organic materials, as well as the basic processes involved in charge transport. It is commonly assumed that good charge transporting properties are a result of close chromophore proximity and a strong level of interaction between transport sites. In contrast, this proximity has been shown to lead to luminescence quenching and an overall decay in emission efficiency [37-48]. By using the dendrons as microscopic spacers between chromophores, the trade off between efficient luminescence and good charge transport can be investigated. In contrast to blend systems, the problem is much better defined in the case of dendrimers, as there is

only one molecule involved in the investigation and there is no danger of phase separation.

The structures of the two dendrimer families are shown in Figs. 4.1 and 4.2. Both material classes are virtually identical except for the choice of the core unit. Three distyrylbenzene (DSB) units are arranged around a central nitrogen atom in the case of ADSB or a central benzene ring in the case of BDSB. The core region is defined as the triangular region containing the three distyrylbenzene units as seen in A0 and B0, respectively. *t-Butyl* units form the surface groups and ensure good solubility in common organic solvents such as tetrahydrofuran (THF), toluene or chloroform. Stilbene units form the dendrons and are joined on to the core in the *meta* position and are hence not conjugated with the core. A detailed comparison of *meta* and *para* linkages has established that the meta position does not allow electron delocalisation [49]. Exciton migration from the dendrons to the core hence occurs by exciton hopping [22]. The number of dendron units in the molecules increases as $6\times(2^{G}-1)$ with generation number G.

A number of standard analytical techniques were used by the Oxford group to asses the chemical composition and purity of the dendrimers, which are synthesised by a convergent and iterative procedure. Spectroscopic tools like UV/VIS and FTIR absorption are used to monitor the reactions. Flash silica column chromatography is used to purify the compounds, which are then checked by thin-layer (TLC) chromatography and combustion analysis. Gel permeation chromatography gives further insight into the purity of the compound and may also be used to estimate the molecular radii. ^{1}H NMR gives insight into the presence of different isomers in the product, but also indicates contamination by hydrogen containing impurities. An important tool used to characterise dendrimers is mass spectrometry, the most commonly used form of which is matrix-assisted laser desorption/ionisation-time-of-flight (MALDI-TOF). MALDI-TOF is particularly suited to characterise dendrimers as it results in little fragmentation of large molecules and gives an accurate idea of the chemical purity of the final product. It also gives an isotope distribution, which can be used to confirm the molecular formula and weight.

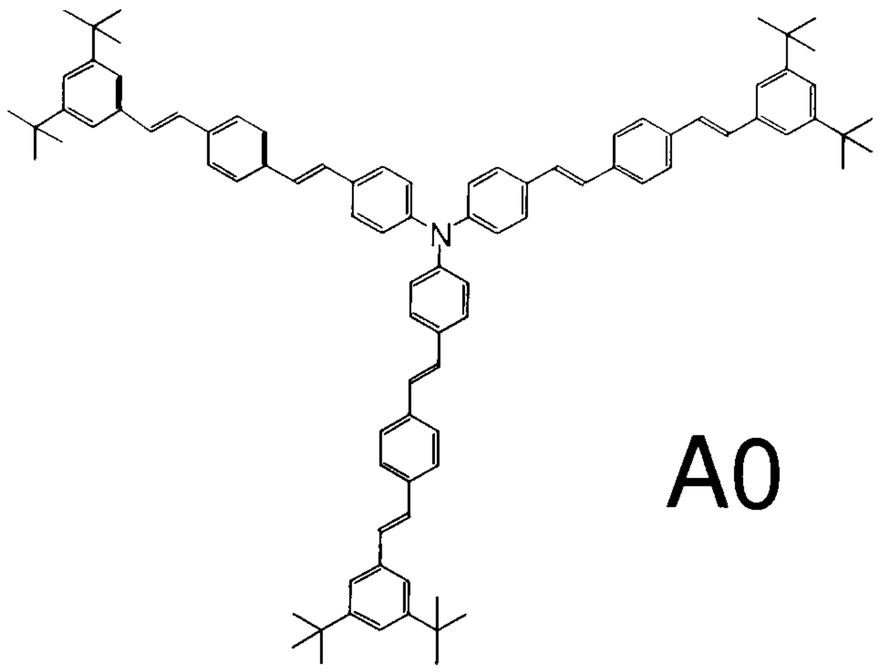

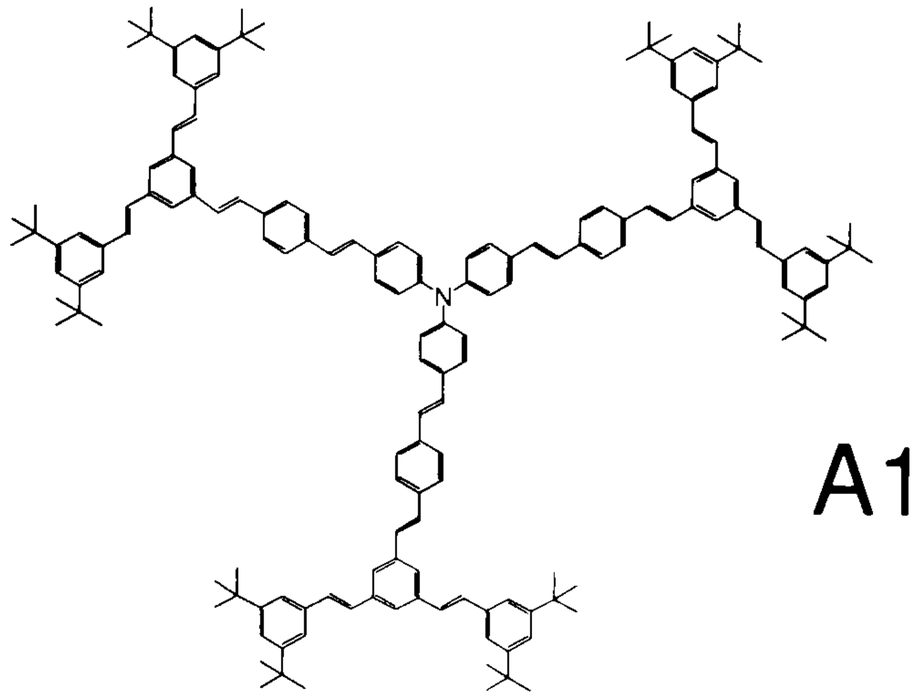

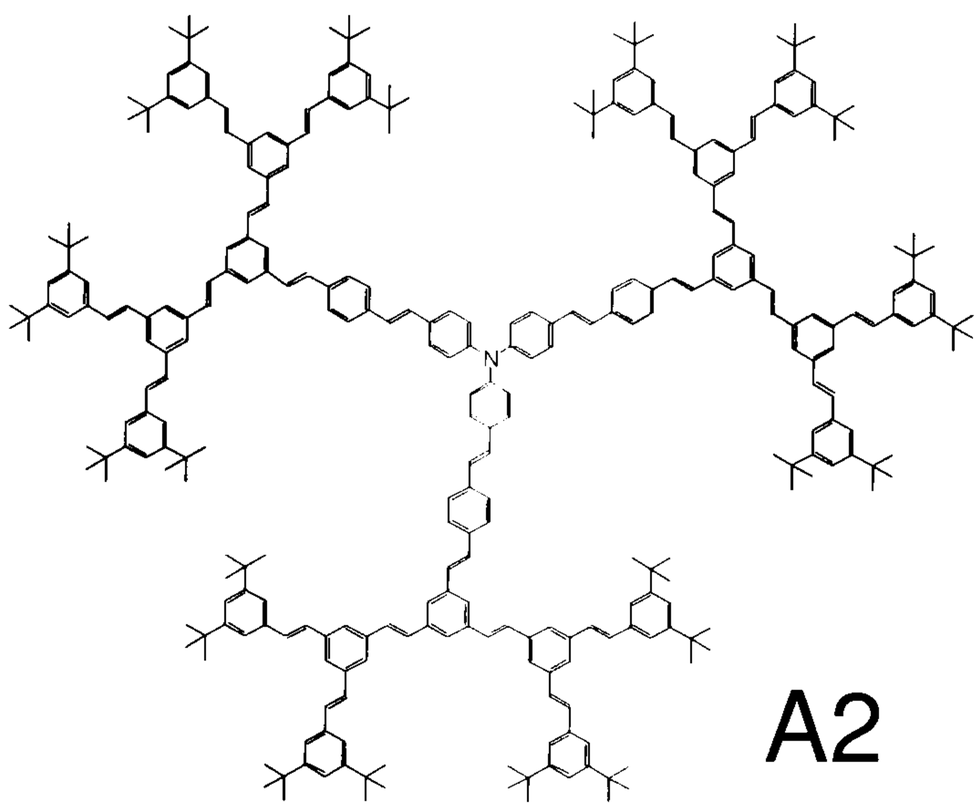

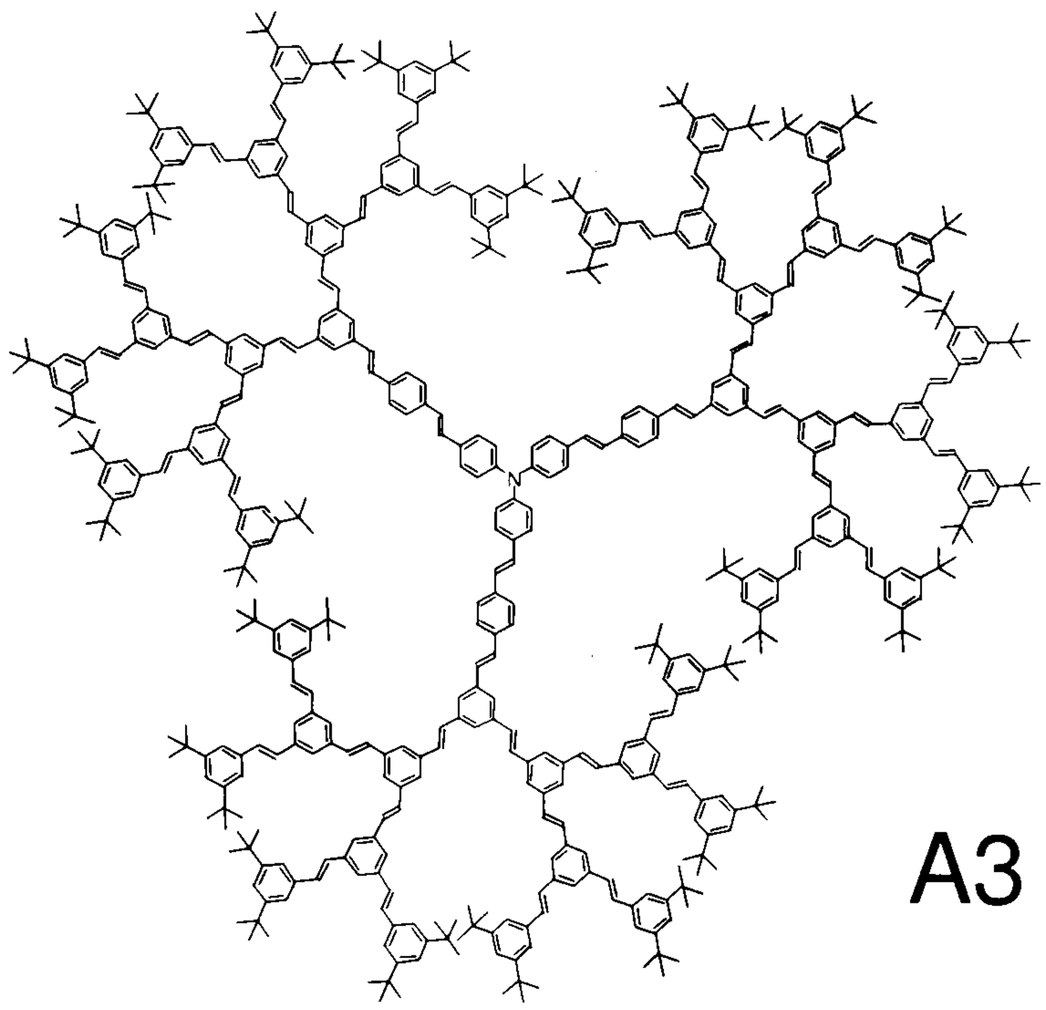

Fig. 4.1. *Structures of the four generations of the nitrogen – or amine – core dendrimer. The family of dendrimers is also referred to as ADSB.*

The chapter begins by discussing the basic photophysical properties of the two dendrimer families showing exciton localisation and the effect of intermolecular interactions in films. Thermochromic effects on absorption and emission are discussed and compared to results obtained for MEH-PPV. Single layer device characteristics are discussed next for a number of electrodes, as well as the temperature dependence of dendrimer device characteristics again in comparison with MEH-PPV. The microscopic control of intermolecular interactions is exploited in bilayer devices, where the dendrimer generation is shown to give rise to a control of the device characteristics. Following the discussion of the material properties, a detailed quantum chemical investigation of the two dendrimer families is presented and the basic features observed are explained in the context of a coupled electronic oscillator model [50].

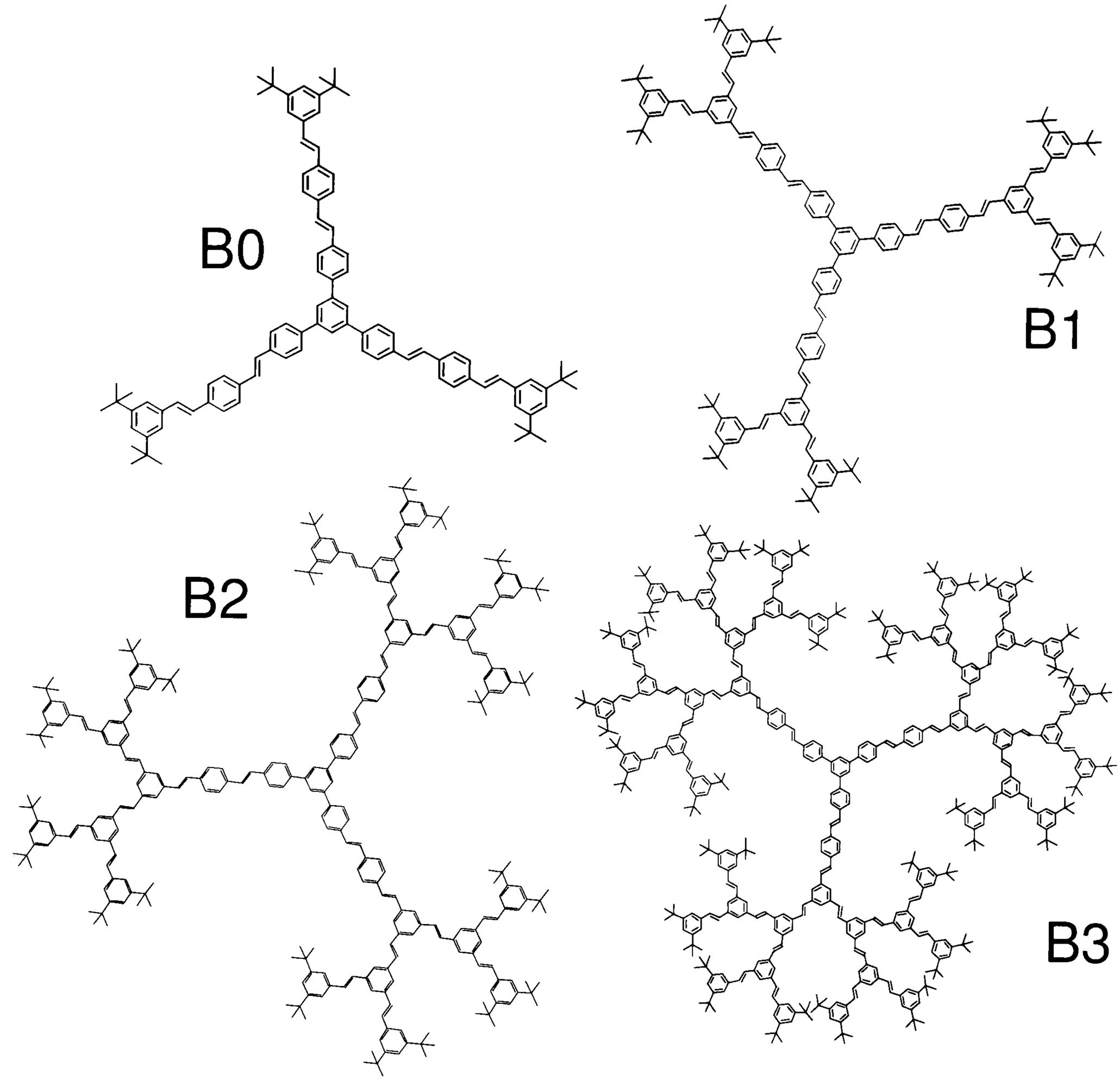

Fig. 4.2. *Structures of the four generations of the benzene core dendrimer. The family of dendrimers is also referred to as BDSB.*

4.2 Photophysics of the dendrimers

4.2.1 Nitrogen core dendrimer

Solutions of all the dendrimers were made by serial dilution in THF to concentrations of approx. 5 mg/l. The absorption spectra of the nitrogen core dendrimers are shown in Fig. 4.3. There are two main absorption features, the first at 420 nm, to which all spectra were normalised, and the second at 320 nm. The absorption at 320 nm can be assigned to the stilbene units as it is in the range of the absorption of lone stilbene [4, 27]. The

dendron absorption increases exponentially with generation, but there is no change in the position of the peak. Remarkably, the lower energy feature, which is assigned to the core absorption, remains virtually unaffected by generation. Such an independence of absorption spectrum on generation has previously been used as an argument of exciton localisation at the core [22]. In the case of these dendrimers, the core and dendron bands are well separated and the absorption spectra can, to a first approximation, be expressed as a superposition of core and dendron absorption. It should be noted that distyrylbenzene absorbs at 360 nm [4-6], whereas the observed absorption here peaks at 420 nm. It is hence concluded that the electronic core region extends across the central amine region and is a result of delocalisation between the three distyrylbenzene units in the core region.

There are a number of further observations to be made. The red absorption tail moves to the red as the generation increases. Such a behaviour has previously been investigated in phenylacetylene dendrimers [22, 19, 20, 25] and is attributed to excitonic splitting between excitons localised on the core region and excitons localised on the dendrons. Interestingly, a feature is seen in the A0 dendrimer in the region of the stilbene band, although there are no dendrons present in this case. In the A1 dendrimer, the stilbene band appears to be split around 320 nm, which may be a consequence of interactions between the core band at 320 nm and the stilbene dendron band at 320 nm. It remains to be pointed out that isolated stilbene absorbs at 300 nm [27], whereas the stilbene bands in all dendrimers studied, and in previous reports on related structures [4, 5], is observed to peak at 320 nm. Upon subtracting the absorption of A0 at 320 nm from the remaining spectra, the stilbene dendron peaks are found to scale as 1:3:7 with generation. As the individual benzene rings are shared between up to three stilbene units, this scaling is somewhat surprising, as it implies that benzene rings are involved in multiple excitations.

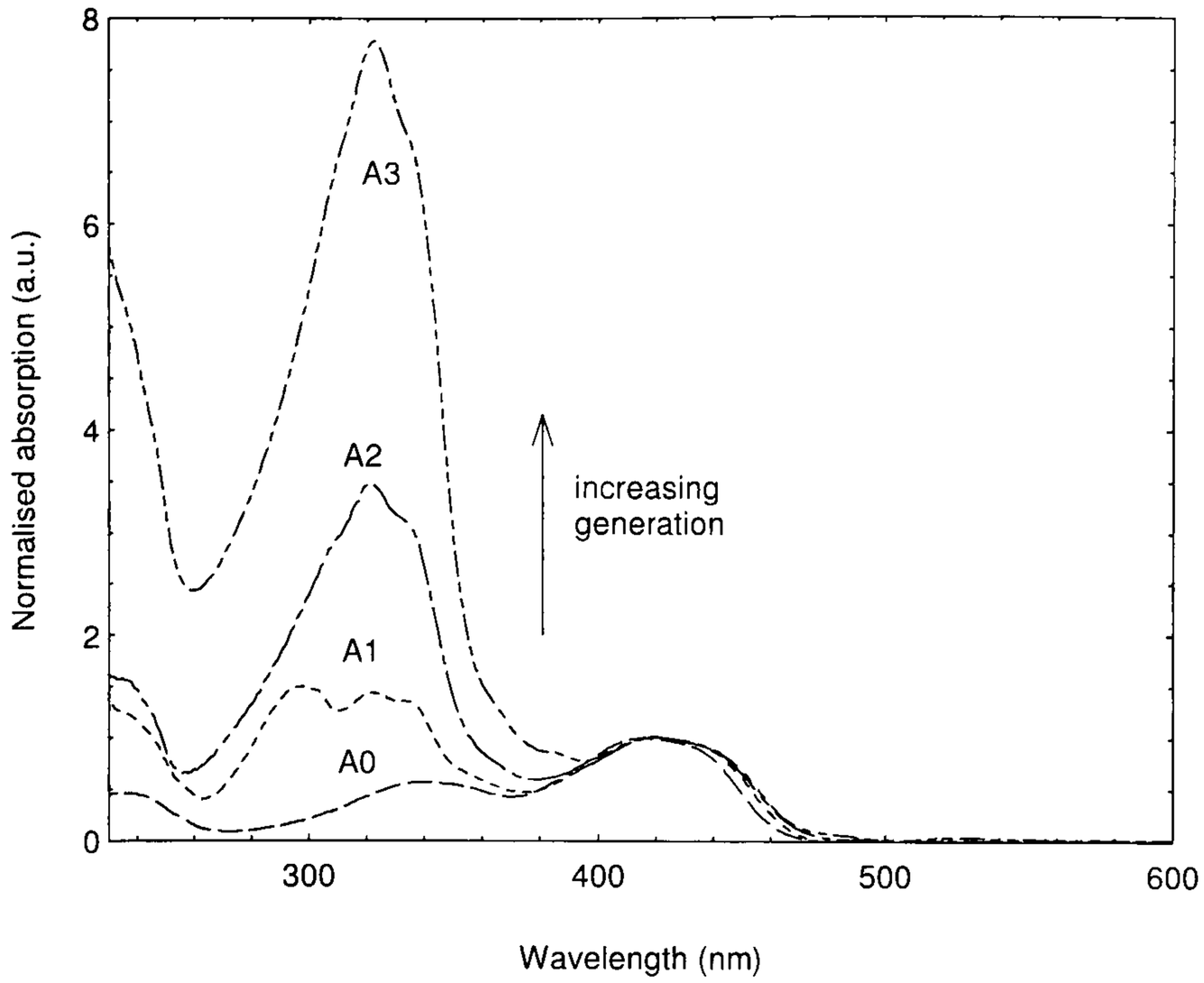

Fig. 4.3. *Normalised solution absorption of the nitrogen core dendrimer.*

The film absorption spectra of ADSB are shown in Fig. 4.4 and are found to be very similar to the solution spectra. The main features are observed at the same wavelengths, but are smoothed out. The core absorption is reduced with respect to the dendron absorption, and in particular with respect to the 320 nm feature of A0. The dendron absorption is found to scale as 1:3:5 with generation. The red-shift of the low lying absorption edge with generation is unchanged from solution to film, however, the feature is broadened by approx. 10 nm in the solid state. There is no significant shift in the absorption peaks between film and solution, which suggests that aggregation of chromophores does not play a role.

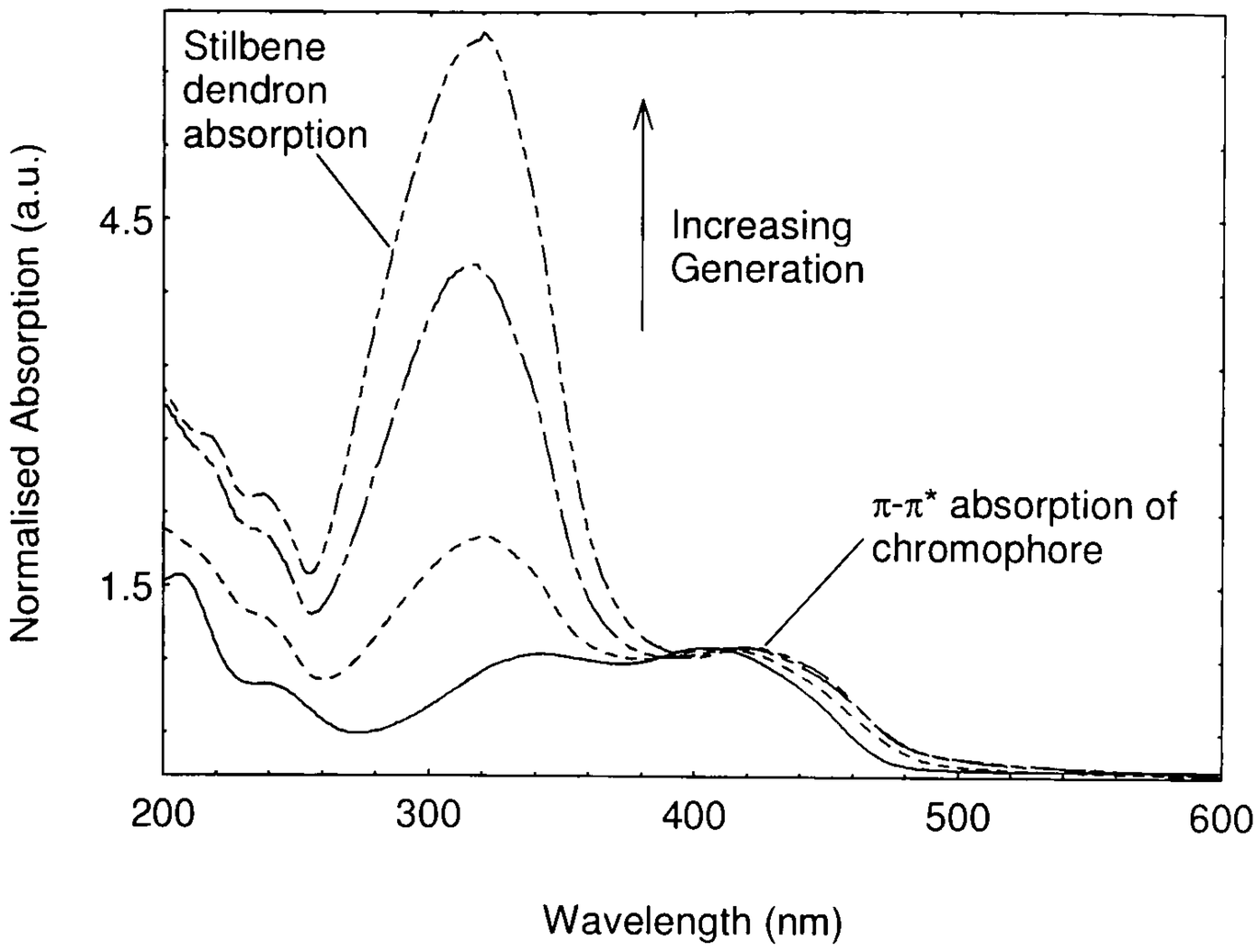

Fig. 4.4. *Normalised absorption of nitrogen core dendrimer films.*

The solution luminescence of the four dendrimer generations is shown in Fig. 4.5. Remarkably, the spectra are identical for all generations, demonstrating that the same excited species is responsible for emission in all cases. This is clear evidence for exciton localisation at the core of the dendrimer. A similar effect has been observed in a family of distyrylbenzene dendrimers by Halim et al. [4] and in anthracene and porphyrin dendrimers studied by Pillow et al. [5]. In contrast, Deb et al. did not observe such an independence on generation, which they attributed to steric effects in the dendrimer [2]. The independence of the solution emission on generation is highly desirable. as it demonstrates the ability to alter the periphery of the molecule without interfering with the emission properties. It remains to be noted that the emission is in the green and is both broad and featureless. In contrast, distyrylbenzene exhibits a narrow emission spectrum in solution in the blue with strong vibronic structure [4-6].

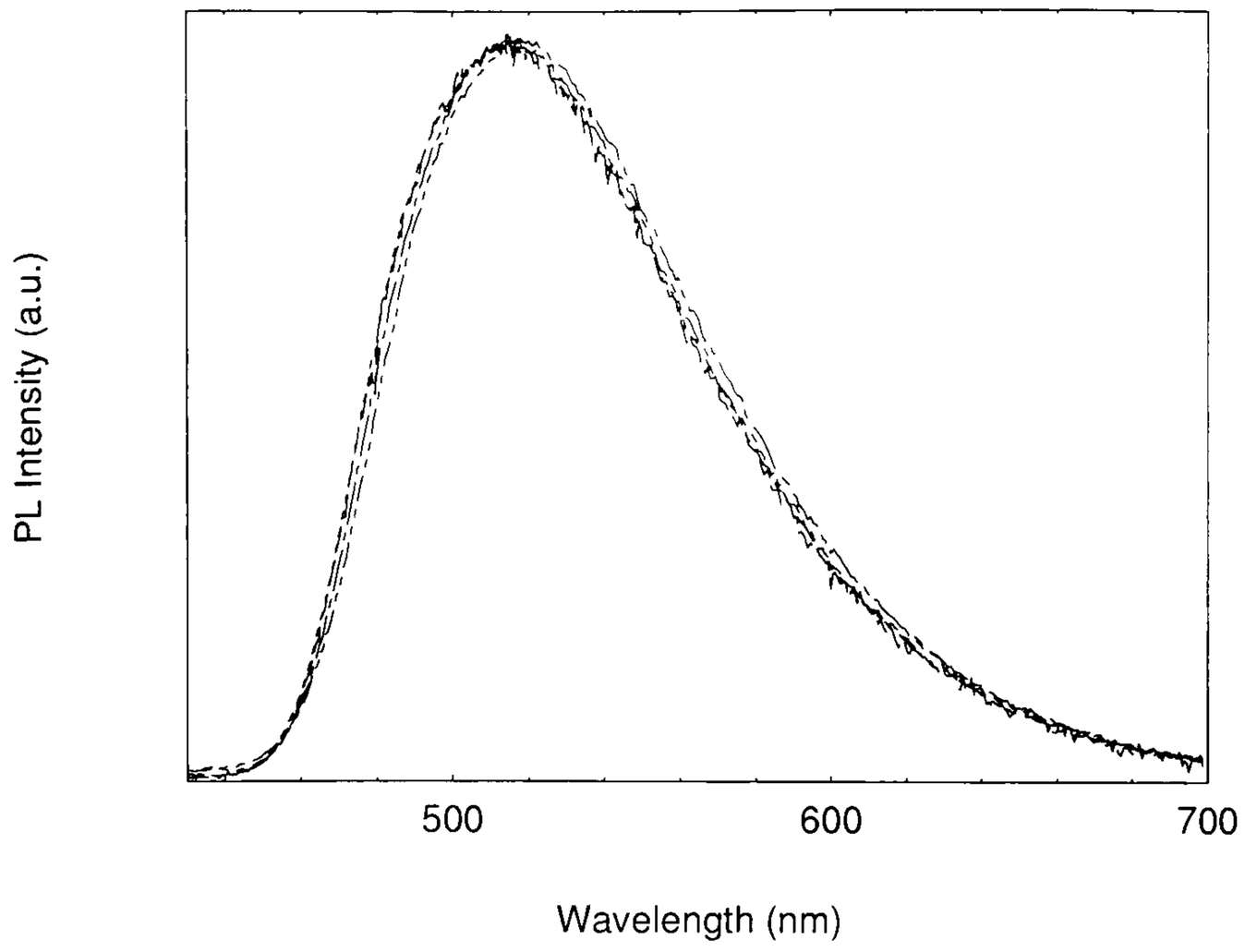

Fig. 4.5. *Solution PL of the four generations of the nitrogen core dendrimers.*

The film PL spectra are shown in Fig. 4.6 in comparison with the solution PL. There is a strong dependence of film emission on generation. As the generation increases, the red tail emission is reduced and the emission peak moves towards the blue, close to that of the solution emission. This effect becomes even clearer in the EL spectra, shown in Fig. 4.7.

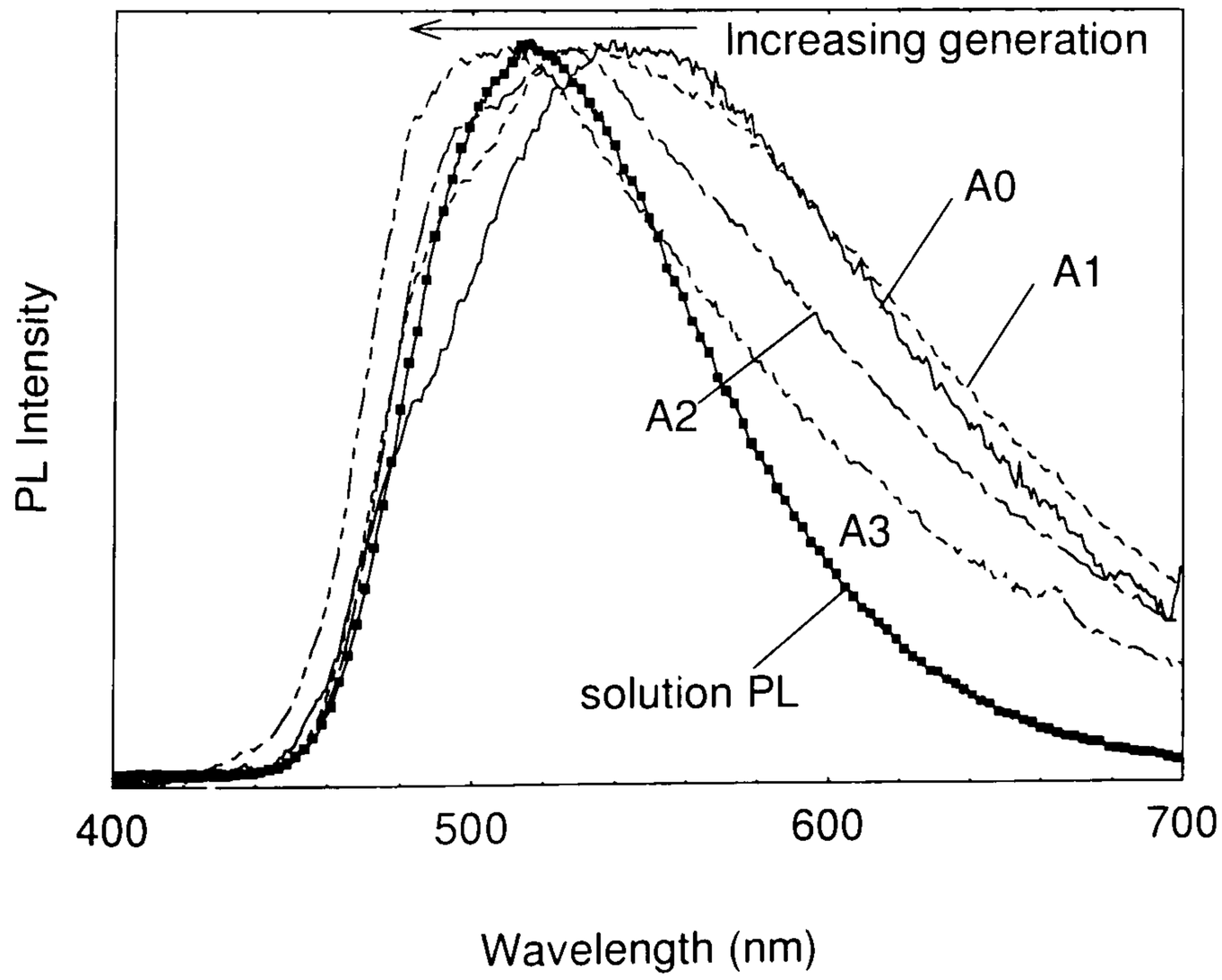

Fig. 4.6. *Film PL of the nitrogen core dendrimer compared to the solution PL.*

The EL spectra are very similar to the PL spectra but are slightly narrower. The red emission, which is reduced with increasing generation, is attributed to the presence of excitations delocalised between adjacent chromophore units. Due to the absence of a corresponding red-shifted feature at low generations in the film absorption of the dendrimers, it is concluded that this red-shift is a characteristic of the excited state resulting from an excited state dimer, or excimer [37-48]. At higher generations, the core chromophores become more shielded from the environment and from interactions with adjacent chromophores due to a reduction in the core to dendron concentration and hence increased chromophore spacing. It is evident from the solid state emission that this gives rise to a reduction in excimer emission, with the high generation emission approaching that of dilute solutions. The dendrimer generation hence allows a direct control of the level of intermolecular interaction, which is directly manifest in the emission properties.

It is interesting to note that the A3 dendrimer emission is slightly blue-shifted with respect to solution. This is believed to result from steric effects, such as increased twisting of the conjugated units, present in the solid state. The film photoluminescence quantum yields were measured and found to be very low in comparison to previous distyrylbenzene based dendrimers of approx. 30 % [4-6]. Values obtained ranged from 7 % for A0 to 9 % for A3, increasing slightly with increasing generation.

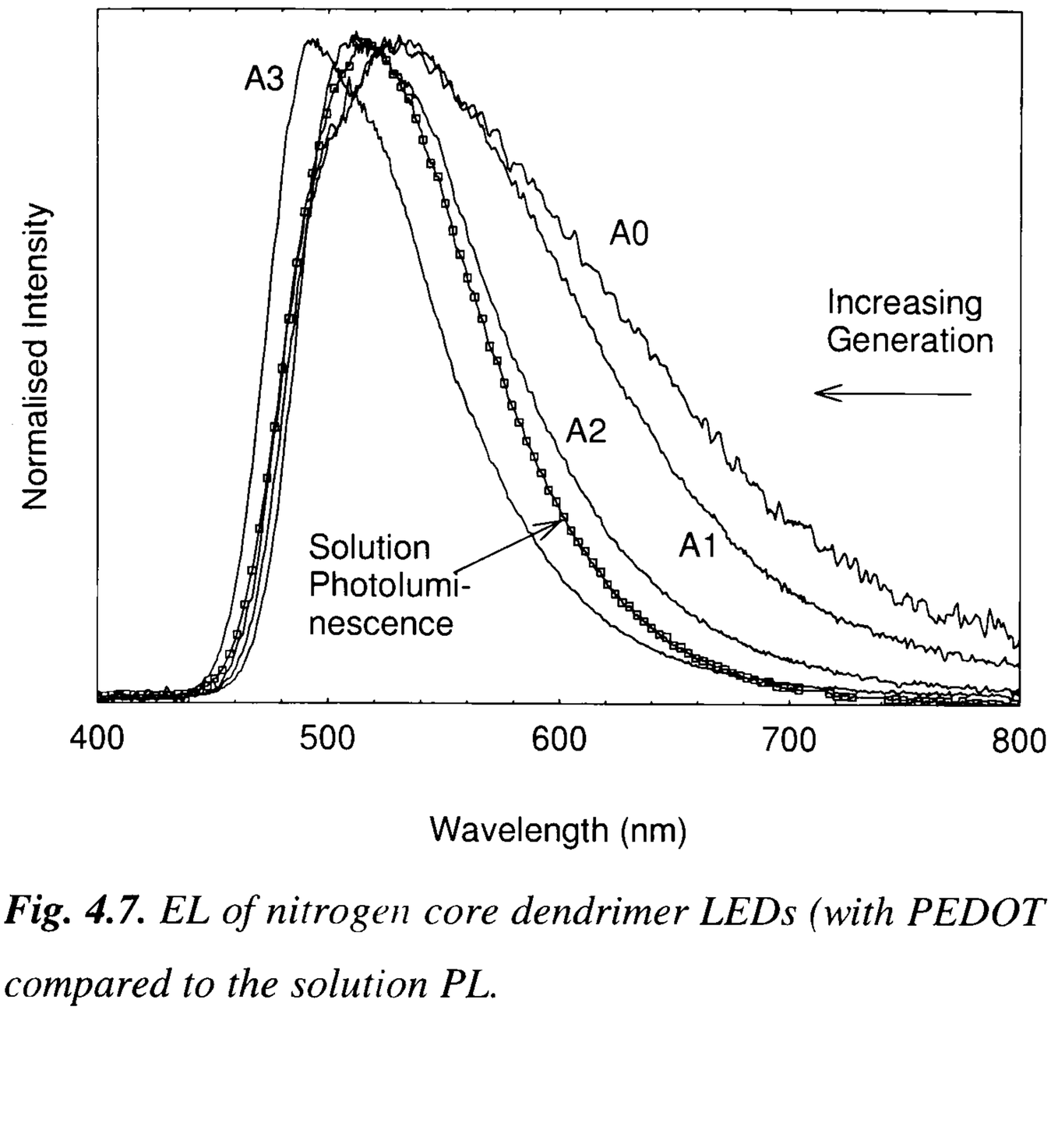

Fig. 4.7. *EL of nitrogen core dendrimer LEDs (with PEDOT and aluminium electrodes) compared to the solution PL.*

4.2.2 Benzene core dendrimer

The solution absorption spectra of the benzene core dendrimers BDSB are shown in Fig. 4.8. The basic features are very similar to those observed for ADSB, however, the core absorption now merges with the dendron absorption and is found to peak at 360 nm, which corresponds to the absorption peak of distyrylbenzene [4-6]. Again, there is a small red-shift of the low-lying absorption edge with generation, although it appears to be strongest between B0 and B1 and is not pronounced for generations above G1. The B0 absorption consists of only one peak, which corresponds to the absorption of distyrylbenzene, and the dendron absorption is found to scale as 1:3:7.

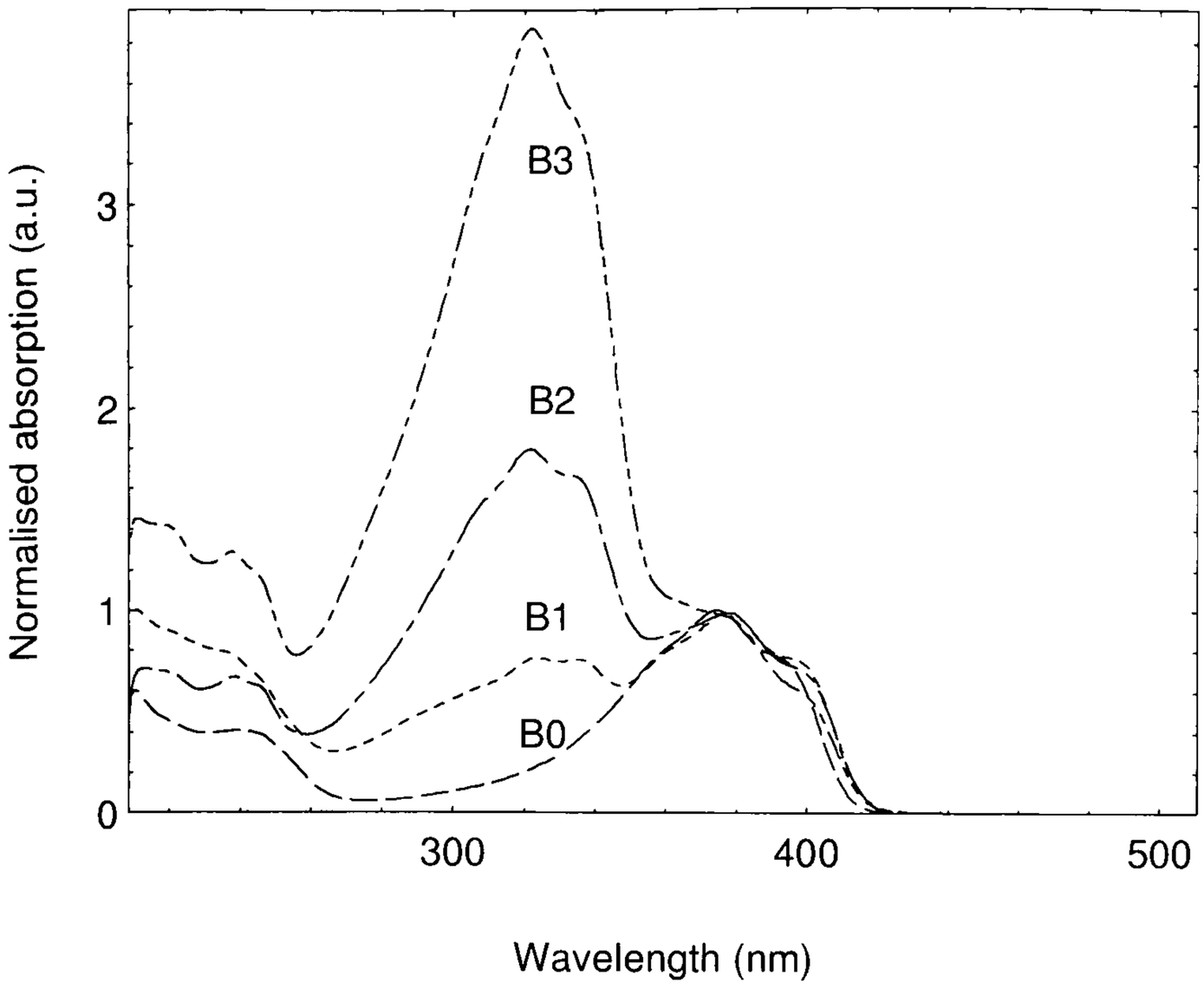

Fig. 4.8. *Normalised solution absorption of the benzene core dendrimer.*

The film absorption spectra are shown in Fig. 4.9. As for ADSB, the features are smoothed out with respect to solution, but due to the proximity of the core and dendron bands, these appear to merge. The B0 absorption is significantly broadened with respect to solution, and the bands extend further into the red of the spectrum, which may be a signature of increased disorder in the films. The dendron peak again increases strongly with generation, but due to the proximity between the broad B0 band and the B1 dendron band, it is not possible to determine an exact scaling relationship. As in solution, there is a shift of the red-edge to the red with increasing generation, which may be attributed to exciton splitting between excitations on the dendrons and on the core. In the normalisation chosen here, this red-shift appears to saturate at the 1st generation. The absence of any generation dependent change in absorption or any significant shift between solution and film suggests that aggregation of the emissive units does not play a significant role. The discontinuity at 321 nm is due to the automated lamp change in the spectrometer.

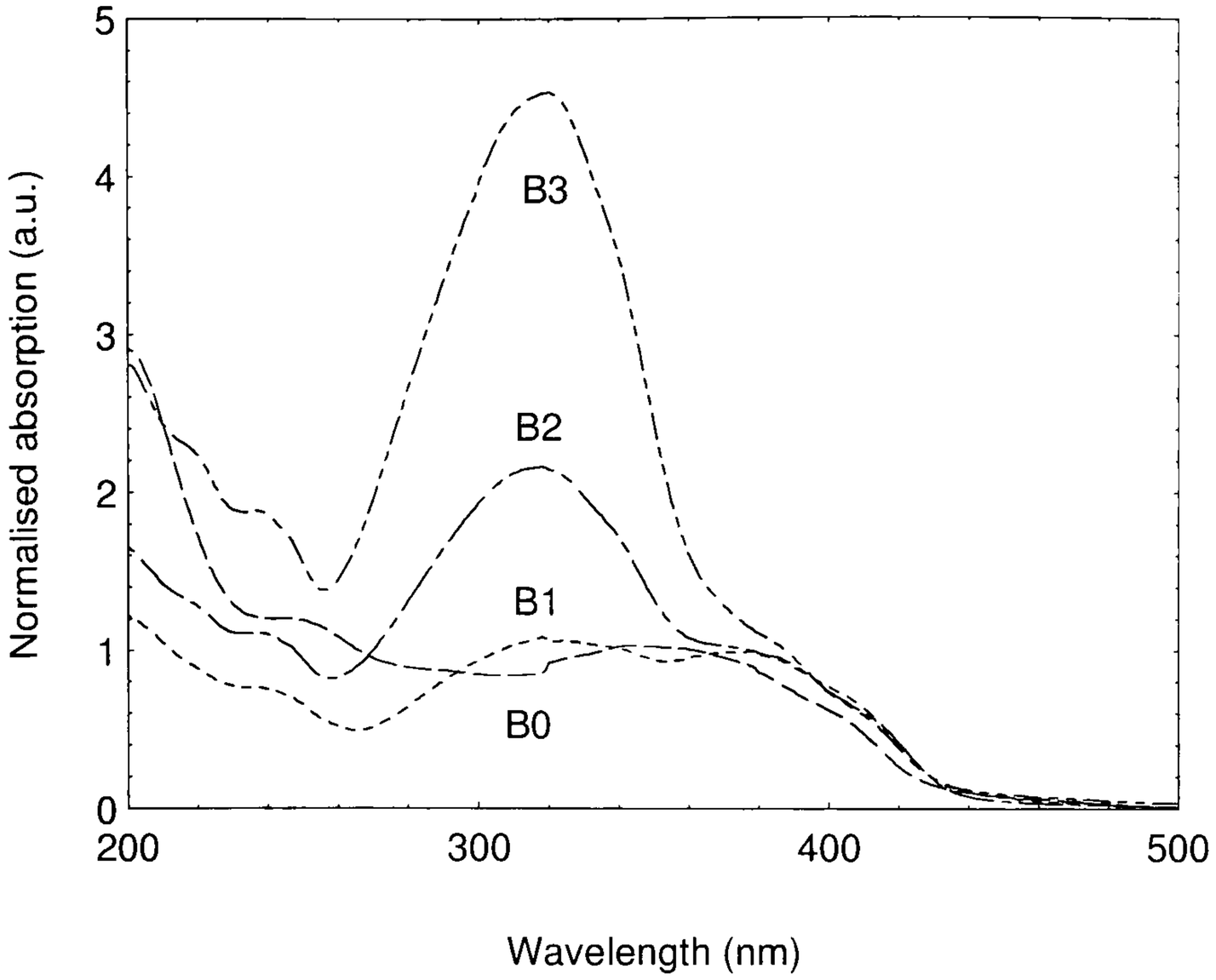

Fig. 4.9. *Normalised absorption of benzene core dendrimer films.*

The solution PL spectra of BDSB dendrimers are shown in Fig. 4.10. As for ADSB, the four generation PL spectra are virtually identical. The spectra resemble closely solution emission of distyrylbenzene and are very different from the solution emission spectra of ADSB. The spectra are relatively narrow and the vibronic peaks are well-resolved. There is a small blue-shift of the B0 spectrum, which also gives rise to a change in weighting of the two vibronic peaks due to increased reabsorption of the emitted light. This small change in emission wavelength with generation is thought to be due to the excitonic energy level splitting observed in the absorption spectra, which appears to be relatively independent of generation above G1.

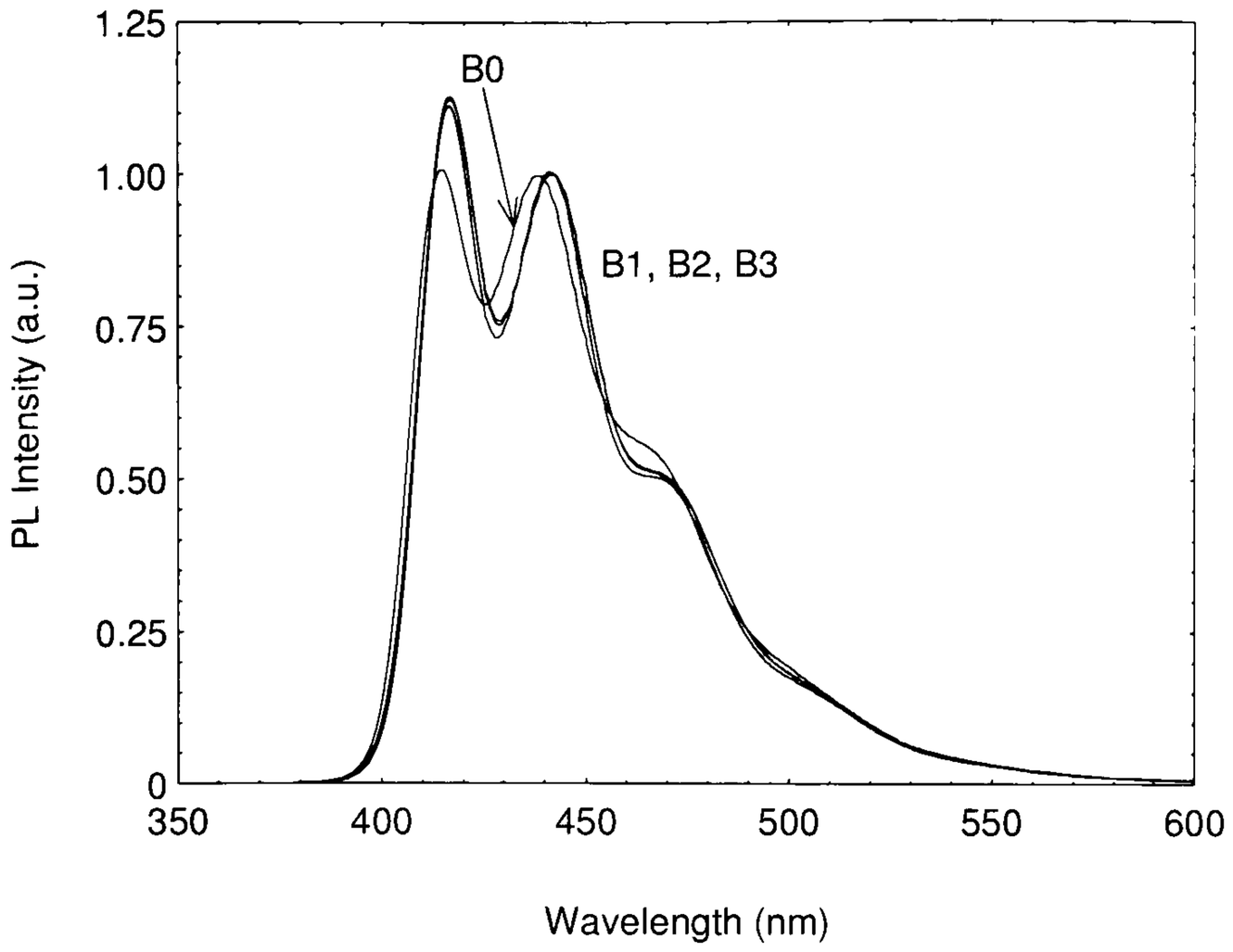

Fig. 4.10. *Benzene core dendrimer solution PL.*

The main difference between ADSB and BDSB becomes clear in the film PL spectra of BDSB shown in Fig. 4.11. A remarkable effect is seen: as the generation increases, the red-tail emission actually increases from B0 to B2. Only for B3 is the red-tail substantially reduced, but the emission remains much broader and red-shifted with respect to the solution emission. There is some vibronic structure visible in B0 and B1, but the B2 emission spectrum is very broad and shows no vibronic structure.

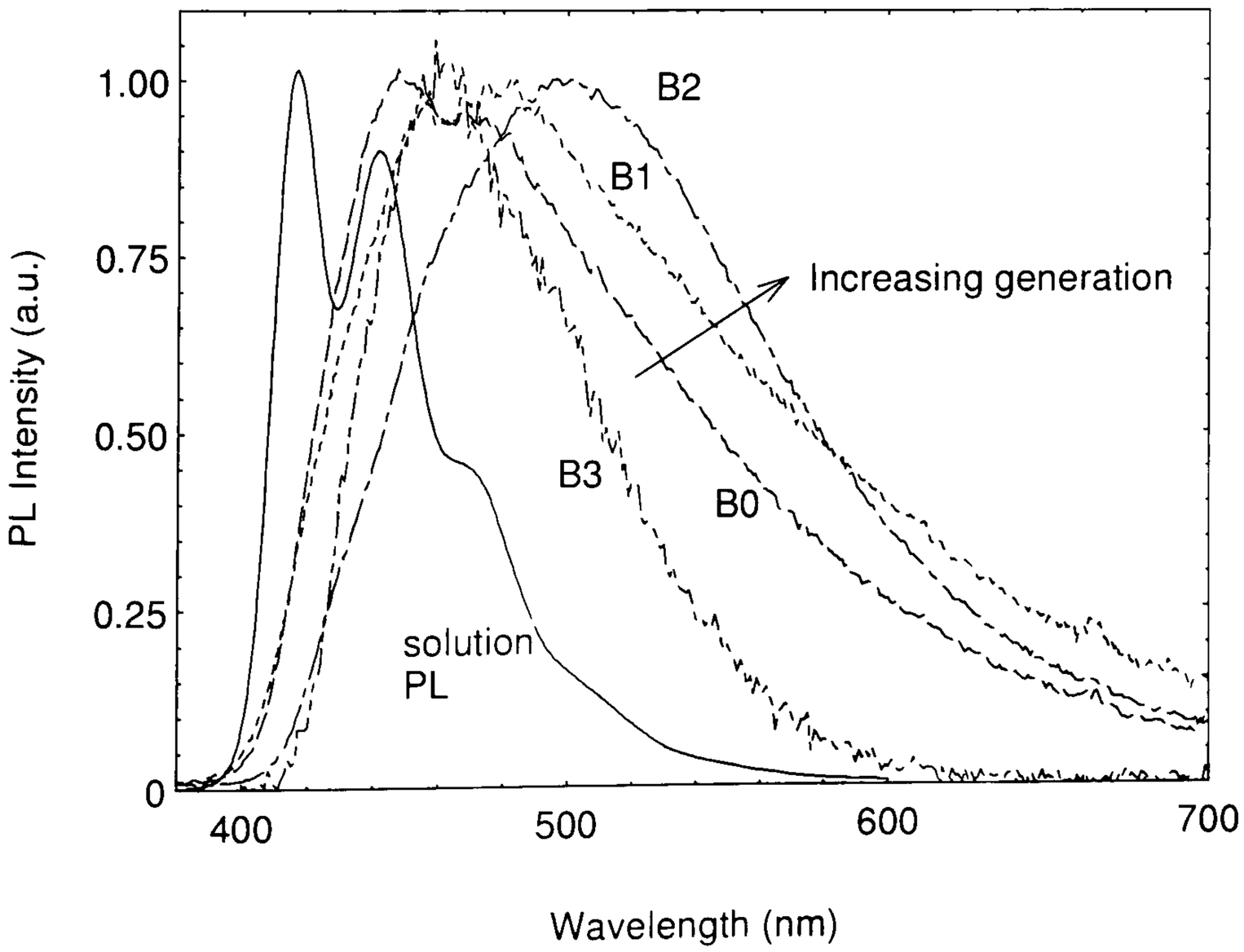

Fig. 4.11. *Benzene core dendrimer film PL compared to solution PL.*

The effect is even more pronounced in EL, as shown in Fig. 4.12. As the generation increases from B0 to B2 the emission becomes much broader. The B2 emission in EL is even broader than in PL. For B3 the EL emission is approximately the same as for B0, but is still much broader than the solution PL and also red-shifted. It is evident from the emission data that the dendrimer generation does allow a microscopic control of the level of interaction between chromophore units and the excimer red-tail emission, which appears to be prevalent in the B2 emission.

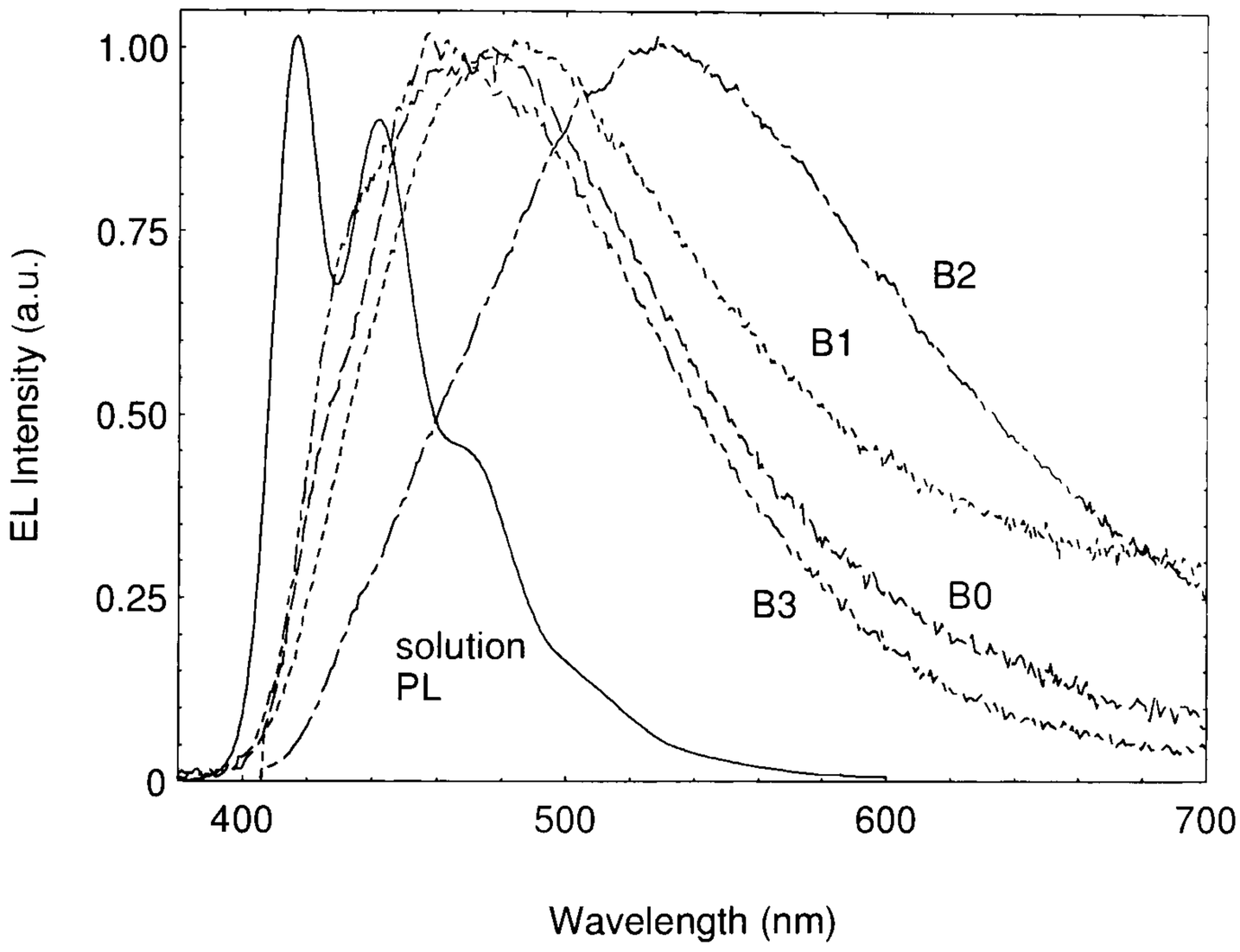

Fig. 4.12. *Benzene core dendrimer EL (PEDOT and aluminium electrodes) compared to solution PL.*

4.2.3 Comparison of the two dendrimer families

Although the chemical structure of the two families of dendrimers studied are very similar, as are molecular weight and size, it is evident from the discussion above that there are a number of significant differences between the photophysical properties of the two materials. Both dendrimers show strong exciton localisation at the core chromophore. However, whereas in the case of the nitrogen core dendrimer ADSB the core unit has to be seen as extending over the three distyrylbenzene units in order to explain the broad green emission band, in the case of the benzene core dendrimer BDSB

there is no or little interaction between the three distyrylbenzene units. The BDSB dendrimer hence practically has three emissive units, which are referred to as core chromophores. This will strongly affect the way excited states on different dendrimers interact with each other and will be discussed further on in more detail in the light of the quantum chemical calculations on the two dendrimer families.

Both material classes exhibit absorption spectra, which can, to a first approximation, be expressed as a linear superposition of the constituents. Such a scaling behaviour has previously been observed in a number of different dendrimer systems [4-6, 22]. As for the case of the benzene core dendrimer emission occurs directly from the distyrylbenzene units, it is instructive to compare these dendrimers with a previous study on a dendrimer which consisted only of one distyrylbenzene unit surrounded by four branching stilbene dendron units [4]. In this case, Halim et al. found that the G2 dendrimer was slightly red-shifted with respect to the G1 and G3 dendrimers. However, they did not observe the trend in EL and the G1 emission was seen to be much broader than the higher generation emission [4].

There are two important conclusions to be drawn from the comparison of the two dendrimer families presented here in view of the microscopic control of the emission properties of films and the level of excimer formation. Firstly, in both cases the desired effect of protecting the excitation from the environment is achieved for B3. The difference between the solution and film PL of the benzene core dendrimer suggest that it may be instructive to synthesise even higher generations to achieve total isolation. In the solid state, the level of interaction between core chromophores hence depends strongly on the dendron architecture. Secondly, the level of interaction also depends on the geometry of the core chromophore. Although aggregation appears to play little or no role in both materials, the broad featureless B2 emission spectrum, particularly in EL, suggests there is a very strong level of interaction between excitations in this case. This suggests that the B2 geometry forces the emissive distyrylbenzene chromophores of adjacent dendrimers closely together, whereas for B0 the individual chromophores are spaced further apart. More detailed structural investigations are required in order to fully understand this effect.

4.2.4 Thermochromic effects

A useful tool for probing the electronic properties of the dendrimers and investigating the characteristics of the excited state is the temperature dependence of absorption and emission spectra. It has been extensively studied in alkyl thiophenes and polydiacetylenes, for example [51]. Conjugated polymers exhibit strong thermochroism in some cases, such as MEH-PPV [52], and a number of connections have been drawn between the temperature dependence of the photophysical properties and the microscopic structure and morphology of films [52]. In general, more rigid materials appear to exhibit a smaller dependence on temperature [46]. In many materials, a reduction in band gap is observed with decreasing temperature, which is often attributed to the freezing out of ring torsions and the conjugated segments becoming more planar [53].

The film absorption spectra of the 0^{th} generation nitrogen core dendrimer are shown in Fig. 4.13 at 10 K and at 300 K. Two main features are seen, at approx. 320 nm and 420 nm. The lower energy feature corresponding to the core absorption moves to the red with decreasing temperature. The vibronic structure also becomes more pronounced at low temperatures. This shift may be explained by the core unit becoming more planar, as in the case of conjugated polymers. In contrast, the higher energy feature remains virtually unchanged with temperature, although the feature due to the lamp change at 321 nm somewhat distorts the shape. This suggests that the higher energy feature results from a geometrically more confined region of the molecule, such as a unit of shorter conjugation length. It is known from x-ray scattering measurements that the benzene rings comprising the triphenylamine core are in a non-planar arrangement [54], so it is expected that this unit becomes more planar with decreasing temperature. It is hence conceivable that the segment of the molecule corresponding to the higher energy absorption does not involve the amine core and hence corresponds to a stilbene unit on the outer end of the distyrylbenzene branch.

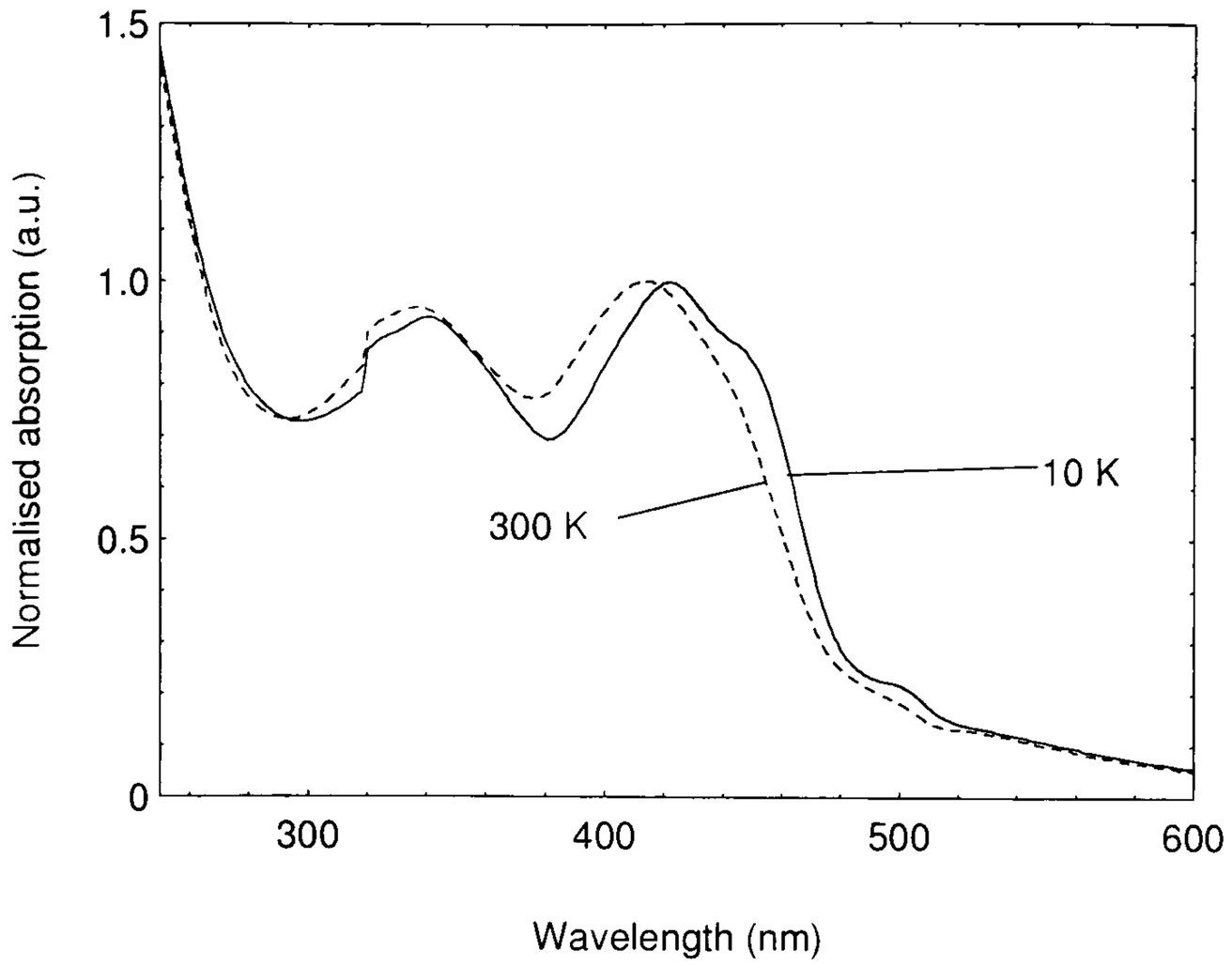

Fig. 4.13. *Temperature dependence of the film absorption of the 0th generation nitrogen core dendrimer A0. (Note that differences to Fig. 4.4 arise due to the experimental geometry in the cryostat. These spectra should be regarded as being for indication purposes only, as the reference beam could not be used in the setup.)*

The temperature dependence of core and dendron are clearly contrasted in Fig. 4.14 for the 2nd generation dendrimer. Whereas the lower energy core feature shows a similar temperature dependence to that of A0, the stilbene absorption is entirely independent of temperature. This suggests that whereas the core has a certain degree of freedom to change conformation, the dendrons are geometrically locked in a certain conformation. This temperature dependence also provides further evidence for the localisation of excitations on the core chromophore, as the absorption is clearly due to two distinct species. The origin of the feature at 500 nm seen at low temperatures in both figures is presently not clear, but it is thought to be related to either light scattering off the cryostat windows or condensation forming on the cryostat.

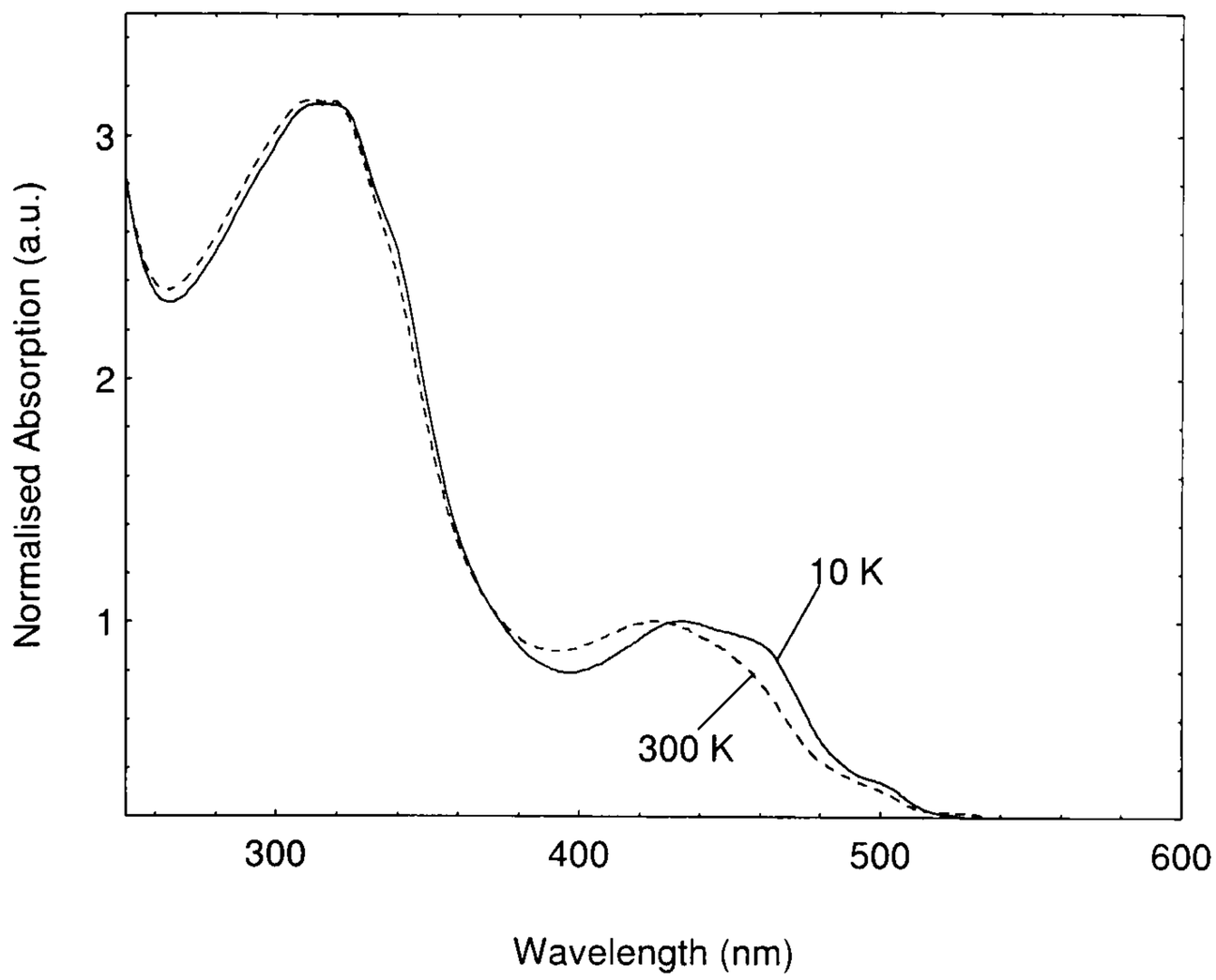

Fig. 4.14. *Temperature dependence of the absorption of a film of the 2nd generation nitrogen core dendrimer A2.*

The luminescence spectra of dendrimer films exhibit an even stronger dependence on temperature. This is investigated further for the case of EL from the 2nd generation nitrogen core dendrimer. Fig. 4.15 shows the evolution of emission spectra as the temperature is increased from 10 K to 300 K. At low temperatures, the emission is more intense and the vibronic structure of the films is more pronounced, which is remarkable considering the broad solution emission discussed earlier. The spectra broaden with increasing temperature. However, due to the presence of two vibronic features it is not possible to discern whether there is an overall blue-shift of the emission with increasing temperature. The spectra do show that any overall blue shift must be considerably smaller than the broadening.

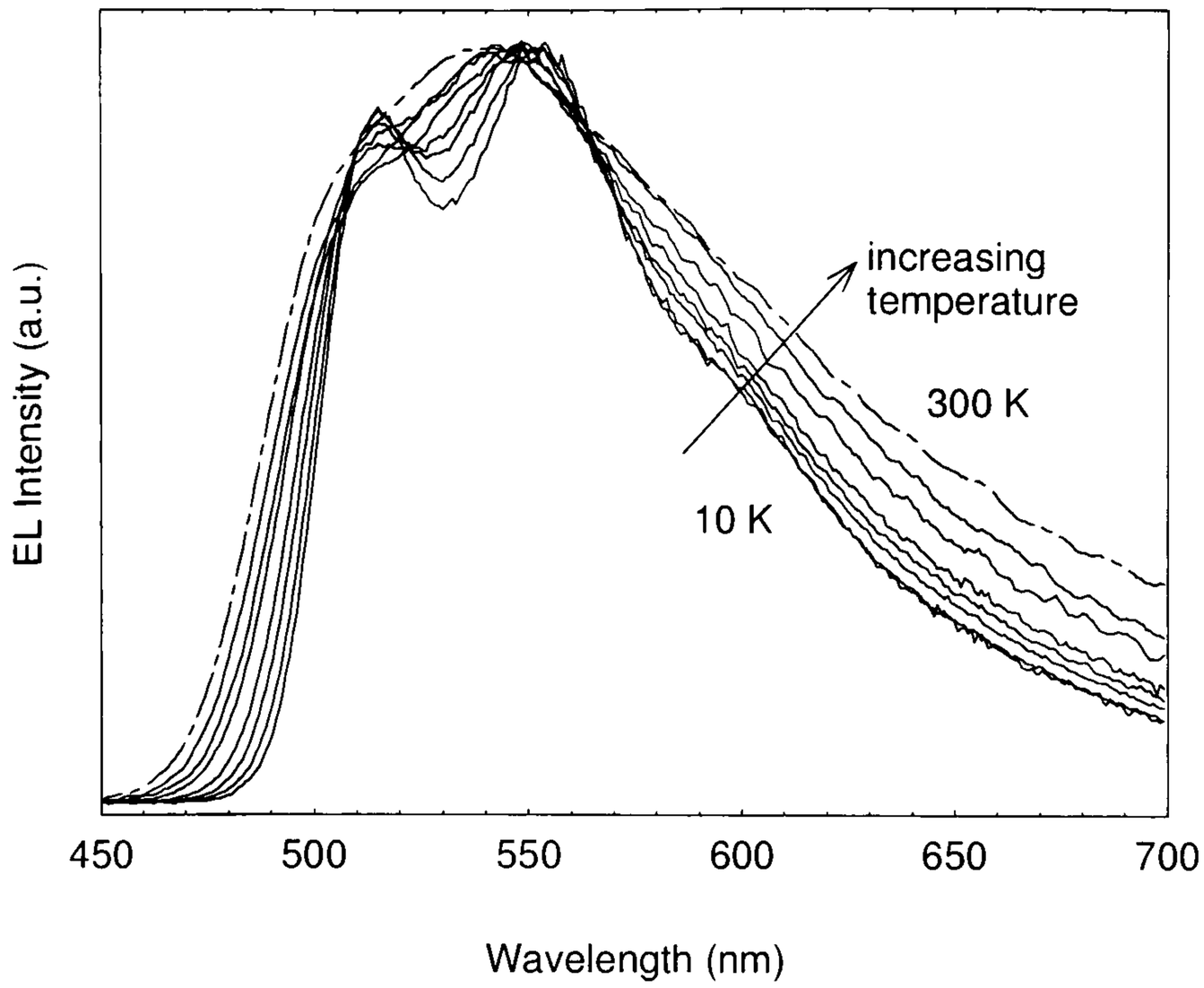

Fig. 4.15. *EL emission spectra of A2 measured at temperatures of 10 K, 70 K, 120 K, 170 K, 200 K, 230 K, 260 K and 300 K (from inside to outside), recorded at the same bias. The diode contained no PEDOT and had aluminium electrodes.*

A direct comparison of the two extremes is given in Fig. 4.16. It appears that the two vibronic peaks seen at 10 K merge directly into the single peak seen at 300 K.

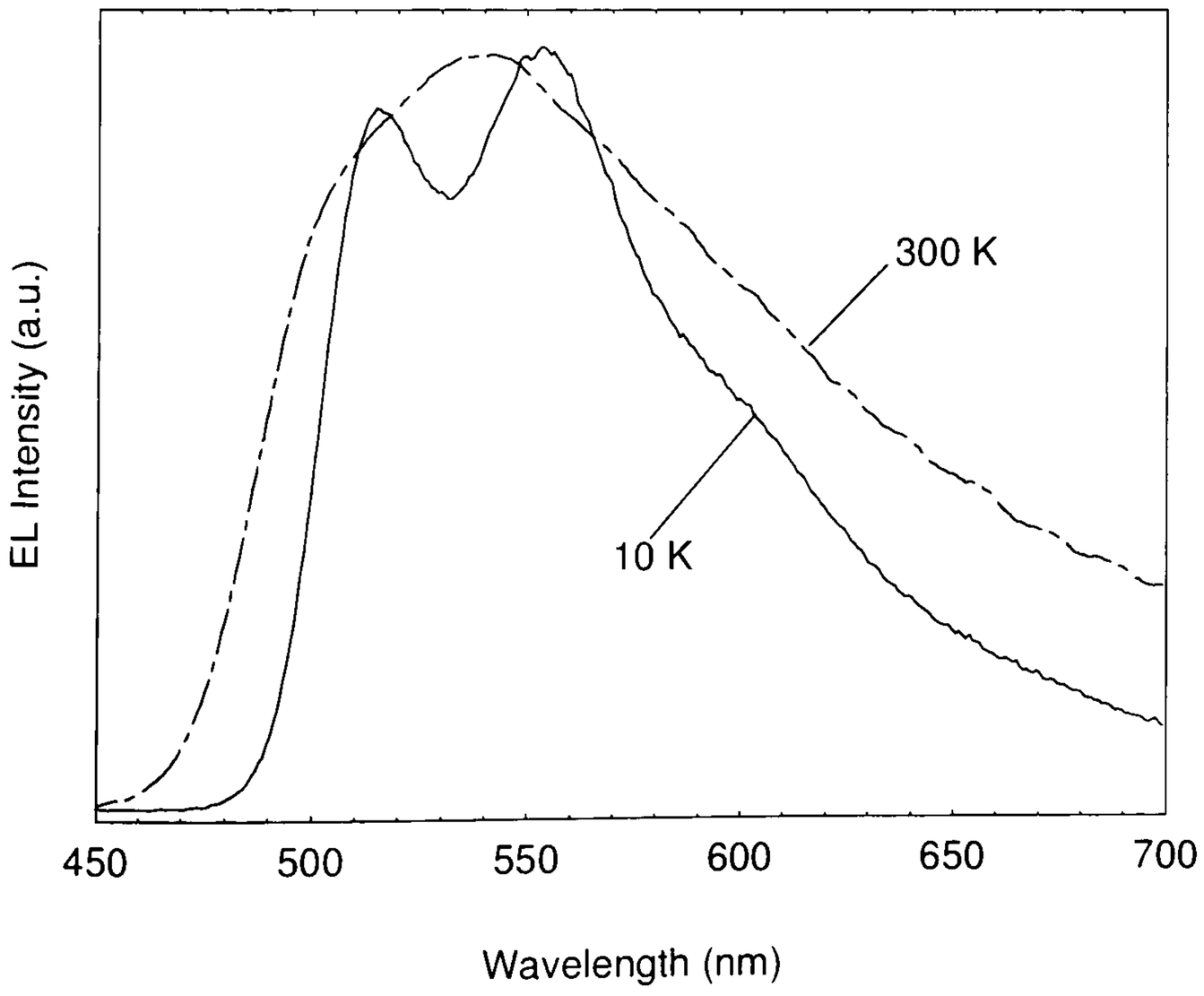

Fig. 4.16. *A2 EL at 300 K compared to EL at 10 K.*

It is most instructive to compare this case with the emission from an MEH-PPV LED. MEH-PPV is known to exhibit strong thermochroism [51, 52]. In Fig. 4.17 the EL spectra of a single layer LED are compared at 300 K and 10 K. The spectrum at 300 K was shifted to the red by 30 nm along the wavelength axis in order to overlay the two spectra. Remarkably, the width of the two spectra is virtually identical. There is more vibronic structure on the 10 K spectrum and the peak separation appears to be slightly reduced at high temperatures, but in contrast to the A2 LED the width remains independent of temperature.

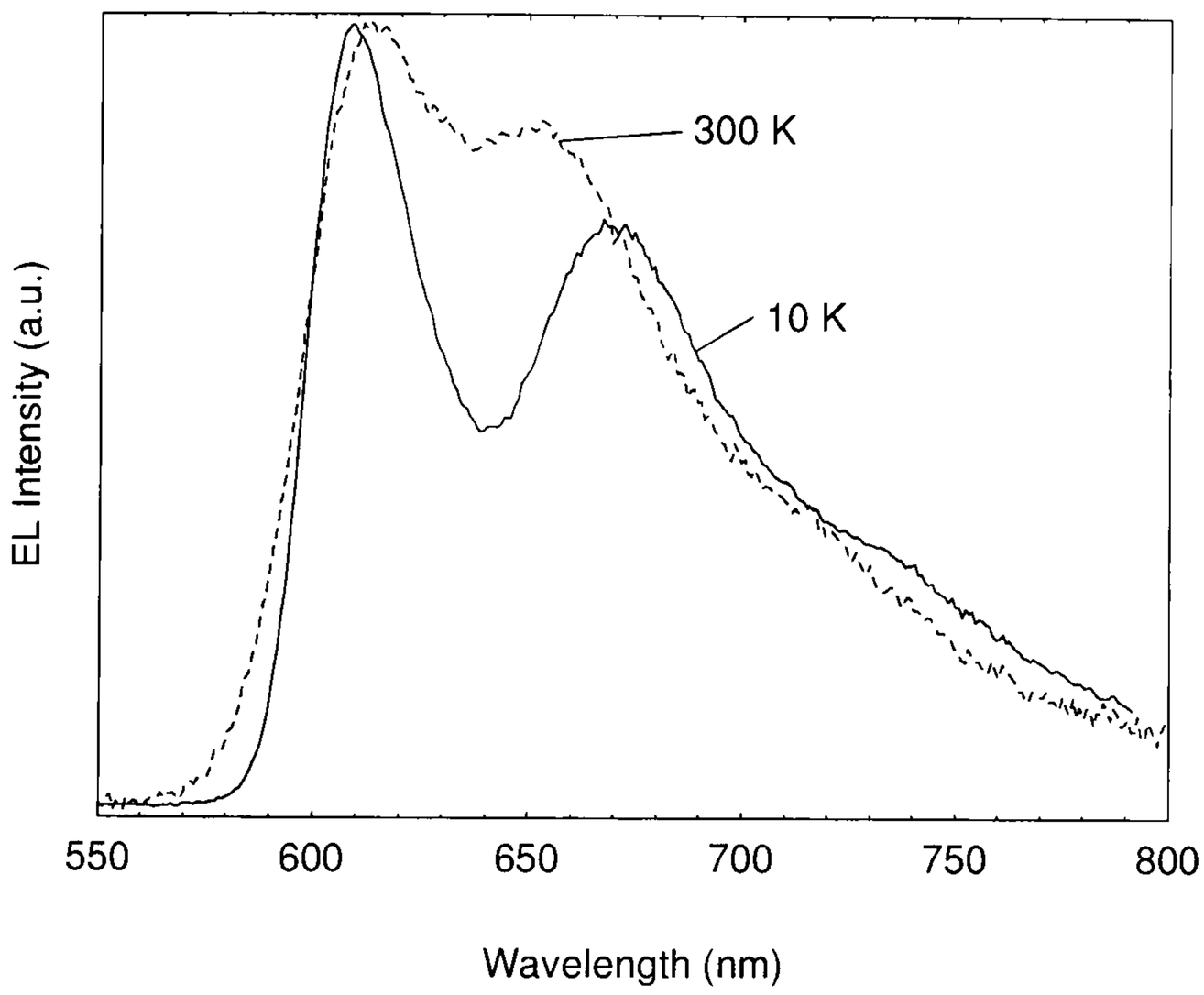

Fig. 4.17. *MEH-PPV EL measured at 300 K and 10 K (LED containing ITO and aluminium electrodes). The 300 K spectrum was shifted to longer wavelengths by 30 nm.*

This comparison between the temperature dependence of A2 and MEH-PPV gives important insight into the origin of spectral broadening in the two materials. A temperature dependent broadening is a result of electron-phonon coupling, which is strong in many organic systems. At lower temperatures, interactions between excitations and phonons are reduced, resulting in a narrower emission. However, in MEH-PPV recent three-pulse-echo studies have shown that the absorption is broadened homogeneously primarily due to electron-electron interactions, rather than electron-phonon interactions [55]. This results in a virtually temperature independent line width. The shift in band gap in MEH-PPV is a direct consequence of conformational effects

rather than broadening. The fact that MEH-PPV shows a strongly temperature dependent band gap, whereas the effect of broadening in A2 is stronger than a possible shift in band gap, also highlights the difference between the more band-like MEH-PPV and the molecular semiconductor A2. The comparison between localisation, in A2, and delocalisation, in MEH-PPV, also gives insight into the relative contributions between electron-electron interactions and electron-phonon interactions. In band-like semiconductors charge carriers move more freely and can hence couple more strongly, whereas in molecular semiconductors the excitation is more sensitive to phonon scattering processes as there are fewer free carriers that can give rise to correlation effects. These phonon scattering processes give rise to the temperature induced spectral broadening observed in Fig. 4.15.

The comparison with the absorption spectra is complicated. There is no direct evidence for thermal broadening in the absorption, and the low temperature absorption appears to be red-shifted by approx. 50 meV. In contrast, the emission at 300 K is broader by 70 meV to the red and the blue, giving rise to a total increase in the FWHM of 140 meV. It remains to be seen whether the dendrimer generation can be used to control the transition from more band-like to more molecular semiconductors by controlling the core chromophore separation. These preliminary results suggest that thermal broadening could increase with decreasing electron-electron correlation. As the electronic interaction can be reduced with increasing dendrimer generation, the nitrogen core dendrimer family may provide a model system in which to study the origin of homogeneous broadening in organic systems.

There is a further interesting temperature dependence of the A2 EL spectra, as shown in Fig. 4.18. This is a dependence of the emission spectrum on applied bias, with convergence reached at higher biases. In particular, at low biases the red emission tail appears to be stronger and the highest energy peak is weaker (the spectra are normalised to the second peak at 540 nm). As seen from the comparison of spectra at different temperatures, this bias dependence increases strongly with increasing temperature. In comparison, no such effect could be observed in MEH-PPV devices. Although this effect is hard to understand quantitatively, it may be related to the thermal broadening discussed previously. As the spectra become broader, the bias dependence increases. At high temperatures, emission occurs from the tail states as charge carriers have relaxed

into these states. As the bias is increased, emission occurs from higher energy levels, as the lower tail states are already filled. One possible explanation of the temperature dependence of this effect is an increase in lifetime of the carriers and the excitations in the tail states with decreasing temperature, which results in a rapid filling of the tail states. It is also conceivable that phonon scattering events modify the population of the tail states. As the effect is strongest at low biases, it should be noted that it cannot be attributed to either exciton dissociation or a Stark shift. The absence of such temperature and bias dependence recombination in more band-like materials such as MEH-PPV provides a further valuable characteristic of excitations on these molecular semiconductors.

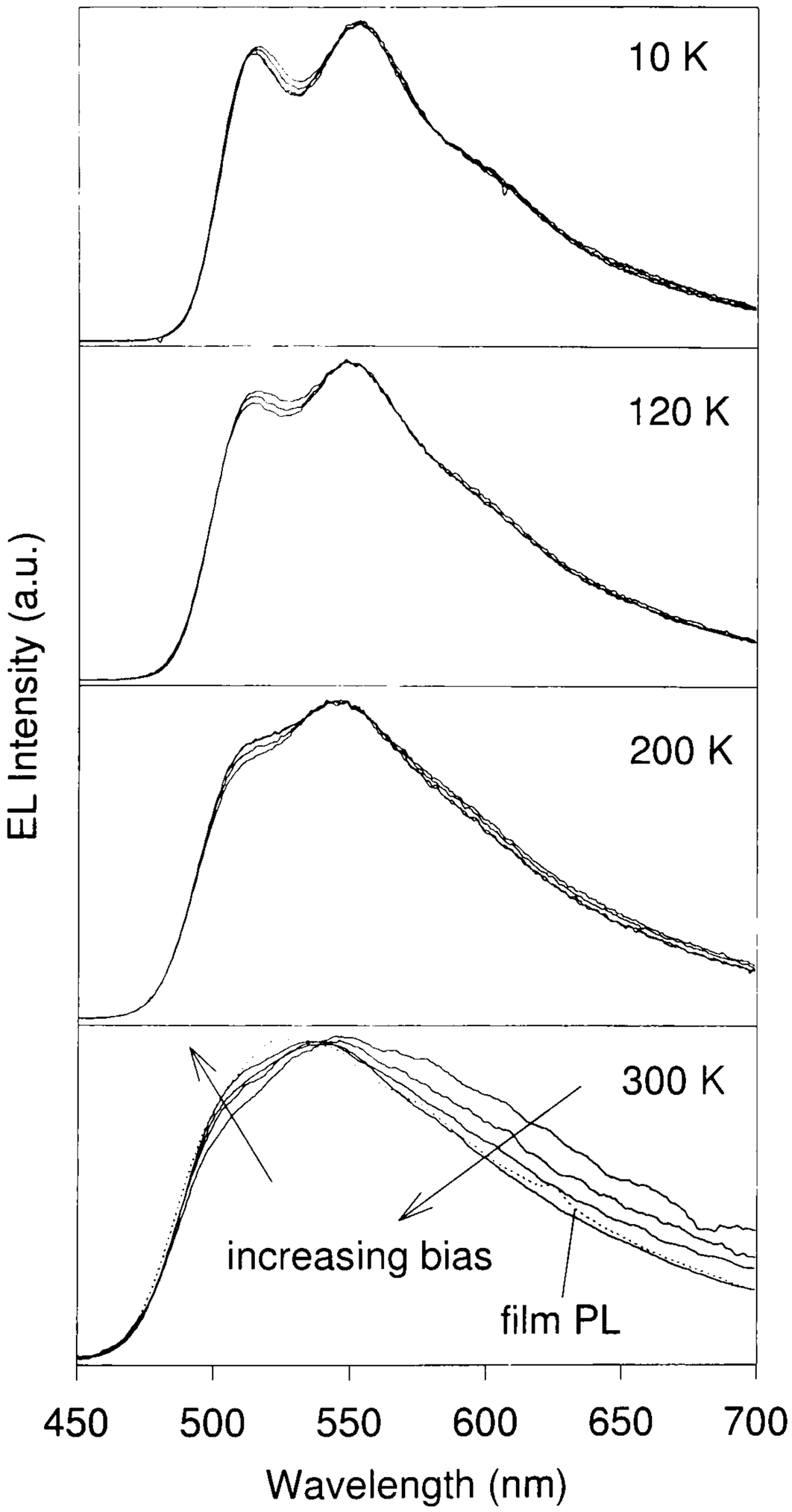

Fig. 4.18. *A2 EL spectra as a function of applied bias measured at different temperatures. The biases used were 17 V, 19 V, 21 V and 23 V at 10 K, 120 K and 200 K. At 300 K biases of 15 V, 18 V, 20 V and 22 V were used. The room temperature film PL of A2 is compared to the 300 K data.*

As a comparison to the previous discussion on the temperature dependence of A2 emission, the B2 EL spectrum is shown in Fig. 4.19 under room temperature operation and cooled under liquid nitrogen. As before, the emission intensity increases with decreasing temperature. In this case, the emission spectrum is very broad but does

narrow with reducing temperature. However, there are no vibronic features visible at all, and as pointed out before, the peak is shifted by over 100 nm to the red with respect to the solution luminescence. The absence of vibronic structure in this spectrum even at low temperatures suggests strongly that the emission in this case be entirely due to an excimer formed between adjacent distyrylbenzene units.

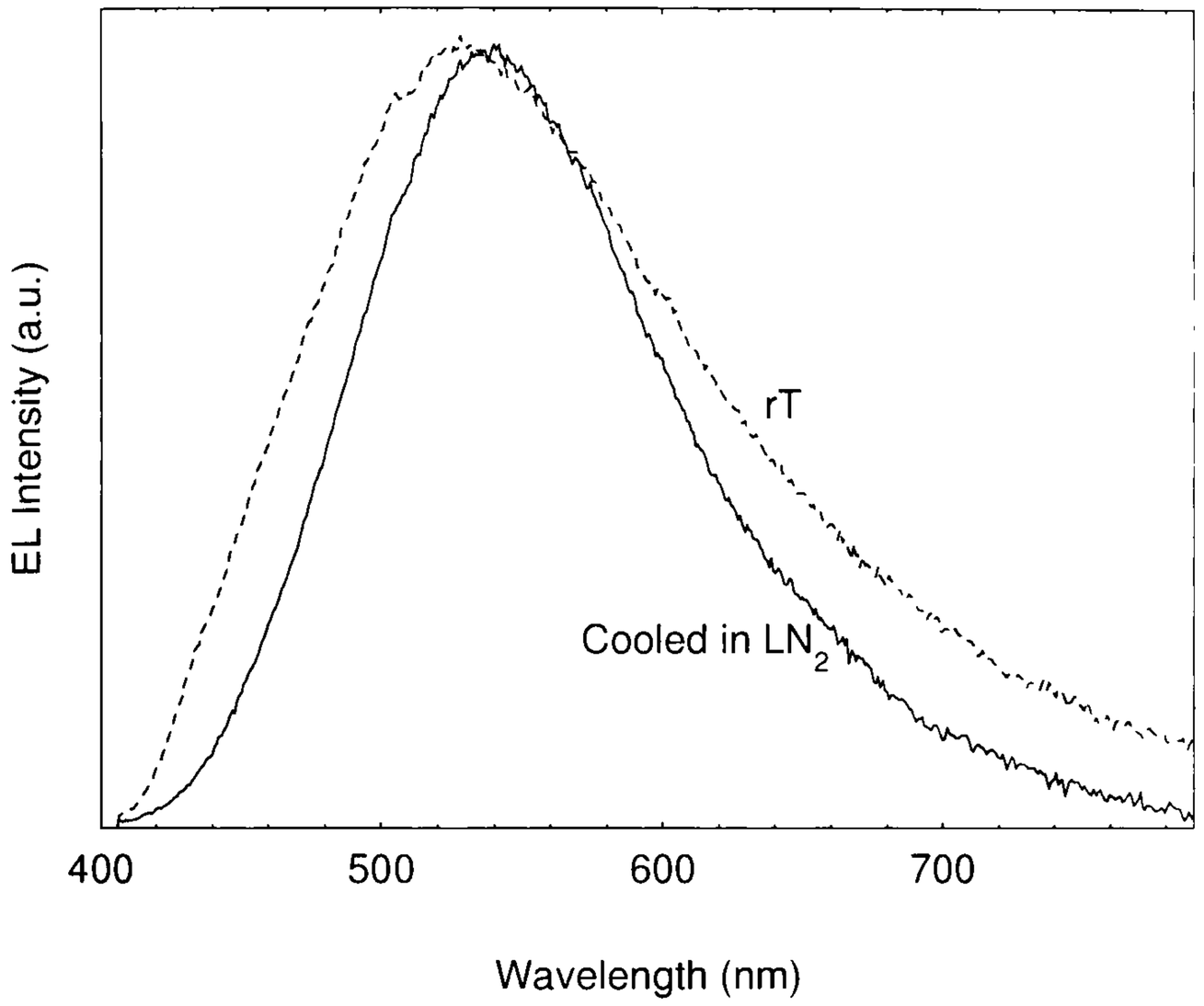

Fig. 4.19. *B2 LED luminescence recorded at room temperature and under liquid nitrogen cooling (exact temperature not known).*

4.2.5 Summary

Two families of conjugated dendrimers have been presented, which differ only in the choice of the central moiety, either a nitrogen atom or a benzene ring. For both materials excitations are found to be localised on the core chromophore, which is a green emitter in the case of the nitrogen core and a blue emitter in the case of the benzene core. In both cases the dendrimer generation is found to have a large effect on the level of intermolecular interactions, giving rise to a generation dependent red-tail emission. Due to the absence of an associated red-shifted absorption feature, this is attributed to the formation of emissive intermolecular excitations. For the case of the nitrogen core dendrimer there is a continuous reduction in the red tail with increasing generation, whereas in the case of the benzene core dendrimer the degree of red

emission initially increases with generation and is accompanied by an overall red-shift and loss in structure.

A dependence of the emission and absorption properties on temperature are observed in both materials, which are in part attributed to an increase in effective conjugated length of the dendrimer with decreasing temperature, but appear to be dominated by the effect of thermal broadening.

4.3. Dendrimer LEDs

4.3.1 Nitrogen core dendrimer device characteristics

The motivation behind the synthesis of these novel families of conjugated dendrimers was the search for new and efficient materials for organic LEDs. In the following section the properties of devices containing ADSB will be described. The temperature dependence of characteristics are compared to those of MEH-PPV LEDs and the most efficient device configurations in the form of bilayer devices are discussed.

The current-field characteristics of a PEDOT/ADSB LED with aluminium contacts are shown in Fig. 4.20. As the generation increases, the device current moves to higher fields, giving rise to an increase in operating field. In fact, the operating field more than doubles as the generation is increased from G0 to G3. This is a significant result, in that it demonstrates that the films become more insulating with generation, which is a direct result of an increase in core chromophore separation. The device characteristics can hence be correlated directly with the reduction in red-tail excimer emission observed in the EL spectra. As the position of the core absorption band is unaffected by generation, this marked change in characteristics must be due to a change in the transport properties rather than a change in the barrier to charge carrier injection. Furthermore, electrochemical studies on related dendritic compounds have shown that that the core energy levels remain unaffected by generation and that injection takes place into the core [56]. It is hence concluded that the barrier to charge carrier injection remains approximately independent of generation. This will be discussed in more detail in Chapter 6. The device stability was also found to increase with generation, and for G0 poor quality characteristics were frequently observed. A similar stability issue has

previously been observed by Halim et al. in distyrylbenzene-stilbene based dendrimers [4], and it is conceivably related to the quality of the dendrimer film. To date there has been no direct correlation of the device characteristics with generation.

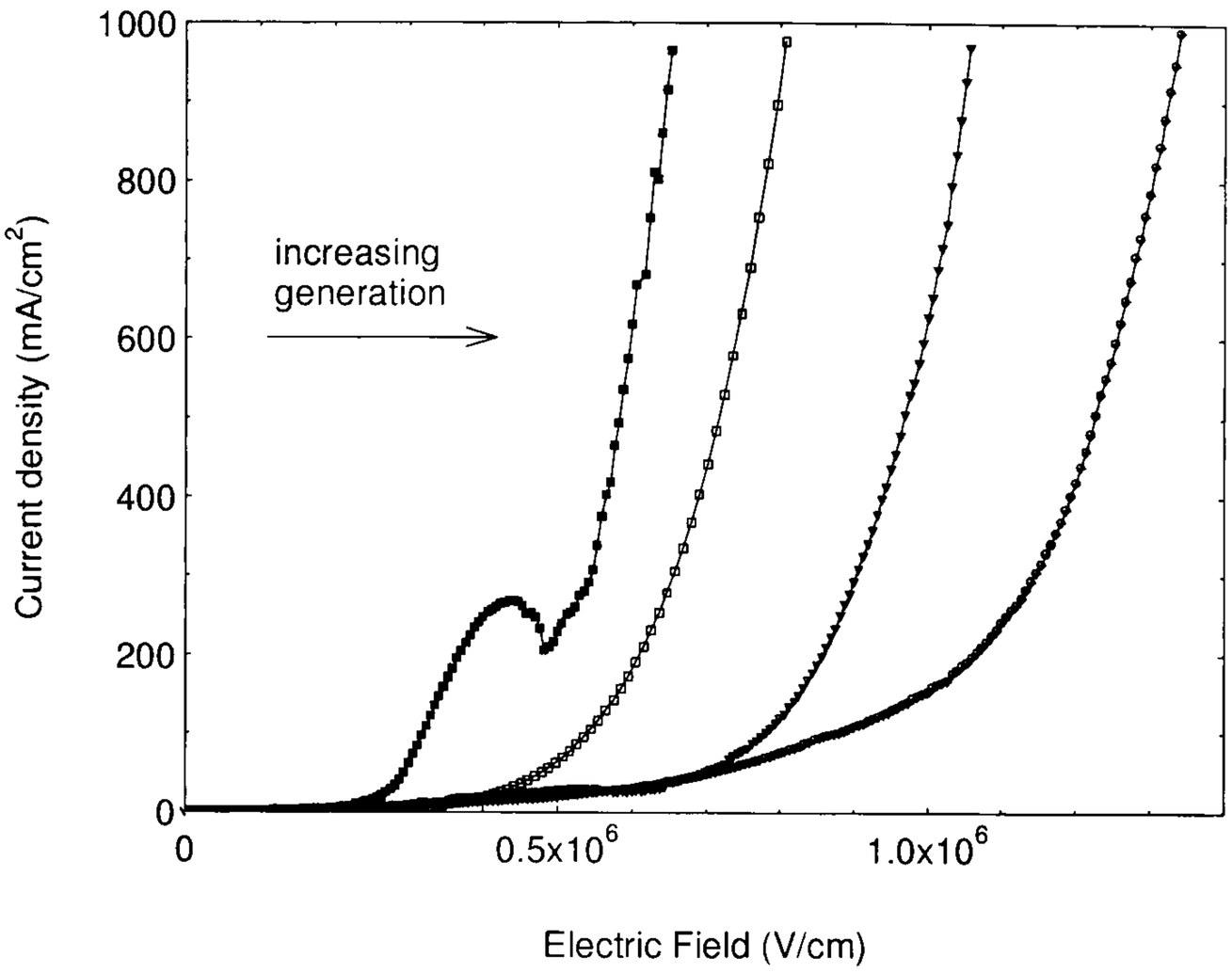

Fig. 4.20. *Current-field characteristic of nitrogen core dendrimer LEDs containing a PEDOT layer and aluminium electrodes.*

The same device characteristics are shown on a logarithmic scale together with the light intensity. The important result is that, as can be seen in the lower panel of Fig. 4.21, the maximal achievable brightness increases with generation. It is also seen that the light emission is observed at the same bias for all generations. There is also a strong exponential dependence of the device efficiency on generation, as is seen in Fig. 4.22.

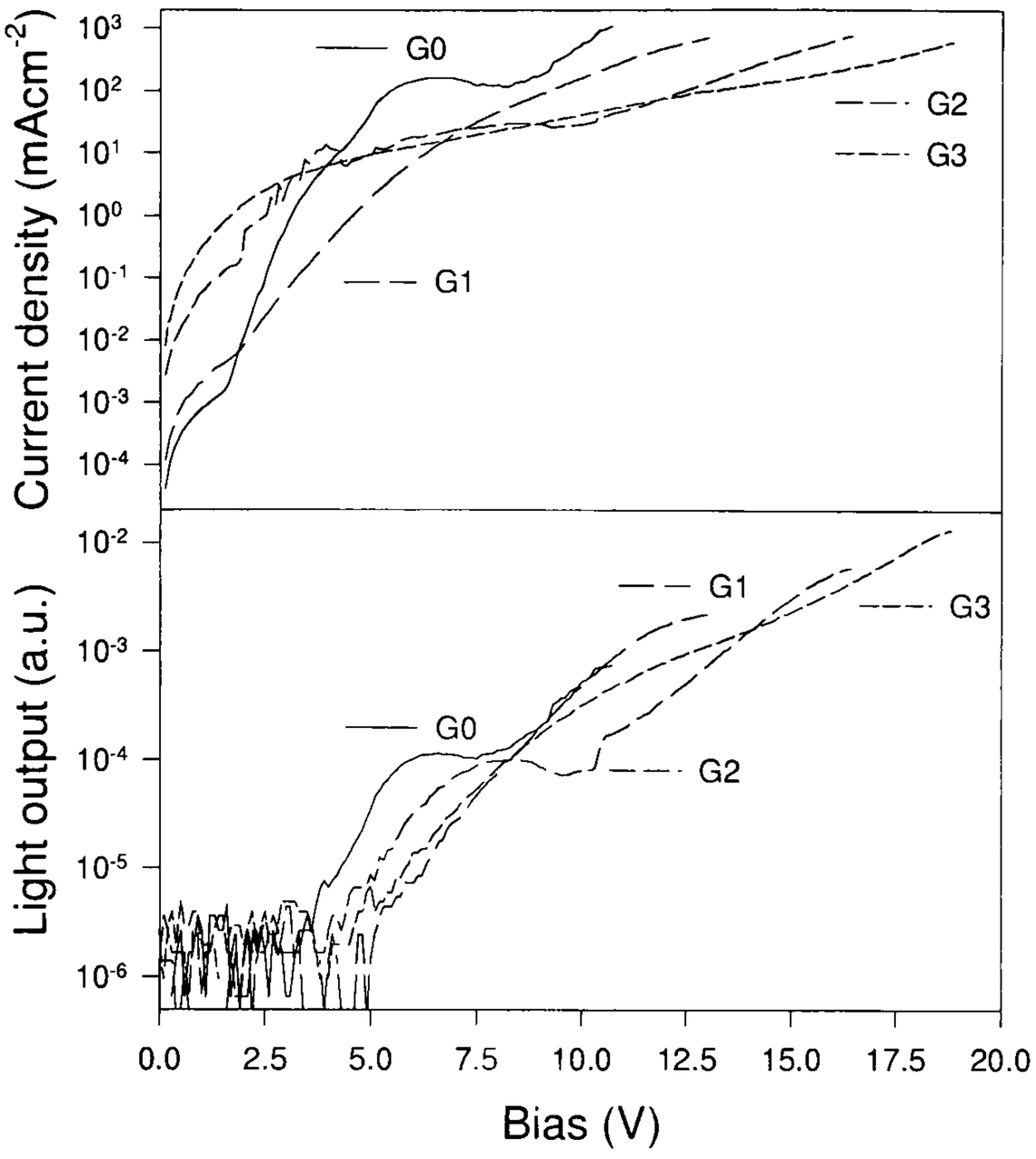

Fig. 4.21. *Device characteristics of nitrogen core dendrimer LEDs containing a PEDOT layer and aluminium electrodes shown on a logarithmic scale.*

Light emission is observed at the same biases independently of generation and appears to have a very similar functional dependence on bias for all generations. This suggests that whereas the current-voltage characteristics, which are governed by the majority carrier transport (holes), are strongly affected by increased chromophore spacing, the minority carrier currents (electrons) remain relatively unchanged. A conclusion of this is that the minority carriers are trapped on the chromophore, as has previously been proposed from analyses of the characteristics of PPV based devices [57]. Recombination hence occurs between relatively mobile holes and trapped electrons. As there is a large surplus of holes, an increase in chromophore spacing results in a reduction in hole current and hence an increase in efficiency and greater achievable brightnesses before device breakdown occurs. The independence of the threshold voltage for light emission also suggests that the electron current is injection limited whereas the hole current is transport limited. It is also important to note that the increase in external quantum efficiency is not related to a change in the PL quantum yield.

Whereas the increase in device efficiency is approx. a factor of 25, the increase in the PL quantum yield measured due to the reduction of excimer luminescence quenching with increasing generation is at most a factor of 1.5.

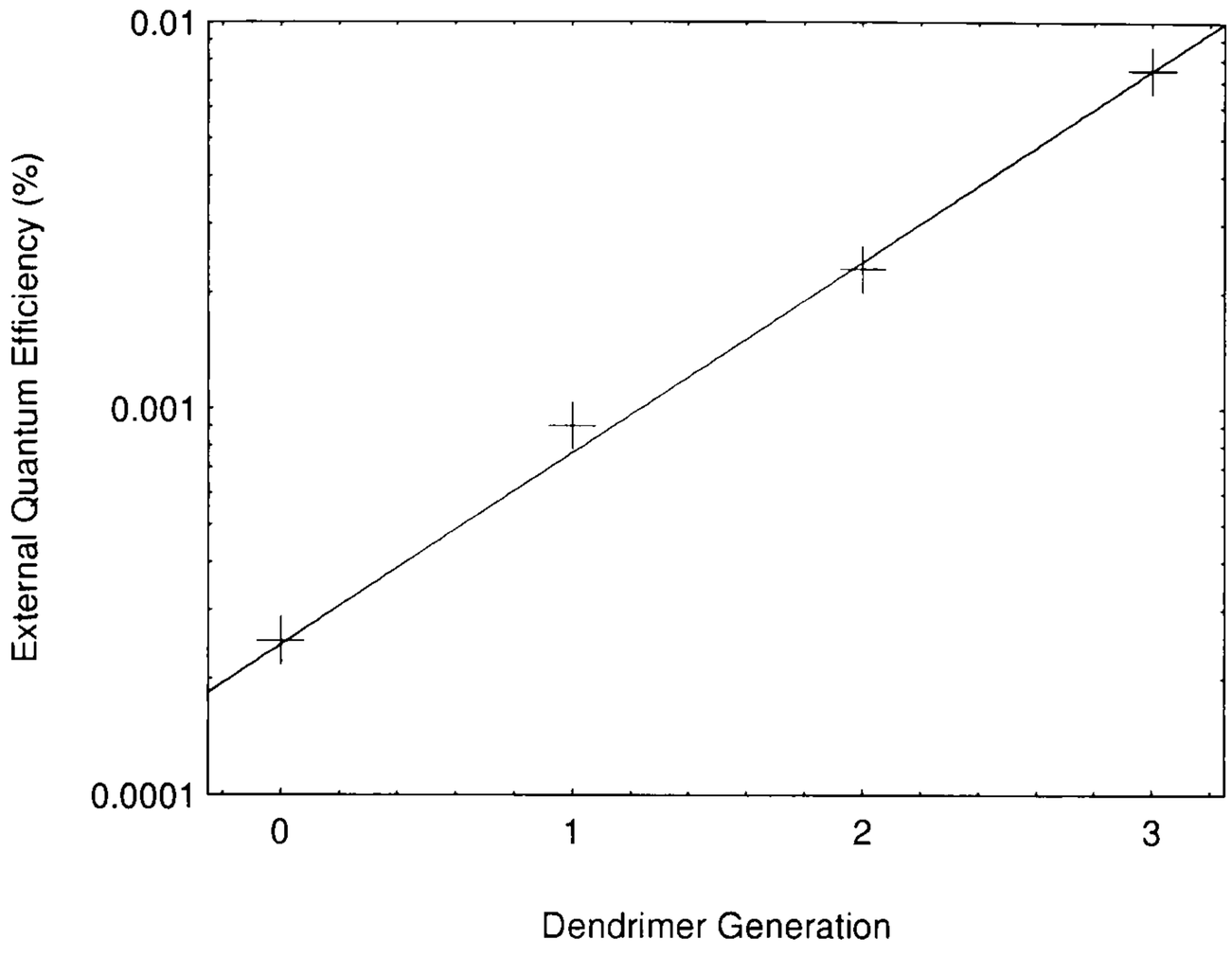

Fig. 4.22. *Dendrimer LED efficiency as a function of generation derived from the above characteristics.*

A further intriguing dependence of the device characteristics on generation is shown in Fig. 4.23, where the current-field characteristics are plotted on a double logarithmic scale. Double logarithmic scales are frequently used to investigate space charge limited transport and charge trapping [58]. As there is such a strong dependence on generation in dendrimer LEDs, charge transport clearly plays an important role and a double logarithmic plot could yield insight into the trapping processes present. Two regions of interest are identified, one in the low bias region, and the second at high biases. It is seen that at low biases below ~0.1 MV/cm the current actually increases with increasing generation, suggesting that some trapping processes and charging of the dendrimer film gives rise to an increase in leakage current with higher generation. This current does not contribute to EL and is hence referred to as a dark current. It is thought to arise from the trapping of charge carriers on the dendrimer cores which results in a significant build-up of space charge within the device and hence a polarisation of the material. Current-voltage characteristics at high generations and low electric fields hence approach the parabolic form of the Child's law description of space charge limited conduction. As the

generation number is increased, the power-law exponent at low fields increases from 1.3 to 1.8, whereas at high electric fields it decreases from approximately 9.5 to 7.0 with increasing generation. These trapping processes are related to the relative energy levels of the core and the dendrons, which can be estimated using cyclic voltametry. Work is currently underway to determine the precise nature of the trapping process, but an initial investigation suggests that the relative positions of core and dendron HOMO and LUMO can give rise to electron trapping on the core [59].

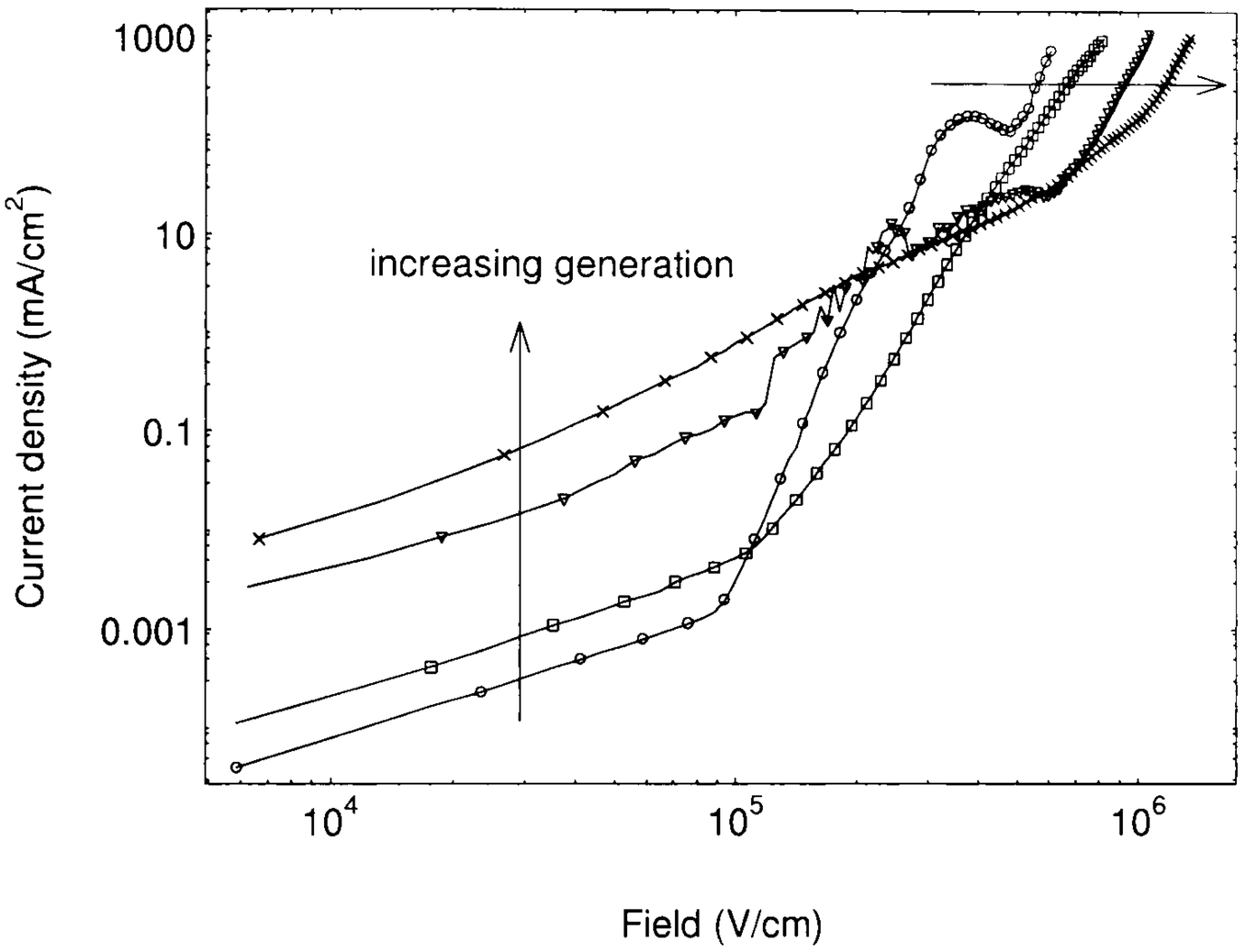

Fig. 4.23. *Dendrimer LED current-field characteristic in double logarithmic representation.*

A further tool for investigating charge transport in dendrimer LEDs is to measure the transient response of EL to an applied voltage pulse [60]. The rise of EL for LEDs operated at a constant field of 1.7 MV/cm is shown in Fig. 4.24. It is seen clearly that the EL rise time increases with increasing generation, suggesting a slowing in charge transport. Although it is not possible to extract any quantitative information regarding the charge transport in dendrimer LEDs, the fact that the rise is more gradual for the G3 LED implies that the time needed for electron and hole currents to reach equilibrium is increased. There is no clear delay visible between the application of the voltage pulse and the start of EL, which suggests that charge transport is highly dispersive and that the charge carrier fronts are spread out across the film. The spread in the carrier waiting time distribution gives rise to the gradual increase in EL with time. As the generation

increases, the waiting time on each hopping site increases, which gives rise to a further slowing in charge transport.

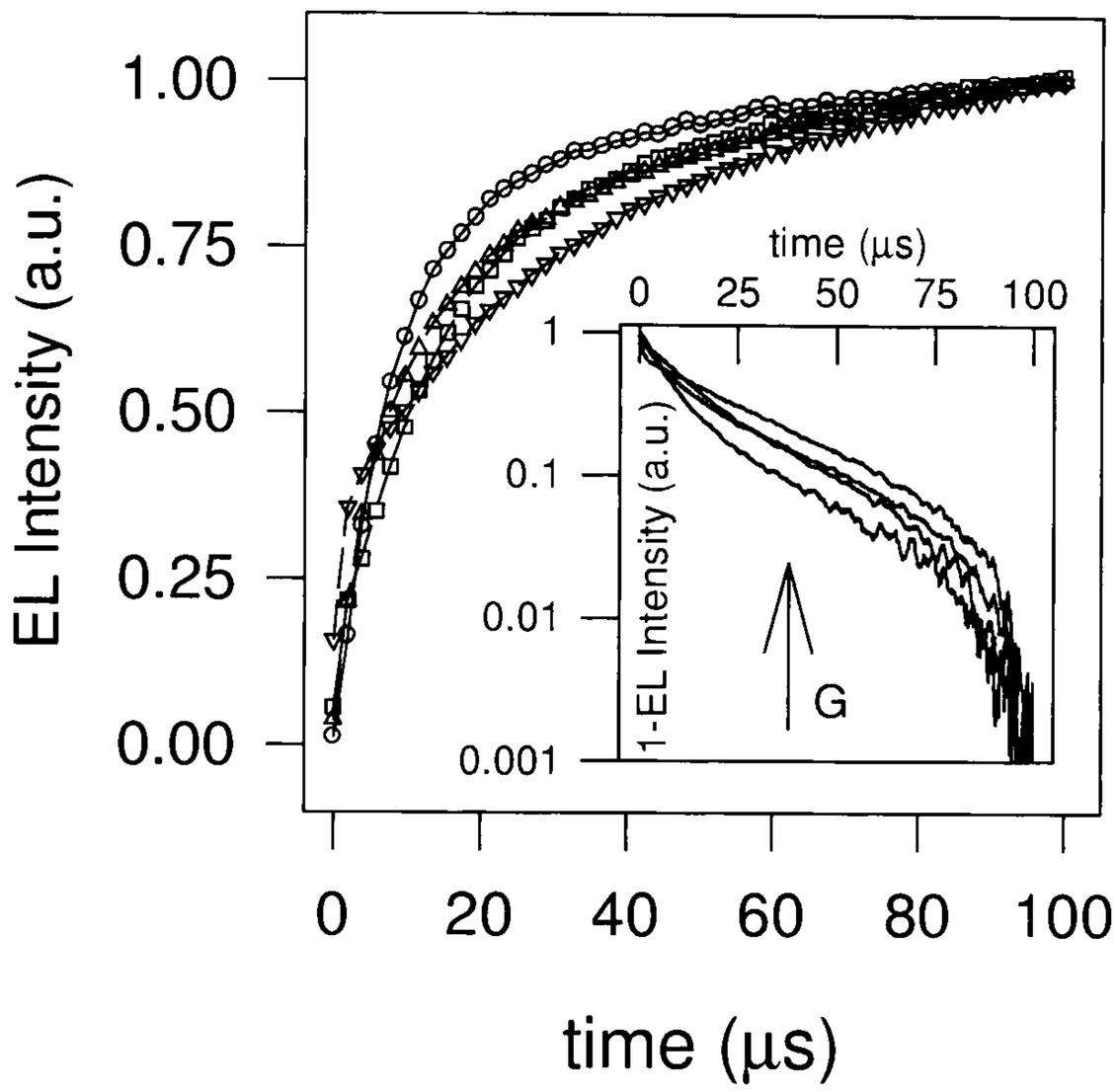

Fig. 4.24. *EL onset and rise of dendrimer LEDs at a field of 1.7 MV/cm,* G=0 (○), G=1 (□), G=2 (△), G=3 (▽). *Inset is the inverse rise on a logarithmic scale. The LEDs did not contain a PEDOT layer in this case. Aluminium was used as the cathode.*

A remarkable consequence of the slowing in charge transport, which may also be thought of as a reduction in charge carrier mobility, is shown in Fig. 4.25. Devices were fabricated on ITO/PEDOT anodes with gold cathodes. The gold work function is slightly higher than that of PEDOT, so the device energy levels were actually reversed with the barrier to electron injection being larger from the cathode than from the anode [61]. As can be seen in the figure, the A0 to A2 devices support very large currents but do not emit any significant amount of light. However, for A3 the current is reduced by orders of magnitude and at high biases above 15 V light emission is observed.

Surprisingly, the A3 device has an efficiency of approx. 0.005 %, which is comparable to that of a device with an aluminium cathode. In comparison, for MEH-PPV the efficiency of devices with gold cathodes has been reported to be over 2 orders of magnitude smaller than that of devices with aluminium cathodes [62]. This observation demonstrates that for A3 devices the charge carrier mobility is so low that the device efficiency becomes virtually independent of the cathode barrier to injection. Due to the increase in the barrier to electron injection of approx. 1 eV between aluminium and gold, the operating bias increases significantly and stable EL is not observed below approx. 15 V.

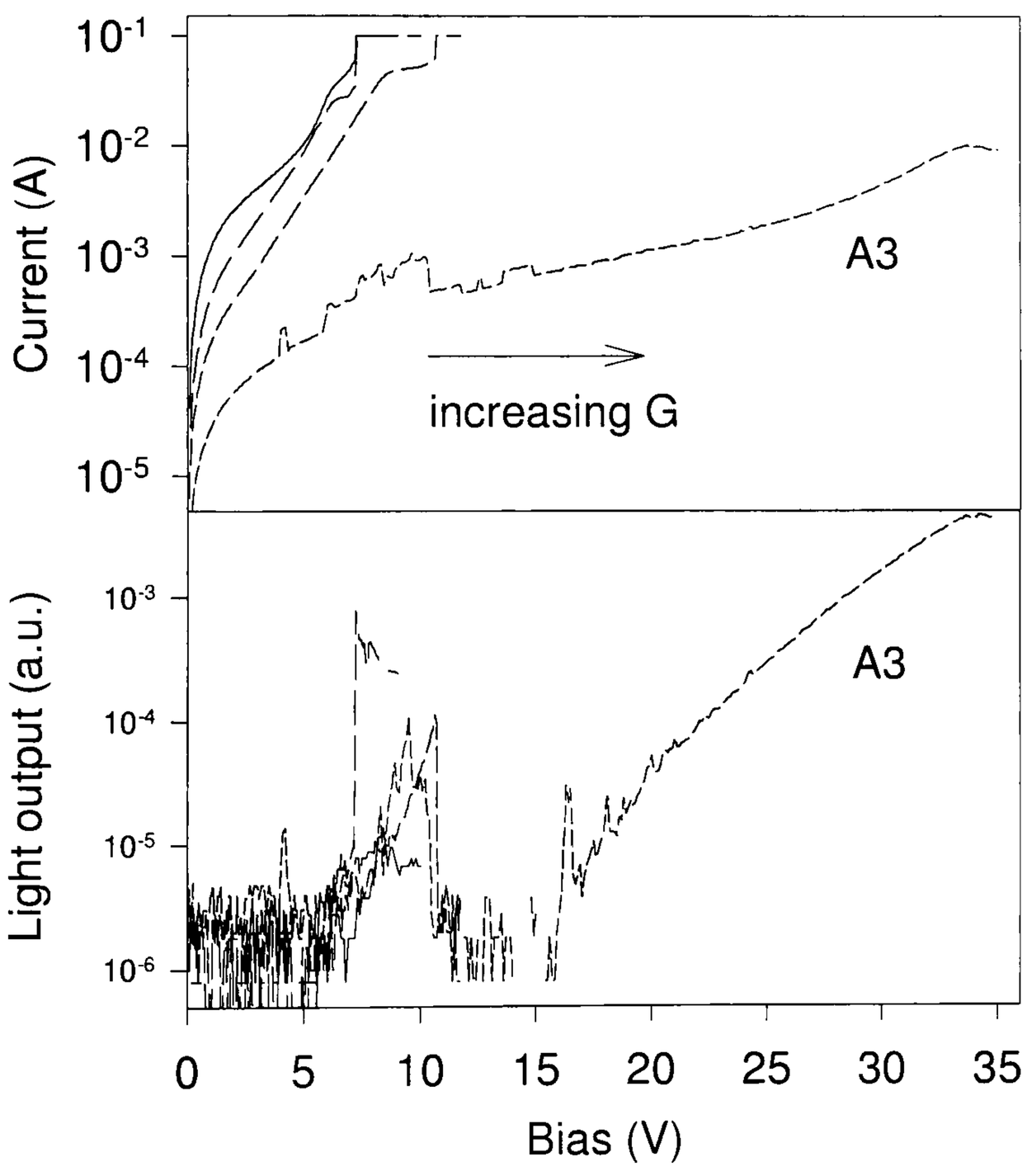

Fig. 4.25. *Dendrimer LED characteristics for devices in the configuration ITO/PEDOT/Dendrimer/Gold, where the gold electrode formed the cathode.*

Devices were also fabricated with calcium electrodes, but similar device characteristics to those of aluminium containing devices were observed. However, upon accidental introduction of an insulating oxide layer in the calcium evaporation, the device efficiency was found to increase by an order of magnitude. An MEH-PPV control

device did not display the same behaviour and in contrast showed a reduction in efficiency by almost 3 orders of magnitude. Calcium is known to be problematic as a cathode material and previous studies on dendrimers have raised concerns regarding the stability of the calcium-dendrimer interface [6]. It is also known from photoelectron spectroscopy measurements on electrode-polymer interfaces that calcium can react with the material at the interface [63]. The best results in terms of efficiency and stability of single layer devices were obtained for devices with magnesium-aluminium cathodes. For single layer devices of A0 with no PEDOT layer a maximum brightness of 24 Cd/m^2 was observed with a peak efficiency of 0.02 %. In contrast, for A3 a peak brightness of 100 Cd/m^2 was measured with a peak efficiency of 0.2 %.

4.3.2 Temperature dependence of nitrogen core dendrimer device characteristics

As established in the previous sections, it is believed that the dendrimers provide model systems of molecular semiconductors. The issue of whether organic semiconductors are intrinsically more band-like or should be treated from a molecular point of view has been at the centre of heated debate for the past years [46, 51, 64-65]. In view of charge transport and in particular the description of device characteristics, it is particularly important to establish whether the treatment of organic semiconductor devices in the conventional framework or semiconductor band theory is correct. A useful tool for investigating the charge transport in organic LEDs is a simple consideration of the temperature dependence of the device properties. MEH-PPV is a well-studied system and many device characteristics have been reproduced within the framework of mainly conventional device models [66-67]. The dependence on temperature of the current-voltage and the brightness-voltage characteristics is shown in Fig. 4.26 for both an A2 device and an MEH-PPV device at 300 K and at 10 K. It is seen that the operating field increases with decreasing temperature and so does the threshold voltage for light emission. The functional dependence of the characteristics on temperature are very similar for the two materials, in particular the relative change in slopes of the curves. For the A2 device the dark current at 10 K is significantly greater than for MEH-PPV, which is thought to be a consequence of doping through either atmospheric impurities or the ITO anode [68]. Also, a hump is seen on the A2 current-voltage characteristic at

300 K, which is believed to be due to such a doping effect and was reproducible upon repeated voltage sweeps. The similarity of the functional dependence of the brightness versus voltage curves on temperature is quite surprising, considering the large difference in the effect of thermal broadening on the emission properties discussed earlier. However, this similarity suggests that the charge transport in organic LEDs can be described by a unique model, independently of the exact electronic structure of the material.

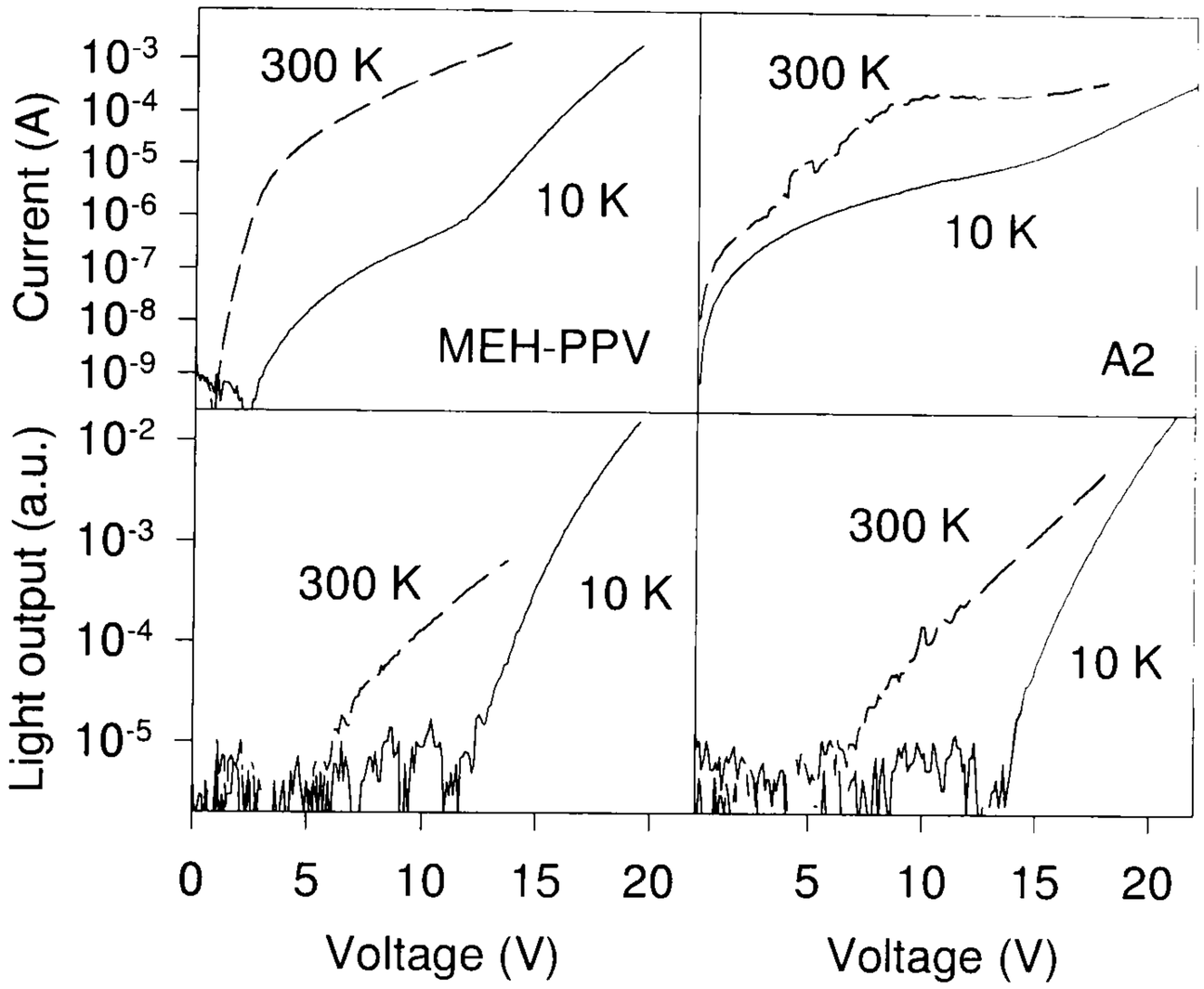

Fig. 4.26. *Temperature dependence of A2 device characteristics compared to MEH-PPV device characteristics (no PEDOT layer in both cases). The temperature was reduced from 300 K to 10 K. During the cycle, the devices were not operated in reverse bias.*

In addition, the functional dependence of the device efficiency on temperature is shown in Fig. 4.27. As seen in the device characteristics, the functional dependence of the device efficiency on temperature is virtually identical for the two materials: it increases strongly with decreasing temperature. However, whereas for A2 the increase from 300 K to 10 K is only by approx. a factor of 8, for MEH-PPV the increase is fifty-fold. It should be noted that this increase of efficiency is due purely to the charge transport

becoming more balanced rather than a change in barrier to injection. Although the band gap of MEH-PPV is reduced by approx. 120 eV as the material is cooled down, the strongest change with temperature is between 200 K and 300 K [67]. Yet in this region the efficiency is virtually constant. The subsequent increase in efficiency is thought to be similar in nature to the process, which gives rise to the generation dependent increase in efficiency. As the temperature is reduced, the majority carrier mobility is reduced more strongly than that of the minority carriers, which are also dispersed in traps throughout the film [57]. It is somewhat surprising that the dependence of this process on temperature should be independent of material, as seen in Fig. 4.27.

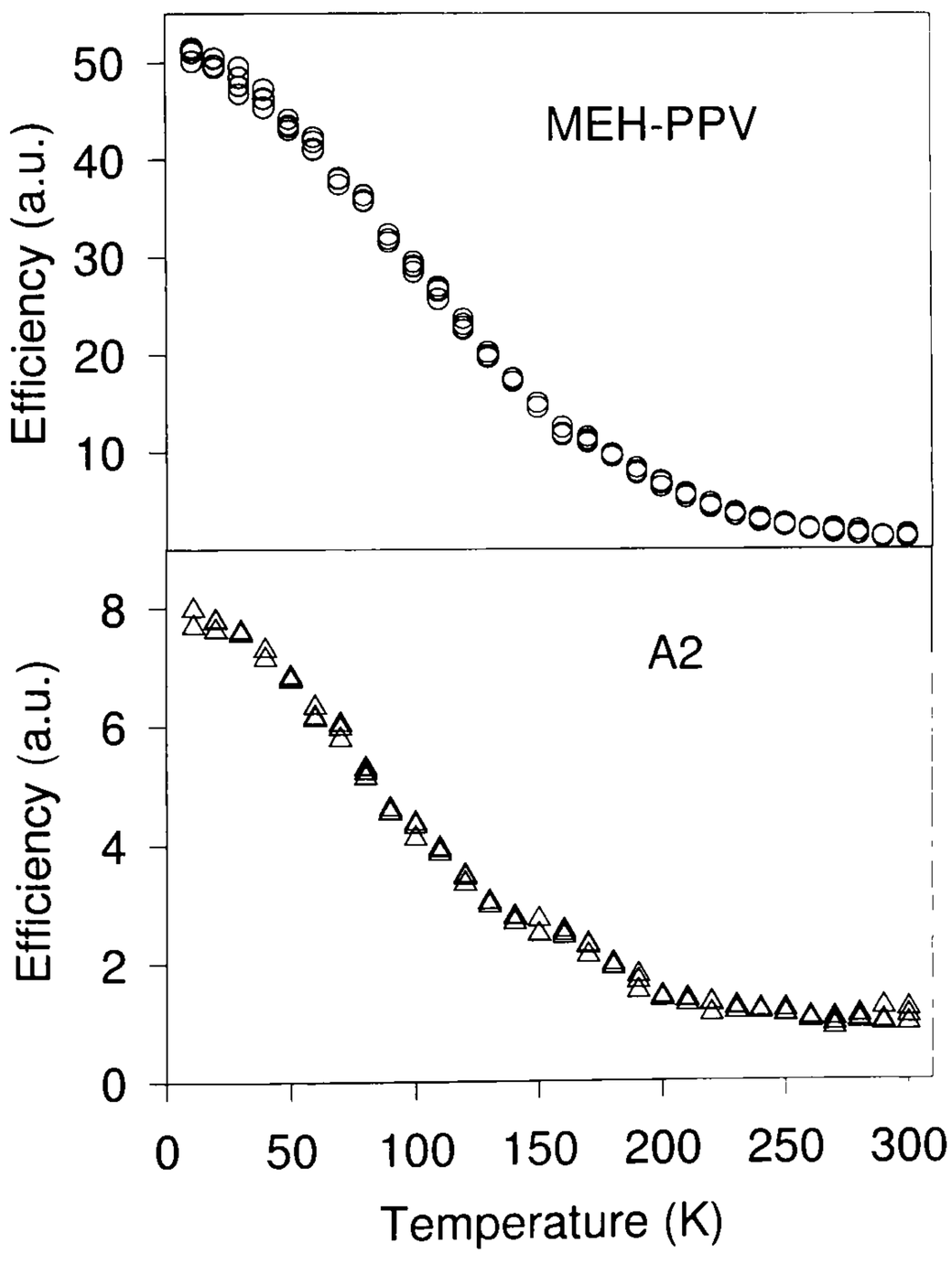

Fig. 4.27. *External quantum efficiency of an A2 device compared to an MEH-PPV device as a function of temperature. The efficiency was normalised to the value at 300 K. Four measurements were made at each temperature.*

This investigation has shown that the characteristics of dendrimer LEDs exhibit a strong dependence on temperature, which is functionally rather similar to that of MEH-PPV LEDs. This is an interesting result, for it has also been established above that the

dendrimer device characteristics depend strongly on generation and hence on the chromophore spacing. Indeed, there is a strong correlation of the device characteristics with the generation dependent excimer red tail emission. Charge transport at low temperatures is likely to be highly dispersive with the carriers not possessing well-defined transit times. The comparison of A2 and MEH-PPV devices hence suggests that there is some universal transport mechanism in thin film organic LEDs which is virtually independent of the material.

4.3.3 Benzene core dendrimer LEDs

LEDs containing the benzene core dendrimers were fabricated following the same route as for the nitrogen core dendrimers. The G0 and G1 devices were found to be very unstable, whereas the G2 and G3 devices were more stable. However, overall the devices were much less stable than devices containing the nitrogen core dendrimer. Approximate efficiencies for the four generations of LEDs with PEDOT and aluminium electrodes are 0.001 %, 0.0001 %, 0.001 % and 0.002 % for G0 to G3, respectively. In contrast to the nitrogen core dendrimers, there is no systematic progression in the efficiency and it is also hard to see a correlation with the photophysics. Sample device current-voltage characteristics are shown in Fig. 4.28. As for the nitrogen core dendrimer there is an increase in the operating bias with increasing generation, except for the 3rd generation device. However, the B3 device was fabricated in a separate run, so there is the possibility of sample to sample variation, although it is unlikely that this would give rise to a change in operating bias by over a factor of two. As the red-shift in the emission is reversed on the transition from B2 to B3, it is not surprising that there is a marked shift in the device characteristics.

It is surprising, however, that the operating bias increases from B0 to B2 whereas the red emission actually increases, suggesting that the emissive sites move closer together. A possible interpretation of this is that the entire core unit, consisting of three distyrylbenzene units, has to be seen as the transport site, rather than the individual distyrylbenzene units. One possible interpretation is then that charge carriers can hop over or tunnel through the central benzene unit. Clearly an increase in the number of stilbene units present in the material will have an insulating effect, which is observed in

the device characteristics. In contrast, the emission occurs only from individual distyrylbenzene units, so excimer formation will be dominated by the minimum distance between these chromophore units rather than the average distance between the entire core units of the dendrimer. Two distyrylbenzene units from different molecules may hence be in close proximity, even when the overall intermolecular spacing increases. For the 3rd generation a significant change in molecular arrangement takes place, which, in contrast to the nitrogen core dendrimers, is discontinuous with generation, giving rise to a reduction in red emission as well as a reduction in operating field.

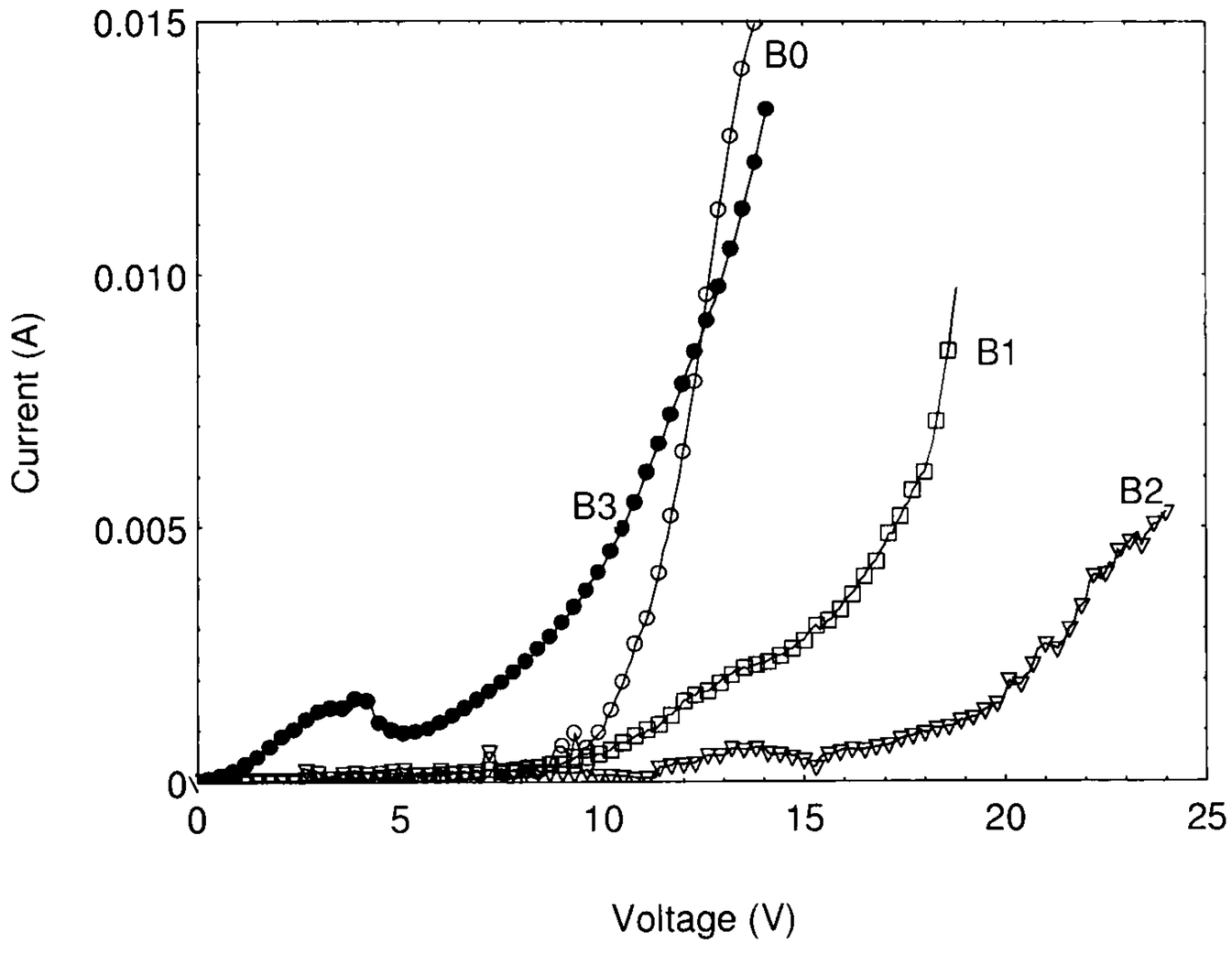

Fig. 4.28. *Current-voltage characteristics of benzene core dendrimer LEDs (PEDOT and aluminium electrodes).*

A further application of the benzene core dendrimer will be discussed in chapter 9. where the suitability as a host material in a doped electrophosphorescent device is investigated.

4.3.4 Bilayer LEDs (Nitrogen core dendrimers)

The device efficiencies of single layer LEDs with aluminium contacts discussed above are not very large compared to the current peak efficiencies of 2 % of MEH-PPV, up to 4 % for other PPV derivatives and even close to 10 % for polyfluorenes [69]. One way of improving the device efficiency is to employ a bilayer configuration. As triphenylamines are commonly used as hole-transporting materials, it is believed that the nitrogen core dendrimers preferentially transport holes. A suitable electron-transporting layer is hence sought to allow more balanced hole and electron transport in the device together with a better definition of the recombination zone, which is located close to the interface of the two materials. Polypyridine (PPY) was initially investigated as an electron transporting material, as it has previously been used in dendrimer bilayer devices [70]. PPY is only soluble in formic acid, which does not dissolve the dendrimer layer. For the A2 dendrimer, an efficiency of 0.005 % was measured in the configuration ITO/A2/PPY/Al, which is not significantly greater than that of a single layer device. The emission spectrum was found to develop a broad red tail, which may be a signature of an exciplex emissive state formed between the PPY and the dendrimer. Exciplex emission in PPY containing devices has previously been reported in bilayer devices with PVK [71].

Electron injection into PPY has been shown to be more effective from an n-type ITO electrode than from an aluminium electrode, which is believed to be due to strong influence of doping states [68]. This remarkable feature allows devices to be fabricated in a reverse configuration of ITO/PPY/Dendrimer/Gold, where holes are injected from the gold electrode and electrons are injected from the ITO. For MEH-PPV, such a configuration was found to yield efficiency values similar to the conventional device configuration with aluminium electrodes. However, for the A2 dendrimer, an efficiency of 0.05 % was measured, giving an order of magnitude improvement. This suggests that the incorporation of an electron transport layer can indeed improve the device efficiency.

The dendrimer generation allows a control of the degree of intermolecular interactions in films, which is manifest both in the emission properties as well as the charge

transport properties. Using the dendrimer generation, it should hence be possible to balance further the charge transport in bilayer devices. This was investigated using vacuum deposited charge transport layers. Evaporating charge transport layers has the advantage over spin-coating that the materials deposited do not intermix or accumulate solvent at the interface. Also, evaporated materials are much purer. Bilayer devices were fabricated using both the common electron transport materials PBD [72] and Alq_3 [73] and the 0^{th} and 3^{rd} generation dendrimers as hole transporting materials. The measurements were carried out in the engineering department at Oxford University.

Dendrimer films approx. 80 nm thick were spin-coated onto substrates, which had not been masked and etched. 50 nm of the electron transport layer, either Alq_3 or PBD, was evaporated, coating the entire device area. Aluminium or magnesium aluminium electrodes were then evaporated through a shadow mask. In the case of magnesium aluminium, a small amount of magnesium was placed in the boat with the aluminium. The magnesium evaporated first, hence forming a thin layer of magnesium on the device, which was then covered by aluminium. Contact to the metallic cathodes was subsequently made through a probe station, paying careful attention not to short circuit the device. The devices were then tested in air rather than under vacuum.

All devices displayed good characteristics. For the case of the PBD electron-transporting layer, emission was observed from the dendrimer, whereas for the Alq_3 containing devices, the Alq_3 was found to emit. The bilayer devices were found to have impressive efficiencies, considering that no attempt was made to optimise the thicknesses of the transport layers, which are known to have a significant impact on the device performance [58]. The efficiencies and peak brightnesses are summarised in Table 4.1. The brightest devices were the LEDs containing Alq_3, where dc brightnesses over 2000 Cd/m^2 were recorded as well as the lowest operating biases (150 Cd/m^2 at 7 V). The highest efficiencies of up to 0.4 % at 65 Cd/m^2 are observed for the devices containing PBD. The dendrimer generation has a clear effect on the brightnesses and efficiencies – with respect to A0, the A3 devices show reduced maximum brightnesses, but increased efficiencies, suggesting more balanced charge transport. This is particularly clear cut for the single layer devices and for the devices containing PBD. It is also interesting to note that for the bilayer devices the choice of cathode material

appears to have little effect other than to increase the maximum brightness for the Alq_3 devices.

Device structure	A0/Al	A3/Al	A0/MgAl	A3/MgAl
single layer EQE (%)	0.00025	0.01	0.02	0.2
Max. Brightness (Cd/m^2)	1	16	24	100
Alq_3 EQE (%)	0.1	0.3	0.1	0.2
Max. Brightness (Cd/m^2)	600	150	2200	590
PBD EQE (%)	0.07	0.4	0.2	0.4
Max. Brightness (Cd/m^2)	60	65	93	65

Table 4.1. *Summary of the key device parameters of nitrogen core dendrimer LEDs. Where possible, the efficiencies were calculated at a brightness of or above 15 Cd/m^2.*

Sample device characteristics are shown in Fig. 4.29 for devices with magnesium aluminium electrodes. The single layer device characteristics for A3 (curve c) are shown by the dashed line. There are two main features to note: firstly, inclusion of the Alq_3 layer lowers the operating bias, whereas the PBD layer results in an increase with respect to the single layer devices. Secondly, the higher generation dendrimer results in an increase in operating bias, too, with respect to the A0 dendrimer. However, for the PBD device, the efficiency is greater for the A3 device, which results in the curves e and d being swapped on the brightness-voltage curve.

The difference in the characteristics between Alq_3 and PBD is related to the relative energy levels of the hole and electron transporters. Whereas PBD is a wide gap material, Alq_3 has a band gap similar to that of the dendrimers. It is hence possible that the LUMO energy levels of Alq_3 and the dendrimers are reasonably well aligned, as are the HOMO levels. The presence of the Alq_3 layer results in an increased electron current and hence the overall operating field is reduced. In contrast, an offset between the PBD and dendrimer energy levels would result in charge accumulation at the interface and the PBD layer acting as a blocking layer for holes, rather than providing a surplus of electrons to the interface as in the case of Alq_3. The functional dependencies of current and brightness on the bias are hence similar to the case of the single layer device. Due to the increased overall device thickness the characteristics are merely shifted to higher

biases. Through the choice of the higher generation dendrimer, the device current is reduced even further. This suggests that in addition to the hole-blocking characteristic of the PBD layer, the impeded hole transport through the dendrimer, i.e. the reduced hole mobility, also plays a role.

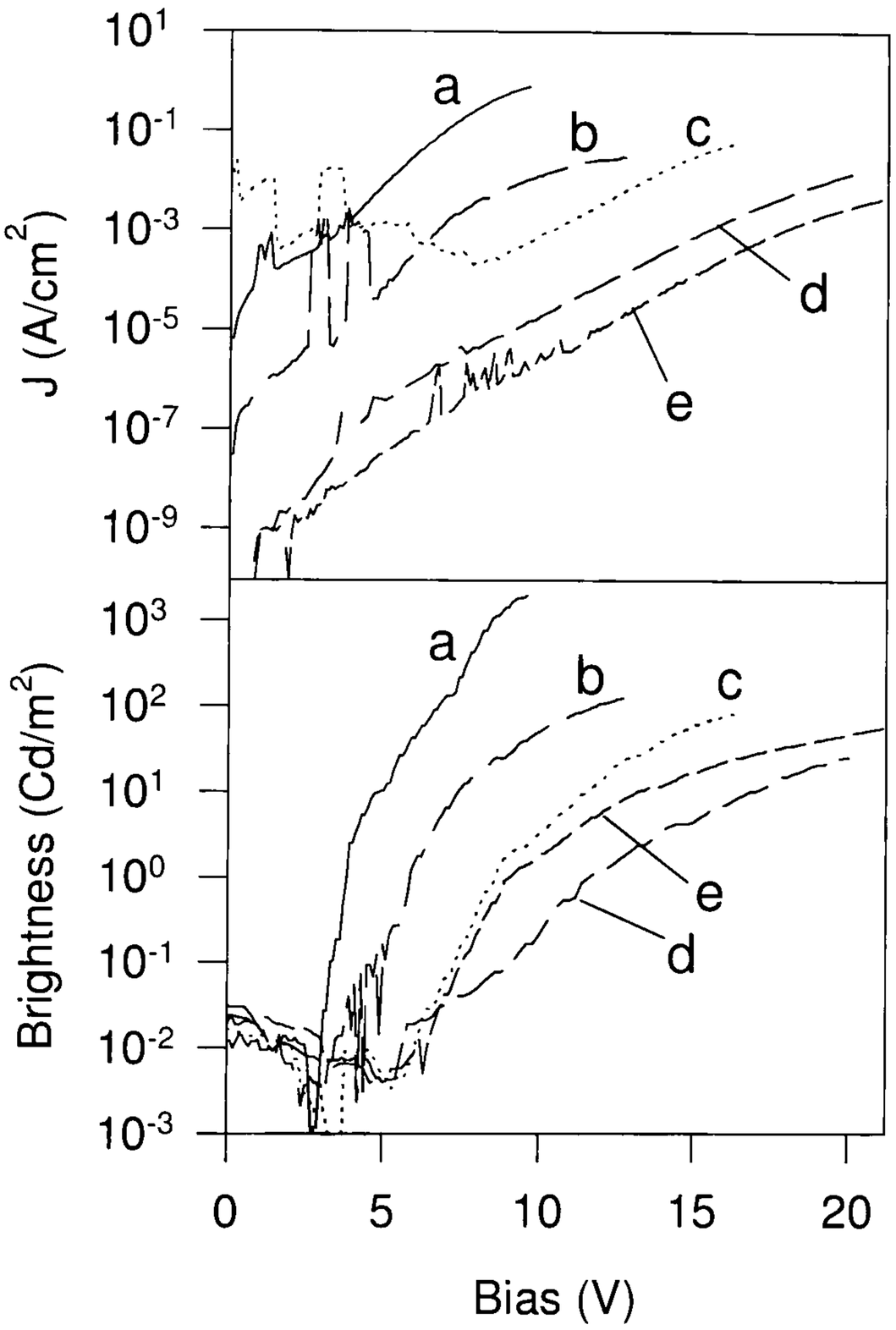

Fig. 4.29. *Current-voltage and brightness-voltage characteristics for single layer and bilayer devices with magnesium aluminium electrodes. a) A0/Alq_3, b) A3/Alq_3, c) A3, d) A0/PBD, e) A3/PBD.*

The increase in efficiency with generation in bilayer LEDs also suggests that the confinement of charge carriers is improved at the interface. An interpretation of the device characteristics d and e in Fig. 4.29 is that the electron leakage current through the

dendrimer layer is reduced with increasing generation. The efficiency is limited by charge carriers passing through the entire device without recombining. As the hole leakage current through the PBD layer is thought to be the same for the A0/PBD and the A3/PBD device, the further reduction in current with an increase in light output may be attributed to a reduction in electron leakage through the dendrimer layer. The electrons in the A3/PBD device are hence more strongly confined at the interface. A consequence of this extreme confinement, which can be tuned using the dendrimer generation, is the occurrence of very high efficiencies at low currents, as shown in Fig. 4.30. The device characteristics of an A3/PBD device are seen with magnesium aluminium and aluminium electrodes. Just above turn-on, the efficiency is found to be in the order of 70 Cd/A for the device with magnesium aluminium electrodes and approx. 5 Cd/A for the device with aluminium electrodes. Although these numbers should be taken as being very approximate and are likely to be overestimated, the characteristics do show that light emission is observed at very low currents in the order of 10 nA. This was also verified visually in a separate experiment. No such extreme efficiencies and strong dependence of the efficiency on operating bias were observed for the other devices studied.

These remarkable efficiencies at low biases demonstrate the unique advantage of being able to control the charge transport properties of a certain material through a single parameter, the dendrimer generation. Although the increase in generation appears to be at first sight detrimental to the charge transport, the above bilayers demonstrate that for certain applications a reduction in mobility may be advantageous. The increased generation does give rise to a limitation on the sustainable currents and hence maximum brightnesses, but it may be possible to improve on this through suitable device configurations. However, for many display applications only medium brightnesses of between 50 and 100 Cd/m^2 are required, so the dendrimer systems studied here could well prove to be of future interest as the emitting layer in LEDs. Alternatively, high brightnesses may be achieved in bilayer configurations using Alq_3 as the emitting layer.

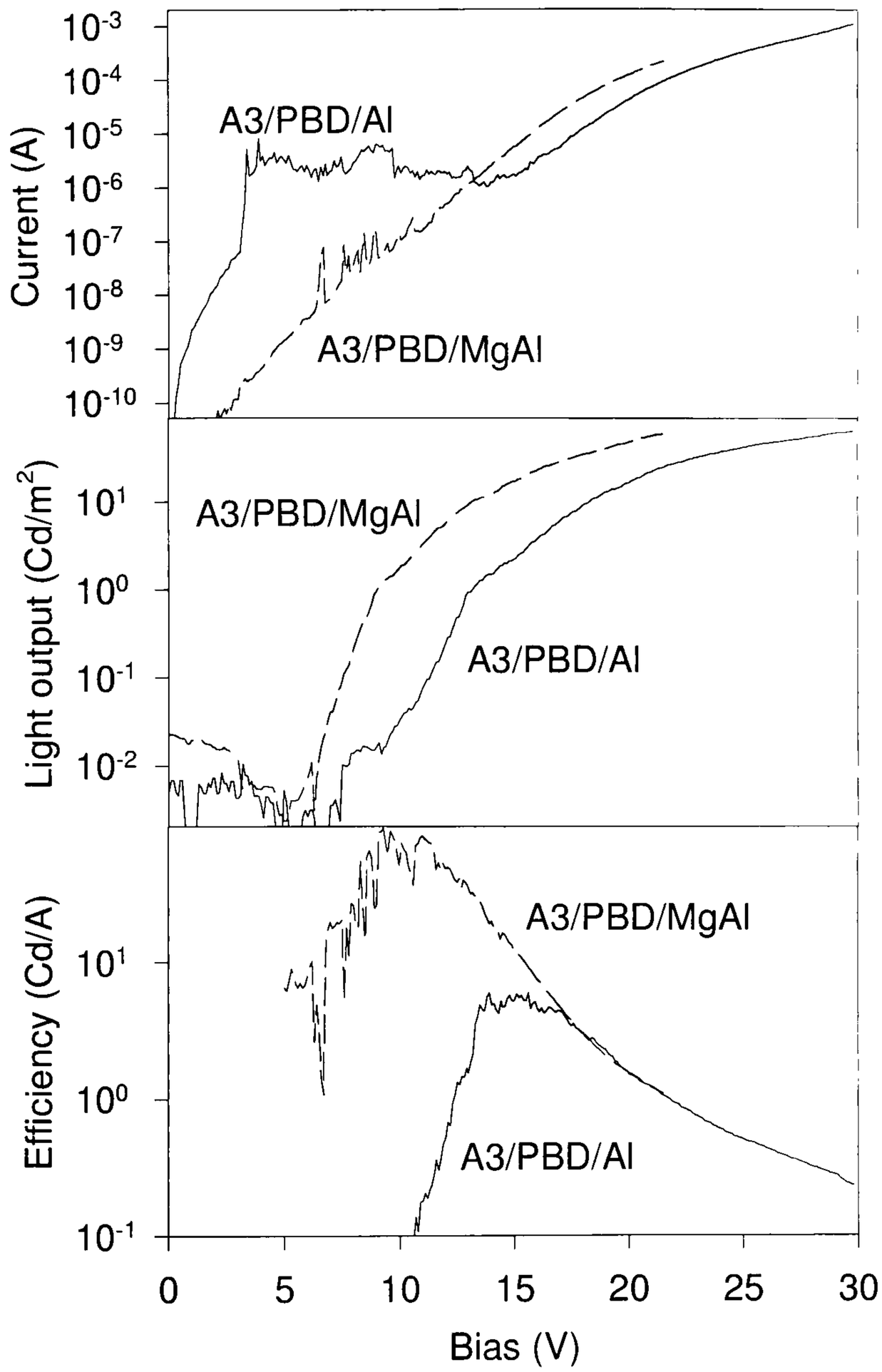

Fig. 4.30. *Device characteristics and EL efficiency of an A3/PBD bilayer device with aluminium and magnesium aluminium electrodes.*

4.3.5 Summary

A detailed study of devices made with the nitrogen core dendrimer as a function of generation, electrode material, temperature and with a variety of electron transporting layers has been presented. There is a strong dependence of the device characteristics on generation with films becoming more insulating with increasing generation. This observation correlates well with the finding that the core chromophores become more

insulated and shielded from the environment with increasing generation, which is manifest in a reduction of the red emission. This correlation demonstrates that the stilbene dendrons act as insulators and neither contribute to charge transport nor act as sites of charge injection. The dendrimer generation hence allows a microscopic control of the level of interaction between chromophores and also of the charge transport properties of the material. Conjugated dendrimers allow a direct correlation to be drawn between the chemical structure of the material, the emission spectrum and the charge transport properties.

An increase in device efficiency with generation is observed in all configurations, which is attributed to a reduction in mobility and an improved balance in charge transport. The most efficient device configurations incorporate a PBD electron-transporting layer and achieve efficiencies of 0.4 %. At low currents this efficiency is greatly enhanced due to strong carrier confinement at the interface between dendrimer and electron transporter.

The device efficiency is also found to increase with decreasing temperature. The functional dependence of the device characteristics on temperature is found to be very similar to that of MEH-PPV devices.

4.4 Coupled electronic oscillator calculations on conjugated dendrimers

4.4.1 Introduction

In the previous sections of this chapter the basic photophysical and transport properties of two families of related dendrimers were discussed. It was found that in spite of the very similar chemical structure, the materials possess very different properties. It is particularly interesting to understand why the nitrogen core dendrimers are green emitters, whereas distyrylbenzene and the benzene core dendrimers emit in the blue. Furthermore, the scaling of dendron to core absorption following the simple proportionality to the number of dendrons of 1:3:7 for G1 to G3 implies double counting of benzene rings within the dendrons. This scaling, which was observed in both material families, is hence counter intuitive and requires further investigation.

The theory of coupled electronic oscillators (CEO) was developed by Mukamel, Cherniak and others in Rochester and has been applied to a variety of systems with great success [19-20, 25, 26-27, 50, 74-75]. It is ideally suited to excitations of strongly correlated electron hole pairs in organic materials and has been used to calculate the energy levels of PPV and a variety of polymers and oligomers. The input to the calculation is the ground state density matrix which is computed by a conventional intermediate neglect of differential overlap (INDO) code. The time dependent Hartree-Fock equations are then solved, giving the energy eigenvalues of the molecule as well as the transition matrix without the need of calculating the excited state eigenfunctions. The transition matrix describes the probability of an electron being excited from the LUMO of carbon atom i to the HOMO of carbon atom j, as discussed in chapter 2. It hence provides a real space representation of where the excitations are localised on the molecule. Diagonal elements correspond to excitations localised on one carbon atom, whereas off-diagonal elements describe the coherences between different sites. The CEO technique provides a very useful tool to study the nature of excitations, as charge transfer states can be identified as well as excitonic coupling and splitting.

Dendrimers have attracted a great deal of interest in this regard, because they are computationally much easier to deal with than polymers [19-20, 25, 64, 76-77]. Both the finite spatial dimensions and the intrinsic symmetry allow a detailed computation of the electronic properties at a relatively low computational cost. Previously, a family of phenylacetylene dendrimers has attracted considerable attention due to the demonstration of exciton localisation on the core [19,20, 22]. In contrast to the systems studied here, these dendrimers are completely symmetrical and consist only of one conjugated unit, rather than distyrylbenzene and stilbene used here. The presence of only one unit allowed the problem to be broken down into the different individual branching units of the dendrimer under the assumption that the *meta* linkage between adjacent conjugated units impedes electron delocalisation effectively. By calculating the energy eigenvalues of the individual segments, the Frenkel exciton coupling parameters could be obtained and the energy level splitting deduced was found to yield excellent agreement with experiment.

In the case of the phenylenevinylene dendrimers studied here, a computational investigation is considerably more complicated. It is evident that the core unit has to be defined as the central three distyrylbenzene units in the case of the amine core dendrimer, as the electronic properties are so different to those of the benzene core dendrimer. In order to understand the electronic processes in the dendrimers, calculations were performed on the entire dendrimer structure. In the case of the benzene core dendrimer, the central *meta* linked benzene ring was thought to impede electron delocalisation throughout the core region allowing the dendrimer to be broken down into three symmetry elements. The localisation of excitations on the core is demonstrated and the energy eigenvalues are found to be in excellent agreement with experimental values.

The calculations presented here were carried out in Rochester. The geometry optimisations were performed on commercial software packages. The CEO calculations were run on a compiled F77 code written by S. Tretiak and coworkers.

4.4.2 Nitrogen core dendrimer

4.4.2.1 Ground state 0th generation

The structure of the 0th generation nitrogen core dendrimer A0 was optimised using the commercial quantum chemistry package SPARTAN employing the Austin Model 1 (AM1) theory with a reduced Hartree-Fock Hamiltonian to calculate the atomic forces and minimise the nuclear displacements. The optimised structures are shown in Fig. 4.31 in stick and space filling representation. The benzene rings are twisted with respect to each other. The central benzene rings of the distyrylbenzene units are twisted with respect to each other by an angle of 35° and the rms deviation from the plane is found to be 0.94 Å. Although the molecule appears to be close to planar, the *t*-butyl groups contribute significantly to the volume of the molecule as seen in the space filling representation. Due to these strong twists and the bulky surface groups it is hence not surprising that these molecules do not π-stack and that there is no signature of aggregation in the absorption of films.

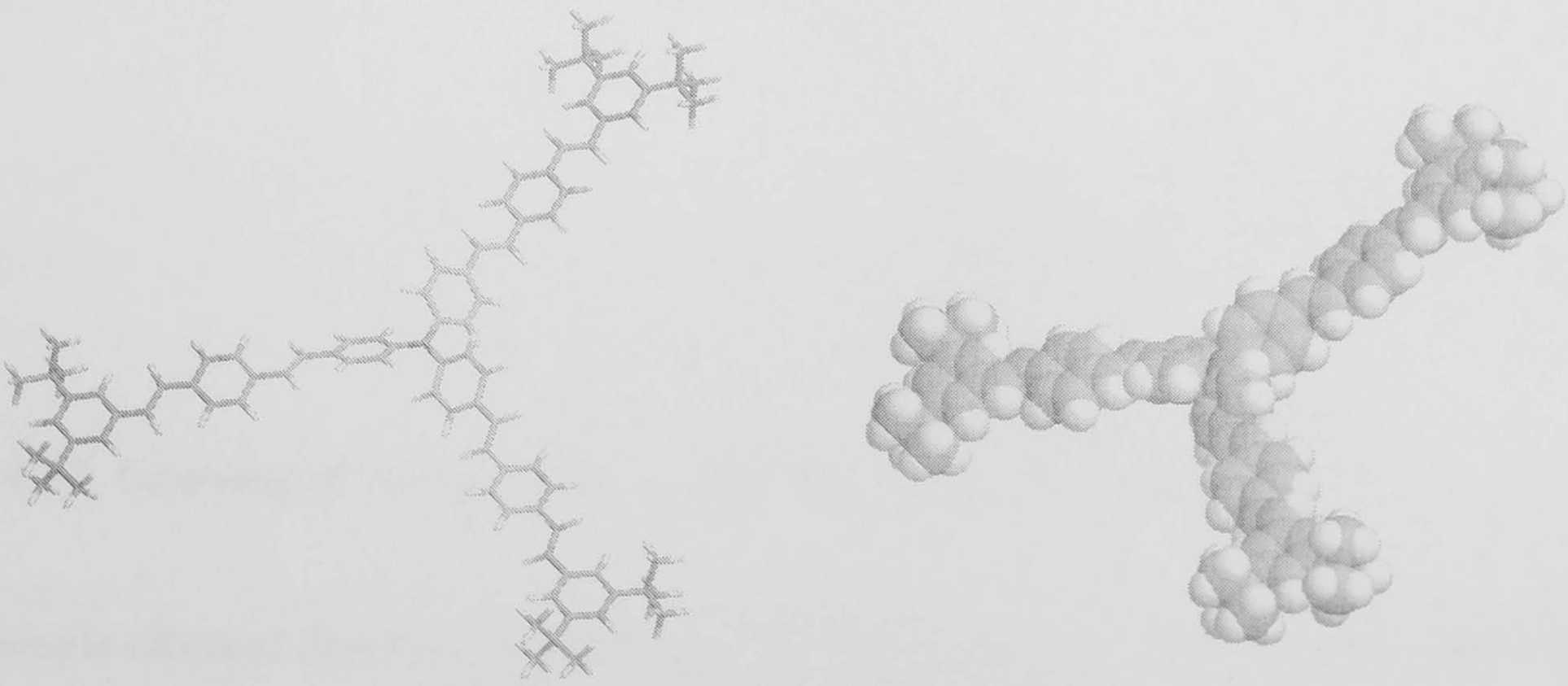

Fig. 4.31. *Geometry optimised structures of A0.*

Fig. 4.32 shows the counting of carbon (and nitrogen) atoms of A0 employed in the CEO calculations. The atoms are counted clockwise around the benzene rings and clockwise around the entire structure. The hydrogen atoms are not shown, but were also labelled in an orderly manner. Although there are a number of conceivable ways to label the atoms, it is important to have a consistent labelling strategy in order to be able to compare different calculations. It is also very beneficial to have a labelling system to be

able to easily relate the transition matrix to the structure of the molecule in terms of building blocks of the molecule, rather than having to locate every individual carbon atom separately.

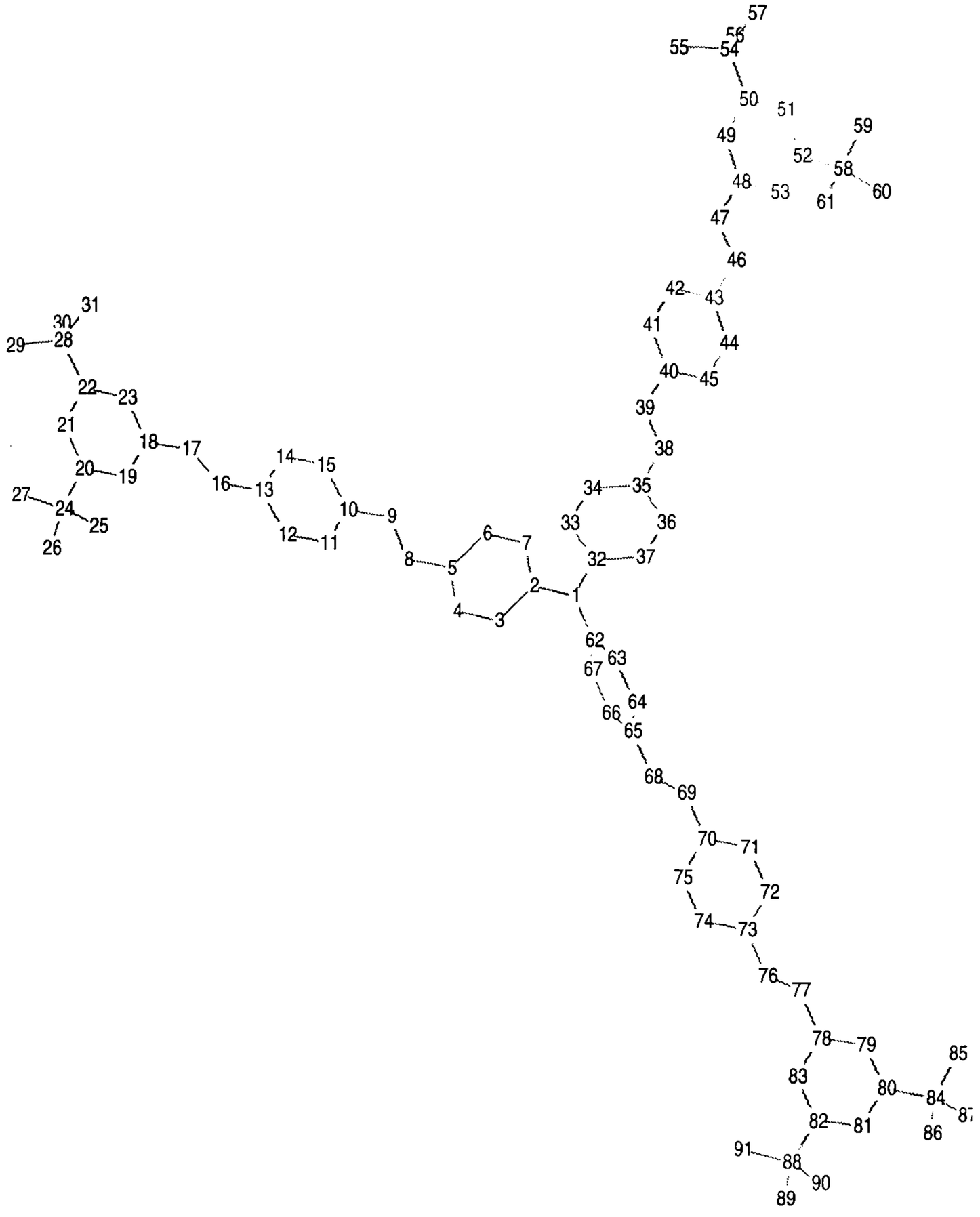

Fig. 4.32. *Counting of carbon atoms used in the CEO calculations on A0.*

The single electron density matrix of A0 is shown in Fig. 4.33 in a 2-d plot. The z-axis uses a logarithmic scale to plot the data. This enhances the clarity of the plots and makes differences easier to spot. All following matrix plots are shown on a logarithmic scale for matrix values from 0.01 to approx. 0.2, unless indicated otherwise. There are three groups of patterns visible in the plot, which are in turn broken down into three subgroups. The groups labelled 1 to 3 correspond to the distyrylbenzene (DSB) units in the dendrimer. The three subgroups result from the three benzene rings comprising distyrylbenzene. The *t*-butyl units are seen at the upper end of the DSB groups. There

are a number of off-diagonal elements corresponding to charge delocalisation across the three central benzene rings comprising the triphenylamine core.

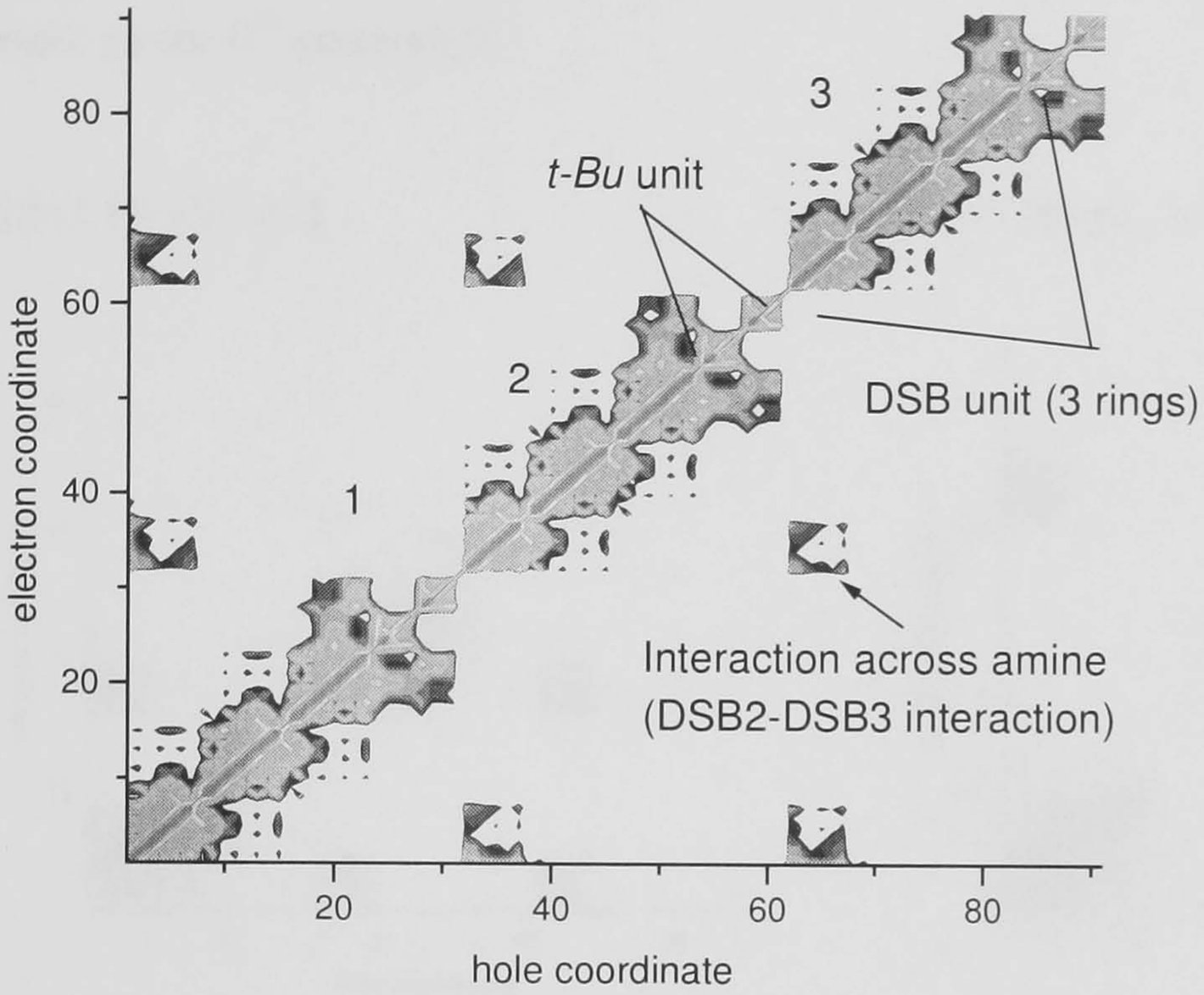

Fig. 4.33. Single electron *density matrix of A0 on a logarithmic scale.*

The CEO calculation found four modes with large oscillator strengths in the A0 dendrimer, two at 3.0 eV which are possibly degenerate although they had slightly different oscillator strengths, and two at 3.6 eV (the energy eigenvalues and the calculated absorption spectra are shown in Fig. 4.36). These four modes are shown in Fig. 4.34. In all cases off-diagonal elements are observed corresponding to delocalisation of excitations across the amine core. The lowest two modes 1 and 2 are similar and show that the excitations are delocalised across the entirety of the distyrylbenzene units. The spaces between the units result from the surface groups, which are not involved in any of these excitations. The comparison of modes 1 and 2 suggests that in any one mode only two distyrylbenzene units are involved in the excitation. This is presumably related to the threefold symmetry of the molecule and would suggest that these two lowest modes are virtually degenerate. A remarkable observation is made in Figs. 4.34 c) and d). Again, two arms of the dendrimer dominate over the third, but this time the triphenylamine core is dissociated from the distyrylbenzene unit and excitations are hence no longer delocalised across the entire

molecule. The result is that the distyrylbenzene unit splits into a benzene ring, which contributes to the triphenylamine core, and a stilbene mode, which gives rise to the observed absorption at 3.6 eV. This observation explains why absorption is seen experimentally in the region of the dendron band, although there are no dendrons present in the 0^{th} generation.

a) Ω=2.99 eV, ν=1

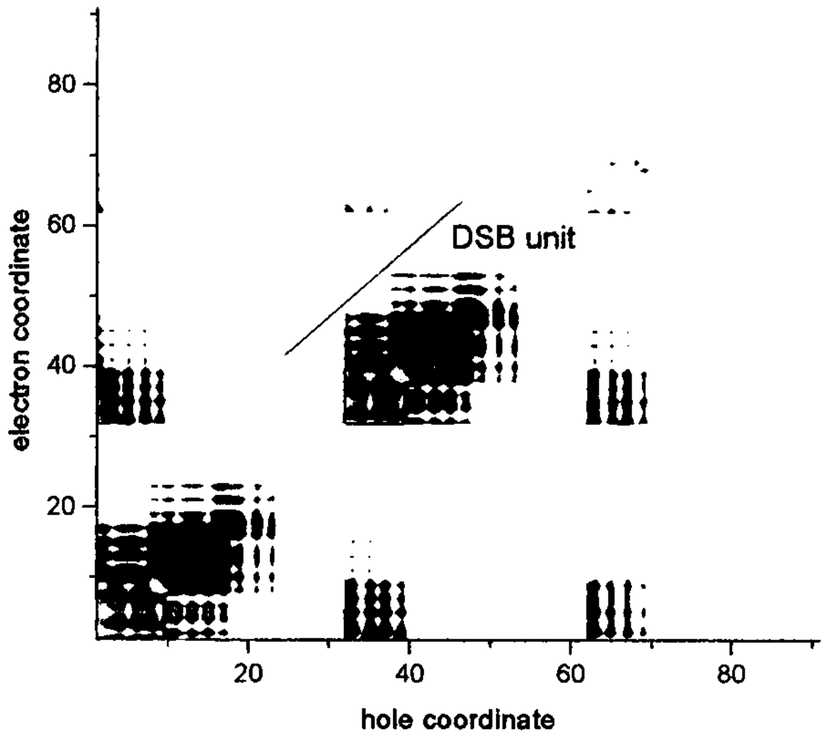

b) Ω=3.00 eV, ν=2

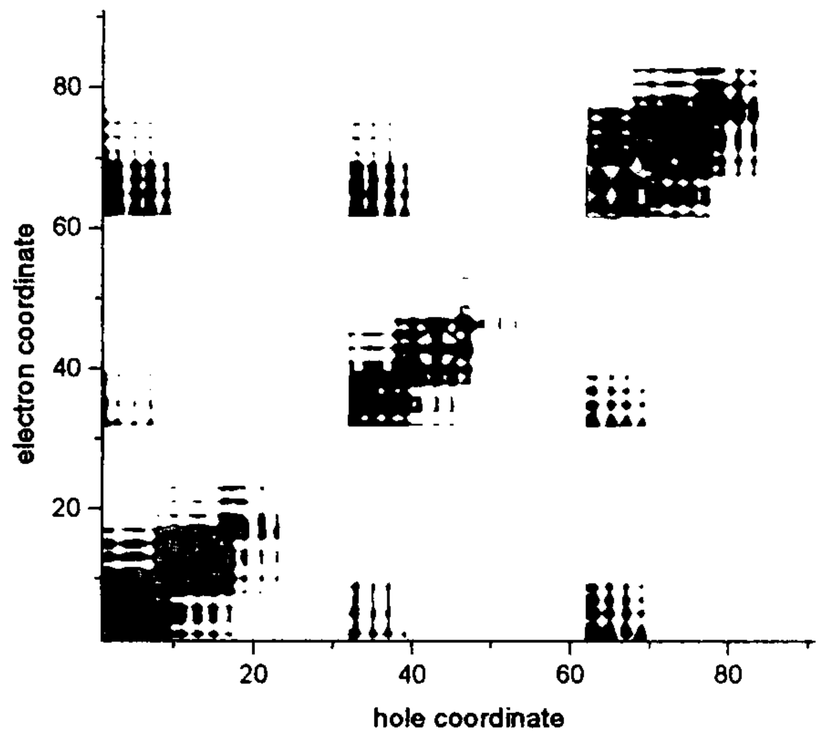

c) Ω=3.33 eV, ν=4

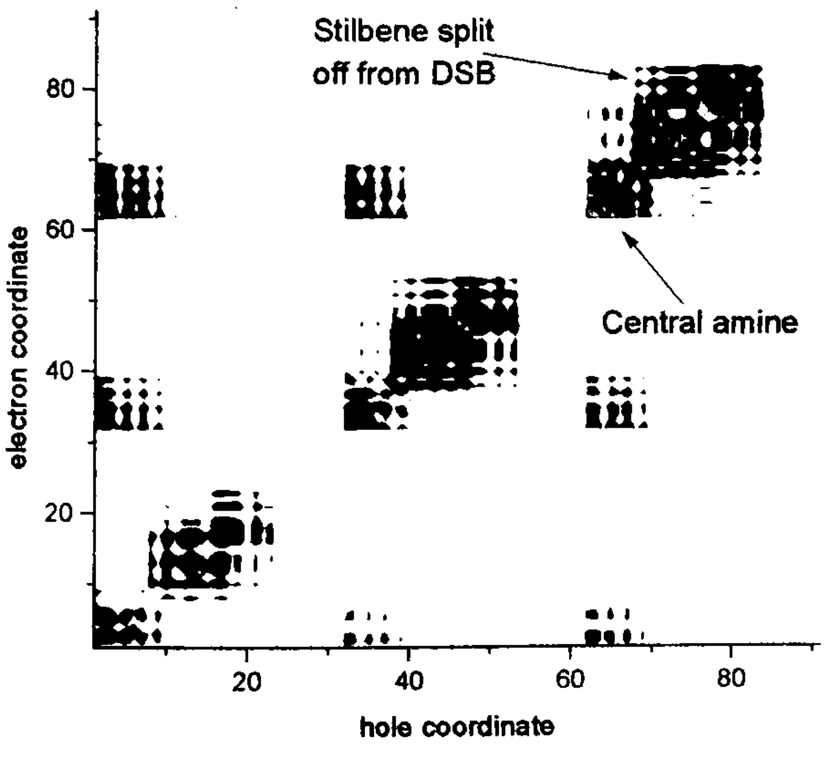

d) Ω=3.59 eV, ν=5

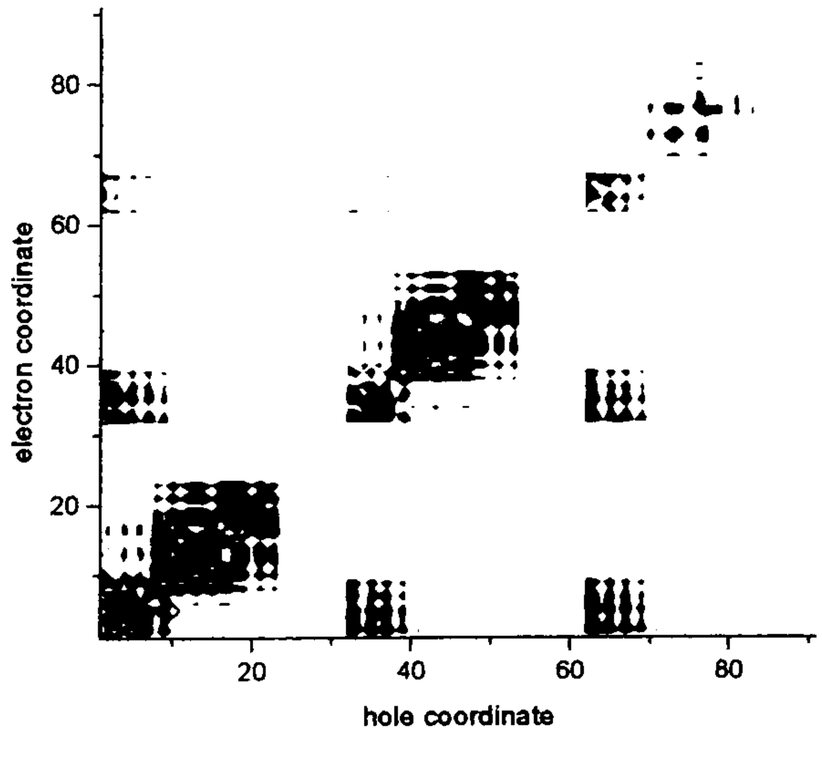

Fig. 4.34. *Strongest CEO modes of A0 (logarithmic scale). Modes 1 (a), 2 (b), 4 (c) and 5 (d).*

4.4.2.2 Triphenylamine and stilbene core modes

To further investigate this remarkable effect, calculations were performed on stilbene and on the triphenylamine core, which were isolated from the optimised A0 structure. The lowest significant mode in the stilbene was found at 3.7 eV, which is comparable to the 3.6 eV observed above. Fig. 4.34 c) suggests that there is still a low level of interaction between the central and the two outer rings of the distyrylbenzene unit as the two blocks are not entirely disjoint, so one would expect this to be slightly lower in energy than the lone stilbene mode. The atoms in the A0 structure forming the triphenylamine core together with a vinylene unit where extracted from the matrices in Fig. 4.34 and renumbered according to the lone triphenylamine studied, which has 27 carbon atoms and 1 nitrogen atom (3×(6 (benzene) + 3 (vinylene) + 1). The upper two diagrams in Fig. 4.35 show the triphenylamine core extracted from A0, whereas the lower panel shows the transition matrix of lone triphenylamine. The main features are very similar for mode 4 of A0, which exhibits stilbene absorption, and the modes on lone triphenylamine: there is strong coherence across the whole unit and interaction between all of the benzene rings. There is an asymmetry between the off-diagonal elements which indicates the motion of a hole from one carbon atom to another. This asymmetry corresponds to a charge transfer state across the triphenylamine, which is thought to be due to the lone electron pair on the nitrogen atom. The triphenylamine extracted from mode 1 of A0 shows strong delocalisation across two of the three benzene rings, as was observed in Fig. 4.34. The similarity between the core excitation of mode 4 of A0 and excitations of lone triphenylamine hence provide further evidence that the dendrimer actually splits into two regions for higher modes, corresponding to triphenylamine and stilbene units. It should be pointed out that whereas the lowest lone triphenylamine modes are observed at 3.33 and 3.34 eV, the mode in Fig. 4.35 b) correspond to an eigenenergy of 3.6 eV. The third mode of lone triphenylamine is found at 3.64 eV with an oscillator strength ~10 % of the first two modes but a very similar transition matrix.

a) Ω=2.99 eV, ν=1

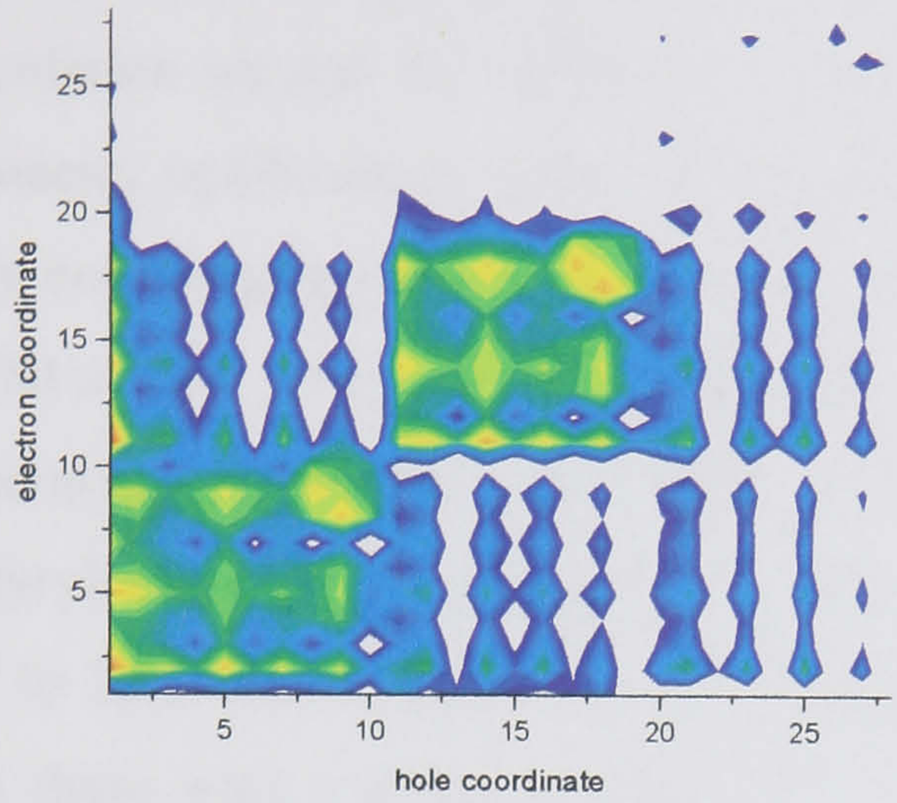

b) Ω=3.59 eV, ν=4

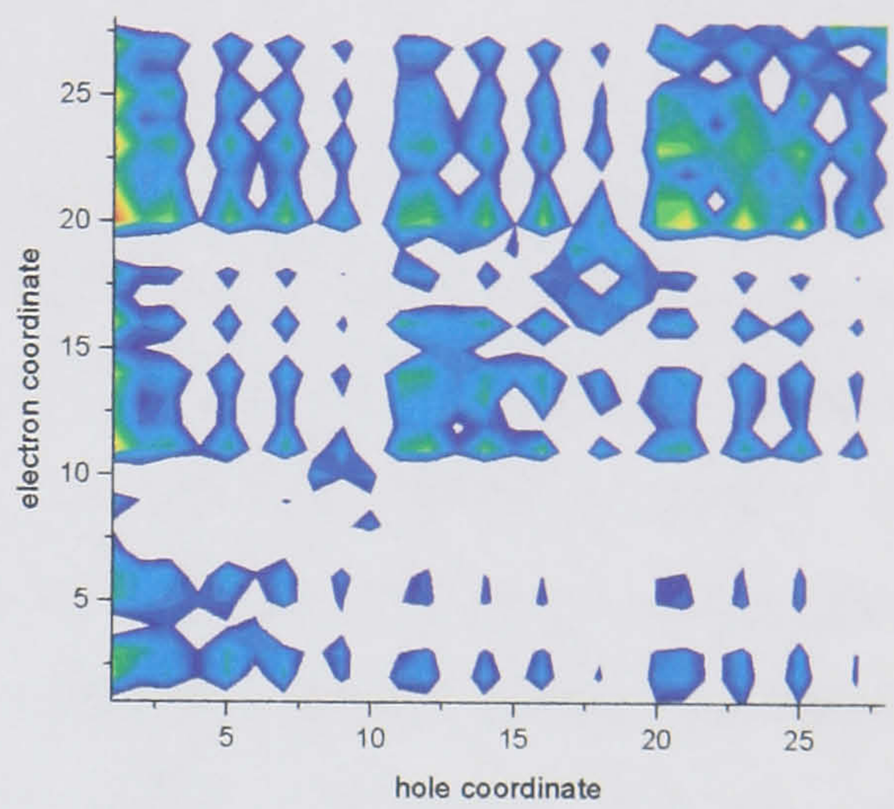

c) Ω=3.33 eV, ν=1

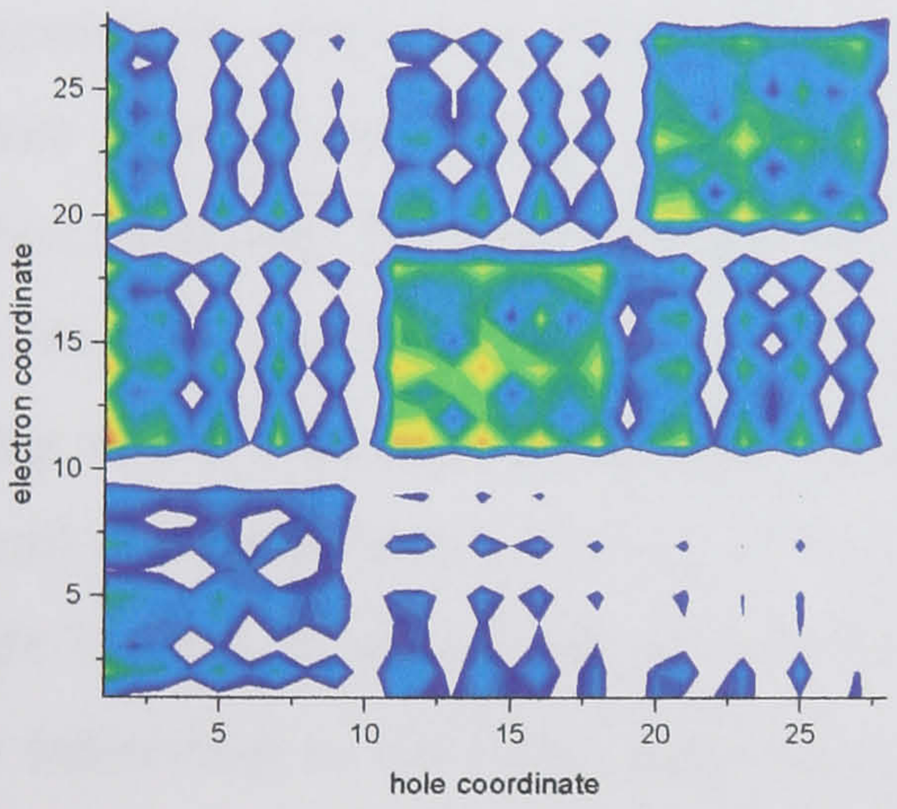

d) Ω=3.34 eV, ν=2

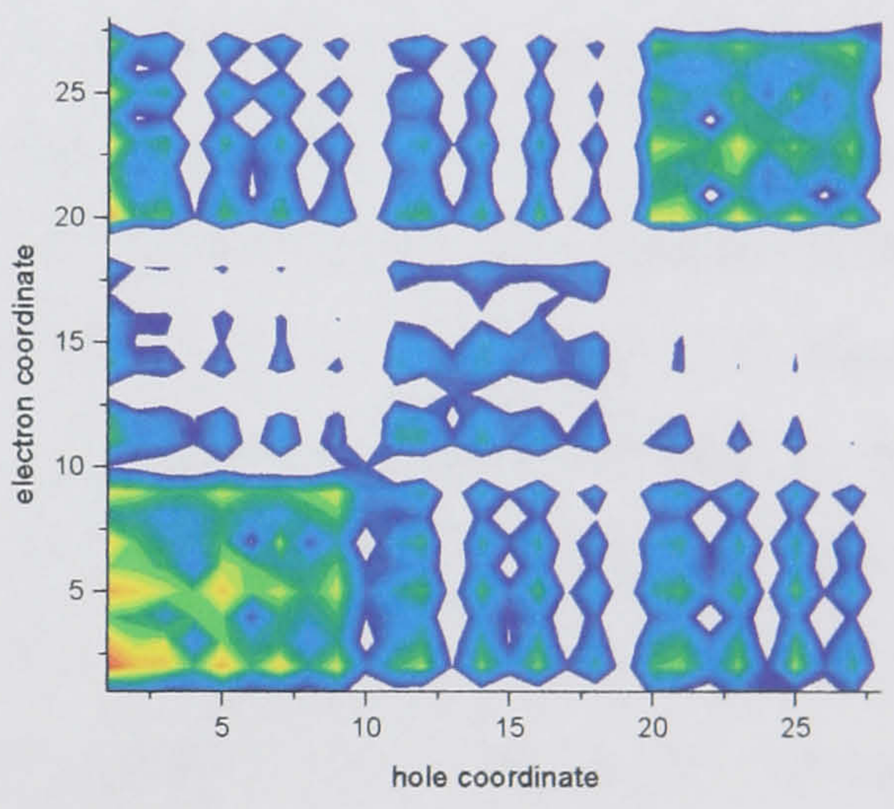

Fig. 4.35. *CEO calculations on molecular triphenylamine (taken from optimised A0 geometry) compared to the elements in the A0 matrix corresponding to the triphenylamine core (logarithmic scale). a) Triphenylamine core of A0, mode 1. b) Triphenylamine core of A0, mode 4. c) Triphenylamine molecule, mode 1. d) Triphenylamine molecule, mode 2.*

4.4.2.3 First generation ground state modes

The computational requirement for the quantum chemical calculations increases as N^3 with the number of atoms in the system N, so higher generation dendrimers become less

accessible to this kind of analysis. As the excitations are delocalised across the whole of the core of the nitrogen dendrimer, there is no further way of reducing the symmetry and hence the computational cost. However, it was possible to perform a CEO calculation on the A1 dendrimer, which took a total of roughly one month for the geometry optimisation (Dual PIII) and the CEO (Alpha workstation). The results are very encouraging and are summarised below. The optimised structure (not shown) was found to have an rms deviation from the plane of 1.82 Å, which is twice that of the 0^{th} generation dendrimer. A small difference in dihedral angles between the distyrylbenzene units across the nitrogen atom was observed, with angles ranging from 32° to 35°. The main modes and the calculated absorption spectra (using a Lorentzian line shape with a width of Γ=0.12 eV) are shown in Fig. 4.36 together with the same data for A0. For both materials the peak of the absorption band is in excellent agreement with experiment. The position of the stilbene band is calculated correctly, but the magnitude in comparison with the core absorption is underestimated. In A1 there is a further strong absorption feature seen in experiment at 4.25 eV, which is not observed in the calculation. This may be associated with a strong vibronic feature neglected in the calculation. It can be seen that the degeneracy of the two lowest modes in A0 is lifted, giving rise to two absorptions split by 80 meV. This gives rise to a red shift in the overall absorption band, which is observed experimentally in both solution and film. Mode 3 is very weak and modes 4 and 5 are found at the edge of the stilbene band. It is also interesting to note that electrochemical measurements of the band gap through pulsed differential cyclic voltammetry have shown a difference between the LUMO and HOMO levels of 3.0 eV, which is in excellent agreement with the value observed here [78].

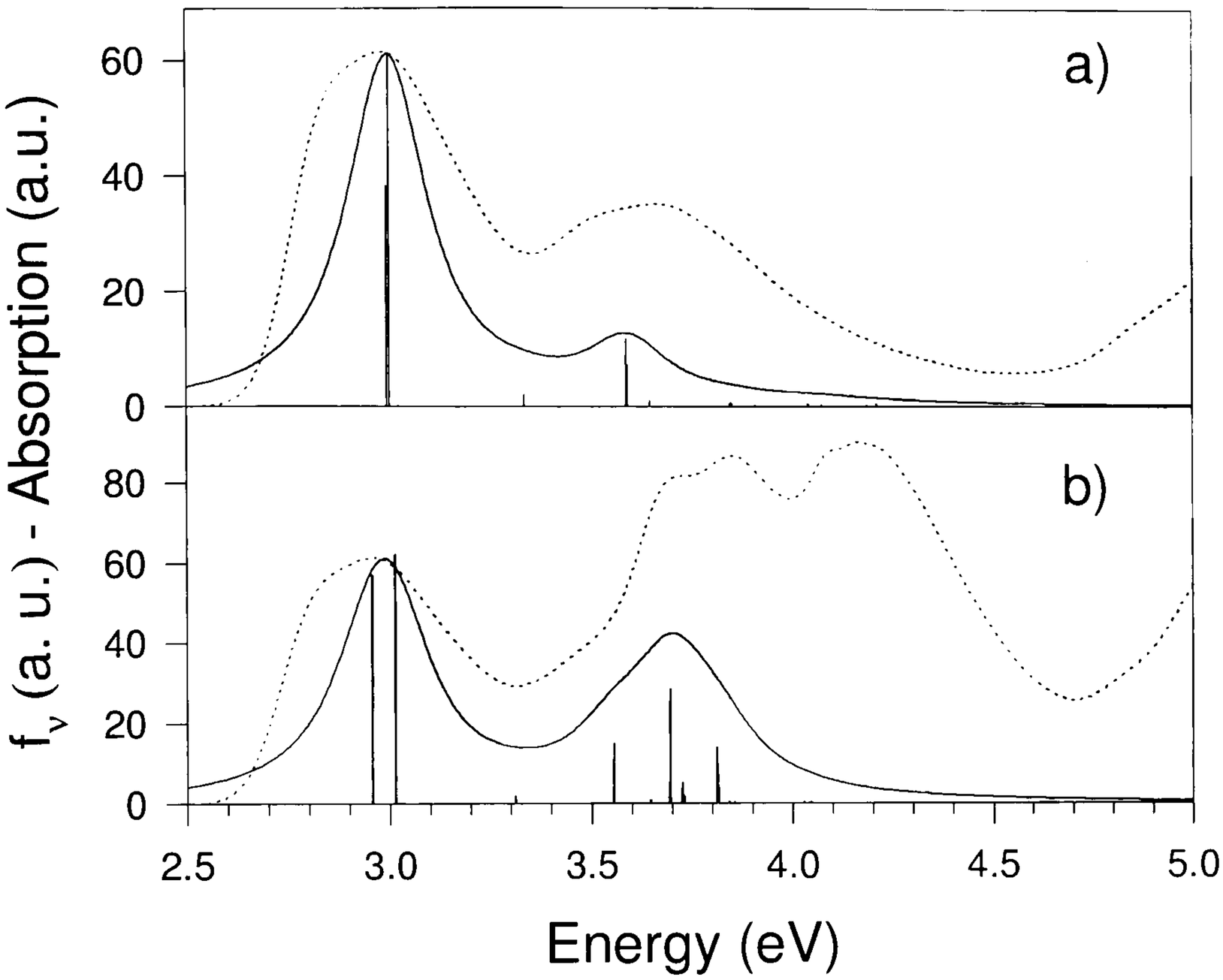

Fig. 4.36. *Calculated absorption (——) and oscillator strength for A0 and A1 dendrimers compared to experiment (……).*

The lowest mode of the A1 dendrimer is shown in Fig. 4.37 on an enhanced logarithmic scaling ranging from 0.001 to 0.2. The core excitations are clearly visible and extend throughout the distyrylbenzene units with strong coherences between the three arms of the dendrimer. The distyrylbenzene units are separated by white regions corresponding to the t-butyl groups, which were counted last and are not excited in this mode. At the end of all three of the distyrylbenzene modes the dendrons are visible with a transition probability 2 orders of magnitude smaller than that of the core. This gives an estimate of the efficiency of confinement of excitations on the core through the energy gradient between the dendrons and the core. The lowest energy excitations are hence strongly localised on the core of the dendrimer. This is the first demonstration of exciton localisation in electroluminescent dendrimers, which is in excellent agreement with the experimental results.

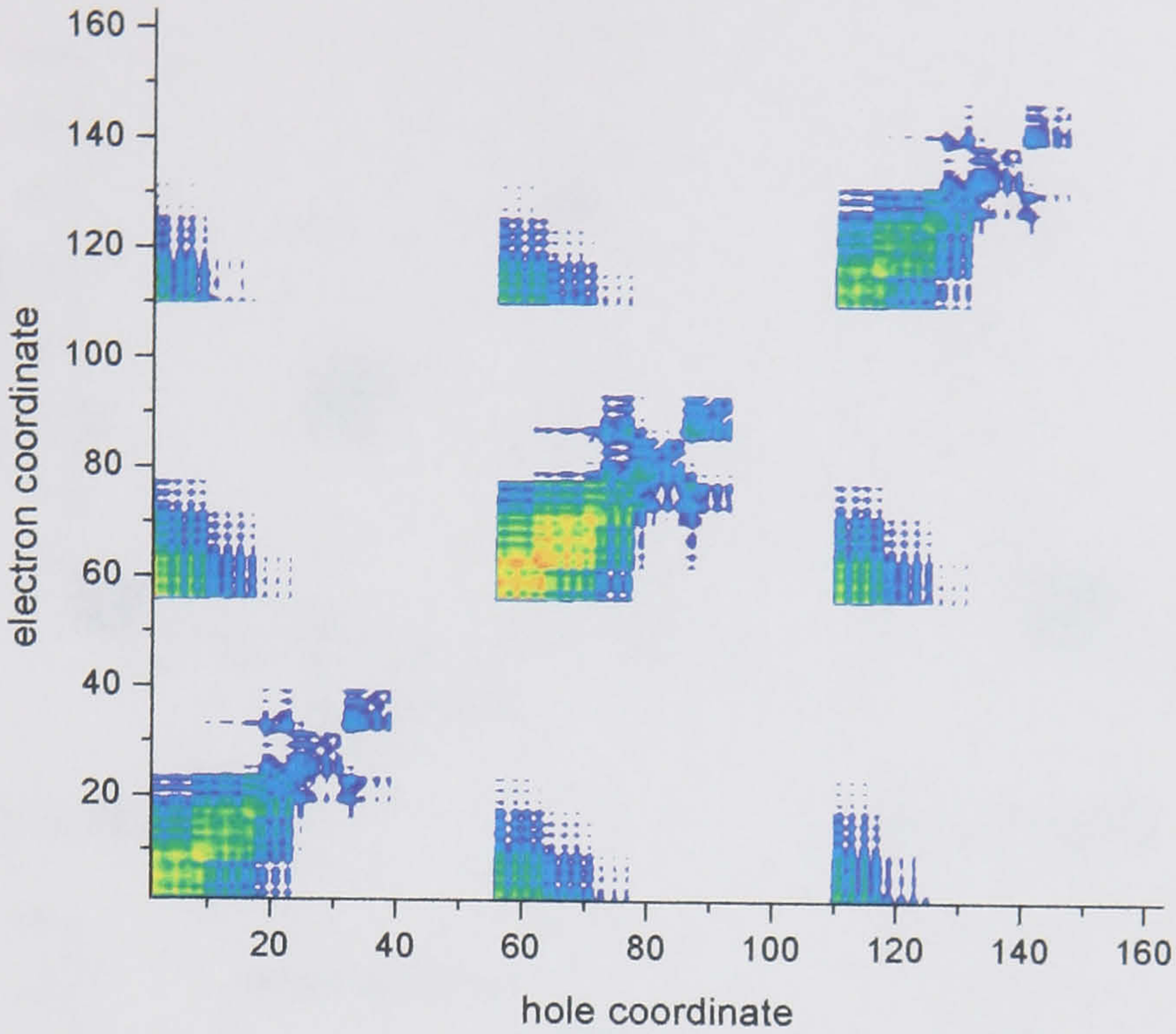

Fig. 4.37. *Lowest mode (Ω=2.96 eV) of A1 dendrimer on a logarithmic scale from 0.001 to 0.2 rather than from 0.01 to 0.2.*

The seven main modes of the A1 dendrimer are shown in Figs. 4.38 and 4.39 on a logarithmic scale from 0.01 to 0.2. The real space representation allows a very simple distinction between core and dendron modes. Again it is seen that only two of the three distyrylbenzene units carry the main excitations of the core modes, as was observed for A0. For the lowest core modes the excitation is delocalised across the amine core. For modes 4 and 5 the triphenylamine core splits off from the core stilbene, as was observed in the A0 dendrimer. Modes 6 and 7 are weak and the first dendron excitation is seen in mode 8. For modes 8 and higher there is no excitation of the core and hence the off-diagonal elements in the transition matrix vanish. Once again, due to the symmetry of the molecule, only two of the three dendron branches are involved in the excitation. The shape of the dendron modes results from the fact that there is a break in the counting of the carbon atoms. The atoms are counted along the distyrylbenzene unit and then along both benzene rings forming the dendrons. One of the stilbene units then does consequentially not have continuously labelled carbon atoms, so an excitation will appear as an off-diagonal excitation, giving rise to the arrow shape observed. This is discussed in more detail later on. For an example of dendron counting the reader is referred to Fig. 4.47.

a) Ω=2.96 eV, ν=1

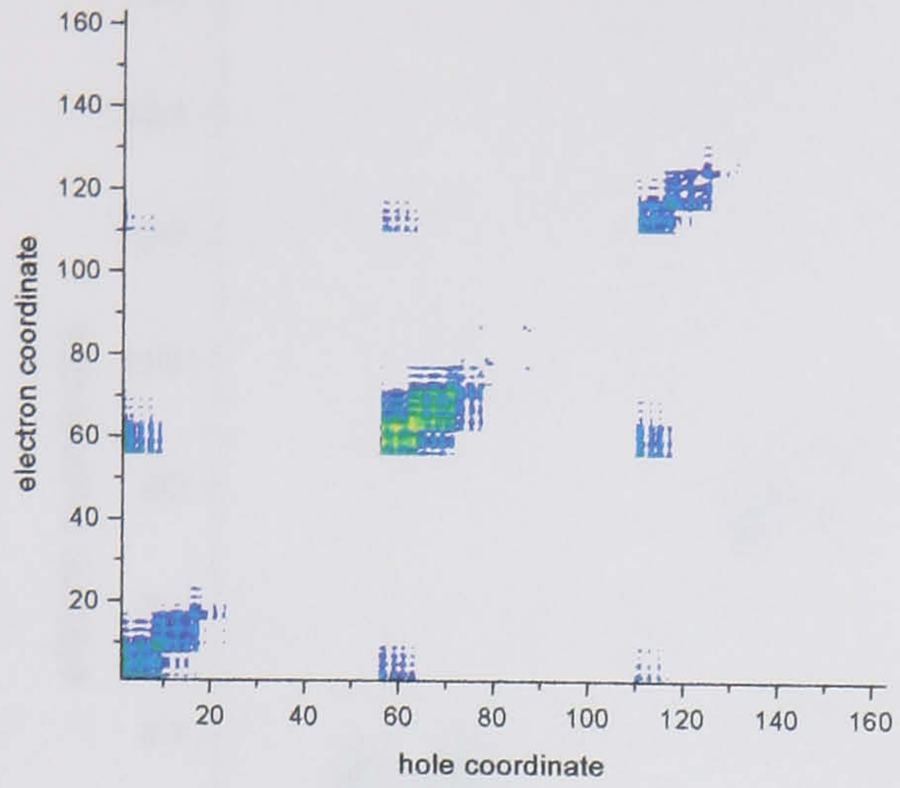

b) Ω=3.01 eV, ν=2

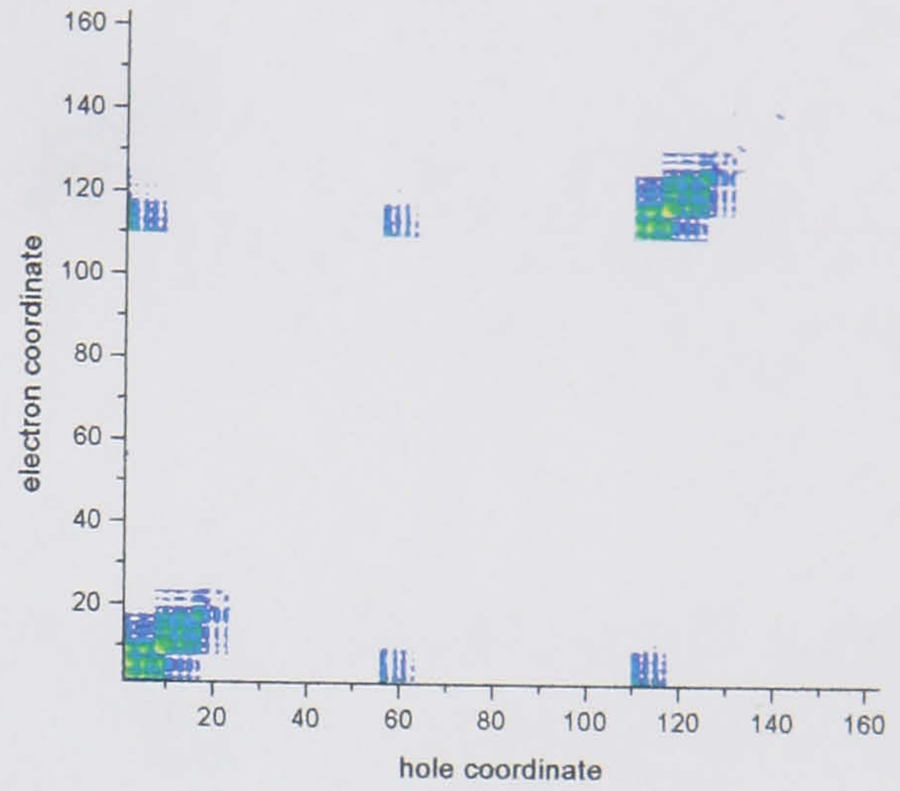

c) Ω=3.55 eV, ν=4

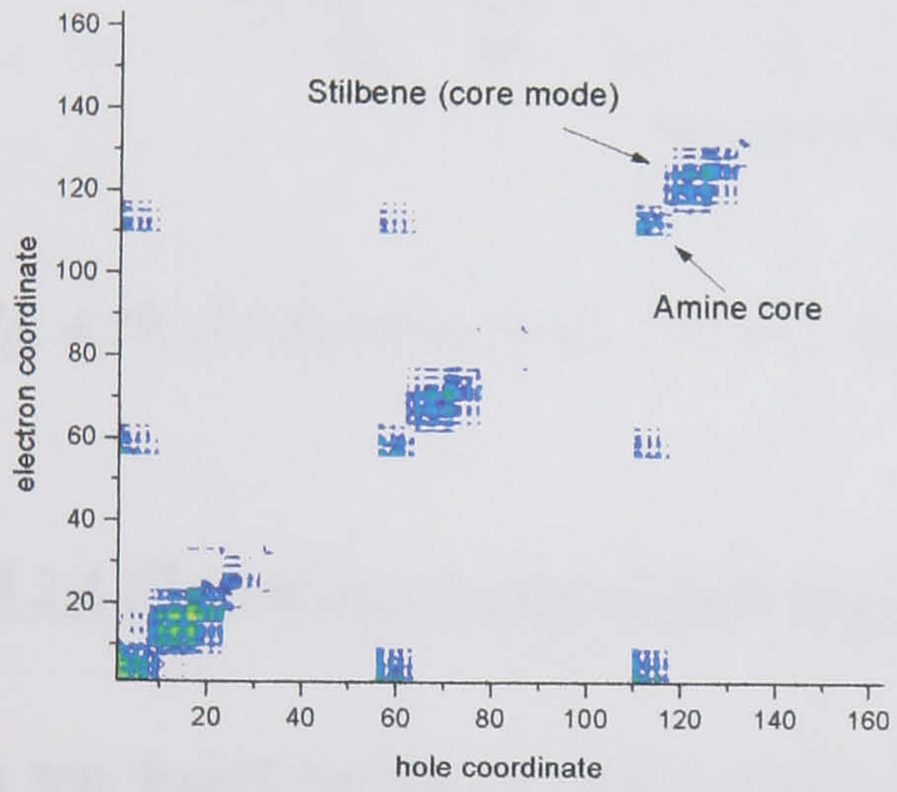

d) Ω=3.56 eV, ν=5

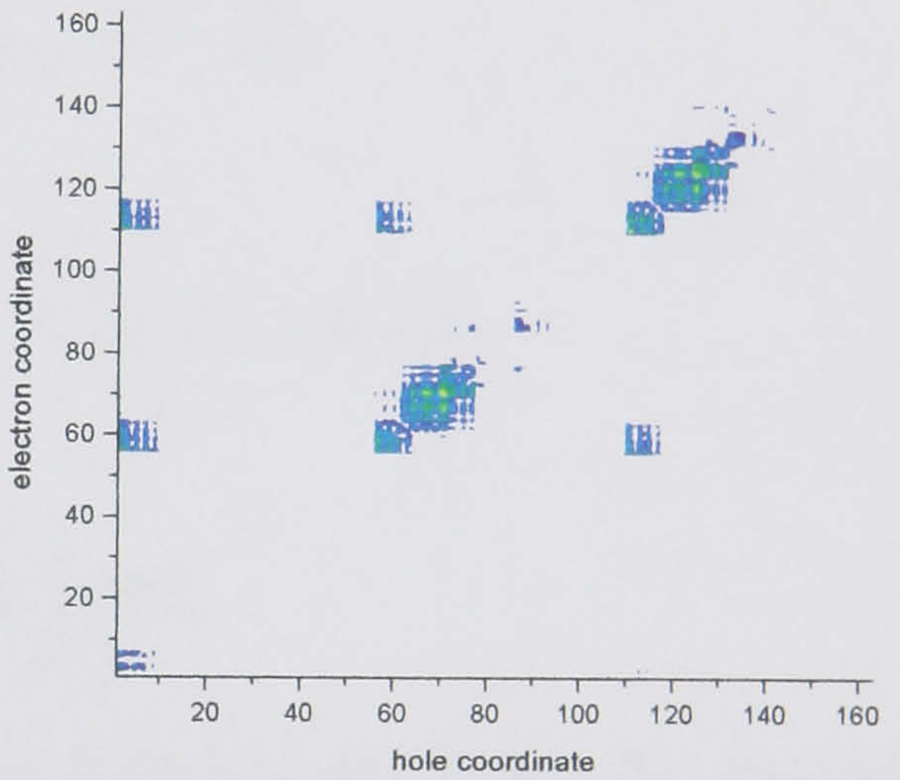

e) Ω=3.69 eV, ν=8

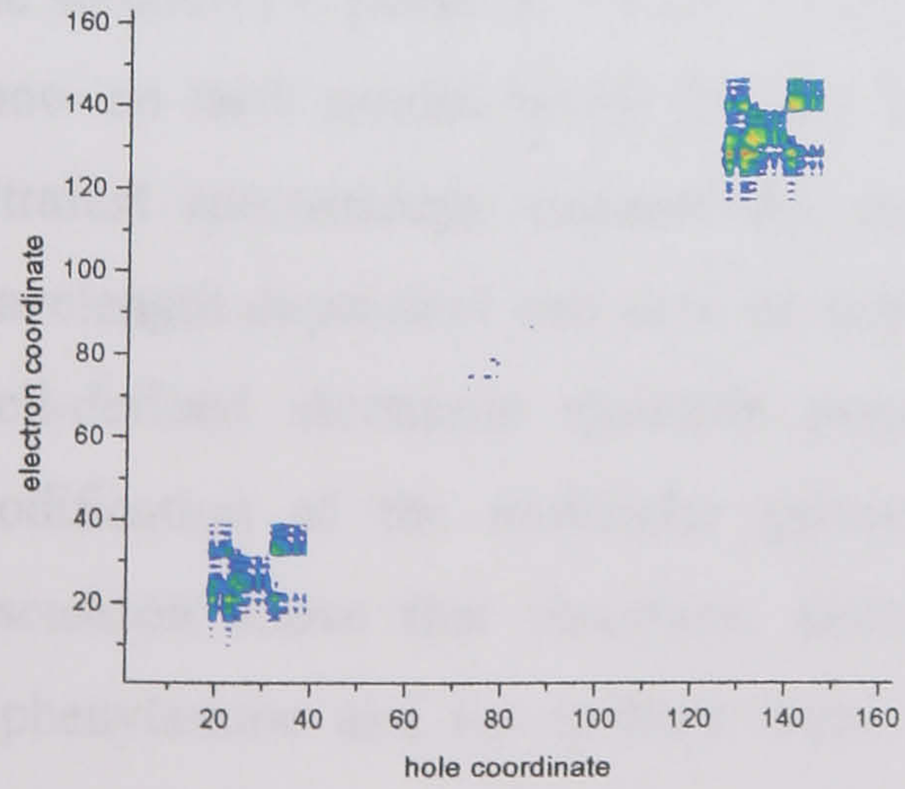

f) Ω=3.70 eV, ν=9

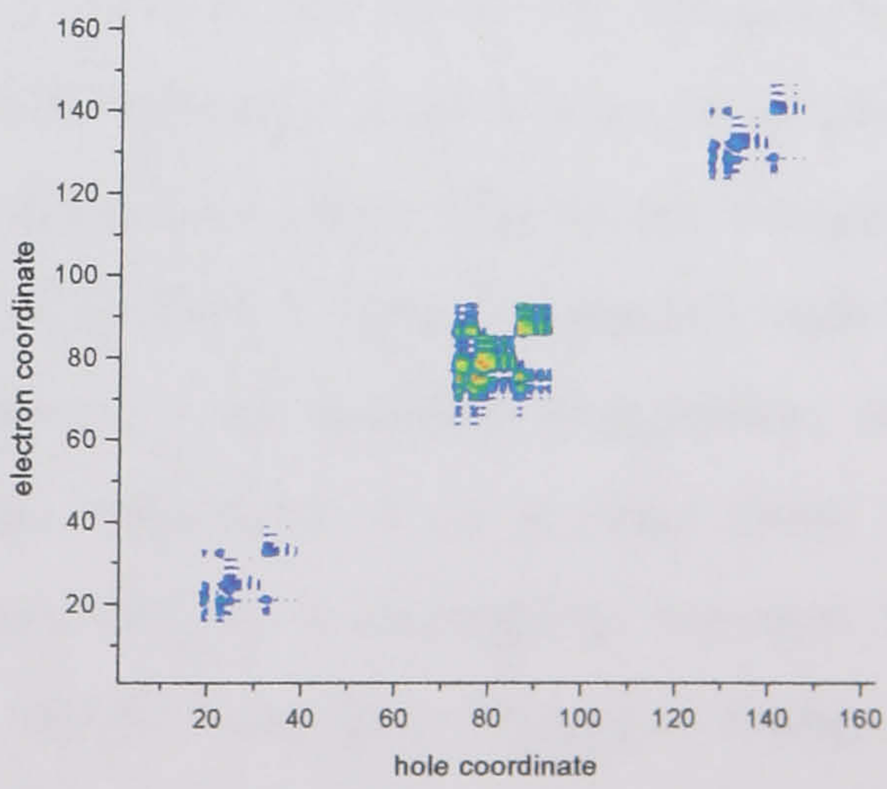

Fig. 4.38. *Strongest modes found in the CEO calculations on the A1 dendrimer plotted on a logarithmic scale. a) Mode 1 (core), b) Mode 2 (core), c) Mode 4 (core, stilbene and triphenylamine split), d) Mode 5 (core, stilbene and triphenylamine split), e) Mode 8 (dendron), and f) Mode 9 (dendron).*

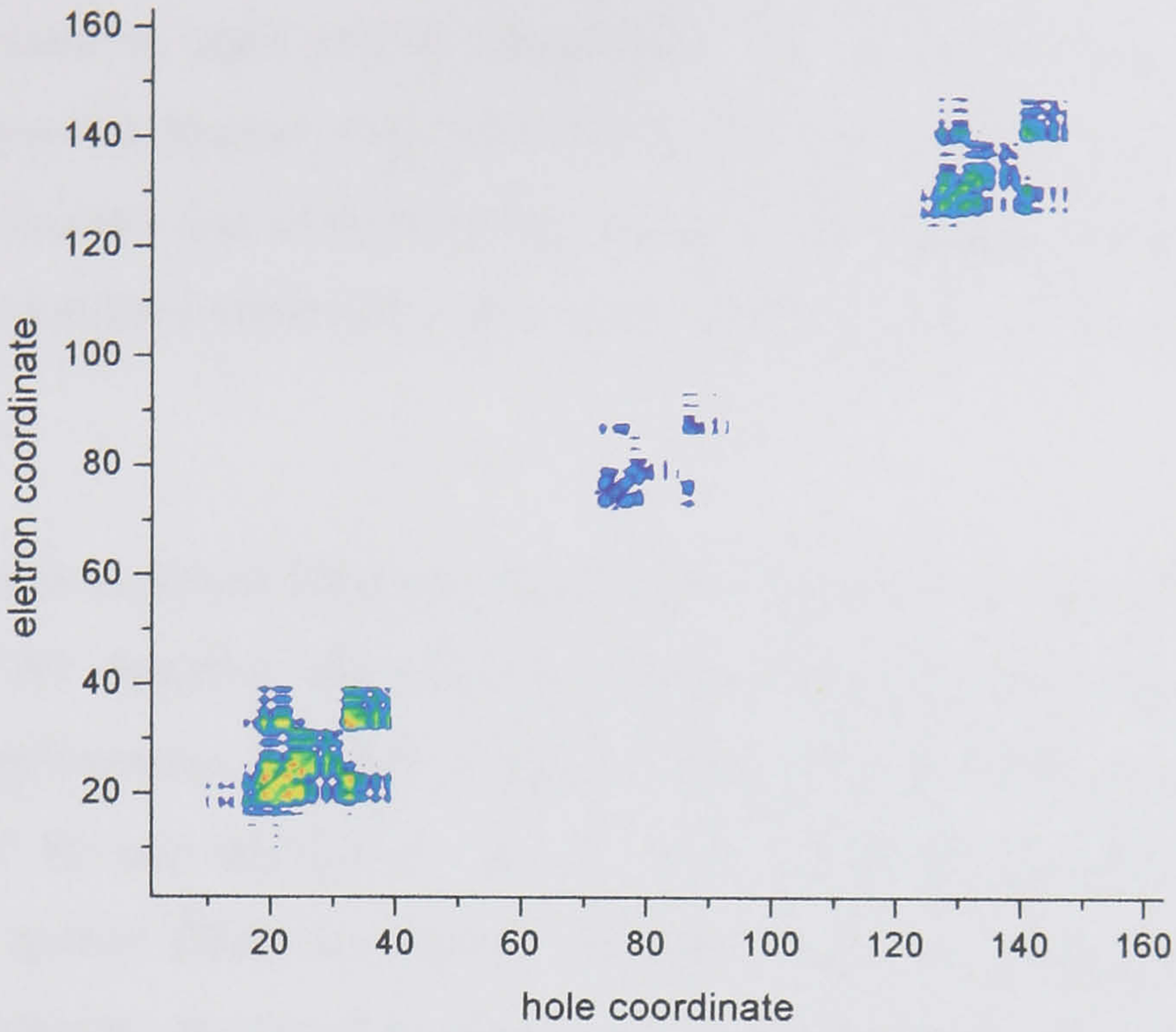

Fig. 4.39. *A1 dendron mode 13 on a logarithmic scale (Ω=3.81 eV).*

4.4.2.4 0^{th} Generation excited state geometry and modes

As was found earlier on in this chapter, there is a strong shift between the absorption and emission of the nitrogen core dendrimer. Whereas the absorption peaks at 3.0 eV, the solution PL peaks at 2.4 eV. However, the CEO calculations on the A0 dendrimer show no dark modes below 3.0 eV from which emission could occur. In addition, ultrafast spectroscopy experiments on these dendrimers have shown an intriguing wavelength dependent rise time on a ps scale [79] which is hard to combine with the well-defined electronic structure presented above. One possible explanation is a modification of the molecular geometry upon excitation. It is evident from the discussion above that electronic processes give rise to a decoupling between the triphenylamine and the stilbene units in A0, which could also suggest a change in charge distribution across the molecule. In order to investigate the possibility of an altered excited state geometry as well as the effect on a change in geometry on the mode structure, the excited state geometry was optimised using a commercial software package. The reduced configuration interaction singles (RCIS) calculation provided by the Gaussian 98 package forces the molecule to be in the first excited state when

performing the geometry optimisation. The previously optimised ground state geometry was used as input to this calculation. The calculation was much more intensive than comparable ground state calculations and the surface groups had to be removed from the structure due to memory constraints. The calculation could not be completed due to computational constraints, but it was found that the geometry converged over the cycles run.

The new structure obtained was found to be slightly distorted with respect to the ground state A0 structure. The dihedral angles measured across the nitrogen atom between the distyrylbenzene units were found to be different for the three units and were measured as 32° for one unit and 42° for the other two. This geometry was then used as the input to a further CEO calculation. The resulting mode energies are shown in Fig. 4.40. Remarkably, the small change in geometry gives rise to a dramatic lowering in energy of the lowest mode by over 0.4 eV. This suggests that the large shift between absorption and emission in this dendrimer may be due to a small change in the geometry of the molecule upon excitation. It is also interesting to note that only one distyrylbenzene unit (corresponding to the least twisted unit) is involved in this mode together with the triphenylamine unit, whereas in higher energy modes and indeed all other modes described earlier, two units were found to be involved. This is shown in the mode plots in Fig. 4.41. A possible, but tentative, conclusion of this is that whereas two distyrylbenzene units are involved in the absorption of a photon, only one is involved in the emission. This imbalance may give rise to the rather low photoluminescence quantum yields observed in the dendrimer.

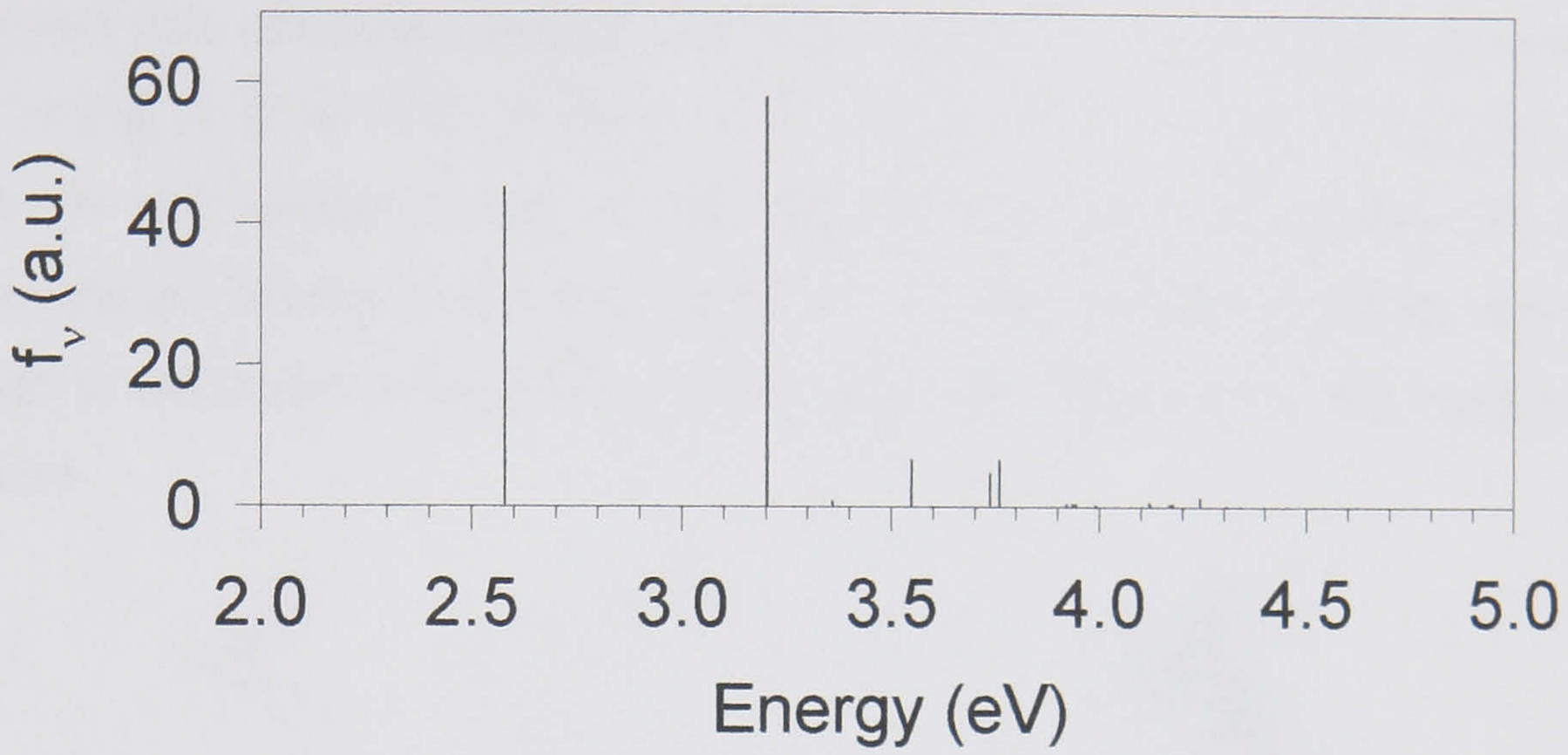

Fig. 4.40. *Modes found in the CEO calculations on the excited state geometry of A0.*

a) Ω=2.58 eV, ν=1

b) Ω=3.20 eV, ν=2

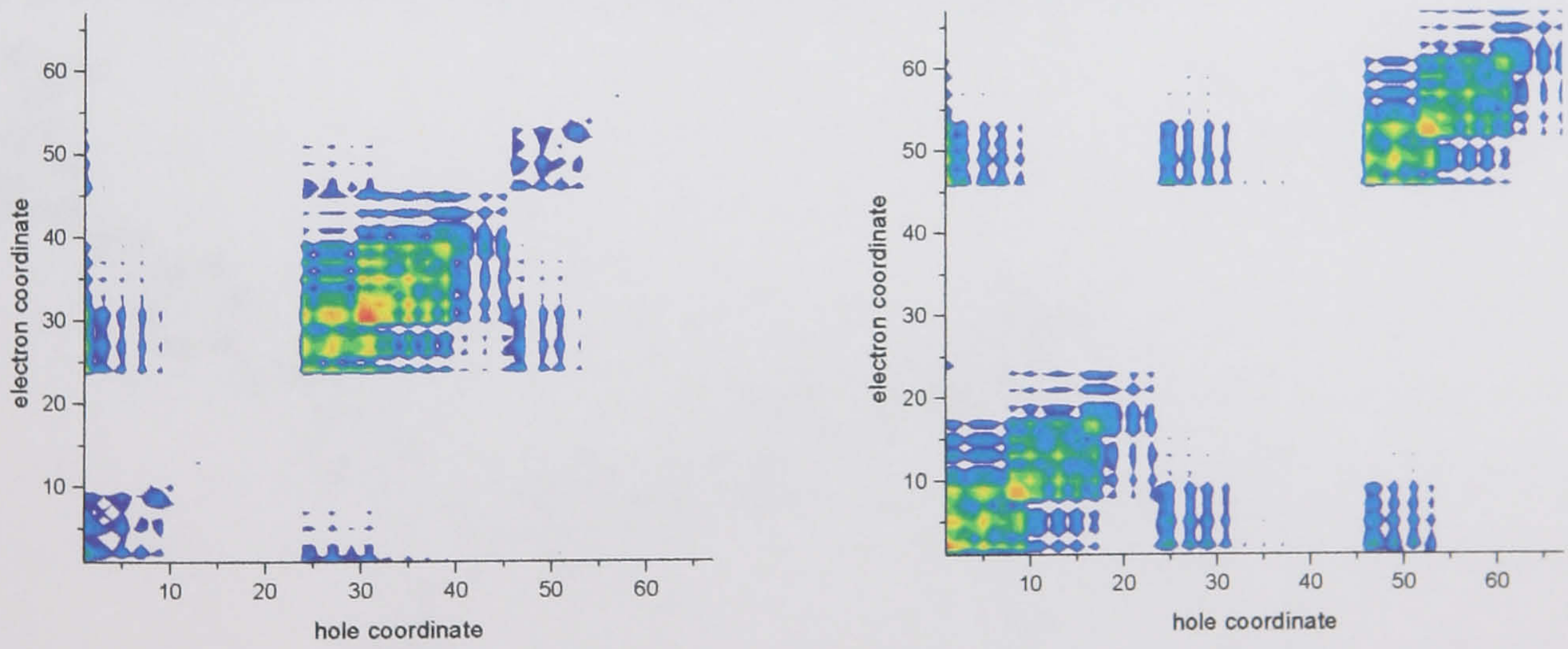

Fig. 4.41. *CEO modes of A0 excited state, a) Mode 1, b) Mode 2 (n.b. the surface groups were excluded from the calculation, hence the counting differs to that above).*

4.4.3 Benzene core dendrimer

The ground state optimised geometry of the 0^{th} generation benzene core dendrimer is shown in Fig. 4.42 and the counting of the carbon atoms is seen in Fig. 4.43. The structure is very similar to that of A0. The benzene rings surrounding the central benzene ring are found to be twisted out of the plane by 44° and the rms deviation from the plane is calculated to be 1.66 A, which is almost twice that of the nitrogen core dendrimer.

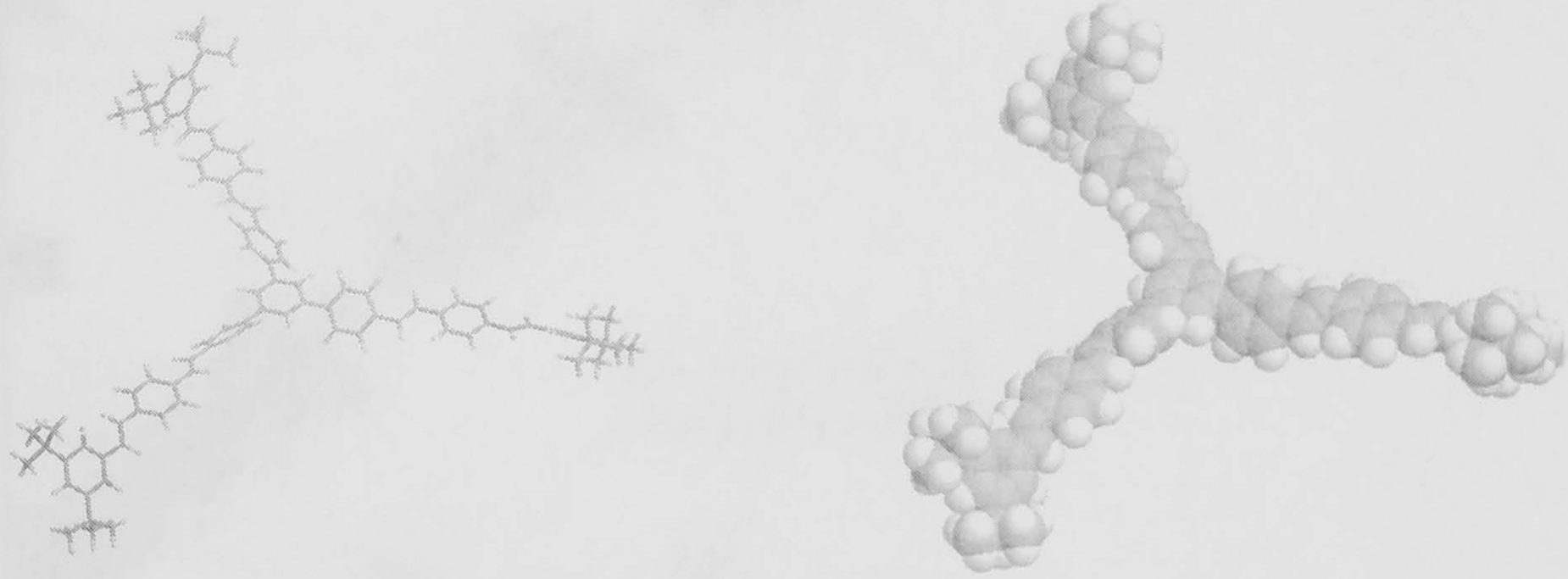

Fig. 4.42. *Ground state optimised geometry of the B0 dendrimer.*

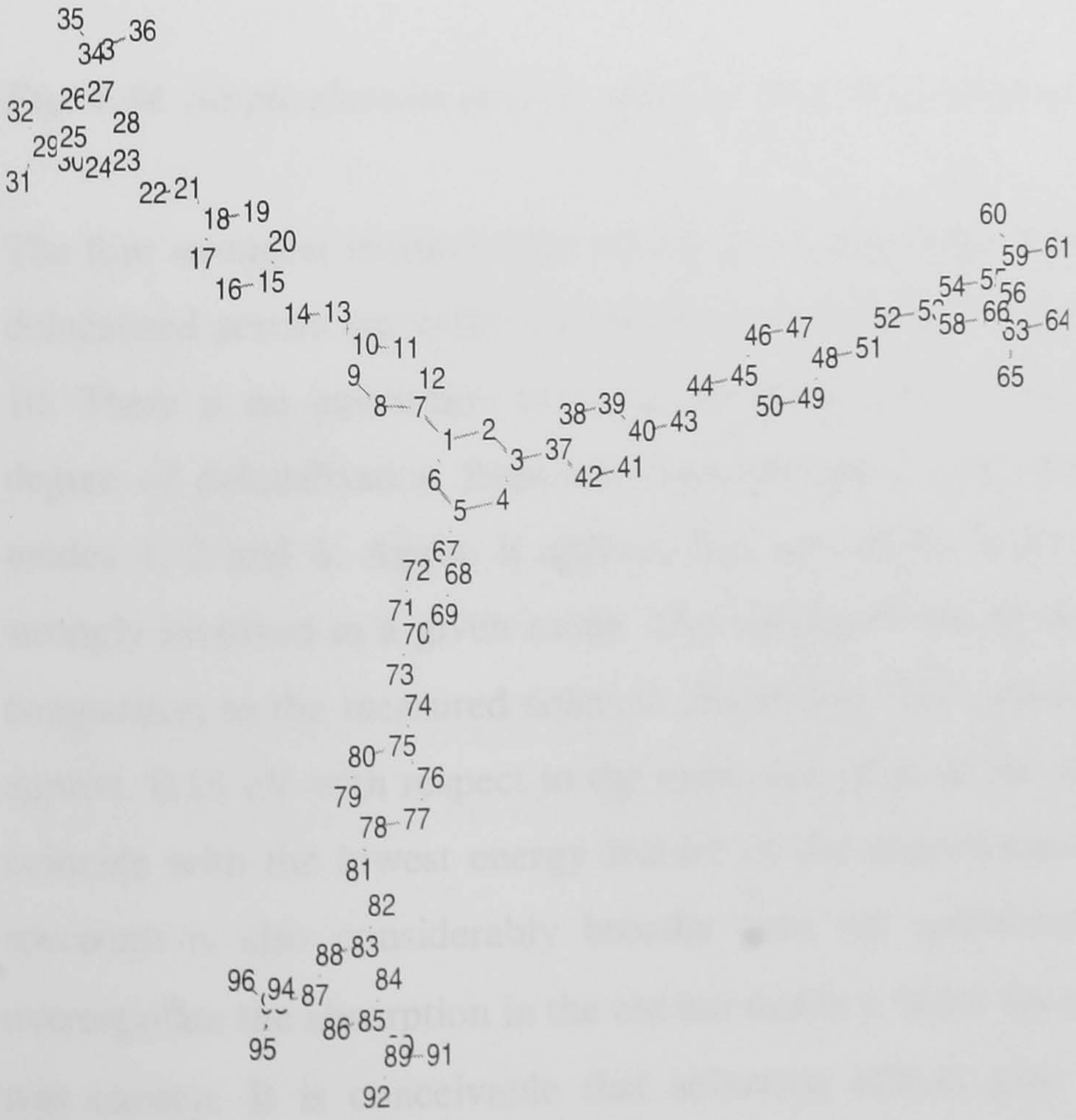

Fig. 4.43. *Carbon atom counting used in the CEO calculations on the B0 dendrimer.*

The single electron density matrix of B0 is shown in Fig. 4.44. As for A0, the three distyrylbenzene units are visible, made up of the individual benzene rings. There is some delocalisation onto the central benzene ring, which gives rise to the off-diagonal elements observed.

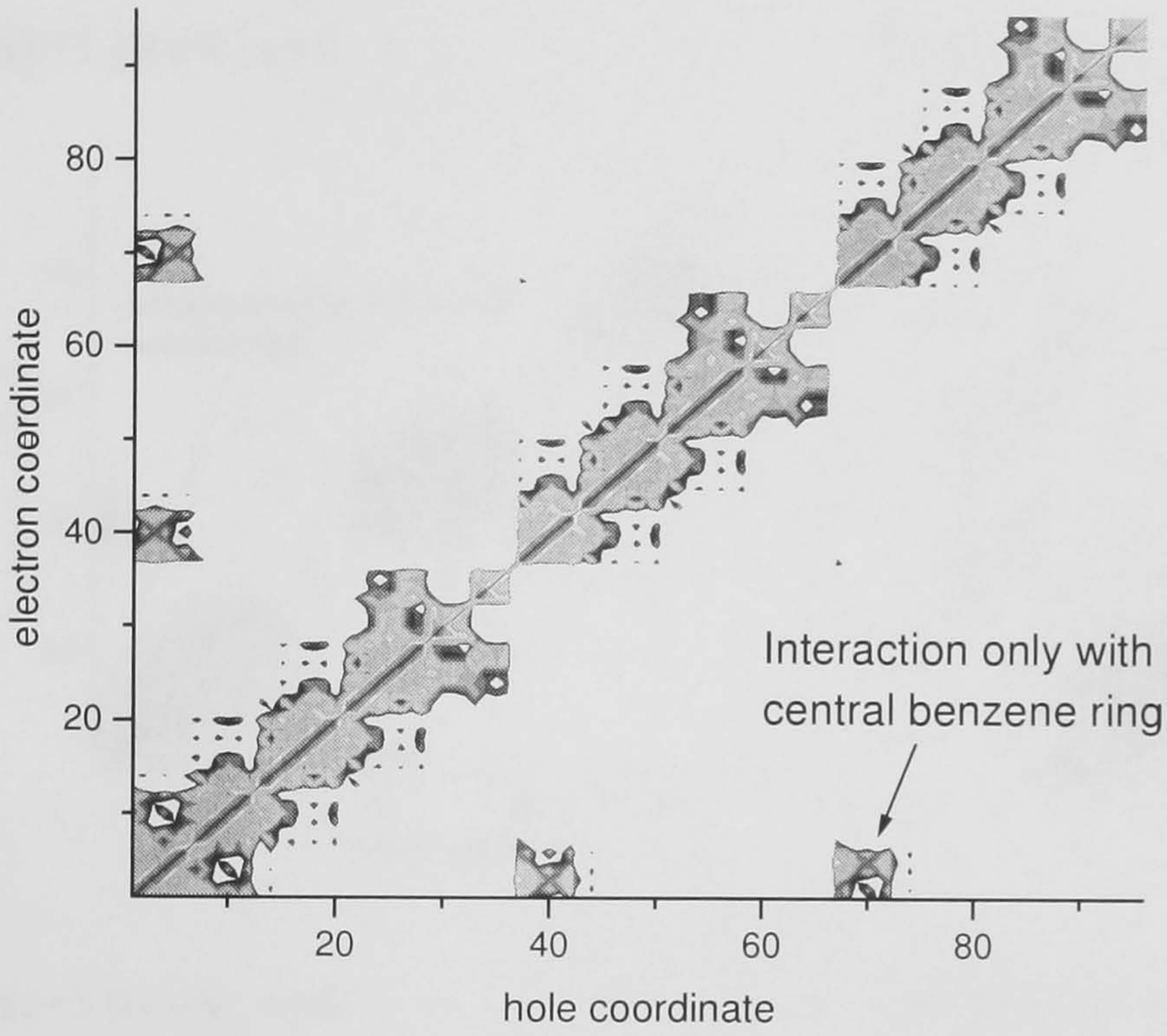

Fig. 4.44. *Single electron density matrix of the B0 dendrimer on a logarithmic scale.*

The four strongest modes of B0 are shown in Fig. 4.45. In all cases the excitations are delocalised across the entire distyrylbenzene branch, except for the high energy mode 10. There is no interaction between the three arms of the dendrimer, but there is a degree of delocalisation from the distyrylbenzene onto the central benzene ring for modes 1, 2 and 6. Again, it appears that two of the three dendrimer arms are more strongly involved in a given mode. The calculated absorption is shown in Fig. 4.46 in comparison to the measured solution absorption. The calculated peak is red-shifted by approx. 0.15 eV with respect to the measured peak of the absorption, although it does coincide with the lowest energy feature of the experimental spectrum. The measured spectrum is also considerably broader than the calculated spectrum. So as not to overestimate the absorption in the red too much, a value for the line shape of Γ=0.12 eV was chosen. It is conceivable that solvation effects give rise to the apparent shift between the calculated and experimental absorption maxima, although it is surprising

that for the nitrogen core dendrimer no such discrepancy is observed. Alternatively, the coherence with the benzene core may be overestimated in the calculation, giving rise to this discrepancy between experiment and calculation. As the calculation coincides with the lower energy feature of the absorption, it is also conceivable that the experimental absorption maximum is a vibronic feature of the spectrum.

a) Ω=3.19 eV, ν=1

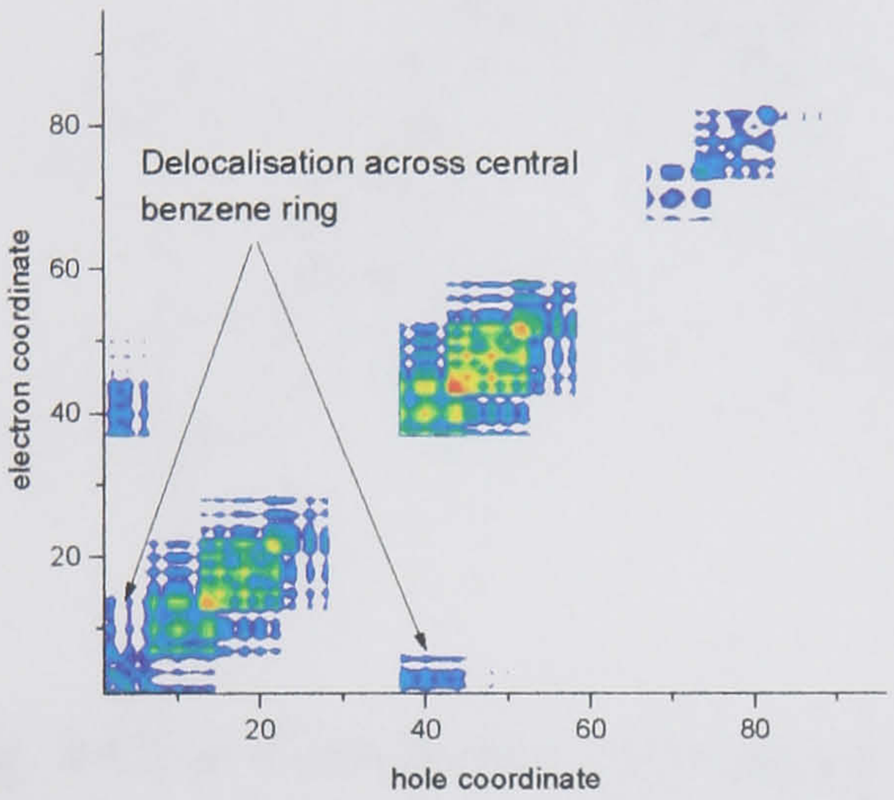

b) Ω=3.19 eV, ν=2

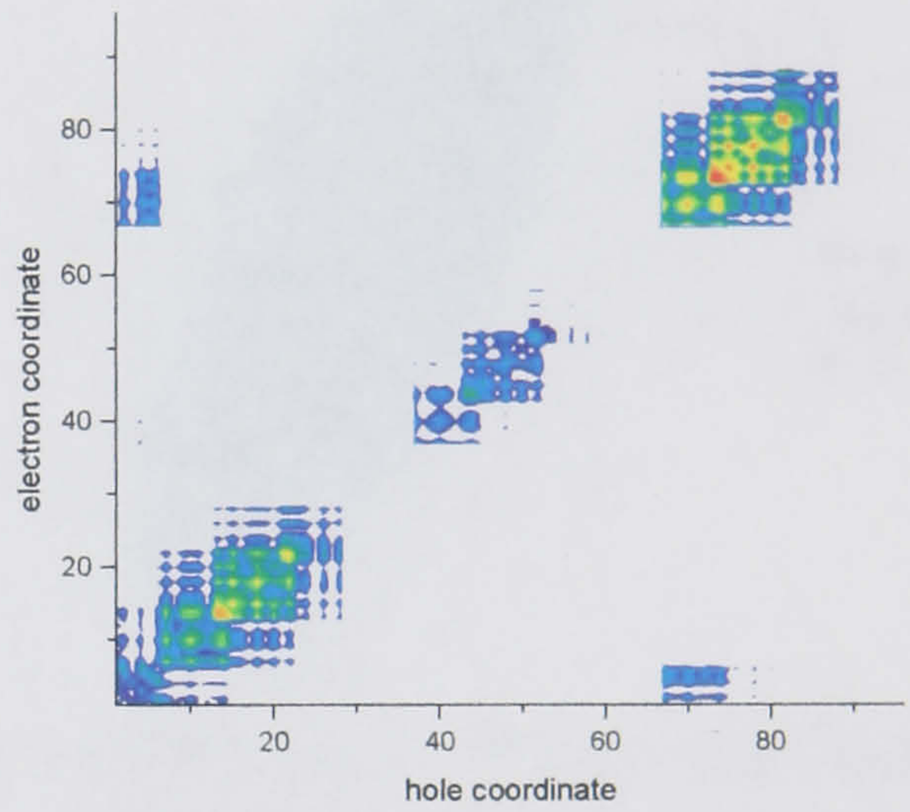

c) Ω=3.91 eV, ν=6

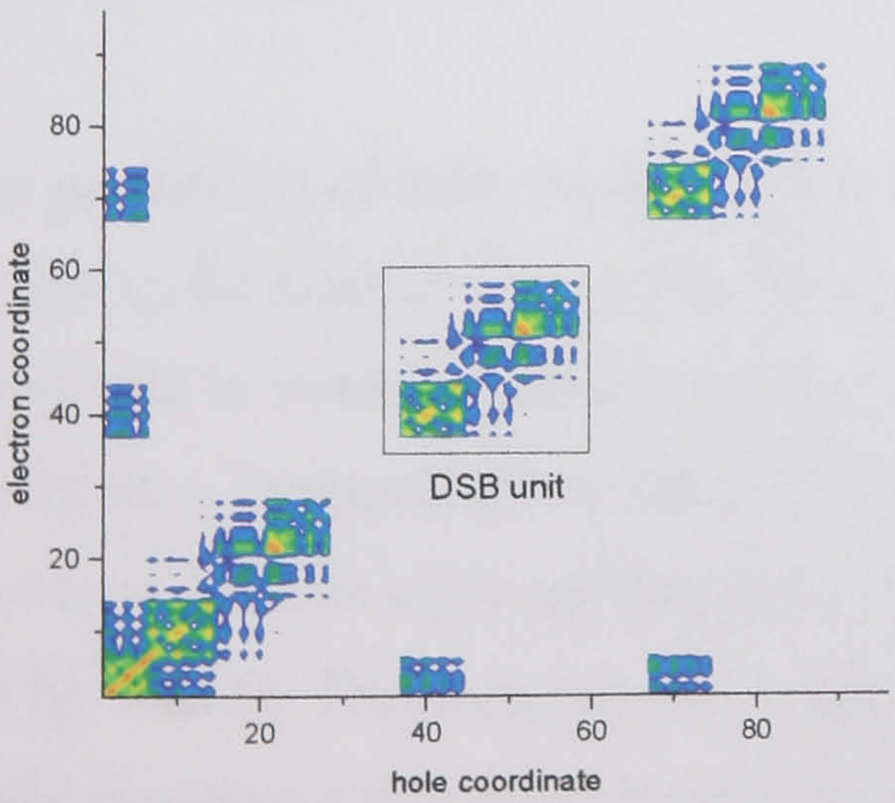

d) Ω=4.05 eV, ν=10

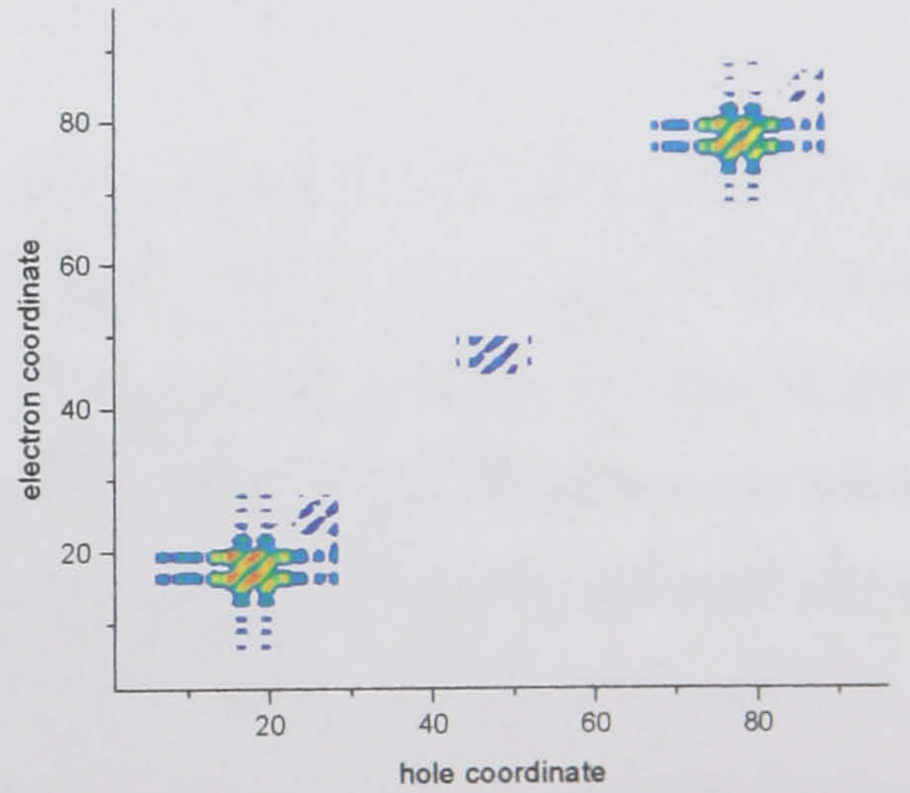

Fig. 4.45. *Strongest modes found in the CEO calculations on the B0 dendrimer. a) Mode 1, b) Mode 2, c) Mode 6, d) Mode 10. Modes 1 and 2 are degenerate.*

PAGE

MISSING

IN

ORIGINAL

PAGE

MISSING

IN

ORIGINAL

PAGE

MISSING

IN

ORIGINAL

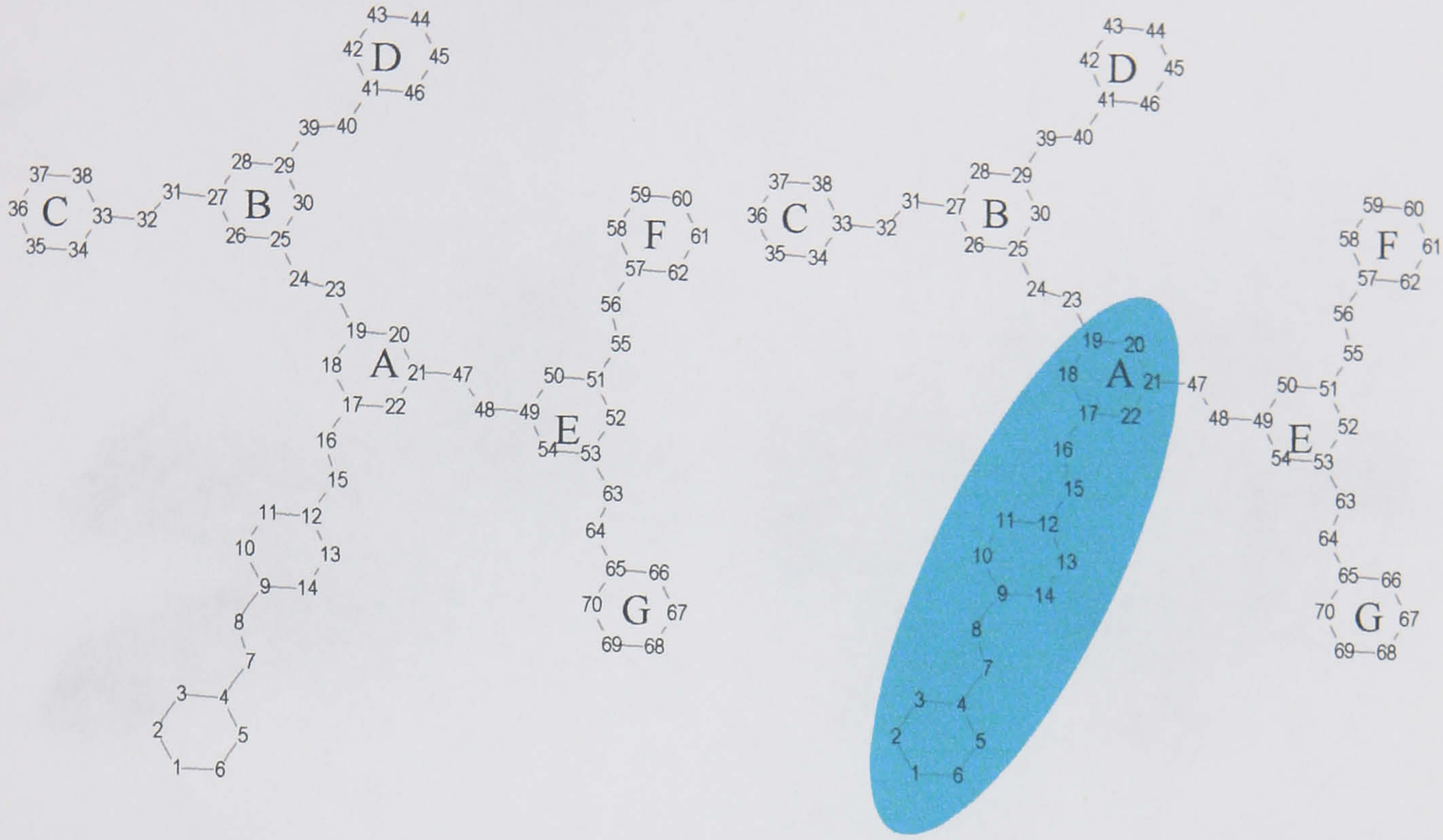

Fig. 4.47. *a) Carbon atom counting used in the calculation on the 2nd generation model compound consisting of a distyrylbenzene core and stilbene dendrons. The benzene rings comprising the dendrons are labelled A to G. b) Core region of the model dendrimer. The counting for the other generations follows a similar pattern.*

The geometries of these model structures are optimised using SPARTAN as before, but appear to be considerably more planar. As is shown in Fig. 4.48 a), the G2 model compound is virtually planar, which is in contrast to the observations on the complete dendrimers. Interestingly, as the generation is increased above G2, the stilbene dendrons start to interact strongly and the outer units are forced out of the plane, as is seen for G3 in Fig. 4.48 b). The presence of *t-butyl* surface groups, which were not included here, is likely to enhance this effect even further. The interaction between the stilbene dendrons can explain why the 3rd generation benzene dendrimer approaches the desired behaviour of excimer free emission, as the dendrons in G3 cannot lie in one plane and must hence act as spacers between molecules. The steric effects of the dendrons may also explain the blue-shifted emission observed in 3rd generation films of the nitrogen core dendrimer with respect to solution. If the dendrons become more constrained, the forces on the core chromophore are likely to increase. In films, the core chromophore structure may become pinned and can hence not relax completely to the lower energy excited

state geometry. The effect of the dendrons is likely to be much more complicated in the presence of the entire dendrimer structure and the surface groups.

a) b)

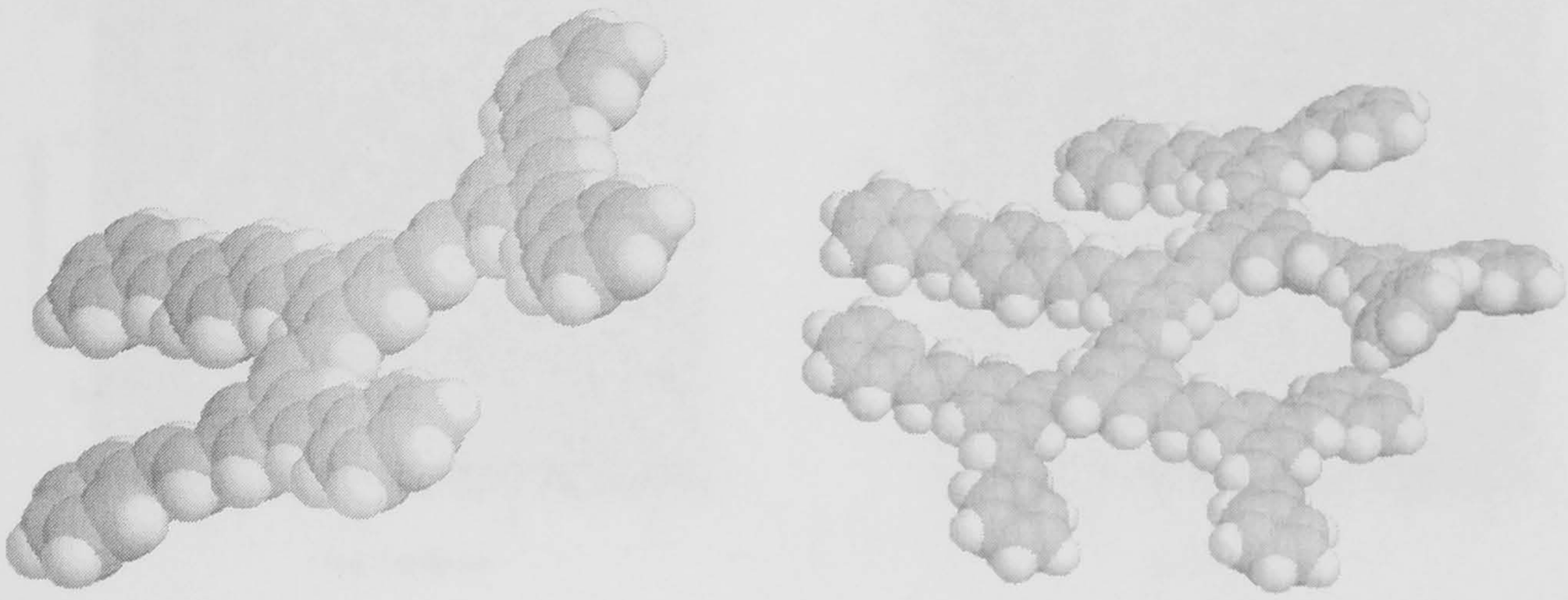

Fig. 4.48. *Optimised geometry of the G2 (a) and G3 (b) model dendrimers consisting of a distyrylbenzene core and stilbene dendrons.*

The lowest energy modes of the four model dendrimers G0 to G3 are shown in Fig. 4.49 on a linear scale. The results are remarkable: for all four generations the lowest mode is localised at the core chromophore of the dendrimer, the distyrylbenzene unit. Indeed, the core mode is independent of generation and is merely found to shrink as the dendron architecture around the core grows. There is a small amount of delocalisation to the inner dendrons and for G2 and G3 a weak excitation of the inner dendrons is observed (the off-diagonal elements result from the discontinuity in counting upon excitation of dendron units A-B and A-E, for example). The second modes of these model systems are plotted in Fig. 4.50. It is evident that the next higher excitation results in an excitation of the dendrons rather than the core. For G1 to G3, the core region in the transition matrix remains dark, whereas the dendrons are excited. These results hence demonstrate two things. Firstly, the lowest energy mode is independent of generation and is always localised on the core. And secondly, the next highest mode excludes the core and comprises merely the dendrons. This analysis hence gives a microscopic real-space picture of the excitations present on a dendrimer molecule. It also demonstrates that the excitations must be funnelled to the core, as this is the lowest energy state. A

molecule excited in the dendrons must hence emit from the core, which is generally observed experimentally.

G0 Ω=3.31 eV, ν=1

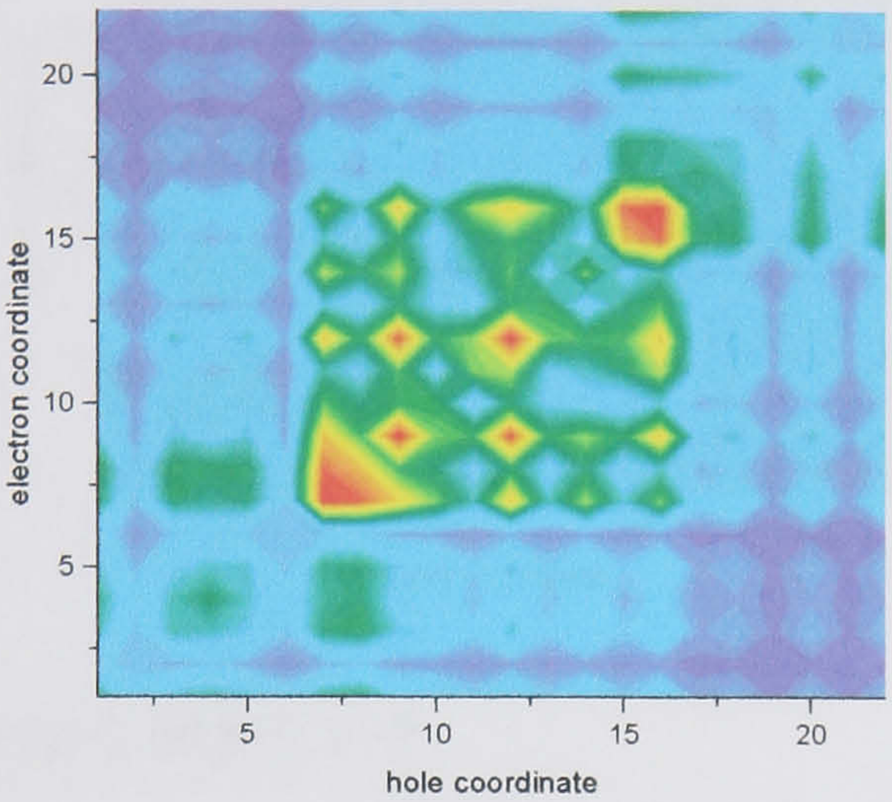

G1 Ω=3.29 eV, ν=1

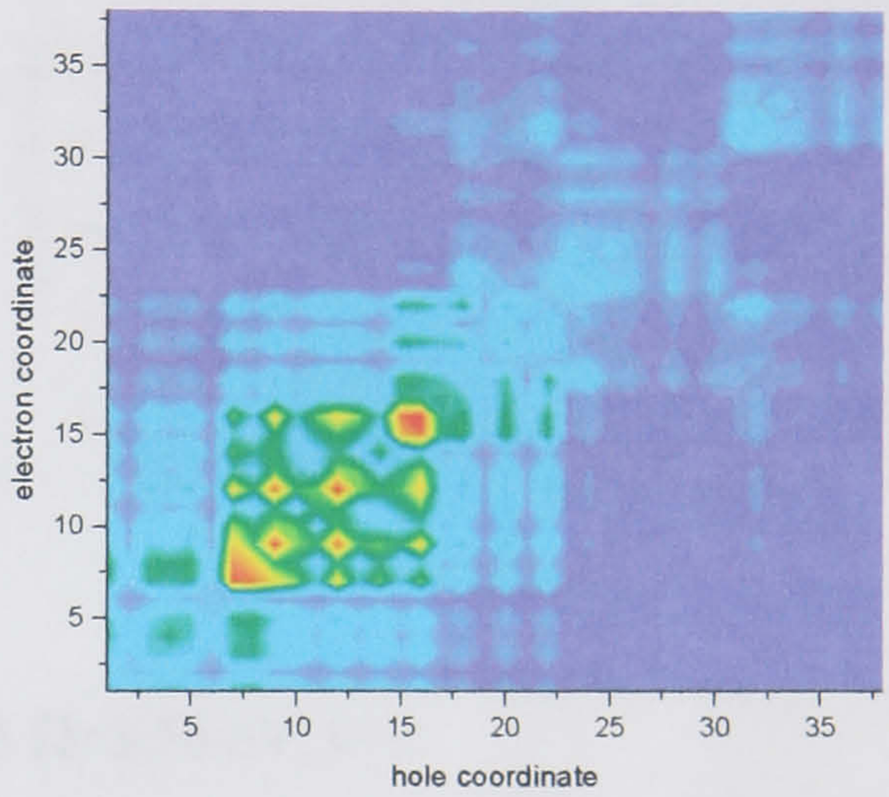

G2 Ω=3.28 eV, ν=1

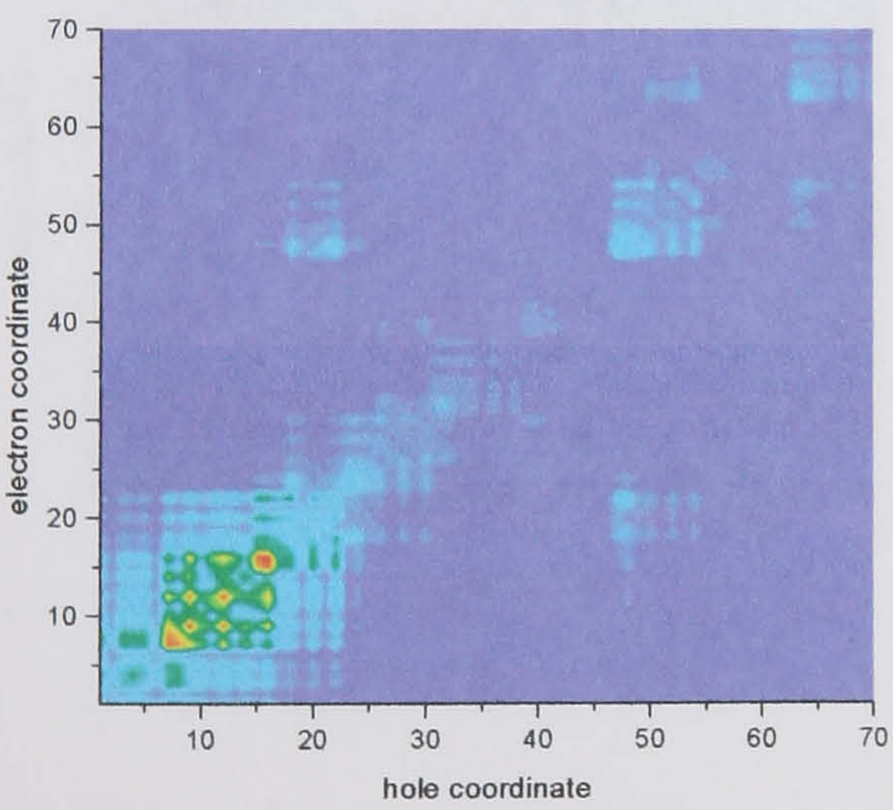

G3 Ω=3.26 eV, ν=1

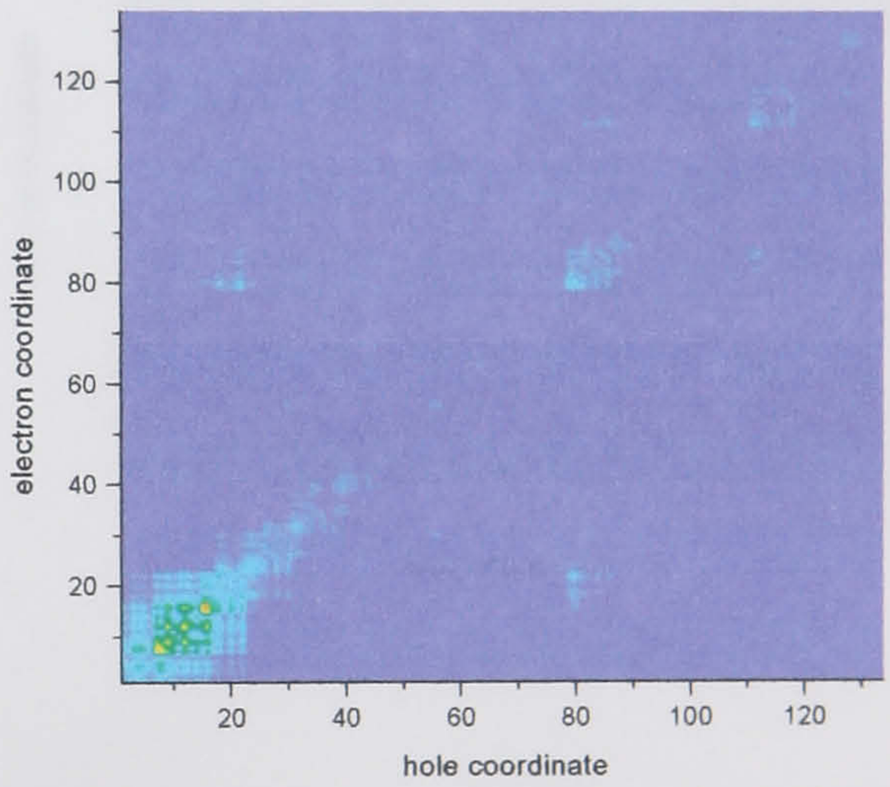

Fig. 4.49. *Plots of the lowest energy (core) modes of the model dendrimers on a linear scale.*

G0 Ω=4.03 eV, ν=2

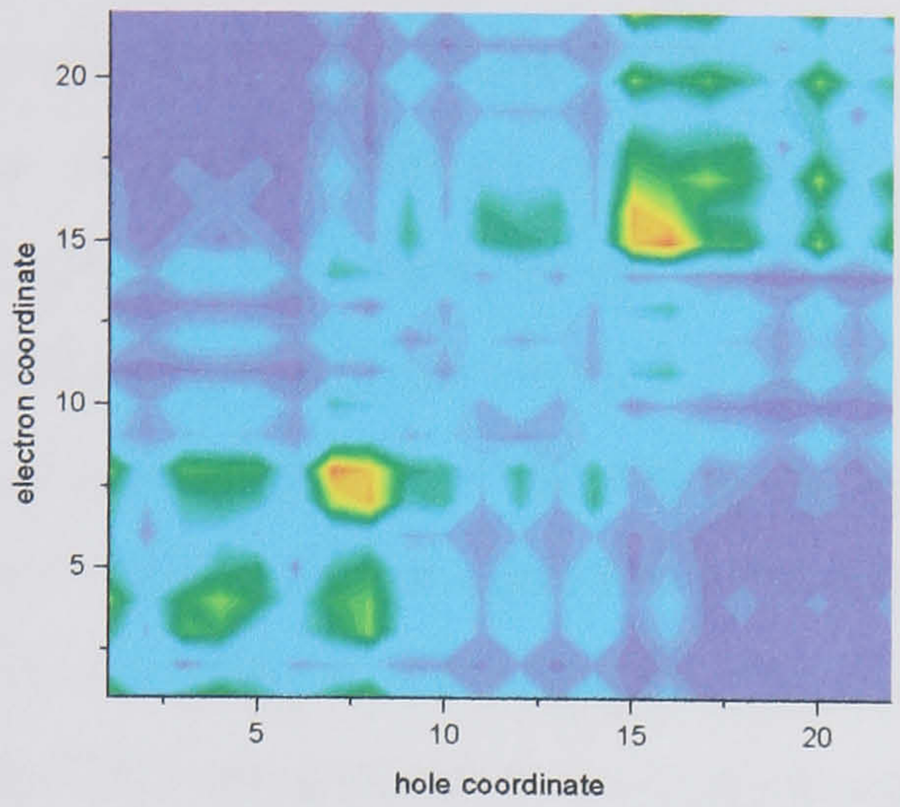

G1 Ω=3.71 eV, ν=2

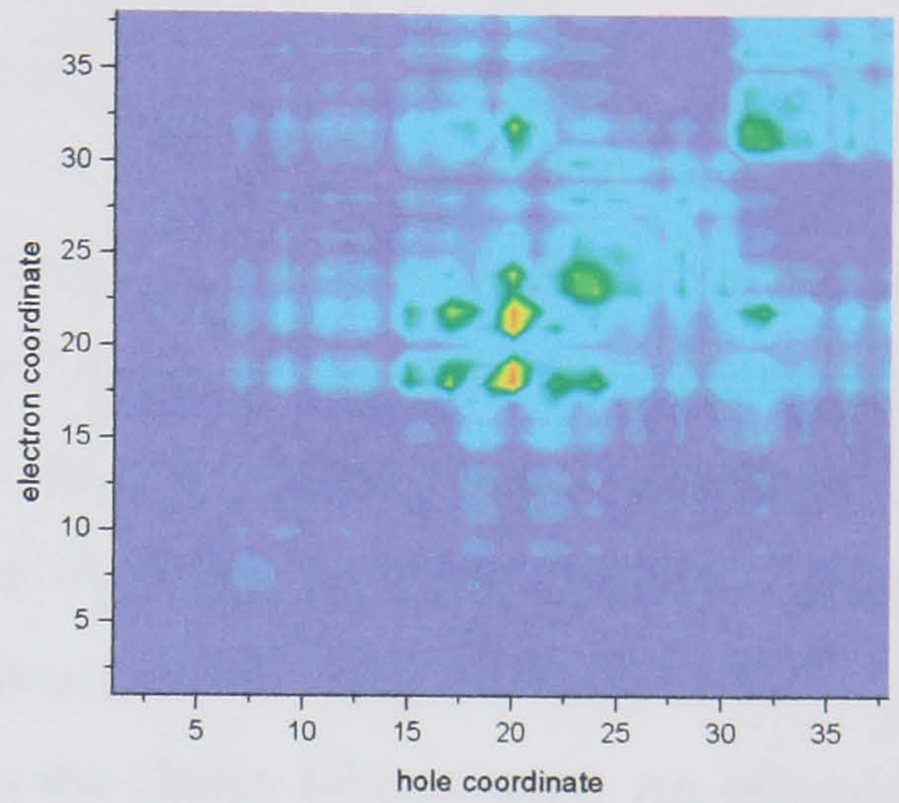

G2 Ω=3.60 eV, ν=2

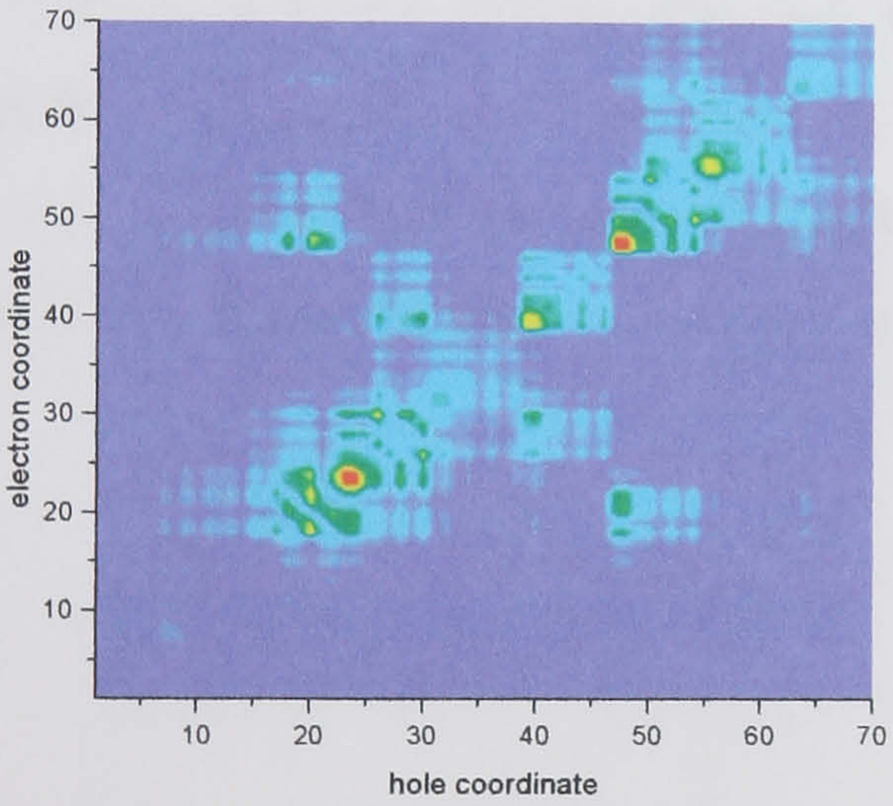

G3 Ω=3.56 eV, ν=2

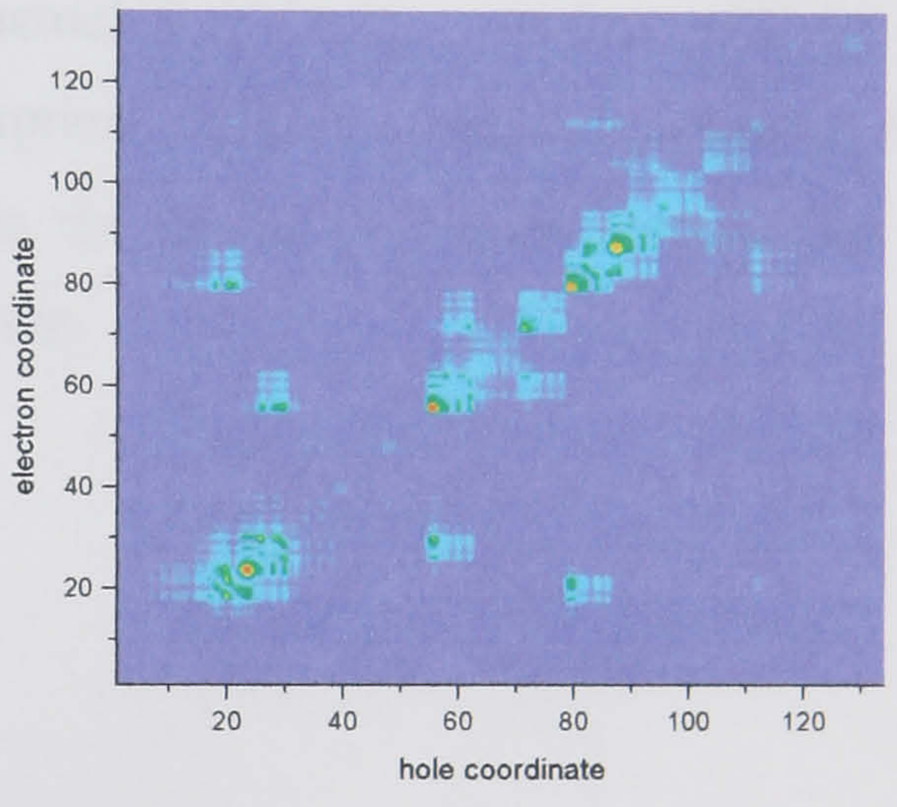

Fig. 4.50. *Second mode observed in the model dendrimers corresponding to dendron modes for G1 to G3. (Linear scale).*

As the number of dendrons increases exponentially with generation, a direct interpretation of the mode diagrams in terms of excitations on the dendrons is possible for G2, as is shown below, but becomes very cumbersome for G3. Whereas G2 exhibits two types of dendron modes, the G3 dendron modes are all different and all involve different regions of the dendrimer.

4.4.5.2 Dendron to core absorption scaling

The modes and calculated absorption spectra are summarised in Fig. 4.51 for all four generations and are compared to the experimental absorption spectra of the benzene core dendrimer. Theory and experiment are in excellent agreement for all four generations. The absorption peak is calculated exactly and the B0 match is much better than for the calculation on the full dendrimer structure. The scaling of the stilbene peaks with respect to the core absorption are well reproduced in the calculation. There appears to be a second higher energy stilbene peak in the experiments, which is not reproduced in the calculations. Lone stilbene absorbs at between 3.8 eV and 4.0 eV, and the result from CEO calculations is strongly dependent on the choice of geometry. An optimised lone stilbene unit absorbs at 3.7 eV, whereas a study of the CEO modes on stilbene using atomic co-ordinates from x-ray diffraction studies yielded a value of approx. 4.0 eV [27]. It is hence conceivable that in the actual dendrimers a variety of stilbene conformations are present. The increase in absorption at higher energies is observed for G0 and G1, although the lack of this feature in the higher generation calculations is most likely due to the limit on the number of modes.

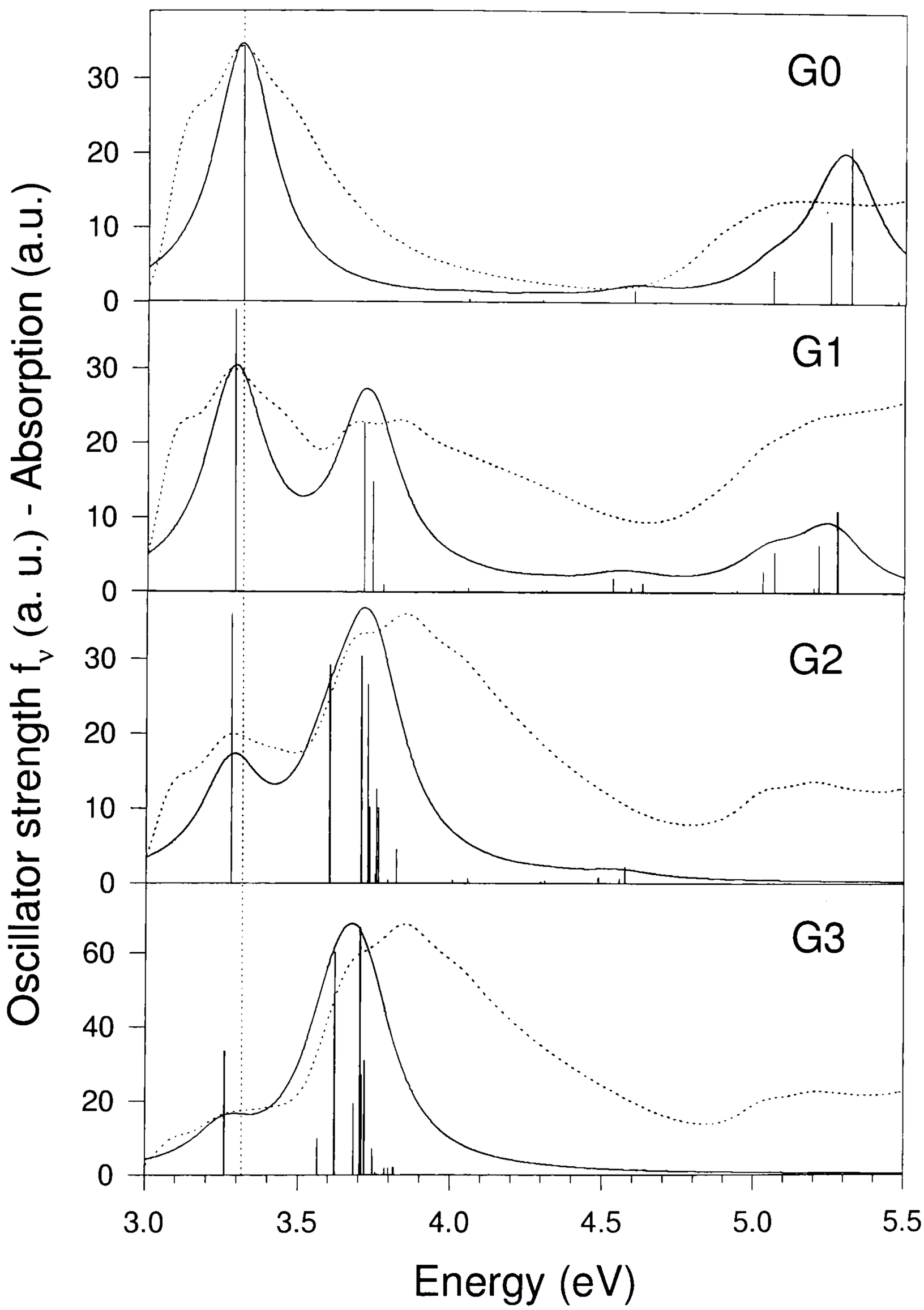

Fig. 4.51. *Calculated absorption (——) and oscillator strength for the model dendrimers compared to experimental absorption (·····) of the* **benzene** *core dendrimers. The dashed line marks the absorption peak of distyrylbenzene.*

The calculation accurately describes the red-shift of the absorption peak with increasing generation. This is a direct result of the core mode coupling to the stilbene modes resulting in excitonic splitting. There is no coherence between the core and the dendron and excitations may be treated in terms of the Frenkel exciton model. It is surprising to note that the core energy level splitting observed in the A1 dendrimer was symmetrical, with transitions appearing at higher and lower energies with respect to the transitions in A0. However, in the model compounds, no second line is observed corresponding to the higher energy transition of the split pair. This suggests that due to the symmetry of the system the higher energy peak becomes forbidden. It is hard to establish from the experimental data whether this really is the case or not, as the higher energy split core peak merges with the dendron band. A comparison of the experimental solution absorption of the two dendrimer families in Figs. 4.3 and 4. 8 does suggest that the band is broadened to the red but not to the blue. If the dipoles on the stilbene dendrons and the core chromophore were aligned in parallel, the higher energy transition would be expected to become forbidden. However, as this is clearly not the case in this system, a discrepancy remains which is presently unresolved. It is conceivable, however, that the excitonic coupling between the core and dendrons is simply too weak to support the feature split to higher energies.

It is surprising that this model system provides a better description of the experimental data than calculations on the complete dendrimer. However, the results suggest that the CEO on the B0 dendrimer overestimates the amount of charge delocalisation onto the central benzene ring. A lone distyrylbenzene unit hence provides a better description of the experimental data. It is also possible that the proximity of the distyrylbenzene units in the B0 dendrimer leads to excitonic coupling and hence a red shift of the spectrum in the calculation, similar to the coupling between core and dendrons observed in the model system. This could depend strongly on the sample geometry and may be overestimated.

One further remarkable consequence of the scaling of core to dendron absorption is the fact that all possible stilbene units contribute to the absorption and the scaling hence goes as 1:3:7. The origin of this effect comes from the presence of different modes with comparable oscillator strengths and energy eigenvalues in the absorption spectrum. This is highlighted in the example of the G2 model dendrimer shown in Fig. 52. It is seen

that for modes 2 and 3, which have identical oscillator strengths (c.f. Fig. 4.51), four different stilbene units may be identified in the transition matrix, of which two are strong and two are weak. For mode 2, the strong stilbene transitions are A-B and E-F, whereas B-D and A-E are weak. For mode 3, B-C and E-G are strong whereas B-D and E-F are weak. Hence in these two modes all benzene rings in the dendrons have been involved. The strong excitations are comprised of benzene rings, which are not shared. The absorption spectrum consists of the sum of all these modes, so there is no danger of double counting the available benzene rings or the free electrons in the system as the dominant transitions result from unshared entities. It is also interesting to note that the dominant stilbene units extend to the adjacent vinylene unit, which can give rise to a further red-shift of the calculated stilbene absorption band.

a)

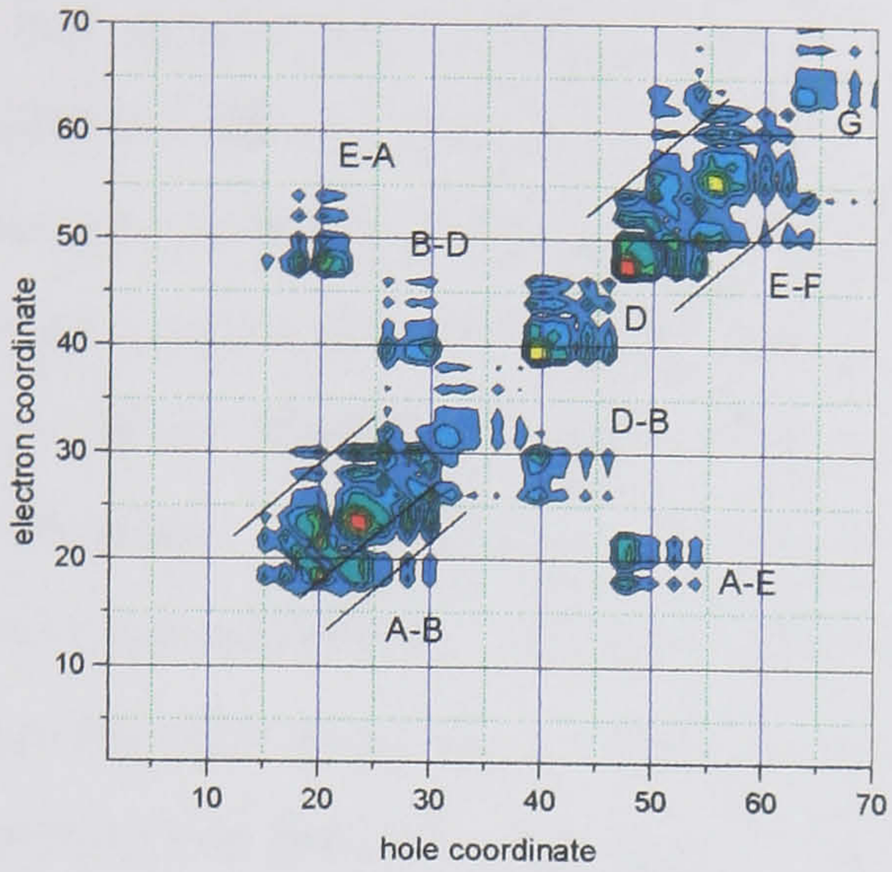

b)

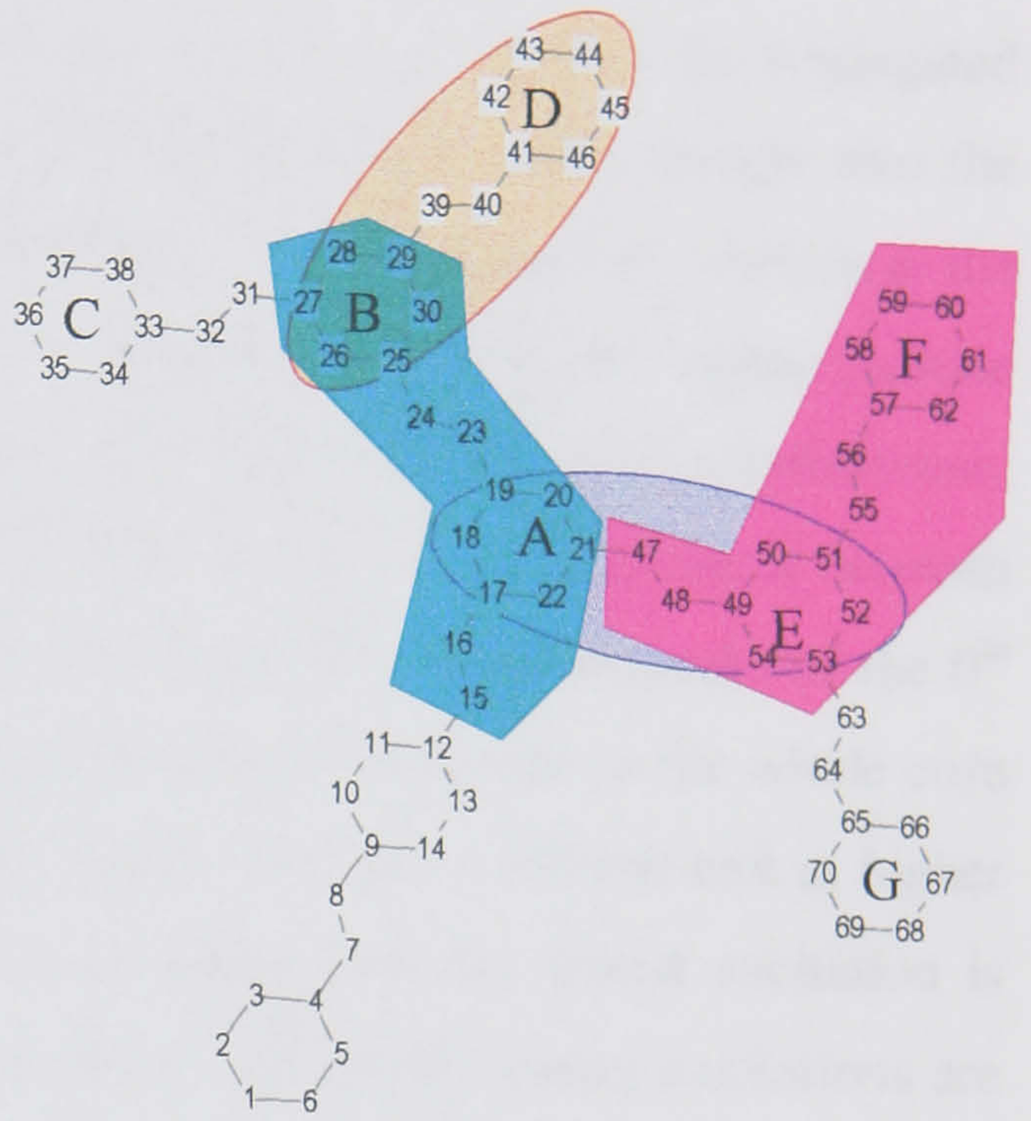

c)

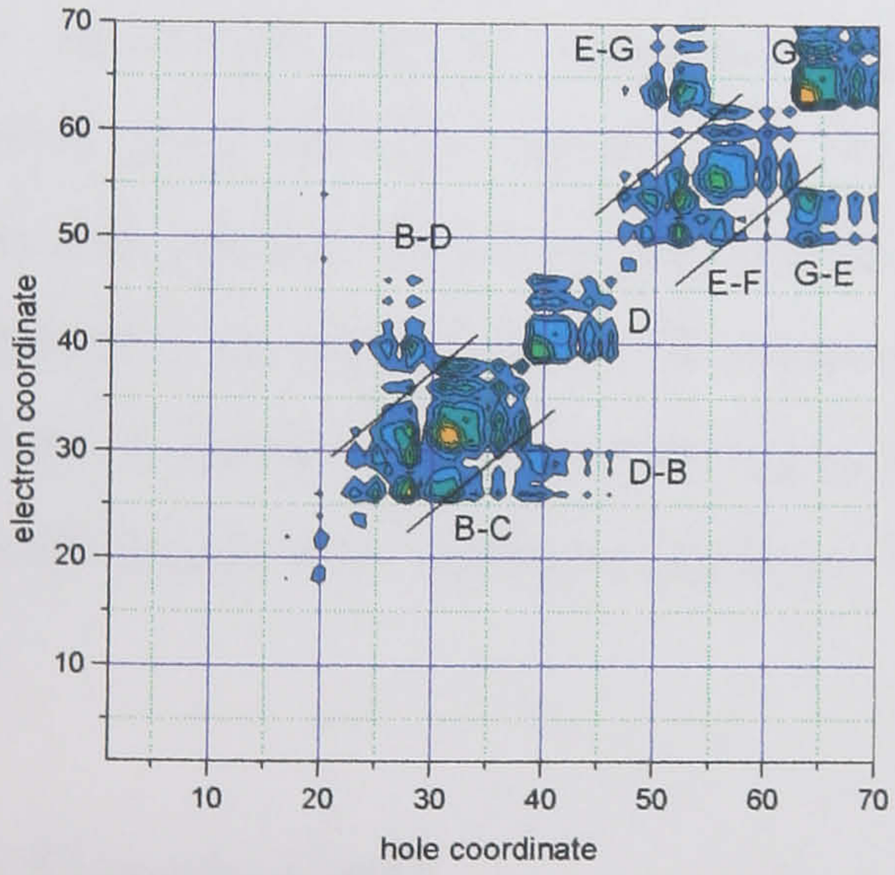

d)

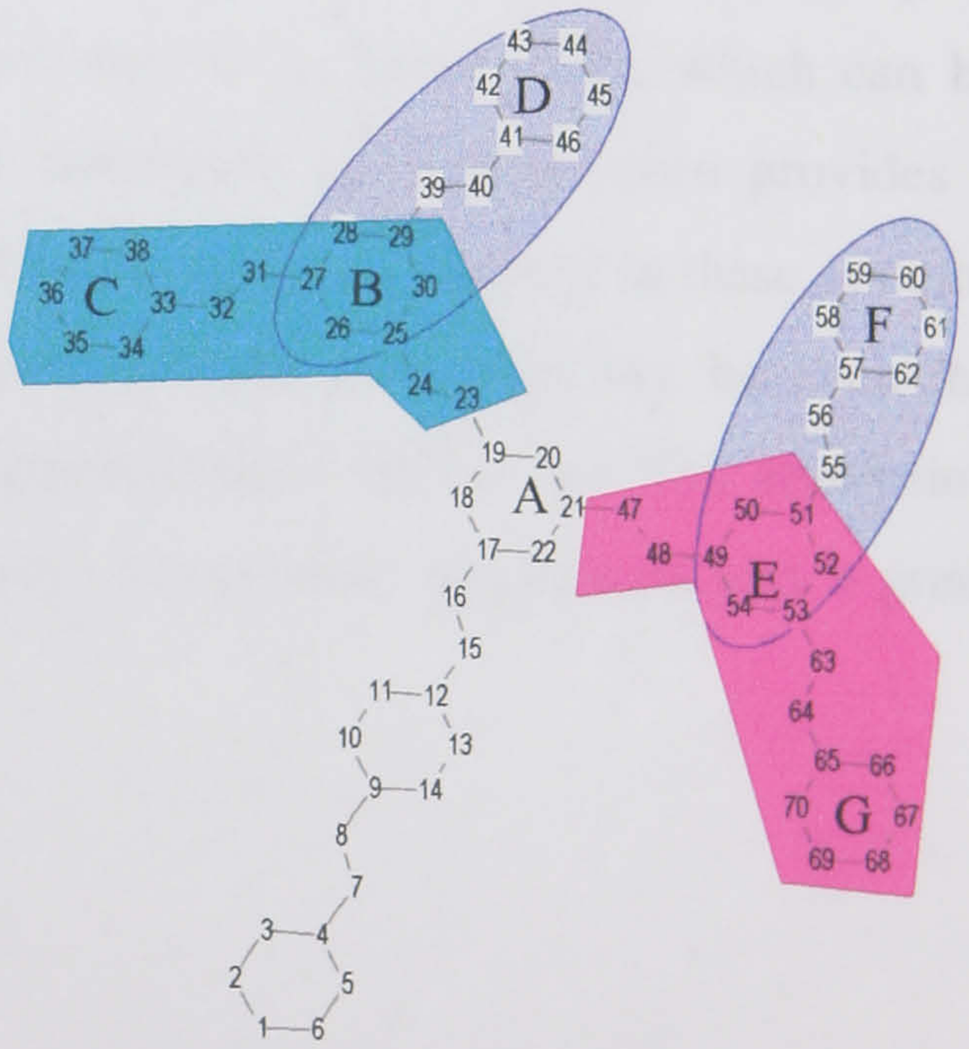

Fig. 4.52. *CEO modes 2 and 3 (linear scale) of the G2 model compound showing the dendron groups involved in the excitations. The shaded ellipses drawn on the structures mark weaker modes. a) Mode 2, b) Dendrons associated with mode 2, c) Mode 3, d) Dendrons associated with mode 3.*

4.4.6 Summary

In this section the coupled electronic oscillator model was applied to conjugated dendrimers for EL applications. The CEO calculations yield valuable insight into the structure of electronic modes present in the dendrimers. It was found that whereas in the nitrogen core dendrimer the core excitation is delocalised across the triphenylamine centre of the dendrimer, reducing the band gap with respect to that of distyrylbenzene, for the benzene core dendrimer no such delocalisation occurs. Good agreement between experiment and theory was found and the two experimental absorption peaks of the 0^{th} generation nitrogen core dendrimer could be interpreted as being due to the whole core absorbing and the core splitting into an triphenylamine unit and a stilbene unit at higher energy. A study of a model core-dendron system shows that the lowest excitation is localised on the core and is independent of generation. All higher energy excitations are present on the dendrons. Dendrimers hence provide an elegant system for localising excitations in space, which is represented very clearly in the real space CEO analysis. The localisation can be compared to quantum dots or quantum wells, which can be probed using the CEO model [24, 74]. The dendrimer generation hence provides a nanoscale control of exciton localisation. Exciton splitting is observed in these systems comparable to that observed in coupled quantum wells. The similarity between the calculated features, and the observations in experimental solution and film absorption spectra suggest that neither solvation effects nor ground state aggregation play a great role.

4.5 Conclusions

In this chapter a detailed investigation into the photophysical and transport properties of two novel families of conjugated dendrimers has been presented. Excitations in all the dendrimers were found to be localised at the core, which allows a deconvolution of the dendritic molecule into core and dendron components. The core emission is found to be independent of the dendrimer generation. It was shown that the dendrimer generation provides a unique and very elegant way of controlling the degree of intermolecular interactions between these core chromophores. A direct correspondence between the generation dependence of the red-tail emission in solid state, which is attributed to the

presence of emissive intermolecular excitations, and the properties of single layer LEDs was established. In particular, for the nitrogen core dendrimer a reduction in excimer emission is observed with increasing generation, which coincides with a doubling in LED operating field and a 25-fold increase in device efficiency.

In contrast, the blue emitting benzene core dendrimer family was found to exhibit the reverse effect, with the level of excited state interaction increasing with increasing generation. The highest generation dendrimer provided a reversal of this trend, demonstrating isolation of the chromophore from the environment.

Temperature dependent measurements show that thermal broadening of excitations on these molecular semiconductors plays an important role, in contrast to conjugated polymers, whereas the temperature dependence of the device properties is comparable to those of MEH-PPV devices. The nitrogen core dendrimers exhibit excellent properties as both transport and emissive layers in bilayer LEDs.

The important photophysical features of the two dendrimer families are reproduced in coupled electronic oscillator calculations. The core units of the two dendrimers are found to be entirely different due to the effect of delocalisation between the distyrylbenzene units. A high degree of exciton localisation is observed in the calculations, as well as the effect of exciton splitting between core and dendron excitations. The excellent agreement of experiment and theory highlights an alternative route to the synthesis of novel compounds. By employing quantum chemical techniques, precise information may be gained about the electronic properties, and most importantly, the emission colour, of the new system prior to synthesis. In the context of conjugated dendrimers this greatly simplifies the search for novel materials.

Besides being of importance to display applications as light-emitting materials, the nanoscale control of core chromophore separation through dendrimer generation gives important new insight into the effect of chromophore spacing in conjugated materials.

References

[1] J. M. J. Frechet, Science **263,** 1710 (1994)

[2] S. K. Deb, T. M. Maddux, and L. P. Yu, J. Am. Chem. Soc. **119,** 9079 (1997)

[3] P. J. Dandliker, F. Diederich, M. Gross, C. B. Knobler, A. Louati, and E. M. Sanford, Angew. Chem.-Int. Ed. **33,** 1739 (1994)

[4] M. Halim, J. N. G. Pillow, I. D. W. Samuel, and P. L. Burn, Adv. Mater. 11, 371 (1999)

[5] J. N. G. Pillow, M. Halim, J. M. Lupton, P. L. Burn, and I. D. W. Samuel, Macromolecules 32, 5985 (1999)

[6] J. M. Lupton, L. R. Hemingway, I. D. W. Samuel, and P. L. Burn, J. Mat. Chem. 10, 867 (2000)

[7] M. Halim, I. D. W. Samuel, J. N. G. Pillow, and P. L Burn, Synth. Met. **102**, 1113 (1999)

[8] J. Issberner, R. Moors, and F. Vogtle, Angew. Chem.-Int. Ed. **33,** 2413 (1995)

[9] L. L. Miller, R. G. Duan, D. C. Tully, and D. A. Tomalia, J. Am. Chem. Soc. **119,** 1005 (1997)

[10] J. S. Moore, Acc. Chem. Res. **30,** 402 (1997)

[11] V. V. Narayanan and G. R. Newkome, Top. Curr. Chem. **197,** 19 (1998)

[12] A. D. Schluter, Top. Cur. Chem. **197,** 165 (1998)

[13] X. T. Tao, Y. D. Zhang, T. Wada, H. Sasabe, H. Suzuki, T. Watanabe, S. Miyata, and I. P. Riken, Adv. Mater. **10,** 226 (1998)

[14] P. W. Wang, Y. J. Liu, C. Devadoss, P. Bharathi, and J. S. Moore, Adv. Mater. **8,** 237 (1996)

[15] A. Kraft, A. C. Grimsdale, and A. B. Holmes, Angew. Chem.-Int. Ed. **37,** 402 (1998)

[16] A. W. Bosman, H. M. Janssen, and E. W. Meijer, Chem. Rev. **99**, 1665 (1999)

[17] J. F. G. A. Jansen, E. M. M. DeBrabandderVandenberg, E. W. Meijer, Science **266**, 1226 (1994)

[18] W. Carl, J. Chem. Soc.-Farad. Trans. **92,** 4151 (1996)

[19] E. Y. Poliakov, V. Chernyak, S. Tretiak, and S. Mukamel, J. Chem. Phys. **110,** 8161 (1999)

[20] S. Tretiak, V. Chernyak, and S. Mukamel, J. Phys. Chem. B **102,** 3310 (1998)

[21] Z. Y. Chen and S. M. Cui, Macromolecules **29,** 7943 (1996)

[22] R. Kopelman, M. Shortreed, Z. Y. Shi, W. H. Tan. Z. F. Xu. J. S. Moore. A. BarHaim, and J. Klafter, Phys. Rev. Lett. **78,** 1239 (1997)

[23] A. BarHaim, J. Klafter, and R. Kopelman, J. Am. Chem. Soc. **119,** 6197 (1997)

[24] C. Weisbuch, H. Benisty, and R. Houdre, J. Lum. **85,** 271 (2000)

[25] T. Minami, S. Tretiak, V. Chernyak, and S. Mukamel, J. Lum. **87,** 115 (2000)

[26] S. Tretiak, W. M. Zhang, V. Chernyak, and S. Mukamel, Proc. Nat. Acad. Sci. USA **96,** 13003 (1999)

[27] G. C. Bazan, W. J. Oldham, R. J. Lachicotte, S. Tretiak, V. Chernyak, and S. Mukamel, J. Am. Chem. Soc. **120,** 9188 (1998)

[28] R. Jakubiak, Z. Bao, and L. Rothberg, Synth. Met. **114,** 61 (2000)

[29] C. Glebeler, H. Antoniadis, D. D. C. Bradley, and Y. Shirota, Appl. Phys. Lett. **72,** 2448 (1998)

[30] K. Itano, T. Tsuzuki, H. Ogawa, S. Appleyard, M. R. Willis, and Y. Shirota, IEEE Trans. Elec. Dev. **44,** 1218 (1997)

[31] Y. Kuwabara, H. Ogawa, H. Inada, N. Noma, and Y. Shirota, Adv. Mater. **6,** 677 (1994)

[32] Y. Shirota, Y. Kuwabara, H. Inada, T. Wakimoto, H. Nakada, Y. Yonemoto, S. Kawami, and K. Imai, Appl. Phys. Lett. **65,** 807 (1994)

[33] Y. Shirota, Y. Kuwabara, D. Okuda, R. Okuda, H. Ogawa, H. Inada, T. Wakimoto, H. Nakada, Y. Yonemoto, S. Kawami, and K. Imai, J. Lum. **72,** 985 (1997)

[34] M. Thelakkat, R. Fink, F. Haubner, and H. W. Schmidt, Macromol. Symp. **125,** 157 (1998)

[35] J. Bettenhausen and P. Strohriegl, Adv. Mater. 8, 507 (1996)

[36] S. C. Chang, J. Bharathan, Y. Yang, R. Helgeson, F. Wudl, M. B. Ramey, and J. R. Reynolds, Appl. Phys. Lett. **73**, 2561 (1998) ; T. Shimoda, S. Kanbe, H. Kobayashi, S. Seki, H. Kiguchi, I. Yudasaka, M. Kimura, S. Miyashita, R. H. Friend, J. H. Burroughes, and C. R. Towns, SID Proceedings, 26.3 (1999)

[37] M. G. Harrison, J. Gruner, and G. C. W. Spencer, Phys. Rev. B **55,** 7831 (1997)

[38] S. A. Jenekhe and J. A. Osaheni, Science **265,** 765 (1994)

[39] I. D. W. Samuel, G. Rumbles, and C. J. Collison, Phys. Rev. B **52,** 11573 (1995)

[40] I. D. W. Samuel, G. Rumbles, C. J. Collison, S. C. Moratti, and A. B. Holmes, Chem. Phys. **227,** 75 (1998)

[41] M. Yan, L. J. Rothberg, E. W. Kwock, and T. M. Miller, Phys. Rev. Lett. **75,** 1992 (1995)

[42] M. Yan, L. J. Rothberg, F. Papadimitrakopoulos, M. E. Galvin, and T. M. Miller, Phys. Rev. Lett. **72,** 1104 (1994)

[43] E. M. Conwell and H. A. Mizes, Phys. Rev. B **51,** 6953 (1995)

[44] E. M. Conwell, Synth. Metals **85,** 995 (1997)

[45] E. M. Conwell, Phys. Rev. B **57,** 14200 (1998)

[46] H. Bassler and B. Schweitzer, Acc. Chem. Res. **32,** 173 (1999)

[47] D. Hertel, B. Schweitzer, H. Bassler, H. Tillmann, and H. H. Horhold, Chem. Phys. **227,** 179 (1998)

[48] I. D. W. Samuel, G. Rumbles, and R. H. Friend, in : N. S. Sariciftci (Ed.), Primary Photoexcitations in Conjugated Polymers: Molecular Exciton versus Semiconductor Band Model, World Scientific (1997)

[49] K. Kondo, S. Yasuda, T. Sakaguchi, and M. Miya, J. Chem. Soc. Chem. Commun. **1**, 55 (1995)

[50] S. Mukamel, S. Tretiak, T. Wagersreiter, and V. Chernyak, Science **277,** 781 (1997)

[51] M. Pope and C. E. Swenberg, Electronic Processes in Organic Crystals, Oxford University Press (1982)

[52] T. W. Hagler, K. Pakbaz, K. F. Voss, and A. J. Heeger, Phys. Rev. B **44,** 8652 (1991) ; A. K. Sheridan, J. M. Lupton, I. D. W. Samuel, and D. D. C. Bradley, Chem. Phys. Lett. **322**, 51 (2000)

[53] J. Yu, M. Hayashi, S. H. Lin, K. K. Liang, J. H. Hsu, W. S. Fann, C.-I. Chao, K.-R. Chuang, and S.-A. Chen, Synth. Met. **82**, 159 (1996)

[54] A. N. Sobolev, V. K. Belsky, I. P. Romm, N. Yu. Chernikova, and E. N. Guryanova, Acta Cryst. C**41**, 967 (1985)

[55] G. D. Scholes, D. S. Larsen, G. R. Fleming, G. Rumbles, and P. L. Burn, Phys. Rev. B **61**, 13670 (2000)

[56] P.L. Burn, M. Halim, M., J. N. G. Pillow, I. D. W. Samuel, SPIE **3797** (1999)

[57] P. W. M. Blom, M. J. M. Dejong, and J. J. M. Vleggaar, Appl. Phys. Lett. **68,** 3308 (1996)

[58] P. E. Burrows, Z. Shen, V. Bulovic, D. M. McCarty, S. R. Forrest, J. A. Cronin, and M. E. Thompson, J. Appl. Phys. **79,** 7991 (1996)

[59] P. L. Burn, University of Oxford, personal communication (2000)

[60] D. Braun, D. Moses, C. Zhang, and A. J. Heeger. Synth. Met. **57,** 4145 (1993)

[61] T. M. Brown, J. S. Kim, R. H. Friend, F. Cacialli, R. Daik, and W. J. Feast. Appl. Phys. Lett. **75**, 1679 (1999)

[62] I. D. Parker, J. Appl. Phys. **75,** 1656 (1994)

[63] W. R. Salaneck and M. Lodglund, Polym. Adv. Technol. **9**, 419 (1998)

[64] A. Kohler, D. A. dosSantos, D. Beljonne, Z. Shuai, J. L. Bredas, A. B. Holmes, A. Kraus, K. Mullen, and R. H. Friend, Nature **392,** 903 (1998)

[65] Primary Photoexcitations in Conjugated Polymers: Molecular Exciton versus Semiconductor Band Model, N. S. Sariciftci (Ed.), World Scientific (1997)

[66] J. M. Lupton and I. D. W. Samuel, J. Phys. D **32**, 2973 (1999)

[67] J. M. Lupton and I. D. W. Samuel, Synth. Met. **112**, 381 (2000)

[68] J. M. Lupton, I. D. W. Samuel, and A. P. Monkman, Synth. Met. **102**, 1079 (1999)

[69] see, for example, http://www.cdt.co.uk

[70] M. Halim, I. D. W. Samuel, J. N. G. Pillow, A. P. Monkman, and P. L. Burn, Synth. Met. **102**, 1571 (1999)

[71] D. D. Gebler, Y. Z. Wang, J. W. Blatchford, S. W. Jessen, D. K. Fu, T. M. Swager, A. G. MacDiarmid, and A. J. Epstein, Appl. Phys. Lett. **70,** 1644 (1997)

[72] A. R. Brown, D. D. C. Bradley, J. H. Burroughes, R. H. Friend, N. C. Greenham, P. L. Burn, A. B. Holmes, and A. Kraft, Appl. Phys. Lett. **61**, 2793 (1992)

[73] C. W. Tang and S. A. Vanslyke, Appl. Phys. Lett. **51**, 913 (1987)

[74] N. J. Wang, J. K. Jenkins, V. Chernyak, and S. Mukamel, Phys. Rev. B **49,** 17079 (1994)

[75] T. Wagersreiter and S. Mukamel, J. Chem. Physics **104,** 7086 (1996)

[76] J. L. Bredas, J. Cornil, D. Beljonne, D. dosSantos, and Z. G. Shuai, Acc. Chem. Res. **32,** 267 (1999)

[77] M. Rohlfing and S. G. Louie, Phys. Rev. Lett. **82,** 1959 (1999)

[78] O. Varnavski, G. Menkir, and T. Goodson III, Wayne State University, personal communication (1999)

[79] M.J. Frampton, University of Oxford, personal communication (2000)

5.

Modelling current-voltage characteristics

5.1 Introduction

In the previous chapter of this thesis a number of novel compounds were discussed, which allow a unique microscopic control of the device properties. This chapter is concerned with developing a device model to understand the operation of LEDs as well as the observed dependence of the device characteristics on dendrimer generation. Despite the thousands of publications which have resulted from the initial reports of organic EL [1, 2], only a few have been concerned with the origin of the wide spread of device properties observed.

Besides the obvious applied interests, organic EL has opened a new chapter of condensed matter physics by demonstrating the unique characteristics of highly anisotropic quasi one-dimensional electronic systems, which, in contrast to most conventional inorganic semiconductors, rely on their amorphous and disordered nature. Despite – or because of – the rapid development of these materials and applications over the past decade there remains much to be understood about the basic physics underlying the operation of organic EL. There have recently been a number of models put forward describing the operation of polymer LEDs, based either on injection limited or space charge limited (SCL) mechanisms [3-18].

Initial studies by Parker [4] on MEH-PPV clearly correlate the device performance, current-voltage characteristics and efficiency, with the work function of the injecting contact, highlighting the importance of charge carrier injection in the description of organic LEDs. Field emission or Fowler-Nordheim (FN) tunnelling theory has found much attention as an explanation of the observed current-voltage characteristics in polymer diodes [3-4, 15-17]. There are a number of problems with models based on tunnelling: the fits are poor in the sense that they typically only follow the measured data over one order of magnitude of current density; the tunnelling theory overestimates the current density by many orders of magnitude [13, 16] which implies the presence of other processes such as image charge effects and carrier recombination; and the barrier heights determined by a FN analysis are typically smaller than values calculated from direct measurements of the built-in electric field and the offset between the metal work function and the highest occupied molecular orbital (HOMO) of the polymer [18-20].

An alternative approach to modelling devices by considering the tunnelling injection current is to assume an ohmic contact and view the low mobility of the material as the current limiting factor. Analytical models have been used successfully to describe SCL conduction in ITO/PPV/Al(Ca) LEDs [9-12, 14]. Using either an exponential distribution of traps in the material or the universal concept of a field and temperature-dependent hopping mobility in the trap free limit or a combination of both, good agreement with experiment has been found. Although capacitance-voltage measurements on MEH-PPV [21] and PPV [22] clearly demonstrate the presence of traps in polymer LEDs and the creation of a Schottky barrier with a charge carrier depletion region, the contributions of these trapping sites to the actual conduction process remains as yet unclear and appears to be linked to the variation of mobility with applied field. Conwell et al. [23] obtained equally good fits to ITO/MEH-PPV/Ca devices considering both the trap-free and the trap-filled limits.

It has recently been shown [6] that the current-voltage characteristics of ITO/MEH-PPV/Al LEDs can be described by a model, which considers single carrier transport (hole polaron only). The model combines the injection processes of the tunnelling, thermionic emission and the interface recombination currents [5] with the bulk transport through the diode. Although the authors demonstrate that the injection terms in their model adapt well to varying work functions [7] of different injecting electrodes, the temperature dependence has not been considered [8] and comparison with data is only at room temperature.

A suitable way to test the device model is to vary one device parameter and examine its effect on device operation and the parameters fitted to the measured characteristics. Two tests of the model are applied here, by examining the temperature dependence of device characteristics and by degrading the device by photo-oxidation. The temperature dependence provides a powerful test of the validity of the model as both injection and transport of charge carriers depend strongly but differently on temperature. The results of the study allow an analysis of the physical significance of the different components in the model, namely the tunnelling currents, the thermionic emission currents and the field-dependent variable range hopping mobility. They also yield valuable information on the variation of the mobility of the majority charge carriers with temperature, which

in turn gives important information on the morphology of the sample through the disorder parameters.

Initially, some qualitative observations relating to the behaviour of the device with temperature are presented. The inadequacy of the tunnelling approach is then demonstrated by considering the temperature dependence of the device current-voltage characteristics and the effects of device ageing and accidental doping. The results of the device model, which was outlined in chapter 2, are then presented and fits to current-voltage characteristics are shown giving fitting parameters in dependence of temperature. New data on photo-oxidation as a test of the device model is then discussed, which demonstrate the significance of bulk transport effects in LEDs with non-ohmic contacts. A final test of the model is the thickness dependence of devices. In a detailed discussion the benefits of the model are examined, the results are compared to literature values and the model is contrasted to recent results from Monte Carlo simulations.

5.2 Transport versus injection models

In the following section a number of qualitative observations relating to device characteristics are made. The effect of temperature is examined as well as the short-comings of tunnelling models. The effect of device degradation on current-voltage characteristics in form of photo-oxidation and ageing is demonstrated and it is shown that a modification of the device characteristics resulting from accidental doping is well described by a Poole-Frenkel emission formalism.

5.2.1 Temperature dependence

The effect of temperature is investigated by measuring the current-voltage characteristics of an LED at different temperatures and considering the variation of current with temperature at a constant applied bias. Fig. 5.1 shows the variation of current density of a 165 nm thick LED with temperature between 13 K and 300 K for forward biases of 10 and 20 V. The current is strongly temperature-dependent at both voltages and decreases with decreasing temperature. Light emission was observed from

the device and the turn-on bias for EL increased from 10 V to 20 V as the device was cooled from 300 K to 13 K. The temperature dependence is non-Arrhenius below about 160 K. Above 160 K the activation energy is approx. 50 meV.

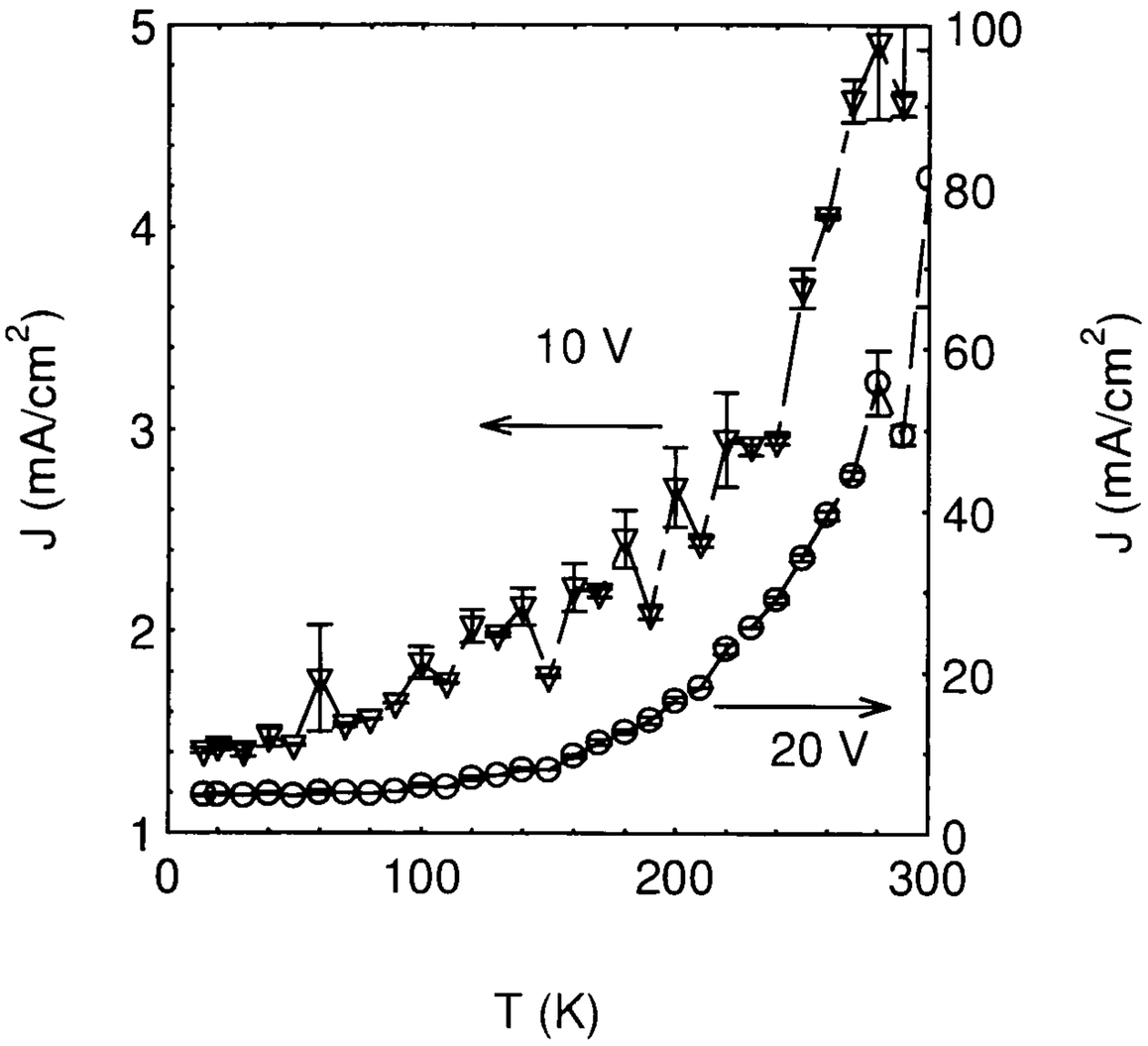

Fig. 5.1. *Measured variation of current density with temperature for an LED at 10 V and at 20 V.*

The FN theory is widely used to analyse current-voltage characteristics in terms of the barrier to injection for majority charge carriers although its shortcomings have been discussed at length in the literature [23]. Here new data is presented illustrating a further problem before going on to a fuller analysis of the operation of devices later on. This problem relates to a strong temperature dependence of the FN barrier height. Following Parker [4], the logarithm of J/E^2 is proportional to the inverse of the field, which allows the determination of the barrier height:

$$J = C \times E^2 \times e^{-\frac{\kappa}{E}} \tag{5.1}$$

$$C = \frac{3e^2}{8\pi h\varphi} \tag{5.2}$$

$$\kappa = \frac{8\pi\sqrt{2em}}{3h}\varphi^{\frac{3}{2}} \tag{5.3}$$

where e is the modulus of the electron charge, h Planck's constant, m the effective mass of the hole polaron which is taken to be the electron mass and φ the barrier height to injection in eV.

The current-voltage characteristics of LEDs were measured at a range of temperatures. Data measured at 20 K and 280 K are shown in Fig. 5.2 in a FN plot, together with a straight line fit. The plots are curved showing that the tunnelling expression at best only holds at high fields but the quality of the fit appears to improve at lower temperatures. Also, the current density calculated by (5.1) is 7 orders of magnitude too high, which is in itself evidence that tunnelling is not the only process involved in charge carrier injection. An estimate of the barrier height can be obtained by approximating the high field values by a straight line as done by Parker.

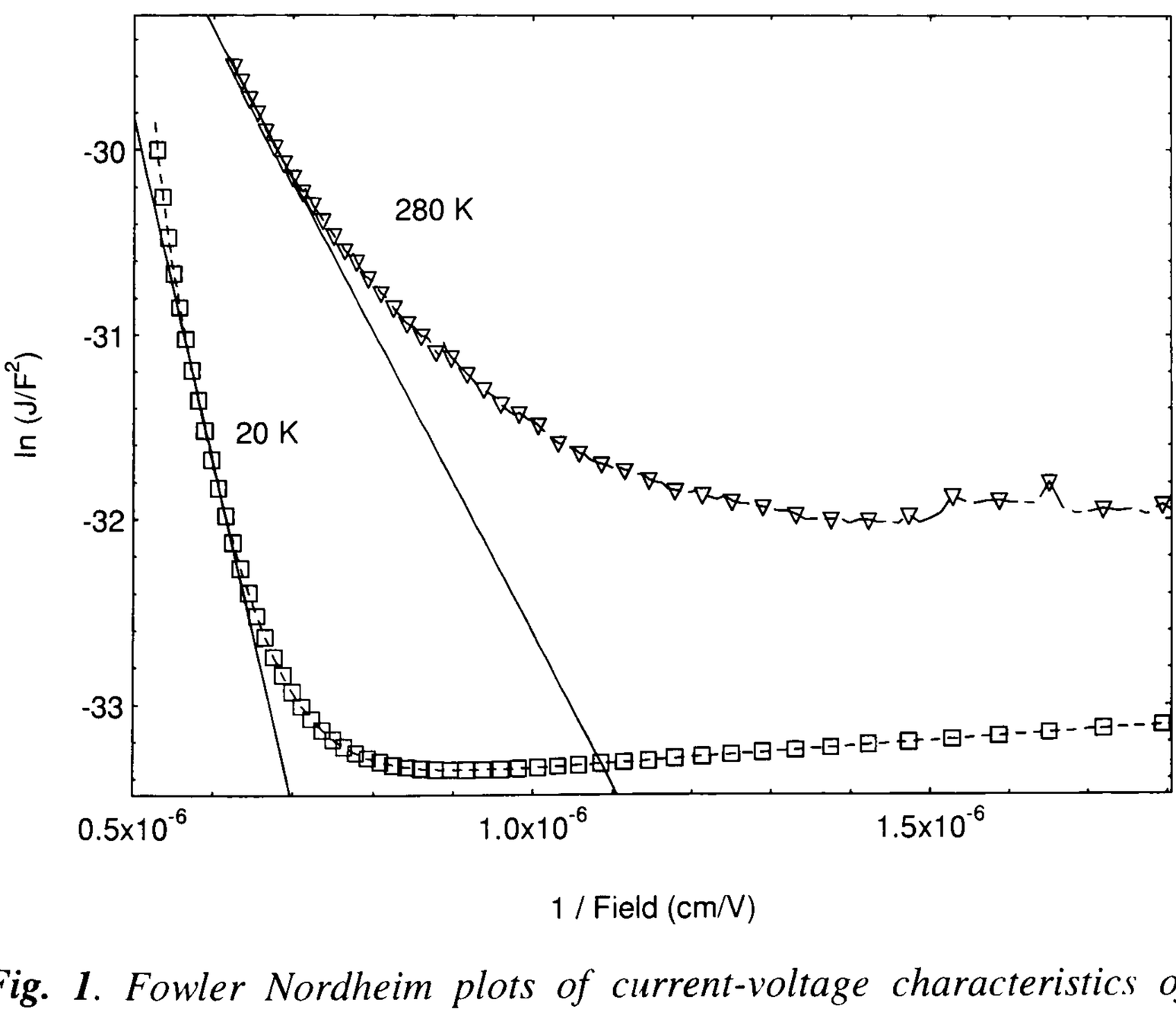

Fig. 1. *Fowler Nordheim plots of current-voltage characteristics of a single layer MEH-PPV LED with ITO and aluminium electrodes at 280 K and 20 K.*

The best fits of a straight line to the FN plots are obtained at each temperature. The resulting tunnelling barrier heights, which are related to the slope of the straight line by equation (5.3), are plotted in Fig. 5.3 as a function of temperature. It is found that the barrier height varies significantly with temperature, changing from 0.2 eV at room

temperature, corresponding to the value found by Parker, to 0.45 eV at 13 K. The apparent increase of barrier height at low temperature indicates that tunnelling is not actually the current-limiting process. The temperature dependence of the barrier height suggests a contribution from thermionic emission between 200 K and 300 K, where the variation is strongest.

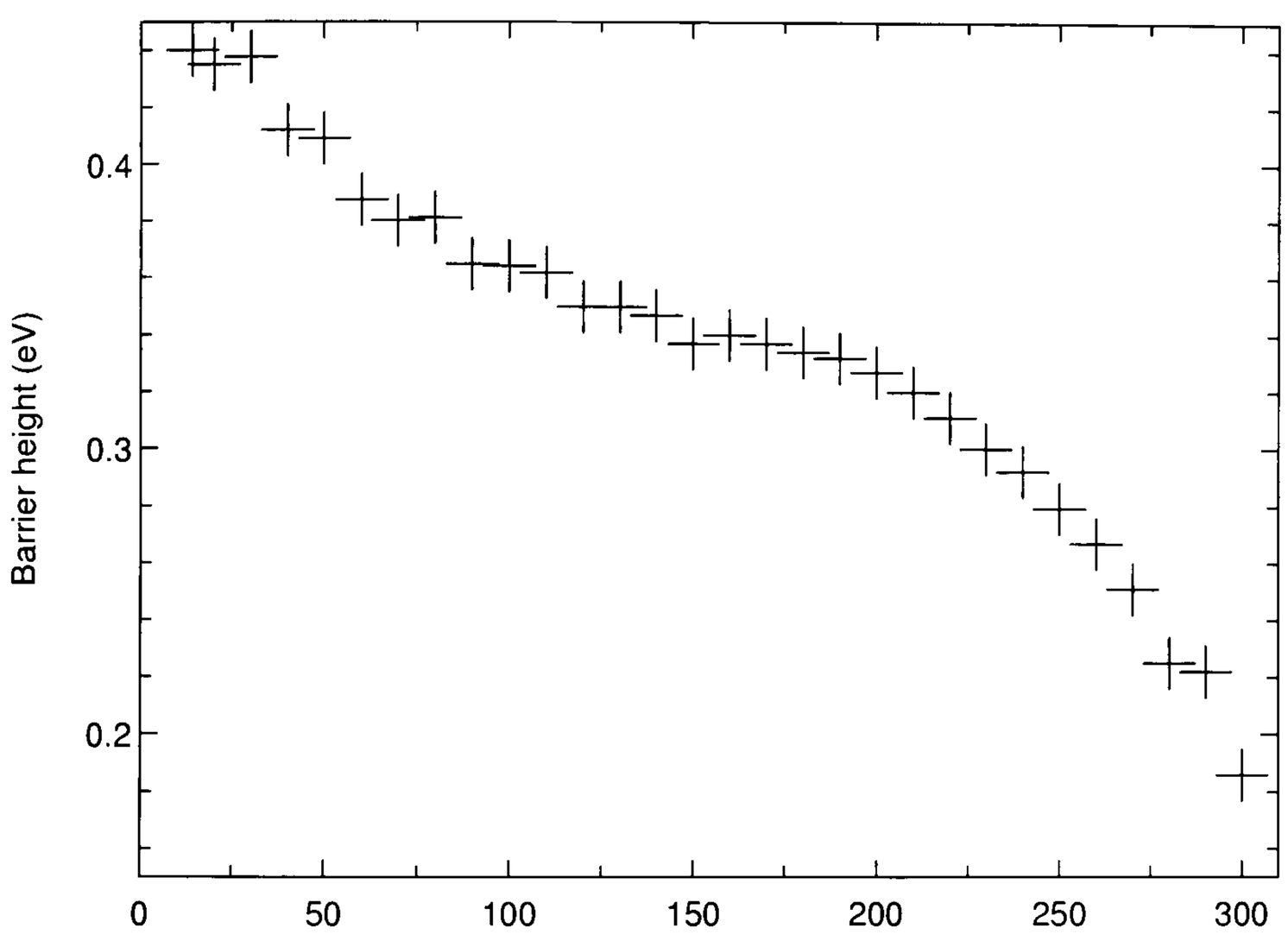

***Fig. 5.3**. Plot of FN barrier height against temperature.*

The variation in barrier height deduced from the FN analysis is significantly larger than any shift in the band structure of the material with temperature and is far greater than the small temperature dependence deduced from a rigorous treatment of the tunnelling formalism [17]. The measured barrier appears to increase with decreasing temperature, which is contrary to what one would expect from a narrowing, red shifted, band gap. The variation of the FN barrier height in PPV samples has been pointed out before [9] and demonstrates that values obtained for the barrier height by the FN analysis are essentially meaningless. However, no detailed study of the intriguing functional dependence of the FN barrier height on temperature has yet been made. The value of 0.45 eV for the barrier height found at 13 K for the fresh sample is in the range of the value expected for the actual barrier height to injection as obtained from photoemission

measurements of the built-in electric field [18] (c. 0.6 eV [6]) considering a reduction in band gap at low temperatures in the order of 0.1 eV.

5.2.2 Bulk effects in device operation

Previous workers have reported the dependence of the current density in a device of the configuration ITO/MEH-PPV/Al on the electric field rather than the applied bias [4]. Parker and subsequent investigators have concluded that for these systems the current is limited by the barrier to hole injection and hence by charge carriers tunnelling through this barrier [4, 16]. It is demonstrated in the following section that although the barriers to injection are crucial in determining the current through the device and the contacts in these devices are not ohmic, bulk transport effects due to the low mobility of the polymer do play a significant role in limiting the current through the device. This is seen clearly by modifying the charge carrier mobility but keeping the barrier height effectively constant [24-26] and exploiting the process of photo-oxidation [27].

Fig. 5.4 shows the current-voltage curves of two identical samples, one fresh and the other stored in air for 4 weeks. The turn-on voltage of the aged sample is found to increase significantly with respect to the fresh sample.

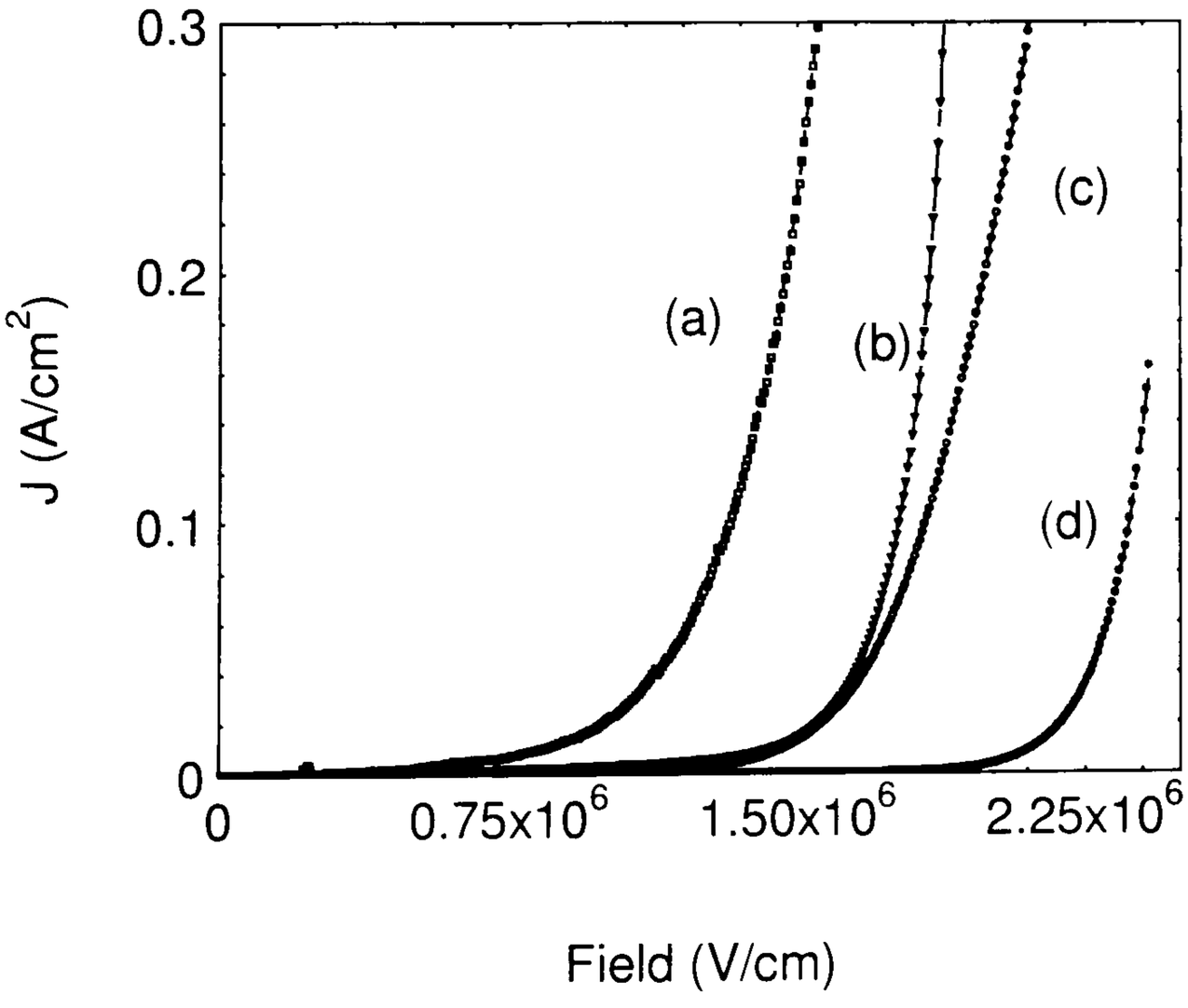

Fig. 5.4. *Difference between current-voltage characteristics of a fresh and aged sample. (a) fresh at 200 K, (b) fresh at 20 K, (c) aged at 200 K, (d) aged at 20 K.*

A similar observation is made in Fig. 5.5 upon exposure of an LED to UV light generated from a Nd:YAG laser in air. The sample was illuminated over an area of 5 mm^2 which covered the entire pixel. Four curves are seen, measured before degradation, after a short exposure to the laser (pulsed at 10 Hz at 355 nm) at low power density (0.1 mJ pulses for 10 seconds) and after a longer exposure at higher power density (1 mJ pulses for 5 minutes). For these exposures the resistance of the sample at higher fields is found to increase after exposure. An increase in the hysteresis upon switching from forward to reverse bias is also observed (not shown) after photo-oxidation as well as an increase in noise (spikes) on the current measurement. It is believed that both effects may be due to the presence of mobile ions resulting from the oxidation process. The noise is reduced in consecutive current-voltage sweeps (curve (d)) and the degradation appears to reach a saturation value above which further exposure does not contribute to a further increase in resistance as the curves (b) and (d) are essentially identical. These observations are inconsistent with FN theory but can be understood to arise from a reduction in mobility, as will be discussed later on. For the exposure conditions employed here the reduction of mobility dominates any possible doping effects, which would lower the effective resistance rather than increasing it.

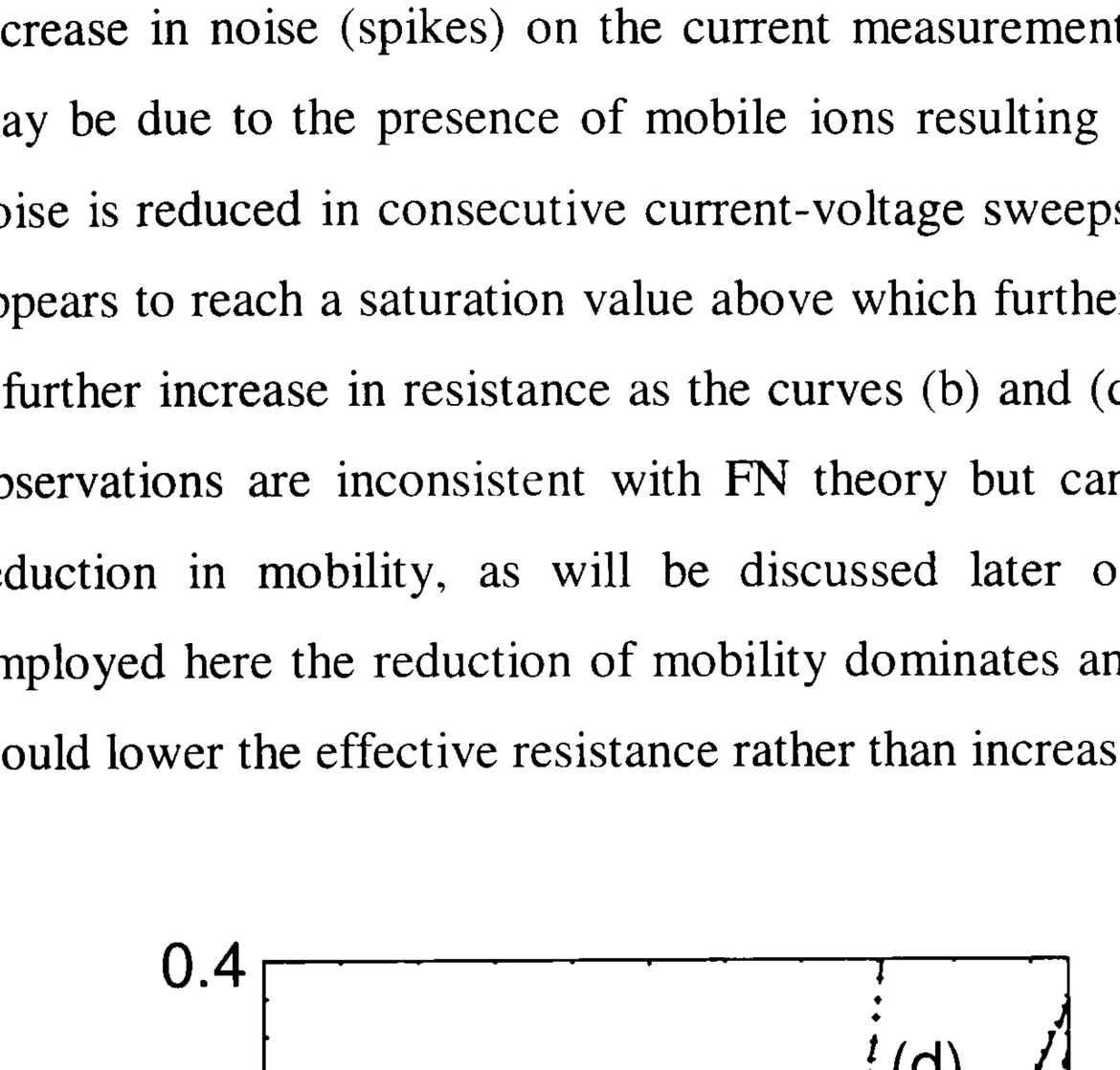

Fig. 5.5. *Effect of photo-oxidation of an LED by laser light on current-voltage characteristics. (a) fresh sample, (b) after 10 s exposure, second measurement, (c) after 5 min. exposure, first measurement, (d) after 5 min. exposure, second measurement.*

A further remarkable consequence of device ageing is shown in Fig. 5.6, where the FN barrier heights of the aged sample discussed in Fig. 5.4 are plotted as a function of temperature. The temperature dependence of this device is entirely different to that of the fresh device seen in Fig. 5.3. The barrier height is again close to 0.2 eV at room temperature, however, it increases rapidly up to 0.65 eV at 13 K. As mentioned above, the increase in barrier height with decreasing temperature is unphysical – the opposite would be expected due to the reduction of the band gap resulting from steric relaxations. There is no apparent physical reason why the aged device should exhibit a more rapid change in barrier height with temperature than the fresh device, and also why there should be such a large difference in barrier height between the two samples at low temperatures but not at room temperatures. If the oxidation process did result in a change in the barrier height and the FN analysis provided an accurate and correct insight into the device properties, the difference between the barrier height of fresh and aged samples should be manifest at all temperatures. This is not the case. It is hence concluded that there are significant further effects, resulting from the presence of space charges and dopants in the device, which render the FN analysis inapplicable.

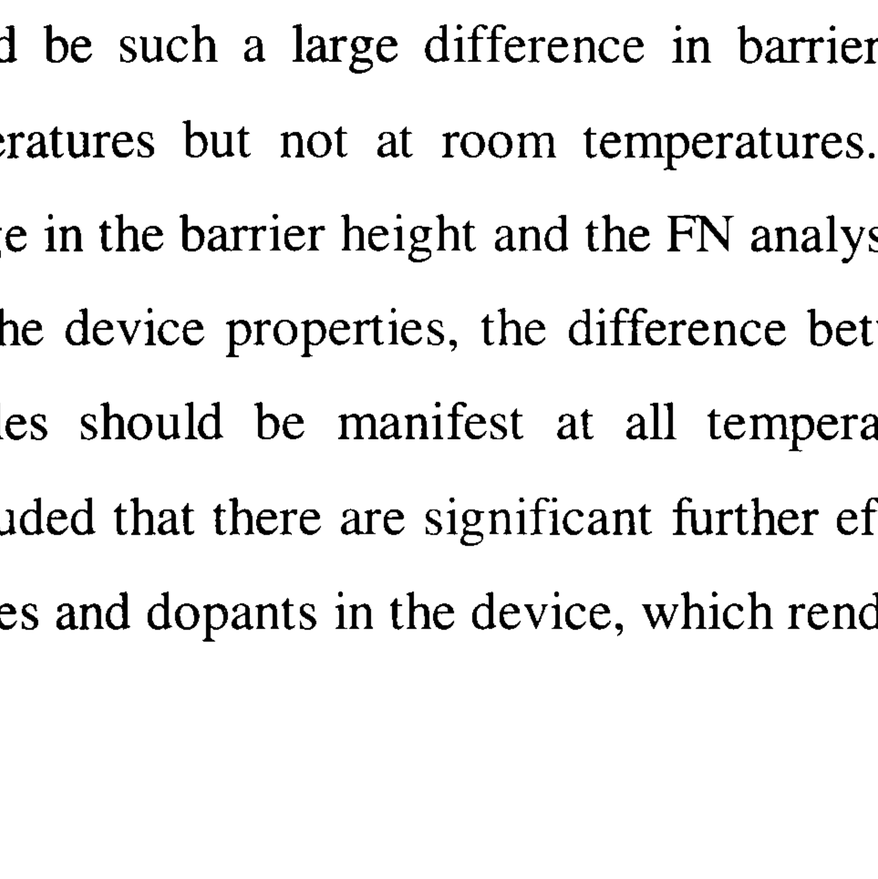

Fig. 5.6. *Temperature dependence of the FN barrier height of a device stored in air for 4 weeks.*

5.2.3 Poole-Frenkel effect

Two experimental results suggest contributions from extrinsic carriers to the device characteristics: symmetric current-voltage characteristics and the change of characteristics upon evacuation. In this subsection a solution is presented to deal with this issue using the concept of Poole-Frenkel emission.

The device model based on the injection of charge carriers into hole polaron levels predicts a strong asymmetry between forward and reverse bias current due to the difference in work function between ITO and aluminium. The experimental results demonstrate, however, that the current is actually symmetric in low forward and reverse biases, as is shown in Fig. 5.7 for a 165 nm LED at 20 K and 200 K. This divergence from pure band injection and conduction is attributed to injection into midgap impurity states, which is qualitatively well described by Poole-Frenkel emission.

The influence of impurities in organic LEDs has been pointed out frequently, in particular the contaminants introduced by the ITO substrate [22, 28-29] and through exposure to air [30]. The current through the device at low forward biases was found to increase by orders of magnitude after application of a reverse bias suggesting that field induced ionic migration of impurities from the ITO electrode into the polymer takes place at reverse biases and modifies the low bias injection characteristics. Ideally, LEDs should be prepared and tested in an inert atmosphere, but this is clearly neither very practical nor close to regular applications. The samples used here were exposed to air during the fabrication process, which leads to a certain degree of p-type doping. The measurements used by Davids et al. to test their device model were performed in an inert atmosphere, whereas the present measurements were conducted under vacuum. The present device characteristics were found to vary with the pressure in the sample chamber, as has been reported by Cumpston et al [30].

The reverse bias characteristics of organic LEDs frequently appear to be inconsistent with the approximation of a rigid barrier to injection and conduction in polaron levels. This issue has been addressed by Davids et al. [31] by considering the sub-gap bipolaron levels to explain capacitance-voltage measurements. For a simplified qualitative treatment discrete energy levels due to the presence of ionic impurities are

considered [29]. As the majority carriers in the device are holes, it is concluded that upon reversal of the bias holes are injected from the aluminium electrode rather than electrons from the ITO. However, the difference in work function between ITO and aluminium is clearly manifest at high biases beyond turn-on, as the diode is indeed rectifying at high biases. This implies that the low bias current is not due to charge carriers being injected into the polaron conduction band but is most likely due to transport through impurity levels in the material, which are spread between the two Schottky junctions. The experimental observations are qualitatively well described by the Poole-Frenkel injection [32] mechanism, which has previously been used to describe some of the transport phenomena observed in PPV oligomers [33] and has the form (5.4):

$$J \propto V \exp\left(2\sqrt{\frac{e}{4\pi\varepsilon d}} \frac{\sqrt{|V|}}{T} - \frac{e\phi_{PF}}{kT} \right) = Va \exp(b\sqrt{|V|}) \qquad (5.4)$$

where d is the thickness of the insulator and ϕ_{PF} is the offset of the dopant site from the valence band, V is the applied bias and a and b are constants. Equation (5.4) is used here to explain the reverse bias characteristics and qualitatively deal with the doping effects of impurities. Fig. 5.7 shows the forward and reverse bias characteristics of a 165 nm LED at 20 K and 200 K with a fit of the Poole-Frenkel expression (using parameters $a=1.5\times10^{-4}$ and b=0.0169 at 20 K and $a=5.13\times10^{-5}$ and b=0.1 at 200 K). The fit accurately describes the transition from forward to reverse bias. In this first approximation only one localised impurity level is assumed. However, there is most probably an energetic and spatial [28] spread in these impurity states which would need to be taken into account to give a complete quantitative temperature-dependent analysis of the doping using the Poole-Frenkel emission.

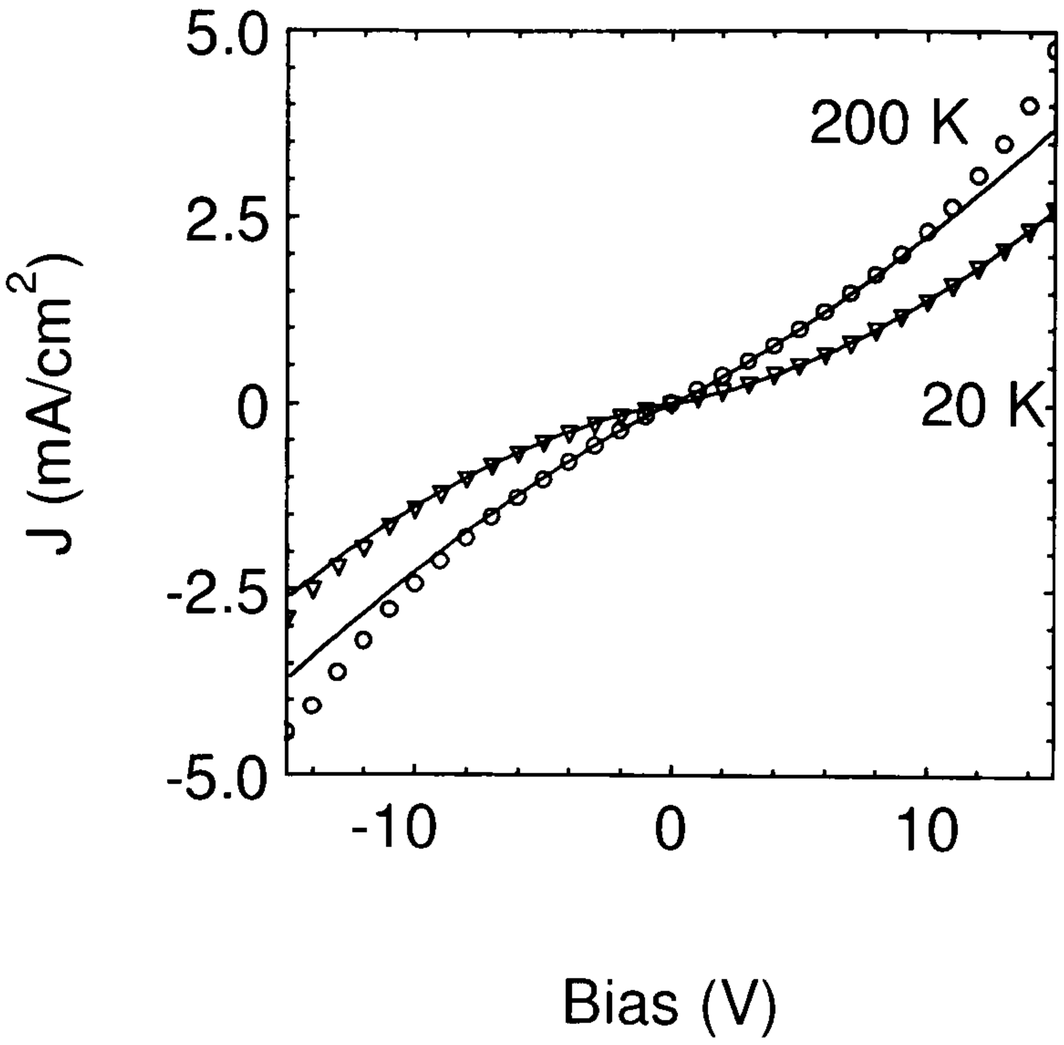

Fig. 5.7. *Fit of the equation of the Poole-Frenkel injection mechanism (solid line) to the low bias region of the measured current-voltage characteristics (dots) of an LED under vacuum at 200 K and 20 K.*

The conduction processes predicted by the band model can now be isolated from the measured data by simply subtracting the contribution of the dopant current (due to Poole-Frenkel emission). An unambiguous fit of the doping expression is obtained by taking the reverse bias characteristics in the low bias region into account. Fig. 5.8 shows the current-voltage characteristics of a sample measured in air (a) and then in vacuum (b) after repeated forward and reverse bias cycling. The functional shape of the current of the sample measured in air is very much like a typical calculation from the model (see next section), although for a given bias the overall current is actually greater, i.e. the electrical resistance is lowered during operation in air. This is a universal effect seen in many different systems such as polymer field effect transistors [34] and is attributed to a greatly increased number of free charge carriers in an oxygen-saturated film. Upon evacuation, the shape changes dramatically and the low bias current rises by many orders of magnitude whereas the high bias current appears to decrease. At present it is not yet fully understood why a rise in the low bias current is observed upon evacuation. The fourth curve (d) in Fig. 5.8 shows the measured current in vacuum with the Poole-Frenkel contribution (curve (c)) subtracted, the contribution having been obtained by fitting to the low bias current region ($a=2.08\times10^{-4}$ and $b=0.0287$ for the sample under vacuum, curve (c)). The functional form characteristic of injection through a rigid

barrier and subsequent hopping transport is restored. The temperature dependence of the b-parameter used here is found to be too weak to be a clear signature of Poole-Frenkel type emission. However, this type of approach gives an excellent qualitative treatment of the forward-reverse bias symmetry and improves the quantitative treatment of the data with the full device model.

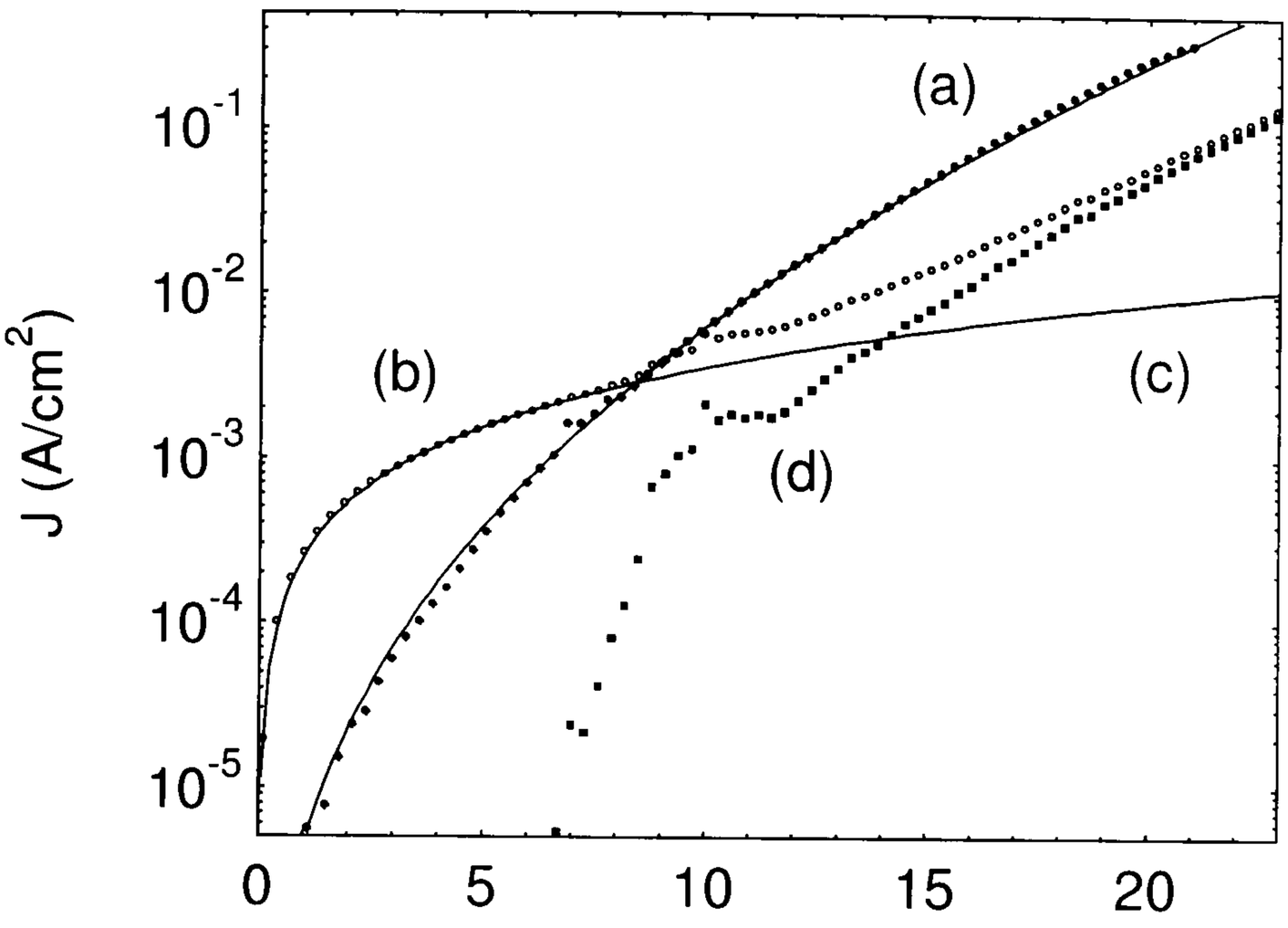

Fig. 5.8. *Effect of doping and Poole-Frenkel type emission on the current-voltage characteristics before and after evacuation of the sample chamber. (a) sample in air, (b) sample under vacuum, (c) Poole-Frenkel injection fit to the low bias region of the sample in vacuum, (d) curve (c) subtracted from curve (b).*

5.3 Device model

5.3.1 Effect of barrier height

In order to test the device model presented in chapter 2, a comparison with calculations found in the literature is made. The current density as a function of applied bias for a 120 nm MEH-PPV sample at 295 K with [6] $n_0=10^{-21}$ cm^{-3} and $\varepsilon=3\varepsilon_0$ is calculated for varying barriers to hole injection, as shown in Fig. 5.9 and previously reported in Ref. [6]. The results are essentially identical to the calculations published by Davids et al. [6], except for a small deviation in the low barrier low bias regime, where diffusion effects, which are not included in the present model, may play a more important role. As

the barrier height is lowered, the current at a given bias increases. Below a barrier height of 0.3 eV the calculated current becomes less sensitive to the barrier height and becomes essentially independent of injection as the barrier is lowered further. This feature has been interpreted [6] as the gradual transition from injection limited to space charge limited behaviour. For low injection barriers the current in the device is limited by the current drift, which is governed by the hopping mobility. For large barrier heights the current is limited by the injection process, which is very sensitive to the energy level offset. The important conclusion of this observation is that there is no rigid transition from the injection to the space charge limited case, and that both processes play a role in the operation of most devices.

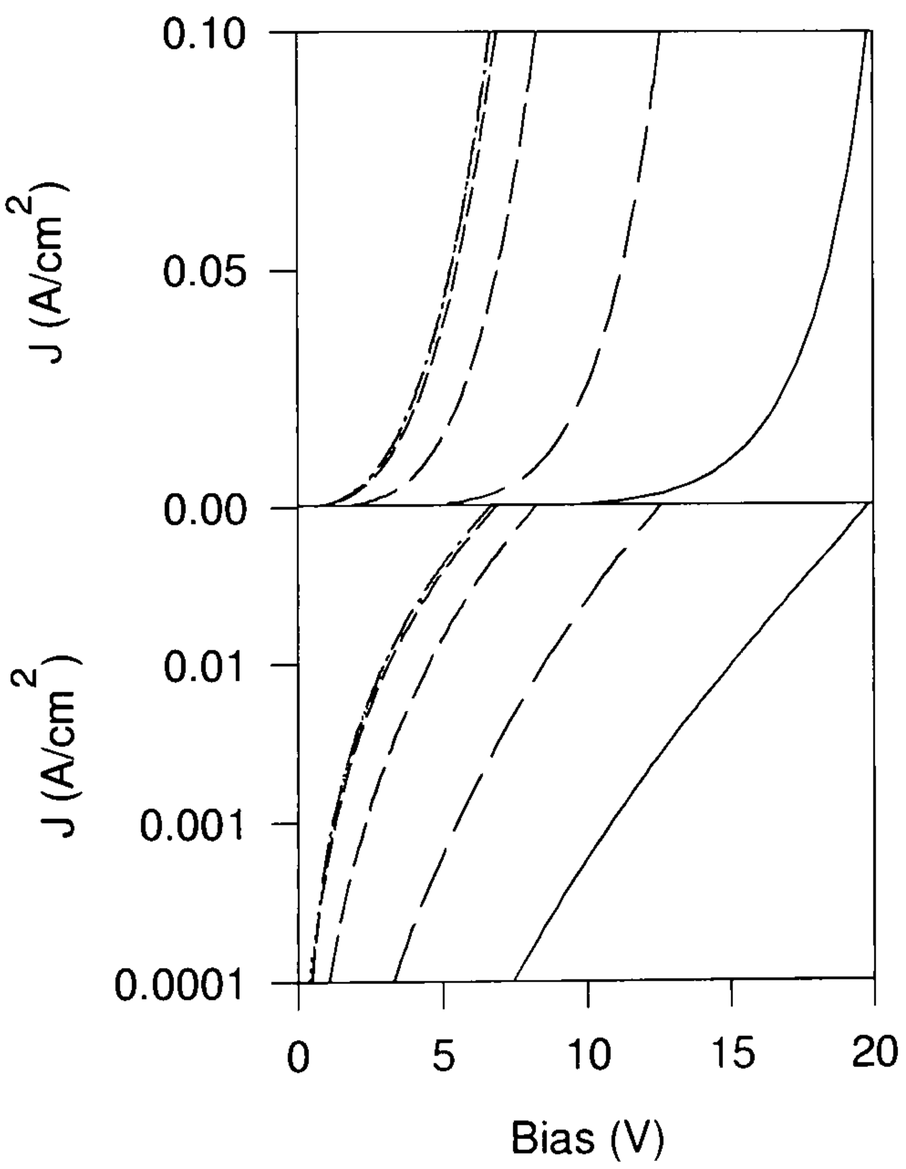

Fig. 5.9. *Variation of calculated current density with barrier height for barriers to hole injection of 0.6, 0.5, 0.4, 0.3, 0.2 and 0.15 eV (curves from right to left) using* $\mu_{(E=0)}=1.7\times10^{-6}$ *cm*^{2}*/Vs and* $E_0=1\times10^5$ *V/cm at 295 K. The upper panel shows the calculations on a linear scale, the lower panel on a logarithmic scale. The calculations for 0.2 eV and 0.15 eV are almost identical and cannot be distinguished here.*

5.3.2 Mobility values deduced from current-voltage characteristics

Next, the three fitting parameters, the barrier height φ and the mobility parameters μ_0 and E_0 are deduced from the current-voltage characteristics. All measured current-voltage curves are treated for the impurity conduction current by subtracting the Poole-Frenkel contribution. This has no effect on the high bias current above turn-on, but does provide a much better fit at low currents. Fitting is performed by choosing a suitable range of fitting parameters and varying the E_0, $\mu_{(E=0)}$ and barrier parameters. The least squares error is calculated for a fit both on the linear and logarithmic scale. As the barrier height changes, a clear variation in the error of the best fit of the mobility parameters is observed giving an unambiguous set of fitting parameters.

Fig. 5.10 shows fits to curves measured at 280 K, 200 K and 100 K. The fits are qualitatively good, as seen on the linear scale (upper panel), however a deviation is seen on the logarithmic scale (lower panel) for low temperatures and low fields.

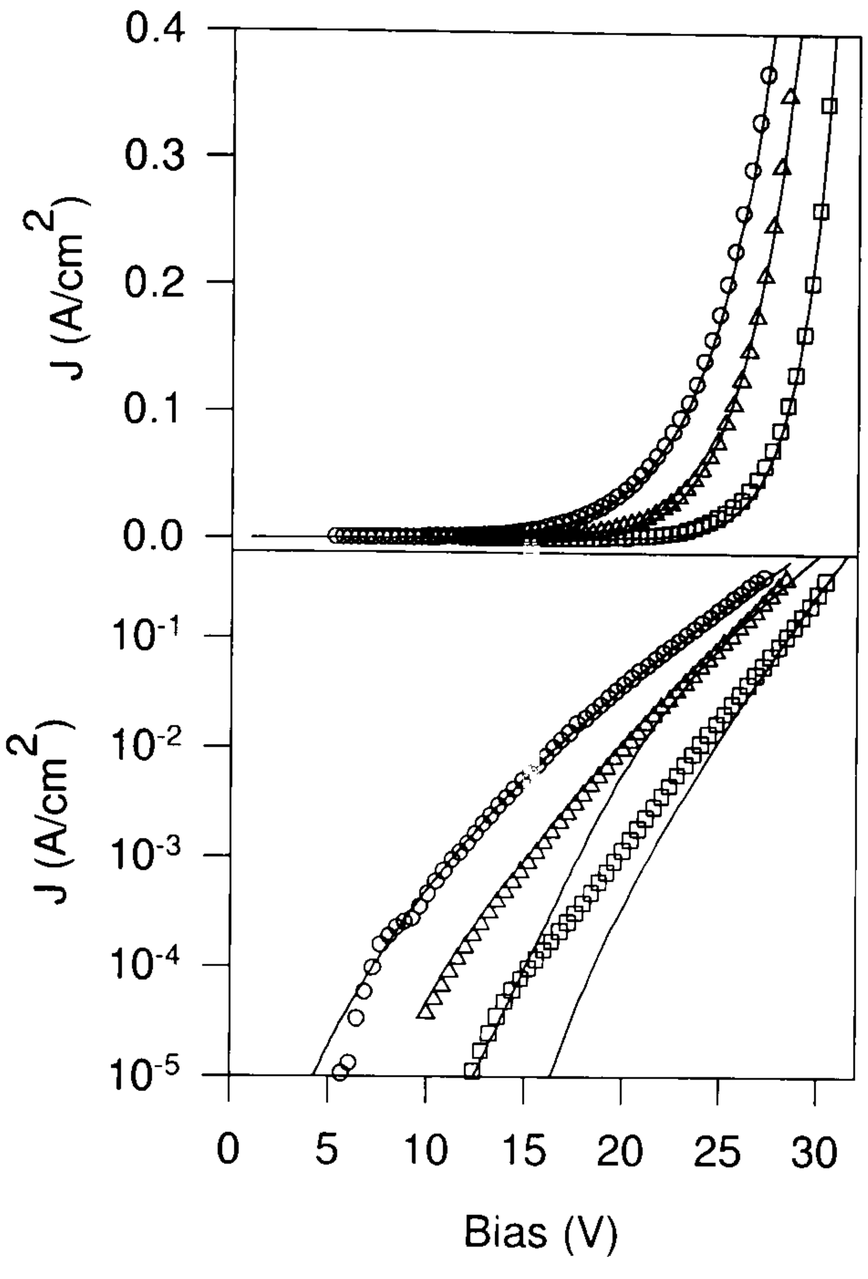

Fig. 5.10. *Calculated and measured current density as a function of bias at 280 K (○), 200 K (△) and 100 K (□) on a linear (upper panel) and logarithmic (lower panel) scale, using parameters T=280: {φ=0.54 eV, $\mu_{(E=0)}=3.9\times10^{-6}$ cm^2/Vs, $E_0=1.9\times10^5$ V/cm}, T=200: {φ=0.44 eV, $\mu_{(E=0)}=6.7\times10^{-12}$ cm^2/Vs, $E_0=7.3\times10^3$ V/cm} and T=100: {φ=0.41 eV, $\mu_{(E=0)}=1.1\times10^{18}$ cm^2/Vs, $E_0=1.9\times10^3$ V/cm}.*

The variation of the $\mu_{(E=0)}$ parameter with temperature is shown in the upper panel of Fig. 5.11. It is found to vary exponentially with inverse temperature and decreases by 12 orders of magnitude between 300 K and 140 K corresponding to the characteristics of hopping transport described by equation (5.5).

$$\mu_{(E=0)} = \mu_0 \exp(-\frac{\Delta}{k_B T}) \qquad (5.5)$$

The variation of the E_0 parameter is shown in the lower panel of Fig. 5.11. The field dependence parameter also decreases strongly with decreasing temperature.

corresponding to an increase in the exponential field dependence at low temperatures. The variation matches well the predictions of the hopping transport as described in equation (5.6) down to 140 K, below which the data appear to diverge from the predicted straight-line relationship.

$$\frac{1}{\sqrt{E_0}} = B\left(\frac{1}{k_B T} - \frac{1}{k_B T_0}\right) \tag{5.6}$$

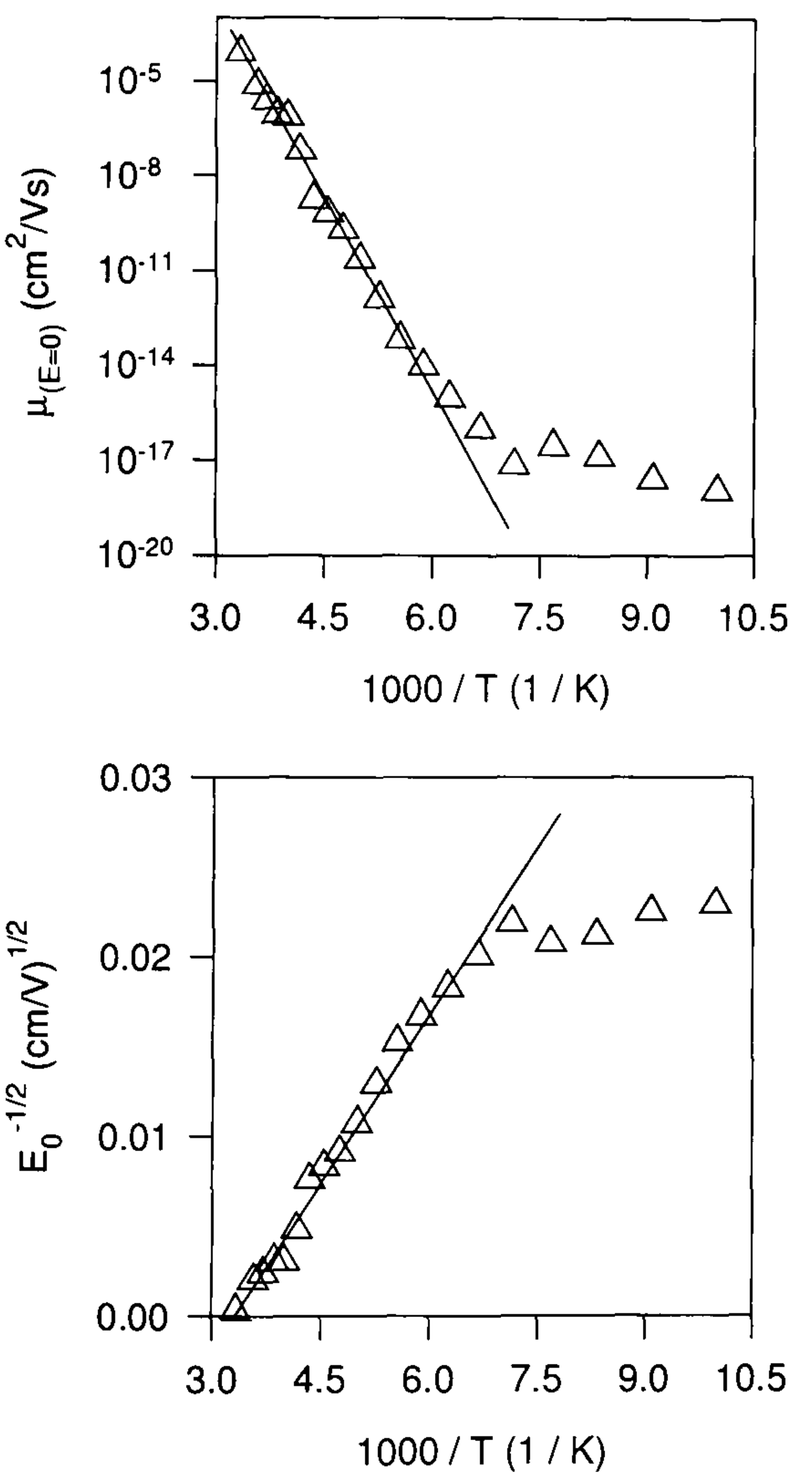

Fig. 5.11*. Arrhenius plot of (a) $\mu_{(E=0)}$ parameter and (b) $E_0^{-1/2}$ parameter from 300 K to 100 K.*

The mobility fitting parameters are shown in summary in Table 5.1 in comparison with the parameters obtained for dialkoxy PPV [10, 11] and recent space charge limited current measurements on MEH-PPV devices [35].

Parameter	PPV [10,11] SCLC	MEH-PPV from p-xylene [35], space charge limited current	MEH-PPV from chlorobenzene. present injection model
Δ / eV	0.59 ; 0.48	0.38±0.02	0.75
μ_0 /cm^2/Vs	1.7×10^3 ; 35	0.15 (interpolated from data	1.5×10^8
T_0 / K	540 ; 520-600	600±90	300
B / eV(cm/V)$^{1/2}$	3.1×10^{-4} ; 2.9×10^{-4}	$2.3\pm0.2\times10^{-4}$	5.5×10^{-4}

Table 5.1. *Comparison of the mobility parameters obtained for MEH-PPV and PPV.*

The activation energy Δ and the μ_0 parameter are found to be larger for the MEH-PPV devices here than for those reported elsewhere. The parameters governing the field dependence of the mobility are smaller in MEH-PPV than in PPV, corresponding to a stronger field dependence in MEH-PPV. This results in the T_0 parameter being smaller in MEH-PPV and the B parameter being larger in comparison to PPV. The decrease of the barrier to injection with temperature as resulting from the fit of the model to the data is shown in Fig. 5.12. It appears to decrease linearly by 0.1 eV down to 220 K.

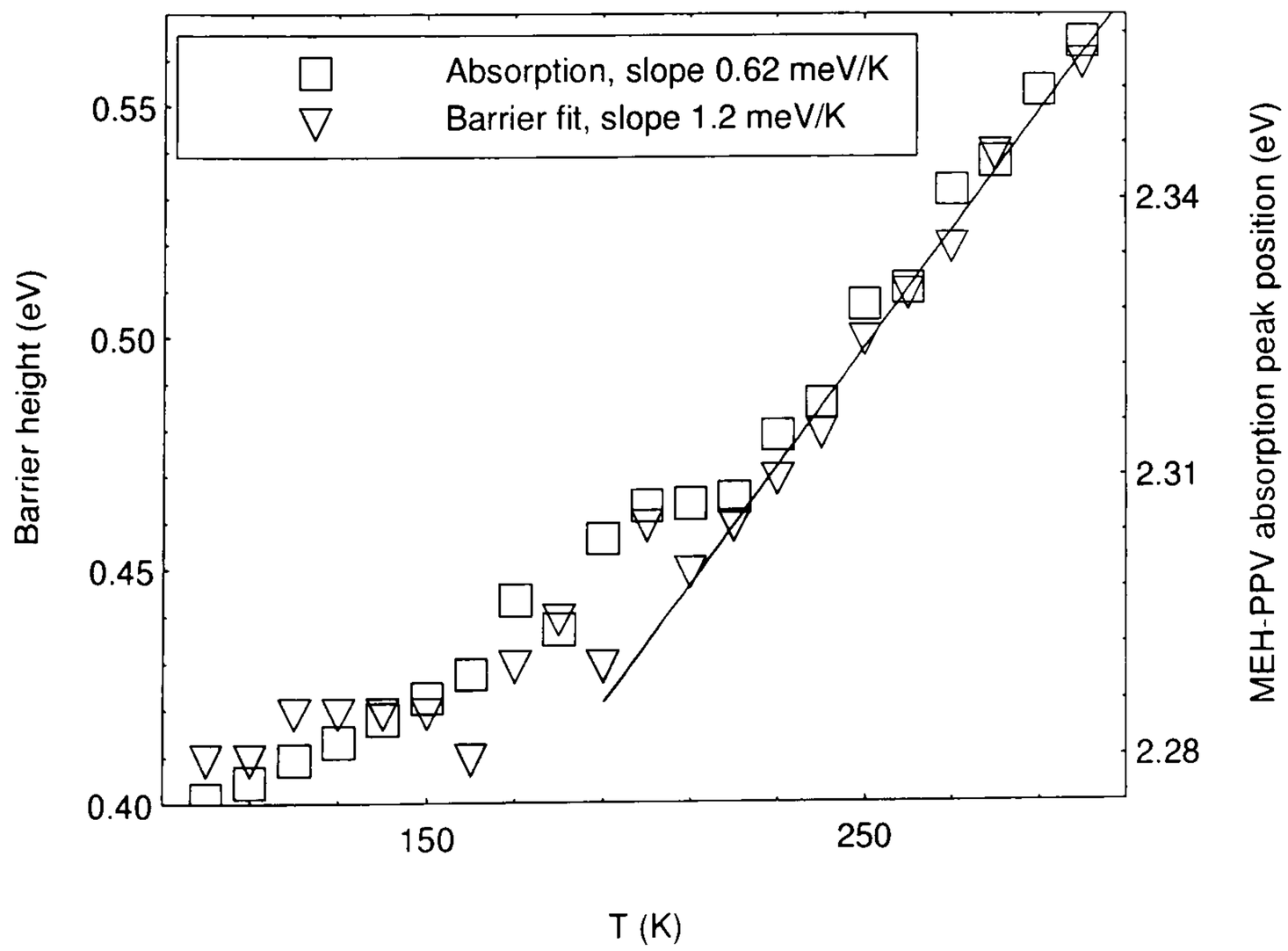

Fig. 5.12. *Decrease of barrier height with temperature compared to the red shift of the absorption of MEH-PPV.*

Also shown in Fig. 5.12 is the decrease in energy of the absorption band of MEH-PPV films spun from chlorobenzene. The absorption spectra were measured as a function of temperature and then fitted using a commercial peak-fitting package (Jandel Peak Fit). A superposition of five asymmetric weighted Gaussians of the form (5.7) with constant asymmetry and width, each separated by approx. 0.18 eV, was used.

$$y(E) = a\exp\left\{-\frac{\ln(2)\ln\left[\frac{(E-b)(c^2-1)}{dc}+1\right]^2}{\ln(c)^2}\right\} \tag{5.7}$$

Here, a is the amplitude, b defines the shape of the peak (i. e. the degree of asymmetry), c is the centre, d is the width of the peak and E is the photon energy. Gaussians with a slight degree of asymmetry have previously been used in the literature to fit to film absorption spectra, which deviate from pure Gaussian or Lorentzian line-shapes due to conformational effects in films and the distribution of conjugation lengths probed by absorption measurements [36, 37].

As is seen in Fig. 5.12, the calculated barrier height and the change of the polymer band gap with temperature are in remarkable agreement. Both decrease linearly down to approx. 200 K and then flatten out. However, the barrier height decreases at twice the rate of the energy of the first absorption band, whereas the opposite would be expected. Assuming an intrinsic semiconductor and charge conjugation symmetry, one would expect a change in band gap to lower the LUMO level an equal amount to raising the HOMO level, hence reducing the barrier to hole injection. It would hence be expected that the reduction in barrier height due to the change in band gap is roughly half the temperature induced change in band gap.

5.3.3 Effect of photo-oxidation

A further test of the model is to establish whether it can account for the effects of photo-oxidation demonstrated above. In the scope of the model presented here, the decrease in current at a given voltage can simply be expressed in terms of a decrease in the hopping

mobility due to the appearance of hole traps and the breaking of conjugation. Fits of the model to data from a fresh and oxidised device at 290 K are shown in Fig. 5.13 using the parameters {φ=0.55 eV, $\mu_{(E=0)}$=6.9×10^{-6} cm^2/Vs, E_0=2.3×10^5 V/cm} for the fresh sample and {φ=0.55 eV, $\mu_{(E=0)}$=2.5×10^{-7} cm^2/Vs, E_0=1.0×10^5 V/cm} for the oxidised sample. With no presupposition of a modification of parameters the model gives a drastic reduction of charge carrier mobility by more than an order of magnitude with no apparent variation in barrier height or the requirement to introduce extrinsic carriers by a doping term in the model.

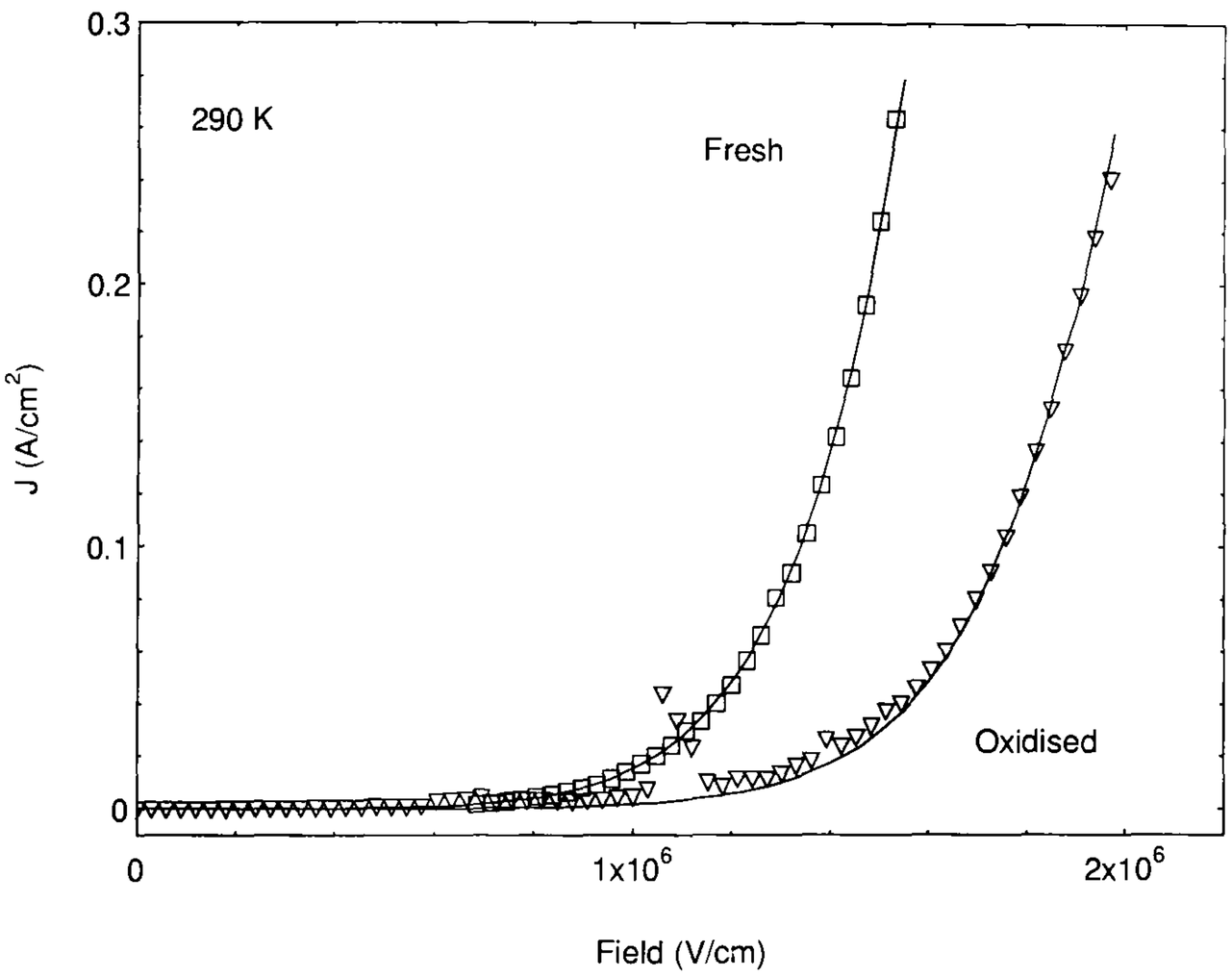

***Fig. 5.13**. Model fit to characteristics of fresh and oxidised sample at 290 K using {φ=0.55 eV, $\mu_{(E=0)}$=6.9×10^{-6} cm^2/Vs, E_0=2.3×10^5 V/cm} for the fresh sample and {φ=0.55 eV, $\mu_{(E=0)}$=2.5×10^{-7} cm^2/Vs, E_0=1.0×10^5 V/cm} for the oxidised sample.*

Photo-oxidation and conjugation breakage are a well-known phenomenon in conjugated polymers and the polymer will hence react with oxygen during the exposure to air and UV radiation [27]. In the scope of a purely injection limited theory, one may argue that the internal bandstructure of the polymer shifts upon oxidation [24, 25] which could change the effective barrier to hole injection. However, the change in fluorescence and absorption is only small and certainly not comparable to the temperature-dependent change in barrier. Microwave conductivity measurements have shown that the number of free charge carriers is more sensitive to photo-oxidation than the bandstructure of the material [26] as deduced from absorption and photoluminescence. This indicates an

energetic structure relatively stable to the effects of conjugation breaking and implies a microscopic influence of the carbonyl groups acting as charge traps or transport inhibitors.

Photo-oxidation demonstrates that even for devices with large barriers to injection, the low mobility of the polymer still remains a significant factor in determining device operation. A rigid distinction between regimes of injection limited and space charge limited current is hence not applicable, and the device model provides a means of investigating this intermediate case. Furthermore, device degradation is an important aspect of the device physics and an improved understanding of the processes involved are essential for the design of long-lifetime devices. The model hence provides a means of identifying deterioration mechanisms in working devices.

5.3.4 Effect of film thickness

As a final test of the model, two devices with different thicknesses are compared. Using the fitting parameters obtained above for the 165 nm thick device, the characteristics are calculated for a 95 nm device and compared to experiment. This is shown in Fig. 5.14. Clearly there are some problems with the model. At 280 K there is reasonable qualitative agreement between the model and the experiment on a linear scale, however, the logarithmic scale reveals some discrepancies. The agreement between the model and the experiment deteriorates dramatically as the temperature is lowered and for 100 K the model significantly overestimates the device current. Also, the calculated characteristics are much steeper.

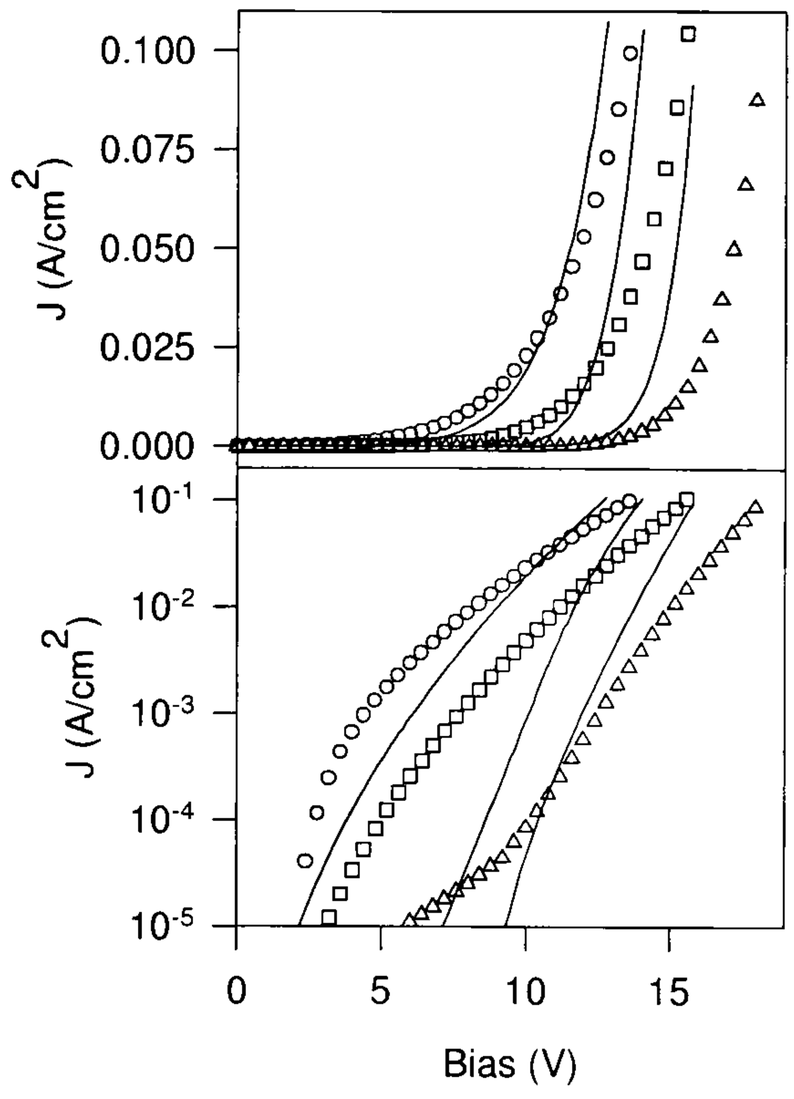

Fig. 5.14. *Model fits to a 95 nm device at 280 K (○), 200 K (□) and 100 K (△) on a linear (upper panel) and logarithmic (lower panel) scale. The same fitting parameters were used as in Fig. 5.10.*

An alternative approach to comparing the two data sets is to run the fitting procedure on the 95 nm thick devices and compare the fitting parameters. This is shown in Figs. 5.15 and 5.16. The comparison of the mobility parameters is seen in Fig. 5.15. Over the range the characteristics could be fitted, there is good agreement between the two sets of parameters.

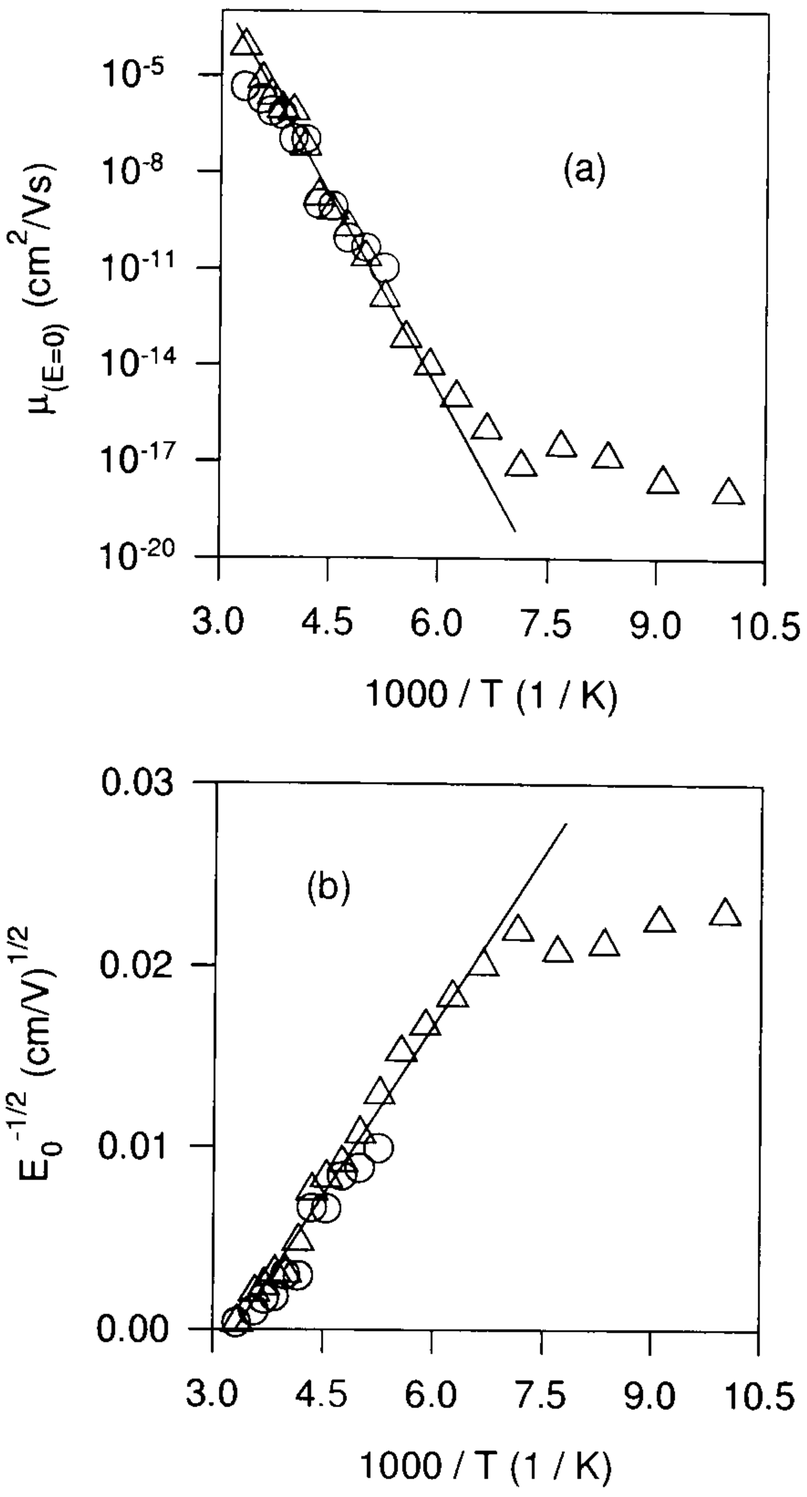

Fig. 5.15. *Comparison of the fitting parameters obtained from a 165 nm device (Δ) and a 95 nm device (O).*

As is seen in Fig. 5.16, however, the barrier height of the thinner device is reduced with respect to the thicker device. This discrepancy is the origin of the poor agreement between experiment and theory seen in Fig. 5.14. Down to 220 K, the fitted barrier height for the 95 nm thick device is 0.05 eV smaller than that for the 165 nm device. Below 220 K the barrier height suddenly drops off and reasonable fits to the data become impossible – the model breaks down.

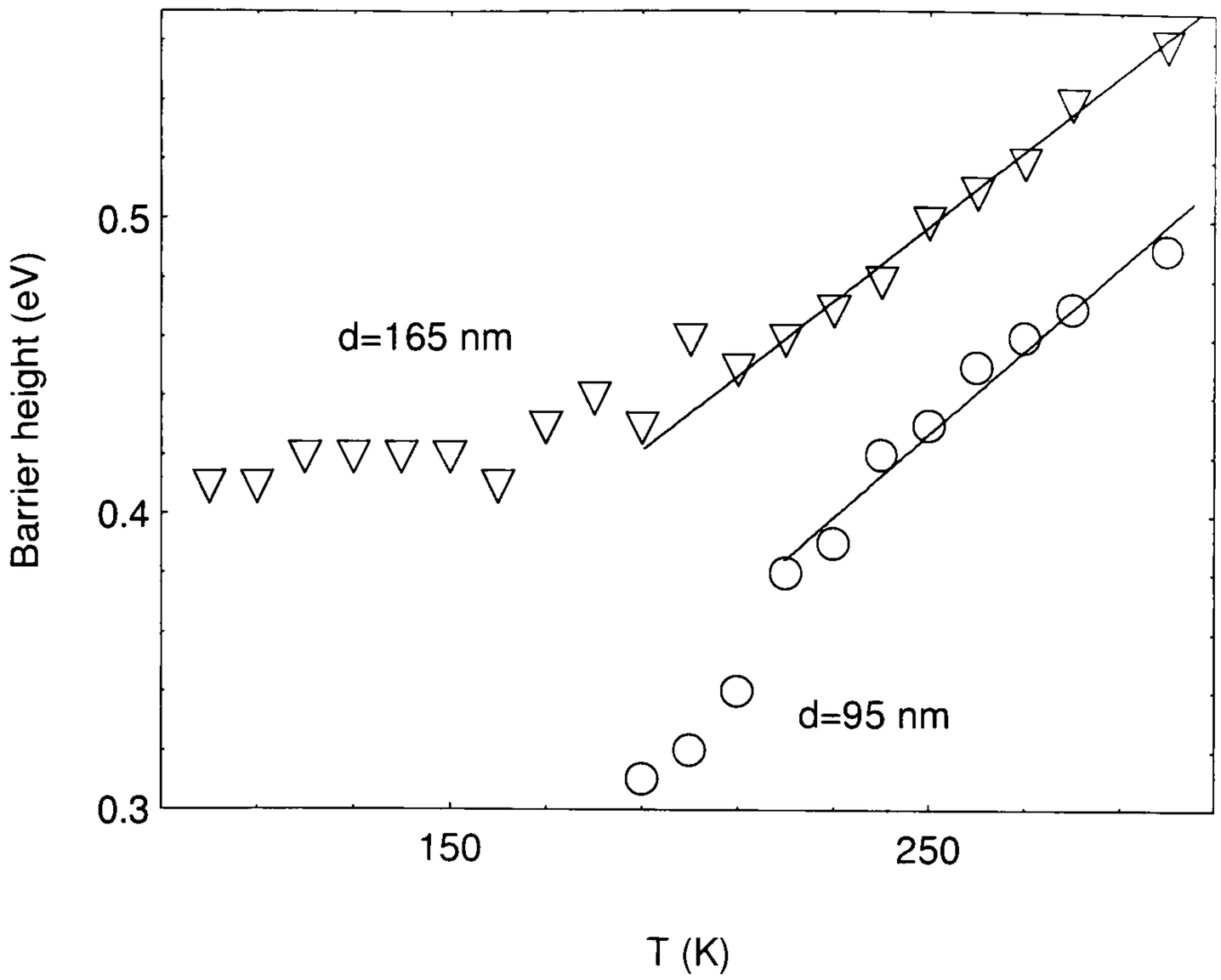

Fig. 5.16. *Values for the barrier height derived from a 165 nm device and a 95 nm device.*

5.4. Discussion

These measurements and calculations show that many aspects of the transport in organic LEDs can be described by a field and temperature dependence of the hopping mobility as seen in a variety of amorphous organic materials. They also show that even for device configurations with large barriers to injection the low mobility of polymeric semiconductors does play a significant role in the device current of polymer LEDs. It was demonstrated above that a variation of the mobility affects the device operation and that in turn using a device model incorporating the field-dependent mobility physically reasonable values for the mobility may be determined through electrical measurements.

5.4.1 FN tunnelling theory

FN tunnelling theory has previously been used to account for the operating characteristics of ITO/MEH-PPV/Al LEDs [4]. Here, a change in the FN barrier height with temperature by more than a factor of 2 was observed, which suggests that the tunnelling theory is not correct. The strong increase of the apparent barrier height as the

temperature is lowered from 300 to 200 K as seen in Figs. 5.3 and 5.6 is attributed to the presence of a further strongly temperature-dependent injection process superimposed on charge carrier tunnelling. It is a manifestation of the decreasing influence of thermionic emission to the injected device current. The more gradual increase of the barrier height towards lower temperatures is due to the increasing importance of space charge effects in the polymer as the hopping mobility is strongly reduced, resulting in a decrease in current density for a given field and hence an increase in the apparent barrier height. An FN analysis cannot yield the barrier height at room temperature, because of the influence of thermionic emission and the low mobility on the device current. At low temperatures the FN barrier height approaches the physical barrier height due to the decrease in the contribution from thermionic emission. However, for the aged device, the mobility is considerably smaller than for the pristine device, so that increased space charge effects are visible near room temperature. This results in a more rapid increase in the FN barrier height with decreasing temperature for the aged device with respect to the pristine device.

5.4.2 Device operation

The single carrier device model gives a good description of the operation of ITO/MEH-PPV/Al devices. Fits at lower temperatures tend to deviate more from the measured data. This is due to diffusion processes at low bias, which were excluded from the model, and sample heating at high currents. At lower temperatures the barrier height is lowered so the transport part of the model becomes more important in describing the device current. The charge carrier density becomes less uniform across the device as the barrier is lowered [6], so the diffusion current, which is proportional to the charge carrier density gradient, will become more important. As the glass substrate is a poor thermal conductor, the polymer film of a device cooled down to 100 K could heat up significantly during continuous operation. As the current does reach a steady state value after a certain time, using the model and the mobility as fitting parameter it is possible to estimate the steady state operating temperature of the luminescing film of the device in contact with a heat sink at a given temperature. This may be used as an alternative to the spectroscopic studies of the device operating temperature recently reported [38]. The variation of the current-voltage characteristics of the devices with temperature is well

described by the change in the hopping mobility and the effective barrier height to injection. The mobility follows a form corresponding to hopping of charge carriers from one conjugated segment to the next, as determined by Pai [39]. Values for the E_0 and $\mu_{(E=0)}$ parameters are overestimated at low temperatures due to diffusion and sample heating. It should be noted that Blom et al. fitted the PPV mobility only over a range from 209 to 296 K [11] but also observe an increasing deviation of the mobility parameters at lower temperatures from the form predicted by equations (5.5) and (5.6). It is conceivable that due to increased dispersion and delocalisation of the charge carriers across conjugated chains the approximation of the hopping mobility becomes less accurate at lower temperatures, as has been indicated by time-of-flight measurements [40].

The mobility parameters obtained here are comparable at temperatures around room temperature to values reported elsewhere for similar materials [10, 11, 35], as summarised in Table 5.1. In the devices tested here, chlorobenzene was used as a spinning solvent. It has been shown by x-ray diffraction experiments that the degree of microscopic order of the film is strongly dependent on the spinning solvent used, with greater crystallinity obtained for solvents such as tetrahydrofuran and lower order for chlorobenzene [41]. The morphology of the films used in Refs. [10] and [11] is not known. The MEH-PPV films studied in Ref. [35] were spun from *p*-xylene which yields slightly more ordered films than chlorobenzene [41]. The structures of the dialkoxy PPVs studied in Refs. [10] and [11] may permit a greater degree of microscopic ordering, which would give rise to a lower energetic disorder [42] and lower activation energies for the zero field hopping mobility and the field dependence when compared to MEH-PPV, whereas the activation energies reported in Ref. [35] for MEH-PPV are actually smaller. Further measurements are required of devices with ohmic contacts spun from different solvents to determine the effect of the microscopic ordering on the mobility parameters. These calculated mobilities suggest that the MEH-PPV films studied here are significantly more disordered than materials used in previous studies, which gives rise to greater activation energies for the mobility parameters.

5.4.3 Photo-oxidation

A reduction in mobility can also account for the difference between fresh and aged samples, the aged samples having a lower charge carrier mobility and hence displaying a stronger increase in apparent tunnelling barrier height with decreasing temperature and hence decreasing mobility. The effects of photo-oxidation which give rise to increased influence of bulk conduction mechanisms on the current through the sample are well described by the model. A significant decrease in the zero field mobility $\mu_{(E=0)}$ is found after exposure to destructive UV laser light, whereas the barrier to injection remains unchanged. This is consistent with the concept of oxidative breaking of conjugated chain segments along the polymer backbone, which inhibit the motion of charge carriers through the sample [26-27] and form traps.

It was shown above that the low bias forward and reverse bias characteristics of devices prepared in air and tested under vacuum are qualitatively well described by a Poole-Frenkel emission expression. This conduction term is only relevant to the understanding of the full physical picture of the device and does not influence the actual device operation above turn-on. As most devices become doped during their lifetime of operation, it is important to isolate this effect.

5.4.4 Critical discussion of the model

It is interesting to note that good quality fits may be obtained even by using the simple superposition of injection terms taken from inorganic semiconductor physics. In fact, conjugated polymers are disordered systems, so microscopic approaches to modelling considering dark injection from a metallic electrode into a random hopping system have a stronger physical grounding. However, it has recently been demonstrated [43-44] that a detailed study of this microscopic injection through Monte Carlo techniques can actually yield current-voltage characteristics similar to both the tunnelling theory and to Richardson-Schottky thermionic emission. At temperatures around room temperature bulk injection terms hence on average provide a good description of the processes at the interface.

The discrepancy between the mobility data obtained here and values reported elsewhere may be related to the simulation of the injection current at the interface. The problem that the barrier height obtained here varies more strongly than the absorption band of MEH-PPV [37] may be an indication that the bulk injection terms used are not applicable at lower temperatures and that the model yields good results and fits only around room temperature. At lower temperatures, the microscopic hopping injection is underestimated by the injection current contribution from the thermionic emission term, as this varies more strongly with temperature than hopping injection [44]. The net result is that the model compensates by requiring a lower barrier height which can give the injection current required to fit the experimental data. Consequently, the mobility fitting parameters vary more strongly with temperature in order to compensate the current resulting from the temperature independent tunnelling approximation which is increased due to the underestimated barrier height. The overestimate of the temperature-independent tunnelling injection current hence requires an underestimate of the mobility to fit the data. It is nevertheless remarkable that the model yields temperature-dependent parameters that follow the functional form of the field-dependent mobility in equations (5.5) and (5.6) albeit with an overestimate of the activation energy. This demonstrates that a consistent set of parameters allows qualitative device modelling over a wide range of temperatures.

The break-down of the model for thin devices at low temperatures is thought to be a further consequence of the deviation of the microscopic thermally assisted injection processes from the approximation of thermionic emission. There are two problems with the comparison of the thick device with the thin device. Firstly, the fits show that the barrier height is smaller for the thin device than for the thick device. And secondly, calculations at low temperatures result in a significant overestimate of the current. It should be noted that meaningful fits could not be obtained below 220 K for the 95 nm device. As seen in Fig. 5.14, the model calculations are much steeper than the measured data. For the 95 nm device it was not possible to reproduce the more gradual shape of the measured characteristics at low temperatures. The exact origins of these discrepancies are presently not clear, but the disagreement between the values for the barrier height and the break-down at low temperatures suggests that the main problem remains the inadequacy of the injection terms discussed above. The important

conclusion is that at room temperature the model adapts relatively well to a change in device thickness.

The variation of the barrier to injection with temperature as predicted by the model is particularly interesting. The barrier height calculated here is slightly smaller (by approx. 50 meV assuming an ITO work function of 4.8 eV and a HOMO level of 5.4 eV [18]) than the value used by Davids et al. [6]. However, it has been shown [45] that the work function of ITO can vary significantly (by up to 0.6 eV) depending on preparation. For the solvent cleansing method applied here, an ITO work function of 4.4 eV [45] has been reported, which would correspond to a barrier height in the order of 1 eV. This value for the ITO work function is within the range of the work function of the aluminium cathode. However, the present devices are rectifying, suggesting that the ITO work function is larger than 4.4 eV. It has been demonstrated that the deposition of self-assembled monolayers between metal and polymer results in a modification of the effective Schottky barrier [46]. Also, photoelectron spectroscopy measurements have suggested a break-down of the strict vacuum level alignment rule between the metal and the organic due to the presence of interfacial dipoles [47]. It is hence concluded that an interfacial layer between polymer and metal resulting from the spin coating process may give rise to a barrier which is somewhat smaller than the offset between HOMO and metal work function.

It is very interesting to note the essentially linear decrease of the injection barrier with temperature down to approx. 220 K. This is not related to the increase of the apparent FN barrier with decreasing temperature, which is attributed to the decrease in significance of thermionic emission. This shift in barrier height by approx. 100 meV is in part related to the spectral shift in MEH-PPV manifest in the absorption and photo-current action spectra [37, 48]. However, the decrease in barrier height is approximately twice that of the decrease in band gap, so that other factors must also contribute. This is a weakness of the model. The linear variation of the barrier height is a signature of the effect of disorder in the system, with the energetic spread of the HOMO level depending approximately linearly on temperature [42] over a certain temperature range (here approx. 220 K to 300 K). Once the ring torsions are frozen out the disorder reaches a static value and the band structure remains relatively unchanged. Also, as the barrier height decreases and the mobility decreases, the device current becomes more and more

influenced by the low mobility, and the barrier height becomes less significant, as demonstrated in Fig. 5.9. This gives rise to the uncertainty in the barrier height at lower temperatures.

The method presented here provides a simple means for the determination of the charge carrier mobility and the barrier heights to injection. The mobility is essential for understanding the device operation, and will give valuable insight into the function of transport layers [49] or polymeric electrodes [50] in multilayer LEDs.

The model does highlight clearly the importance of the barrier to injection from the ITO electrode, which is used in most device configurations. In a recent study of different anode materials, it was demonstrated that the barrier for hole injection is the efficiency-limiting factor in MEH-PPV devices with calcium cathodes [51]. Hence the study of single layer single carrier device structures is extremely useful in understanding the efficiency limiting mechanisms in polymer LEDs.

The model does not give any explanations of the transients and dynamic capacitances measured in organic LEDs [9]. However, it has been shown that these are mainly extrinsic properties greatly dependent on the manufacturing process and contamination with impurities [22]. As the charge carrier mobility within the polymer is an intrinsic property, the intrinsic model presented here may supply sufficiently correct physical information. Detailed investigations and comparisons of mobility data may allow an improvement of the understanding of the difference in efficiency between different materials in single layer and bilayer configuration. This model can provide valuable insight into the charge carrier and field distribution that could be used to optimise multilayer devices.

5.5 Conclusions

The temperature dependence of a single carrier device model to describe organic LEDs has been successfully tested. The calculations and measurements demonstrate that charge carrier hopping in the disordered polymer may be approximated around room temperature by injection into a band like continuum combined with a field and

temperature-dependent mobility. This approximation allows a very simple characterisation of the organic LED in terms of mobility and barrier to injection, which are the key parameters leading to increased device efficiency [52], brightness and also lifetime. The need to include both injection and transport effects in a complete analysis of devices was demonstrated and the influence on the device characteristics of reducing the mobility through photo-oxidation was shown. The model could be used for a preliminary distinction between intrinsic (hopping conduction between polaron states) and extrinsic (transport in doping states) conduction processes which suggests that this kind of approach will be useful in identifying undesired behaviour in LEDs such as impurity conduction and doping, which may lead to luminescence quenching and ultimately device breakdown. The incorporation of the barrier height in the model ensures applicability to a wide range of materials, particularly novel large bandgap blue luminescent polymers, which are likely to have non-ohmic contacts. The larger temperature dependence of the fitting parameters obtained here in comparison with independent experiments suggests that a complete description of injection and transport in these disordered semiconductors requires a microscopic treatment of the hopping injection process. Bulk approximations of injection and transport appear to give quantitatively reasonable results only over a limited temperature range.

References

[1] C. W. Tang and S. A. Vanslyke, Appl. Phys. Lett. **51,** 913 (1987)

[2] J. H. Burroughes, D. D. C. Bradley, A. R. Brown, R. N. Marks, K. Mackay, R. H. Friend, P. L. Burn, and A. B. Holmes, Nature **347,** 539 (1990)

[3] D. Braun and A. J. Heeger, Appl. Phys. Lett. **58,** 1982 (1991)

[4] I. D. Parker, J. Appl. Phys. **75,** 1656 (1994)

[5] P. S. Davids, S. M. Kogan, I. D. Parker, and D. L. Smith, Appl. Phys. Lett. **69,** 2270 (1996)

[6] P. S. Davids, I. H. Campbell, and D. L. Smith, J. Appl. Phys. **82,** 6319 (1997)

[7] I. H. Campbell, P. S. Davids, D. L. Smith, N. N. Barashkov, and J. P. Ferraris, Appl. Phys. Lett. **72,** 1863 (1998)

[8] B. K. Crone, P. S. Davids, I. H. Campbell, and D. L. Smith, J. Appl. Phys. **84**, 833 (1998)

[9] A. J. Campbell, D. D. C. Bradley, and D. G. Lidzey, J. Appl. Phys. **82,** 6326 (1997)

[10] P. W. M. Blom, M. J. M. Dejong, and J. J. M. Vleggaar, Appl. Phys. Lett. **68,** 3308 (1996)

[11] P. W. M. Blom, M. J. M. deJong, and M. G. van Munster, Phys. Rev. B **55,** R656 (1997)

[12] J. C. Scott, S. Karg, and S. A. Carter, J. Appl. Phys. **82,** 1454 (1997)

[13] Y. Kawabe, G. E. Jabbour, S. E. Shaheen, B. Kippelen, and N. Peyghambarian, Appl. Phys. Lett. **71,** 1290 (1997)

[14] S. Karg, M. Meier, and W. Riess, J. Appl. Phys. **82,** 1951 (1997)

[15] A. J. Heeger, I. D. Parker, and Y. Yang, Synth. Met. **67,** 23 (1994)

[16] H. Vestweber, J. Pommerehne, R. Sander, R. F. Mahrt, A. Greiner, W. Heitz, and H. Bässler, Synth. Met. **68,** 263 (1995)

[17] M. Koehler and I. A. Hummelgen, Appl. Phys. Lett. **70,** 3254 (1997)

[18] I. H. Campbell, T. W. Hagler, D. L. Smith, and J. P. Ferraris, Phys. Rev. Lett. **76,** 1900 (1996)

[19] M. Gross, K. Meerholz, and C. Brauchle, Synth. Met. **102**, 1147 (1999)

[20] M. Fahlman, O. Lhost, F. Meyers, J. L. Bredas, S. C. Graham, R. H. Friend, P. L. Burn, A. B. Holmes, K. Kaeriyama, Y. Sonoda, M. Logdlund, S. Stafstrom, and W. R. Salaneck, Synth. Met. **55,** 263 (1993)

[21] I. H. Campbell, D. L. Smith, and J. P. Ferraris, Appl. Phys. Lett. **66,** 3030 (1995)

[22] J. Scherbel, P. H. Nguyen, G. Paasch, W. Brutting, and M. Schwoerer. J. Appl. Phys. **83,** 5045 (1998)

[23] E. M. Conwell and M. W. Wu, Appl. Phys. Lett. **70,** 1867 (1997)

[24] K. Z. Xing and N. Johansson, Adv. Mat. **9,** 1027 (1997)

[25] G. D. Hale, S. J. Oldenburg, N. J. Halas, and D. E. Rice, Appl. Phys. Lett. **71,** 1483 (1997)

[26] G. H. Gelinck and J. M. Warman, Chem. Phys. Lett. **277,** 361 (1997)

[27] L. J. Rothberg, M. Yan, F. Papadimitrakopoulos, M. E. Galvin, E. W. Kwock, and T. M. Miller, Synth. Met. **80,** 41 (1996) ; N. T. Harrison, G. R. Hayes, R. T. Phillips, and R. H. Friend, Phys. Rev. Lett. **77**, 1881 (1996)

[28] L. M. Do, K. J. Kim, T. Zyung, H. K. Shim, and J. J. Kim, Appl. Phys. Lett. **70,** 3470 (1997)

[29] J. M. Lupton, I. D. W. Samuel, and A. P. Monkman, Synth. Met. **102**, 1079 (1999)

[30] B. H. Cumpston, I. D. Parker, and K. F. Jensen, J. Appl. Phys. **81** (3716) 1997

[31] P. S. Davids, A. Saxena, and D. L. Smith, J. Appl. Phys. **78,** 4244 (1995)

[32] S. M. Sze, Phys. of Semiconductor Devices 2nd Edition (John Wiley and Sons, New York, 1981)

[33] P. Le Rendu, T. P. Nguyen, O. Gaudin, and V. H. Tran, Synth. Met. **76**, 187 (1996)

[34] H. Sirringhaus, N. Tessler and R. H. Friend, Science **280**, 1741 (1998)

[35] L. Bozano, S. A. Carter, J. C. Scott, G. G. Malliaras, and P. J. Brock, Appl. Phys. Lett. **74**, 1132 (1999)

[36] M. Liess, S. Jeglinski, Z. V. Vardeny, M. Ozaki, K. Yoshino, Y. Ding. and T. Barton, Phys. Rev. B **56**, 15712 (1997)

[37] A. K. Sheridan, J. M. Lupton, I. D. W. Samuel, and D. D. C. Bradley, Chem. Phys. Lett. **322**, 51 (2000)

[38] N. Tessler, N. T. Harrison, D. S. Thomas, and R. H. Friend, Appl. Phys. Lett. **73**, 732 (1998)

[39] D. M. Pai, J. Chem. Phys. **52,** 2285 (1970)

[40] I. H. Campbell, D. L. Smith, C. J. Neef, and J. P. Ferraris, Appl. Phys. Lett. **74**, 2809 (1999)

[41] C. Y. Yang, F. Hide, M. A. Diaz-Garcia, A. J. Heeger, and Y. Cao, Polymer **39**, 2299 (1998)

[42] D. H. Dunlap, P. E. Parris, and V. M. Kenkre, Phys. Rev. Lett. **77**, 542 (1996)

[43] V. I. Arkhipov, E. V. Emelianova, Y. H. Tak, and H. Bassler, J. Appl. Phys. **84**, 848 (1998)

[44] U. Wolf, V. I. Arkhipov, and H. Bässler, Phys. Rev. B **59**, 7507 (1999)

[45] J. S. Kim, M. Granstrom, R. H. Friend, N. Johansson, W. R. Salaneck, R. Daik, W. J. Feast, and F. Cacialli, J. Appl. Phys. **84**, 6859 (1998)

[46] I. H. Campbell, J. D. Kress, R. L. Martin, D. L. Smith, N. N. Barashkov, and J. P. Ferraris, Appl. Phys. Lett. **71,** 3528 (1997)

[47] I. G. Hill, A. Rajagopal, A. Kahn, and Y. Hu, Appl. Phys. Lett. **73,** 662 (1998)

[48] M. G. Harrison, J. Gruner, and G. C. W. Spencer, Phys. Rev. B **55,** 7831 (1997)

[49] S. Dailey, M. Halim, E. Rebourt, L. E. Horsburgh, I. D. W. Samuel, and A. P. Monkman, J. Phys. CM **10**, 5171 (1998)

[50] S. A. Carter, M. Angelopoulos, S. Karg, P. J. Brock, and J. C. Scott, Appl. Phys. Lett. **70**, 2067 (1997)

[51] J.C. Scott, G. G. Malliaras, W. D. Chen, J.-C. Chen, J.-C. Breach, J. R. Salem, P. J. Brock, and S. B. Sachs, Appl. Phys. Lett. **74**, 1510 (1999)

[52] D. D. C. Bradley, Adv. Mat. **4**, 756 (1993)

6.

Mobility measurements on dendrimers

Acknowledgements

I am indepted to H. Bässler for hosting a visit to Marburg and the use of the Marburg time-of-flight set-up as well as many helpful discussions. I would particularly like to thank C. Im for training me on the time-of-flight equipment. The dendrimers studied were synthesised by R. Beavington and P. Burn at Oxford University. I am grateful to M. Frampton of Oxford University for performing cyclic voltammetry measurements on the dendrimers studied here.

6. 1 Introduction

Studies of the nature of charge transport in highly disordered organic semiconductors have experienced a renaissance since the discovery of efficient EL in small organic molecules [1] and polymers [2]. Progress on materials and devices has led to a vast array of electronic and opto-electronic applications [3]. Most organic materials have low mobilities in comparison to their inorganic counterparts and hence there has been considerable interest in increasing these mobilities to find materials capable of sustaining the currents required for field-effect transistors and organic lasers [4,5]. Although there have been attempts to correlate the chemical and physical structure of these materials with their mobilities, little is known about the origin of the low mobilities found in most organic materials for EL applications. Conjugated polymers in particular do not lend themselves readily to structural studies due to their inherent disorder, and many previous discussions have hence been based on stochastic models [6]. The charge carrier mobility in luminescent polymers is related to the chemical structure of the polymer and the microscopic conformation. Martens et al. have used the concept of energetic disorder to explain the wide range of mobilities observed in a recent comparison of different PPV based polymers [7]. In contrast, geometrical considerations have been invoked to explain the large difference in mobilities between highly disordered materials such as MEH-PPV and more rigid polymers such as polyfluorenes [8]. In this chapter the effect of increased spacing of the luminescent conjugated segments through dendrimer generation is investigated. This intuitive microscopic control of the interaction between individual chromophores allows an unambiguous study of the effect of molecular arrangement on the transport properties within the organic material. In addition, it is of interest to investigate the correspondence between the device properties and the excimer formation observed in dendrimer films, as discussed in chapter 4. The direct control of the intermolecular interactions through dendrimer generation can shed light on the correlation between chemical structure, optical properties and device performance.

One key advantage of using conjugated dendrimers in the study of charge transport in organic materials is the fact that they can be synthesised in an orderly manner such that the precise structure and molecular weight are known. This is in contrast to some

polymers where batch to batch variations of the molecular weight can occur. Batch to batch variations in polymer synthesis have been shown to give rise to dramatic variations of device properties [9], which greatly complicates attempts to relate the chemical structure to the charge transport in polymers. Conjugated dendrimers can also be seen as a bridge between small organic molecules and conjugated polymers. The chromophore unit may be based on either small organic compounds such as porphyrins, anthracene or hydroxyquinolines, or oligomer units of commonly used polymers. The dendrimer generation can be exploited as a direct control of the spacing between the core units of the dendrimers.

In the present chapter, the charge transport properties of films of the nitrogen cored dendrimer are studied using both transient and cw methods. Charge transport in emissive conjugated materials for LEDs is of particular interest. The potential imbalance between electron and hole mobilities was identified early on in the research of organic LEDs as a stumbling block in the design of efficient devices [3, 10-12]. Charge transport in molecularly doped polymers and organic crystals has been studied extensively for over thirty years, but few systematic studies have been made on systems directly relevant to LEDs [13-15]. The most common tool for studying charge transport in organic materials is the time-of-flight (TOF) technique, which was developed by Haynes and Shockley [16] and Lawrance and Gibson [17] in the Fifties. A sheet of charge carriers is generated optically at one side of the sample and then swept through the film under application of an external field, resulting in a current. During the transit of charge carriers through the film, a constant current is measured, as long as the characteristic waiting time distribution of a charge carrier on a transport site is narrow. Once the carrier front reaches the counter electrode, the number of free carriers in the film is rapidly reduced and the current hence falls. Although this method yields excellent results for many materials, the extremely low mobility of many conjugated polymers has rendered many initial attempts to measure the mobility using TOF unsuccessful [18]. Correlations of mobility data obtained by TOF have been made with results from carrier concentration measurements using transient absorption and Monte Carlo simulations [19]. The Bayreuth group have found consistent mobilities through measurements of space charge limited currents and TOF on precursor PPV [15]. However, the two samples used differed in film thickness by up to an order of magnitude and there were also differences in the film preparation. In addition, precursor

PPV has been found to exhibit extrinsic semiconducting properties due to doping impurities introduced in the conversion process [20, 21], which further complicates the analysis. In the following, a correlation is drawn between TOF measurements and data from LEDs. The fact that the charge transport properties can be systematically engineered using the dendrimer generation rules out the possibility that the observed correlations may be coincidental.

6.2 Time-of-flight measurements

6.2.1 Introduction

The interpretation of TOF data can be extremely complicated and has attracted a huge amount of research interest over past decades [22-29]. It soon became apparent in the study of current transients that many materials exhibit patterns deviating from the behaviour expected for a sheet of charge carriers moving under the diffusion limit through the sample. The ground-breaking model on dispersive transport by Scher and Montrol [23-24] unified many open problems at the time and has since found frequent application to numerous systems. However, with the increased interest in highly amorphous materials such as molecularly doped or conjugated polymers, the effect of spatial and energetic disorder on the charge transport has been of central interest [6, 24, 25, 30]. In the ideal case, charge carriers are generated in a narrow sheet within the film, or within a charge generation layer, and swept through the material as shown in Fig. 6.1. [31].

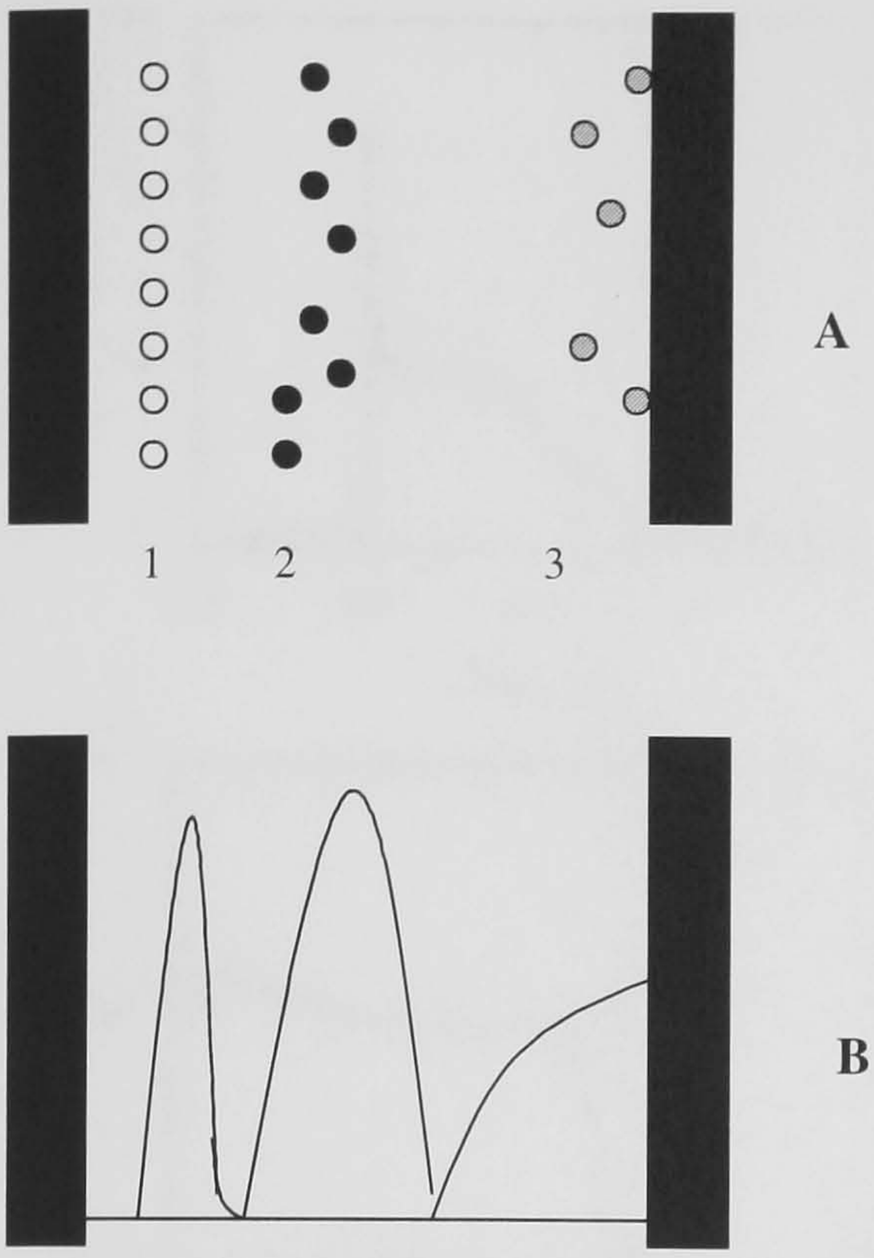

Fig. 6.1. *Non-dispersive transport. 1: Carrier generation. 2: Carrier transport. 3: Carriers annihilate at counter electrode. A: Plot of charge carriers. B: Plot of carrier density. C: Plot of transient photocurrent against time. The current begins to drop at the transit time t_{tr} which marks the arrival of the charge carrier front at the counter electrode.*

A typical non-dispersive transient is shown in Fig. 6.2. A peak is seen at short times which is due to capacitative effects of the sample and to the relaxation of charge carriers within the density of states distribution [32, 33] as well as initial charge trapping [34]. A clear plateau region is observed, which corresponds to region 2 in Fig. 6.1 and the transit time is obtained through the extrapolated asymptotes of the photocurrent at short and long times.

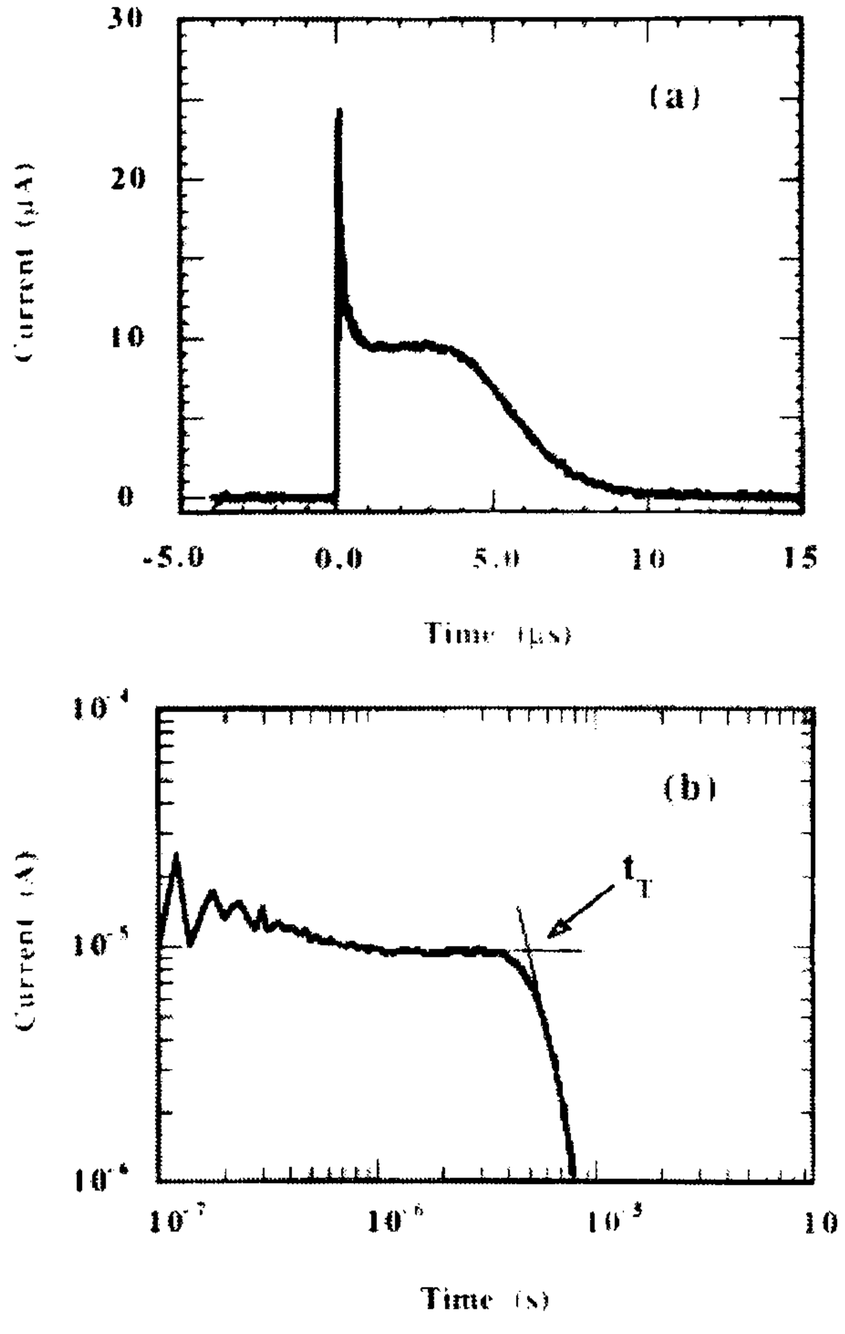

Fig. 6.2. *A typical non-dispersive TOF signal. Taken from Redecker et al. [35], measured on a polyfluorene film.*

In the case of non-dispersive transport, to a first approximation the one-dimensional law of diffusion holds which results in a Gaussian distribution of the charge carrier density in space. Under the assumption of the validity of the Einstein equation, the diffusivity is proportional to the mobility and the spread of the Gaussian distribution hence depends on the field applied to the sample. In contrast, in many materials including the conjugated dendrimers discussed in the following, this Gaussian diffusion is not observed and the stochastic model of dispersive transport [24] is used to explain the observed behaviour. Additionally, deviations from the Einstein equation have also been observed in disordered materials [36]. The case of dispersive transport is shown schematically in Fig. 6.3 [24, 31].

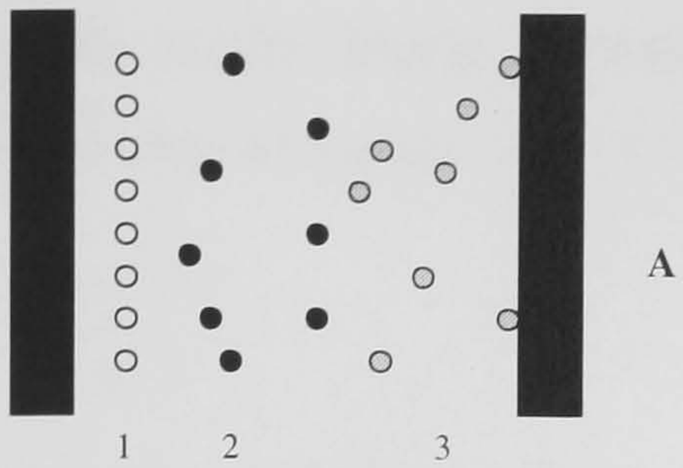

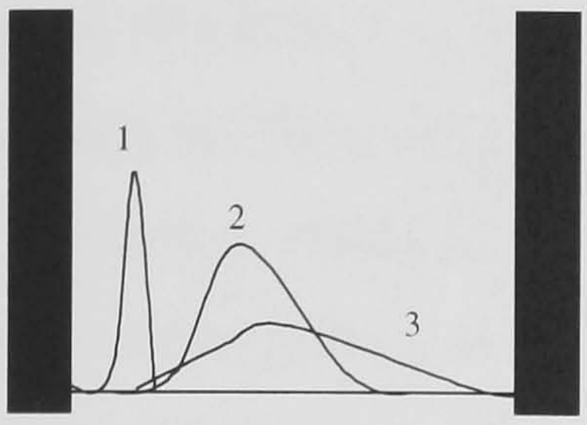

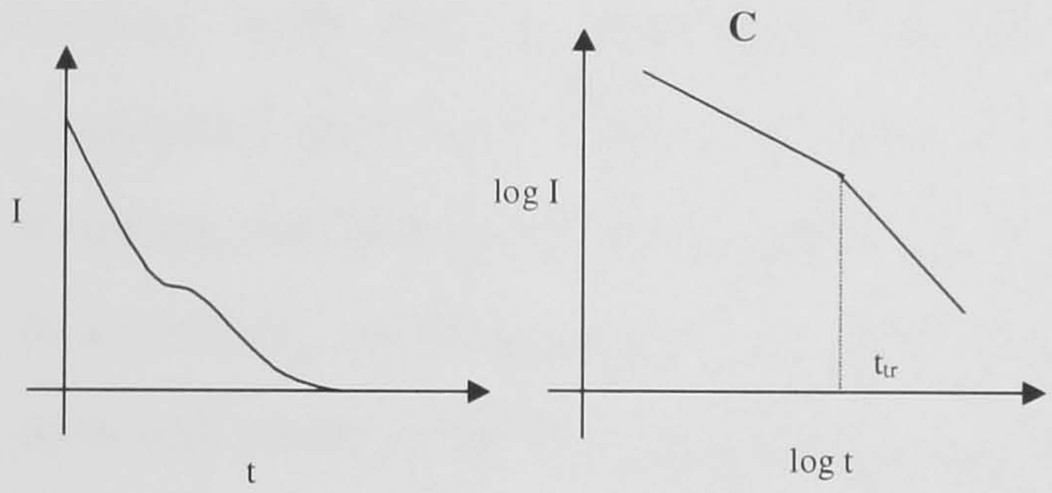

Fig. 6.3. *Dispersive transport. 1: Carrier generation. 2: Carrier transport. 3: Carrier annihilation at counter electrode. A: Plot of charge carriers. B: Plot of carrier density. C: Plot of transient photocurrent against time on a double linear and double logarithmic scale. The point of inflection on the log-log plot marks the transit time.*

In the case of dispersive transport the charge carrier packet is broadened throughout the sample due to a large distribution of waiting times of the individual charge carriers on the transport sites. In the continuous time random walk theory developed by Scher, Montrol and Lax [23-24] a waiting time distribution of the form $\Psi(t)=t^{-1-\alpha}$ is postulated. This gives rise to a temporal evolution of the current following

$$I(t)\sim t^{-(1-\alpha)} \quad \text{for } t<t_{tr}$$
$$I(t)\sim t^{-(1+\alpha)} \quad \text{for } t>t_{tr} \qquad (6.1)$$

where t_{tr} is the transit time and α is the dispersion parameter ($0<\alpha<1$). In general, a decrease in α results in more dispersive transport which is a consequence of increased

disorder in the sample. A further consequence of the stochastic transport model is the dependence of transit time on film thickness d and applied field E according to

$$t_{tr} \sim \left(\frac{d}{E}\right)^{\frac{1}{\alpha}} \tag{6.2}$$

This scaling behaviour of the transit time implies that the mobility is not a universal material property but rather depends on the field and the sample thickness. In the context of LEDs it is hence imperative that comparisons of the mobility of the material are made for films of comparable thickness. Frequently, deviations from the above laws of dispersive transport are observed, in particular the two exponents describing the decay of the photocurrent do not always add up to -2 (if α=const., $-(1-\alpha)+(-(1+\alpha))=-2$) [28, 37]. This has led to numerous modifications of the continuous time random walk theory, particularly in the light of the Gaussian disorder theory of conjugated polymers [38]. The main result of the work of Scher and Montrol is, however, the definition of the transit time in dispersive transport, which turns out to be an extremely useful quantity. A further consequence of the broad power-law distribution of transit times in the continuous time random walk model is the invariance of the shape of the photocurrent transient to the applied field. Whereas Gaussian transport gives rise to a field dependent broadening of the carrier packet, the stochastic model describes the probability of carrier release from a hopping site rather than a spatial distribution and hence employs a scale invariant distribution function Ψ. The result is that all transients of a sample scale by the transit time.

The charge carrier mobility, which is defined as the ratio of drift velocity to applied electric field, is defined in equation 9.3 as

$$\mu = \frac{d^2}{Vt_{tr}} \tag{6.3}$$

where V is the applied bias.

6.2.2 Results and discussion

TOF transients were measured on devices of thicknesses 185 nm, 300 nm, 250 nm, and 200 nm, for A0 to A3, respectively. Fig. 6.4 shows typical traces recorded for all four

generations with a 15 nm rhodamin 6G charge generation layer between the dendrimer and the aluminium electrode.

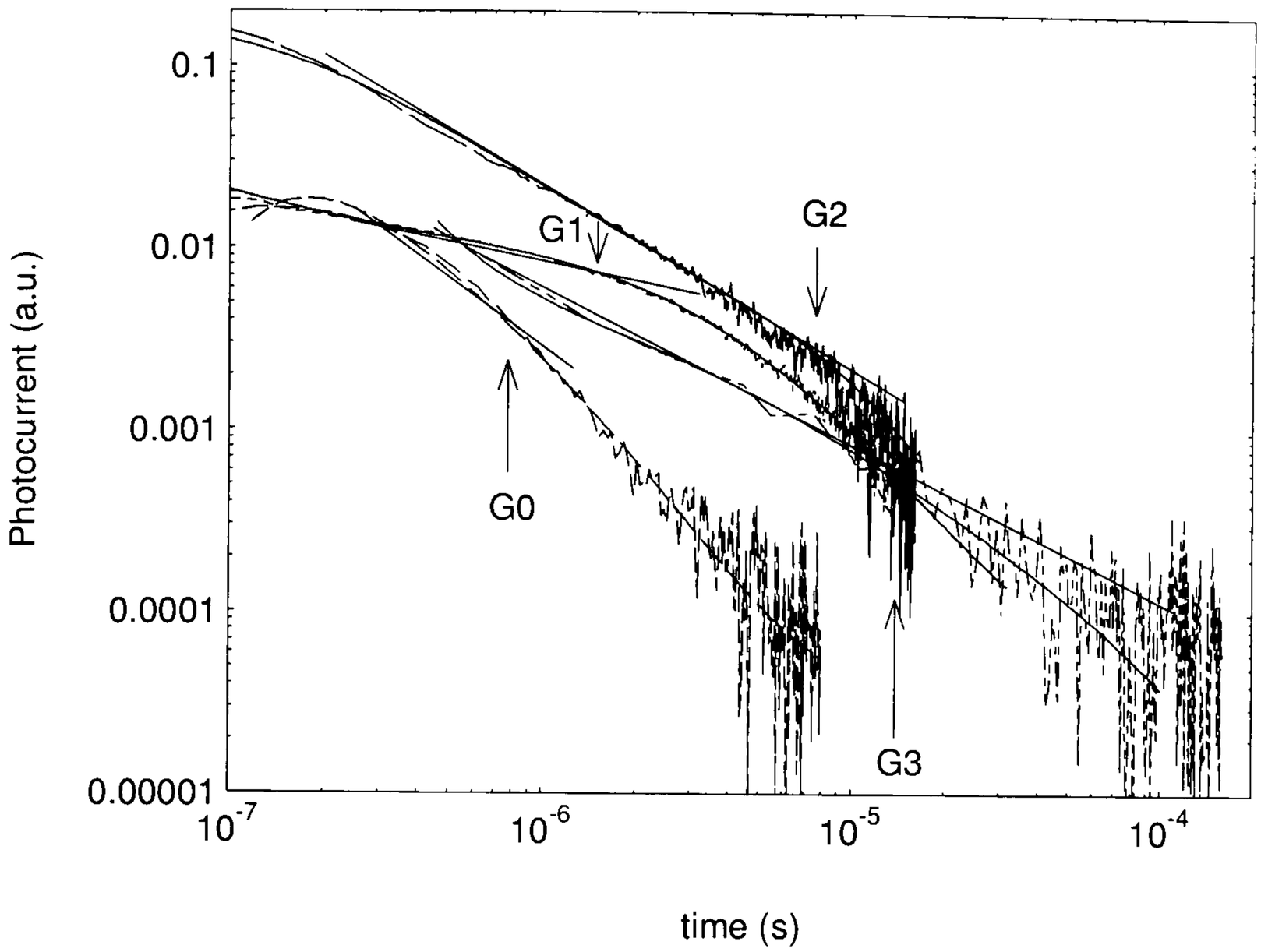

Fig. 6.4. *Typical TOF transients for dendrimer films. Straight lines have been fitted to the decay at short times. The arrows mark the transit times.*

The traces seen in Fig. 6.4 are virtually featureless. However, the remarkable observation is that the time scale over which the transients were measured, which were all recorded at biases in the range 5 to 30 V, increases by 2 orders of magnitude as the generation increases. This is clear evidence that the TOF data contains useful information regarding the charge transport in films of conjugated dendrimers. It also demonstrates that the injection of charge carriers from the charge generation layer into the dendrimer layer is not the rate limiting step of the photocurrent [29], as a change in dendrimer generation has a large effect on the current. Transit times were estimated by fitting straight lines to the transients at short and long times and are marked by arrows in the plot. It is seen that the transit times increase by almost 2 orders of magnitude as the generation increases, quantifying a dramatic slowing in charge transport for higher generations.

Great care has to be taken to ensure that the measured transient corresponds to an intrinsic property of the sample and is not due to the experimental set-up. Good evidence that the measured data relates directly to the chemical structure of the dendrimers comes from the fact that there is a strong change in the photocurrent with generation. A common source of error is the response of the voltage source unit, which is required to keep the voltage constant despite the rapidly changing current. This was achieved with a voltage source built in-house in Marburg. An example of a poor choice of voltage source is shown below in Fig. 6.5 where a Keithley source measure unit was used to apply the field.

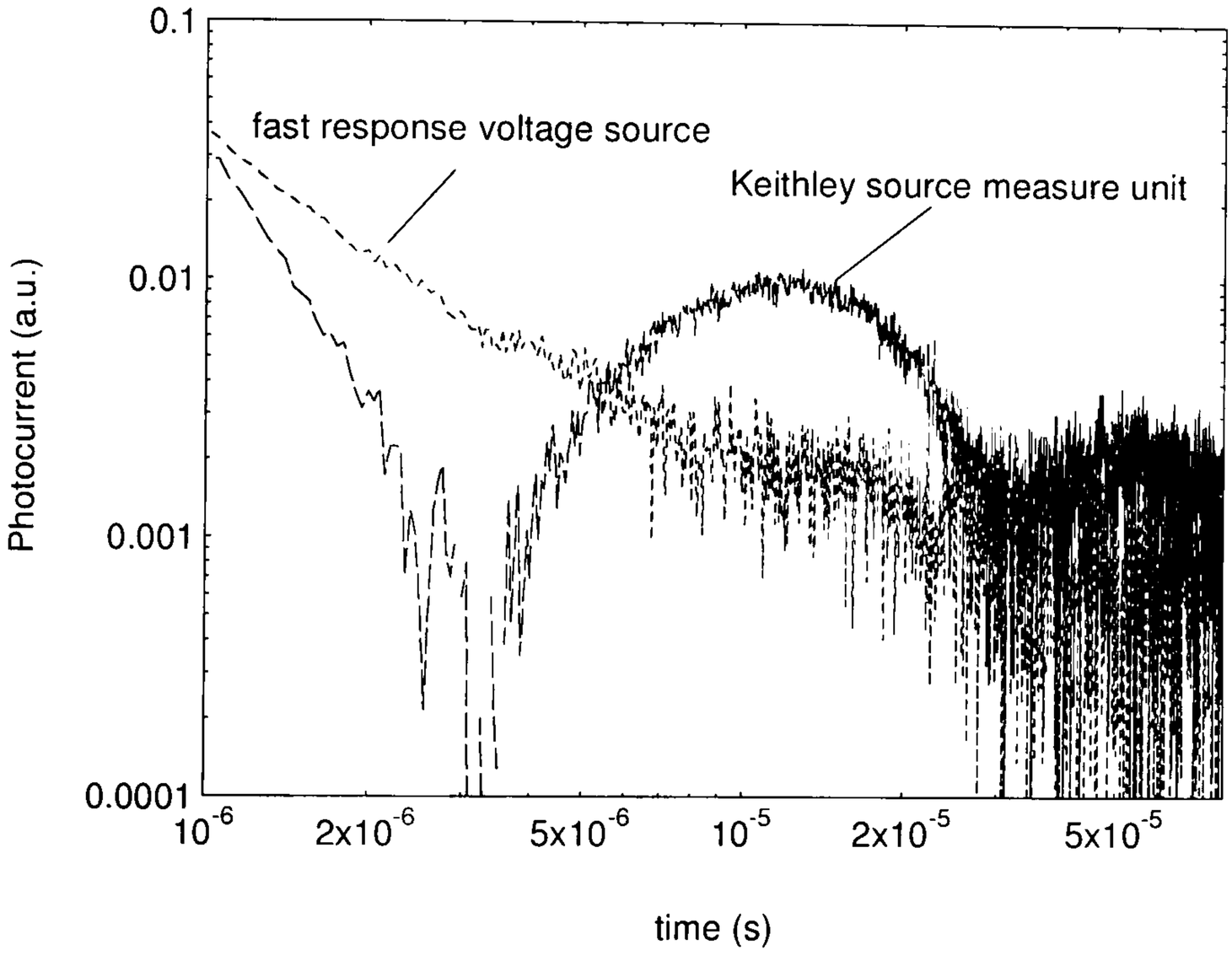

Fig. 6.5. *A1 dendrimer film photocurrent measured using a fast response voltage supply and a standard Keithley source measure unit.*

The transients shown above are entirely different from each other, although they were measured in succession at the same bias of 30 V. There is a rapid decay in the current in the measurement with the Keithley source, and the current is subsequently seen to rise again on a microsecond time-scale as the source measure unit compensates for the change in current flowing through the device. All traces measured with the fast response voltage source showed a monotonous decrease in current with time, which suggests that the voltage source response time was smaller than 100 ns.

In order to establish the presence of dispersive transport in dendrimer films, the scale invariance of traces obtained for the first generation dendrimer are considered. Plotted in Fig. 6.6 are transients measured for the G1 dendrimer at different biases. The upper panel shows the raw data of the traces, whereas in the lower panel, the traces are scaled to the transit time on the time axis and normalised to the current at 400 ns on the current axis.

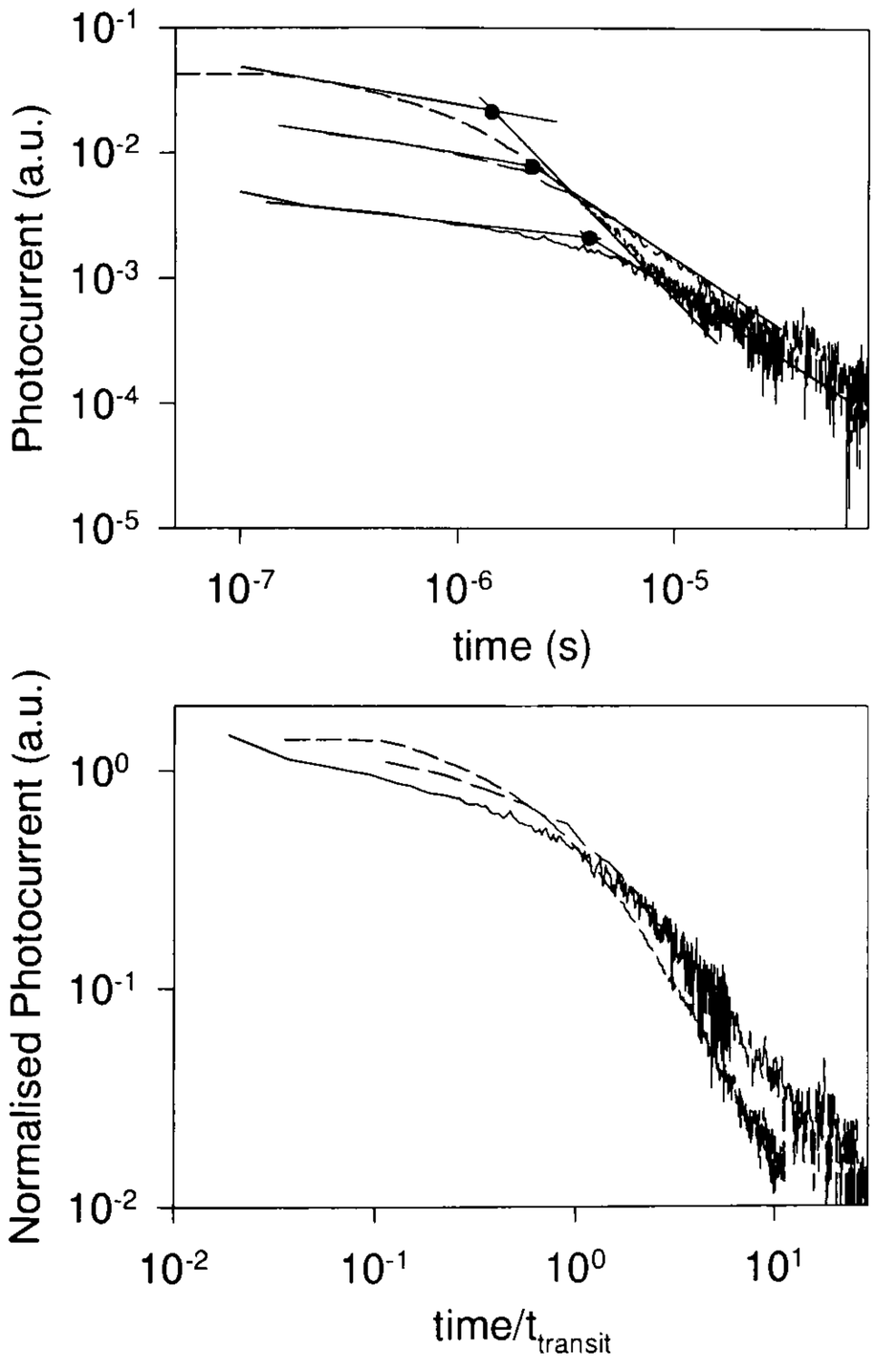

Fig. 6.6. *Upper panel: transient photocurrent for a G1 dendrimer film (300 nm) at fields of 0.2 MV/cm, 0.33 MV/cm and 0.47 MV/cm. The filled circles mark the transit time, which increases with increasing field. Lower panel: The same traces normalised to the current at 400 ns and scaled by the transit time.*

It is seen in Fig. 6.6 that the shapes of the photocurrent transients are independent of the applied field and when scaled to the transit time all traces overlay. This scaling behaviour has been studied extensively in, for example, amorphous As_2Se_3 [24] and in polymers [28]. The absence of a field-dependent broadening of the traces hence

demonstrates that the transport process is non-Gaussian in origin. In addition, having established the scale invariance, the overlap between traces measured at different fields may itself be used as a tool for estimating the transit time. In order to obtain the transit times, the data were smoothed by fitting a 5^{th} order polynomial to the measured data. This greatly reduced the number of data points and allowed an estimate of the transit time to be made by extrapolating the two power-law regions of the curve. An alternative method was to find the best fit of overlaid curves of the same generation with the aid of a computer program in order to determine the relative change in transit time. Both methods were found to yield equivalent results.

An interesting question is the effect of the dendrimer generation on the dispersion parameter α. A change in α with generation implies that the transients have different shapes depending on generation, but are invariant to changes in thickness or applied field. Fig. 6.7 shows the raw data of transients for the 4 generations normalised to the current at 400 ns and scaled by the transit time. Apparently, the curves do not overlap. This is made clearer in Fig. 6.8 where the polynomial fits to the raw data are plotted in the identical scaling.

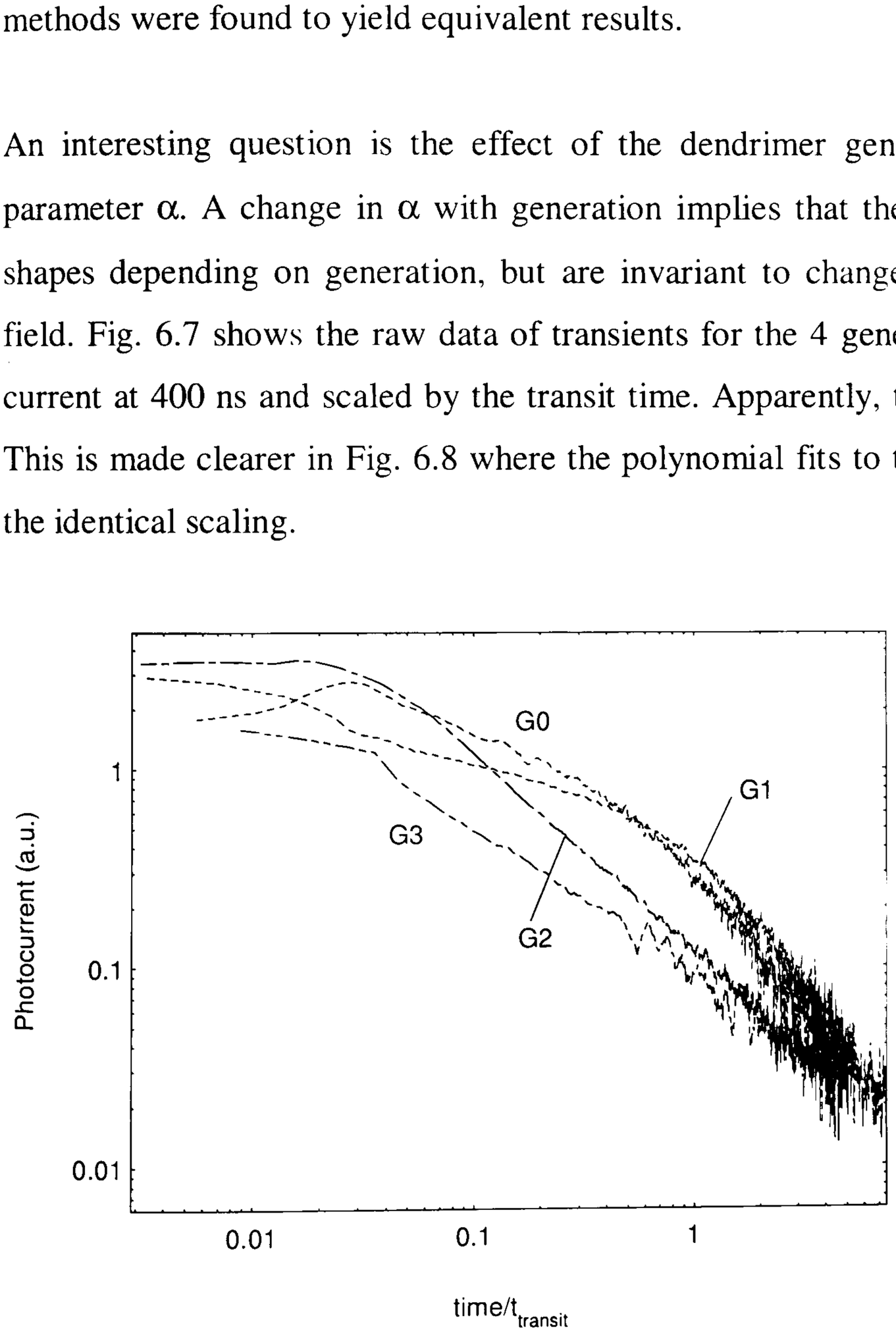

Fig. 6.7. *Photocurrent transients scaled to the transit time for all four generations.*

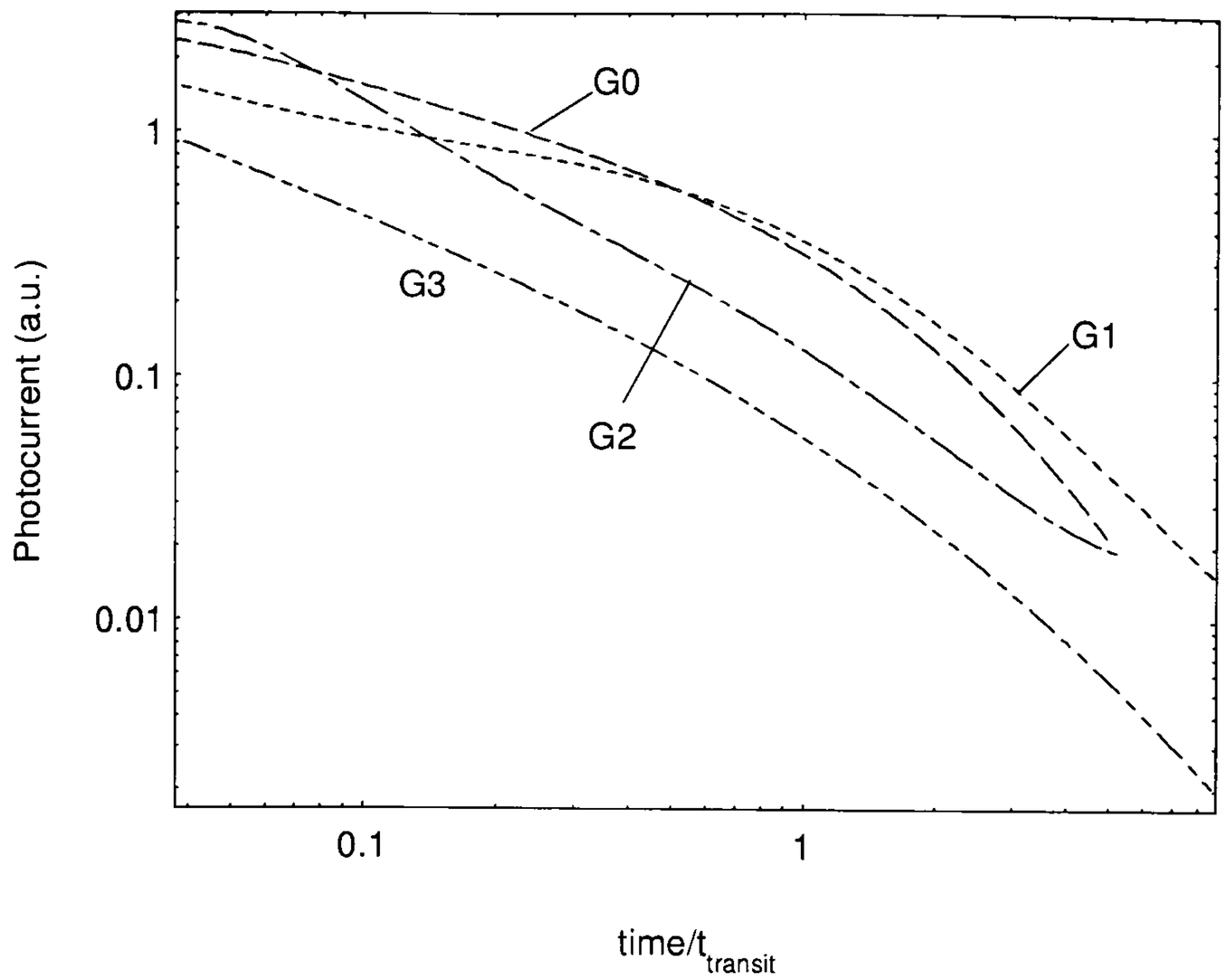

Fig. 6.8. *Photocurrent transients of A0 to A3 smoothed by fitting of a polynomial.*

Although the data is not sufficient to extrapolate any systematic correlation between the dispersion parameter α and the dendrimer generation, the disagreement between the curves demonstrates that α is indeed dependent on generation. The slope of the initial decay of the photocurrent appears to become somewhat stronger with increasing generation, which suggests that the dispersion parameter decreases with increasing generation. This would be consistent with an increase in structural disorder in the material.

To further investigate the presence of dispersive phenomena in the dendrimer films, we shall next look at the temporal evolution of the photocurrent in the first generation dendrimer as well as the scaling behaviour of the transit time with applied field. Fig. 6.9 shows two tangents fitted to the short and long time-scale evolution of the photocurrent. The exponents obtained from this fit indeed add up to -1.94, which is close to the sum of -2 suggested by equation (6.1). The corresponding value for α is hence approx. 0.64. In comparison, a value of 0.45 has been found for α in a soluble PPV derivative by Blom et al. [30]. However, their results were based on measurements of transient electroluminescence, where the interpretation of the data is greatly complicated due to the presence of two charge carriers. In contrast, Lebedev et al. [13] used a multiple trapping model to explain their observed photocurrents in a precursor PPV film.

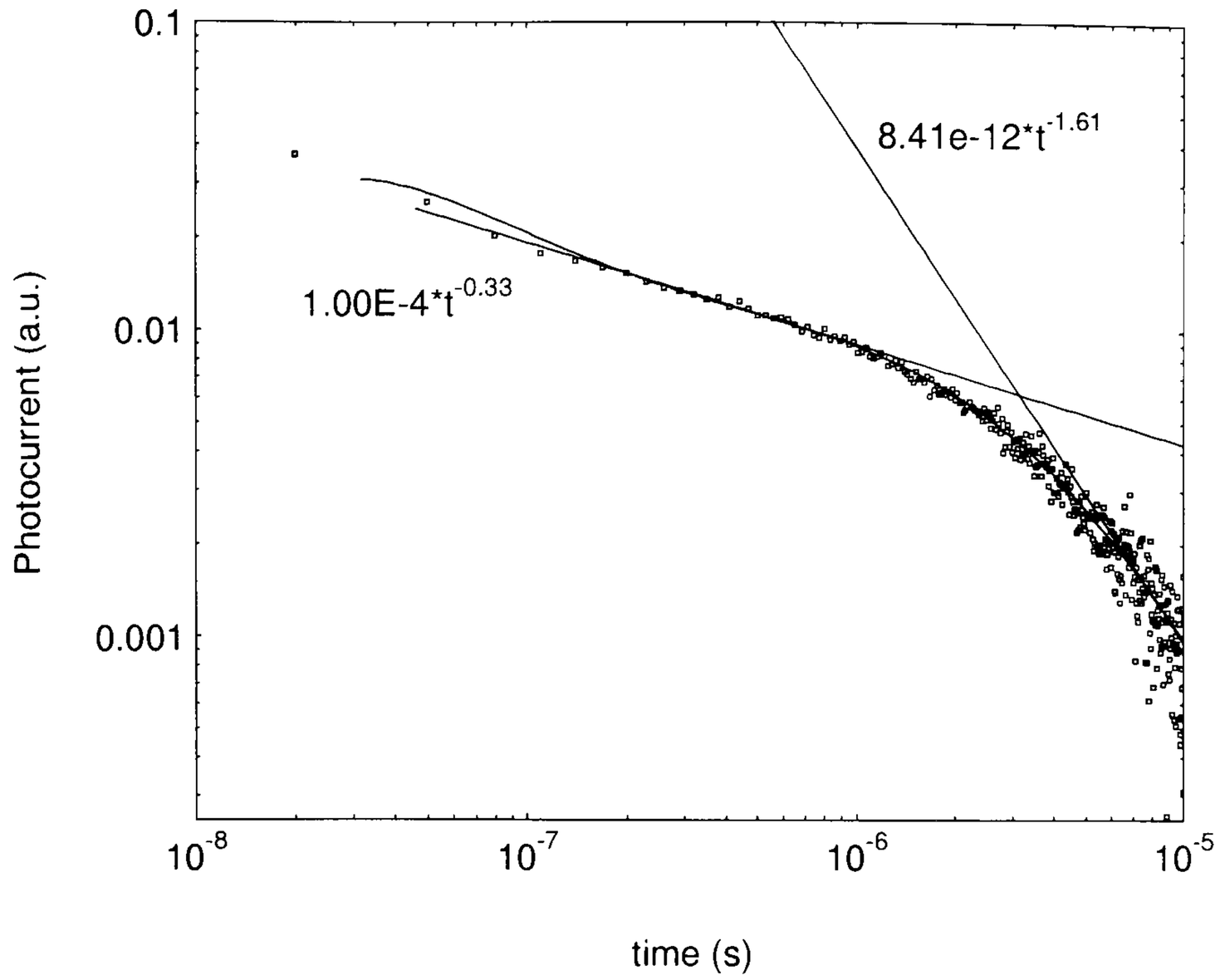

Fig. 6.9. *Transient photocurrent for first generation dendrimer with power-law fits.*

The transit time is also found to scale with the applied field according to a power-law as in equation (6.2). This scaling is shown in Fig. 6.10 and an exponent of between ~1.6 and 2.0 is found for $1/\alpha$. These two sets of data are consistent with a value for α of approx. $\alpha=0.6\pm0.05$.

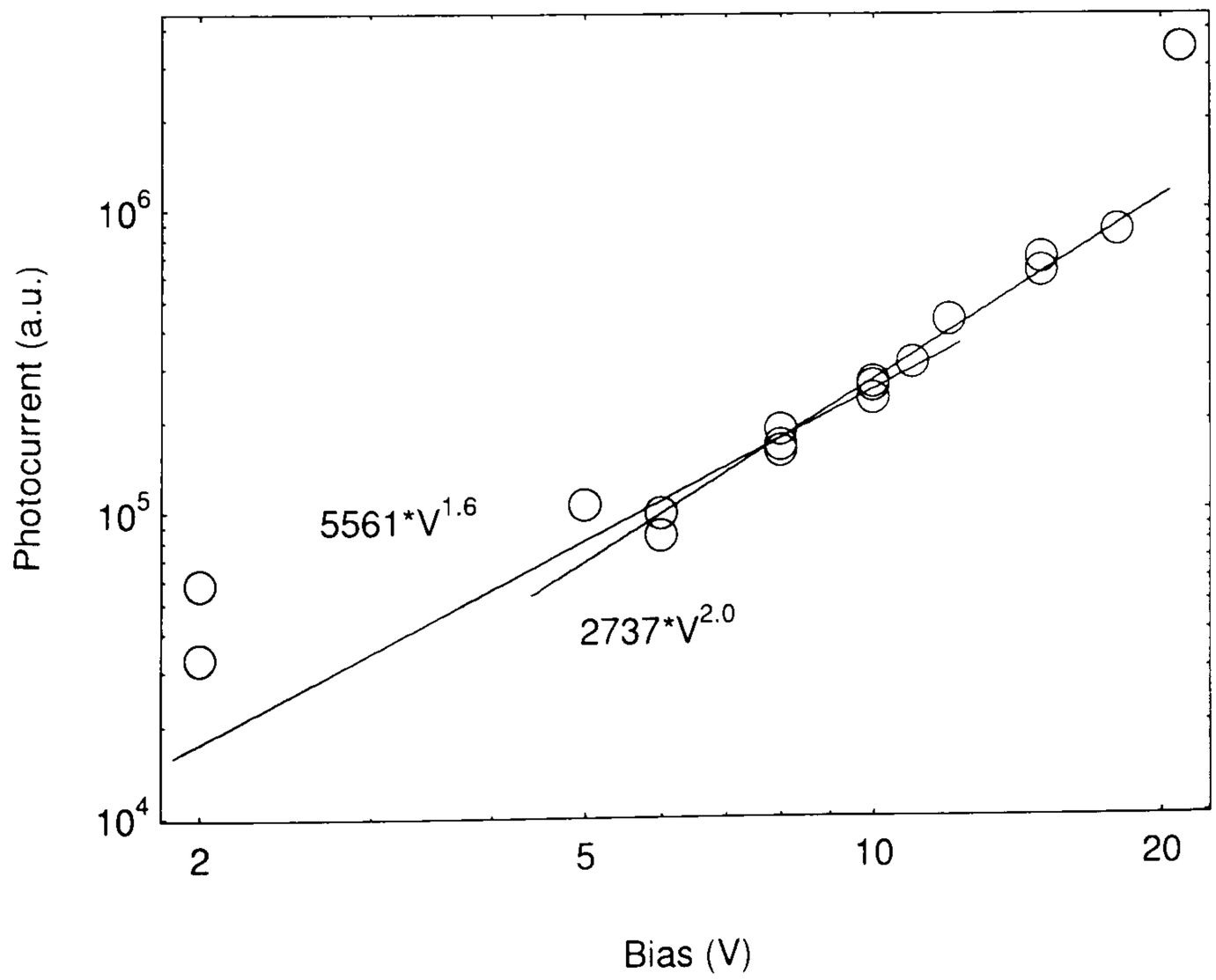

Fig. 6.10. *Scaling of the transit time with the applied bias in an Al film according to equation (6.2). The two lines mark the range of possible fits.*

No such agreement was observed for the other three generations, and in particular only the A1 measurements exhibited the same value for α before and after the transit time, whereas for the other generations the exponents of the power-law photocurrent decay did not add up to -2. The observation of the agreement between the decay parameter and the field scaling in the A1 dendrimer may hence be either coincidental or an indication of a narrow range of structural and disorder parameters over which the basic form of the stochastic transport model holds [37].

Finally, the mobility values for all generations were obtained at different fields from equation (6.3) and are plotted in Fig. 6.11. The results are quite remarkable. The dendrimer generation allows a direct control of the charge carrier mobility. It is seen that the mobility decreases by 2 orders of magnitude from G0 to G3. There is also an increase in mobility with field, which appears to get stronger with higher generation. It is presently not clear whether the main origin of the field dependence in these materials is due to the commonly observed pseudo Poole-Frenkel effect [6] or due to dispersion. From the experimental data obtained on the dendrimers it was not possible to distinguish unambiguously between the two functional dependencies of the mobility on the applied field. In the context of device models discussed in the previous chapter, both the power-law and the exponential form of the field-dependence yield a similar functional dependence over a limited range of field values. This may be sufficient to fit to the high-field behaviour of LEDs, which is the most relevant region. It should be noted that an exponential field dependence fitted to a power-law dependence leads to an overestimate of the mobility in the low-field region. This in turn could lead to an overestimate of the barrier height in the model.

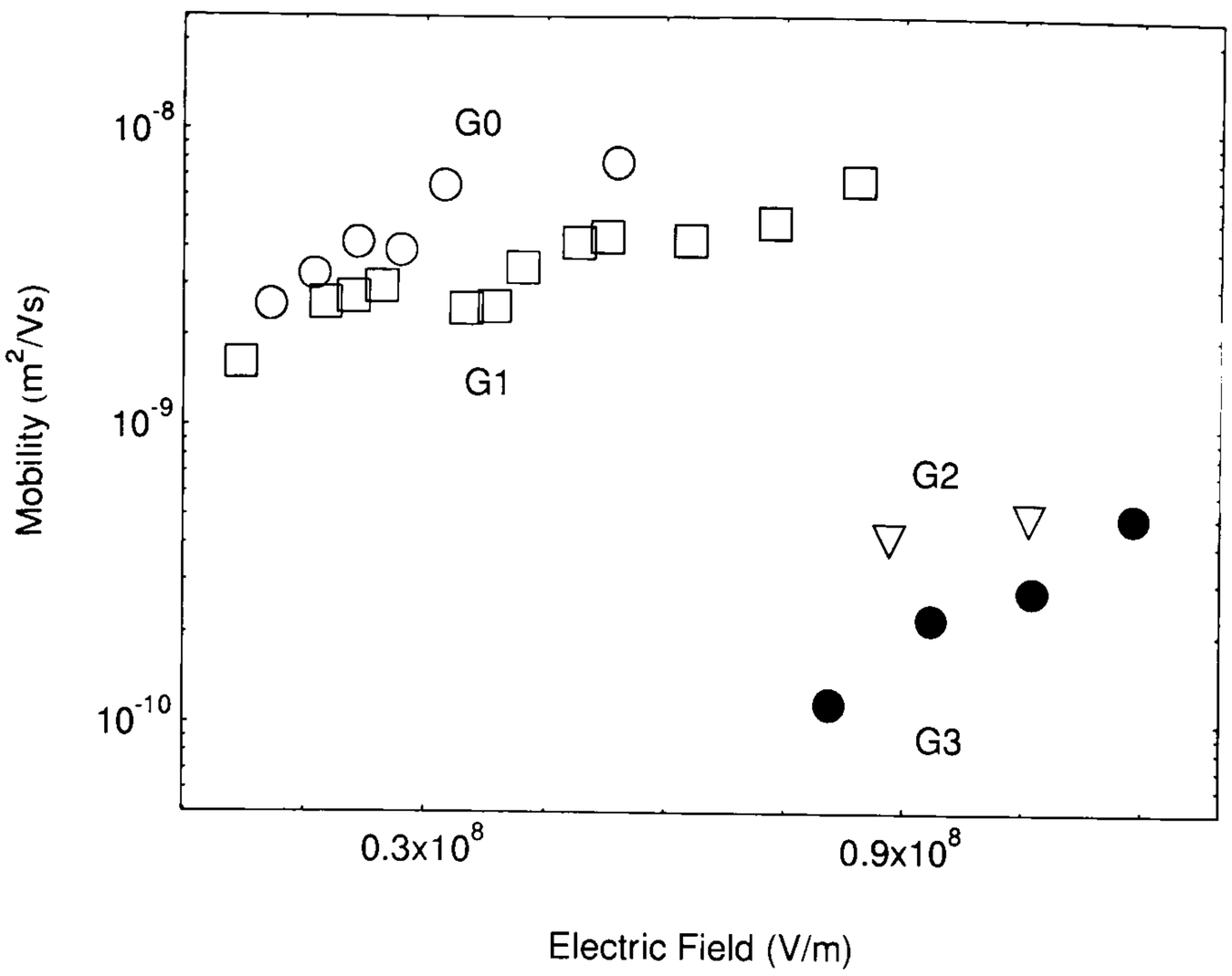

Fig. 6.11. *Change of mobility with dendrimer generation.*

6.3 Fitting current-voltage characteristics

Conjugated dendrimers provide model systems in which to study the microscopic nature of charge transport in organic semiconductors. The control of mobility discussed in the previous section can be used to test device models which describe the operation of polymer LEDs [9, 14, 39-42]. Good quality fits have previously been achieved with this model and mobility parameters determined in MEH-PPV devices were found to agree well with those obtained from TOF measurements on the identical structure at room temperature [14]. Fig. 6.12 shows the current-electric field characteristics of devices of different generations with ITO/PEDOT and aluminium electrodes. The lines in Fig. 6.12 show model fits to the data using the barrier height and the parameters μ_0 and E_0 as fitting parameters. The thickness of the device was taken to be the thickness of the dendrimer layer and the PEDOT hole-injecting layer was taken to be ohmic. Studies of the charging of capacitor structures in the configuration ITO/SiO_x/PEDOT/Al have shown that the device capacitance does not depend significantly on the PEDOT layer thickness [43]. This hence suggests that the charge carrier density in PEDOT is, to a first approximation, sufficient to provide metallic properties as an injecting electrode and hence zero field drop across the layer.

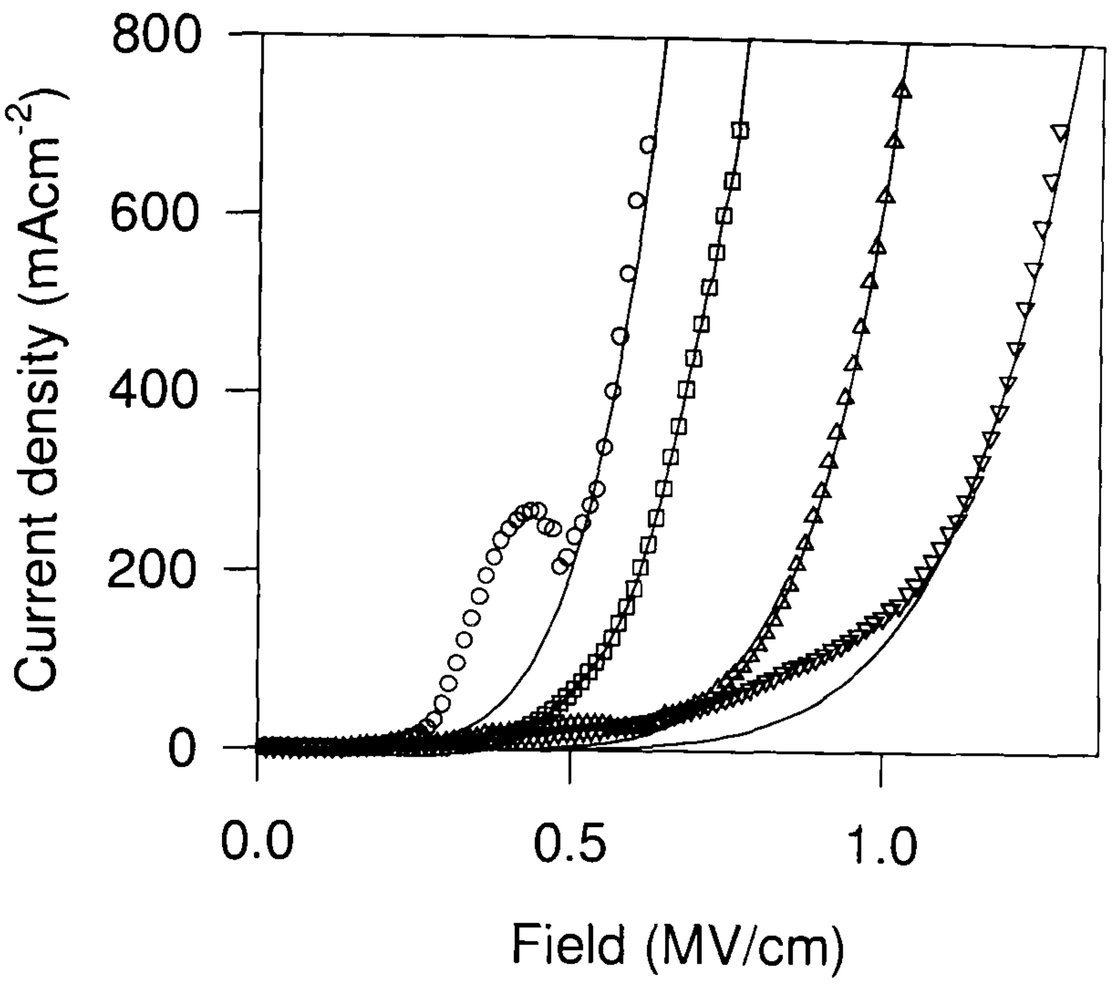

Fig. 6.12. *Measured IV characteristics of dendrimer LEDs (points) with model fits (lines).*

The fits qualitatively follow the shape of the current-voltage characteristics and quantitatively describe the measured current. At lower fields there are some deviations due to the influence of space charge on carrier injection, which is not incorporated into the model. There may also be some charge trapping and bulk polarisation effects which give rise to an increase in dark current with generation, as discussed in chapter 4. The fitting parameters are summarised in Table 6.1.

	G0	G1	G2	G3
Barrier / eV	.47	.48	.48	0.49
μ_0 / m^2/Vs	5.1×10^{-10}	3.4×10^{-10}	6.2×10^{-13}	5.5×10^{-13}
E_0 / V/m	7.3×10^{6}	9.6×10^{6}	2.1×10^{6}	3.3×10^{6}

Table 6.1. *Fitting parameters obtained by fitting to IV characteristics in Fig. 6.12.*

It is apparent from the values in Table 6.1 that the mobility parameters depend strongly on generation, with the mobility decreasing with increasing generation. In contrast, the barrier height is found to be unaffected by generation and approx. 0.48 eV, which is a reasonable value for hole injection into a green-blue emitter on a PEDOT layer [44]. As seen in Fig. 6.12, there is some discrepancy between the data and the fits and depending on the choice of fit the resulting mobility $\mu = \mu_{E=0} e^{\sqrt{\frac{E}{E_0}}}$ was found to vary by approx. a factor of 2. However, the overall decrease in mobility predicted by the model is in the order of 2 orders of magnitude, which is a significant result and can explain the large increase in operating field observed in the IV characteristics.

The value of the barrier height obtained in the fits is effectively independent of generation, which suggests that injection takes place into the core of the dendrimer. The electronic properties of the core hence remain unaffected by further branching of the dendrons. In order to confirm this conclusion, cyclic voltammetry was performed on solutions of the dendrimer of different generations by M. Frampton in Oxford. Previous measurements on related compounds showed little effect of the dendrimer generation on ionisation of solutions [45]. Cyclic voltammetry was performed on dendrimer solutions of concentration 0.1 mol/l in tetrabutylammonium hexafluorphosphate (1.0 mol/l) in dichloromethane. The traces for the oxidation are shown in Fig. 6.13.

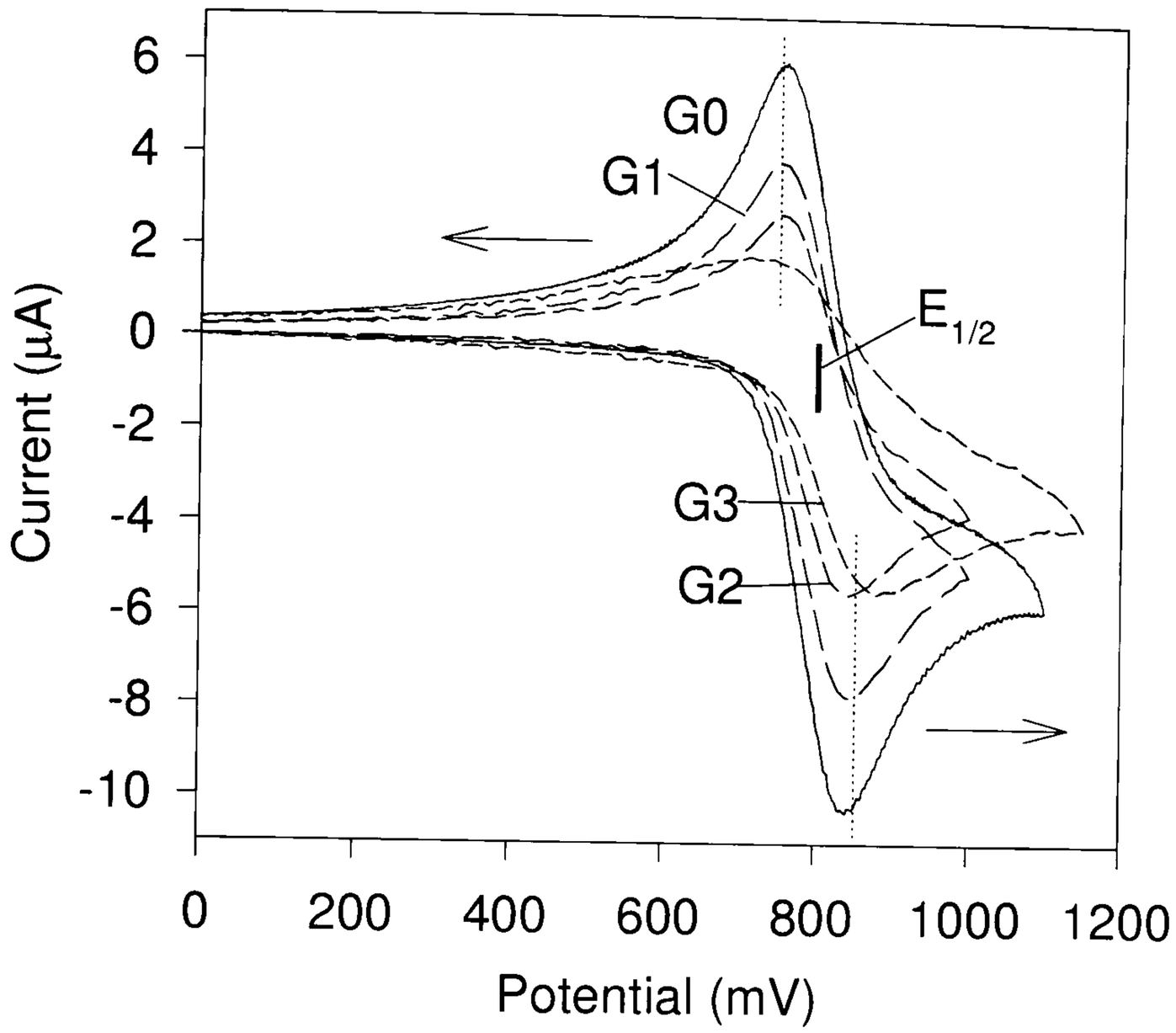

Fig. 6.13. *Cyclic voltammetry (oxidation) of dendrimer solutions. (Courtesy of M. Frampton).*

Remarkably, the oxidation traces show very little dependence on generation. The turning points of the cycles are observed at 750 mV and 850 mV with the $E_{1/2}$ values at 800 mV and are found to be virtually independent of generation, which demonstrates that the energy levels of the chromophore remain unaffected by the dendrons. The results obtained from cyclic voltammetry are hence in excellent agreement with the model calculations on dendrimer LEDs. The change in hysteresis with generation may be related to the reduction in actual concentration of the chromophore units with increasing number of stilbene dendrons. By using ferrocene as a standard, absolute values for the HOMO levels of the dendrimers were determined and found to be in the range 5.4 to 5.7 eV [46]. This value is comparable to that expected from the results of the model. The ionisation potential of PEDOT is known to be approx. 5.0 eV [44], hence according to the model the HOMO level of the dendrimers should lie between 5.4 eV and 5.5 eV. There is a significant error in the order of 0.3 eV associated with the electrochemical analysis and the literature values of the ionisation potential of the

ferrocene reference [46], so the value for the dendrimer HOMO level should be treated as a rough approximation. It is also conceivable that interfacial barrier effects between the PEDOT and the dendrimer give rise to a modification of the effective barrier in LEDs [47].

6.4 Discussion

In the two previous sections two independent methods were applied to measure the charge carrier mobility in dendrimer films. For both measurements it is found that the mobility decreases by two orders of magnitude as the generation is increased from zeroeth to third and the hydrodynamic dendrimer radius doubles. Fig. 6.14 shows the mobility values found by the TOF technique plotted together with the mobility parameters obtained in the previous section.

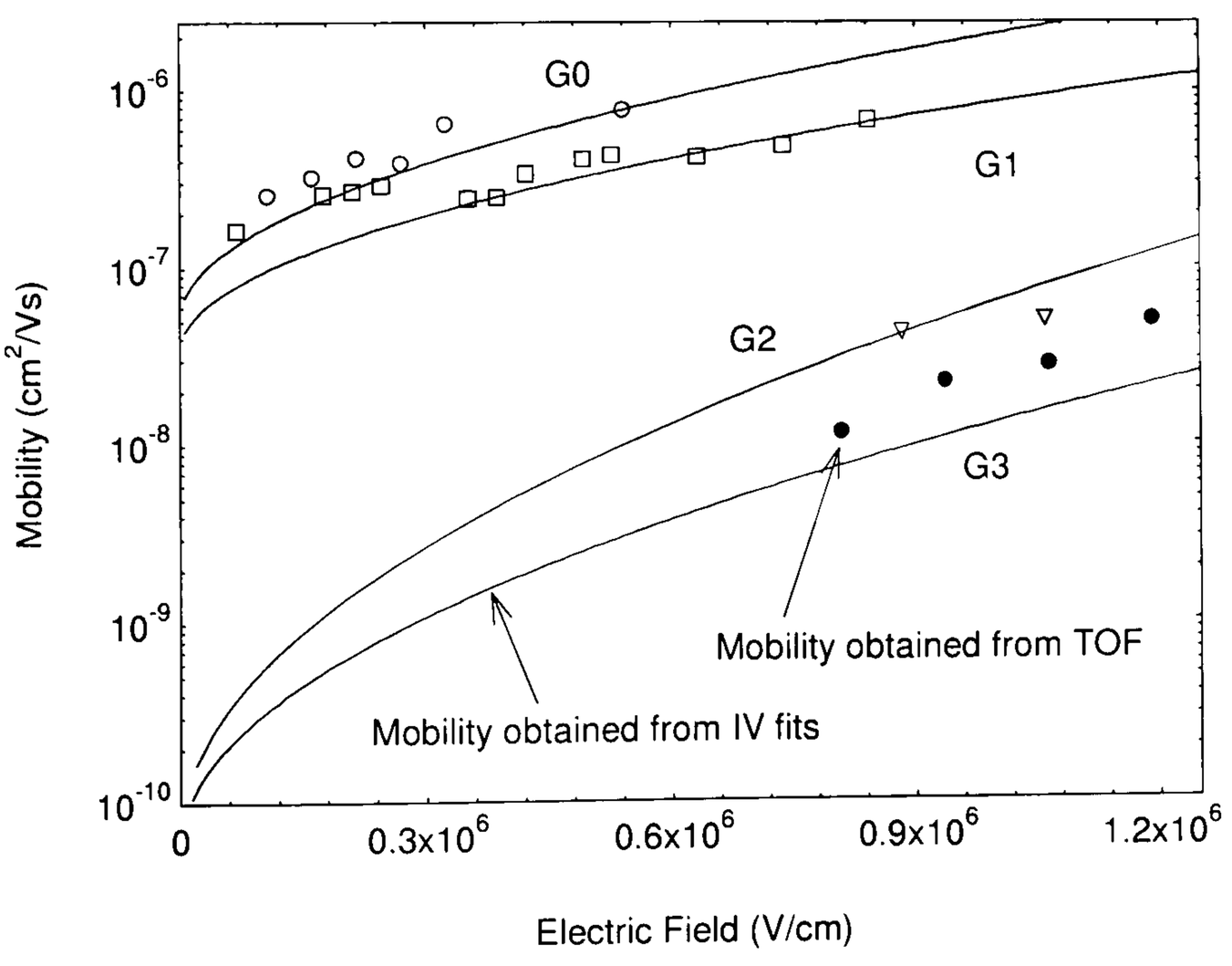

Fig. 6.14. *Mobility values obtained through TOF and IV characteristics.*

The correspondence between these two sets of results is striking. The agreement between the mobility values obtained through TOF and those obtained through the IV characteristics demonstrates the validity of both approaches to determine the mobility. Previously, only few attempts have been made to correlate TOF data with device data [14-15], and the comparisons have been limited in the range of mobility covered by the

system. In the present case of the dendrimers, the mobility is varied by the dendrimer generation over two orders of magnitude and correspondence between the two sets of data is demonstrated. It is also seen that the field dependence E_0 of the mobility decreases with increasing generation both in the IV fits and in the TOF data. This is in accord with previous experimental observations and recent theoretical predictions. TOF measurements have shown that whereas the mobility of MEH-PPV [14] is much smaller than that of polyfluorene [35], the field dependence in the latter is much less pronounced than in MEH-PPV (corresponding to a much larger value for E_0 in polyfluorene). Yu et al. have related this large variation in field dependence via a geometric model to an effective spring constant of the system [8]. Clearly, a more ordered system with a greater level of rigidity has less geometric flexibility upon application of a field and will hence exhibit a less pronounced dependence on field. This is consistent with the present observation that the increase in dendrimer size results in a decrease of the core to dendron concentration ratio and hence a greater geometric core flexibility at higher generations. It appears that in the case of the dendrimers, the mobility is determined by structural rather than energetic disorder [7, 23]. However, it should be noted that this distinction is not clear cut. Whereas a systematic comparison of soluble PPV derivatives recently found the origin for the difference in mobility in varying degrees of energetic disorder [7], a former study on one of these materials led to the conclusion that the dispersive transport is governed by structural rather than energetic effects [30, 48-49]. The relative contributions of inter- and intrachain transport have a strong influence on the transport properties [28] and it is possible that some confusion arises from the trade-off between these effects. In dendrimers, interchain transport does not play a significant role due to the limited dimensions of the macromolecule. The microscopic transport is hence mostly governed by the structural properties of the material.

Hopping mobilities have been shown to have a dependence on site separation 2R according to $\mu \propto R^2 e^{\frac{2R}{R_0}}$ due to the nature of field assisted polaron hopping [50-52]. This was initially investigated in TOF measurements on films of molecularly doped PVK, where a concentration dependence of the mobility could be explained [50]. The functional form derives from the overlap integral of polarons on a lattice site with adjacent sites [51-52]. The hydrodynamic radii of the dendrimers are used as estimates

of the separation between chromophores. This is most likely an overestimate of the distance between adjacent sites, as the lower generation dendrimers are not space filling. However, the packing in three dimensions in films is not clear but it is evident from the absorption data that the dendrimers do not π-stack and are hence not in a fully planar configuration. The scaling of the mobility with dendrimer radius is shown in Fig. 6.15 together with the inverse quantum efficiency as discussed in Fig. 4.22.

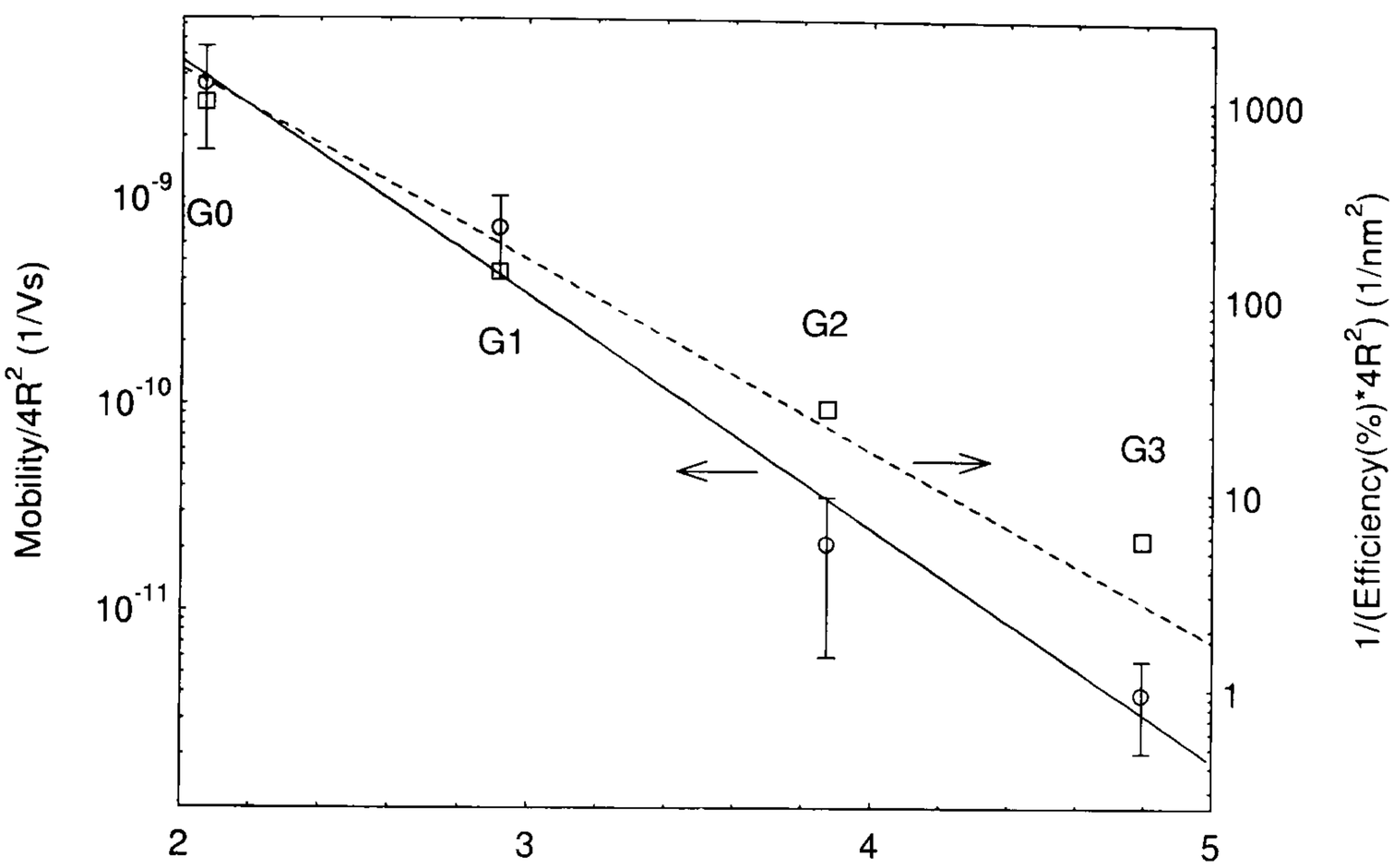

Fig. 6.15. *Plot of mobility and inverse quantum efficiency against average dendrimer-dendrimer separation following [50].*

A value of 0.39 nm is found here for R_0 from the mobility measurements, which compares to 0.5 nm for trinitrofluoreneone poly-vinylcarbazole complexes [50]. The inverse of the external quantum efficiency scales with the dendrimer separation similarly to the mobility, giving a value for R_0 of 0.45 nm. This correlation between the decrease in mobility and the increase in efficiency suggests that the increase in efficiency with increasing generation is due primarily to a reduction in hole mobilitiy. In the case of unbalanced transport the device efficiency is approximately proportional to the ratio of photon flux to majority charge carrier current [53]. In the approximation of an ohmic hole injecting contact, the current is proportional to the mobility and hence the inverse quantum efficiency gives a value proportional to the hole mobility. The data in Fig. 6.15 hence suggest that the increase in quantum efficiency is mainly due to the decrease in hole mobility. An implication of this is that the electron mobility decreases

less strongly with dendrimer radius than the hole mobility. This can be understood in terms of electrons being more readily trapped on the chromophores than holes, as has previously been suggested [12]. The device operation may be understood in terms of mobile holes meeting up with trapped electrons. Triphenylamine is a commonly used hole transporting material, so it is not surprising that the amine centred dendrimers studied here exhibit hole transporting properties. An alternative explanation is that the hole current in the device is transport limited whereas the electron current is injection limited. Decreasing the mobility of the majority carrier clearly increases the operating field of the LED as seen in Fig. 6.12, which should give rise to a greater electron injection current over the aluminium/LUMO barrier. In combination with this, more balanced electron and hole currents will also result in a change in the position of the recombination zone [54], with the zone moving away from the quenching metal electrode [55] as the generation is increased. The dependence of efficiency on generation demonstrates an intrinsic asymmetry between electron and hole transport, which is in contrast to recent proposals that the electron and hole mobility in MEH-PPV are virtually identical [11]. However, TOF measurements generally exhibit an asymmetry between electron and hole transport (e.g. [35]), so this assignment remains an open issue.

By controlled variation of a device parameter, namely the mobility, a further way of exploring the parameter space of physical models for LEDs has been demonstrated, alongside the barrier height [41], intense electrical operation [43], oxidation [40] and temperature [40]. Due to the high level of reproducibility in the synthesis of dendrimers resulting from the exact molecular weight, these results are not affected by batch to batch variations of molecular weight, which is a considerable problem when trying to model the transport properties of conjugated polymers [9].

6.5 Conclusions

In this chapter, a direct correspondence to the effect of dendrimer generation on the emission properties of dendrimer films has been observed in the charge transport properties. Using both TOF and a device model, it was found that the dendrimer generation allows a microscopic control of the mobility by 2 orders of magnitude

whereby maintaining the basic electronic properties of the material. The increase in device efficiency with generation is found to be directly related to the change in mobility. Charge transport is identified as being due to hopping and found to be strongly dispersive. The observed properties are thought to be due to structural disorder rather than energetic disorder.

Besides being of interest in bilayer devices, where it is desirable to be able to balance the electron and hole transport in the respective layer by matching the mobilities, the control of mobility is also a useful tool for studying the physics of LEDs and the validity of device models. By varying the mobility, a further parameter has been explored to test the model discussed, yielding good agreement between experiment and theory.

References

[1] J. H. Burroughes, D. D. C. Bradley, A. R. Brown, R. N. Marks, K. Mackay, R. H. Friend, P. L. Burn, and A. B. Holmes, Nature **347,** 539 (1990)

[2] C. W. Tang, and S. A. Vanslyke, Appl. Phys. Lett. **51,** 913-915 (1987)

[3] R. H. Friend, R. W. Gymer, A. B. Holmes, J. H. Burroughes, R. N. Marks, C. Taliani, D. D. C. Bradley, D. A. Dos Santos, J. L. Brédas, M. Lögdlund, and W. R. Salaneck, Nature **397**, 121 (1999)

[4] H. Sirringhaus, P. J. Brown, R. H. Friend, M. M. Nielsen, K. Bechgaard, B. M. W. LangeveldVoss, A. J. H. Spiering, R. A. J. Janssen, E. W. Meijer, P. Herwig, and D. M. deLeeuw, Nature **401,** 685 (1999)

[5] R. Österbacka, C. P. An, X. M. Jiang, and Z. V. Vardeny, Science **287**, 839 (2000)

[6] H. Bässler, Phys. Stat. Sol. B **175,** 15 (1993)

[7] H. C. F. Martens, P. W. M. Blom, and H. F. M. Schoo, Phys. Rev. B **61,** 7489 (2000)

[8] Z. G. Yu, D. L. Smith, A. Saxena, R. L. Martin, and A. R. Bishop, Phys. Rev. Lett. **84**, 721 (2000)

[9] B. K. Crone, I. H. Campbell, P. S. Davids, D. L. Smith, C. J. Neef, and J. P. Ferraris, J. Appl. Phys. **86,** 5767 (1999)

[10] D. D. C. Bradley, (1993)

[11] L. Bozano, S. A. Carter, J. C. Scott, G. G. Malliaras, and P. J. Brock, Appl. Phys. Lett. **74**, 1132 (1999)

[12] P. W. M. Blom, M. J. M. Dejong, and J. J. M. Vleggaar, Appl. Phys. Lett. **68,** 3308 (1996)

[13] E. Lebedev, Th. Dittrich, V. Petrova-Koch, S. Karg and W. Brütting, Appl. Phys. Lett. **71**, 2686 (1997)

[14] I. H. Campbell, D. L. Smith, C. J. Neef, and J. P. Ferraris, Appl. Phys. Lett. **74,** 2809 (1999)

[15] S. Forero, P. H. Nguyen, W. Brutting, and M. Schwoerer, Phys. Chem. Chem. Phys. **1,** 1769 (1999)

[16] E. M. Conwell in : H. S. Nalwa (Ed.) Handbook of Organic Conductive Molecules and Polymers: Vol. 4. Conductive Polymers: Transport, Photophysics and Applications (1997)

[17] J. R. Haynes and W. Shockley, Phys. Rev. **81**, 835 (1951)

[18] R. Lawrence and A. F. Gibson, Proc. Phys. Soc. B **65**, 994 (1952)

[19] M. Redecker, H. Bassler, and H. H. Horhold, J. Phys. Chem. B **101,** 7398 (1997)

[20] J. Scherbel, P. H. Nguyen, G. Paasch, W. Brutting, and M. Schwoerer, J. Appl. Phys. **83,** 5045 (1998)

[21] W. Brutting, E. Buchwald, G. Egerer, M. Meier, K. Zuleeg, and M. Schwoerer, Synth. Met. **84,** 677 (1997)

[22] M. Pope and C. E. Swenberg, Electronic Processes in Organic Crystals, Oxford University Press (1982)

[23] H. Scher and M. Lax, Phys. Rev. B **7**, 4491 (1975)

[24] H. Scher, E. W. Montroll, Phys. Rev. B **12**, 2455 (1975)

[25] P. M. Borsenberger, L. T. Pautmeier, and H. Bassler, Phys. Rev. B **48,** 3066 (1993)

[26] H. Meyer, D. Haarer, H. Naarmann, and H. H. Hörhold, Phys. Rev. B **52**, 2587 (1995)

[27] M. Gailberger, and H. Bässler, Phys. Rev. B **44**, 8643 (1991)

[28] D. Hertel, H. Bässler, U. Scherf, H. H. Hörhold, J. Chem. Phys. **110**, 9214 (1999)

[29] J. Bondkowski, I. Bleyl, D. Haarer, and D. Adam, Chem. Phys. Lett. **283,** 207 (1998)

[30] P. W. M. Blom and M. Vissenberg, Phys. Rev. Lett. **80,** 3819 (1998)

[31] J. Mort and G. Pfister in : J. Mort and G. Pfister (Eds.), Electronic Properties of Polymers, John Wiley & Son, New York 1982

[32] C. Im, Diploma Thesis, University of Marburg (1999)

[33] E. Müller-Horsche, D. Haarer, and H. Scher, Phys. Rev. B **35**, 1273 (1987)

[34] B. Reimer and H. Bässler, Phys. Status Solidi A **51**, 445 (1979)

[35] M. Redecker, D. D. C. Bradley, M. Inbasekaran, and E. P. Woo, Appl. Phys. Lett. **73,** 1565 (1998)

[36] R. Richert, L. Pautmeier, and H. Bassler, Phys. Rev. Lett. **63,** 547 (1989)

[37] P. M. Borsenberger, L. T. Pautmeier, and H. Bassler, Phys. Rev. B **46,** 12145 (1992)

[38] P. M. Borsenberger, R. Richert, and H. Bassler, Phys. Rev. B **47,** 4289 (1993)

[39] P. S. Davids, I. H. Campbell, and D. L. Smith, J. Appl. Phys. **82**, 6319 (1997)

[40] J. M. Lupton and I. D. W. Samuel, J. Phys. D: Appl. Phys **32**, 2973 (1999)

[41] I. H. Campbell, P. S. Davids, D. L. Smith, N. N. Barashkov, and J. P. Ferraris, Appl. Phys. Lett. **72,** 1863 (1998)

[42] I. H. Campbell, D. L. Smith, C. J. Neef, and J. P. Ferraris, Appl. Phys. Lett. **75**, 841 (1999)

[43] K. Book, University of Marburg, personal communication (1999)

[44] T. M. Brown, J. S. Kim, R. H. Friend, F. Cacialli, R. Daik, and W. J. Feast, Appl. Phys. Lett. **75,** 1679 (1999)

[45] P. L. Burn, M. Halim, J. N. G. Pillow, and I. D. W. Samuel, SPIE **3797**, 66 (1999)

[46] M. J. Frampton, University of Oxford, personal communication (2000) ; M. J. Frampton, R. Beavington, J. M. Lupton, I. D. W. Samuel and P. L. Burn, Synth. Met. (in Press)

[47] P. K. H. Ho, J. S. Kim, J. H. Burroughes, H. Becker, S. F. Y. Li, T. M. Brown, F. Cacialli, and R. H. Friend, Nature **404,** 481 (2000)

[48] M. Vissenberg and P. W. M. Blom, Synth. Met. **102,** 1053 (1999)

[49] H. C. F. Martens, H. B. Brom, and P. W. M. Blom, Phys. Rev. B **60,** R8489 (1999)

[50] W. Gill, J. Appl. Phys. **43,** 5033 (1972)

[51] M. H. Cohen, J. Non-cryst. Sol. **4,** 391 (1970)

[52] T. Holstein, Ann. Phys. **8**, 325 (1959)

[53] H. Bassler, Y. H. Tak, D. V. Khramtchenkov, and V. R. Nikitenko, Synth. Met. **91,** 173 (1997)

[54] H. Vestweber, H. Bassler, J. Gruner, and R. H. Friend, Chem. Phys. Lett. **256,** 37 (1996)

[55] H. Becker, S. E. Burns, and R. H. Friend, Phys. Rev. B **56,** 1893 (1997)

7.

Electrophosphorescence from a conjugated dendrimer blend device

Acknowledgements

This work was carried out in collaboration with P. Burn, R. Beavington and M. Frampton of the Dyson Perrins Laboratory, Oxford. The materials used in the investigation were synthesised in Oxford. The cyclic voltammetry discussed below was measured by M. Frampton in Oxford. I am grateful to P. Burn for helpful discussions.

7.1 Introduction

The operation of organic light-emitting diodes (LEDs) is based on the injection of oppositely charged carriers, which pair to form excitons. Analysis of spin statistics associated with the injected charge carriers suggests that only 25% of the excitons formed in the device are in the singlet state [1-2]. Although it has been proposed that the barrier of 25% for singlet excitons may be exceeded under certain circumstances, it is known to be far from 100% [3-5]. The singlet excited state can decay radiatively with the emitted light generally in the visible range. The remaining excitations are in the triplet state and for most organic materials, these triplet excitations decay non-radiatively as radiative transitions are forbidden due to the molecular symmetry. The possibility to extract luminescence from the triplet excited state has recently been demonstrated by inclusion of phosphorescent guest metallic complexes in host matrices [2-3, 6-10]. However, blends of materials are sensitive to the concentration of the guest in the host. Even at relatively low concentrations the guest can phase separate leading to aggregation and luminescence quenching.

To avoid phase separation it is necessary for the two components to have similar "surface functional" groups. Dendrimers offer two advantages over common materials when attempting to fabricate blends of two materials. Firstly, different cores can be surrounded by the same dendrons and surface groups, rendering different molecules with identical surface functional properties. Secondly, the use of dendritic structures attached to luminescent chromophores has been shown to inhibit luminescence quenching. Therefore a good technique for avoiding aggregation of a guest chromophore within a host matrix is to incorporate it within a dendritic structure.

It has previously been demonstrated with a new class of conjugated dendrimers consisting of stilbene dendrons and luminescent chromophores that the emission colour in solution is determined by the chromophore at the "core" and is independent of the dendron architecture [11-14]. In this work an extension of this concept to the formation of a phosphorescent dendrimer is described, which provides a channel for triplet excitations to decay radiatively. A dendrimer host is used in the LED, which is then doped with a phosphorescent dendrimer guest to allow triplet harvesting. The common

dendrons of the singlet emitting host dendrimer and the triplet emitting guest dendrimer ensure excellent phase compatibility and uniform miscibility. In the following, the harvesting of triplet excitations from an organic LED based on either a blue or a green emitting host dendrimer is demonstrated by doping the host with a red emitting platinum porphyrin based dendrimer. The materials A3 and B3 discussed in Chapter 4 are used as the host materials. The guest dopant, labelled P1, is shown in Fig. 7.1. The platinum porphyrin dendrimer is a novel compound, but it is conceptionally related to previously studied free-base porphyrin dendrimers [11].

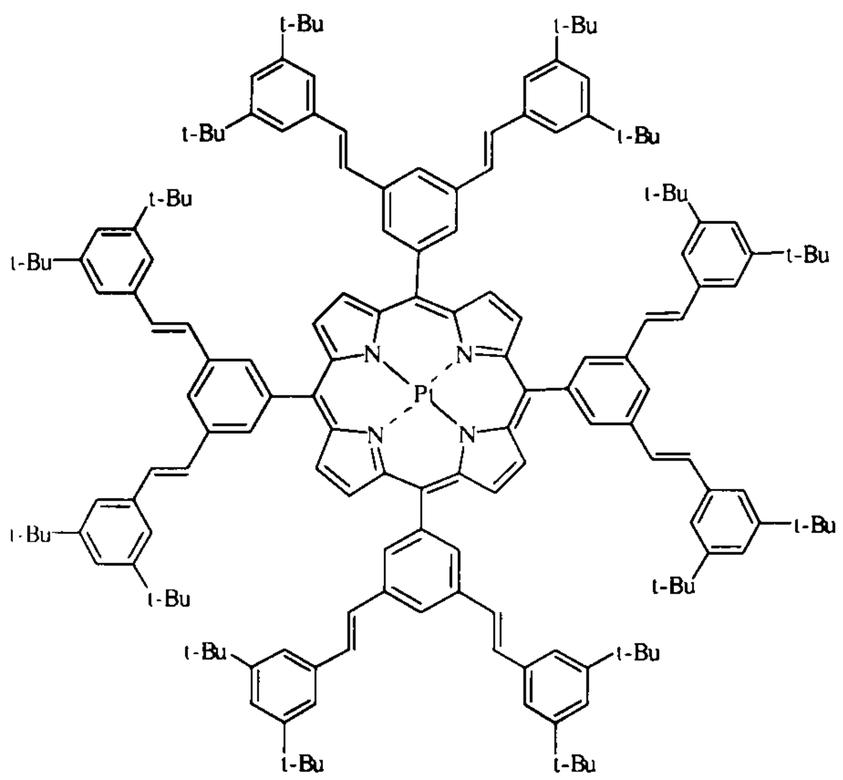

Fig. 7.1. *Structure of the first generation platinum porphyrin dendrimer P1.*

In this chapter the unique properties of devices containing blends of a fluorescent and a phosphorescent dendrimer are considered. The luminescence spectra are investigated in order to establish the absence of singlet excitation energy transfer from the fluorescent host to the phosphorescent guest. The remarkable difference between EL and PL spectra of the blends can be explained by trapping of charge carriers on the guest, which is investigated by cyclic voltammetry. Pulsed operation of the LEDs is found to give rise to a substantial spectral modification depending on the pulse period, which can be attributed to quenching of long lived triplet excitations. This is investigated further using a simple kinetic model.

7.2 Emission and absorption spectra

Films of PtPOR/host blends were formed by spin-coating THF solutions of the two dendrimers (10 mg/ml) in a w/w ratio of host to guest of 10:1 corresponding to a molar

ratio of approximately 3:1. The PL spectra were measured both on an ISA Fluoromax Fluorimeter and on an ISA Spectrum One CCD spectrometer. EL spectra were measured with the CCD spectrometer.

7.2.1 A3:P1 host:guest blends

The chapter begins by discussing the absorption and luminescence properties of blends of materials A3 and P1. The absorption spectra of the materials are shown in Fig. 7.2. The absorption is characterised by two main bands, which are due to electronic transitions in the chromophores and the stilbene dendrons. The *meta*-linkage of the dendrons to the emissive central units limits electron delocalisation, so that the electronic properties of the material can to a first approximation be expressed as a linear superposition of the properties of the stilbene and core chromophores. For A3 and P1 the stilbene moieties are found to give rise to an absorption peak at 320 nm. The core gives rise to an additional absorption at 420 nm for A3, whilst for P1 absorption bands are observed at 420 nm, 514 nm and 544 nm and correspond to the Soret and Q-bands of the PtPOR.

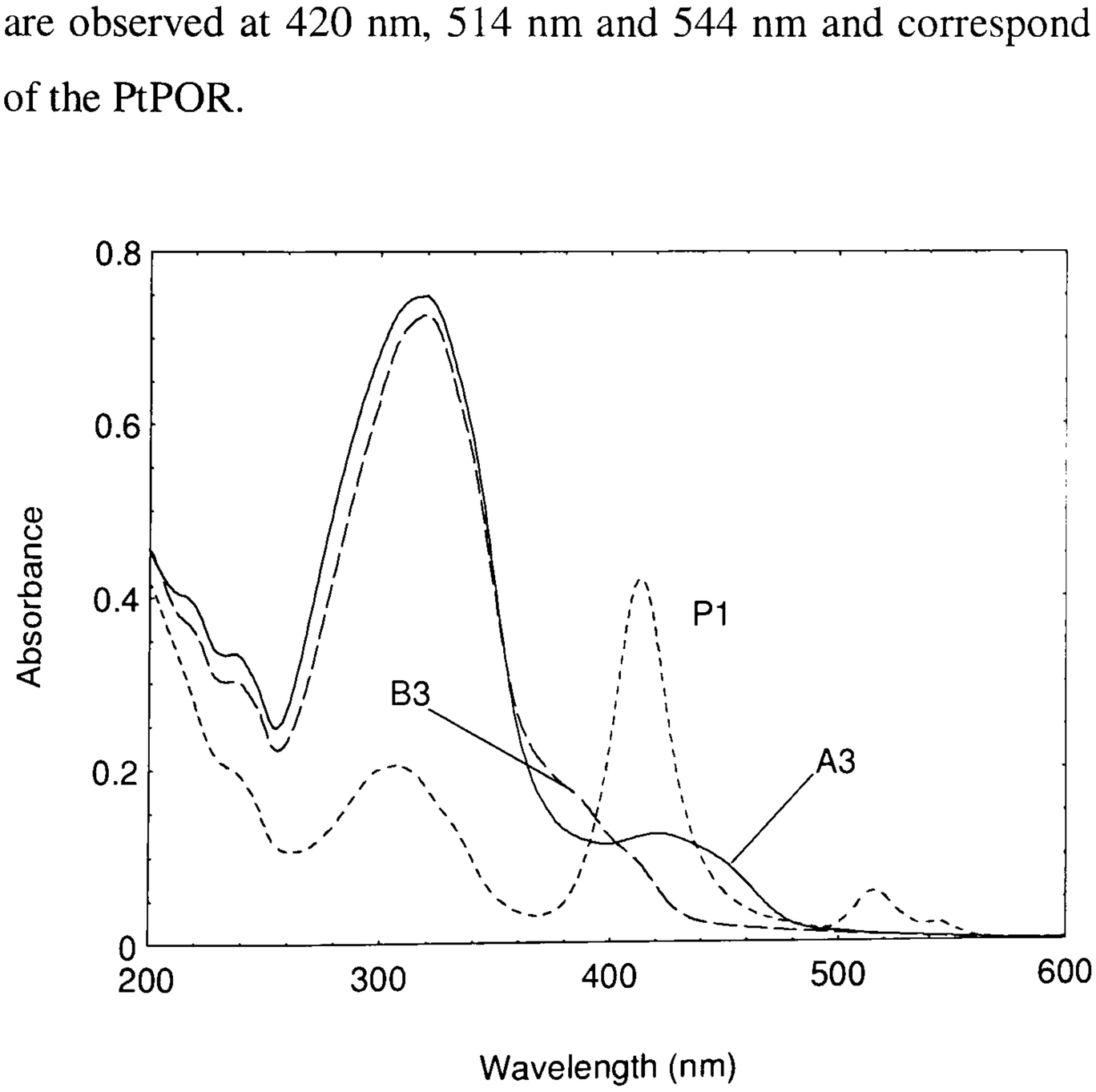

Fig. 7.2. *Absorption spectra of neat dendrimer films A3, B3 and P1.*

Fig. 7.3 shows PL and EL spectra of blends of the materials under continuous excitation. To begin with, the PL results are discussed. Upon optical excitation, the emission of A3 is in the green and peaks at 495 nm and the guest dendrimer P1 emits in the red to near IR with peaks at 662 nm and 737 nm. The emission of the host dendrimer A3 is attributed to fluorescence, whereas the emission of the guest P1 is believed to be due to phosphorescence, as platinum porphyrins are known as phosphors [3, 6]. For the A3:P1 blend the host emission is much stronger than the guest emission. In order to investigate the energy transfer from host to guest in the blends, films of the blends were excited at 320 nm, which corresponds to the stilbene dendron absorption of the two materials, and 420 nm which coincides with the peak absorption of the guest. It was found that the host can be efficiently excited in the dendron absorption band, indicating energy transfer from the dendrons to the core. For blend A3:P1, the guest and host core absorption bands both peak at 420 nm. As is seen in Fig. 7.3a, the guest emission is reduced upon excitation in the dendron band at 320 nm with respect to excitation in the core absorption bands of A3 and P1 at 420 nm. As there are more stilbene units in the host than in the guest and the optical density of the host is hence greater at 320 nm than that of the guest, this indicates that there is little singlet energy transfer between the host and the guest. The large contribution of host emission in the blend A3:P1 upon excitation in the dendron band at 320 nm suggests that Förster type energy transfer from the host to the guest plays little role, if any.

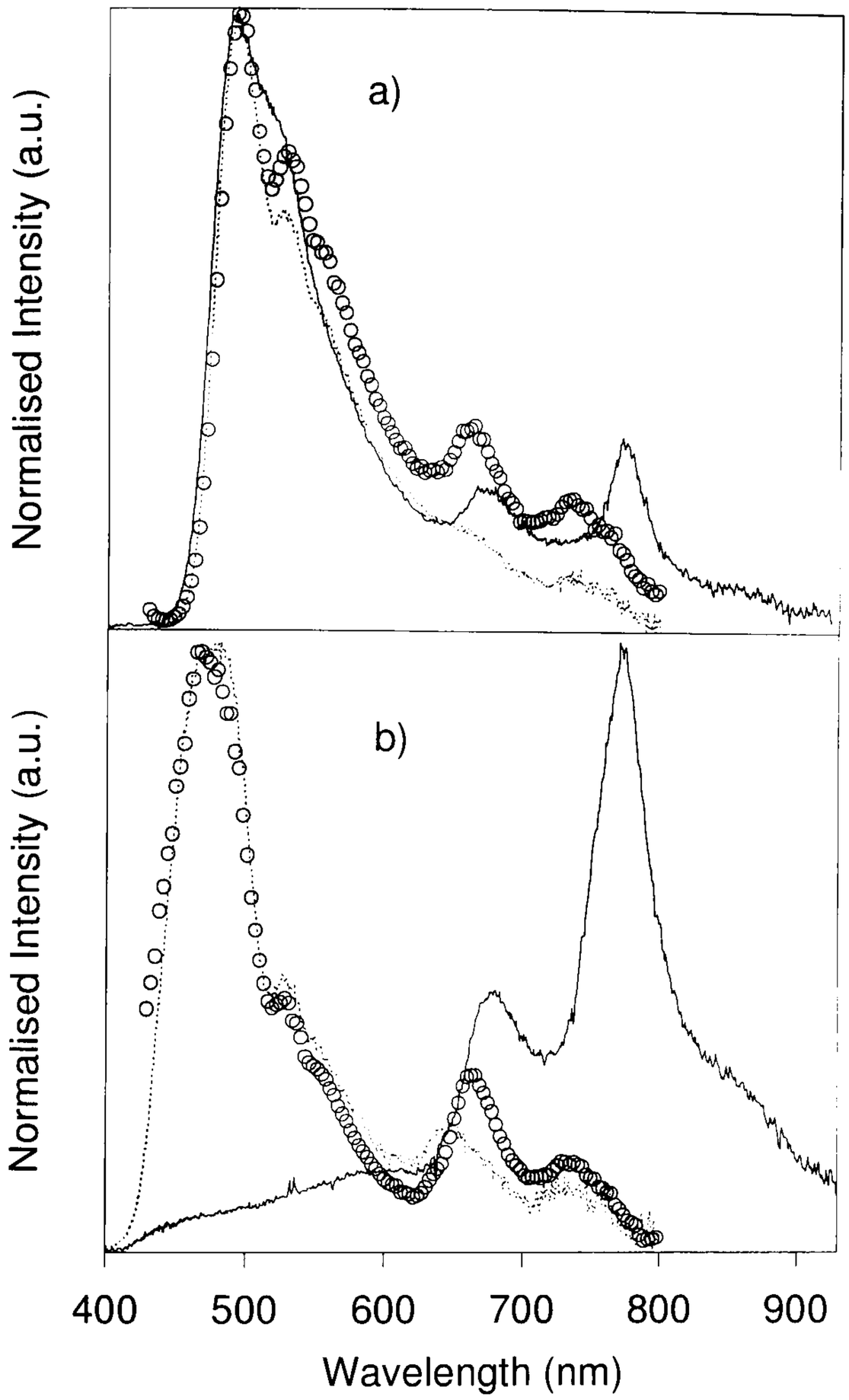

Fig. 7.3. *Luminescence of films of dendrimers A3 and B3 doped with guest dendrimer P1 in both EL and PL. a) Blend of A3:P1, PL excited at 320 nm (·····), PL excited at 420 nm (○) and EL (——). b) Blend of B3:P1, PL excited at 320 nm (·····), PL excited at 420 nm (○) and EL (——). Devices were fabricated in the configuration ITO/PEDOT/blend/Aluminium.*

This was further investigated by considering the PL excitation (PLE) of the blend. The PLE spectra of the blend A3:P1 are shown in Fig. 7.4 with detection at 530 nm (host emission) and 660 nm (guest emission). The PLE data provide clear evidence that radiative energy transfer does not play a significant role in the A3:P1 blend. Upon

detection in the A3 emission band at 530 nm, the absorption of the host is clearly resolved. However, upon detection in the P1 emission band at 660 nm, there is no trace of the host absorption in the PLE spectrum, as excitations are not transferred from the host to the guest. In this case, only a narrow feature at 420 nm is observed, corresponding to the absorption of the guest. Due to the close proximity of the A3 and P1 absorption bands as seen in Fig. 7.2, the A3 excitation spectrum appears to peak slightly offset to the red at 440 nm. This implies that excitation in the region of 420 nm results also in strong excitation of the guest, dramatically reducing the host excitation efficiency in this region. In the P1 PLE spectrum, the P1 Q-band is also clearly resolved.

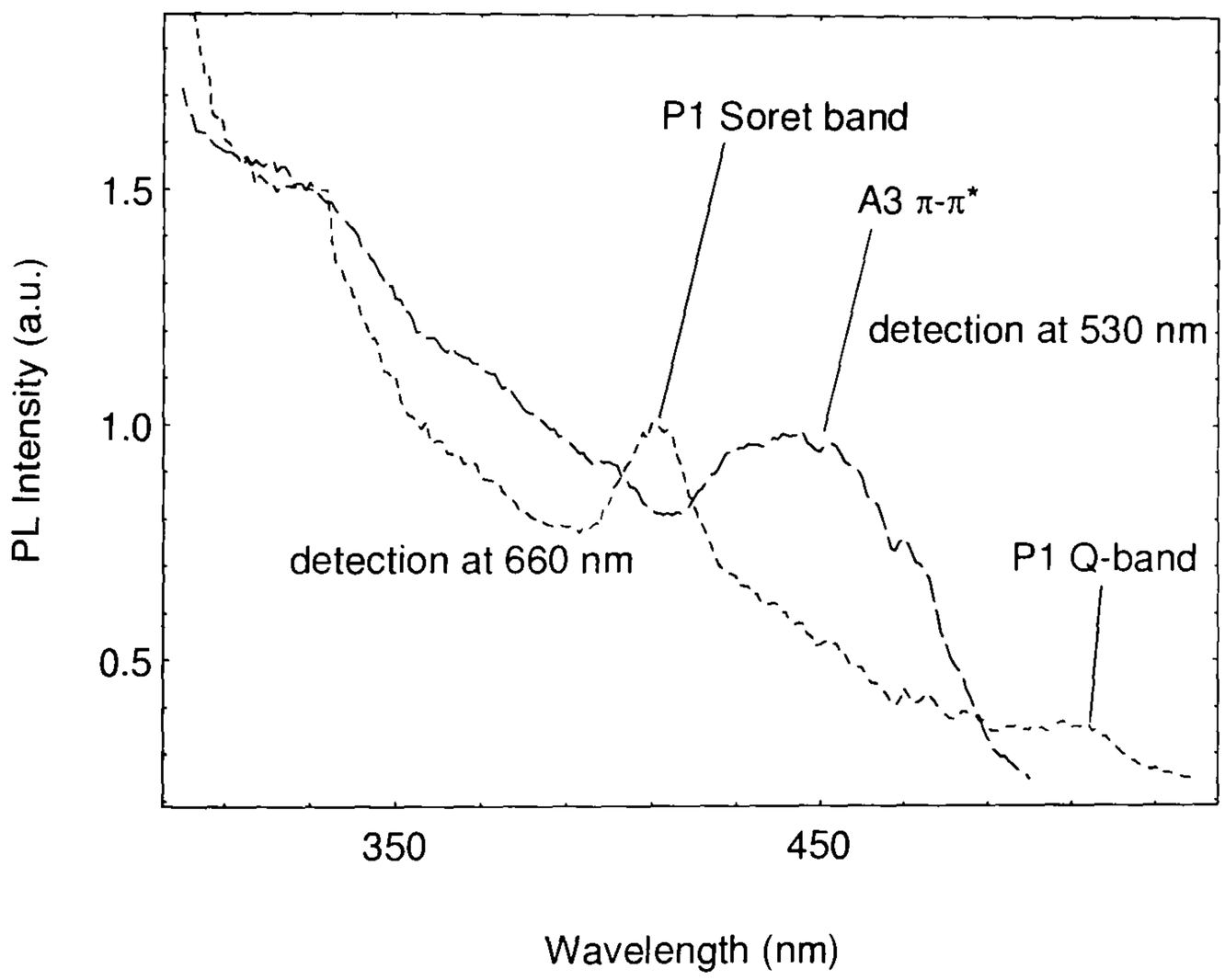

Fig. 7.4. *PLE spectra of blend A3:P1.*

7.2.2 B3:P1 host:guest blends

As for materials A3 and P1, dendrimer B3 exhibits an absorption peak at 320 nm corresponding to the stilbene dendrons, which can be seen in Fig. 7.2. The core of the dendrimer B3 gives rise to a further absorption at 370 nm. The PL results are shown in the lower panel of Fig. 7.3. Upon optical excitation, the emission is in the blue and peaks at 470 nm. As before, the host emission is much stronger than the guest emission. For the blend B3:P1 the reduction in guest emission with excitation at 320 nm is not as pronounced as for A3:P1. However, as the emission band of B3 overlaps the absorption

band of P1, one would expect to observe energy transfer from the host to the guest. The PLE measurements shown in Fig. 7.5 demonstrate the absence of energy transfer. As before, the P1 Soret and Q-bands are clearly resolved. Despite the overlap of B3 emission and P1 absorption in this case, excitation in the B3 absorption band does still not result in any significant emission from P1. As before, the absorption of P1 at 420 nm results in a reduction in the excitation spectrum upon detection of the host emission.

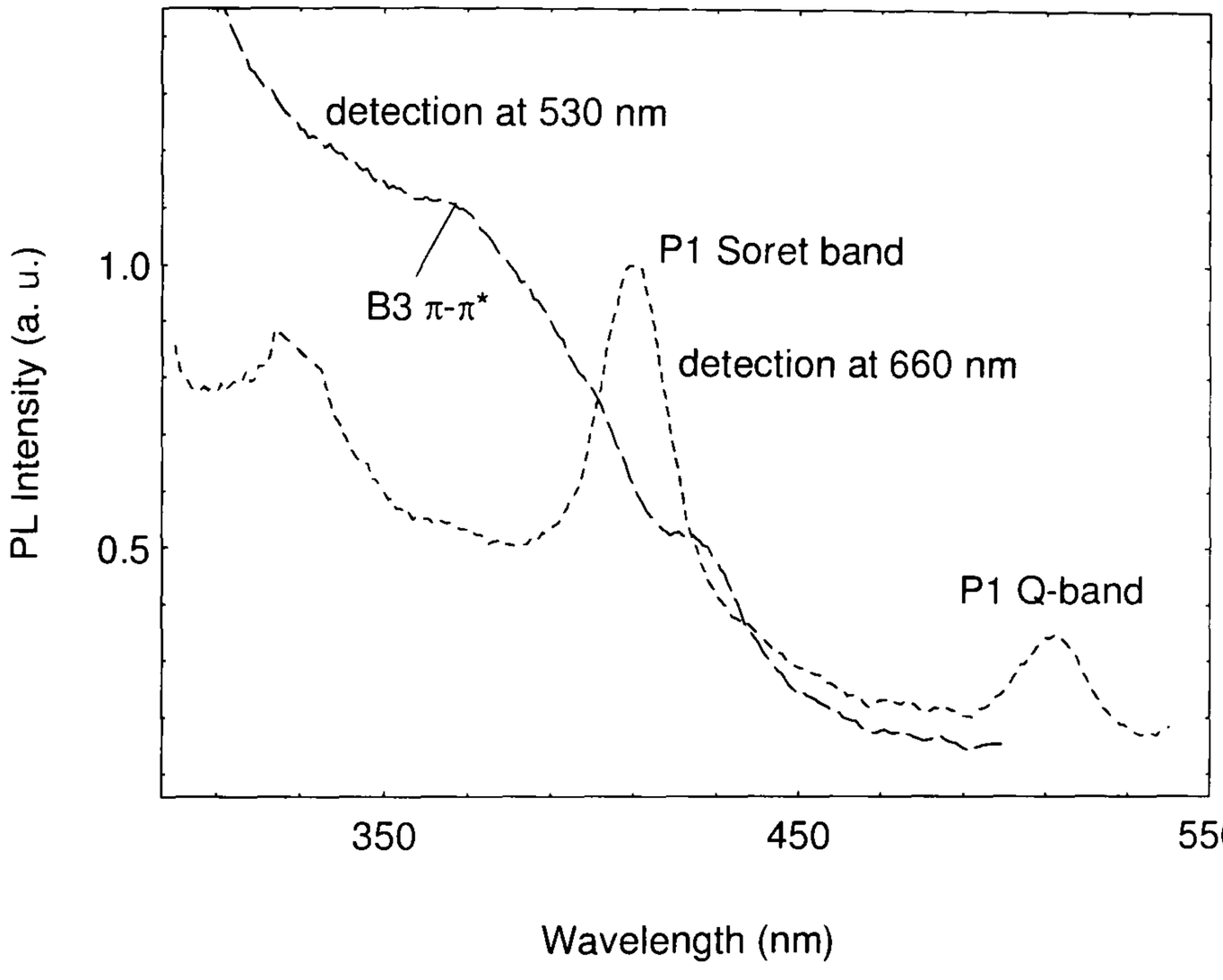

Fig. 7.5. *PLE spectra of films of blend A3:P1.*

From the large contribution of host emission in blend B3:P1 upon excitation in the common stilbene dendron band at 320 nm it is concluded that singlet exciton energy transfer from the host to the guest does not occur in these blends. Finally, in all PL spectra an emission "maximum" is observed close to 520 nm. The local minimum associated with this feature coincides with the first Q-absorption band of the guest dopant P1. This feature is therefore assigned to a proportion of the host PL being re-absorbed by the guest dendrimer.

7.3 Charge trapping

The most striking result of Fig. 7.3 is the large difference between EL spectra of the blend B3:P1 compared to the PL spectra. In contrast to the PL, in EL the guest emission

is much stronger than the host emission. For the A3:P1 blend, the same host emission is observed in EL as in PL, but the guest emission is increased in EL, particularly towards the red. This difference between the EL and PL spectra can be rationalised by considering the relative HOMO and LUMO energies of the host and the guest, which were determined by cyclic voltammetry. The relative offsets in energy levels between the hosts A3 and B3 and the guest dendrimer P1 are summarised in Table 7.1.

	HOMO level	LUMO level
Offset B3 to P1	0.1 eV	0.7 eV
Offset A3 to P1	0.4 eV	0.8 eV

Table 7.1. *Relative offsets of energy levels of guest and host dendrimers (courtesy of M. Frampton).*

The HOMO energies of P1 and B3 are similar with a difference of only 0.1 eV. In contrast there is an offset of approximately 0.7 eV in their relative LUMO energies with dendrimer P1 being more easily reduced. This indicates that the guest dendrimer P1 will be a trap for electrons in the blend with host B3 whereas the holes will not be trapped preferentially on either material as the difference in the HOMO levels is within the order of the thermal energy. Therefore, as the electrons are trapped on the guest and the holes are dispersed throughout the blend, the majority of the emission will occur from the guest P1. The fact that efficient emission from the guest in blend B3:P1 is observed is remarkable since from the analysis of the PL Förster transfer is not effective.

In contrast, for the A3:P1 blend, electrochemistry indicates that the two components would be expected to trap different charged species. Dendrimer A3 is more easily oxidised by about 0.4 eV compared to the guest P1, whilst the guest is more easily reduced by about 0.8 eV. This means that the guest will act as a trap of electrons, whereas the host A3 will trap holes. The probability of an exciton being formed on either A3 or P1 will hence be closer to the ratio of the two materials in the blend as the charge carriers are not preferentially located on either a guest or host site. As a consequence the EL and PL spectra are more similar for the blend A3:P1. The trapping processes are summarised in a schematic energy level diagram in Fig. 7.6.

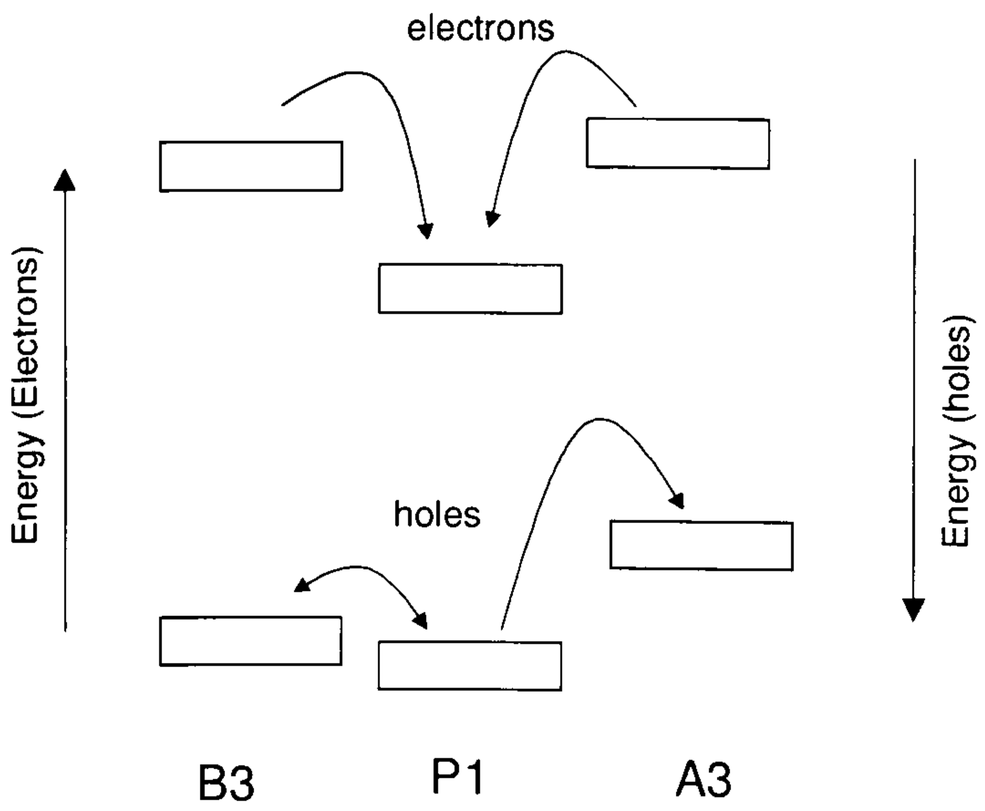

Fig. 7.6. *Schematic energy level diagram showing trapping of electrons on dendrimer P1 in both blends. In blend A3:P1, holes are trapped on A3, whereas in blend B3:P1 holes are not preferentially trapped on either material.*

There is another significant difference between the EL and PL spectra which is the positions of the peaks in the range 600 to 800 nm. In PL these are observed at 662 nm and 737 nm for both A3:P1 and B3:P1. In EL the peaks of the two blends are at 675 nm and 772 nm. This suggests that there is a difference in the light emitting state or its environment. This substantial shift in emission spectrum could be a result of the porphyrin charging under electrical excitation, giving rise to a change in energy levels and a change in molecular geometry. It should be noted that there is a significant difference between the EL spectra reported here and those found in previous studies of platinum porphyrin compounds. Without the use of the dendrimer architecture, platinum porphyrin compounds have been found to show an emission maximum at 650 nm and mostly do not display the lower energy peak observed here [3, 6]. In the present case, the lower energy emission is stronger than the higher energy peak. However, the guest concentrations used here are much greater than those in previously described devices, which is bound to influence the emission spectrum and may give rise to an increase in the red emission. Also, the effect of charge carriers on the emission in EL may be stronger in these devices due to the higher guest concentration. It is also found that the feature at 520 nm observed in the PL of the blends is not seen in the EL.

7.4 Pulsed Device Operation

A further remarkable consequence of combined fluorescence and phosphorescence devices is a strong dependence of the emission spectrum on excitation density. In the following, a novel method of controlling the emission colour is demonstrated by exploiting the large difference in the lifetime of excitations on the guest and the host. The phosphorescence lifetime for platinum octaethylporphyrin has previously been estimated at around 70 μs [3], although this value appears to be strongly dependent on the environment of the molecule. Baldo et al. reported a decrease in lifetime from approx. 40 μs to 10 μs with increasing excitation density [6] and a similar lifetime is expected for P1, whereas the singlet emission lifetime of the host is of the order of 1 ns. Changing the driving conditions and the duty cycle should hence give rise to different excited state populations and control the level of interactions between long lived excitations, which gives rise to emission quenching. This allows a tuning of the relative emission intensity of host to guest.

Fig. 7.7 demonstrates this effect for both host materials for pulses of 100 ns duration. As the driving pulse period (inverse repetition rate) is increased from 300 ns to 20 μs, the porphyrin emission increases relative to that of the host dendrimer, as is seen in Fig. 7.7a for dendrimer A3 and in Fig. 7.7b for dendrimer B3.

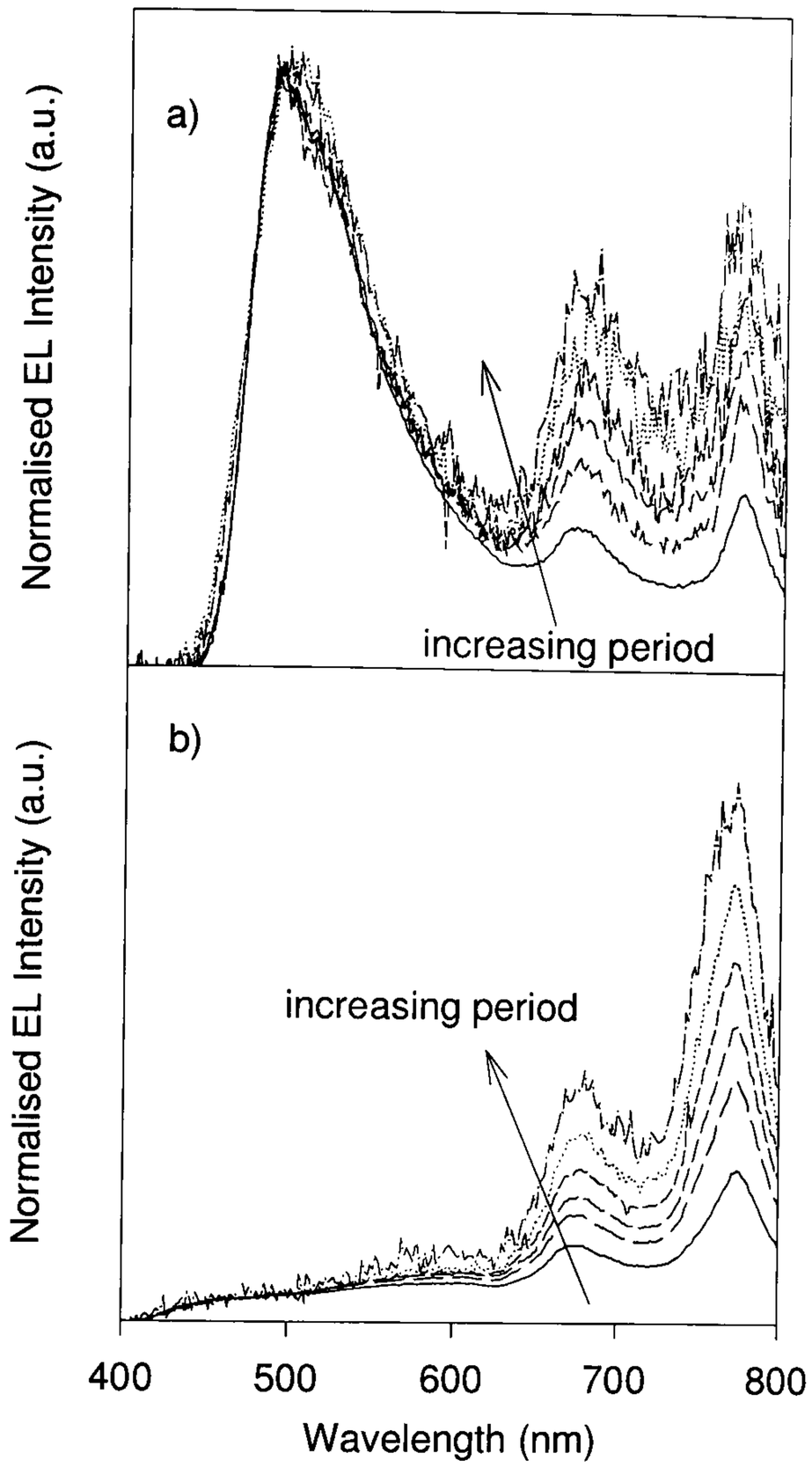

Fig. 7.7. *EL spectra of blend devices under pulsed operation. a) Device with blend A3:P1 at 18 V pulses of 100 ns duration over periods of 300 ns (lowest curve), 600 ns, 1 μs, 2 μs, 5 μs and 20 μs (upper most curve). b) Device with blend B3:P1 at 24 V pulses of 100 ns duration over periods of 300 ns (lowest curve), 600 ns, 1 μs, 2 μs, 5 μs and 20 μs (upper most curve).*

For longer periods the emission is unchanged with a change in period, as is seen in Fig. 8 for EL spectra of an A3:P1 blend device driven with 10 μs pulses at periods of 50 μs and 300 μs. There is no difference between the two spectra, other than a decrease in signal to noise ratio for the spectrum with the longer pulse period, which suggests that the long lived excited state population has decayed over a time scale of the order of 50 μs. A similar behaviour is also observed for A3 blend devices.

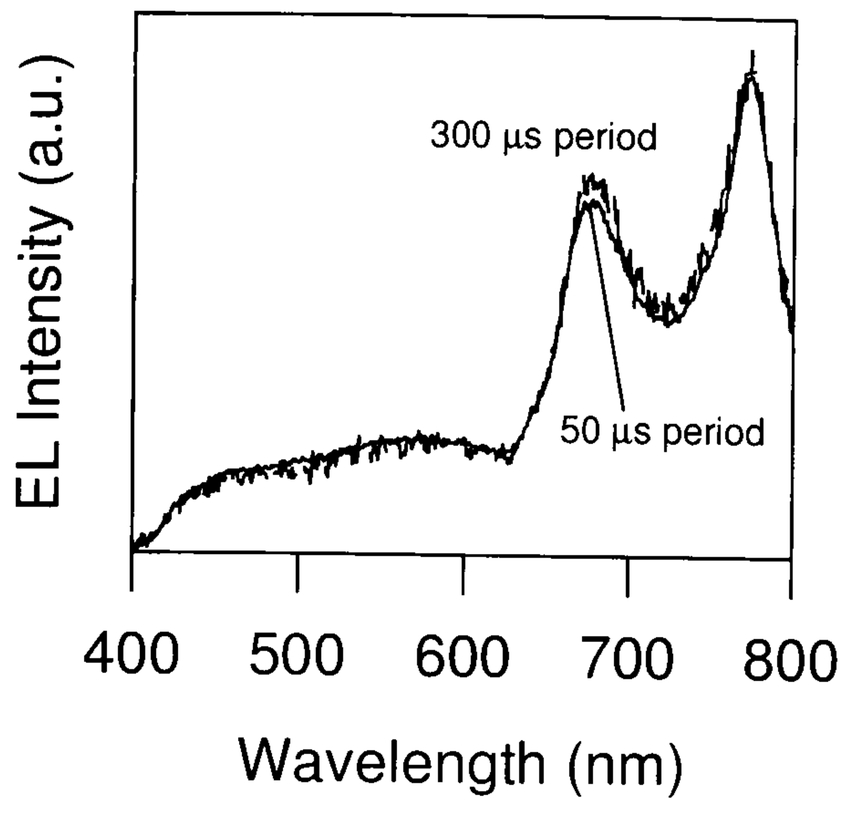

Fig. 7.8. *EL spectra of a B3:P1 blend device at pulses of 10 µs over periods of 50 µs and 300 µs showing no dependence on duty cycle for longer periods and pulse lengths.*

The increase in guest emission can be analysed by comparing the relative integrated intensities of the two components of the emission, as is shown in Fig. 7.9. As the period increases, the ratio of phosphorescence to fluorescence (emission of guest P1 to host emission) increases following a square root exponent. Remarkably, as is seen in the figure, the scaling with period is identical for both host materials, despite the large difference in EL spectra, providing evidence that the frequency dependence of the emission is due to a common process.

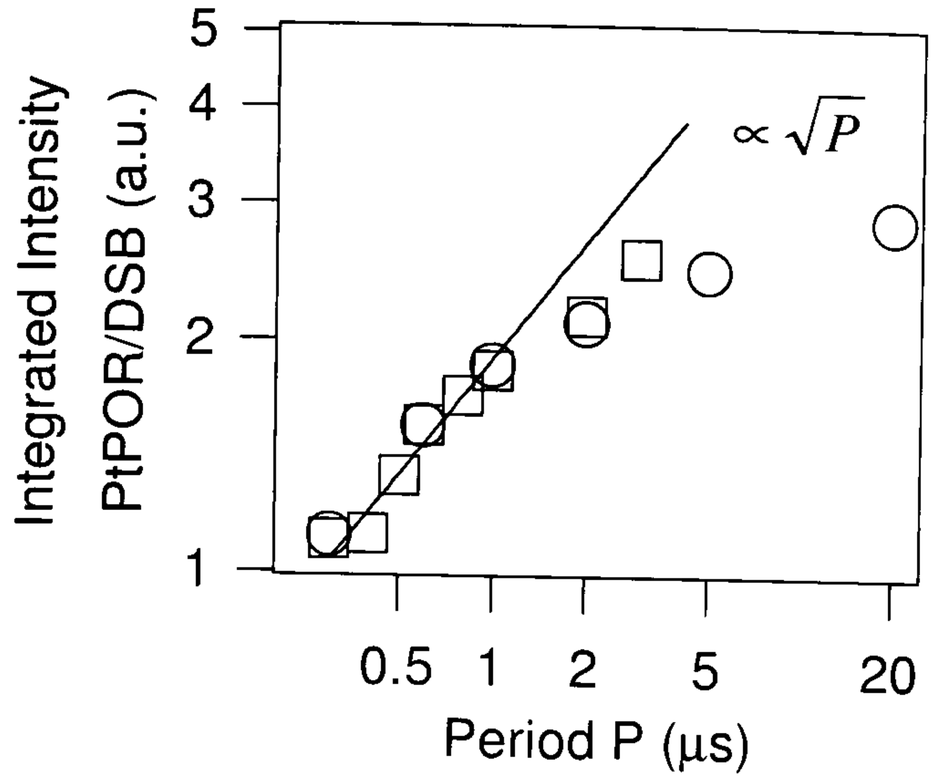

Fig. 7.9. *Plot of ratio of guest emission to host emission for blends containing dendrimer A3 (○) and B3 (□) on a double logarithmic scale. The drive pulse duration was 100 ns. The line indicates the region of square root scaling due to bimolecular recombination.*

The square root exponent observed in Fig. 7.9 is a characteristic of bimolecular decay resulting from interactions between the long lived excited states. One possible explanation of this behaviour is a direct destructive interaction between triplets present in the material, which is known to be a serious problem in electrophosphorescent devices [6,10,15]. However, it is also possible that interactions with charged species give rise to luminescence quenching. As the pulse period increases, the total number of long lived emissive excitations in the blend (the excitation density) decreases, giving rise to a reduction in interaction between these species and hence an increase in the emission of P1. This power-law scaling is comparable to the singlet-singlet annihilation observed in polymeric microcavity lasers with increasing pump intensity [16]. However, in the present case it is apparent at much lower concentrations of excitation due to the longer lifetime of the emitting species. At very long periods the data points deviate from the simple square root law as the signal to noise ratio decreases with decreasing excitation density and the period approaches the lifetime of the porphyrin emissive state. Alongside the quenching, it is also conceivable that filling of the

porphyrin sites [6] resulting in saturation of the emission can contribute to the frequency dependence observed.

7.5 Exciton-exciton annihilation

In the following the results are investigated using a model of bimolecular recombination in order to provide evidence for the occurrence of triplet-triplet annihilation in these devices. As there is no insight available into the actual excitation density, the model should be seen as a qualitative description of the physical processes.

Bimolecular decay can be described through the bimolecular rate equation [17]

$$\frac{dn}{dt} = -\gamma_1 n - \frac{1}{2}\gamma_2 n^2$$

where n is the exciton concentration and γ_1 and γ_2 are the radiative lifetime and the interaction rate, respectively. The integrated emission detected by the CCD camera corresponds to the integral of the exciton density as a function of time. The pulsed operation can be modelled by adding a fixed number of excitations, n_0, to the overall density at fixed time intervals corresponding to the period. The iteration is repeated until the integrated excitation decay reaches steady state after every pulse. The numerical solution of the bimolecular rate equation as a function of pulse period is shown in Fig. 7.10 for γ_1=1/70μs, γ_2=3.8×10^{-5} cm^{3}s^{-1}, and n_0=10^{12} cm^{-3} (the parameters arise from the best fit discussed below). It is seen that the overall shape of the calculated integral on pulse period is in excellent agreement with the measured data. For short periods the integrated density follows a square root dependence on the period and then flattens off at longer periods.

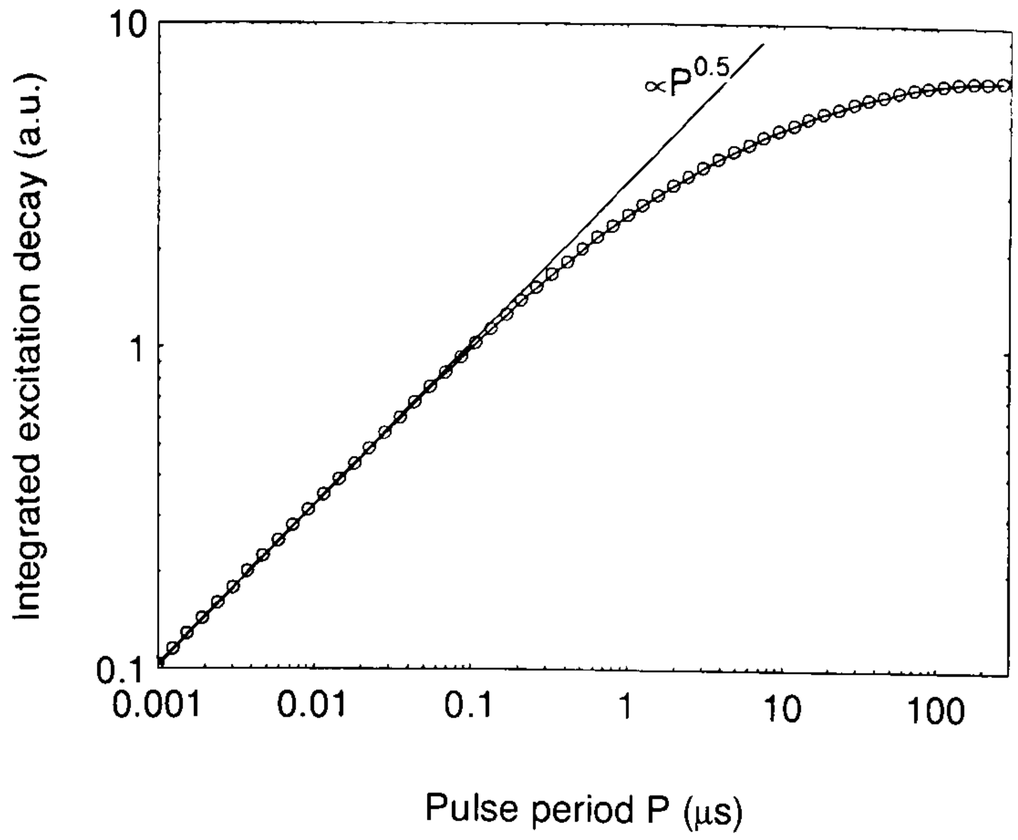

Fig. 7.10. *Calculated dependence of the integrated excitation decay on pulse period for* $\gamma_1=1/70\mu s$, $\gamma_2=3.8\times10^{-5}$ cm^3s^{-1}, $n_0=10^{12}$ cm^{-3}. *The straight line shows the square root dependence on perdiod.*

Although little is known about the total excitation density and the number of excitons generated with every pulse, n_0, it is possible to fit to the measured data using combined sets of the density n_0 and the interaction rate γ_2. It should be noted that identical fits can be achieved using larger densities and smaller rates. Fig. 7.11 shows fits of the calculated integrated excitation decay to the measured data seen in Fig. 7.9 using $n_0=10^{12}$ cm^{-3}. Three different radiative lifetimes are used and it is found that the observed quenching is best described by a radiative lifetime $\tau_1=1/\gamma_1$ of 3.5 μs. This suggests that the lifetime of the phosphorescent porphyrin dendrimer is considerably shorter than that previously reported, which may be a consequence of the high concentrations used and the presence of charge carriers. The excellent agreement between the two data sets obtained for the two host materials and the calculated quenching provides strong evidence that the observed dependence of the emission spectrum on pulse period is due to interactions between triplet excitations.

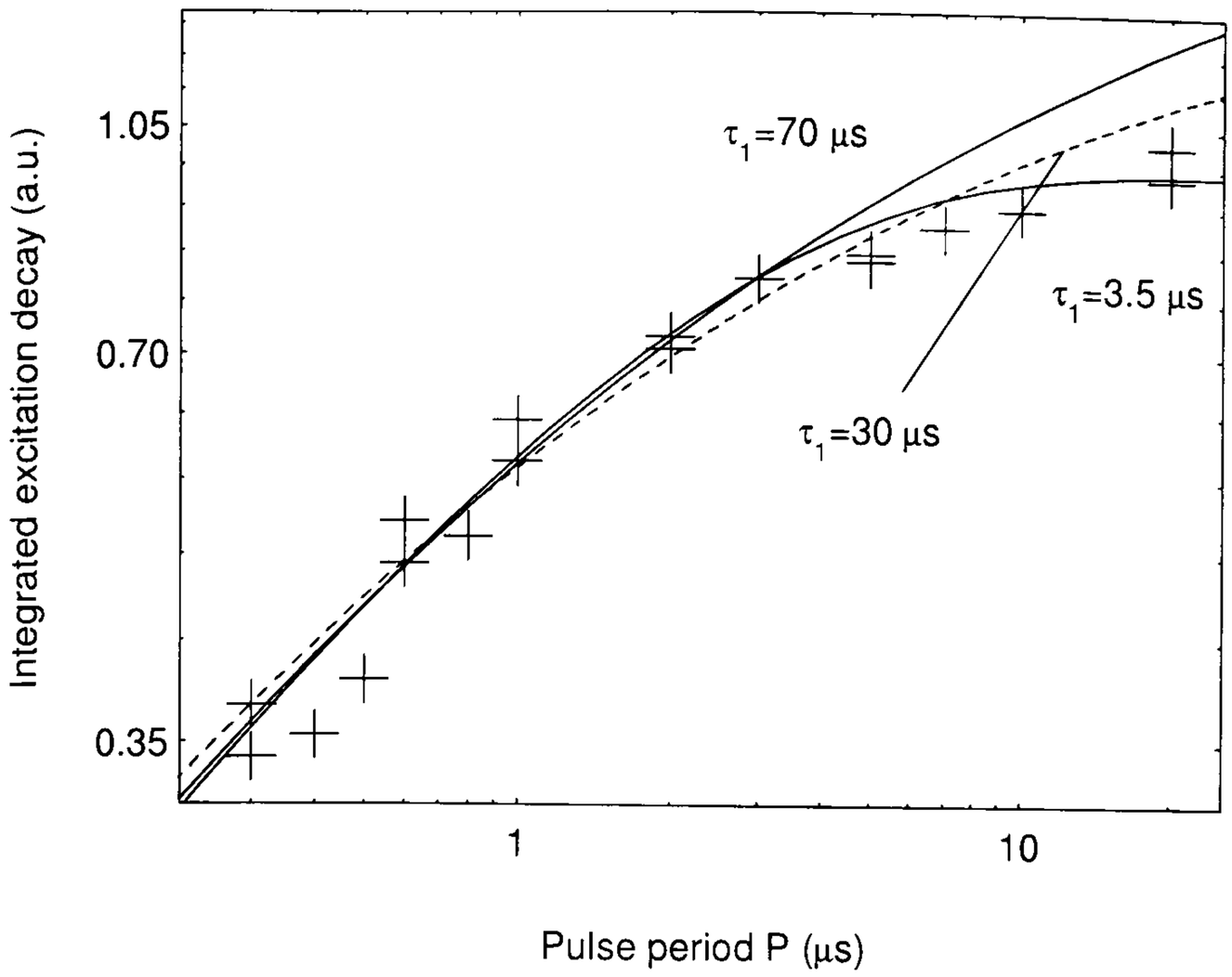

Fig. 7.11. *Comparison of experimental results to the calculated bimolecular quenching for* $\{\gamma_1=1/70\mu s,\ \gamma_2=3.8\times10^{-5}\ cm^3s^{-1},\ n_0=10^{12}\ cm^{-3}\}$; $\{\gamma_1=1/30\mu s,\ \gamma_2=3.0\times10^{-5}\ cm^3s^{-1},\ n_0=10^{12}\ cm^{-3}\}$; $\{\gamma_1=1/3.5\mu s,\ \gamma_2=7.6\times10^{-6}\ cm^3s^{-1},\ n_0=10^{12}\ cm^{-3}\}$.

Using the model of bimolecular decay, it is also possible to investigate the effect a filling of emissive sites may have on the dependence of the emission spectrum on pulse period. The above calculation is run again with a limit on the number of excitations, n, imposed by the parameter n_{max}. Fig. 7.12 shows the calculated quenching with different limits on the number of sites. It is seen that the power law dependence of the integrated decay on the period yields larger exponents for the case where filling of sites plays a role. As the total number of available sites increases, the power law tends towards the observed square root dependence. It is hence concluded that filling of emissive sites does not account for the spectral dependence on pulse period observed here.

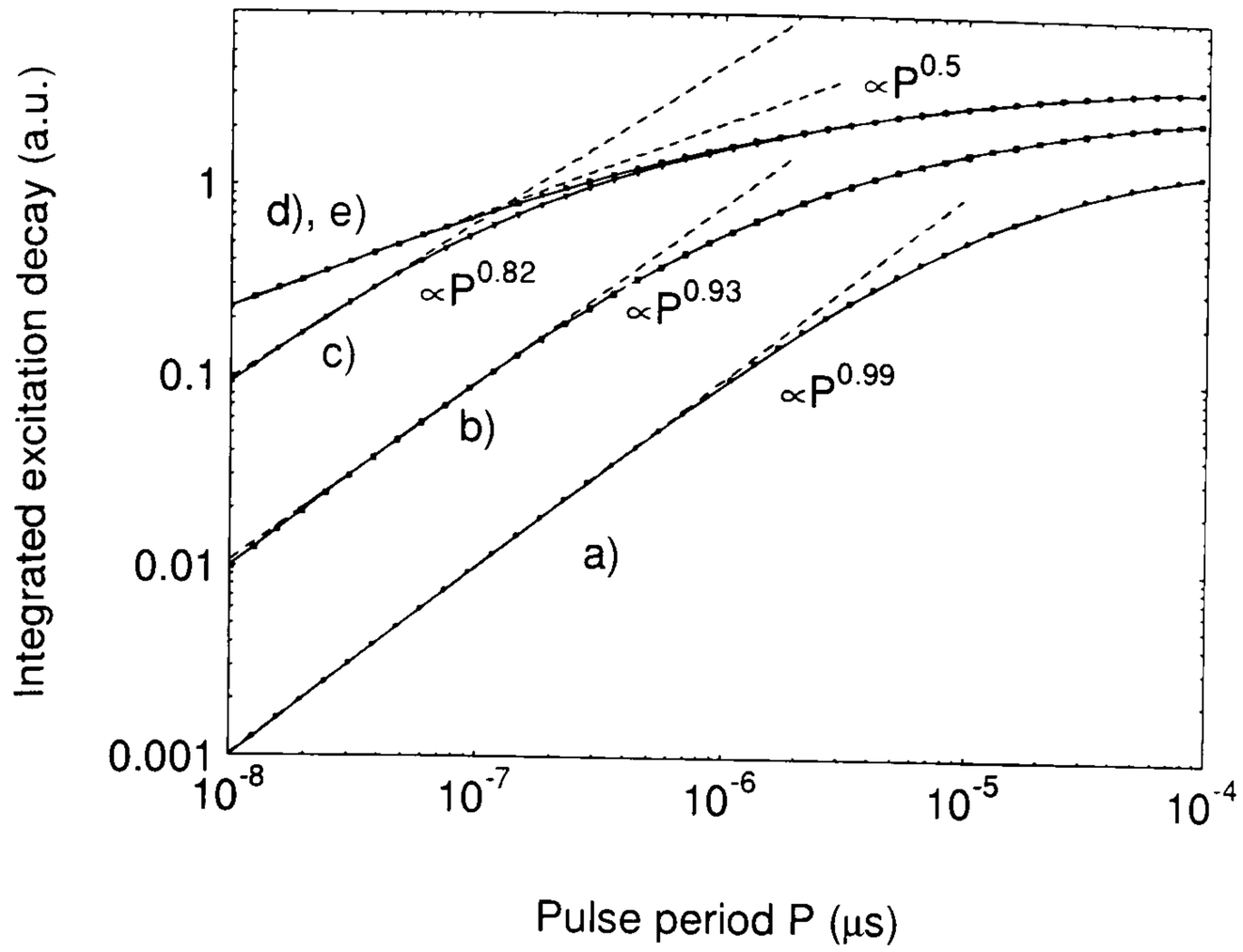

Fig. 7.12. *Calculated quenching for different maximum number of sites using {$\gamma_1=1/70\mu s$, $\gamma_2=3.8\times10^{-5}$ cm^3s^{-1}, $n_0=10^{12}$ cm^{-3}}. a) $n_{max}=10^{10}$ cm^{-3}, b) $n_{max}=10^{11}$ cm^{-3}, c) $n_{max}=10^{12}$ cm^{-3}, d) $n_{max}=10^{13}$ cm^{-3}, e) $n_{max}=10^{14}$ cm^{-3}.*

7.6 Conclusions

A dependence of the emission spectrum on excitation density has been pointed out previously as a result of the applied bias and current density flowing through the device [9]. For the guest/host combinations used in this study a shift in weighting from the guest emission to the host emission is also observed as the bias and hence the current and excitation density is increased. This means that the drive voltage can also be used to control the colour of light emission. However, a limitation of this form of spectral control is that different colours are achieved at different brightnesses. With regards to the physics of the quenching process the dependence on duty cycle is also more clear cut. It is found that these devices, and indeed electrophosphorescent devices studied by the Author prepared with alternative phosphors in bilayer configurations, can yield power-laws of the singlet to triplet emission ratio as a function of current or light output and hence excitation density. Exponents extracted from these analyses are generally in the order of 0.1, which suggests that the quenching processes present upon electric driving are considerably more complicated than a mere dependence on excitation density.

In view of these new results, the dependence on pulse period demonstrated above may be used in conjunction with the bias dependence of the emission spectrum to tune the perceived colour of the LED. A suitable choice of red and green dopants with different triplet lifetimes dispersed in a blue emitting host should allow tunability over the entire visible spectrum and paves the way for novel, more compact backlights and high resolution RGB pixel. Finally, the above experiment also demonstrates the probing of excited state dynamics using steady state spectroscopy under suitable driving conditions.

The application of a new PtPOR containing dendrimer as a triplet harvesting phosphorescent dopant for EL devices has been demonstrated. Due to the common dendrimer architecture of host and guest molecules, excellent miscibility of the materials in thin films is achieved. Efficient emission is observed from the guest despite a lack of radiative energy transfer. It is shown that charge carriers are preferentially trapped on the lower energy dopant sites which then affects the ratio of EL emission from each component in the blend. The long phosphorescence lifetime of the guest porphyrin dendrimer gives rise to a frequency dependent quenching process, which is independent of the host material. The use of conjugated dendrimers hence provides an elegant way of controlling the phosphorescence, trapping and quenching of excitations in organic LEDs.

References

[1] A. R. Brown, K. Pichler, N. C. Greenham, D. D. C. Bradley, R. H. Friend, and A. B. Holmes, Chem. Phys. Lett. **210**, 61 (1993)

[2] M. A. Baldo, D. F. O'Brien, M. E. Thompson, and S. R. Forrest, Phys. Rev. B **60,** 14422 (1999)

[3] V. Cleave, G. Yahioglu, P. LeBarny, R. H. Friend, and N. Tessler, Adv. Mat. **285,** 11 (1999)

[4] Z. Shuai, D. Beljonne, R. J. Silbey, and J. L. Bredas, Phys. Rev. Lett. **84,** 131 (2000)

[5] Y. Cao, I. D. Parker, G. Yu, C. Zhang, and A. J. Heeger, Nature **397**, 414 (1999)

[6] M. A. Baldo, D. F. O'Brien, Y. You, A. Shoustikov, S. Sibley, M. E. Thompson, and S. R. Forrest, Nature **395**, 151 (1998)

[7] Y. G. Ma, C. M. Che, H. Y. Chao, X. M. Zhou, W. H. Chan, and J. C. Shen, Adv. Mat. **11**, 852 (1999).

[8] D. F. O'Brien, M. A. Baldo, M. E. Thompson, and S. R. Forrest, Appl. Phys. Lett. **74**, 442 (1999)

[9] M. A. Baldo, S. Lamansky, P. E. Burrows, M. E. Thompson, and S. R. Forrest, Appl. Phys. Lett. **75**, 4 (1999)

[10] M. A. Baldo, M. E. Thompson, and S. R. Forrest, Nature **403**, 750 (2000)

[11] J. N. G. Pillow, M. Halim, J. M. Lupton, P. L. Burn, and I. D. W. Samuel, Macromolecules **32**, 5985 (1999)

[12] M. Halim, J. N. G. Pillow, I. D. W. Samuel, and P. L. Burn, Adv. Mater. **11**, 371 (1999)

[13] M. Halim, I. D. W. Samuel, J. N. G. Pillow, and P. L Burn, Synth. Met. **102**, 1113 (1999)

[14] J. M. Lupton, L. R. Hemingway, I. D. W. Samuel and P. L. Burn, J. Mat. Chem. **10**, 867 (2000)

[15] I. D. W. Samuel and A. Beeby, Nature **403**, 710 (2000)

[16] G. J. Denton, N. Tessler, N. T. Harrison, and R. H. Friend, Phys. Rev. Lett. **78**, 733 (1997)

[17] V. Sundstrom, T. Gillbro, R. A. Gadonas, and A. Piskarsaks, J. Chem. Phys. **89**, 2754 (1988)

8.

Bragg-scattering from periodically microstructured light-emitting diodes

Acknowledgements

I would like to thank B. Matterson at Durham University for introducing me to this interesting research area and for many helpful discussions. The gratings used in this study were fabricated by M. Jory and M. Salt at Exeter University in the group of W. Barnes, to whom I am grateful for many stimulating exchanges. I would also like to thank A. Safonov at Durham University for a fruitful collaboration and for performing the photoluminescence quantum yield measurements on corrugated samples.

8.1 Introduction

Low dimensional photonic structures are becoming increasingly important for optical applications, in particular for optical fibres, solid state semiconductor lasers and LEDs [1]. Periodic structure on the scale of the wavelength of the radiation concerned has been used to control the photonic density of states, and leads to intriguing modifications of the interactions of light with matter [2]. One significant problem with using photonic structures in practical devices lies in the fabrication process of wavelength scale periodicity with sufficient contrast in refractive index [3], as well as the actual physical modulation of the optically active material. The fact that semiconducting polymers are both mechanically soft and solution processable makes them ideal for imprinting structures on them, which can be achieved through lithographic means [4], or by stamping [5]. In this chapter an attractive and effective alternative moulding technique is presented whereby one-dimensional photonic structure is induced in an optically active conjugated polymer using a high resolution Bragg diffraction grating as the mould [6-8]. The emitting material takes up the form of the microstructure mould when cast onto a corrugated substrate. In particular, the simple processibility of conjugated polymers allows a detailed investigation of the effect of periodicity in the emitting layer on electrically driven devices in an LED configuration. This simple photonic structure is shown to be advantageous with respect to a planar device configuration.

The relatively high refractive index of the emitting polymer results in a significant contribution of trapped waveguide modes to the total amount of light generated [9-10]. In the following it is demonstrated that the device efficiency can be increased by scattering out these modes from the device by enforcing a periodic modulation on the emitting layer. Periodic modulation of organic thin films has been investigated in a number of examples, most notably in the context of lasing [6-8]. Although it has previously been shown that random structures and surface roughening or substrate shaping can lead to a significant improvement in light extraction [11-12], the advantages of periodical modulation of the emitting layer have only been considered in device-like configurations which do not comprise injecting contacts [13]. Some work has focused on extracting light from waveguide modes trapped in the substrate of an organic LED [14-16]. However, as the refractive index of the emitting layer in an organic LED is

generally much greater than that of the glass substrate, structuring the emitting layer should be far more effective.

8.2 Control of film emission through lateral microstructure

In order to establish the effect of periodic microstructure on the emission from a thin polymer film, the PL efficiency of films in a device-like configuration was measured by A. Safanov [17]. The grating substrates were fabricated on photoresist following an established technique using the interference pattern of two laser beams [18]. The integrated emission of a polymer film deposited on a gold covered (50 nm) substrate was measured in an integrated sphere under excitation by the 488 nm line of an argon ion laser. The film thickness was approx. 220 nm and the corrugation pitch and period were 13 nm and 388 nm, respectively. The results of this measurement are shown in Fig. 8.1. The spectra were normalised by the amount of light absorbed so that the area beneath the curves becomes proportional to the emission efficiency. It is clearly seen that the emission efficiency is doubled upon introduction of the corrugation with respect to the planar sample. Also, it should be noted that due to the presence of the metal layer all emission occurs in the forward direction. The increase in efficiency is hence believed to be due to an increase in emission from the polymer film itself rather than from the substrate of the sample.

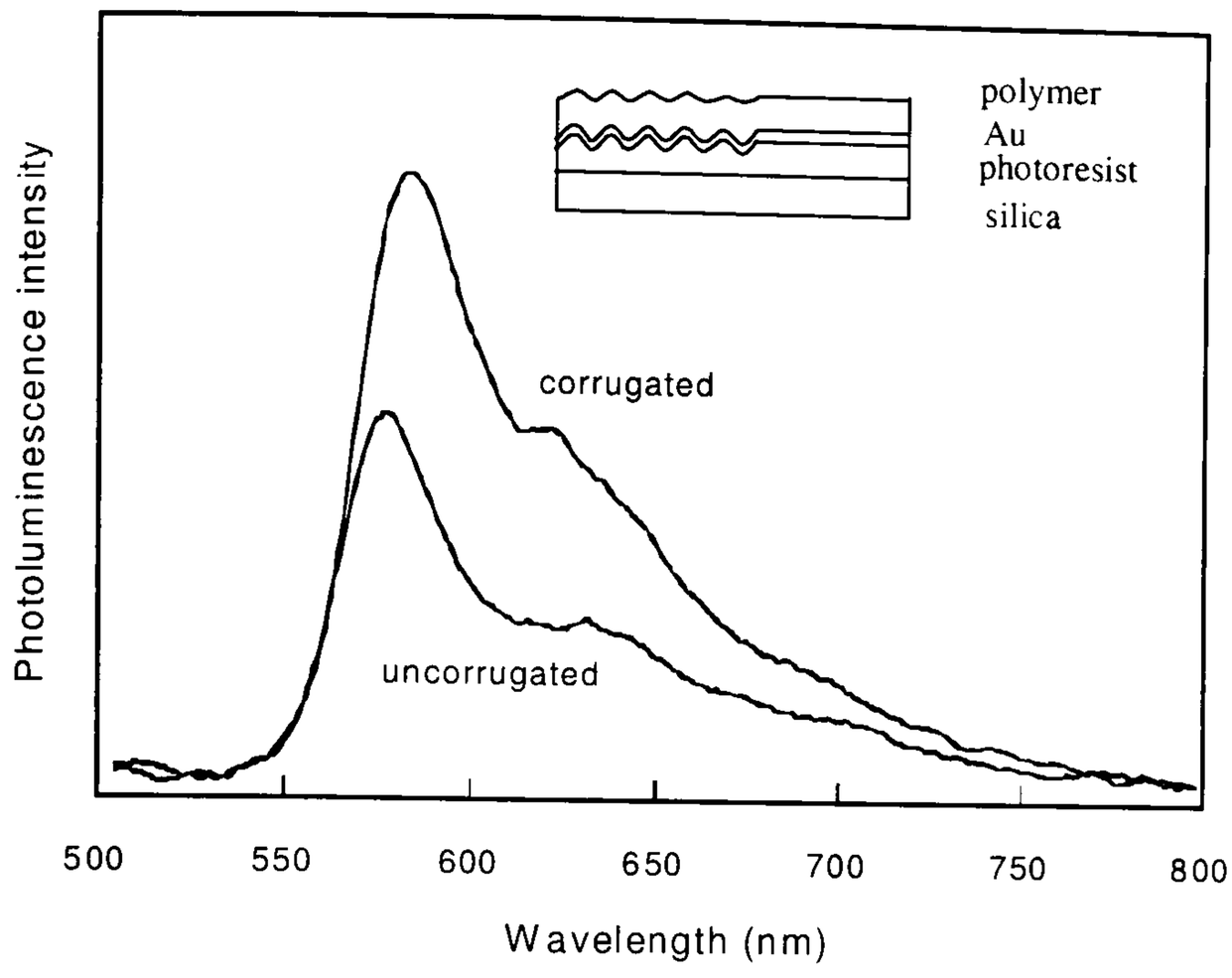

Fig. 8.1. *Effect of corrugation on luminescence efficiency. The figure shows the integrated PL spectra of corrugated and uncorrugated layers measured in an integrating sphere. Inset is the sample structure. (Courtesy of A. Safanov, ref. [17]).*

This relatively straightforward measurement compares to PL yield measurements on device-like structures carried out on inorganic materials with engineered photonic properties [13]. However, the spin-coating process allows a much simpler implementation of photonic structure and control of the photonic density of states of the device than, for example, lithographic means.

8.3 Microstructured LEDs

8.3.1 Device structure

The simple sandwich structures of LEDs mean that the incorporation of a photonic structure discussed above should be relatively straightforward. However, there are valid concerns that the electrical properties of the device may be affected by the corrugation, which can typically be of the order of the film thickness. The structure of the devices

studied is given in Fig. 8.2. Gratings of pitch 388 nm with depths of 10 nm to 100 nm were studied. The corrugation only extends across half of the substrate to allow direct comparison of corrugated and uncorrugated LEDs on one substrate. A thin strip of gold is evaporated onto the substrate, forming the anode and providing the index contrast between substrate and film necessary to achieve scattering. The semiconducting polymer MEH-PPV is spin-coated onto the gold, which is optionally covered with a standard hole-injecting layer of PEDOT. Calcium capped by aluminium is used as the cathode to provide sufficient electron injection. Remarkably, the corrugation is found to carry through all layers of the LED to the top of the aluminium cathode. A small amount of silver paint was used to dissolve the polymer layer and make a rigid contact with the thin gold anode. This proved sufficient for use in the conventional spring mount testing rig.

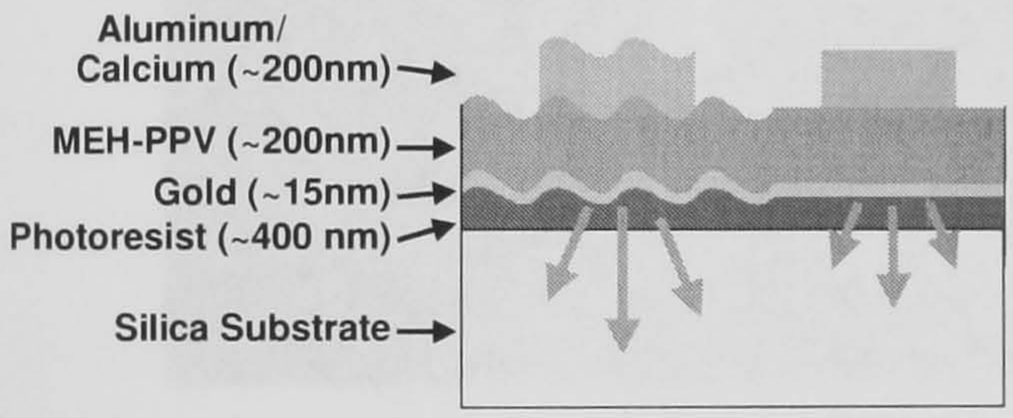

Fig. 8.2. *Device structure used in the study of corrugated LEDs.*

The use of the PEDOT layer on top of the gold electrode was motivated by two concerns. Firstly, the gold electrode is very sensitive to oxygen adsorbtion [19], which dramatically reduces the hole injection efficiency. It was hoped that by introducing a PEDOT layer between the gold and the semiconducting polymer, efficient injection could be achieved. Secondly, the PEDOT layer increases the overall thickness of the device and hence allows longer wavelength modes to be present in the two polymer films. Whereas the inclusion of the PEDOT layer did give rise to some remarkable photonic effects, devices fabricated in ambient conditions with a standard PEDOT layer were found to have efficiencies two orders of magnitude lower than conventional devices fabricated on ITO. However, it was found that by immersing the gold coated substrate in the spinning solvent prior to coating, and then spin-coating the polymer under dry nitrogen in a glove-box, efficiencies in the order of 0.1 % could be achieved.

Fig. 8.3 shows a photograph of an operating LED with 0.1 % external efficiency and a brightness of over 1000 Cd/m^2, demonstrating that the grating structure allows the fabrication of efficient devices with high yields. There are two features visible in Fig. 8.3, the actual LED pixel marked A and a weaker feature B, which changes colour from yellow-green to deep red (from left to right). Feature B arises from the angular dispersion by the grating of modes scattered out of the *substrate*. Similar features have been observed in devices employing silica spheres to scatter out substrate modes [14]. Our device, however, also scatters out *film* modes, which gives rise to polarisation and angular peak splitting.

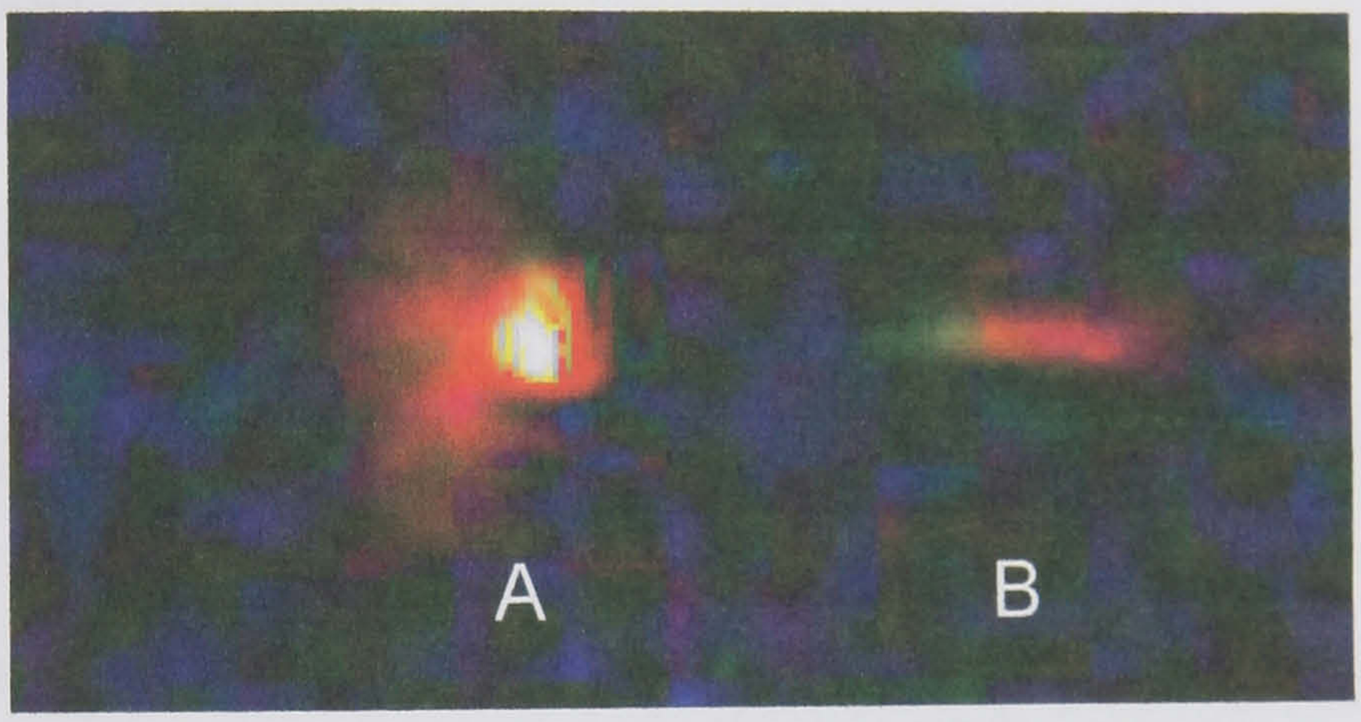

Fig. 8.3. *Photograph of an operating LED showing the direct emission A and a spectrally resolved faint feature B approx. 5 mm from the pixel. The colour of B changes from yellow-green to deep red from left to right, which corresponds to a change in scattering angle of substrate modes.*

The origin of the two features seen in Fig. 8.3 is outlined in the sketch in Fig. 8.4 with respect to the grating lines.

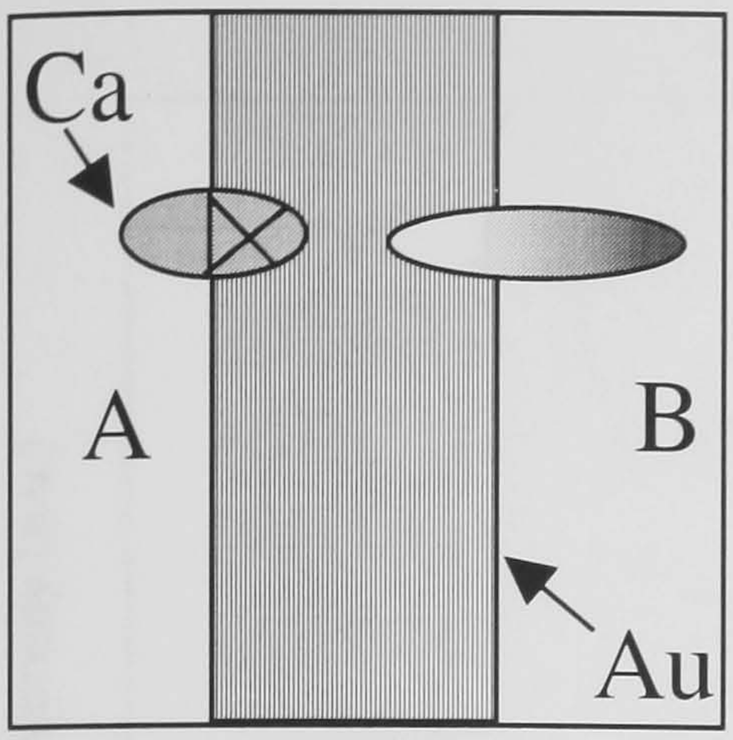

Fig. 8.4. *Top view of the device structure. The active pixel area is marked by X and labelled A. The weak feature B results from the angular dispersion of the substrate waveguide mode scattered out of the device.*

8.3.2 Efficiency enhancement

Devices were fabricated side by side on a substrate with both a planar and a corrugated (pitch 388 nm and groove amplitude 60 nm) region of photoresist. Fig. 8.5 shows the EL spectra measured in the forward direction for a planar and corrugated pixel on opposite sides of the substrate. The device current for both pixel was approx. 5 mA. The result is remarkable: the light emission is enhanced by a factor of 4 in the forward direction due to the presence of the grating structure. Also, a modification of the spectrum is observed. This result demonstrates that a modification of the photonic structure of an LED allows both a marked improvement of the device efficiency as well as a control of the actual emission spectrum within a certain level.

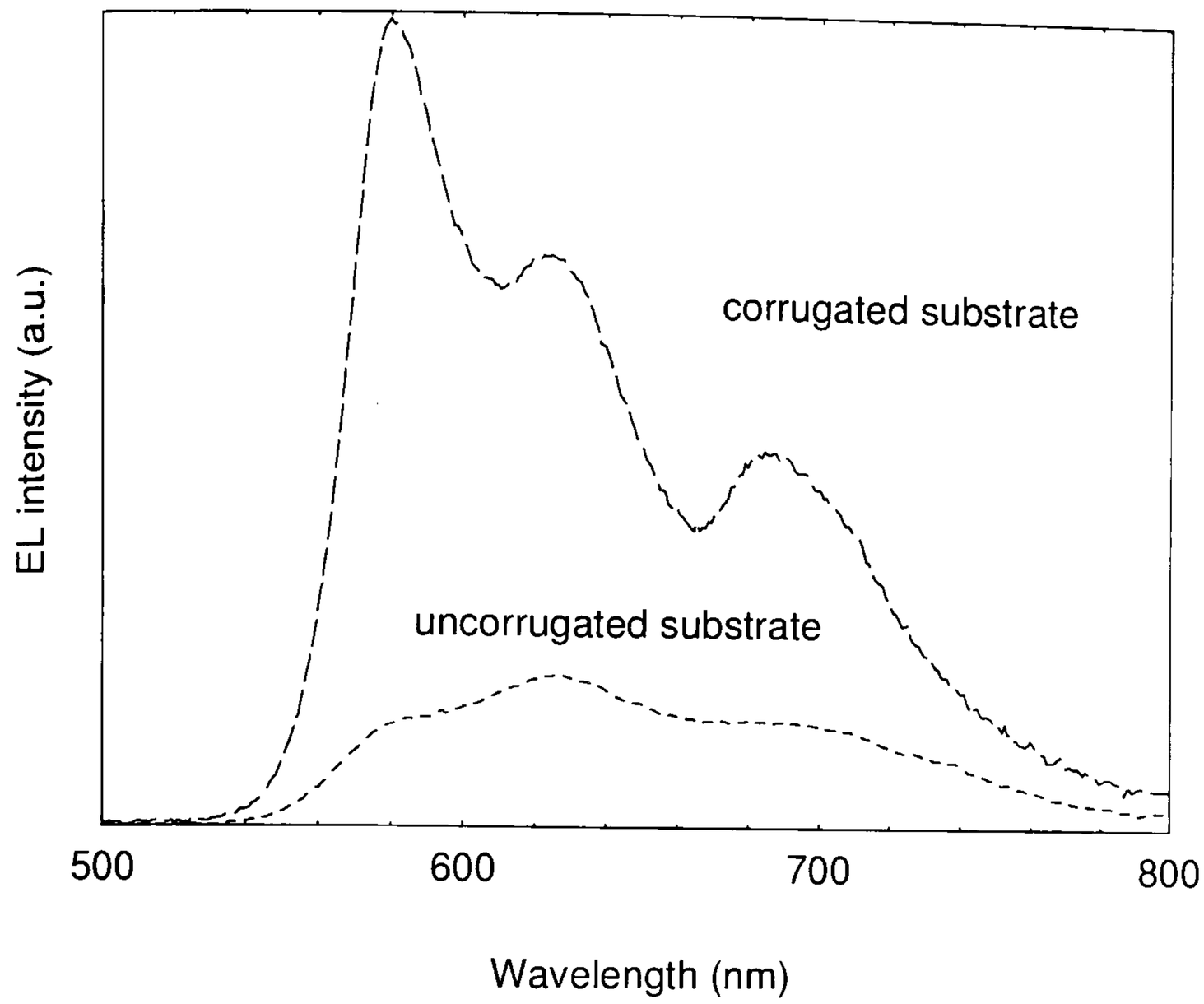

Fig. 8.5. *EL spectra of uncorrugated and corrugated LEDs containing PEDOT.*

In order to assess whether the modification of the photonic device properties affects the electrical device properties in any way, the device characteristics of corrugated and uncorrugated LEDs are compared next. The EL intensity was measured by placing a large area silicon photodiode directly on top of the LED and is hence integrated over all emission angles in the forward direction. The current-voltage and EL intensity-voltage characteristics are shown in Fig. 8.6. It is seen that the current-voltage characteristics of pixels on the corrugated and uncorrugated part of the substrate are very similar and follow each other closely over orders of magnitude on the current scale. In contrast, the corrugated LED exhibits a stronger luminescence at the same current, as is seen in the inset plot of intensity as a function of current, indicating that more light is escaping from the film. An increase in the external efficiency by a factor of 2.0±0.2 is observed, similar to that seen above for the PL yield measurements. The fact that the current is unchanged with the corrugation is important evidence that the injection characteristics are not modified by the grating structure and that the increase in emission intensity observed in Fig. 8.5 is not due to electric field effects resulting from the corrugation. Indeed, also the light-output curves of the corrugated and uncorrugated LEDs are identical over orders of magnitude, but merely shifted in magnitude. This demonstrates that the injection processes of both electrons and holes are unchanged, which is

remarkable considering the dimensions of the grating of amplitude 60 nm with respect to the film thickness of 200 nm.

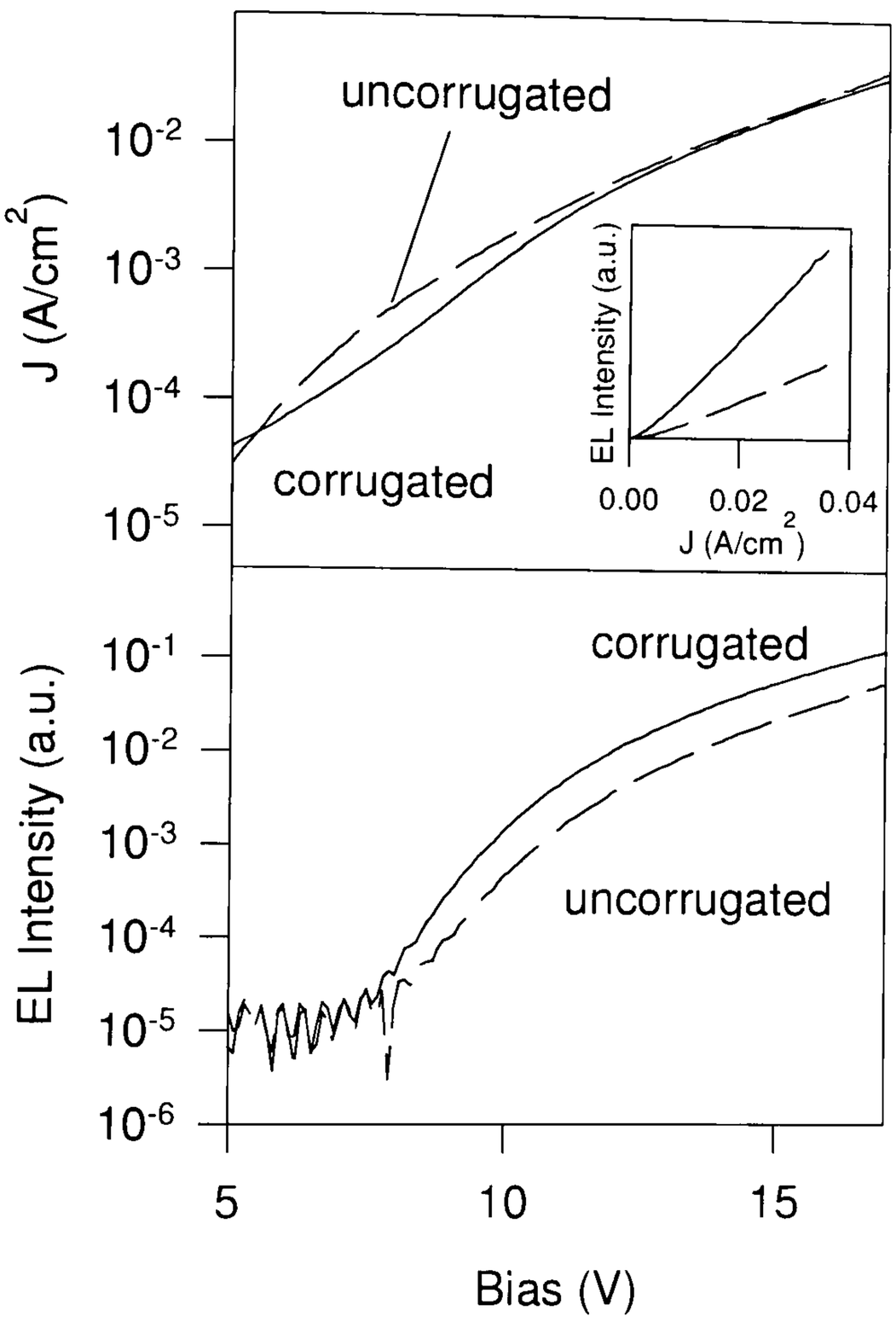

Fig. 8.6. *Current-voltage and EL-voltage of an uncorrugated and corrugated LED. The current is very similar for both devices, whereas more light is observed from the corrugated LED. Inset is the EL intensity as a function of current. The device contained PEDOT.*

8.3.3 Peak splitting

Evidence that the enhancement in emission is due to Bragg-scattering comes from the emission spectra. Fig. 8.7 displays the angular dependence of the emission spectrum of

a strongly corrugated LED, recorded using a fibre coupled CCD spectrometer in a plane perpendicular to the grating grooves. As the angle at which emission spectra are recorded is increased, the middle peak at 625 nm splits symmetrically into two peaks which move to higher and lower wavelengths, respectively, as seen in the inset plot of peak wavelength versus angle. A similar angular dependence in PL spectra of MEH-PPV spun on gratings covered with a non-transparent metal layer has been observed [17] and could be used to deduce the dispersion of the refractive index, as described in chapter 2. In the case of the device structure, the calculation of the internal angle of mode propagation is considerably more complicated than for the case of a simple polymer/metal structure due to the presence of a semitransparent contact and the resulting interference and microcavity effects [20]. However, the fact that the main peak splits into two as the detection moves off-normal is clear evidence for Bragg-scattering. As substrate modes are suppressed in the PL measurement by the metal film between polymer and grating, the peak splitting is attributed unambiguously to scattering of film modes. One possible concern of this observation is that the angular dispersion may be detrimental to the colour purity required in display applications. However, a calculation [21] of the colour co-ordinates of the extreme spectra showed that due to the broad reddish emission band of the polymer, the dispersion has a negligible effect on the colour co-ordinates of smaller than 1 %.

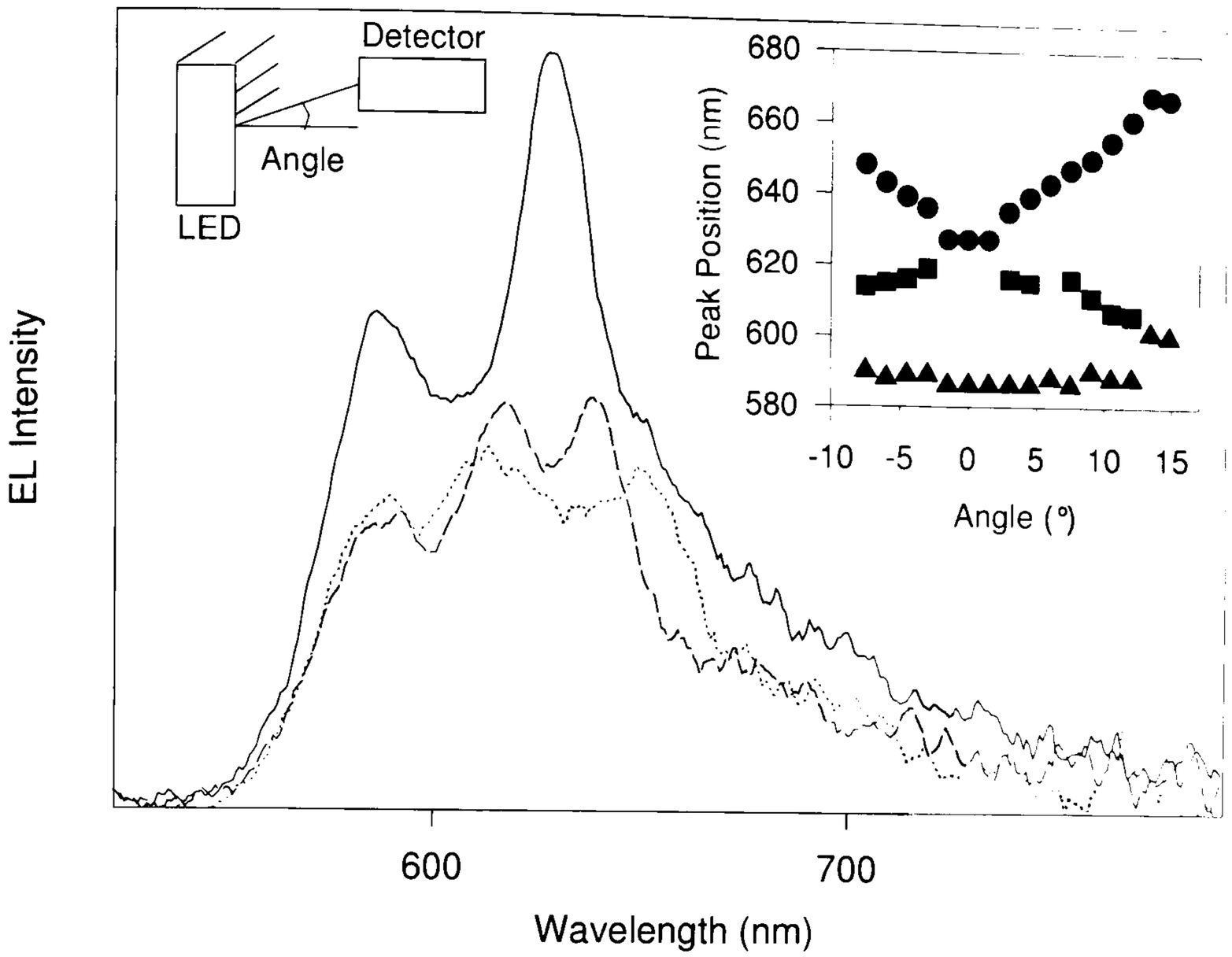

Fig. 8.7. *Angular dependence of the emission from a corrugated LED for normal emission (——), emission at –4.5° (---) and +9.0° (·····). The left inset shows the experimental alignment relative to the grating. The peak at 625 nm splits into two peaks as the detection moves off normal. The right inset shows the positions of the emission peaks as a function of angle: normal emission at 590 nm (▲), split part of 625 nm peak moving to shorter wavelengths (■) and split part of 625 nm peak moving to longer wavelengths (●). The device contained PEDOT.*

An interesting way of representing all the angular dependent data is by plotting the EL intensity on an intensity map as a function of wavelength and angle. This is shown in Fig. 8.8 for the same data discussed in Fig. 8.7. The X-shape structure is visible as in the inset in Fig. 8.7. However, a close analysis of the measured spectra shows that the central peak does not split into two peaks of equal weighting, but rather a peak and a shoulder. Although the measurement was somewhat complicated by the low intensity of the LED emission, it is believed that this suppression of a full peak may be due to the coupling of the scattered mode to a further photonic mode such as a surface plasmon

with different film thicknesses on gratings of various depths. The unpolarised EL is shown together with polarised EL, which is of lower intensity due to the absorption of the polarisation filter. For all devices, the emitted light exhibits a degree of polarisation, which increases with increasing film thickness and grating depth. A detailed analysis of this effect is complicated by the presence of two metal electrodes, one of which is semi-transparent, resulting in contributions from surface plasmons and interference within the cavity. However, the polarisation effect does demonstrate that there is a contribution in the forward emission from scattered light, which gives rise to the observed increase in efficiency.

The coupling of light out of the LED structure depends on the polarisation, wavelength and direction of propagation of the waveguided light. A mode propagating perpendicular to the corrugation lines will be scattered out of the device effectively, whereas a mode propagating parallel to the grating lines will not couple to radiation. Both transverse electric (TE) and transverse magnetic (TM) modes will be coupled out of the structure, but at different wavelengths because of their different dispersion relations. For a metal clad polymer structure, the lowest TM mode is at longer wavelength than the lowest TE mode of the same wavevector [24]. This explains the observation in Fig. 8.9 that for thicker films there is also a broad polarised feature at long wavelength with polarisation perpendicular to the grating direction, whereas the higher energy TE modes are polarised parallel to the grating and scatter out as relatively narrow features. The comparison of Figs. 8.9 b) and c) also shows that the scattered TE mode moves to longer wavelengths with increasing film thickness, as discussed in chapter 2.

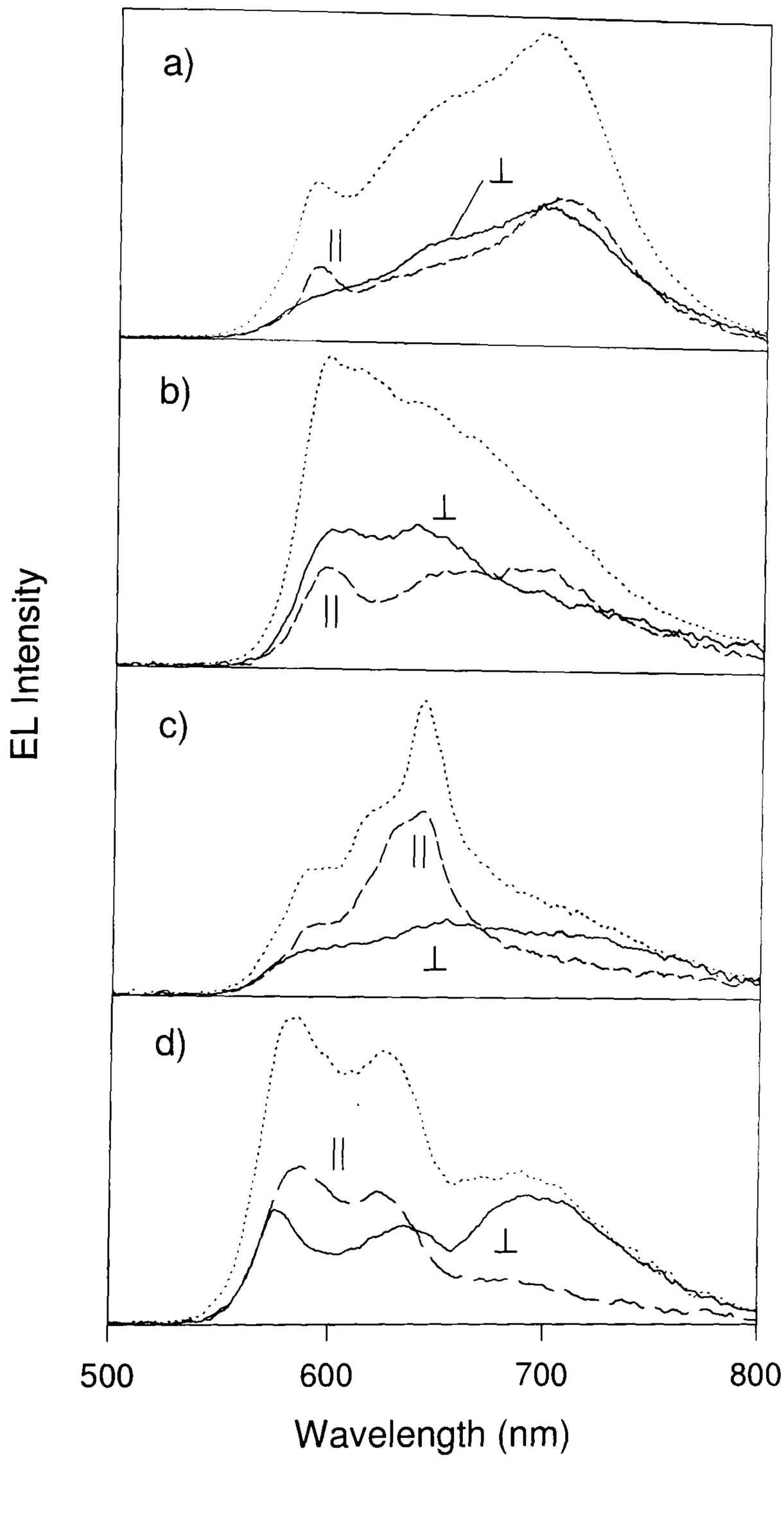

Fig. 8.9. *Emission spectra in the forward direction, unpolarised (·····), polarised parallel to the direction of the grating (---) and orthogonal to the direction of the grating (-------). a) Thin film (120 nm) on shallow grating (10 nm). b) Thin film (120 nm) on deep grating (80 nm). c) Thick film (200 nm) on deep grating (70 nm). d) Thick film (200 nm) plus a PEDOT layer (50 nm) on a deep grating (80 nm).*

It is interesting to note that the spectrum of the emitted light depends sensitively on the device structure under investigation and is readily modified by grating depth and film thickness. Although in the above example this modification is accidental, further studies could determine a systematic relationship, which would be useful as a direct photonic control of the emission spectrum. The absorption of the green photoresist layer as well as the gold layer, in conjunction with interference effects in the device cavity as well as the strength of scattering, give rise to this wide range of spectra measured.

The observation of polarised EL in the forward direction is not only of importance in understanding the structure of waveguided modes in the device and the nature of the efficiency enhancing scattering process. It is particularly important in view of backlight applications for LC displays, where conventional devices rely on a polarisation filter, which results in a loss of at least 50 % of the emitted light. The microscale control of polarisation and emission through lateral microstructure provides a novel route to efficient display components. The simple processing of organic materials makes them well suited to being formed as corrugated structures, and it is evident that such structures may provide a significant contribution to increasing the overall device efficiency. In view of applications to backlights and displays, the use of a gold electrode has previously been shown to be preferable as a hole injecting contact due to the higher work function with respect to conventional indium tin oxide [19]. Also, gold electrodes are readily evaporated and are ideally suited for shadow masked electrodes in matrix displays. As up to 80 % of the generated light is believed to be trapped in the polymer film [9, 15], a suitable structure could be fabricated which extracts most of this light polarised in the plane of the film. Although the implementation of the microstructure concept has been limited here to the context of organic systems, it should also be applicable to a wider selection of materials.

8.4 Practical device considerations

Clearly there are numerous benefits related to the use of microstructured LED technology, the most obvious being an increase in efficiency. The fact that the scattering process also allows a control of polarisation is of particular significance to the design of backlights for LC displays. Although the research to date has been of more fundamental

rather than applied interest, one should expect to be able to extract a significant fraction of the light in the desired polarisation, which would dramatically reduce the losses by polarisation filters.

As is seen from Fig. 8.9, the polarised scattered peak of the TE mode extends only over a relatively small wavelength range. This means that the scattering is more effective for narrow band emitters such as organolanthanides. The effect of efficiency enhancement could hence be increased by the use of narrow band emitters. Also, a strong scattering would imply that most of the emission is polarised, which could potentially mean that backlights could be constructed without the need of absorbing polarisation filters. These two combined facts suggest that a backlight employing both narrow band emitters and wavelength scale microstructure should be superior to previously suggested device concepts. The use of a diffuser in the backlight should eliminate any parasitic dispersion effects with viewing angle.

Gold electrodes have previously not found much attention as anode materials, although the work function of ~5.2 eV is far more suited to hole injection than that of ITO. It has been shown that the efficiency of an MEH-PPV LED using gold as an anode is doubled with respect to that of a conventional ITO-anode device [19], due to the preferential alignment of the energy levels. In wide-gap materials such as organolanthanides hole injection is a significant problem and could be considerably enhanced by the use of a higher workfunction electrode.

Gold is extremely sensitive to the adhesion of atmospheric impurities. However, if the anode deposition is performed in the same step as the deposition of the organic, this problem is not an issue – quite the opposite is the case, an anode and organic layer evaporated in one step would exhibit much greater stability and purity than a chemically cleaned ITO substrate coated with an organic, as there is no possibility for impurities to reach the anode/organic interface.

Contacting is a potential problem, but by preventing a part of the gold anode from being covered with the organic, contact can readily be made by conductive epoxy/paint as in the case of ITO. Contacting is a much more severe problem in the case of spin-coated

materials, as this process relies on covering the entire substrate to achieve a uniform film. There are, however, conceivable ways of circumventing this problem.

A thin 10 nm gold layer has an optical transmission of 60 % to 70 %, yet electrical properties far superior to those of ITO. The resistivity ρ of sputtered ITO is typically 200 μΩcm (for a 100 nm thick film), whereas the resistivity of most metals, such as gold, is 2 μΩcm. To estimate the sheet resistance, a film of the structure seen in Fig. 8.10 is considered,

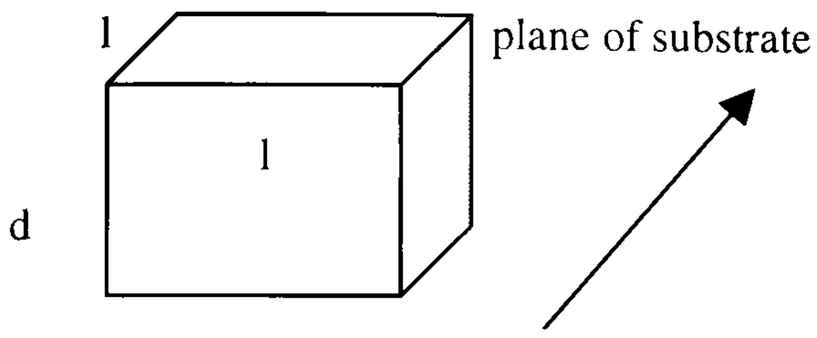

Fig. 8.10. *Calculation of the sheet resistance of gold.*

where d is the thickness of the metal film, and l are the lengths of the sides of a square. The resistance of the film is then defined as the resistance to conduction across an area d*l over a length l, hence ρ*l/(d*l). The length hence drops out and one is left with the quantity of resistance per square. In the case of a 100 nm thick ITO film this give a resistance of 20 Ω/□, whereas a 10 nm thick gold layer gives 2 Ω/□. This lower resistance means that gold is actually the ideal material of choice for passive matrix displays. In addition, patterning of electrodes is much simpler for shadow mask deposition than through chemical etch and lithography, and also gives the advantages in cleanliness and purity as discussed above.

Furthermore, corrugations of 200 nm to 400 nm period can be embossed mechanically on polyethylene films heated above the glass transition temperature (~80° C) [5-6, 8]. In terms of large scale processing this provides a substantial advantage over ITO covered glass in that a flexible substrate allows continuous processing on rolls rather than on individual substrates.

It is hence thought that the requirement of microstructure results in only limited additions to the manufacturing process of LEDs. The advantages of control of

polarisation, increase in efficiency and the use of gold electrodes are most likely to outweigh any constraints on manufacturing steps.

8.5 Conclusions

Lateral microstructure provides an elegant and effective way of controlling the photonic mode structure of organic LEDs. Through the use of wavelength scale microstructure a control of the emission and polarisation is achieved. In comparison to planar devices, the external efficiency is found to double without any measurable changes of the electrical characteristics of the device. This device structure is the first application of controlled photonic structure to an electrically driven light-emitting device, and should be distinguished from alternative techniques such as photon recycling [11-12], which have been used to increase the efficiency of inorganic diodes.

Although it appears that the increase in efficiency observed here results purely from scattering, a combination with a blocking of waveguide modes through an alteration of the photonic band structure could provide an even greater increase in efficiency. Hence suitable tailoring of the photonic band-structure of the LED through appropriate periodic microstructure can allow for the preferential excitation of a desired waveguide mode. This may allow for an additional increase in efficiency over and above that due to extracting guided modes by Bragg-scattering. The higher mode density associated with a mode at the edge of a photonic band gap [2] would further enhance the overall efficiency of the device by ensuring that dipole emission into waveguide modes preferentially produces waveguide modes that propagate in an in-plane direction that the microstructure is able to couple to useful radiation. Additionally, flattened photonic bands and increased emission efficiency lead to an increase in the emission decay rate [25], which may prove to be advantageous when high modulation rates are required or emitters lose a significant amount of energy through non-radiative decay channels.

References

[1] C. Weisbuch, H. Benisty, and R. Houdré, J. Lum. **85**. 271 (2000)

[2] E. Yablonovitch, Phys. Rev. Lett. **58,** 2059 (1987)

[3] E. Yablonovitch and T. J. Gmitter, Phys. Rev. Lett. **63,** 1950 (1989)

[4] J. Wang, X. Y. Sun, L. Chen, and S. Y. Chou, Appl. Phys. Lett. **75,** 2767 (1999)

[5] T. Granlund, T. Nyberg, L. S. Roman, M. Svensson, and O. Inganäs, Adv. Mater. **12**, 269 (2000)

[6] M. Berggren, A. Dodabalapur, R. E. Slucher, A. Timko, and O. Nalamasu, Appl. Phys. Lett. **72**, 26 (1998)

[7] M. D. McGehee, M. A. DiazGarcia, F. Hide, R. Gupta, E. K. Miller, D. Moses, and A. J. Heeger, Appl. Phys. Lett. **72,** 1536 (1998)

[8] C. Kallinger, M. Hilmer, A. Haugeneder, M. Perner, W. Spirkl, U. Lemmer, J. Feldmann, U. Scherf, K. Müllen, A. Gombert, and V. Wittwer, Adv. Mater. **10,** 920 (1998)

[9] N. C. Greenham, R. H. Friend, and D. D. C. Bradley, Adv. Mater. **6,** 491 (1994)

[10] J. S. Kim, P. K. H. Ho, N. C. Greenham, and R. H. Friend, J. Appl. Phys. **88**, 1073 (2000)

[11] R. Windisch, P. Heremans, A. Knobloch, P. Kiesel, G. H. Dohler, B. Dutta, and G. Borghs, Appl. Phys. Lett. **74,** 2256 (1999)

[12] I. Schnitzer, E. Yablonovitch, C. Caneau, T. J. Gmitter, and A. Scherer, Appl. Phys. Lett. **63**, 2174 (1993)

[13] M. Boroditsky, T. F. Krauss, R. Coccioli, R. Vrijen, R. Bhat, and E. Yablonovitch, Appl. Phys. Lett. **75,** 1036 (1999)

[14] T. Yamasaki, K. Sumioka, and T. Tsutsui, Appl. Phys. Lett. **76**, 1243 (2000)

[15]G. Gu, D. Z. Garbuzov, P. E. Burrows, S. Venkatesh, S. R. Forrest, and M. E. Thompson, Opt. Lett. **22,** 396 (1997)

[16] C. F. Madigan, M. H. Lu, and J. C. Sturm, Appl. Phys. Lett. **76,** 1650 (2000)

[17] A. N. Safonov, M. Jory, J. M. Lupton, W. L. Barnes, and I. D. W. Samuel, Synth. Met. **116**, 145 (2001)

[18] S. C. Kitson, W. L. Barnes, and J. R. Sambles, IEEE Photon. Tech. Lett. **8**, 1662 (1996)

[19] J. C. Scott, G. G. Malliaras, W. D. Chen, J. C. Breach, J. R. Salem, P. J. Brock, S. B. Sachs, and C. E. D. Chidsey, Appl. Phys. Lett. **74,** 1510 (1999)

[20] V. Bulovic, V. B. Khalfin, G. Gu, P. E. Burrows, D. Z. Garbuzov, and S. R. Forrest, Phys. Rev. B **58,** 3730 (1998)

[21] M. Halim, PhD Thesis, University of Durham (1999)

[22] M. J. Jory, I. D. W. Samuel, and W. L. Barnes, Phys. Rev. B (submitted)

[23] H. Becker, S. E. Burns, and R. H. Friend, Phys. Rev. B **56,** 1893 (1997)

[24] M. G. Salt and W.L. Barnes, Opt. Comm. **166,** 151 (1999)

[25] E. P. Petrov, V. N. Bogomolov, I. I. Kalosha, and S. V. Gaponenko, Phys. Rev. Lett. **81,** 77 (1998)

9.

Conclusion

polariton mode [22]. This gives rise to an apparent asymmetry in Fig. 8.8 with the lower left-hand section of the cross vanishing close to the origin. Such deviations from the simple Bragg-scattering expected have been observed in polymer/metal structures and have also been treated theoretically in the framework of surface plasmons [22]. Clearly more experimental work is required to clarify whether there are effects which may add to the observed Bragg-scattering and to which extent microcavity and interference effects also play a role in these devices.

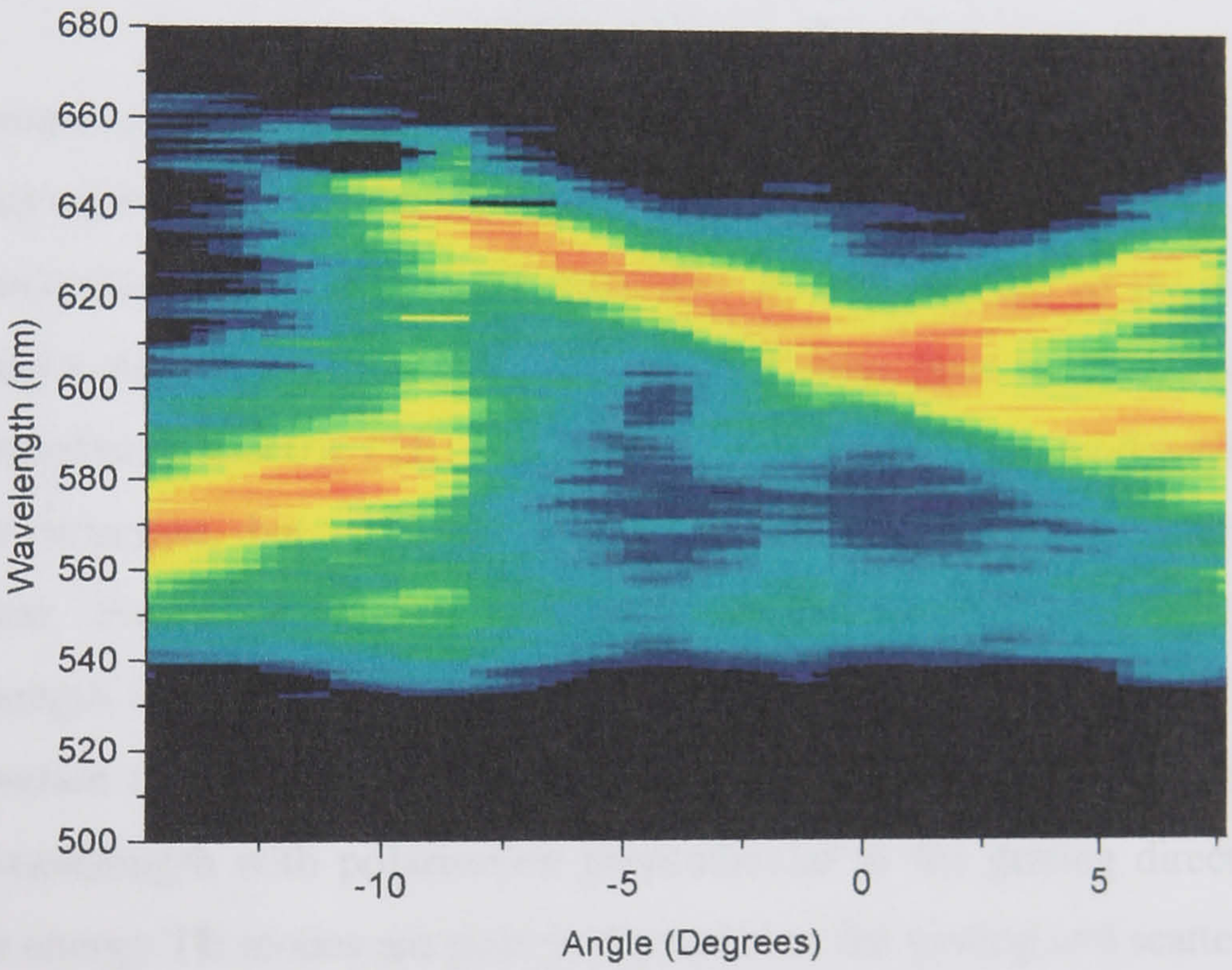

Fig. 8.8. *Intensity map of the scattered mode shown in Fig. 8.7. Plotted is the EL intensity (z-axis) as a function of the angle and wavelength. The X-shape of the scattered mode can be identified and is centred at 0°.*

8.3.4 Polarisation of the forward emission

It has previously been demonstrated that the emitting dipoles in spin-coated MEH-PPV lie preferentially in the plane of the substrate [23]. Their random distribution in this plane results in unpolarised emission in the forward direction. In contrast, waveguided light in the plane of the substrate is expected to be strongly polarised due to the presence of oriented dipoles. This effect is highlighted in Fig. 8.9 for LEDs fabricated

Organic semiconductors are ideally suited to explore the possibilities of electronic, structural and photonic nanoengineering in LEDs. Complex molecular semiconductors can be created by elegant synthesis rather than complicated epitaxial processes. In this thesis a novel group of molecular semiconductors for organic EL applications was presented. These dendritic materials were shown to give rise to strong exciton localisation at the core region, which has profound effects on the electronic interactions between adjacent molecules as well as the charge transport properties.

Dendrimers exhibit three key advantages over conventional materials for LEDs. Firstly, the emissive core can be chosen independently of the dendron architecture, allowing a tuning of the emission colour or even a choice of the nature of the excited state, i.e. whether singlet or triplet. Secondly, the dendron architecture, described by the dendrimer generation, shields the emissive core and allows a direct control of the level of protection with respect to the environment and neighbouring emissive species. As the dendrons are wider gap than the core in the systems studied, injection occurs into the core region and the separation of cores is hence directly related to the charge transport. Thirdly, the surface groups may be chosen independently of the core and dendron region of the dendrimer, allowing solution processing of these nanoscopic compounds.

The dendrimer generation provides a direct control of the charge carrier hopping mobility. The significance of this was demonstrated in this thesis in the context of bilayer devices. Additionally, it was realised very recently, that the power efficiency of an LED depends sensitively on the mobility [1]. Due to the quenching processes present at the cathode, LEDs exhibit a distinct maximum in power efficiency at a mobility of 10^{-11} m^2/Vs for a brightness of 100 Cd/m^2. Depending on the application envisaged for the LED, whether as a bright pixel or a dim backlight, the optimal power efficiency depends strongly on the mobility. There is hence an optimal mobility, to which the material can be tuned by varying the dendrimer generation.

A microscopic route to nanoengineer the emission properties of organic LEDs was explored by incorporating a wavelength scale periodic Bragg grating structure into the emitting layer of the LED. This was found to yield a control of the spontaneous emission from LEDs. With no measurable change in the device current-voltage characteristics, a doubling in light output was detected for corrugated LEDs. This could

be understood in terms of Bragg scattering of lossy waveguide modes within the organic film, which would otherwise be reabsorbed. Signatures of the scattering process were found in the angular dependence of the emission as well as the polarisation of the emission in the forward direction. It remains to be seen whether such a microstructure is viable in commercial devices. However, the preliminary experiments do not suggest any detrimental effect of the grating structure on the device operation. It is also of interest to investigate whether narrow-band emitters, such as organolanthanides, exhibit stronger scattering than the broad band emitter used in the present study. The preliminary results suggest that the scattered feature is relatively narrow and that an optimised device structure tuned to scatter out light of the emission peak of a narrow band emitter may exhibit much greater polarisation ratios and an improvement in efficiency significantly above the factor of 2.

LEDs offer an exciting ground for exploring the physics of molecular organic semiconductors. In this thesis a link has been drawn between the chemical structure of an electro-optically active material and the macroscopic device properties. A numerical device model as well as quantum chemical calculations complement the investigation and offer a good description of the experimental results. Future effort should concentrate on the systematic development of new materials with increased luminescence yield and optimised charge transport. The blending of dendrimers in order to harvest triplet excitations has shown the feasibility of combining different electronically active components in one layer. The dendrimer concept may be extended to very large macromolecular materials, which comprise a number of electronically active components in the core such as a singlet emitter and a triplet harvester.

An obvious application of the dendrimer concept is to use the materials as artificial light harvesting complexes in photovoltaic devices. However, this would require much narrower band gap dendrons, which ideally absorb in the red end of the spectrum. In combination with a suitable choice of energy level offsets, donor and acceptor functions could be assigned to the core and dendron regions, respectively, allowing charge carriers to be generated within one molecular unit and to subsequently be swept out of the device. The fact that different components in a blend structure can be assigned to trap differently charged species was demonstrated in this thesis in the context of platinum porphyrin doped dendrimer films.

Organic electronics covers a vast array of fields from basic science to applications. It is the feedback between the material structure, synthesis and properties which gives this research area its unique dynamics and will ensure the development of many more exciting systems and applications in the future.

References

[1] P. W. M. Blom, M. C. J. M. Vissenberg, J. N. Huiberts, H. C. F. Martens, and H. F. M. Schoo, Appl. Phys. Lett. 77, 2057 (2000)

Appendix

Publications arising from this work

J. M. Lupton and I. D. W. Samuel, "Temperature dependent single carrier device model for polymeric light emitting diodes", Journal of Physics D **32**, 2973-2984 (1999)

J. M. Lupton and I. D. W. Samuel "Temperature dependent device model for polymer light-emitting diodes: Significance of barrier height", Synthetic Metals **111-112**, 383-386 (2000)

J. M. Lupton and I. D. W. Samuel, "Device Model for Polymer Light Emitting Diodes: Effect of Temperature and Oxidation", SPIE Proceedings **3797**, 340-347 (1999)

J. M. Lupton, B. J. Matterson, I. D. W. Samuel, M. J. Jory, and W. L. Barnes, "Bragg-scattering from periodically microstructured light-emitting diodes", Applied Physics Letters **77**, 3340-3342 (2000)

A. N. Safonov, M. Jory, B. J. Matterson, J. M. Lupton, M. G. Salt, J. A. E. Wasey, W. L. Barnes, and I. D. W. Samuel, "Modification of polymer light emission by lateral microstructure", Synthetic Metals **116**, 145-148 (2001)

J. M. Lupton, R. Beavington, P. L. Burn, and I. D. W. Samuel, "Nanoengineering of organic semiconductors for light-emitting materials: Control of charge transport", Synthetic Metals **116**, 357-362 (2001)

B. J. Matterson, J. M. Lupton, A. F. Safanov, M. G. Salt, W. L. Barnes, and I. D. W. Samuel, "Increased efficiency and controlled light output from a microstructured light-emitting diode", Advanced Materials **13**, 123 (2001)

J. M. Lupton, I. D. W. Samuel, R. Beavington, P. L. Burn, and H. Bässler, "Control of charge transport and intermolecular interactions in dendrimer organic light-emitting diodes", Advanced Materials in Press (publication 16/02/01) and issue cover design

J. M. Lupton, R. Beavington, M. J. Frampton, P. L Burn, and I. D. W. Samuel, "Control of mobility in molecular organic semiconductors by dendrimer generation", Physical Review B in Press (publication 15/04/01)

O. Varnavski, G. Menkir, I. D. W. Samuel, J. M. Lupton, R. Beavington, P. L. Burn and T. Goodson III, "Ultrafast polarized fluorescence dynamics in an organic dendrimer", Applied Physics Letters in Press

P.L. Burn, R. Beavington, M.J. Frampton, J.N.G. Pillow, M. Halim, J.M. Lupton, and I.D.W. Samuel, "Structure/Property relationships in conjugated molecules", Materials Science and Engineering B in Press

J. M. Lupton, R. Beavington, P. L. Burn, I. D. W. Samuel and H. Bässler, "Charge transport in conjugated dendrimers for light-emitting diodes", Synthetic Metals in Press

M. J. Frampton, R. Beavington, J. M. Lupton, P. L. Burn and I. D. W. Samuel, "The optoelectronic properties of novel conjugated dendrimers", Synthetic Metals in Press

J. M. Lupton, M. Frampton, R. Beavington, P. L. Burn, and I. D. W. Samuel, "Control of electrophosphorescence in conjugated dendrimer light-emitting diodes", submitted to Advanced Functional Materials

J. M. Lupton, I. D. W. Samuel, R. Beavington, P. L. Burn and S. Mukamel, "Exciton confinement in organic dendrimer light-emitting diodes" (in preparation)

J. M. Lupton, I. D. W. Samuel, P. L. Burn and S. Mukamel, "Control of interchromophore coherence in electroluminescent conjugated dendrimers" (in preparation)

L. O. Palsson, J. P. J. Markham, R. Beavington, P. L. Burn, I. D. W. Samuel and J. M. Lupton, "The nature of the excited state in Amine-cored dystyryl-benzene-stilbene dendrimers probed by optical spectroscopy" (in preparation)

D. Ma, J. M. Lupton, I. D. W. Samuel and P. L. Burn, "Novel heterolayer organic light-emitting diodes based on a conjugated dendrimer" (in preparation)

I. D. W. Samuel, J. M. Lupton, B. J. Matterson, W. L. Barnes, and M. G. Salt, "Light emitting diode with improved efficiency", Patent WO 00/70691

P. L. Burn, R. Beavington, J. M. Lupton and I. D. W. Samuel, "Improved Dendrimers", UK patent application (2000)

Publications arising from related work

J. M. Lupton, I. D. W. Samuel, and A. P. Monkman, "Temperature dependence of current-voltage characteristics of poly(p-pyridine) light-emitting diodes", Synthetic Metals **102**, 1079 (1999)

J. N. G. Pillow, M. Halim, J. M. Lupton, P. L. Burn, and I. D. W. Samuel, "A Facile Iterative Procedure for the Preparation of Dendrimers Containing Luminescent Cores and Stilbene Dendrons", Macromolecules **32**, 5985 (1999)

J. M. Lupton, L. R. Hemingway, I. D. W. Samuel, and P. L Burn, "Electroluminescence from a novel distyrylbenzene based triazine dendrimer", Journal of Materials Chemistry **10**, 867 (2000)

A. K. Sheridan, J. M. Lupton, I. D. W. Samuel and D. D. C. Bradley, "Temperature dependence of the spectral line-narrowing and photoluminescence of MEH-PPV", Synthetic Metals **111-112**, 533-536 (2000)

A. K. Sheridan, J. M. Lupton, I. D. W. Samuel, and D. D. C Bradley, "Effect of temperature on the spectral line-narrowing in MEH-PPV", Chemical Physics Letters **322**, 51-56 (2000)

J. M. Lupton, V. R. Nikitenko, I. D. W. Samuel, and H. Bässler, "Time delayed electroluminescence overshoot in single layer polymer light-emitting diodes due to electrode luminescence quenching", Journal of Applied Physics **89**, 311 (2001)